SINGLE PARTICLE, HIGH TEMPERATURE, GAS-SOLID REACTIONS IN AN ELECTRODYNAMIC BALANCE

by

David Robert Dudek

B.S. Chemical Engineering, University of Akron (1983).
M.S. Chemical Engineering Practice, MIT (1985).

Submitted to the Department of Chemical Engineering
in Partial Fulfillment of the Requirements of the Degree of
Doctor of Philosiphy

at the

Massachusetts Institute of Technology

May 1988

Signature of Author _____
Department of Chemical Engineering
May 5, 1988

Certified by _____
Adel F. Sarofim
Professor of Chemical Engineering
Thesis Supervisor

Certified by _____
John P. Longwell
Professor of Chemical Engineering
Thesis Supervisor

Accepted by _____
Robert C. Armstrong
Chairman, Committee on Graduate Students

SINGLE PARTICLE, HIGH TEMPERATURE, GAS-SOLID REACTIONS IN AN ELECTRODYNAMIC BALANCE

by

DAVID ROBERT DUDEK

Submitted to the Department of Chemical Engineering
on May 5, 1988 in partial fulfillment of the
requirements for the Degree of Doctor of Philosophy
in Chemical Engineering

ABSTRACT

The electrodynamic balance (EDB) has been further developed and found to be a viable tool for studying single particle, high temperature, gas-solid reactions. This thesis dealt with developing new experimental techniques for single particle characterization, characterizing the natural convective drag force induced on heated, levitated particles, understanding charge loss from heated particles, and studying single particle char oxidation.

Single particle diameter measurements are performed to within ± 3 μm with an optical microscope. The aerodynamic drag force technique is used to measure single particle mass, density, porosity, and excess charge. Finally, carbon dioxide adsorption and the Dubinin-Polanyi equation have successfully been used to measure single particle surface areas. Therefore, experimental techniques now exist to measure diameter, mass, density, porosity, surface area, temperature, and reactivity of a single levitated particle versus extent of reaction in the EDB.

The computational method of Geoola and Cornish (*Int. J. Heat Mass Transfer* **24**, 1369-1379 (1981); **25**, 1677-1687 (1982)) for describing the heat transfer and fluid mechanics surrounding a heated solid sphere was modified to correctly calculate the drag force due to natural convection. The experimental steady-state and transient results of the natural convective drag force agree well with the Boussinesq numerical solutions, indicating that the Boussinesq approximation is valid over the experimental parameter range examined. The numerical calculations were used to develop empirical correlations to approximate the steady-state natural convective drag force and the dimensionless time required to reach 90% of the steady-state drag coefficient. The steady-state and transient empirical correlations may be used to cancel out the natural convective drag force from the reacting particle force balance, thereby, allowing continuous mass versus time measurements to be calculated from balancing voltage versus time measurements.

"Catastrophic" charge loss due to particle heating has experimentally been found to represent the most serious limitation in studying single particle gas-solid reactions in the EDTGA. Experimentally, charge loss was found to be primarily a function of particle work function and particle temperature. The electric field strength at the particle surface and surface contamination were seen to be of secondary

importance and could be thought of as acting to lower the particle work function. A literature survey also indicated the importance of surface irregularities in lowering the particle work function. Of all the possible mechanisms of charge loss from heated particles, thermionic emission of ions was determined to be the most viable, and a modified Richardson-Dushman equation has been proposed to predict the temperature range that can effectively be studied in the EDB for a given material.

Uncatalyzed and catalyzed "Spherocarb" oxidations were performed in the EDB to test its overall potential and uniqueness in studying single particle gas-solid reactions. Diameter, density, charge, and surface area were measured versus percent conversion. "Spherocarb" particles were observed to undergo shrinkage while reacting under kinetically controlled conditions. "Spherocarb" specific surface area also decreased with conversion. The extent of "Spherocarb" shrinkage and surface area decrease is a strong function of conversion, a slight function of catalyst type, but not a function of temperature or reacting gas.

Nineteen separate "Spherocarb" particles were reacted in the EDB in air at temperatures ranging from 740 to 1170 K. Corresponding reaction times required for 50% conversion covered almost four orders of magnitude, ranging from 2.2 to 17,000 sec. The reaction rates obtained from the EDB agree favorably with those obtained from a conventional TGA, with both apparatuses yielding an activation energy of 36 kcal/mol for the "Spherocarb"-air reaction.

Density measurements on individual "Spherocarb" particles revealed a large variability in "Spherocarb" apparent density from particle to particle. A systematic study of "Spherocarb" density versus reactivity showed no correlation.

A study of particle-to-particle variability in reactivities revealed a standard deviation in reaction rates of 21% for uncatalyzed "Spherocarb", 88% for Fe catalyzed "Spherocarb", and 32% for K catalyzed "Spherocarb".

Thesis Supervisors: Professor Adel F. Sarofim
Professor John P. Longwell

ACKNOWLEDGEMENTS

I would like to first thank Exxon Research and Engineering Corporation for sponsoring this reseach project and my graduate studies. Next, I would like to thank my research advisors, Professor A.F. Sarofim and Professor J.P. Longwell, for their advice, encouragement, enthusiasm, and never ending lists of interesting ideas. Their support has been greatly appreciated. I would also like to thank the rest of my thesis committee, J.M. Beer, J.B. Howard, and especially R.E. Spjut whose knowledge of the electrodynamic balance was invaluable. Special thanks also goes to Tom Fletcher of Sandia National Lab for help on the natural convection problem, Tony Modestino for help on just about any engineering problem, Bob Hurt for conversations on shrinkage, Matteo D'Amore, for his enthusiasm and uncanny ability to get things done, Jacob Yeheskel for his knowledge on charge loss, and Ezra Bar-Ziv for his ideas on the electrodynamic balance. The technical contributions of Maria Tsiakkas, Bashar Zeitoon, and Dave Wright are also greatly appreciated.

Special thanks also goes to friends, fellow students, office mates, and all who consider themselves Worthless and Weak for making MIT a very enjoyable as well as a very educational experience. In this regard, I would like to thank the participants in the scholarly MIT chemical engineering traditions of intramural sports, Friday afternoons at the Muddy, and poker at Tang.

I would very much like to thank my parents, parents-in-law, and family for their encouragement, love, and support throughout this work. Finally, I would like to thank my wife, Mary Kay, whose companionship, sense of humor, and patience have contributed so greatly to this thesis and to my life.

TABLE OF CONTENTS

LIST OF FIGURES

LIST OF TABLES

LIST OF SYMBOLS

$A = 4\pi emk^2/h^3 = 120$ amps/cm^{2}K^2 = the Richardson constant.

A = cross-sectional area of hole in bottom electrode (m^2).

A = cross-sectional area of hole in ring electrode (m^2).

A_d = sensitive area of photodetector (cm^2).

A_r = cross-sectional area of hole in ring electrode (m^2).

B = constant.

c = speed of light = 2.9979×10^{10} cm/sec.

c_1 = Planck's first constant = $2\pi hc^2 = 3.740 \times 10^{-5}$ erg cm^2/sec.

c_2 = Planck's second constant = ch/k = 1.4388 cm K.

C = dimensionless chamber constant = 0.4.

C_{DP} = dimensionless pressure drag force coefficient.

C_{DF} = dimensionless viscous drag force coefficient.

C_{DT} = dimensionless total drag force coefficient.

C_p = heat capacity of surrounding gas at constant pressure per unit mass (m^2/sec^2 K).

d = particle diameter (m).

d_s = diameter of a sphere of equivalent volume to a nonspherical particle (m).

d_n = diameter equal to the diameter of a circle having an area equal to that of the projected area of a particle (m).

e = elementary charge = 1.6×10^{-19} coul.

E = electric field strength in vertical direction (volts/m).

E = electric field strength at the surface of the material (volts/m).

E_d = energy gap between the valence band and the conduction band (eV).

E_f = the Fermi energy level or the highest filled energy level of a metal at T = 0 K (eV).

E_{th} = energy required to bring an electron from the highest occupied level to the vacuum level (eV).

E_{DC} = electric field experienced by a levitated particle due to the DC voltage (volts).

E_{AC} = electric field experienced by a levitated particle due to the AC voltage (volts).

E_s = electric field experienced by a levitated particle due to excess charge on the particle (volts).

E_{total} = total electric field experienced by a levitated particle (volts).

fdρ = fraction of particles with densities between ρ and ρ+dρ (dimensionless).

F_{dp} = viewfactor between detector and particle.

$F_{a,s}$ = drag force encountered by a sphere (N).

$F_{a,ns}$ = drag force encountered by a nonspherical particle (N).

$F_{gravity}$ = net gravity on particle (N).

F_{nat} = natural convective drag force (N).

F_a = aerodynamic drag force on suspended particle (N).

g = gravitational acceleration = 9.81 m/sec^2.

G = modified dimensionless vorticity.

G = gain of photodetector.

Gr = Grashof number = $g\beta(T_s-T_\infty)R^3/v^2$ (dimensionless).

h = Planck's constant = 6.6256 x 10^{-27} erg sec.

I = total emitted current per unit area (amp/cm^2).

I = ionization energy of the atom evaporated (eV).

$I_{\lambda a}$ = monochromatic emissive power at wavelength λ_a (erg/cm^3 sec).

k = surrounding gas thermal conductivity (kg m/sec^3 K).

k = Boltzmann's constant = 1.3805 x 10^{-16} erg/K.

K = shape correction factor (dimensionless).

K = complex part of index of refraction (dimensionless).

K = proportionality constant between gas velocity and volumetric flow rate (m^{-2}).

$\bar{K}$ = proportionality constant = 18μK/g = 0.848 kg sec m^{-4}.

K_0 = dimensionless pressure at the front stagnation point.

K_θ = dimensionless pressure at the sphere surface.

L = distance of the particle surface from the chamber center (m).

m = mesh size in the z-direction.

m = mass of particle (kg).

m = mass of an electron = 9.107 X 10^{-31} kg.

m_i = initial mass with no CO_2 adsorption (kg).

M = number of mesh points in the z-direction.

n = mesh size in the θ-direction.

n = mols of CO_2 adsorbed (mols).

N = number of mesh points in the θ-direction.

Nu = overall Nusselt number (dimensionless).

Nu_θ = local Nusselt number (dimensionless).

P = CO_2 equilibrium pressure (atm).

P_0 = saturation vapor pressure of CO_2 (atm).

Pr = Prandtl number = $C_p\mu/k$ (dimensionless).

q = total excess charge on particle (coul).

Q = volumetric flow rate of gas through the chamber (m^3/sec).

r = dimensionless radial direction.

r = the fraction of electrons reflected back at the surface (dimensionless).

$\tilde{r}$ = dimensional radial distance (m).

r = resistivity (ohms cm).

R = particle radius (m).

Re = Reynold's number = $\langle v \rangle \rho d/\mu$ (dimensionless).

t = dimensionless time.

$\tilde{t}$ = dimensional time (sec).

T = dimensionless temperature.

$\tilde{T}$ = dimensional temperature (K).

T_s = particle surface temperature (K).

T_∞ = ambient gas temperature (K).

ΔT = particle surface temperature - ambient gas temperature (K).

u = dimensionless velocity.

$\tilde{u}$ = dimensional velocity (m/sec).

v = velocity of surrounding gas (m/sec).

v_s = velocity around sphere (m/sec).

v = settling velocity of any shaped particle (m/sec).

$\langle v \rangle$ = average velocity of gas through the chamber (m/sec).

$\bar{v}$ = mean specific volume of the distribution (m^3/kg).

V = balancing DC voltage across endcap electrodes (volts).

V_a = signal voltage from photodetector a (volts).

V_i = balancing voltage of unheated particle in absence of aerodynamic drag and CO_2 adsorption (volts).

ΔV_{nat} = change in balancing voltage between unheated and heated particle

(volts).

ΔV_{aero} = change in balancing voltage between particle experiencing aerodynamic drag and particle not experiencing aerodynamic drag (volts).

W = general continuous function representing T, G, and ψ.

W = the vacuum level or energy of an electron at rest outside at a large distance from the metal (eV).

X = microscopic or point electric field around irregularity (volts/m).

X_m = macroscopically imposed electric field (volts/m).

z = modified dimensionless radial direction.

z_0 = characteristic chamber dimension = 0.004 m.

Z_∞ = dimensionless outer boundary location.

α = the thermal expansion coefficient (eV/K).

β = coefficient of volume expansion (1/K).

β = affinity coefficient of CO_2 relative to N_2 (dimensionless).

β = correction factor (dimensionless).

γ = statistical weight ratio (dimensionless).

ϵ = convergence criteria.

ϵ_a = emissivity at wavelength λ_a (dimensionless).

ϵ_0 = permittivity constant = 8.85×10^{-12} farad/m.

ϵ_r = relative permittivity of particle (dimensionless).

λ_a = wavelength (cm).

$\Delta\lambda$ = optical bandwidth of photodetector.

θ = angular coordinate.

μ = surrounding gas viscosity (kg/m sec).

ν = surrounding gas kinematic viscosity (m^2/sec).

ν_i = number of ions evaporated per second.

ν_a = number of atoms evaporated per second.

ζ = dimensionless vorticity component in the ϕ-direction.

ρ = surrounding gas density (kg/m^3).

ρ_p = apparent particle density (kg/m^3).

ρ_s = density of sphere (kg/m^3).

ρ_f = density of fluid (kg/m^3).

$\rho_{n,s}$ = density of a nonspherical particle (kg/m^3).

ϕ = coordinate representing the angle of rotation about the axis of symmetry of the flow.

Φ = the work function or the energy required to bring an electron from the Fermi level to the vacuum level (eV).

Φ = lowering of the work function due to surface contamination (eV).

Φ_0 = the work function at some reference temperature (eV).

Ψ = dimensionless stream function.

Ψ = sphericity = ratio of the surface area of a sphere to the surface area of a nonspherical particle of equivalent volume (dimensionless).

ω = relaxation factor.

ξ = lowering of the work function due to electric field (eV).

Ω = oscillating frequency of AC field (Hz).

Subscripts:

G = vorticity.

i = mesh point index in the z-direction.

i = initial or CO_2-free.

j = mesh point index in the θ-direction.

m = mass fraction.

n = number fraction.

r = radial direction.

s = surface.

T = temperatue.

w = general function.

z = modified radial direction.

∞ = ambient.

θ = tangential direction.

Ψ = stream function.

Superscripts:

L = L^{th} iteration.

L-1 = $(L-1)^{th}$ iteration.

THESIS DIGEST

D1. INTRODUCTION.

Probably the most celebrated single particle levitation device was the flat-plate capacitor used by Milliken [1] to suspend oil droplets and determine the charge of an electron. Today's version of Milliken's flat-plate capacitor is the electrodynamic balance (EDB), which is a device capable of stably suspending a single, micron-sized, charged particle in a dynamic electric field which is produced by three electrodes in a hyperboloidal configuration. Electrodynamic balances such as these have been used by many workers [2-6] to study ambient temperature phenomenon, such as light scattering, condensation, or evaporation. More recently, Spjut et al. [7-9] extended the diversity of the EDB by successfully heating a single suspended particle with a CO_2 laser. Spjut et al. [7-9] were also able to measure single particle temperatures using two color infrared pyrometry. Postion control systems have been built [7,10] that automatically adjust the balancing DC voltage across the endcap electrodes to keep the particle in the center of the chamber. Since the balancing voltage across the endcap electrodes is proportional to the particle mass to charge ratio, the EDB was now potentially capable of following reacting particle mass versus time much in the same way as a conventional thermogravimetric analyzer (TGA). In this sense, a true electrodynamic thermogravimetric analyzer (EDTGA) had been born.

The motivation behind the development of the EDTGA was the study of single particle gas-solid reactions, since a single particle device offered many potential advantages over traditional gas-solid reaction apparatuses such as conventional TGA's, laminar flow furnaces, entrained flow reactors, fluidized beds, packed beds, and moving beds. Some of these advantages of studying single particle reactions in the EDTGA are: 1) minimal heat and mass transfer limitations, 2) rapid heating/quenching capabilities (10^6 K/sec) due to heating by CO_2 laser, 3) ability to systematically study effects of specific vari-

ables (such as particle density, particle size, coal composition, etc.) on particle reactivity, and 4) easy measurement of diameter shrinkage or growth.

The EDTGA also possesses two experimental difficulties brought about by particle heating, charge loss and the creation of a natural convective drag force. The particle must retain some of its charge in order to be levitated, therefore, charge loss potentially represents a very serious limitation of the EDTGA. The natural convective drag force, which is caused by a natural convective flow field set up around a heated particle, makes the DC balancing voltage no longer proportional to particle mass, therefore, without prior knowledge of the natural convective drag force, continuous mass versus time measurements via voltage versus time measurements would not be valid.

The overall objective of this thesis was to determine the usefulness of the EDB in studying single particle gas-solid reactions. This objective was satisfied in the following four parts:

1) Develop experimental measurement techniques for characterizing single particles suspended in the EDTGA. More specificly, develop techniques for measuring single particle diameter, mass, density, porosity, surface area, and reactivity versus particle conversion.
2) Determine the feasibility of continuous mass versus time measurements in the EDTGA in light of the induced natural convective drag force on heated particles. Ideally, identify the major variables important in determining the natural convective drag force and develop predictive capabilities.
3) Attempt to understand the charge loss phenomenon from heated particles. Ideally, develop predictive capabilities that can be utilized in defining the limitations of the EDTGA.
4) Study uncatalyzed and catalyzed "Spherocarb" oxidations in an attempt to more fully understand the role of the EDTGA in gas-solid reaction studies. Examine particle-to-particle variations in reactivity and changes in diameter, density, and surface area versus conversion for both uncatalyzed and catalyzed "Spherocarb" particles.

D2. EXPERIMENTAL APPARATUS.

The electrodynamic balance (EDB) consists of three electrodes in a hyperboloidal configuration, the theory of which is completely described by Wuerker et al. [11], Frickel et al. [12], Davis and Ray [4], Ray [6], and Spjut [7]. An exploded view of the electrodynamic balance is shown in Figure D2.1. The EDB chamber stably contains a single, charged particle in a dynamic electric field, with the electric field strength in the vertical direction being directly proportional to the mass-to-charge ratio of the particle. The position control system automatically adjusts the electric field to keep the particle in the chamber center. This is very important when the particle mass is changing due to reaction. A 20 W CO_2 laser supplies heat to the levitated particle and two color infrared (2 μm and 4 μm) pyrometry is used for temperature measurement. A CO_2 laser control system is required to minimize laser power fluctuations, and finally, a gas flow system allows for particles to be reacted in various gaseous environments.

D3. EXPERIMENTAL MEASUREMENT TECHNIQUES.

In this section, three different experimental measurement techniques which involve characterizing the suspended particle, both initially and at various extents of reaction will be discussed.

D3.1 Single particle diameter measurements.

Diameters of single particles suspended in the EDTGA are measured via one of two microscopes attached to the system. A (x70) Ealing microscope has associated with it a graticule that allows for diameter measurements to ± 5 μm. A 35 mm camera may be attached to a (x100) Wild microscope and photographs can be taken for diameter measurements good to within ± 3 μm.

D3.2 Use of aerodynamic drag in measurement of single particle mass, charge, and density.

D3.2.1 Introduction.

The most straightforward method of studying single particle gas-

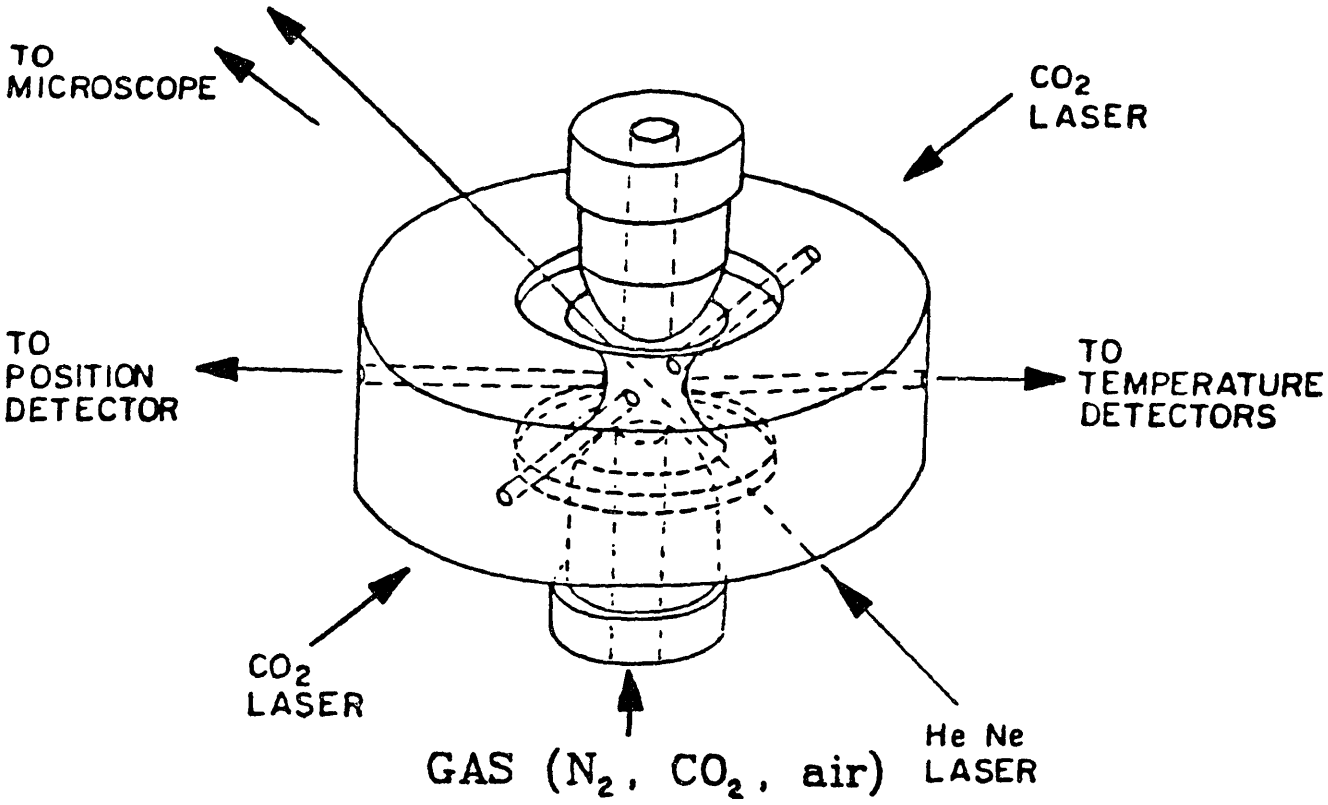

Figure D2.1 : Exploded view of electrodynamic balance.

solid reactions is to follow the particle weight versus time. A force balance on an unheated particle levitated in an EDB yields:

$$mg = qCV/z_0 \qquad (D3.1)$$

or

$$V = (gz_0/C)(m/q) \qquad (D3.2)$$

where m is the particle mass, g is the gravitational acceleration , q is the excess charge on the particle, C is the chamber constant, V is the balancing DC voltage across the endcap electrodes, and z_0 is the characteristic length of the EDB chamber. The term (gz_0/C) is a constant. If the number of charges on the particle remains constant, and the initial mass is known, a voltage versus time curve will be sufficient to determine the reaction rate. Under these conditions the electrodynamic balance can be used as a TGA (i.e. collecting continuous weight versus time data). If some charge is lost, but the particle is still able to be levitated, the particle will require periodic reweighing in order to follow particle mass versus time. In either case, in order to follow single particle gas-solid reactions in the EDTGA, a simple method of weighing levitated particles is necessary.

D3.2.2 Theory.

In this work an aerodynamic drag method of particle mass measurement is utilized. If the particle is spherical and the diameter can be determined, the particle mass can be calculated by measuring the drag force as a function of volumetric flow rate of gas around the suspended particle. The volumetric flow rates of gas were selected to yield velocities well under the terminal velocity.

A vertical force balance on an unheated, levitated particle with an upward gas flow yields:

$$mg = qCV/z_0 + F_a \qquad (D3.3)$$

where F_a is the aerodynamic drag force on the particle.

Since Re << 1, the aerodynamic drag on the particle is described by Stokes' law:

$$F_a = 3\pi\mu vd \qquad \text{(D3.4)}$$

where μ is the gas viscosity, v is the gas velocity, and d the particle diameter. If the velocity of gas is assumed to be proportional to the volumetric flow rate of gas through the chamber, Q, and the mass of a spherical particle is written as:

$$m = (\pi/6)d3\rho_p \qquad \text{(D3.5)}$$

where ρ_p is the apparent particle density, equation D3.3 can be solved under both flow and nonflow conditions. If these two equations are then combined and rearranged, the following equation results:

$$\Delta V_{aero} = \bar{K}V_i Q/(\rho_p d^2) \qquad \text{(D3.6)}$$

where $\Delta V_{aero} = V_i - V$, V_i = the DC voltage across the endcap electrodes required to balance the levitated particle in the absense of aerodynamic drag, V = the DC voltage across the endcap electrodes required to balance the levitated particle in the presense of aerodynamic drag, and $\bar{K} = 18\mu v/gQ$. $\bar{K}$ is a proportionality constant that can be determined by means of a calibration procedure using particles of known density. From equation D3.6, the apparent particle density, and hence its mass and charge, can be determined from measurement of V_i and ΔV_{aero} versus Q for a particle of known diameter.

D3.2.3 Calibration Runs.

Because the flow field of gas through the chamber is not known, calibration runs must be performed to back out the velocity of gas over the suspended particle as a function of volumetric flow rate. Eight calibration runs were performed on glass spheres with a known density of 2.5 g/cm^3 and diameters ranging from 50 μm to 130 μm. Typical results are shown in Figure D3.1 for spheres of 72, 74, 109, and 124 μm. The linearity of the data shown in Figure D3.1 indicates the validity of the aerodynamic drag technique in the range of gas flow rates tested. The slopes of the voltage versus flow rate data, togeth-

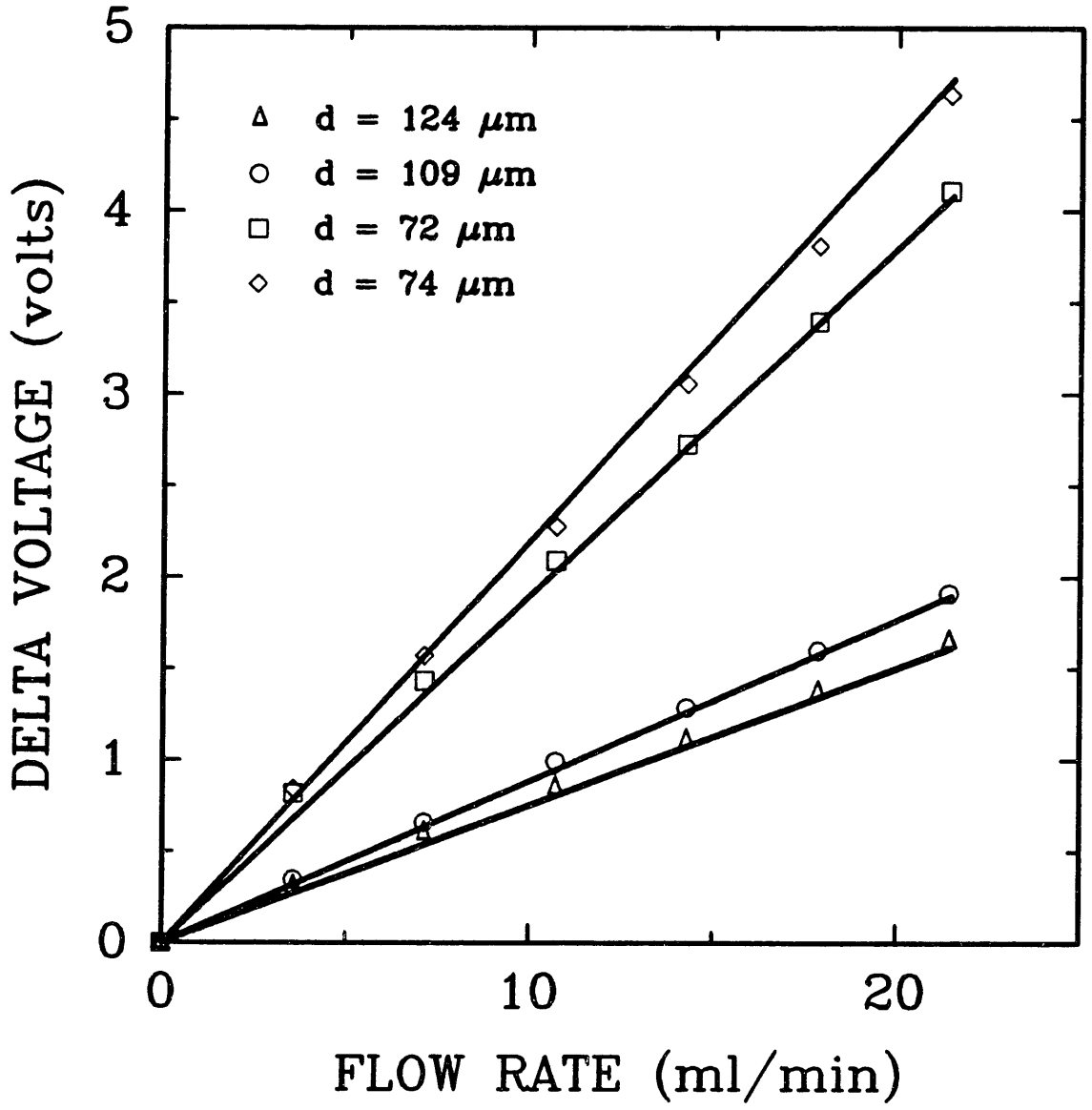

Figure D3.1 : Change in balancing voltage versus volumetric flow rate for four calibration runs performed on glass spheres with a density of 2.5 g/cm^3.

er with measurements of V_i and particle diameter, can be substituted in equation D3.6 to determine the constant $\bar{K}$, which was found to have a value of 0.848 kg sec m^{-4}. The standard deviation for the eight calibration runs was 0.0153.

D3.2.4 Example of aerodynamic drag force technique.

An example of the aerodynamic weighing technique is presented in Figure D3.2. Two separate weighings were performed on a 245 μm diameter "Spherocarb" particle and the results are presented in the form of DC balancing voltage versus volumetric flow rate. The small systematic difference in balancing voltage at each flow rate between the two weighings was due to a movement of the microscope between the weighings. Also, the upward curvature of the data at flow rates close to zero is probably due to diffusion of water into the chamber and absorption in the "Spherocarb" which results in a real weight gain.

D3.3 Single particle surface area measurements.

D3.3.1 Introduction.

Since the overall rate of reaction of the levitated particle is a function of its surface area available to gaseous reactants, it is desirable to measure this surface area. In this work, single particle surface areas of synthetic chars are evaluated from the adsorption isotherm of CO_2 at 298 K using the Dubinin-Polanyi equation.

D3.3.2 Dubinin-Polanyi theory.

The use of the Dubinin-Polanyi equation is discussed by Lamand and Marsh [13] and is written as follows:

$$\log(n/mg) = \log(n/mg)_0 - (BT^2/\beta)\log^2(P_0/P) \qquad (D3.7)$$

where (n/mg) is the number of mols of CO_2 adsorbed at the CO_2 equilibrium pressure P, $(n/mg)_0$ is the micropore capacity of the sample, P_0 is the saturation vapor pressure of CO_2 at temperature T (K), β is the affinity coefficient of CO_2 relative to N_2, and B is a constant. A plot of log(n/mg) versus $\log^2(P_0/P)$ should yield

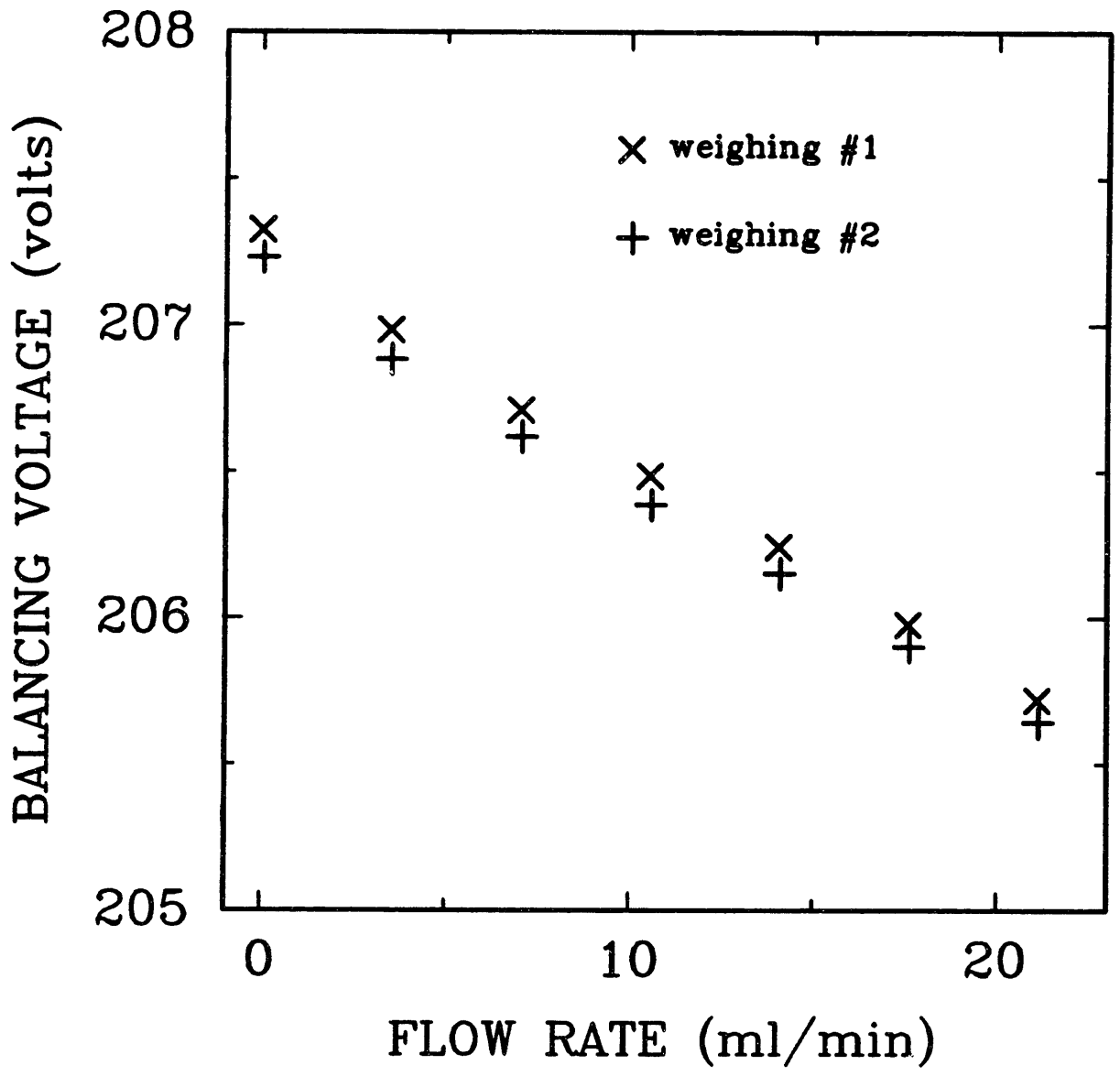

Figure D3.2 : Balancing voltage versus volumetric flow rate for two separate weighings of a 245 μm diameter "Spherocarb" particle.

a straight line with the intercept at $\log^2(P_0/P) = 0$ equal to $\log(n/m_g)_0$. If the adsorption of CO_2 is restricted to a monolayer then $(n/m_g)_0$ multiplied by the cross-sectional area of a CO_2 molecule and Avagadro's number yields the microporous surface area. The cross-sectional area of the CO_2 molecule is a function of temperature and was taken from Walker and Kini [14].

D3.3.3. Experimental procedure.

If equation D3.1 is solved twice for the same particle, once with CO_2 adsorption and once without, and the equations are subtracted from each other, the following expression results:

$$(m-m_i)/m_i = (V - V_i)/V_i \qquad \text{(D3.8)}$$

where m_i and V_i are the initial mass and voltage when no CO_2 has been adsorbed and m and V are the mass and voltage when CO_2 has been adsorbed. In other words, the change in particle mass due to CO_2 adsorption divided by initial mass is equal to the change in DC voltage required for balancing divided by the initial voltage. The (n/mg) ratio can be measured directly from the balancing voltages (equation D3.8) and dividing by the molecular weight of CO_2.

Five different gas mixtures were utilized in these adsorption studies, pure N_2, a 20% CO_2/80% N_2 mixture, a 35% CO_2/65% N_2 mixture, a 50% CO_2/50% N_2 mixture, and pure CO_2. Some raw data for a "Spherocarb" particle is plotted in Figure D3.3 in the form of balancing voltage versus the mass flow meter reading. The mass flow meter reading was used instead of volumetric flow rate because the mass flow meter is only calibrated for nitrogen. A mass flow meter reading of 600 corresponds to a nitrogen flow rate of 42 ml/min. Three balancing voltage measurements (at mass flow meter readings of 400, 500, and 600) were taken for each gas mixture. These measurements are shown as the open boxes in Figure D3.3. Since the chamber is not leak proof, in order to ensure that the levitated particle is experiencing the environment of the gas cylinders, a finite gas flow rate must be maintained. Gas flow rates corresponding to mass flow meter readings of 400, 500, and 600 have been shown to be experimentally adequate.

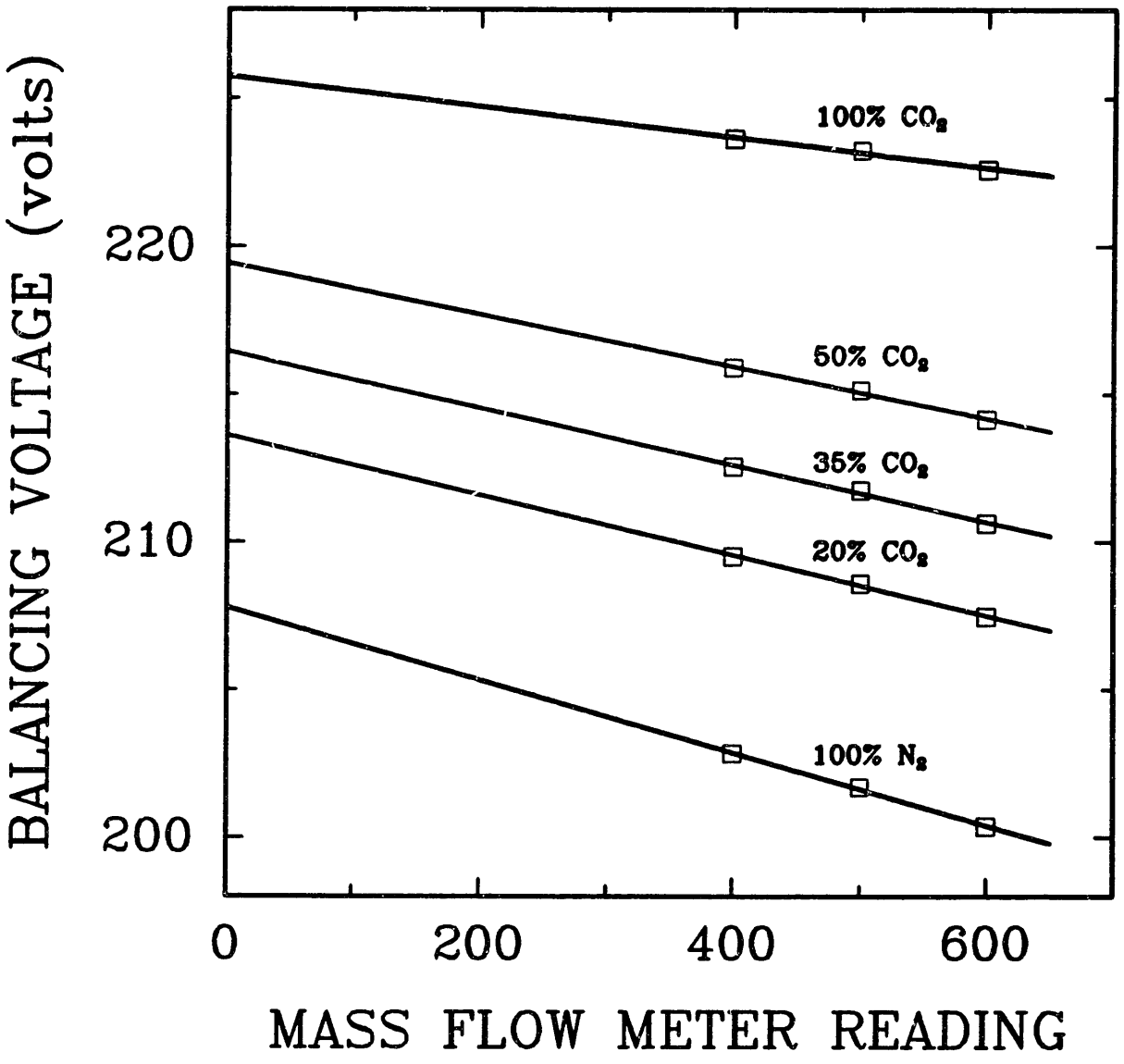

Figure D3.3 : Balancing voltage of a single "Spherocarb" particle versus mass flow meter reading for five different gas mixtures.

Unfortunately, the introduction of a gas flowing upward past the suspended particle produces an aerodynamic drag force which affects the DC voltage required for stable balancing of the particle. The solid lines in Figure D3.3 represent a least squares linear regression that was performed on each group of three experimental points. By extrapolating the experimental data to a zero mass flow meter reading, the "true" balancing voltage without the aerodynamic drag force included can be obtained. These "true" balancing voltages can then be used directly to form a Dubinin-Polanyi plot and thus a surface area calculation. One surface area measurement performed in this fashion takes approximately 1.5 hours.

D3.3.4. Examples of surface area measurements.

Figure D3.4 is a Dubinin-Polanyi plot for a 181 μm diameter "Spherocarb" particle. The data points are represented as open squares, and the line is a least squares linear regression through these points. The slope of this line is -0.1524, the intercept is -2.229, and the correlation coefficient is 0.9994. An intercept of -2.229 corresponds to a surface area of 860 m^2/g.

D4. NATURAL CONVECTIVE DRAG.

D4.1 Introduction.

Upon laser heating of the levitated particle, the fluid near the particle surface is heated due to conduction. Since the ambient fluid is cool, the fluid near the particle surface rises, and a natural convective flow field is set up which introduces a natural convective drag force, F_{nat}, on the particle. The vertical force balance of equation D3.1 now becomes:

$$mg = qCV/z_0 + F_{nat} \qquad \text{(D4.1)}$$

This upward drag force on the particle complicates interpretation of the particle weight change data. Arnold and Lewittes [15] were the first to report such a force, and later, Spjut [7] reported drag force

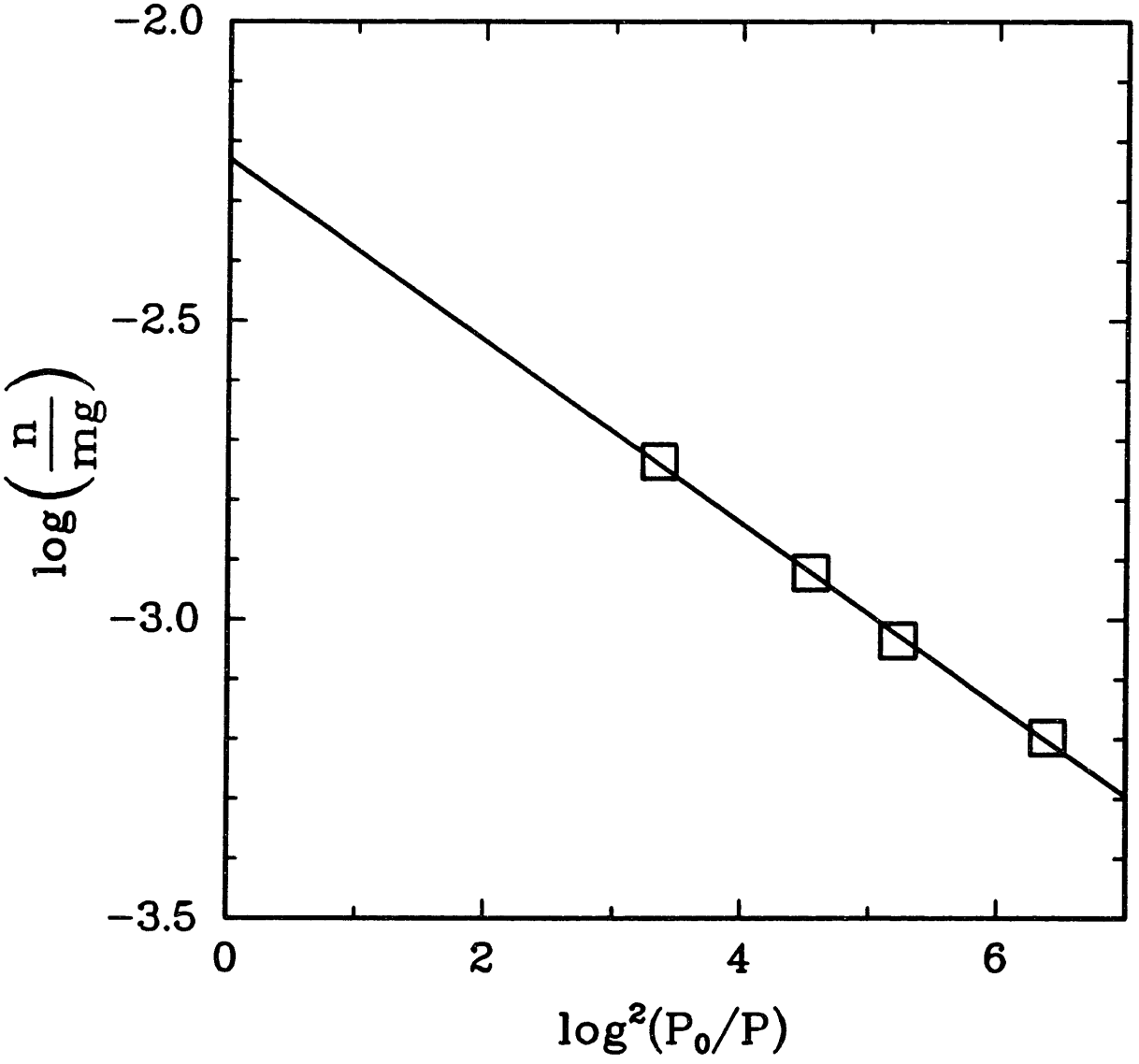

Figure D3.4 : Dubinin–Polanyi plot for a 181 μm diameter "Spherocarb" particle.

magnitudes as great as the particle weight. In order to determine the true particle reaction rate, changes in particle mass must be distinguished from changes in drag force. Therefore, characterization of the natural convective drag force is necessary if the electrodynamic balance is to be used for continuous mass versus time measurements.

An example of how the natural convective drag affects the balancing voltage of a heated "Spherocarb" particle is depicted in Figure D4.1. At time zero, the 183 μm diameter "Spherocarb" particle is balanced in the chamber and is at ambient temperature. Laser heating begins at 0.28 sec and ends at 1.94 sec and was performed in an inert N_2 environment to prevent any chemical reaction. After the particle is heated to 610 K, the natural convective drag force develops and the voltage required for balancing decreases. The initial, unheated balancing voltage is 125 volts, therefore, a 6.5 volt decrease represents a 5% decrease in balancing voltage that is caused solely by the natural convective drag force.

D4.2 Previous work.

Due to the small size of the particles being examined in the EDB, the corresponding Grashof number will also be small, with the range of interest being between 0.0005 and 1.0. The Reynold's number based on the maximum convective velocity is much less than one.

Experimental studies of natural convection around a heated sphere at small Grashof number have been conducted [16-21], however, the authors were interested in heat transfer, and only measured the overall Nusselt number. No experimental measurements of the drag force induced on a sphere by a natural convective flow field are found in the literature.

The classic references to analytical treatments of natural convection around spheres at small Grashof numbers are Mahony [22], Fendell [23], Hossain and Gebhart [24], and Hieber and Gebhart [25]. Each attempted to solve the problem by a perturbation method, but a suitable outer solution could not be obtained so as to match with the inner expansion. This problem can, however, be solved by a series truncation method [26] or using finite difference methods to obtain solutions [27-30]. The Boussinesq approximation is used in all of the

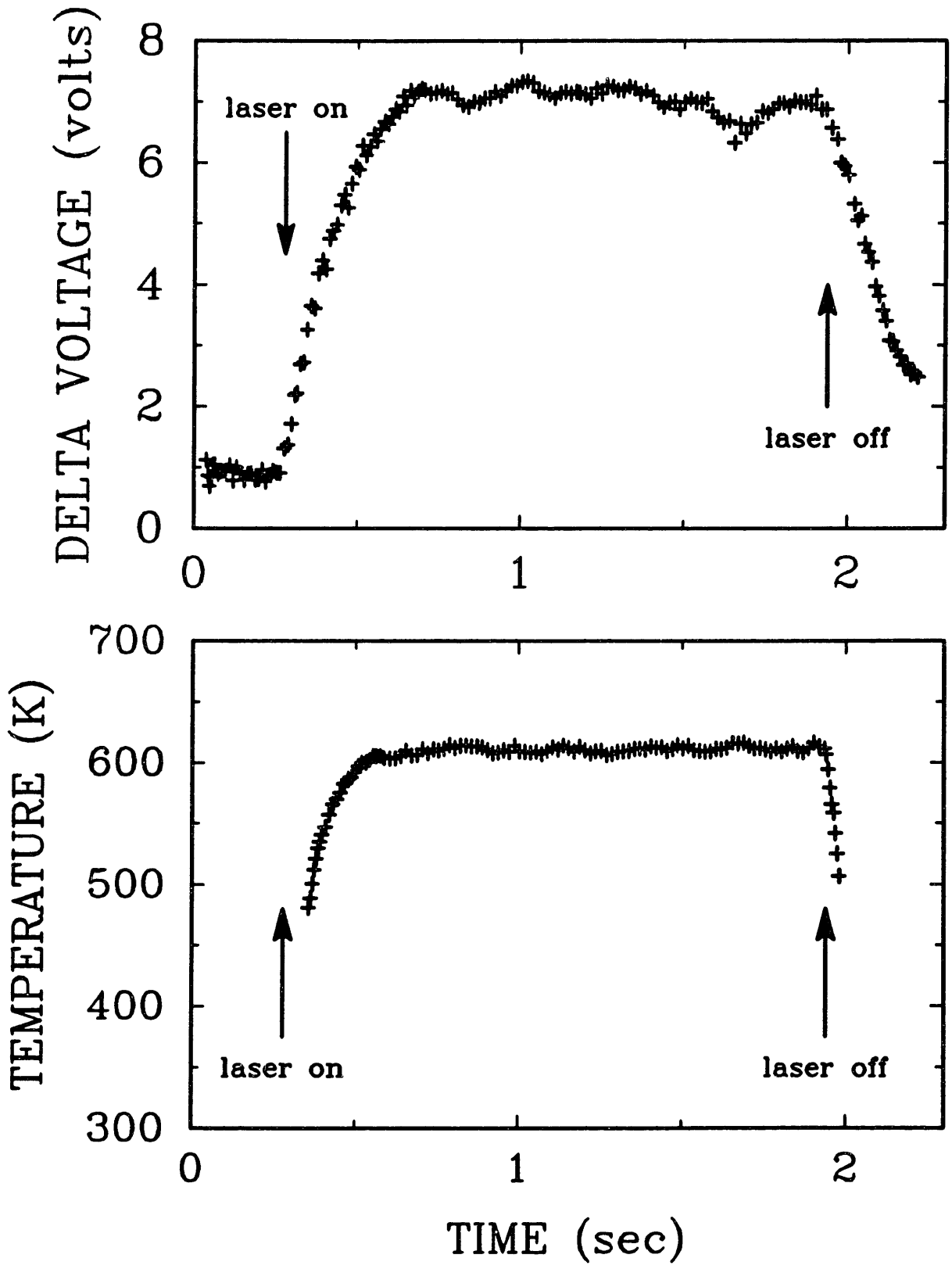

Figure D4.1 : Change in balancing voltage and temperature for a 183 μm diameter "Spherocarb" heated to 610 K in nitrogen.

above-referenced studies. Only Geoola and Cornish [29-30] calculate a natural convective drag force; all previous studies concentrate on the heat transfer aspects of the problem.

D4.3 Dimensional analysis.

Dimensional analysis reveals that:

$$F_{nat} = \frac{\mu^2}{\rho} C_{DT} \qquad (D4.2)$$

where: μ is the surrounding gas viscosity, ρ is the surrounding gas density, and C_{DT} is the dimensionless drag force coefficient.

The dimensionless drag force coefficient is some unknown function of the Grashof number, Gr, and the Prandtl number, Pr, which are defined as follows:

$$Gr = g\beta(T_s - T_\infty)R^3/v^2 \qquad (D4.3)$$

$$Pr = C_p\mu/k \qquad (D4.4)$$

where: β is the coefficient of volume expansion, T_s is the particle surface temperature, T_∞ is the ambient gas temperature, R is the particle radius, v is the gas kinematic viscosity, C_p is the gas heat capacity at constant pressure per unit mass, and k is the gas thermal conductivity.

Note that we have used the convention of Geoola and Cornish to define Gr, where R is used as the characteristic length instead of particle diameter. All gas properties are evaluated at the gas film temperature, T_f, defined as $(T_s + T_\infty)/2$, and the value of β used in the definition of Gr is $1/T_\infty$ [31]. The numerical results will be presented primarily as a function of the dimensionless drag force coefficient and the Grashof number.

D4.4 Theoretical model and numerical methods.

A numerical technique modeled after that of Geoola and Cornish [29,30] is used to solve the conservation equations of mass, momentum, and energy in two dimensions for the gas phase near the particle.

Methods were developed to obtain both a steady-state and a transient solution. The assumptions used in this model are that: 1) the particle is spherical; 2) the particle has a uniform, constant surface temperature; 3) the particle is not rotating; 4) flow is axisymmetric (all the dependent variables are independent of ϕ); 5) the only body force is gravity; 6) the Boussinesq approximation applies; and 7) other fluid properties (such as viscosity, specific heat, and thermal conductivity) are constant.

In the steady-state case, the energy, vorticity, and stream function equations were solved simultaneously using an extrapolated Gauss-Seidel method [32]. In the transient computations, the energy and vorticity transport equations were solved using Peaceman and Rachford's ADI method [33]. The stream function equation was solved at each time step using an extrapolated Gauss-Seidel method.

D4.6 Discussion of numerical results.

A linear regression on the numerical solution of the steady-state drag force coefficient versus Prandtl number reveals that C_{DT} varies with $Pr^{-0.25}$.

Figure D4.2 is a plot of the steady-state dimensionless pressure, viscous, and total drag coefficients versus Grashof number. The ratio of the dimensionless viscous drag over the dimensionless pressure drag remains constant at a value of 2.0 over the range of Grashof number examined. This implies that there is no change in the basic flow patterns, such as the separation of the boundary layer.

A log-log plot of the dimensionless time required to reach 90% of the steady-state total drag force coefficient versus Grashof number is plotted in Figure D4.3.

D4.7 Experimental program.

The experimental program examined the effect of three parameters, particle temperature, particle size, and surrounding gas on the natural convective drag force. Particle temperature was varied in the range of 600 to 1200 K. Five different diameter spheres were examined, 127, 153, 168, 192, and 236 μm. In each case, the material used was the synthetic char "Spherocarb". Also, two different surrounding gases

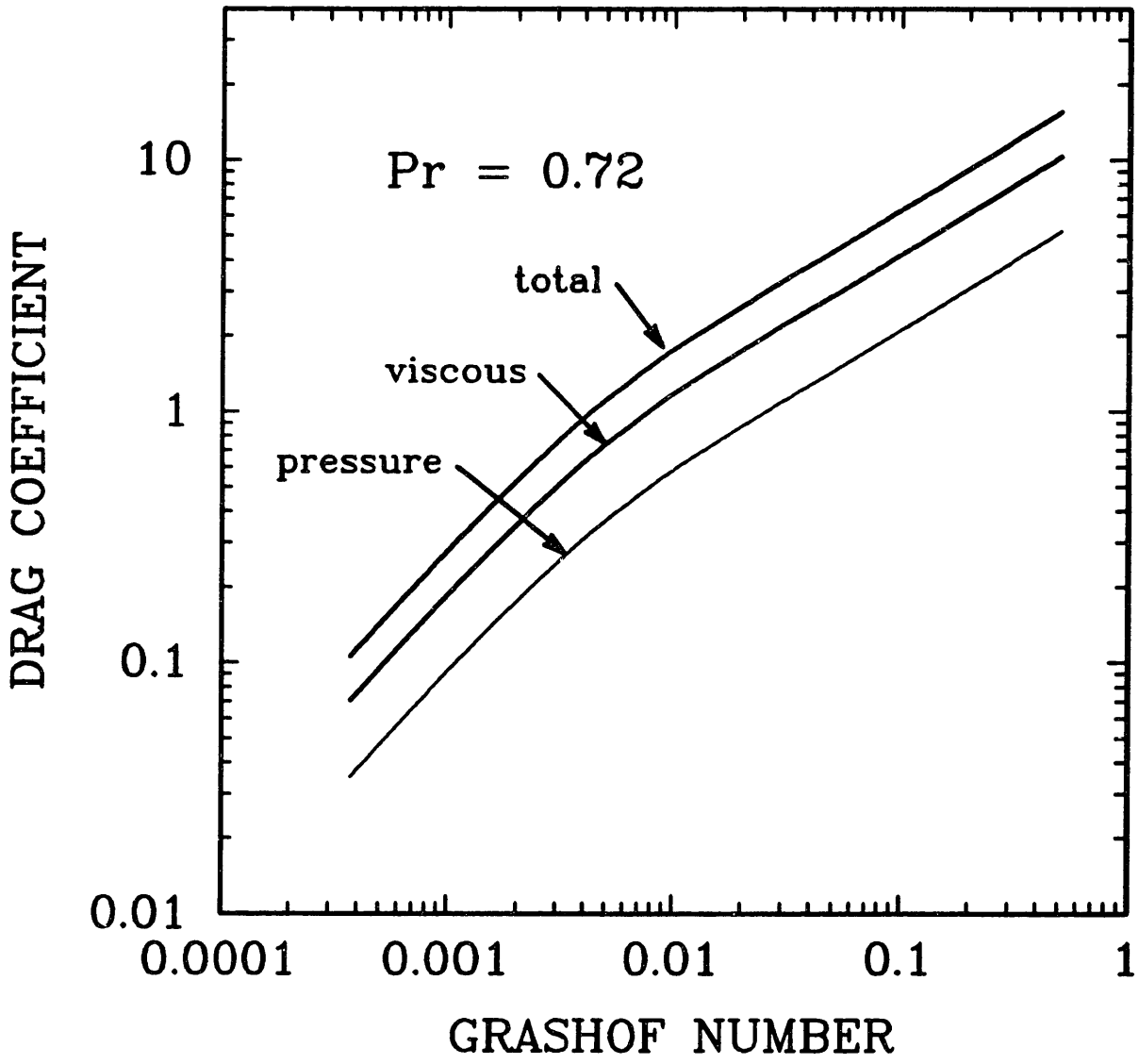

Figure D4.2 : Steady-state dimensionless pressure, viscous, and total drag force coefficients versus Grashof number for Pr = 0.72.

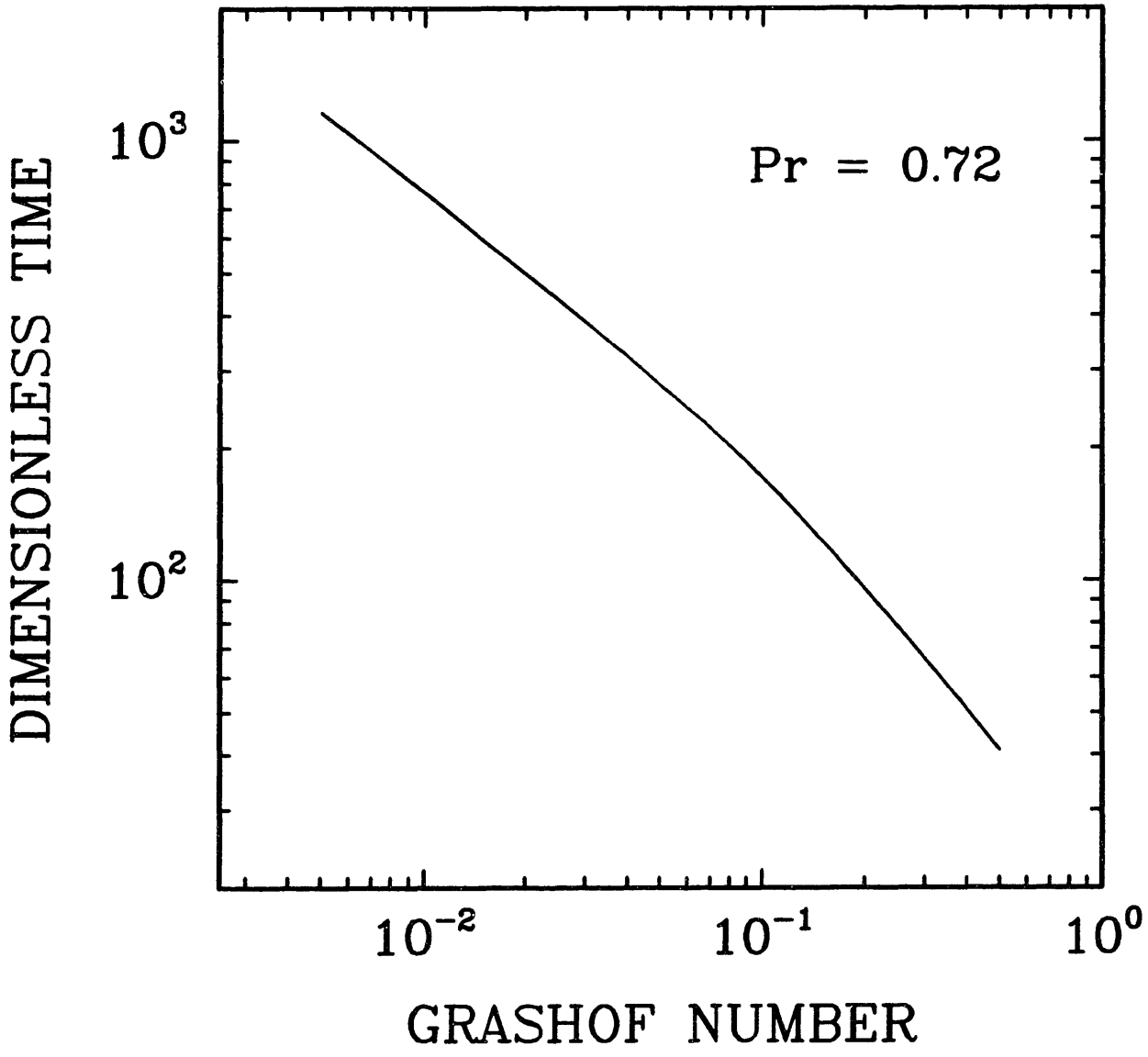

Figure D4.3 : Dimensionless time versus Grashof number for Pr = 0.72.

were used, N_2 and CO_2.

A force balance on the heated particle yields:

$$\Delta V_{nat}/V_i = F_{nat}/mg \qquad (D4.5)$$

where: ΔV_{nat} is the change in balancing voltage between an unheated and a heated particle and V_i is the balancing voltage of an unheated particle.

D4.8 Comparison of experimental and numerical results.

Figure D4.4 is a plot of F_{nat}/mg versus particle temperature for a 192 μm diameter "Spherocarb" particle. The open triangles represent experiments performed in nitrogen, the open circles represent experiments performed in carbon dioxide, and the solid lines represent the numerical solutions.

Figure D4.5 is a plot of steady-state dimensionless drag force coefficient versus Grashof number. Again, the triangles represent experiments performed in nitrogen, the circles represent experiments performed in carbon dioxide, and the solid line represents the numerical solution. The numerical solutions agree well with the experimental results, even though the Boussinesq criterion has been violated due to the large temperature differences in the problem [34].

Figure D4.6 is a plot of the change in balancing voltage versus real time for a 183 μm diameter "Spherocarb" particle heated to 610 K in nitrogen. The initial, unheated voltage was 125 volts. The small points represent experimental results and the smooth solid line represents the transient numerical solution. The experimental points were smoothed with a moving average filter. Again we see good agreement between experiment and theory. According to the heat transfer model developed by Spjut [7], the particle should reach 90% of its equilibrium temperature in 70-80 msec.

D4.9 Numerical predictions.

Figure D4.7 is a plot of the numerical solution of the steady-state natural convective drag force for a heated sphere in ambient nitrogen divided by the particle weight versus particle radius for a

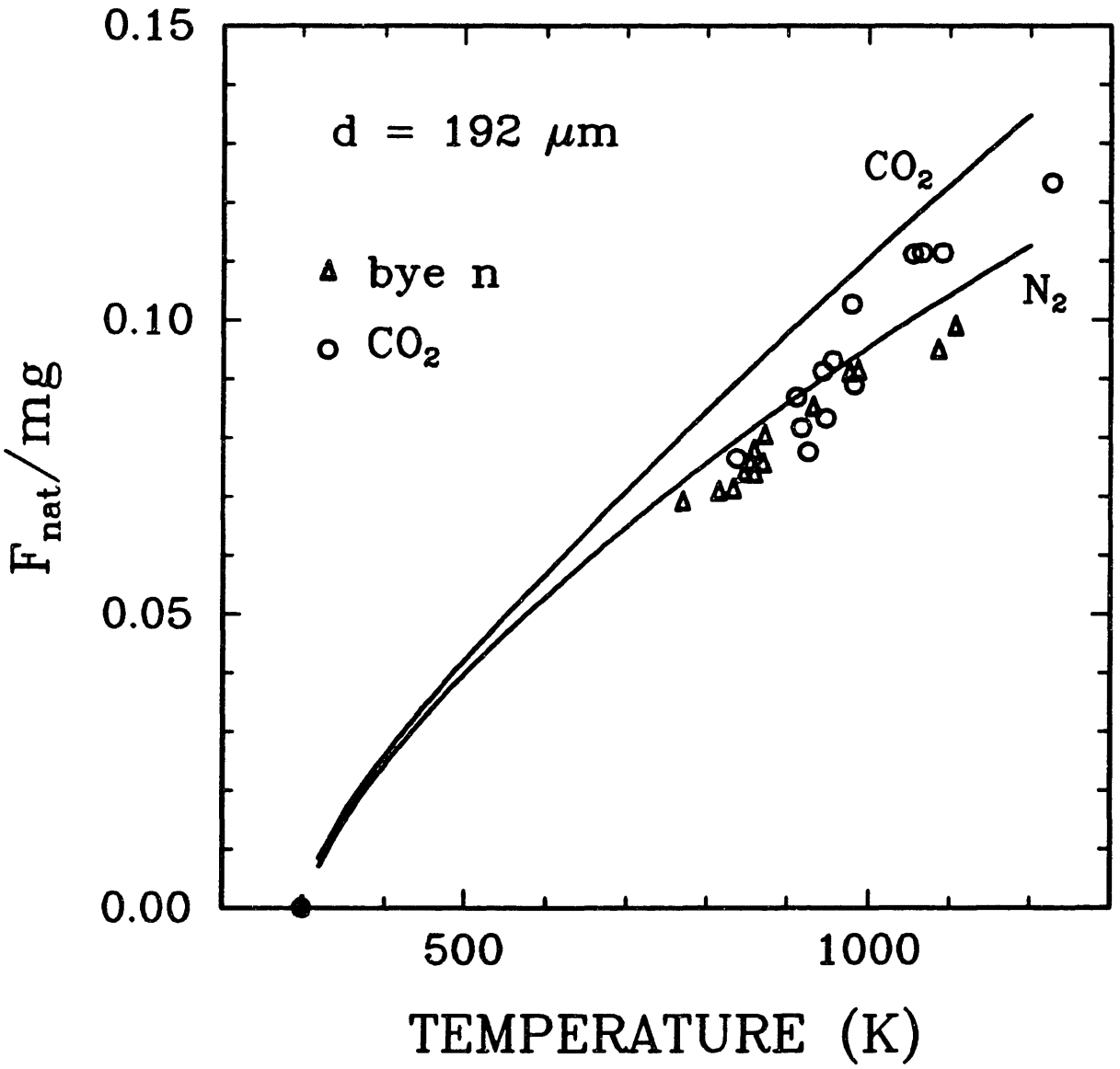

Figure D4.4 : Experimental measurements and numerical calculations of the ratio of natural convective drag force to particle weight versus temperature for a 192 μm diameter "Spherocarb" particle in nitrogen and carbon dioxide.

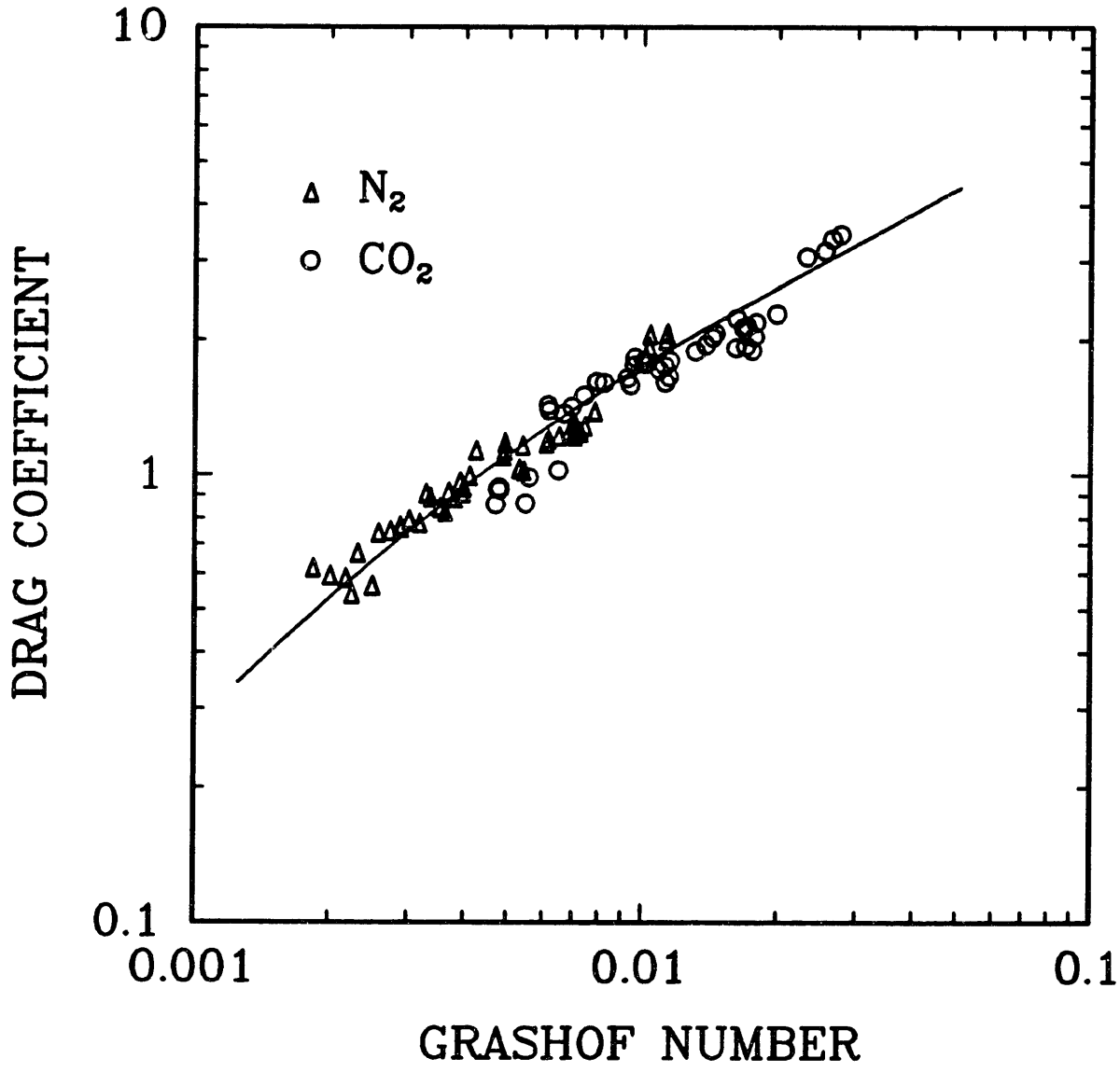

Figure D4.5 : Experimental measurements and numerical calculations of the steady-state dimensionless drag coefficient versus Grashof number for five different diameter "Spherocarb" particles heated in nitrogen and carbon dioxide.

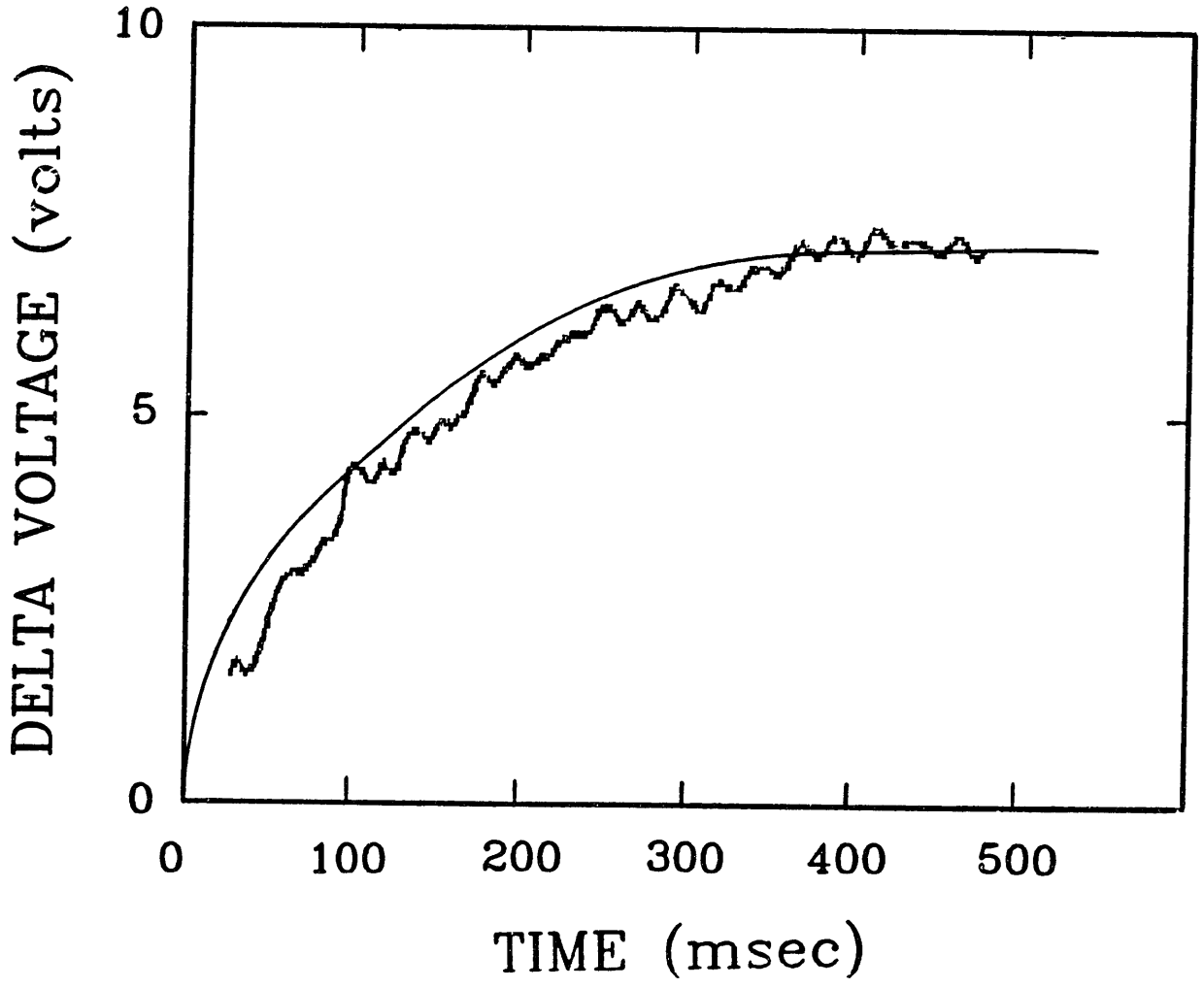

Figure D4.6 : Experimental measurements and numerical calculations of the change in balancing voltage versus time for a 183 μm diameter "Spherocarb" particle heated to 610 K in nitrogen.

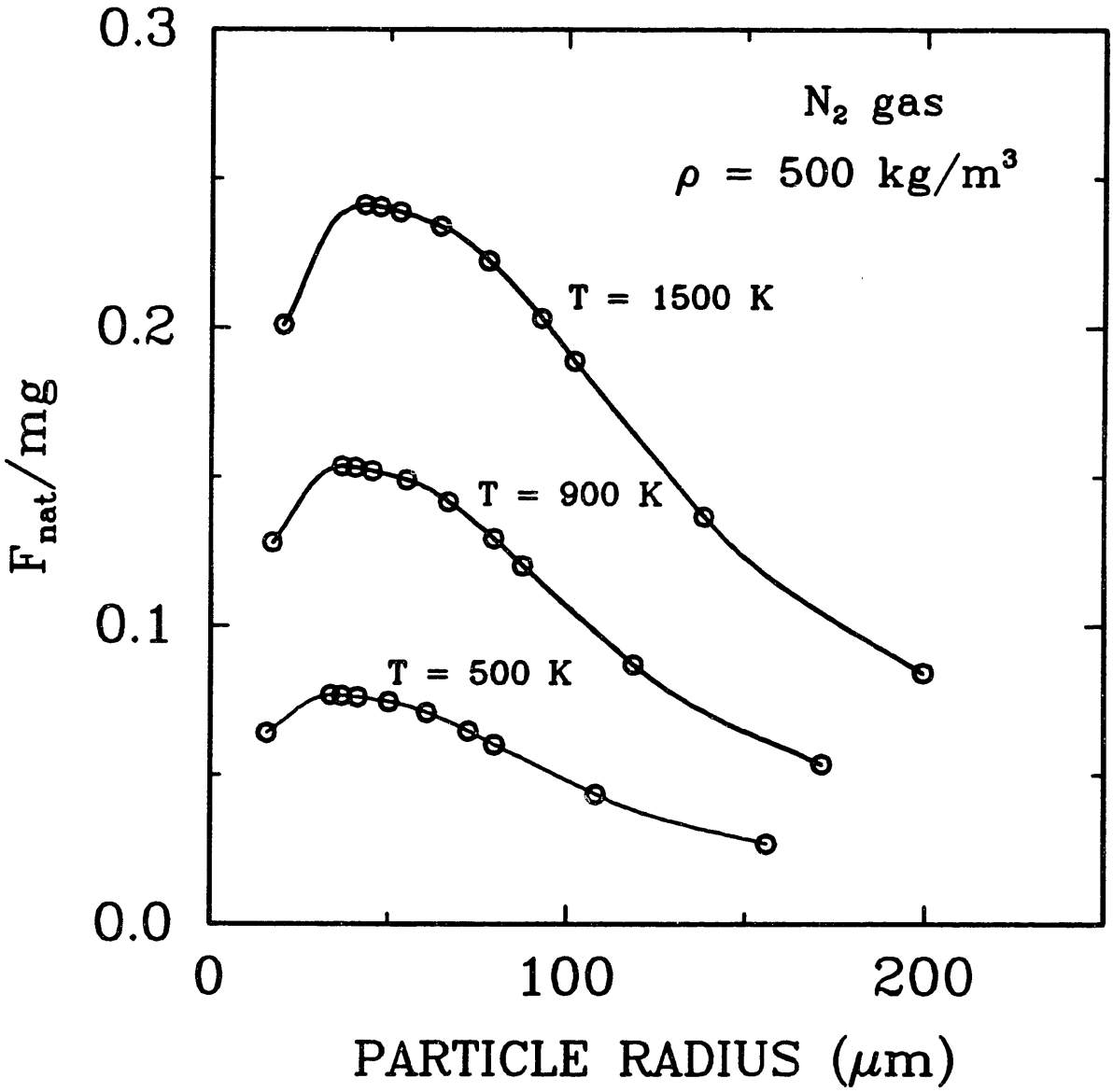

Figure D4.7 : Numerically predicted ratio of the steady-state natural convective drag force to particle weight versus particle radius for a particle density of 500 kg/m^3 and three different particle temperatures, 500 K, 900 K, and 1500 K.

particle density of 500 kg/m^3 and three different particle surface temperatures, 1500 K, 900 K, and 500 K. The circles represent predictions of the drag force/weight using the numerical solution and the solid lines are "best fit" lines through these points. The numerical solution predicts a peak in drag force divided by weight for a particle radius of approximately 40 μm. This solution predicts that the natural convective drag force around aerosol particles less than 10 μm in diameter with a density greater than 500 kg/m^3 will be less than 5% of the particle weight, if particle temperatures are kept under 1500 K. Furthermore, since the drag force divided by weight is inversely proportional to particle density, heavy particles with densities greater than 2500 kg/m^3 will also not experience drag forces greater than 5% of their weights if particle temperatures are kept under 1500 K.

Figure D4.8 is a prediction based on the transient numerical results of the real time required to reach 90% of the steady-state drag coefficient in nitrogen versus particle temperature for three different particle radii of 40, 80, and 120 μm. The time required to set up the natural convective flow field decreases with increasing particle temperature and decreases with decreasing particle radius.

A discrete least squares method [35] was used to obtain the following second-order polynomial which describes the steady-state dimensionless total drag force coefficient as a function of Grashof number:

$$\log(C_{DT}) = 1.25 + 0.31[\log(Gr)] - 0.097[\log(Gr)]^2 \qquad (D4.7)$$

This correlation is good to within 5% over the range $0.0004 < Gr < 0.5$ for Pr = 0.72.

The same discrete least squares method was used to obtain the following second-order polynomial that approximates the dimensionless time required to reach 90% of the steady-state drag force coefficient:

$$\log(t_{90\%}) = 1.32 - \log(Gr) - 0.11[\log(Gr)]^2 \qquad (D4.8)$$

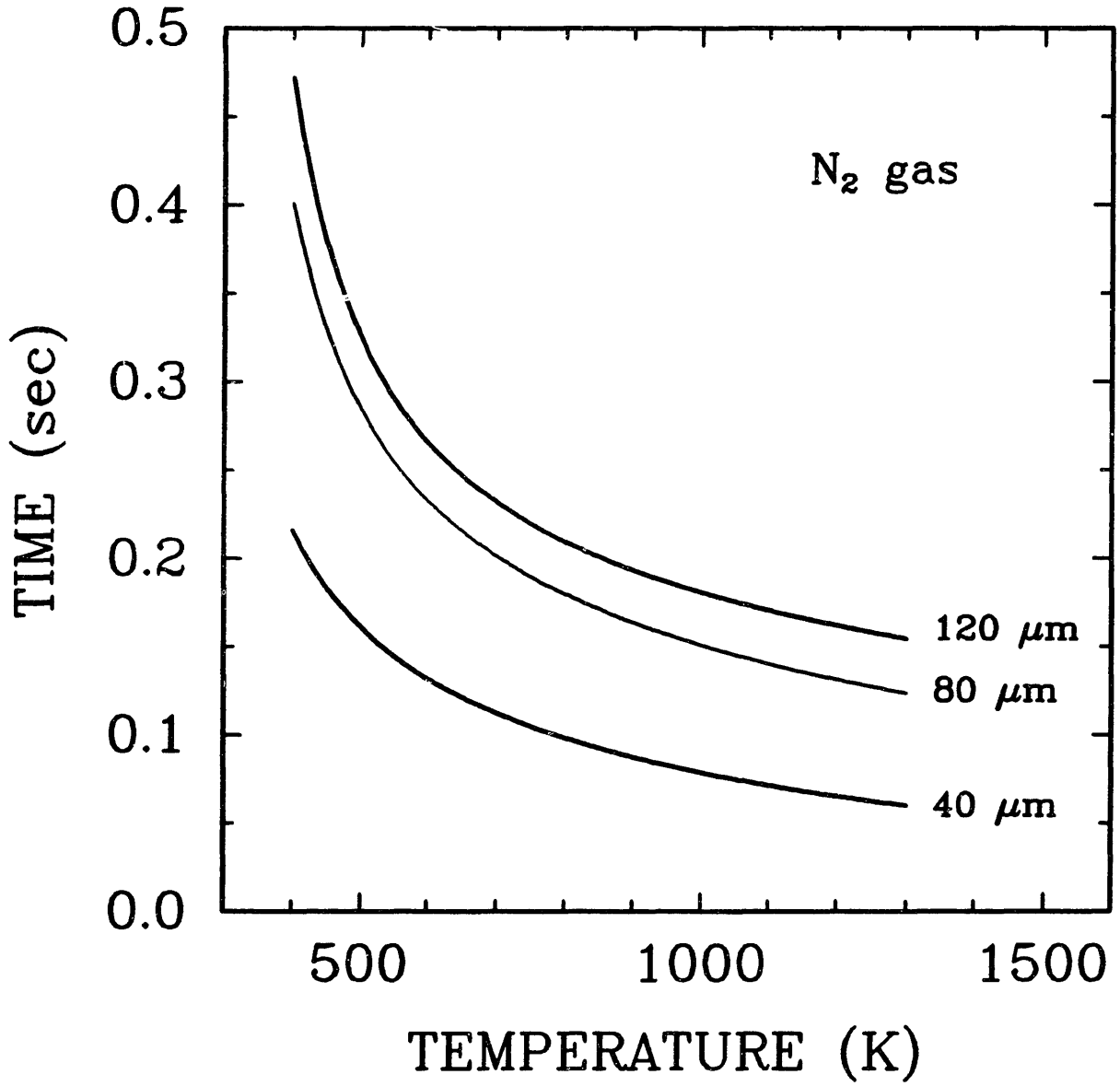

Figure D4.8 : Numerical predictions of real time required to reach 90% of the steady-state drag force coefficient versus particle temperature for particle radii of 40, 80, and 120 μm.

These polynomial approximations may be used to predict the magnitude and response time of the natural convective drag force on a particle levitated in the EDTGA, allowing particle mass to be continuously measured by continuously measuring the DC voltage required for stable balancing.

D5. CHARGE LOSS FROM HEATED PARTICLES LEVITATED IN THE EDB.

D5.1 Motivation.

The vertical force balance shown in equation D3.1 reveals the extreme importance of the charge on a particle. If charge equal zero, then particle levitation in the EDTGA becomes impossible. The term "catastrophic" charge loss will be used to describe an event where enough charge is lost from a particle to prevent it from being stably balanced.

Experimentally, it has been found that initial charging of particles (most probably by tribo or frictional electrification) is not a problem. Particles with both positive and negative excess charge have been successfully captured in the EDB. A typical number of excess charges on a captured particle in our EDB is in the range of 10^6 to 10^8.

Although initial charging of particles is not difficult, keeping the particle charged during heating has been shown experimentally to be a problem. All particles suspended in our EDB, regardless of material, polarity of charge, size, or shape, have been shown to experience charge loss at some temperature. To date, C, SiO_2, BaO, CaO, KI, KCl, NaCl, $Ca(OH)_2$, $CaSO_4$, Al coated SiO_2, Fe coated SiO_2, Ag coated Cu, and Au coated Ni particles have all been shown to experience charge loss. The size range examined was between 20 and 250 μm.

D5.2 Experimental results.

Two sets of experimental measurements were performed. The first set of experiments examines the effect of particle temperture and particle work function on charge loss from heated particles levitated

in the EDTGA. The work function can be defined as the minimum energy required to extract the weakest electrons from their maximum natural surface excursion distance to infinity [36]. The second set of experiments looks at the effect of temperature, surface contamination, and electric field strength on charge loss from a heated metal thermocouple.

D5.2.1 Charge loss from heated particles.

Since excess charge on a levitated particle is inversely proportional to the DC voltage required for stable balancing, charge loss can be measured by an increase in the DC voltage required for balancing. Figure D5.1 is a plot of the change in balancing voltage due to a 2.8 msec CO_2 laser pulse versus the incident power of the CO_2 laser for seven different "Spherocarb" particles. Four of the experiments were performed on negatively charged "Spherocarb" particles and three of the experiments were performed on positively charged "Spherocarb" particles, with no noticable difference in charge loss detected between negatively and positively charged particles. Below 0.5 W, no charge loss was ever detected. Above 2 W, catastrophic charge loss always occurred, with subsequent loss of the particle from the chamber.

Figure D5.2 is a plot of absorbed laser power required for charge loss versus particle work function for seven different materials, BaO, CaO, C, SiO_2, KI, KCl, and NaCl. It appears that the larger the work function of the particle, the more laser power is required before charge loss occurs. Caution must be exercised when trying to draw conclusions from this plot, however, due to uncertainties in material absorptivities of 10.6 μm radiation and laser intensities.

D5.2.2 Charge loss from heated metal wires.

The experimental system utilized in this section was designed to measure charge transfer in the form of current from an isolated thermocouple inside the EDB to the surrounding electrode walls. A DC voltage was supplied to the surrounding electrodes to create an electric field similar to the electric field experienced by a charged par-

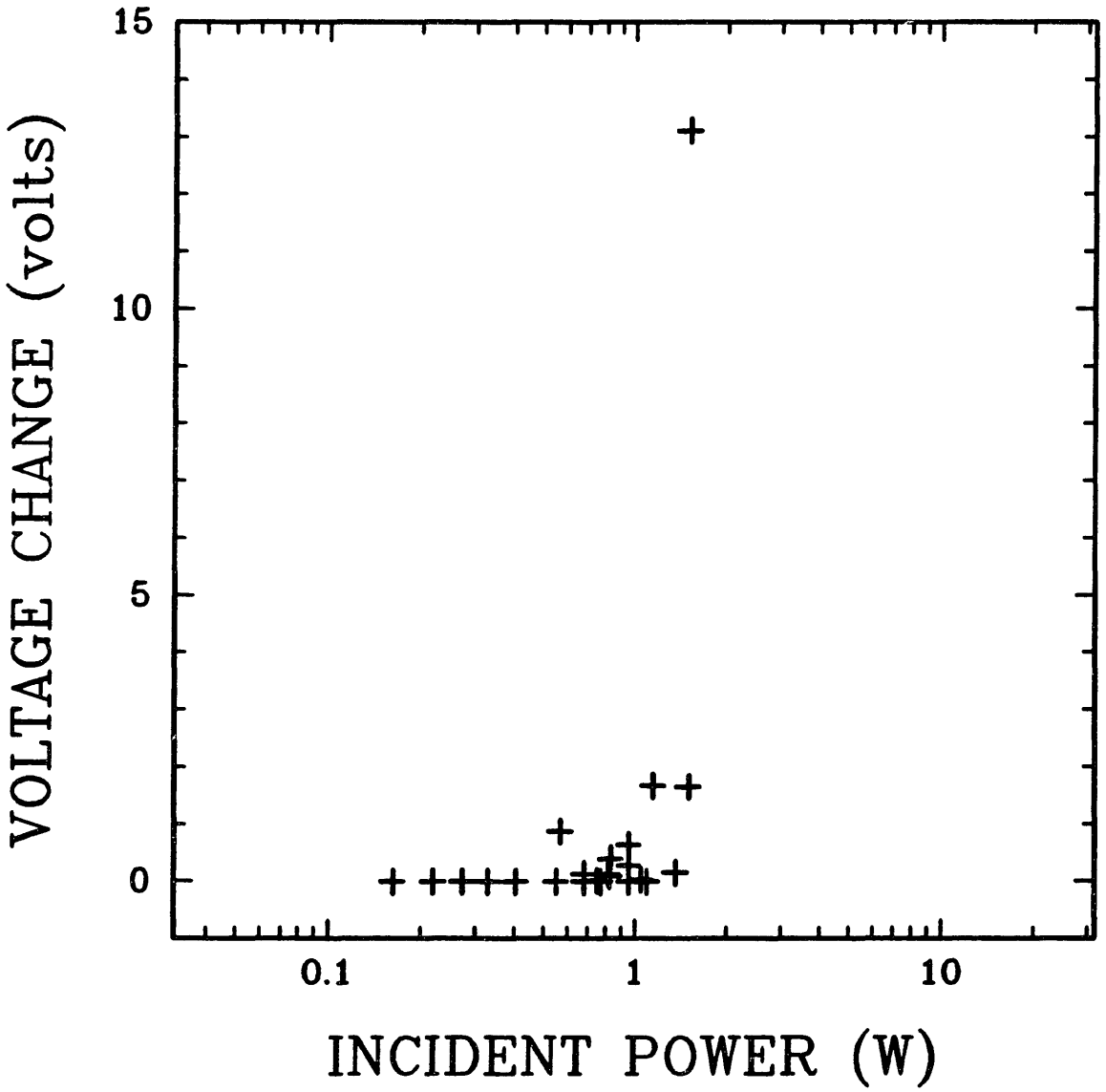

Figure D5.1 : Change in balancing DC voltage due to charge loss from a series of seven different "Spherocarb" particles versus incident CO_2 laser power for a 2.8 msec laser pulse.

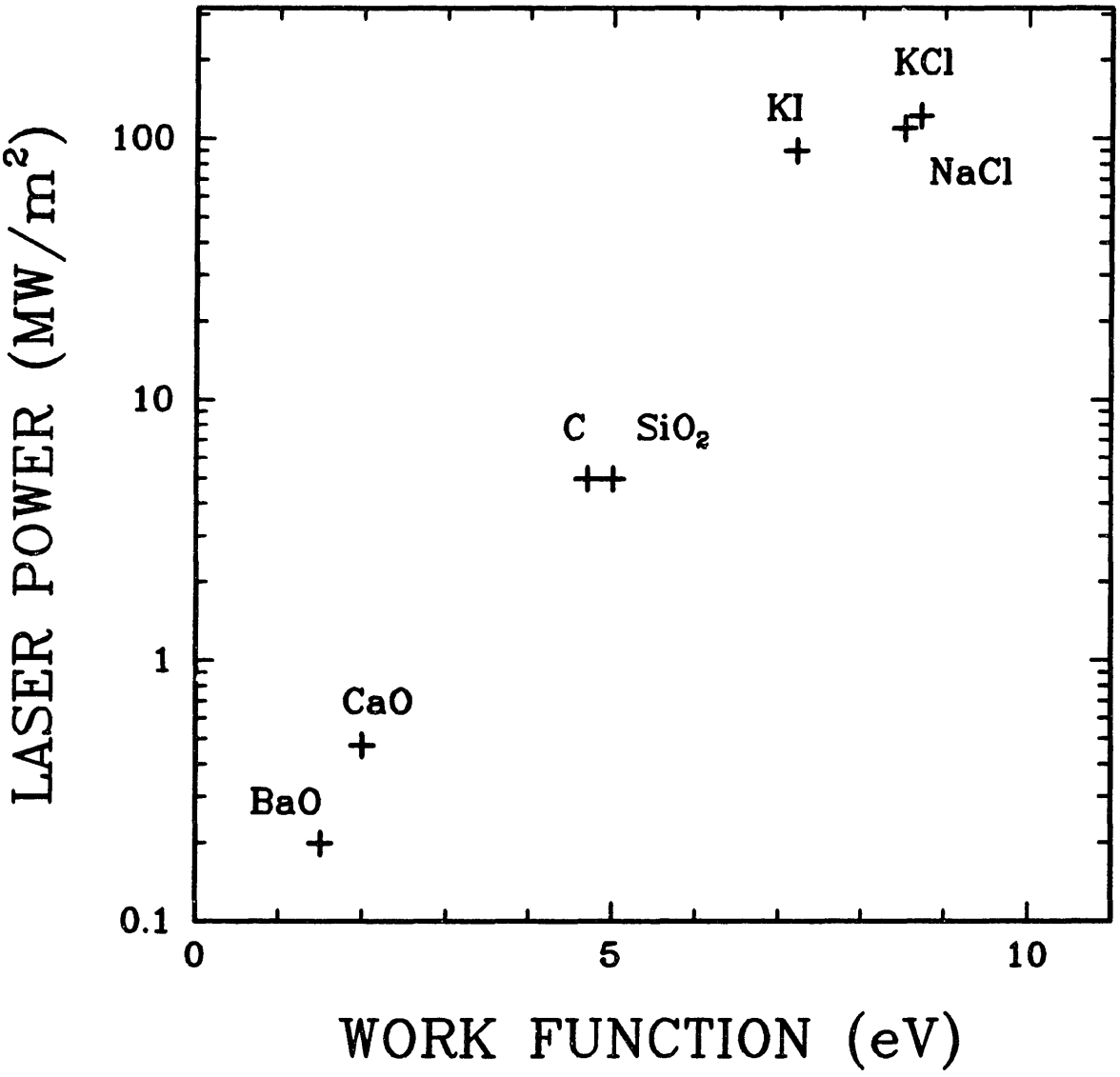

Figure D5.2 : Absorbed CO_2 laser power required for charge loss versus particle work function for seven different materials, BaO, CaO, C, SiO_2, KI, KCl, and NaCl.

ticle. By dipping the thermocouple bead into ethanol solutions, various compounds such as SiO_2, ZrO_2, carbon black, $Ca(Ac)_2$, and KCl could be used as surface coatings.

Figures D5.3 and D5.4 highlight results taken from a thermocouple held in place by a ceramic tube with heat being provided by a CO_2 laser. Figure D5.3 is a plot of positive ion current versus negative DC voltage being applied to the electrodes, with type K thermocouple temperatue as a parameter. Here we see a very systematic dependence of positive ion current versus thermocouple temperature and electric field strength.

Figure D5.4 is a plot of positive ion current versus negative DC voltage applied to the electrodes, with type R thermocouple temperature as a parameter. This plot highlights the results of work performed with doped thermocouples. In this case, a ZrO_2 coating was attached to the thermocouple. The solid lines in Figure D5.4 represent results with no coating on the thermocouple and the dotted lines represent results with a ZrO_2 coating. The ZrO_2 coating increases the positive ion current by approximately one order of magnitude.

D5.3 Theory.

Charge may be lost from a particle suspended in the EDB by six different mechanisms, 1) photoemission, 2) field emision, 3) secondary emission, 4) thermionic emission of electrons or ions, 5) fragmentation, and 6) surrounding gas ionization.

After examining evidence from experiments performed in this lab as well as evidence presented in the literature, thermionic emission of ions remains the most viable mechanism for charge loss. The Richardson-Dushman equation describes thermionic emission from a clean surface and predicts the maximum temperature at which a material can be heated without experiencing charge loss.

An electric field can lower the apparent work function of the material by $[eE/(4\pi\epsilon_0)]^{0.5}$. This is called the Schottky effect [37,38] where E is the electric field strength at the surface of the material and ϵ_0 is the permittivity of free space. The total electric field at the particle surface, E_{total}, is a combination of the electric fields

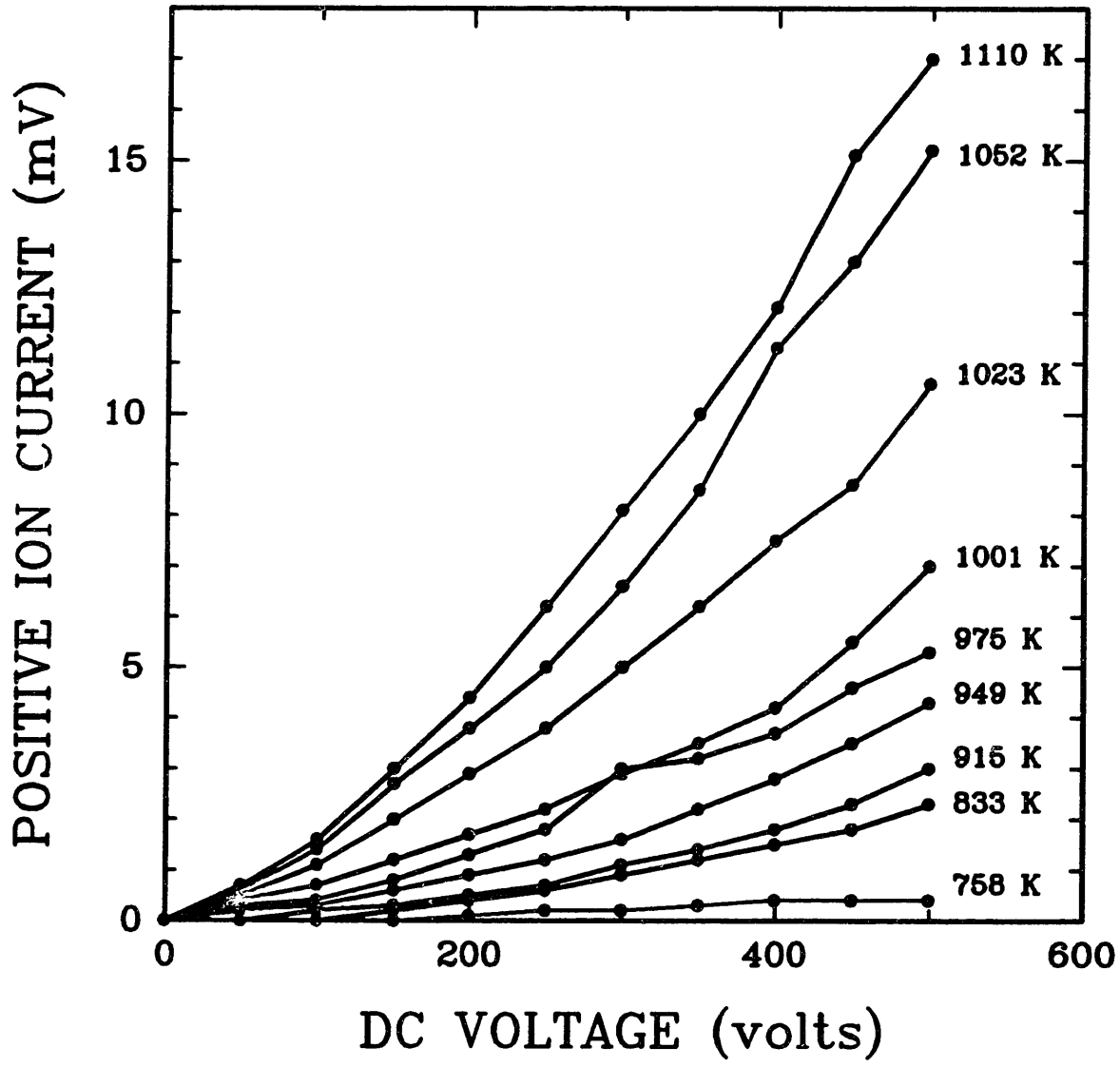

Figure D5.3 : Positive ion charge loss from a CO_2 laser heated, type K thermocouple versus DC voltage applied to surrounding electrodes. Thermocouple temperature is a parameter.

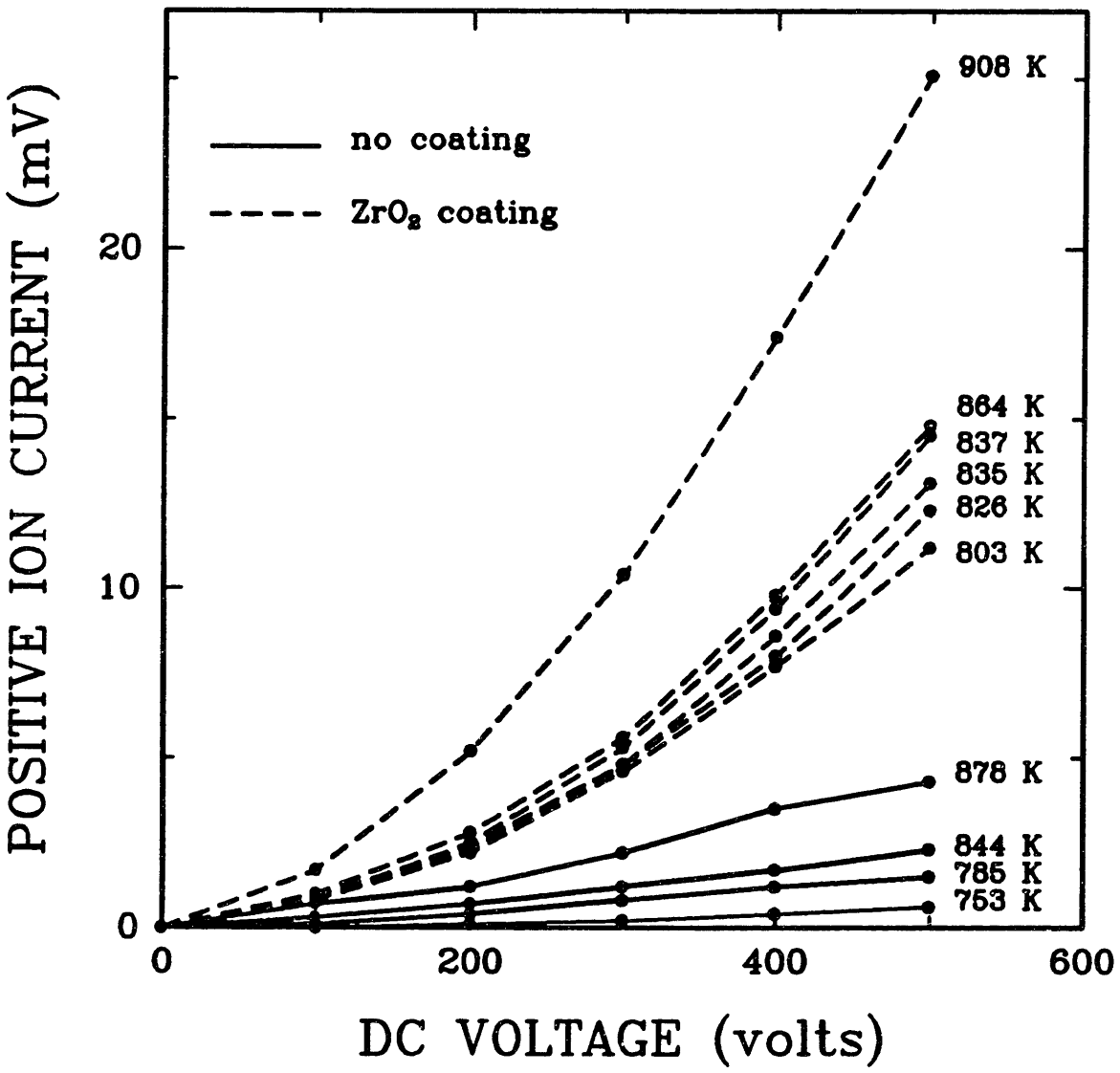

Figure D5.4 : Positive ion charge loss from a CO_2 laser heated, type R thermocouple versus DC voltage applied to surrounding electrodes for an uncoated and a ZrO_2 coated thermocouple. Thermocouple temperature is a parameter.

produced by 1) the DC endcap electrodes, E_{DC}, 2) the AC ring electrode, E_{AC}, and 3) the excess surface charge, E_s. The electric field produced by the excess surface charge dominates the total electric field at the particle surface, and can be minimized by minimizing the total amount of excess charge on the levitated particle.

Jenkins [39] discusses how surface contamination can greatly modify the potential barrier at the solid surface and can lower the work function by two or three eV. Loeb [40] and Lawton and Weinberg [41] concluded that surface irregularities act in a way as to magnify the electric field found on charged particles by as much as 200 times, and this in turn can be thought of as decreasing the particle work function.

If the particle work function and particle temperature are assumed to be of primary importance in describing charge loss, and that electric field strength, surface contamination, and surface irregularities are of secondary importance and act to lower the particle work function, a modified Richardson-Dushman equation can be written:

$$I = AT^2 \exp[(-\phi+\xi+\Phi)/(kT)] \qquad (D5.1)$$

where ϕ is the particle work function at some reference temperature, ξ is defined as $[e\beta(E_s+E_{AC}+E_{DC})/(4\pi e_0)]^{0.5}$ which describes the lowering of the work function due to the electric field strength at the particle surface, and Φ is the decrease in work function due to surface contamination. The other variables are defined as follows:

A = the Richardson constant = 120 amps/cm^2 K^2.

k = Boltzmann's constant = 8.63 x 10^{-5} eV/molecule K.

e = elementary charge = 1.6 x 10^{-19} coul.

β = correction factor due to surface irregularities (dimensionless).

This equation can be used to predict the importance of charge loss and the range of feasible operating temperatures for any material that is to be studied in the EDTGA.

D6. SINGLE PARTICLE "SPHEROCARB" OXIDATION.

In this section, we utilize the EDTGA to measure diameter, mass,

density, surface area, and reactivity of single particles as a function of conversion. The uncatalyzed synthetic char "Spherocarb" was chosen as a base case. Since "Spherocarb" has been widely studied, results from the EDTGA can be compared with those of conventional gas-solid reaction apparatuses to test the overall usefulness, credibility, and uniqueness of the EDTGA in studying gas-solid reactions. "Spherocarb" particles doped with Fe, K, and Ca are also examined in this section to determine the effect of catalyst on the evolution of diameter and surface area as a function of conversion. The effect of catalyst on particle-to-particle variations in reactivity is also examined.

D6.1 Uncatalyzed "Spherocarb".

D6.1.1 Density and porosity versus conversion.

Figure D6.1 is a plot of density versus percent conversion for nine separate, uncatalyzed "Spherocarb" oxidations. Intitial densities ranged from 670 to 920 kg/m^3. Percent conversion is defined as follows:

$$\% \text{ conversion} = (1.0 - m/m_1)100\% \qquad \text{(D6.1)}$$

Five of the oxidations were performed in oxygen, one in air, two in carbon dioxide, and one in a dilute stream of oxygen in nitrogen. Density measurements were performed discretely using the aerodynamic drag force technique discussed in section D3.2. From Figure D6.1 it can be seen that "Spherocarb" density decreases with conversion, independent of the oxidation environment. Reaction times for 50% conversion ranged from 2 minutes in oxygen to 30 minutes in carbon dioxide, with a corresponding temperature range of 750-830 K for reactions in oxygen and 1200-1250 K for reactions in carbon dioxide. It is believed that the "Spherocarbs" are oxidizing in the kinetically controlled regime under these conditions [42]. The data suggest a minimum density (approximately 400 kg/m^3) that "Spherocarb" can obtain, even at high conversions of 60-90%.

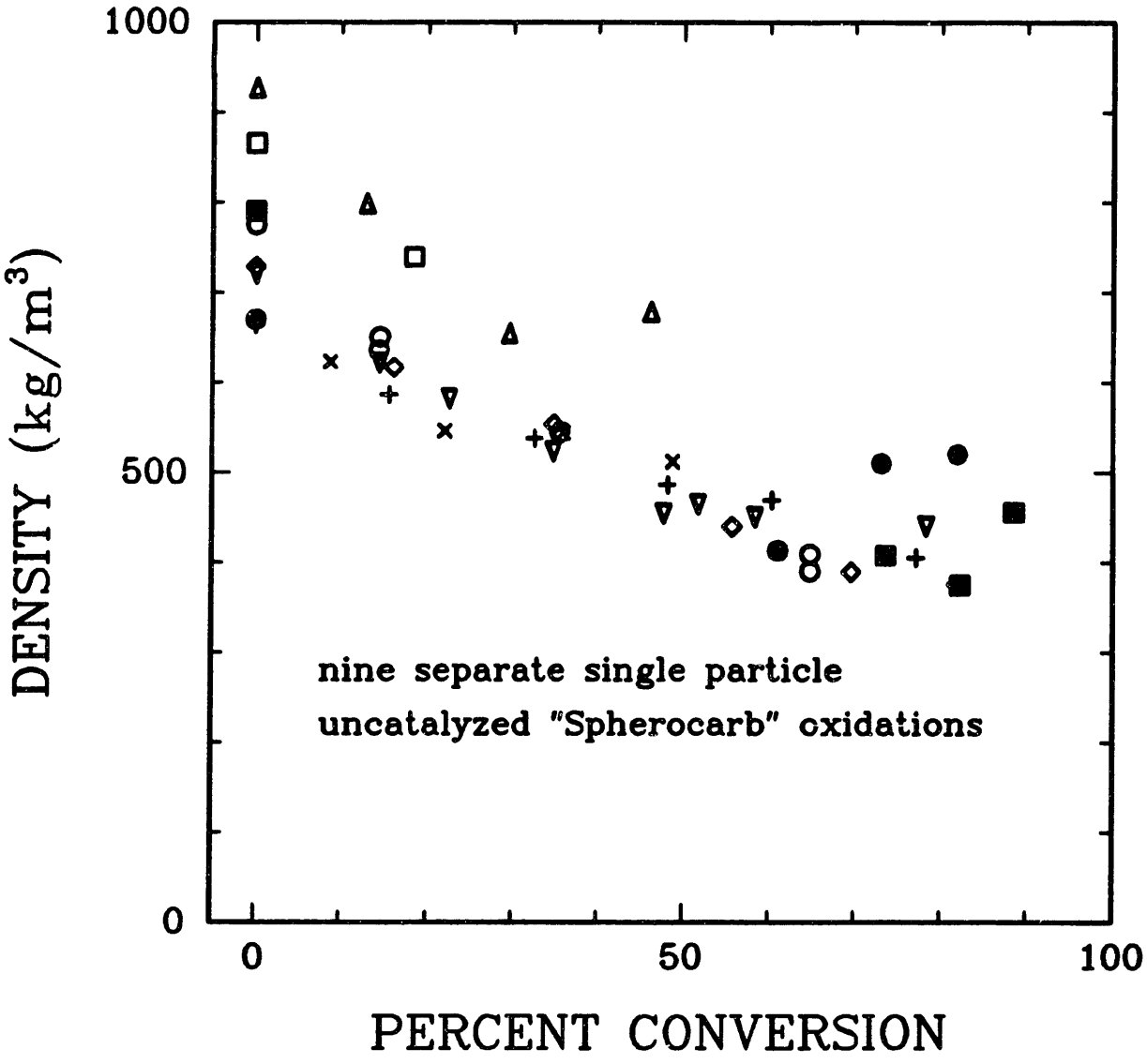

Figure D6.1 : Apparent density versus percent conversion for nine separate, single particle, uncatalyzed "Spherocarb" oxidations performed in the EDTGA.

D6.1.2 Shrinkage versus conversion.

Diameter versus conversion measurements were obtained for 13 separate, single particle, uncatalyzed "Spherocarb" reactions, with the results depicted in Figure D6.2 in the form of diameter/intial diameter versus percent conversion. Nine of the runs were performed in oxygen, three in carbon dioxide, and one in air. Reaction times and temperatures were similar to those described in section 6.1.1. At 50% conversion, the "Spherocarb" diameter is typically 90% of its original value, and at 90% conversion, the diameter is reduced to 50% of its original value. Since it is believed that all of the runs took place under kinetically controlled conditions, the Hurt shrinkage-densification model [43] must be incorporated to interpret the data. The data indicate that the extent of "Spherocarb" shrinkage is not a function of temperature or reacting gas, but only a function of conversion.

D6.1.3 Surface area versus conversion.

Single particle surface areas are obtained using CO_2 adsorption and the Dubinin-Polanyi equation. Figure D6.3 is a plot of specific surface area versus percent conversion for eight single particle "Spherocarb" oxidations. Five of the runs were performed in oxygen, two in carbon dioxide, and one in air. Again, the reaction times and temperatures were similar to those described in section 6.1.1. The initial specific surface area varied from 821 to 1116 m^2/g, with the average initial surface area being 960 m^2/g. These surface areas can be compared to a value of 965 m^2/g obtained from a 0.294 g sample of "Spherocarb" particles from Hurt [44] in a conventional volumetric adsorption apparatus. The surface area appears to increase slightly up to a conversion of 10-15% and then monotonically decrease to an average value of 660 m^2/g at about 81% conversion. A value of 647 m^2/g was obtained at 65% conversion from Hurt [44] using a conventional volumetric adsorption apparatus. The data indicate that "Spherocarb" surface area evolution is not a function of temperature or reacting gas, but only a function of conversion.

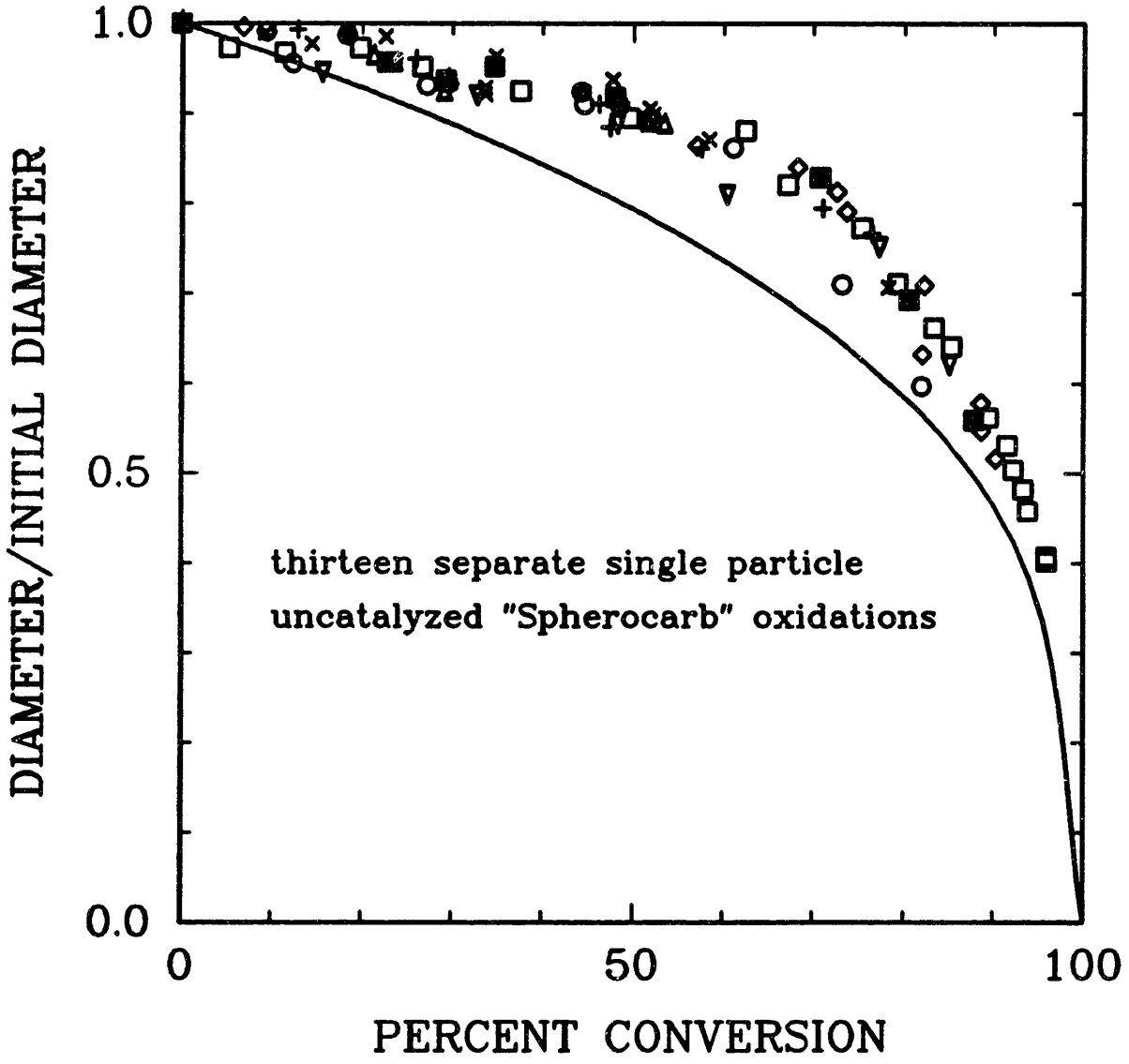

Figure D6.2 : Ratio of diameter to initial diameter versus percent conversion for 13 separate, single particle, uncatalyzed "Spherocarb" oxidations performed in the EDTGA.

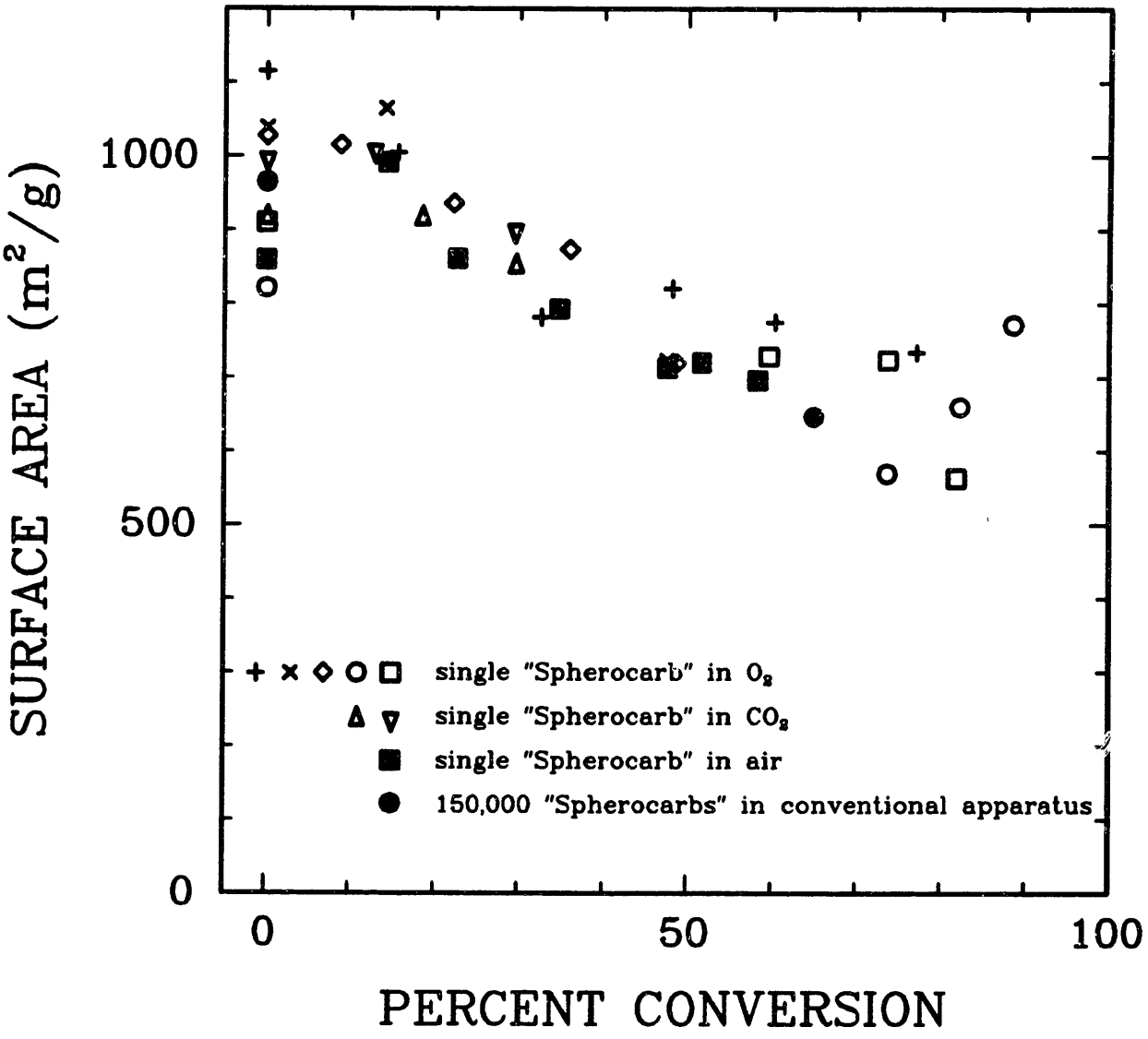

Figure D6.3 : Specific surface area versus percent conversion for eight separate, single particle, uncatalyzed "Spherocarb" oxidations performed in the EDTGA.

D6.1.4 Reactivities.

A total of 19 separate, uncatalyzed "Spherocarb" particles were reacted in air. Particle temperatures ranged from 740 to 1170 K and the corresponding times required for 50% conversion ranged from 2.2 to 17,000 sec.

Figure D6.4 is a plot of the natural log of $1/\tau_{0.5}$ versus 1/T for all of the 19 "Spherocarb" particles that were reacted in air. $\tau_{0.5}$ is defined as the time in seconds required for 50% of the particle to have reacted. In this figure, the solid black circles represent data collected by Floess [45] and Hurt [42] in a conventional TGA. Their data cover the range of $\tau_{0.5}$ = 372 to 167,900 sec, approximately 2.5 orders of magnitude in reaction rate. The x's represent data collected in the EDTGA. These data cover the range of $\tau_{0.5}$ = 2.2 to 17,000 sec, almost 4 orders of magnitude in reaction rate. The EDTGA results are reproducible at rates over 2 orders of magnitude faster than obtainable in a conventional TGA. Both TGA and EDTGA results yield an activation energy of 36 kcal/mol for the "Spherocarb"-air reaction. These results indicate for the first time that the EDTGA is a viable tool in studying the kinetics of high temperature gas-solid reactions.

D6.1.5 Density distribution.

A wide variability in apparent density has been observed from the weighing of individual "Spherocarb" particles in the EDTGA. The results indicate that the "Spherocarb" particle density varies from a minimum of 0.42 to a maximum of 0.94 g/cm^3. The reason for the variability in particle density may be appreciated from an optical examination of polished cross-sections of "Spherocarb" particles in Figure D6.5 [46]. A systematic study on nine "Spherocarb" particles reacting at the same temperature of 880 K revealed no correlation between "Spherocarb" density and reactivity.

D6.1.6 Particle-to-particle variations in reactivity.

A total of nine individual "Spherocarb" particles were reacted at approximately the same temperature and the results are depicted in the Arrhenius plot of Figure D6.6. Individual "Spherocarbs"

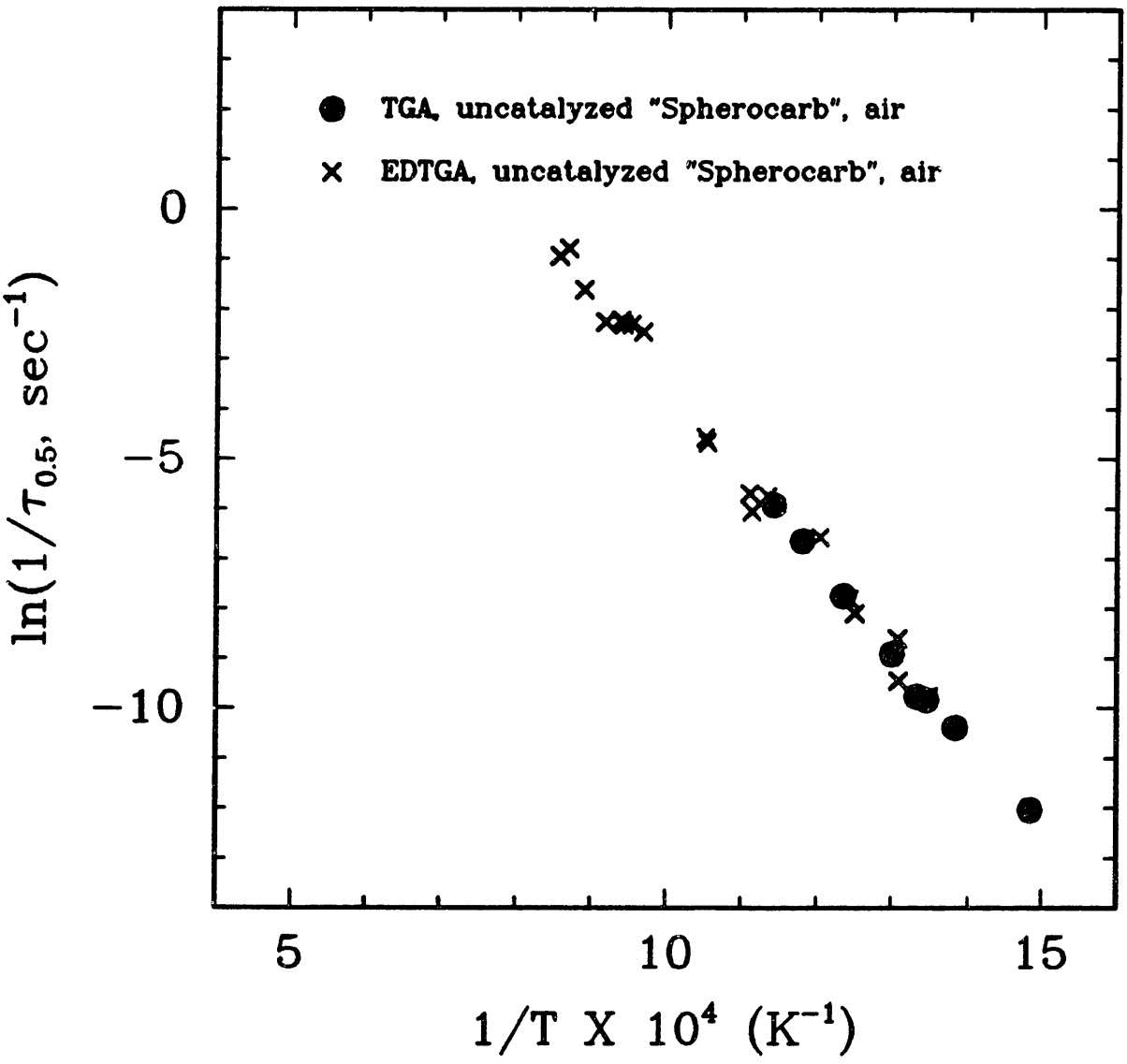

Figure D6.4 : $\ln(1/\tau_{0.5})$ versus 1/T for 19 separate, single particle, uncatalyzed "Spherocarb"–air reactions performed in the EDTGA and eight "Spherocarb"–air reactions performed in a conventional TGA.

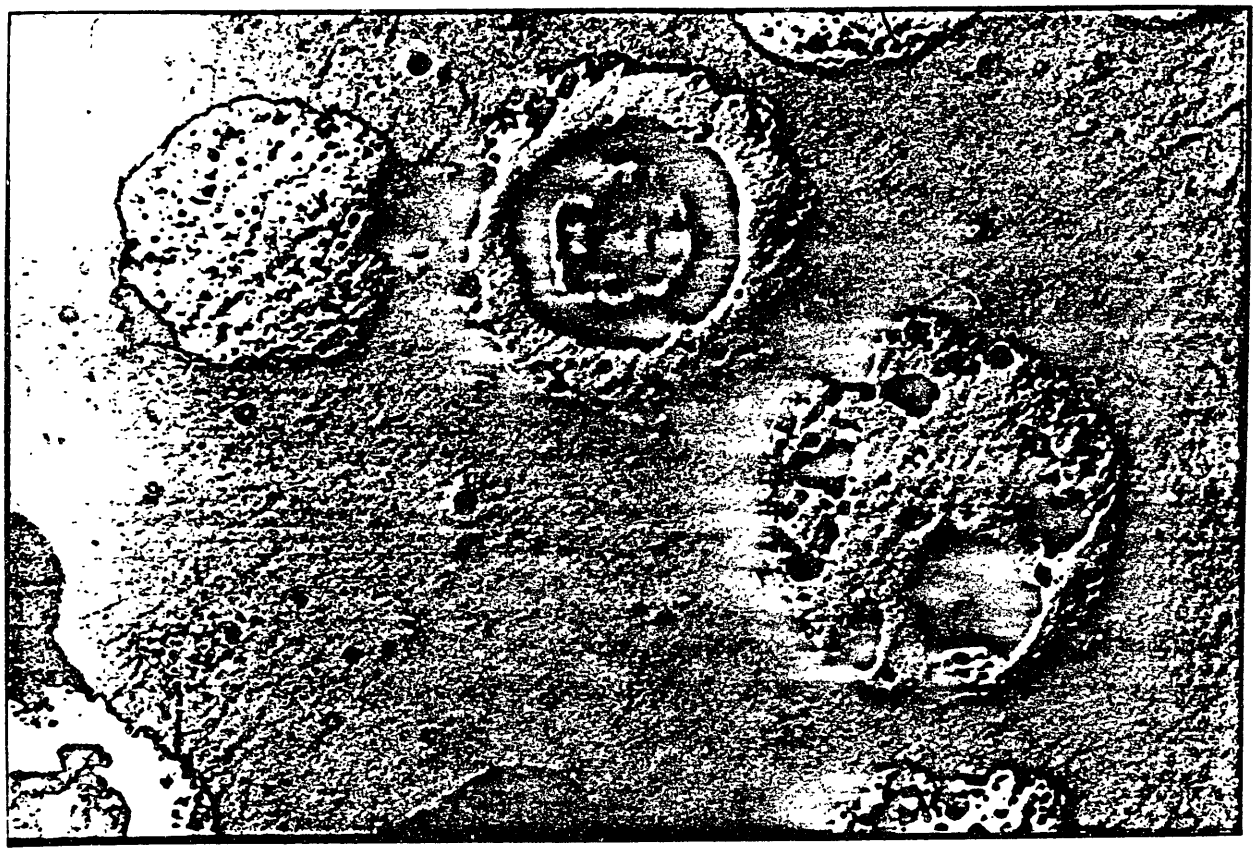

Figure D6.5 : Polished cross sections of "Spherocarb" particles.

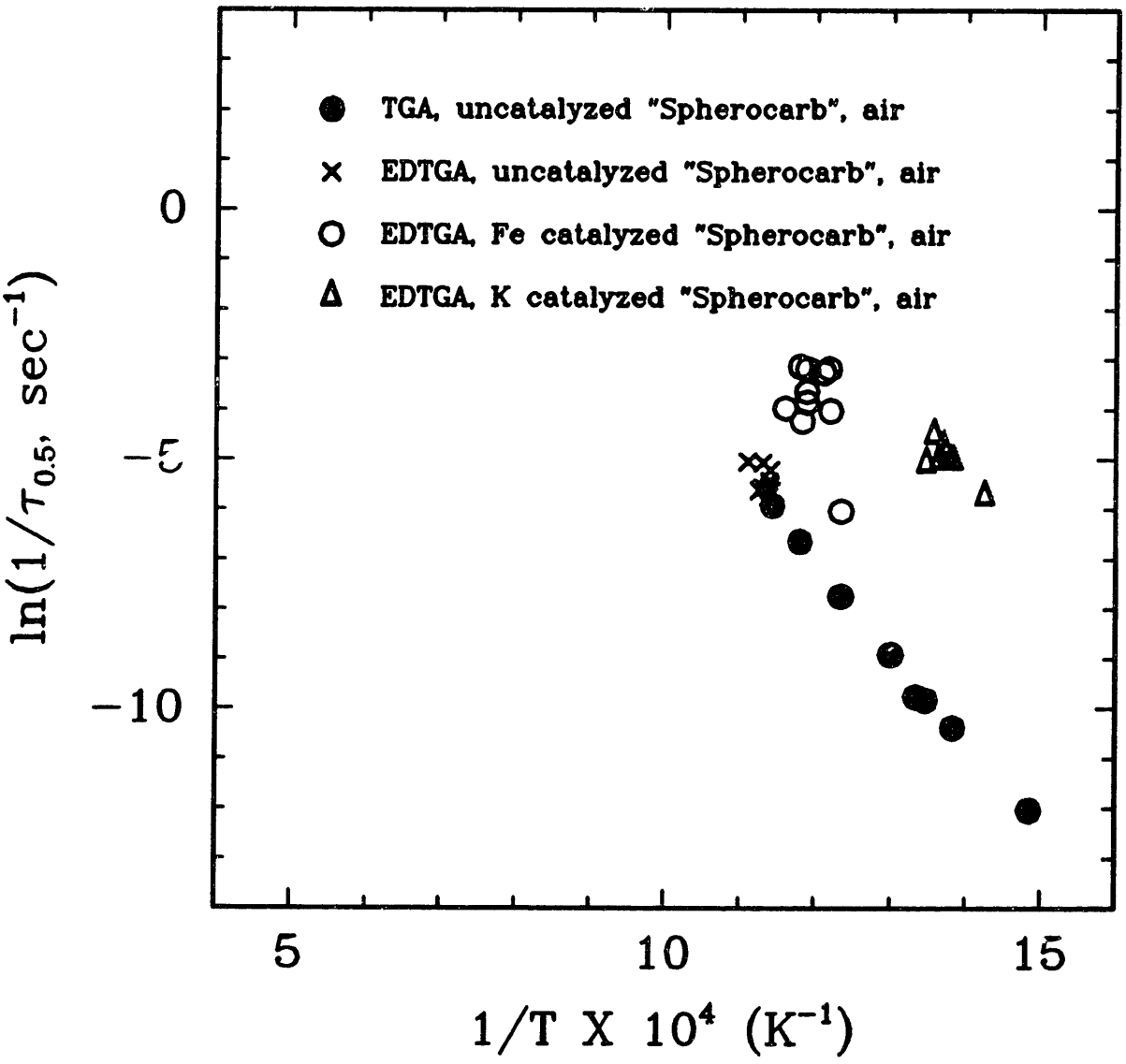

Figure D6.6 : Arrhenius plot for single particle uncatalyzed, Fe catalyzed, and K catalyzed "Spherocarb"–air reactions performed in the EDTGA.

possess amazingly uniform reactivities with a standard deviation in reactivity of only 21%.

D6.2 Catalyzed "Spherocarb".

Three different catalysts (Fe, K, and Ca) were examined to determine their effect on "Spherocarb" oxidation. Potassium has been shown by Mims and Pabst [47] and Mims et al. [48] to be very mobile and to completely wet the reacting surface. Iron has been shown by McKee [49] and Baker et al. [50] to be an immobile, pitting catalyst. Calcium is ion exchanged on the "Spherocarb" surface and is assumed to be immobile.

The presence of Fe or Ca catalyst in "Spherocarb" does not change the magnitude of shrinkage with conversion as compared with uncatalyzed "Spherocarb". Potassium, however, does increase shrinkage slightly. For Fe catalyzed "Spherocarb" the surface area decreases in the same manner as the uncatalyzed "Spherocarb". For K catalyzed "Spherocarb" the surface area decreases more with conversion than the uncatalyzed "Spherocarb".

A series of 10 separate Fe catalyzed "Spherocarb" particles were reacted in air at approximately the same temperature. Likewise, a series of seven separate K catalyzed "Spherocarb" particles were reacted in air at approximately the same temperature. The results from both sets of experiments are compared to the uncatalyzed results and depicted in the Arrhenius plot of Figure D6.6. The standard deviation in reactivities was 88% for Fe and 32% for K. The "Spherocarb" doped with the pitting Fe catalyst shows the highest particle-to-particle variation in reactivity. The "Spherocarb" injected with the wetting K catalyst, on the other hand, shows only slightly more variability in reactivity than the uncatalyzed "Spherocarb".

D7. CONCLUSIONS.

D7.1 Experimental techniques for single particle characterization.

By taking photographs of suspended particles, single particle

diameter measurements can be performed to within ± 3 μm. The aerodynamic drag force technique has been shown to be useful in measuring single particle mass, density, porosity, and excess charge. Carbon dioxide adsorption and the Dubinin-Polanyi equation have successfully been used to measure single particle surface areas of the synthetic char "Spherocarb". Experimental techniques now exist to measure diameter, mass, density, porosity, surface area, temperature, and reactivity of a single levitated particle versus extent of reaction in the EDTGA.

D7.2 Natural convection.

The computational method of Geoola and Cornish [29,30] for describing the heat transfer and fluid mechanics surrounding a heated solid sphere was modified to correctly calculate the drag force due to natural convection. The experimental steady-state and transient results of the natural convective drag force agree well with the Boussinesq numerical solutions, indicating that the Boussinesq approximation is valid over the experimental parameter range examined. The numerical calculations were used to develop empirical correlations to approximate the steady-state natural convective drag force and the dimensionless time required to reach 90% of the steady-state drag coefficient. The steady-state and transient empirical correlations may be used to cancel out the natural convective drag force from the reacting particle force balance, thereby, allowing continuous mass versus time measurements to be calculated from balancing voltage versus time measurements.

D7.3 Charge loss from heated particles levitated in the EDTGA.

"Catastrophic" charge loss due to particle heating has experimentally been found to represent the most serious limitation in studying single particle gas-solid reactions in the EDTGA. Experimentally, charge loss appears to be a function of particle work function, particle temperature, electric field strength, and surface contamination. There is also no noticable difference in charge loss from positively charged particles as compared to negatively charged particles.

From a literature survey, it was determined that particle surface irregularities coupled with the electric field at the particle surface could drasticly increase the charge loss from the particle at a specific temperature, potentially decreasing the particle surface work function by a couple of electron volts. Surface impurities can also lead to a drastic increase in charge loss.

After examining evidence from experiments performed in this lab as well as evidence presented in the literature, thermionic emission of ions was determined to be the most viable mechanism for charge loss. The Richardson-Dushman equation describes thermionic emission from a clean surface and predicts the maximum temperature at which a material can be heated without experiencing charge loss.

By incorporating the effect of electric field strength, surface contamination, and surface irregularities on lowering the particle work function, a modified Richardson-Dushman equation was proposed. This modified Richardson-Dushman equation can be used as in an initial screening of the reactions that can be effectively studied in the EDTGA.

D7.4 Single Particle "Spherocarb" Oxidation.

"Spherocarb" particles have been observed to undergo shrinkage while reacting under kinetically controlled conditions. The extent of "Spherocarb" shrinkage is not a function of temperature or reacting gas, a slight function of catalyst type, and a strong function of conversion. K catalyzed "Spherocarb" appears to shrink slightly more than the uncatalyzed or Fe or Ca catalyzed "Spherocarbs".

Uncatalyzed "Spherocarb" specific surface area, as measured by CO_2 adsorption, has an initial average value of 960 m^2/g. The surface area appears to increase slightly up to a conversion of 10-15% and then decreases monotonically to an average value of 660 m^2/g at approximately 80% conversion. Uncatalyzed "Spherocarb" surface area evolution is not a function of temperature or reacting gas, but only a function of conversion. The surface area evolution of Fe catalyzed "Spherocarb" behaves in the same manner as uncatalyzed, however, the surface area of K catalyzed "Spherocarb" decreases more with conversion.

Nineteen separate "Spherocarb" particles were reacted in the EDTGA in air at temperatures ranging from 740 to 1170 K. Corresponding reaction times required for 50% conversion covered almost four orders of magnitude, ranging from 2.2 to 17,000 sec. The reaction rates obtained from the EDTGA agree favorably with those obtained from a conventional TGA, with both apparatuses yielding an activation energy of 36 kcal/mol for the "Spherocarb"-air reaction. No pore diffusion limitations are detectable over the entire four orders of reaction rates examined, indicating that the "Spherocarbs" are reacting in the kinetic regime.

Density measurements on individual "Spherocarb" particles revealed a large variability in "Spherocarb" apparent density from particle to particle. A systematic study of "Spherocarb" density versus reactivity showed no correlation.

A study of particle-to-particle variability in reactivities revealed a standard deviation in reaction rates of 21% for uncatalyzed "Spherocarb", 88% for Fe catalyzed "Spherocarb", and 32% for K catalyzed "Spherocarb".

REFERENCES FOR DIGEST

[1] Milliken, R.A., "The Isolation of an Ion, A Precision Measurement of its charge," *Phys. Rev.*, 32, 349 (1911).

[2] Davis, E.J., "Transport Phenomena with Sigle Aerosol Particles," *Aerosol Sci. Tech.*, 2, 121-144 (1983).

[3] Blau, H.H. Jr., McCleese, D.J., and Watson, D., *J. Atmos. Sci.*, 9, 2522-2528 (1970).

[4] Davis, E.J., and Ray, A.K., "Single Aerosol Particle Size and Mass Measurements Using an Electrodynamic Balance," *J. Colloid Int. Sci.*, 75, no. 2, 566-576 (1980).

[5] Rubel, G.O., "Measurement of the Condensational Growth of Single Hygroscopic Acid Aerosol Droplets," *J. Aerosol Sci.*, Vol. 12, no. 6, 551-558 (1981).

[6] Ray, A.K., "A Study of Rate Processes Associated with Single and Multiple Aerocolloidal Particles," Ph.D. Thesis, Clarkson College of Technology (1980).

[7] Spjut, R.E., "Heat Transfer to and Position Control of Electrodynamically Suspended Micron-sized Particles," Ph.D. Thesis, Massachusetts Institute of Technology, Cambridge, MA (1985).

[8] Spjut, R.E., Bar-Ziv, E., Sarofim, A.F., and Longwell, J.P., "Electrodynamic Thermogravimetric Analyzer," *Rev. Sci. Instrum.*, 57(8), 1604-1610 (1986).

[9] Spjut, R.E., Sarofim, A.F., and Longwell, J.P., "Laser Heating and Particle Temperature Measurement in an Electrodynamic Balance," *Langmuir*, 1, 355-360 (1985).

[10] Arnold, S., "Determination of Particle Mass and Charge by One Electron Differentials", *J. Aerosol Sci.*, 10, 49-53 (1979).

[11] Wuerker, R.F., Shelton, H., and Langmuir, R.V., "Electrodynamic Containment of Charged Particles," *J. Appl. Phys.*, 30, no. 3, 342-349 (1959).

[12] Frickel, R.H., Shaffer, R.E., and Stamatoff, J.B., Technical Report ARCSL-TR77041, U.S. Command, Aberdeen, MD (1978).

[13] Lamond, T.G., and Marsh, H., "The Surface Properties of Carbon-II

The Effect of Capillary Condensation at Low Relative Pressures Upon the Determination of Surface Area," *Carbon*, 1, 281-292 (1964).

[14] Walker, P.L., Jr., and Kini, K.A., "Measurement of the Ultrafine Surface Area of Coals," *Fuel*, 44, 453-459 (1965).

[15] Arnold, S., and Lewittes, M., "Size Dependence of the Photophoretic Force," *J. Appl. Phys.*, 53(7), 5314-5319 (1982).

[16] Meyer, P., "Heat Transfer to Small Particles by Natural Convection," *Inst. Chem. Engrs.*, 15, 127-131 (1937).

[17] Elenbaas, W., "The Dissipation of Heat by Free Convection of Spheres and Horizontal Cylinders," *Physica*, 9, no. 3, 285-296 (1942).

[18] Ranz, W.E., and Marshall, W.R. Jr., "Evaporation from Drops," *Chem. Engng. Prog.* 48, no. 4, 173-180 (1952).

[19] Mathers, W.G., Madden, A.J. Jr., and Piret, E.L., "Simultaneous Heat and Mass Transfer in Free Convection," *Ind. Engng. Chem.*, 49, no. 6, 961-968 (1957).

[20] Tsubouchi, T., and Sato, S., "Heat Transfer from Fine Wires and Particles by Natural Convection," res. of the Inst. of high speed mech., Tohoku Univ. 12, pp. 127-132 (1960).

[21] Yuge, T., "Experiments on Heat Transfer from Spheres Including Combined Natural and Forced Convection," *Trans. ASME*, C82, 214-220 (1960).

[22] Mahony, J.J., "Heat Transfer at Small Grashof Numbers," *Proc. R. Soc., London*, A238, 412-423 (1956).

[23] Fendell, F.E., "Laminar Natural Convection about an Isothermally Heated Sphere at Small Grashof Number," *J. Fluid Mech.*, 34, part 1, 163-176 (1968).

[24] Hossain, M.A., and Gebhart, B., "Natural Convection about a Sphere at Low Grashof Number," Fourth International Heat Transfer Conference, Paris-Versailles, 5, NC1.6, A.I.Ch.E., New York (1970).

[25] Hieber, C.A., and Gebhart, B., "Mixed Convection from a Sphere at Small Reynolds and Grashof Numbers," *J. Fluid Mech.*, 38, part 1, 137-159 (1969).

[26] Singh, S.N., and Hasan, M.M., "Free Convection about a Sphere at Small Grashof Number," *Int. J. Heat Mass Transfer*, 26, no. 5, 781-783 (1983).

[27] Farouk, B., "Natural Convection Heat Transfer from an Isothermal Sphere," *Therm. Sci.*, **16**, vol. 1, 347-364 (1982).

[28] Fujii, T., Honda, T., and Fujii, M., "A Numerical Analysis of Laminar Free Convection around an Isothermal Sphere: Finite-Difference Solution of the Full Navier-Stokes and Energy Equations Between Concentric Spheres," *Num. Heat Transfer*, **7**, 103-111 (1984).

[29] Geoola, F., and Cornish, A.R.H., "Numerical Solution of Steady-State Free Convective Heat Transfer from a Solid Sphere," *Int. J. Heat Mass Transfer*, **24**, no. 8, 1369-1379 (1981).

[30] Geoola, F., and Cornish, A.R.H., "Numerical Simulation of Free Convective Heat Transfer from a Sphere," *Int. J. Heat Mass Transfer*, **25**, no. 11, 1677-1687 (1982).

[31] Sparrow, E.M., and Gregg, J.L. Jr., "The Variable Fluid-Property Problem in Free Convection," *Trans. ASME*, **a46**, 879-8867 (1958).

[32] Smith, G.D., *Numerical Solution of Partial Differential Equations*, Chapters 2 and 5, Oxford University Press, London (1965).

[33] Peaceman, D.W., and Rachford, H.H. Jr., "The Numerical Solution of Parabolic and Elliptic Differential Equations," *J. Soc. Ind. Appl. Math.*, **3**, 28-41 (1955).

[34] Boussinesq, J., *Theorie analytique de la chaleur*, Paris: Gathier-Villars, vol. 2 (1903).

[35] Burden, R.L., Faires, J.P., and Reynolds, A.C., *Numerical Analysis*, Prindle, Weber, and Schmidt, Boston, Massachusetts, 136-145 (1978).

[36] Gallo, C.F., and Lama, W.L., "Some Charge Exchange Phenomena Explained by a Classical Model of the Work Function," *J. of Electrostatics*, **2**, 145-150 (1976).

[37] Schottky, V.W., *Physik. Zeitschr.*, **XV**, 872-878 (1914).

[38] de Bruyne, N.A., "The Action of Strong Electric Fields on the Current from a Thermionic Cathode," *Proc. Roy. Soc. (London)*, **120A**, 423-437 (1928).

[39] Jenkins, R.O., and Trodden, W.G., *Electron and Ion Emission from Solids*, Dover Publications, Inc., New York (1965).

[40] Loeb, L.B., *Fundamental Processes of Electrical Discharge in Gases*, John Wiley and Sons, Inc., New York, 310-335 (1939).

[41] Lawton, J., and Weinberg, F.T., *Electrical Aspects of Combustion*,

Clarendon Press, Oxford, (1969).

[42] Hurt, R.H., "Chemical and Physical Phenomena Determining Carbon Gasification Reactivity," Ph.D. Thesis, Massachusetts Institute of Technology, Cambridge, MA (1987).

[43] Hurt, R.H., Dudek, D.R., Longwell, J.P., and Sarofim, A.F., "The Phenomenon of Gasification-Induced Carbon Densification and its Influence on Pore Structure Evolution," *Carbon*, **26**, 3 (1988).

[44] Hurt, R.H., personal communication, conventional volumetric adsorption apparatus data, Massachusetts Institute of Technology, Dept. of Chemical Engineering (1987).

[45] Floess, J.K., "The Effect of Calcium on the Gasification Reactions of Carbon," Ph.D. Thesis, Massachusetts Institute of Technology, Cambridge, MA (1985).

[46] D'Amore, M., personal communication, Massachusetts Institute of Technology, Dept. of Chemical Engineering (1987).

[47] Mims, C.A., and Pabst, J.K., "Role of Surface Salt Complexes in Alkali-Catalyzed Carbon Gasification," *Fuel*, **62**, 176-179 (1983).

[48] Mims, C.A., Chludzinski, J.J. Jr., Pabst, J.K., and Baker, R.T.K., "Potassium-Catalyzed Gasification of Graphite in Oxygen and Steam," *J Catalysis*, **88**, 97-106 (1984).

[49] McKee, D.W., "Metal Oxides as Catalysts for the Oxidation of Graphite", *Carbon*, **8**, 623-635 (1970).

[50] Baker, R.T.K., Chludzinski, J.J. Jr., and Sherwood, R.D., "A Comparison of the Catalytic Influence of Nickel, Iron, and Nickel-Iron on the Gasification of Graphite in Various Gaseous Environments," *Carbon*, **23**, no. 3, 245-254 (1985).

LIST OF SYMBOLS FOR DIGEST

$A = 4\pi emk^2/h^3 = 120$ amps/cm^{2}K^2 = the Richardson constant.

B = constant.

C = dimensionless chamber constant = 0.4.

C_{DT} = dimensionless total drag force coefficient.

C_p = heat capacity of surrounding gas at constant pressure per unit mass (m^2/sec^2 K).

d = particle diameter (m).

e = elementary charge = 1.6×10^{-19} coul.

E = electric field strength at the surface of the material (volts/m).

E_{DC} = electric field at particle surface due to DC electric field (V/m).

E_{AC} = electric field at particle surface due to AC electric field (V/m).

E_s = electric field at particle surface due to surface charge (V/m).

$E_{total} = E_{DC} + E_{AC} + E_s$ (V/m).

F_{nat} = natural convective drag force (N).

F_a = aerodynamic drag force on suspended particle (N).

g = gravitational acceleration = 9.81 m/sec^2.

Gr = Grashof number = $g\beta(T_s-T_\infty)R^3/v^2$ (dimensionless).

h = Planck's constant = 6.6256×10^{-27} erg sec.

I = total emitted current per unit area (amp/cm^2).

k = surrounding gas thermal conductivity (kg m/sec^3 K).

k = Boltzmann's constant = 1.3805×10^{-16} erg/K.

$\bar{K}$ = proportionality constant = $18\mu K/g = 0.848$ kg sec m^{-4}.

m = mass of particle (kg).

m = mass of an electron = 9.107×10^{-31} kg.

m_i = initial mass with no CO_2 adsorption (kg).

n = mols of CO_2 adsorbed (mols).

P = CO_2 equilibrium pressure (atm).

P_0 = saturation vapor pressure of CO_2 (atm).

Pr = Prandtl number = $C_p\mu/k$ (dimensionless).

q = total excess charge on particle (coul).

Q = volumetric flow rate of gas through the chamber (m^3/sec).

R = particle radius (m).

Re = Reynold's number = $\langle v \rangle pd/\mu$ (dimensionless).

$t_{90\%}$ = dimensionless time required to reach 90% of the steady-state dimensionless drag force coefficient.

T = temperature (K).

T_s = particle surface temperature (K).

T_∞ = ambient gas temperature (K).

v = velocity of surrounding gas (m/sec).

V = balancing DC voltage across endcap electrodes (volts).

V_i = balancing voltage of unheated particle in absence of aerodynamic drag and CO_2 adsorption (volts).

ΔV_{nat} = change in balancing voltage between unheated and heated particle (volts).

ΔV_{aero} = change in balancing voltage between particle experiencing aerodynamic drag and particle not experiencing aerodynamic drag (volt).

z_0 = characteristic chamber dimension = 0.004 m.

β = coefficient of volume expansion (1/K).

β = affinity coefficient of CO_2 relative to N_2 (dimensionless).

β = correction factor due to surface irregularities (dimensionless).

ϵ_0 = permittivity constant = 8.85×10^{-12} farad/m.

μ = surrounding gas viscosity (kg/m sec).

ν = surrounding gas kinematic viscosity (m^2/sec).

ρ = surrounding gas density (kg/m^3).

ρ_p = apparent particle density (kg/m^3).

ϕ = coordinate representing the angle of rotation about the axis of symmetry of the flow.

ϕ = work function (eV).

$\tau_{0.5}$ = time required for 50% conversion (sec).

ξ = describes the lowering of the work function due to the electric field strength at the particle surface (eV).

1. INTRODUCTION.

1.1 Background.

Probably the most celebrated single particle levitation device was the flat-plate capacitor used by Milliken [1] to suspend oil droplets and determine the charge of an electron. Today's version of Milliken's flat-plate capacitor is the electrodynamic balance (EDB), a three electrode device capable of stably levitating a single, charged, micron-sized particle in a dynamic electric field. Electrodynamic balances such as these have been used by many workers [2-6] to study ambient temperature phenomenon, such as light scattering, condensation, or evaporation. More recently, Spjut et al. [7-9] extended the diversity of the EDB by successfully heating a single suspended particle with a CO_2 laser. Spjut et al. [7-9] were also able to measure single particle temperatures using two color infrared pyrometry. Postion control systems have been built [7,10] that automatically adjust the balancing DC voltage across the endcap electrodes to keep the particle in the center of the chamber. Since the balancing voltage across the endcap electrodes is proportional to the particle mass to charge ratio, the EDB was now potentially capable of following reacting particle mass versus time much in the same way as a conventional thermogravimetric analyzer (TGA). In this sense, a true electrodynamic thermogravimetric analyzer (EDTGA) had been born.

1.2 Motivation, advantages, and problems.

The motivation behind the development of the EDTGA was

the study of single particle gas-solid reactions, since a single particle device offered many potential advantages over traditional gas-solid reaction apparatuses such as conventional TGA's, laminar flow furnaces, entrained flow reactors, fluidized beds, packed beds, and moving beds. Some of these advantages of studying single particle reactions in the EDTGA are: 1) minimal heat and mass transfer limitations, 2) rapid heating/quenching capabilities (10^6 K/sec) due to heating by CO_2 laser, 3) ability to systematically study effects of specific variables (such as particle density, particle size, coal composition, etc.) on particle reactivity, and 4) easy measurement of diameter shrinkage or growth.

The EDTGA also possesses three experimental difficulties brought about by particle heating: 1) the creation of photophoretic forces, 2) the creation of a natural convective drag force, and 3) charge loss. These difficulties will be discussed individually in the following paragraphs and will become the basis for much of this thesis.

Photophoretic forces on levitated particles arise from temperature variations on the particle surface caused by uneven particle heating. An example of the potential magnitude of the photophoretic force was discussed by Spjut [7] and is depicted in Figure 1.1 in the form of the ratio of photophoretic force to particle weight versus particle diameter for a particle with a density of 2500 kg/m^3, an equilibrium temperature of 1000 K, and a complex index of refraction of 2 - Ki. K, the complex part of the index of refraction is a parameter. These photophoretic forces, which can be minimized by heating the particle from at least two sides, have been shown in this lab to potentially cause particle movements of greater than 500 μm from the chamber center. Particle movements of this magnitude

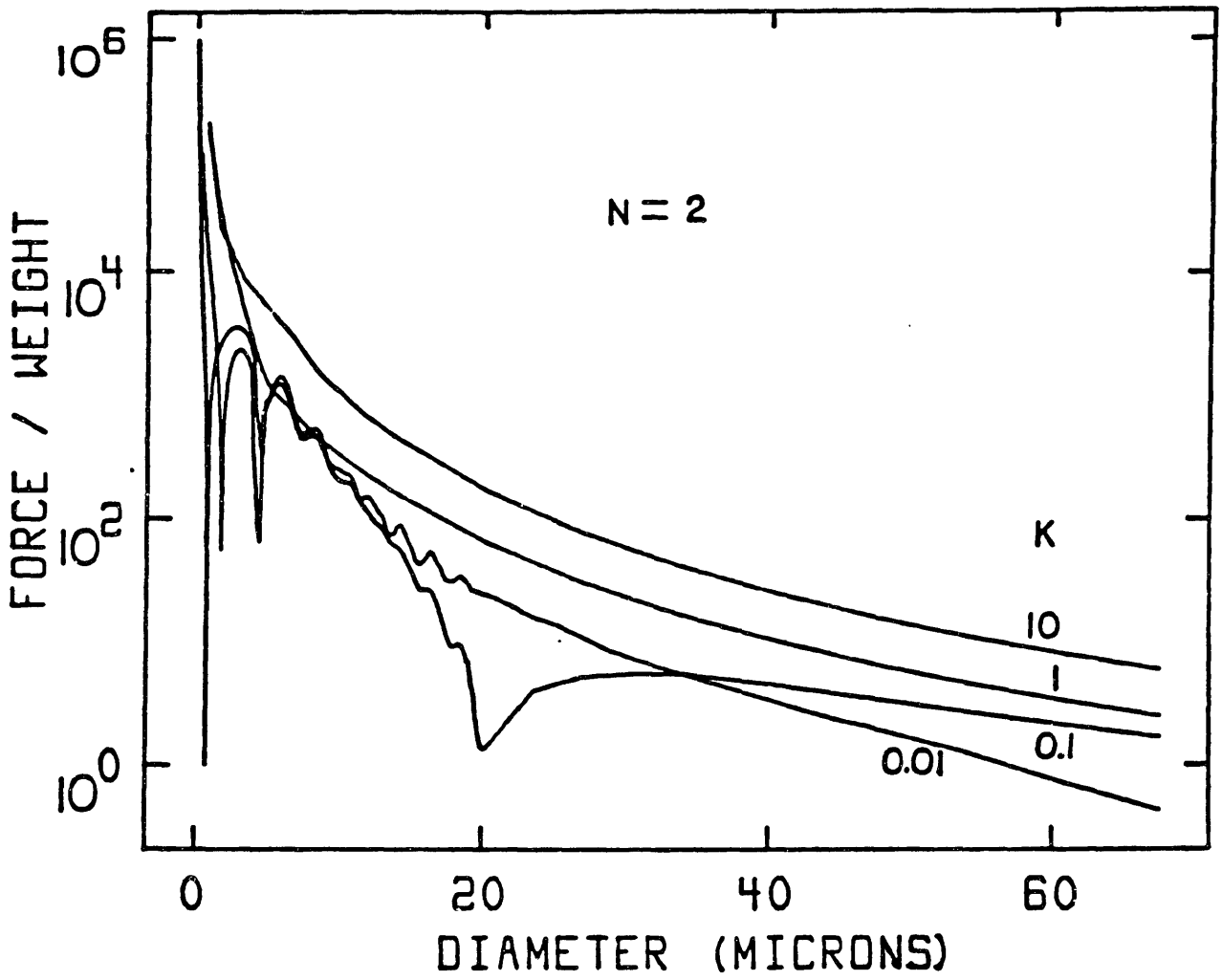

Figure 1.1 : Ratio of photophoretic force to particle weight versus particle diameter for a particle with a density of 2500 kg/m^3, an equilibrium temperature of 1000 K, and a complex index of refraction of 2 – Ki.

can reek havoc on temperature measurements by pushing the particle out of the field of view of one or both of the temperature detectors used in infrared pyrometry. Movements of this magnitude may also cause actual changes in the particle temperature by moving the particle to less intense parts of the CO_2 laser beam. It can be seen in Figure 1.1 that use of larger particles will minimize the relative magnitude of the photophoretic force on the levitated particle as compared to the particle weight. The restoring forces which act to keep the particle in the center of the chamber are the same order of magnitude as the particle weight. In this work, the role of photophoretic forces were minimized by working with particles greater than 100 μm in diameter. Although sucessful in combating the photophoretic forces, use of >100 μm particles created a problem of particle weighing. The previous method of weighing particles involved electron stepping [11], which unfortunately, can only be used to weigh particles less than 20 μm in diameter [7]. Since it is desirable to use larger particles, a method for weighing these larger particles must be developed.

The second experimental difficulty was the introduction of an upward acting natural convective drag force, which is caused by a natural convective flow field set up around a heated particle and makes the DC balancing voltage no longer proportional to particle mass. This natural convective drag force was first reported by Arnold and Lewittes [12]. Since then, Spjut [7] has reported natural convective drag forces as great as the particle weight. Without prior knowledge of the natural convective drag force, continuous mass versus time measurements via voltage versus time measurements are not valid.

The third experimental difficulty is charge loss from heated particles. The particle must retain some of its

charge in order to be levitated, therefore, charge loss due to heating potentially represents a very serious limitation of the EDTGA for some reactions.

1.3 Thesis objectives.

The overall objective of this thesis was to determine the usefulness of the EDB in studying single particle gas-solid reactions. This objective was satisfied in the following four parts:

1) Develop experimental measurement techniques for characterizing single particles suspended in the EDTGA. Most importantly, develop a technique for weighing single particles that are greater than 100 μm in diameter. In addition, develop techniques for measuring single particle diameter, density, porosity, surface area, and reactivity versus particle conversion.
2) Determine the feasibility of continuous mass versus time measurements in the EDTGA in light of the induced natural convective drag force on heated particles. Ideally, identify the major variables important in determining the natural convective drag force and develop predictive capabilities.
3) Attempt to understand the charge loss phenomenon from heated particles. Ideally, develop predictive capabilities that can be utilized in defining the limitations of the EDTGA.
4) Study uncatalyzed and catalyzed "Spherocarb" oxidations in an attempt to more fully understand the role of the EDTGA in gas-solid reaction studies. Examine particle-to-particle variations in reactivity and changes in diameter, density, and surface area versus conversion for both uncatalyzed

and catalyzed "Spherocarb" particles.

2. EXPERIMENTAL APPARATUS.

The electrodynamic thermodynamic analyzer (EDTGA) is a device capable of studying single particle, high temperature, gas-solid reactions. It can be divided into six separate parts, 1) the electrodynamic balance (EDB) chamber, 2) the position control system, 3) the heating system, 4) the temperature measurement system, 5) the CO_2 laser control system, and 6) the gas flow system. The EDB chamber stably contains a single, charged, micron-sized particle in a dynamic electric field, with the electric field strength in the vertical direction being directly proportional to the mass-to-charge ratio of the particle. The position control system automatically adjusts the electric field to keep the particle at the chamber center. This is very important when the particle mass is changing due to reaction. A 20 W CO_2 laser supplies heat to the suspended particle and two color infrared (2 μm and 4 μm) pyrometry is used for temperature measurement. A CO_2 laser control system is required to minimize laser power fluctuations, and finally, a gas flow system allows for particles to be reacted in various gaseous environments. These six parts will be discussed individually in the remainder of this chapter.

2.1 Electrodynamic balance chamber.

The electrodynamic balance (EDB) consists of three electrodes in a hyperboloidal configuration, the theory of which is completely described by Wuerker et al. [13], Frickel et al. [14], Davis and Ray [4], Ray [6], Philip [15], and Spjut [7]. An exploded view of the electro-

dynamic balance is shown in Figure 2.1, and a cross-sectional view is given in Figure 2.2. The characteristic length, z_0, of our chamber is 4 mm. The chamber creates a dynamic electric field capable of suspending a single, charged, less than 250 μm particle. The AC or ring electrode provides lateral stability to the particle through an imposed AC field oscillating sinusoidally ±2000 volts at 100 Hz. The generated potential field is in the shape of a saddle, and by inverting this saddle 100 times per second, a net time averaged force toward the center is obtained. Since the frequency of the oscillating AC field is faster than the suspended particle's inertial response time, the particle does not drift laterally from side to side. However, if the particle is pushed from the center by an external force, the restoring force on the particle is proportional to the distance from the chamber center. The particle's weight is an external force that pushes the particle below the chamber center. If a DC electric field is introduced across the top and bottom electrodes, the gravitational force can be cancelled out and the particle can be raised to the chamber center where the time varying fields vanish. Therefore, the DC top and bottom electrodes provide vertical stability by cancelling out the gravity force, thus stably suspending the charged particle in the EDB.

The AC and DC electrodes are separated by teflon rings. The majority of the access ports into the center of the chamber are through holes in the teflon through the gaps between the ring and endcap electrodes. These holes allow for the introduction of HeNe laser light for particle illumination, ultraviolet light for charge removal, a syringe for particle injection, and an optical path for particle observation through a microscope. Four other holes are drilled through the AC ring electrode, two for

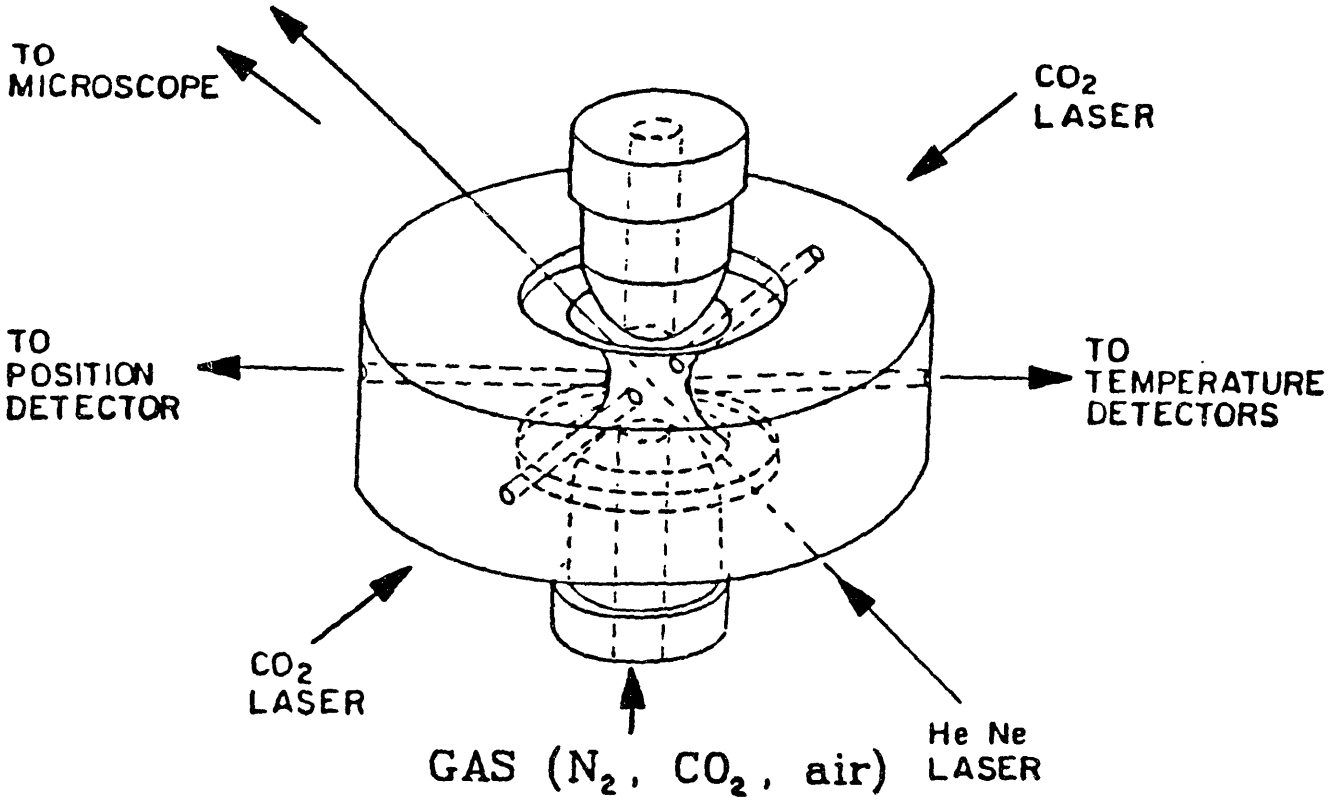

Figure 2.1 : Exploded view of electrodynamic balance.

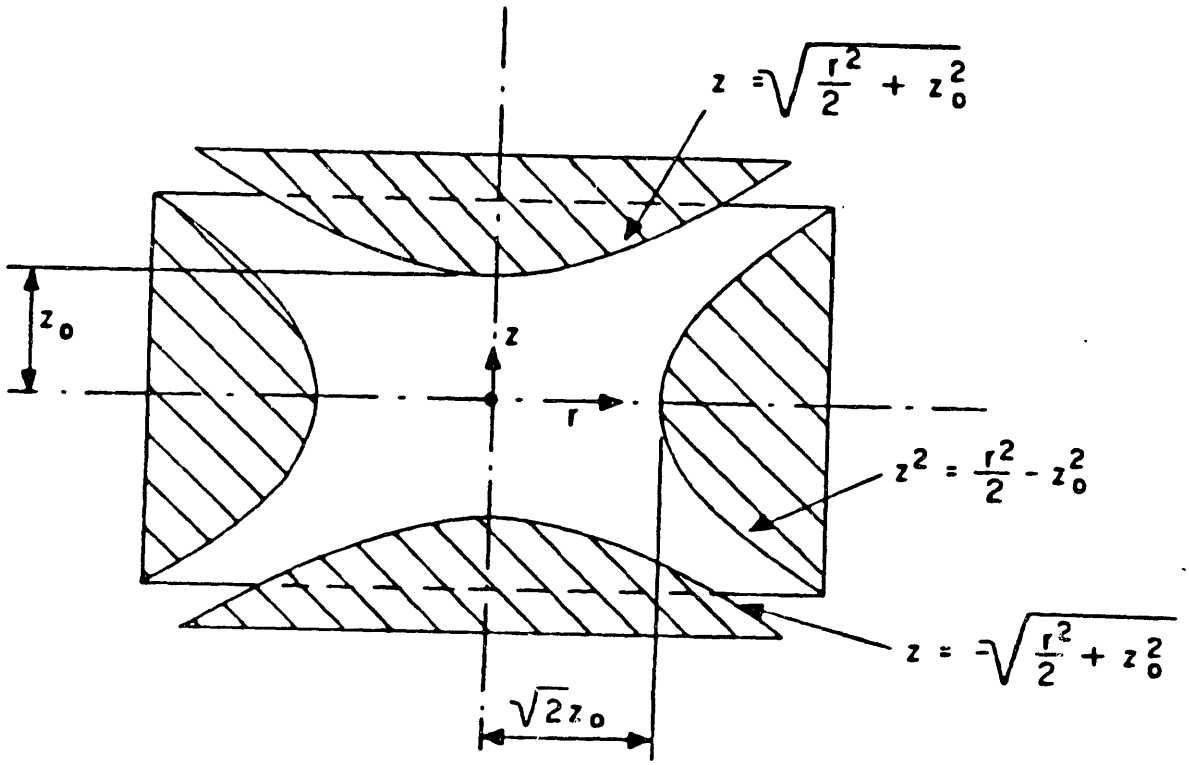

Figure 2.2 : Cross-sectional view of electrodes in electrodynamic balance.

the CO_2 laser beams to enter the chamber, one for the collection of thermal radiation from the particle, and one for the collection of scattered HeNe light from the particle. All holes are sealed by windows to prevent drafts in the chamber from disturbing the particle.

In order to capture a single particle in the center of the electrodynamic balance, many particles (2-50) are injected into the chamber with a 2 cc Micro-mate syringe. The particles are naturally charged by tribo-electrification, half being positively charged, half being negatively charged. Only particles with near the correct mass to charge ratio can be captured. If more than one particle fits the criterion of having near the correct mass to charge ratio, manipulation of the manual AC and DC voltage controls allows for quick capture of a single particle.

The suspended particle is illuminated by a 5 mW Spectra-Physics helium-neon laser or a Dolan-Jenner white light source and can be observed by the experimenter with a x70 Ealing microscope. A graticule in the microscope allows for particle diameter measurements to within ±5 μm. Photographs have been taken of suspended particles with a 35 mm camera attached to a x100 Wild microscope. Examination of these photographs allows for particle diameter measurements to within ±3 μm. High speed movies (2000 frames/sec) have been made using the same Wild microscope.

2.2 Position control system.

Spjut [7] installed a position control system in the electrodynamic balance which automatically adjusts

the voltage on the DC electrodes to keep the particle balanced in the center of the chamber. A schematic of the position control system, taken from Spjut [7], is shown in Figure 2.3. Scattered HeNe light from the particle is collected by a CaF_2 lens located 13 mm from the center of the chamber and is focused down onto a knife-edge prism by a BaF_2 lens. Both CaF_2 and BaF_2 are transparent to HeNe laser radiation. The knife-edge prism and photomultiplier tubes are enclosed in a light-tight steel box. Only HeNe laser light at 632.8 nm is able to pass into the box through a laser-line transmission filter. The signals from the photomultiplier tubes are sent to a log ratio amplifier (AD757P) which takes the log of the ratio of the signal strengths and produces an error signal which is sent to a proportional-integral-derivative (PID) controller. The signal from the PID controller is then amplified by high voltage amplifiers (AD171K) and sent to the top and bottom electrodes. When the particle is exactly centered, the photomultiplier tubes each collect the same amount of HeNe light and produce the same signals. The log ratio is zero, therefore, the position control system acts to keep the voltage on the electrodes the same. If the particle were to move up or down from the center position, more HeNe light would pass over the prism into PMT A or more HeNe light would be reflected up into PMT B. The log of the signal ratio would no longer be zero and an error signal would be produced. The position control system would then increase or decrease the voltage on the electrodes to bring the particle back to the center of the chamber. A complete circuit diagram of the position control system and accompanying PID controller is provided by Spjut [7].

2.3 Heating system.

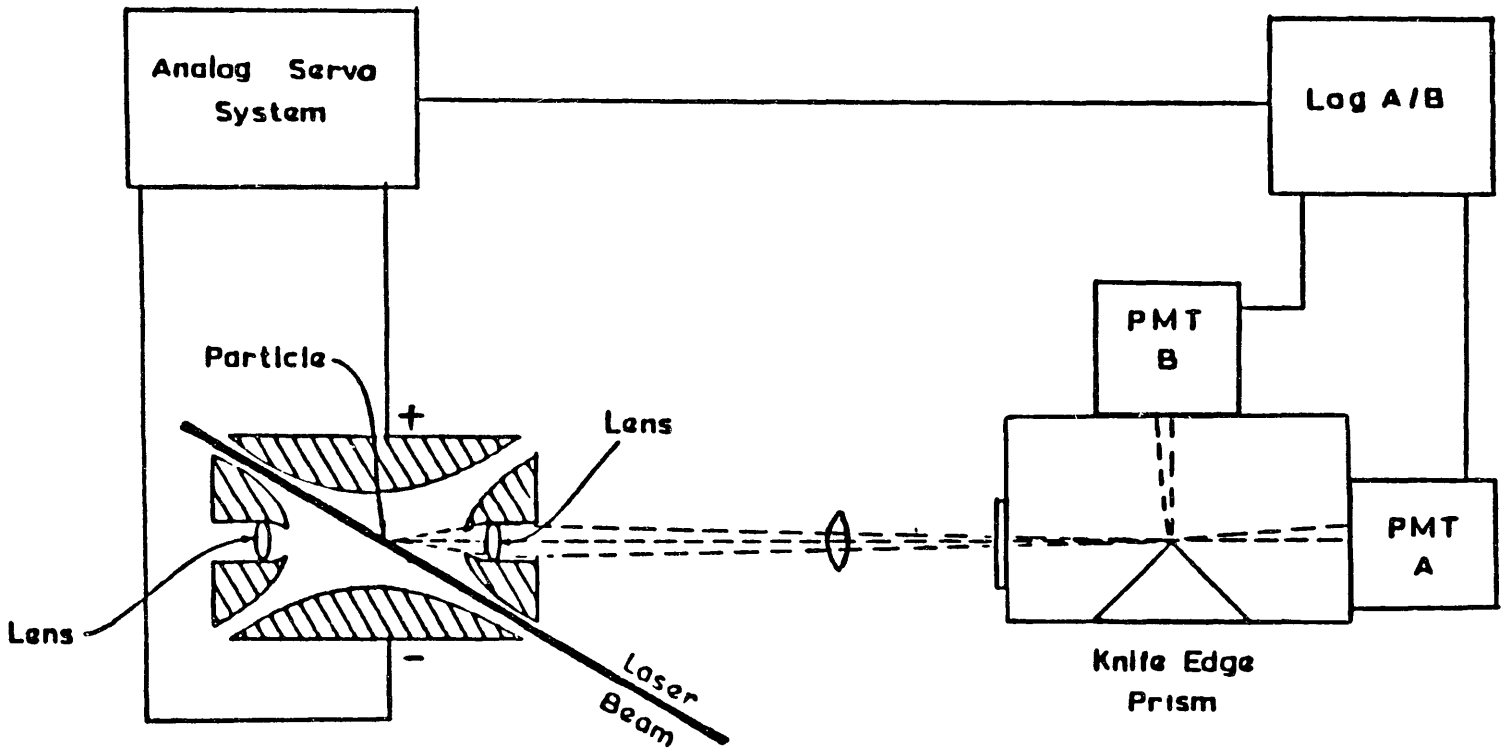

Figure 2.3 : Schematic of position control system for electrodynamic balance from Spjut [7].

The particle is heated by an air-cooled, 20 W, RF165 Laakmann, CO_2 laser with a nominal wavelength of 10.6 μm. Uneven particle heating can cause nonymmetrical photophoretic forces that move the particle from the center of the chamber. Photophoretic forces great enough to cause the particle to be lost from the chamber have been observed. The uneven heating of the particle is due to nonuniform amounts of CO_2 laser radiation being absorbed on or in different sections of the particle, and can be caused by: 1) a nonuniform energy flux incident on the particle, 2) an irregular particle shape, or 3) nonuniform particle absorptivity. Little can be done about the particle shape or absorptivity, but if the particle is heated from two sides, a more uniform energy flux will result. A nonuniform energy flux may still result, however, due to a nonuniform CO_2 laser beam or CO_2 laser power fluctuations.

Two experimental set-ups have been used successfully for heating the particle from two sides. The first set-up has the 20 W CO_2 laser beam split by a ZnSe beamsplitter and each beam focused onto opposite sides of the particle by a ZnSe lens. This set-up has the advantage of easier alignment. Since the two beams are separate, each may be aligned onto the particle separately. The disadvantage is that since the 20 W CO_2 laser beam is initially split in two, each 10 W beam must be focused down to a smaller beam width in order for the same energy flux to reach the particle that would occur if the entire 20 W beam were used. This results in potentially greater particle temperature fluctuations. The ideal CO_2 laser beam is a very large, flat beam. Small particle movements would not cause the particle to move outside the CO_2 laser beam, therefore, the particle would still absorb the same energy flux. By focusing the Gaussian CO_2 laser beam down, the

probability is increased that small particle movements will push it into a region with a different energy flux, resulting in a particle temperature change.

The second experimental set-up has the entire 20 W CO_2 laser beam focused onto one side of the suspended particle by a ZnSe lens. Since only a small fraction of the 20 W beam is actually absorbed by the particle, essentially the entire beam passes all the way through the chamber and is refocused back onto the opposite side of the particle with a gold-plated spherical mirror. The advantage to this experimental set-up is that since the beam is not split, a larger CO_2 laser beam can be used. The disadvantage of this set-up is more difficult alignment. The laser beam that heats one side of the particle is also the laser beam that heats the other side, therefore, the alignment of one side can not be done independent of the other.

2.4 Temperature measurement system.

Temperature measurement is by two color (2 μm and 4 μm) infrared pyrometry, shown schematically in Figure 2.4 and the theory of which is discussed in section 3.4. The suspended particle is heated by a CO_2 laser. This heated particle emits thermal radiation in all directions, a certain solid angle of which is collected by a flouride glass fiber optics bundle 0.144 inches in diameter and 3.5 inches long produced by Infrared Fiber Systems, Inc. These fibers are packed in a 0.156 inch outside diameter brass tube. The transmission loss curve for flouride glass is shown in Figure 2.5. The thermal radiation is then passed through 1) an optical modulator (Laser Precision Corp. #CTX534) with a

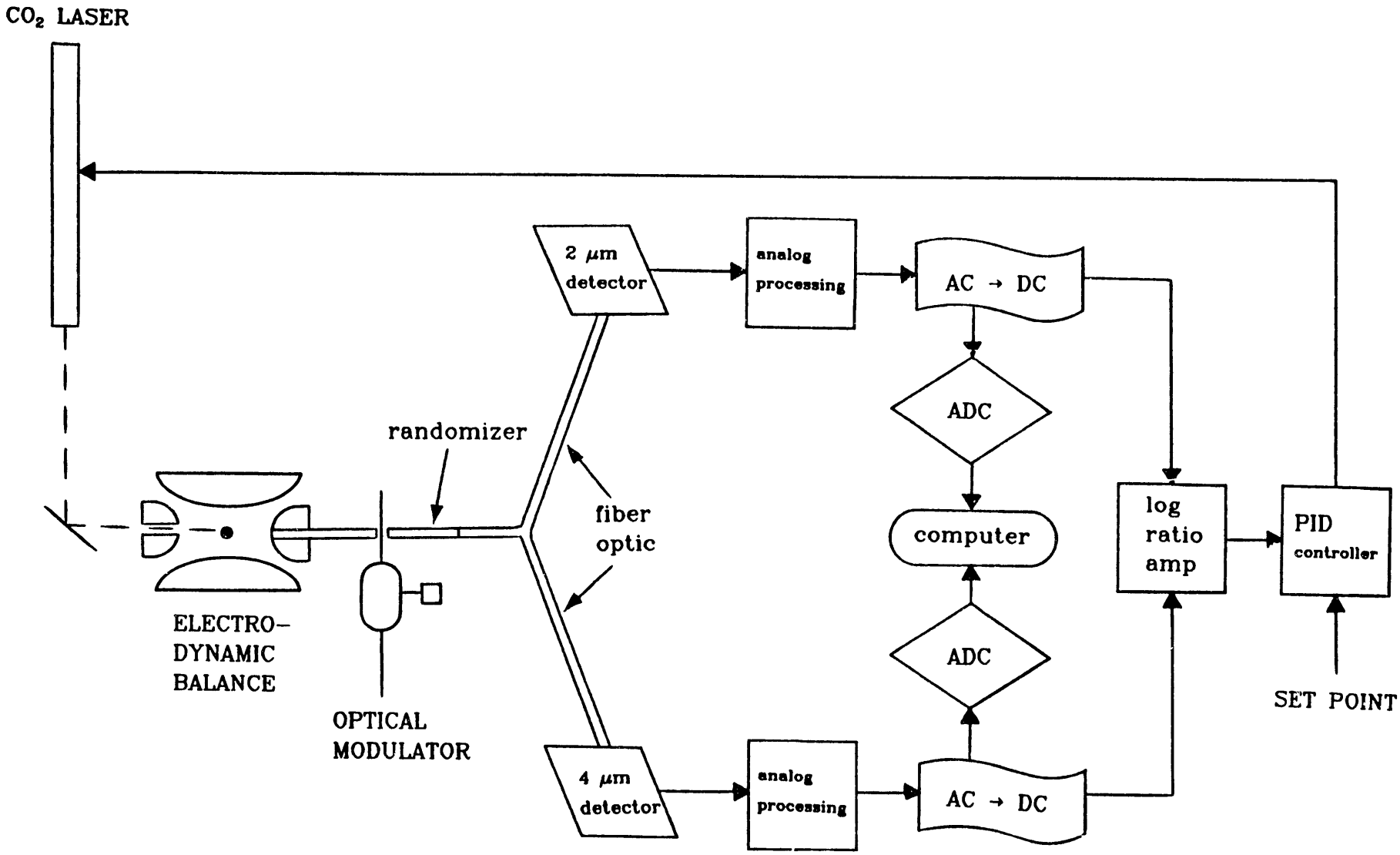

Figure 2.4 : Temperature measurement and CO_2 laser control system for electrodynamic balance.

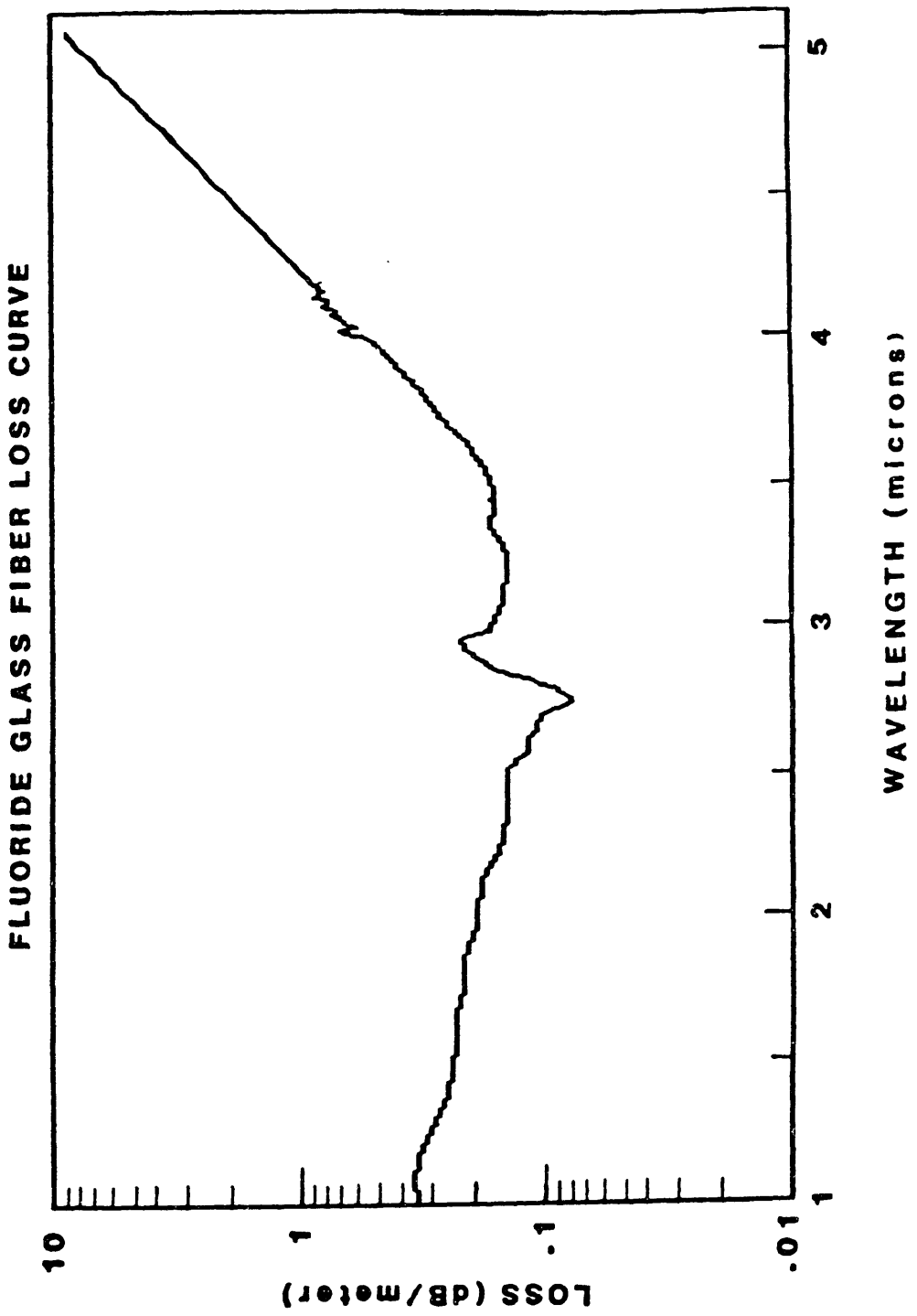

Figure 2.5 : Flouride glass fiber transmission loss curve (from Infrared Fiber Systems, Inc.).

chopping frequency of 1000 Hz, 2) a randomizer, 3) a bifurcated flouride glass fiber optic bundle, and 4) interference filters, which are centered at 2 μm and 4 μm, before entering the liquid nitrogen cooled infrared semiconductor photodiodes (Barnes InSb and Infrared Associates HgCdTe). The signal outputs from the detectors are sent first to Barnes and Infrared Associates preamplifiers, and then amplified and passed through electronic bandpass filters centered at 1000 Hz (Evan Associates 4110), before being sent to true rms-to-DC converters (AD536A). The analog DC signals from the converters are converted to digital signals and sent to the computer for storage.

2.5 CO_2 laser control system.

The need for a temperature control system arises from CO_2 laser power fluctuations that occur over time. Figure 2.6 shows the magnitude of these power fluctuations. A 50 μm type R Omega thermocouple was inserted into the center of the electrodynamic balance and heated by the CO_2 laser beam. The voltage from this thermocouple is plotted versus time for 10 minutes. The thermocouple voltage varied between 5 and 12 mV or 600 and 1110 C in an oscillatory manner. The frequency and magnitude of these oscilliations decrease with time, however, the average value of the thermocouple voltage increases with time.

Figure 2.7 is a similar plot of thermocouple voltage versus time for a run of 92 minutes. The same wild fluctuations (±40%) are seen to occur in the first ten minutes. The fluctuations are dampened in the final 82 minutes but there is still thermocouple drift (±15%).

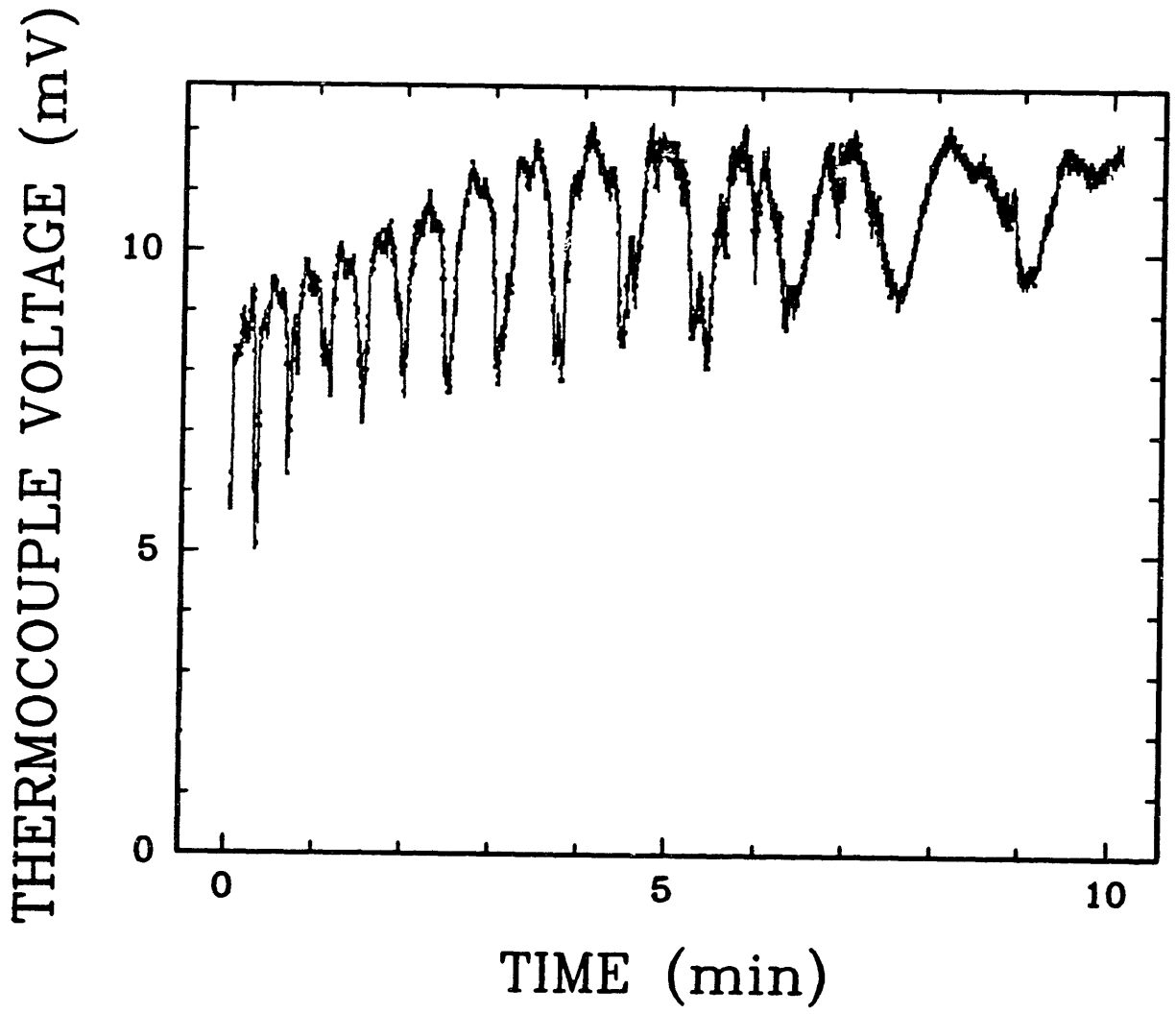

Figure 2.6 : Voltage fluctuations of a 50 μm type R Omega thermocouple being heated by the CO_2 laser for 10 min.

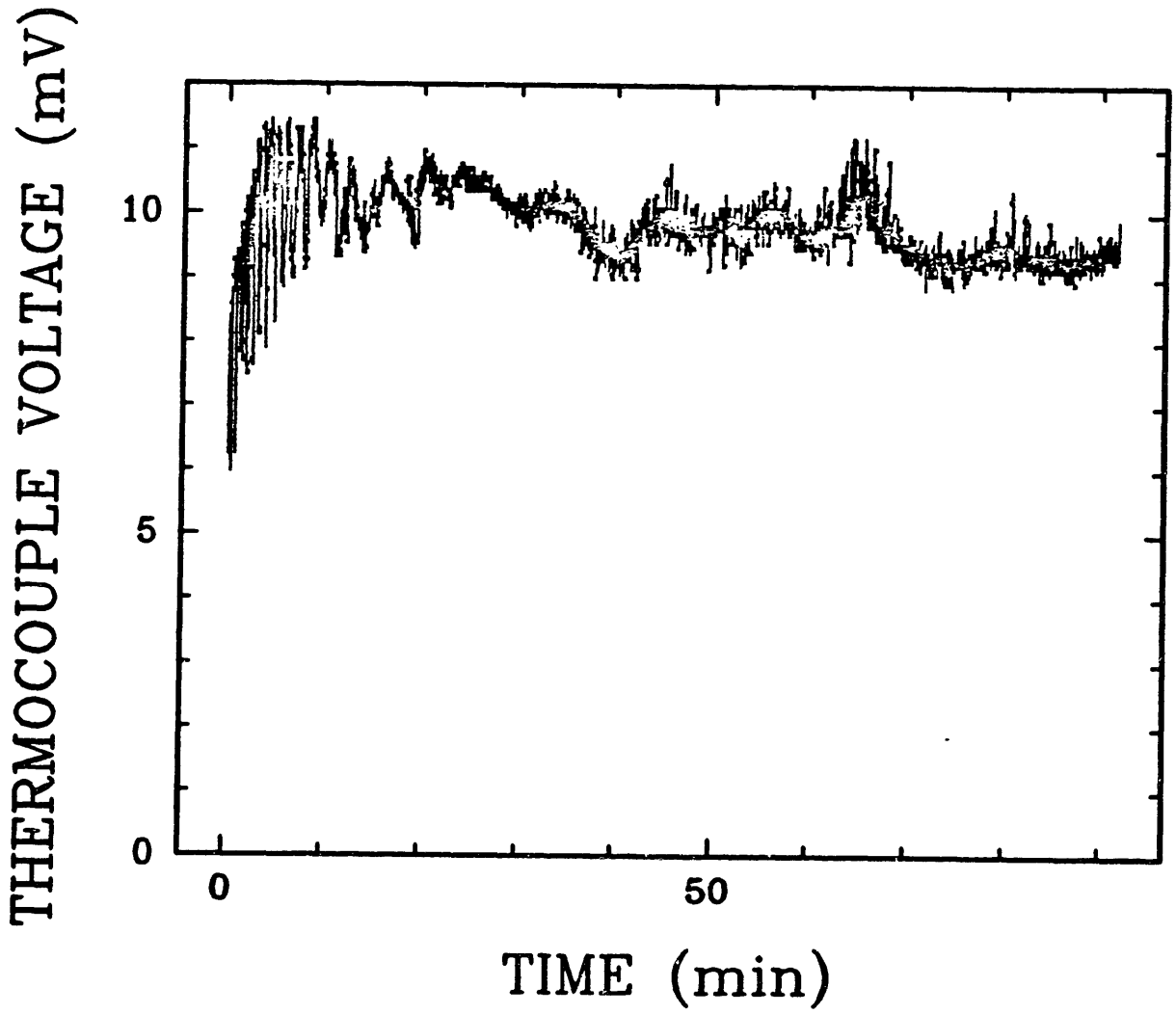

Figure 2.7 : Voltage fluctuations of a 50 μm type R Omega thermocouple being heated by the CO_2 laser for 92 min.

Laser output as measured from an Oriel thermopile is plotted versus time for another ten minute run in Figure 2.8. The thermopile voltage does not vary as much as the thermocouple voltage, but this is probably due to the slower response time of the thermopile. The same decrease in oscillation frequency is seen in Figure 2.8 as in Figures 2.6 and 2.7.

Particle temperature fluctuations can be caused by CO_2 laser power fluctuations or particle movements. From Figures 2.6-2.8, it can be concluded that the CO_2 laser power is not constant, therefore, in an attempt to keep particle temperature fluctuations to a minimum, a CO_2 laser control system has been developed and will be discussed in this section.

As seen in Figure 2.4, the DC signals from the 2 μm and 4 μm detectors are sent to a log ratio amplifier (AD757P) for comparison. The log ratio of the 2 μm and 4 μm signals is used as an error signal and sent to a PID controller, which turns on and off the 20 W CO_2 laser to heat up or cool down the suspended particle. Therefore, a specific 2 μm to 4 μm signal ratio can be held constant throughout an experiment. Since the 2 μm to 4 μm signal ratio is directly related to particle temperature, the temperature control system can be used to maintain a specific temperature throughout an experiment. The control system was developed by Spjut [16] and the circuit diagram is shown schematically in Figures 2.9 and 2.10. It should be pointed out that any temperature sensitive device can be used as the error signal feeding into the PID controller and controlling CO_2 laser output.

Figure 2.11 is a plot of thermopile output voltage versus time with the laser control system in place. In

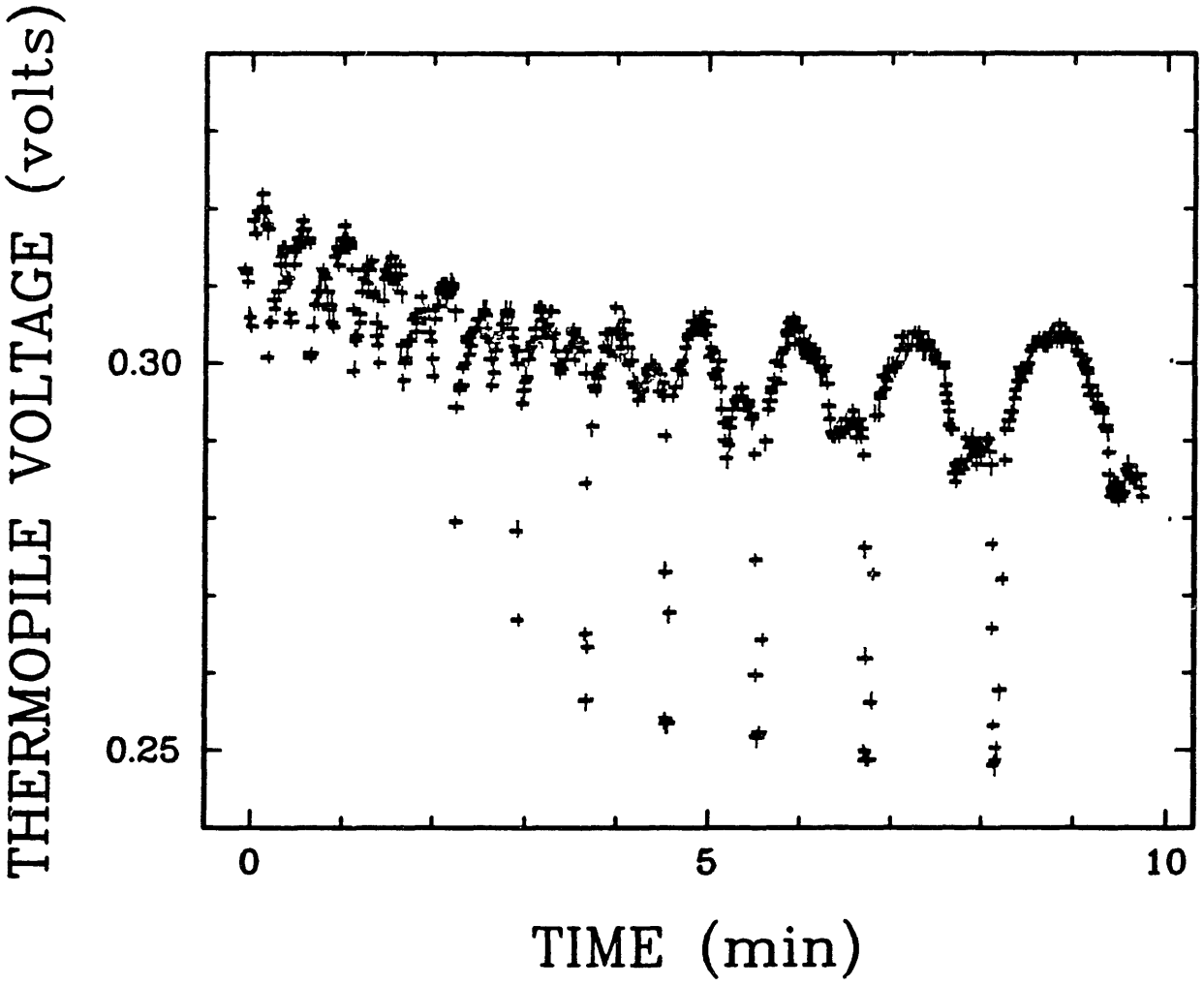

Figure 2.8 : CO_2 laser output as measured by an Oriel thermopile versus time for 10 min.

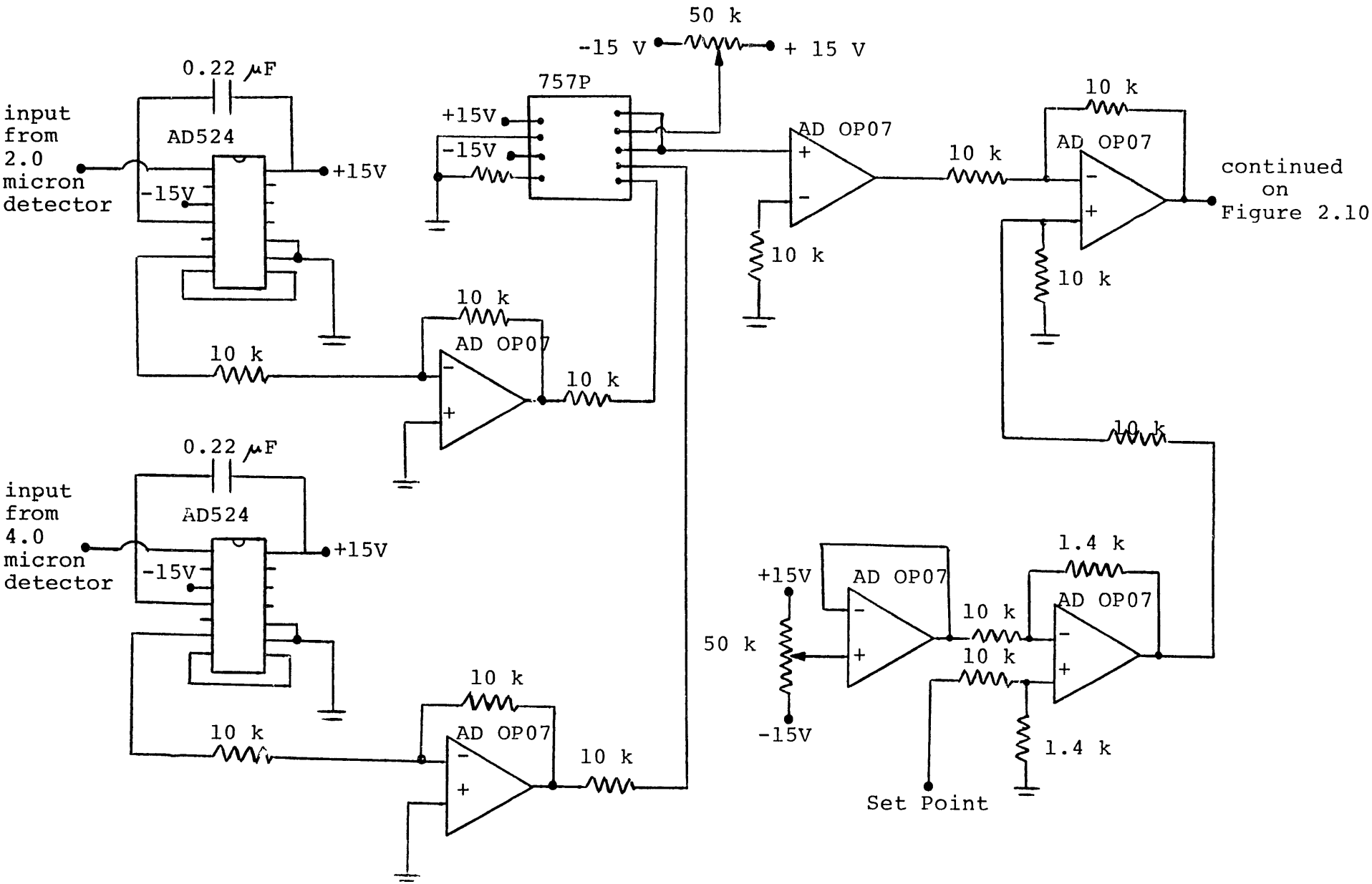

Figure 2.9 : Circuit diagram of the CO_2 laser control system. Continued on Figure 2.10.

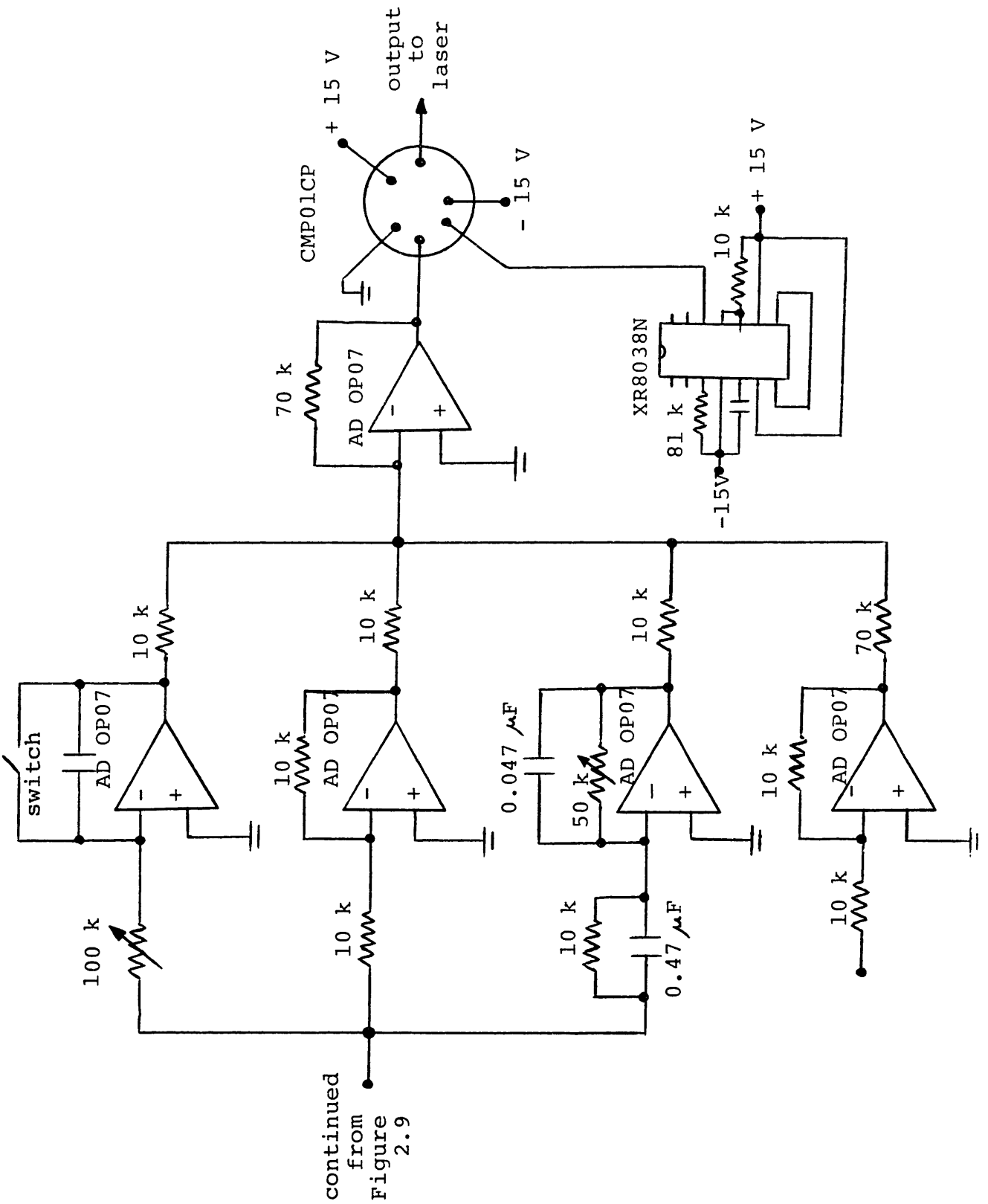

Figure 2.10 : Circuit diagram of the CO_2 laser control system. Continued from Figure 2.9.

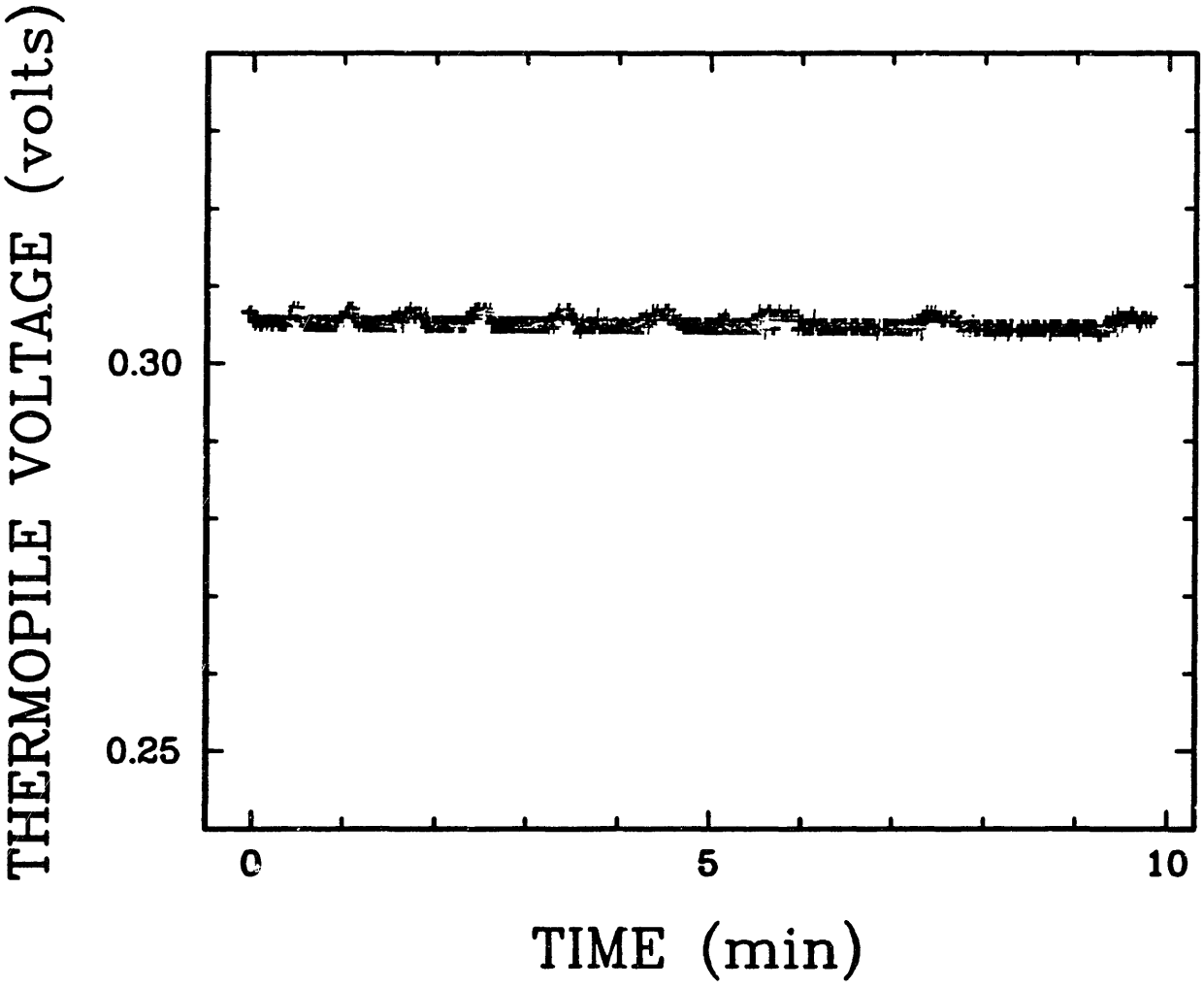

Figure 2.11 : CO_2 laser output (as measured by an Oriel thermopile) with the control system in place versus time for ten min.

this case the thermopile voltage is used as the error signal to the PID controller. Since the error signal comes from a stationary object, temperature control is easy. Temperature control is more difficult when the error signal comes from the levitated particle, which is not stationary.

It can be concluded that CO_2 laser power fluctuations, like those of Figures 2.6, 2.7, and 2.8, could seriously complicate the interpretation of kinetic data obtained in the EDTGA. These fluctuations, which are probably caused by the expansion and contraction of the CO_2 laser tube due to temperature variations, can be minimized somewhat by allowing the CO_2 laser to warm up for at least ten minutes. A much more reliable solution, however, is to use the laser control system described in this section. This can be done in two ways, either the CO_2 laser power output is held constant or the particle temperature is held constant. By splitting off a fraction of the CO_2 laser beam, measuring its energy by thermocouple or other temperature sensitive device, and using this signal as the error signal to the PID controller, the CO_2 laser power output can be held constant. The particle temperature would still be a function of particle size, however. If the log ratio of the temperature detector signals is used as the error signal to the PID controller, the particle temperature can be held constant. This temperature control system greatly simplifies the interpretation of kinetic data obtained in the EDTGA because a constant average particle temperature can be maintained throughout a reaction. Without the temperature control system, the average particle temperature would vary as a function of CO_2 laser power and particle size. Unfortunately, even though a constant average temperature can be maintained, the particle undergoes rapid temperature fluctuations due to control system overshoot

caused by particle movement. A discussion of how to deal with these temperature fluctuations is presented in section 3.6.

2.6 Gas flow system.

The gas flow system of the EDTGA is depicted schematically in Figure 2.12. Cylinder gas is fed through 0.25 inch plastic tubing to a silica gel desicator and into a Brook's mass flow meter (0-60 ml N_2/min). The gas is then transported via 0.25 inch plastic tubing to the electrodynamic balance where it enters the chamber through a 5.56 mm diameter hole in the bottom DC electrode. The gas passes through the chamber and out a similar 5.56 mm diameter hole in the top DC electrode to the atmosphere. To date, the following gases: nitrogen, oxygen, carbon dioxide, and sulfur hexaflouride have been injected successfully in the EDTGA.

It is very important to check the breakdown strength of the gas before injecting it into the chamber. Figure 2.13 is a plot taken from Meek and Craggs [17] of breakdown voltages versus pd for various gases. The gas pressure, p, is in mm Hg, and d is the distance between the closest electrodes. Our system is only capable of atmospheric conditions. Along the asymptotes, the ring and DC electrodes have a gap of approximately 1.5 mm. If the breakdown voltage of the gas is less than the amplitude of the AC field, sparks will fly across the gap and very high voltages will propagate through the electronic system. In our system, pd = (760)(0.15) = 114 mm Hg cm. The amplitude of the AC voltage is approximately 1800 volts. From Figure 2.13, air and

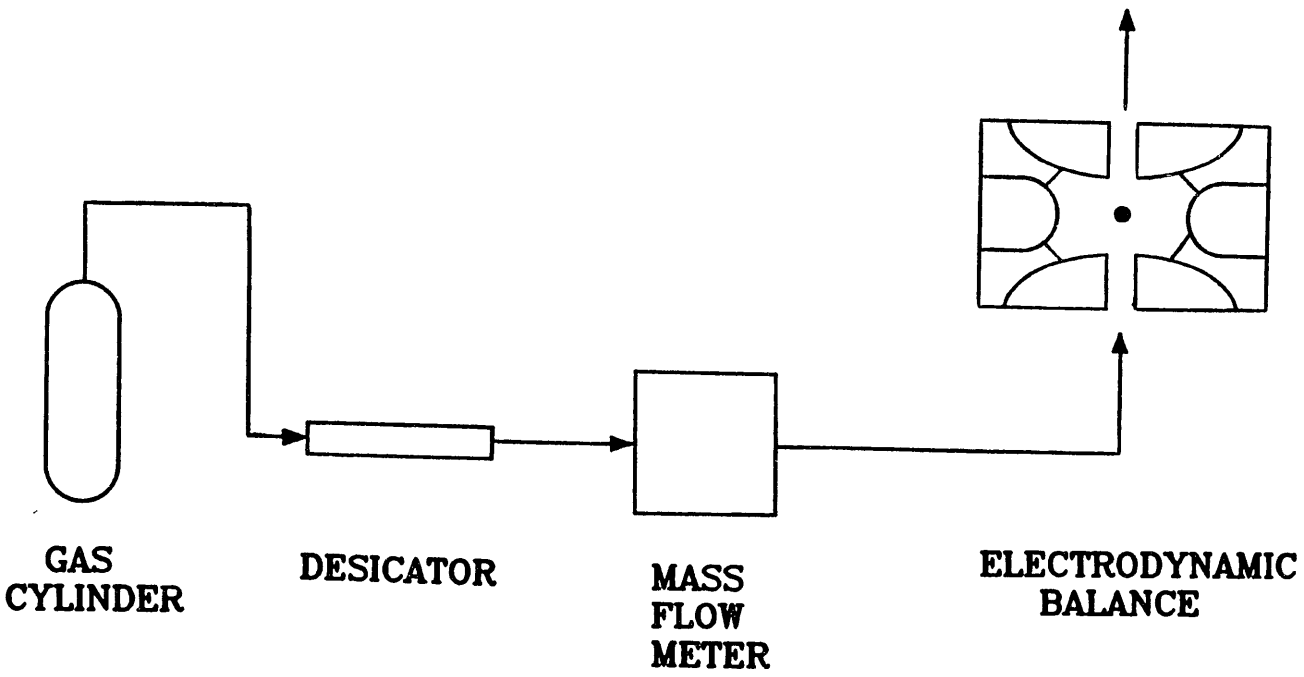

Figure 2.12 : Schematic view of the gas flow system of the electrodynamic balance.

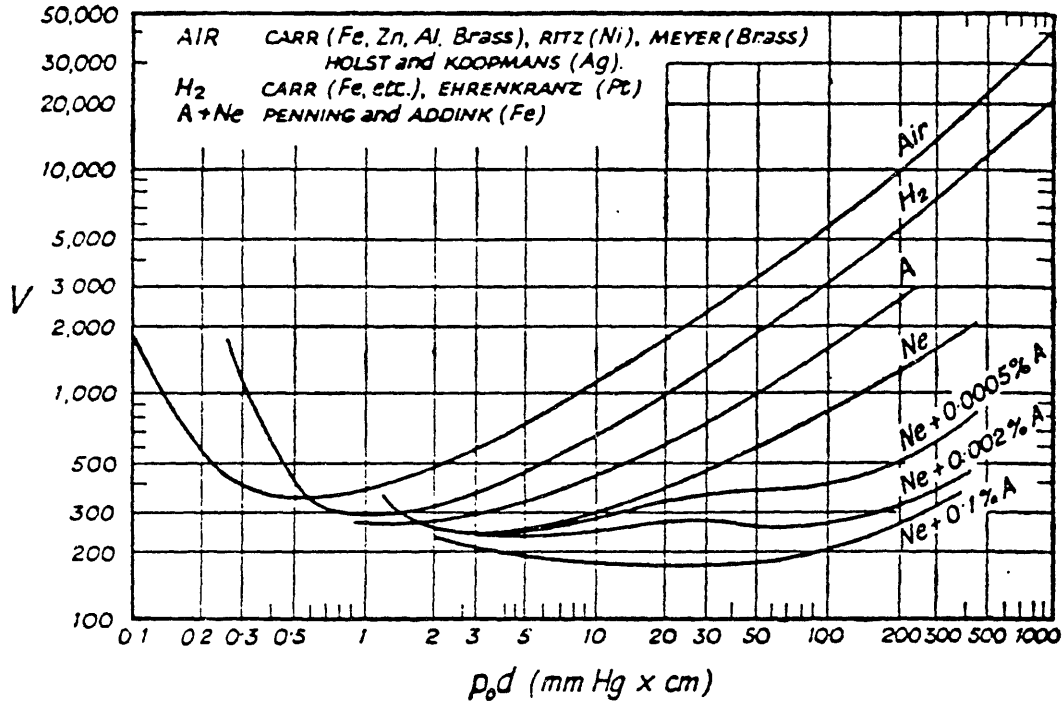

Figure 2.13 : Typical breakdown voltage curves for different gases between parallel plate electrodes. p_0 is the gas pressure in mm Hg corrected to 0 °C. (from Meek and Craggs [17]).

hydrogen appear relatively safe. Argon, however, is boarderline and neon is unsafe. Helium has an even lower breakdown voltage than neon. This unfortunate fact has been experimentally verified.

3. EXPERIMENTAL MEASUREMENT TECHNIQUES.

In this chapter, six different experimental measurement techniques useful in studying single particle gas-solid reactions will be discussed individually. The first three measurement techniques involve characterizing the suspended particle, both initially and at various extents of reaction. The technique for particle diameter measurement via optical microscope is discussed in section 3.1. Particle mass, density, porosity, and excess charge are measured using the aerodynamic drag force technique described in section 3.2, and particle surface area is measured using the technique of CO_2 adsorption and the Dubinin-Polanyi equation as discussed in section 3.3. By utilizing these three measurement techniques, the electrodynamic thermogravimetric analyzer (EDTGA) is capable of measuring the diameter, mass, density, porosity, excess charge, and surface area of a single levitated particle at any stage of its reaction.

The second three measurement techniques enable the electrodynamic balance (EDB) to be used as a thermogravimetric analyzer (TGA) in measuring kinetics of gas-solid reactions. The technique of two color infrared pyrometry (2 μm and 4 μm) is utilized for particle temperature measurement and is discussed in section 3.4. The ability to study and characterize the natural convective drag force is critical before balancing voltage versus time measurements can be converted to mass versus time measurements. The natural convective drag force is discussed extensively in Chapter 4, and the technique of measuring the natural convective drag force is discussed in section 3.5. Finally, kinetic measurement techniques are discussed in section 3.6.

3.1 Single particle diameter measurements.

Diameters of single particles suspended in the EDTGA are measured via one of two microscopes attached to the system. A (x70) Ealing microscope can be used to observe the particle through the asymptote between the top and ring electrodes. This observation angle allows for measurement of the vertical movement of the particle. The Ealing microscope is used for particle capturing, balancing, and weighing. It is also used for measuring the natural convective drag force of heated particles and the surface area of unheated particles. The Ealing microscope also has associated with it a graticule that allows for diameter measurements to ± 5 μm.

A Wild (x100) microscope allows observation of the particle through the top DC electrode. A 35 mm camera may be attached to the Wild microscope and photographs can be taken for more exact diameter measurements. An example of one of these photographs of a "Spherocarb" particle is shown in Figure 3.1 along with a partial photograph of a scale which can then be used to measure the particle diameter. The 100 unit scale (of which only 54 units are shown) is 1.0 mm in length. The particle in Figure 3.1 is 202 μm in diameter. Particle diameter measurements taken in this fashion are good to within ± 3 μm.

A high speed (2000 fps) movie camera may also be attached to the Wild microscope to allow for particle observation during a very fast reaction.

3.2 Use of aerodynamic drag in measurement of single particle

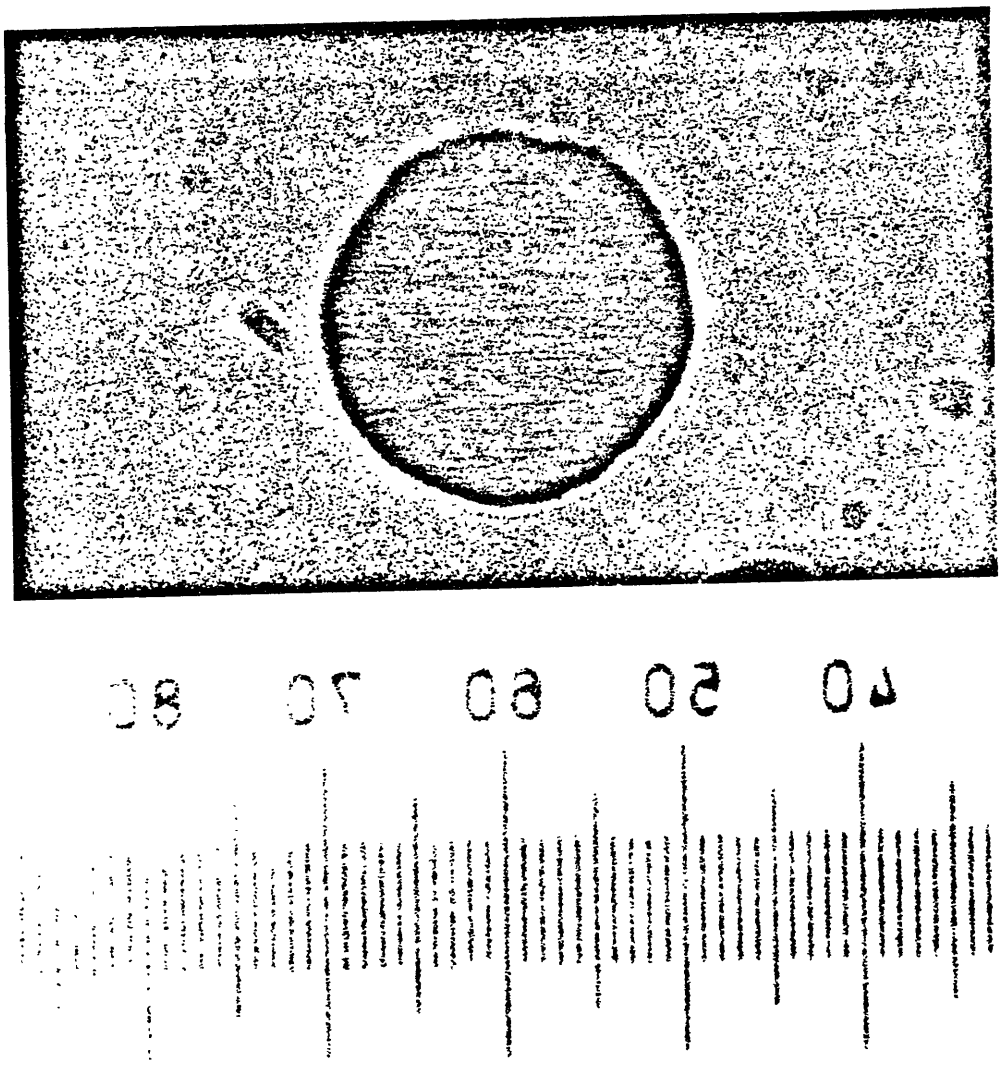

Figure 3.1 : Photographs of a 202 μm diameter "Spherocarb" particle in the electrodynamic balance and a scale. 100 units on scale = 1 mm.

mass, charge, and density.

3.2.1 Motivation.

The most straightforward method of studying single particle gas-solid reactions is to follow the particle weight versus time. A force balance on a suspended particle in an electrodynamic balance yields:

$$mg = qE \tag{3.1}$$

where: m = particle mass (kg).
g = gravitational acceleration (m/sec^2).
q = excess charge on the particle (coul).
E = Electric field strength in the vertical direction (volt/m).

The electric field strength in the vertical direction in an EDB can be written:

$$E = CV/z_0 \tag{3.2}$$

where: C = chamber constant = 0.4 (dimensionless).
V = balancing DC voltage across the endcap electrodes (volts).
z_0 = characteristic length of the EDB chamber = 0.004 m.

Combining equations 3.1 and 3.2 yields:

$$mg = qCV/z_0 \tag{3.3}$$

or

$$V = (gz_0/C)(m/q) \qquad (3.4)$$

The term (gz_0/C) is a constant. If the number of charges on the particle remains constant, and if no unknown vertical forces are present, and if the initial mass is known, a voltage versus time curve will be sufficient to determine the reaction rate. Under these conditions the electrodynamic balance can be used as a TGA (i.e. collecting continuous weight versus time data). It will be seen later (Chapter 4) that a natural convective drag force also acts in the vertical direction upon particle heating. This force is characterized in Chapter 4 and is therefore a known force. If the number of charges on the particle is not constant, the electrodynamic balance will have to be operated in a discrete mode. After a certain conversion, the reaction will be stopped and the particle reweighed. The number of reweighings will depend on the number of points desired on the particle weight versus time plot. Regardless of the mode in which the EDB is to be operated, in order to follow single particle gas-solid reactions, a simple method of weighing particles in the EDB is necessary.

3.2.2 Previous methods.

The mass of spherical particles with known density can be calculated by measuring the particle diameter, which can be done by microscope (for larger particles, $>$ 50 μm), by light scattering (for smaller particles, $<$ 10 μm), or by terminal velocity measurements for any size particle. The mass of a suspended liquid droplet or a nonporous solid particle of known density can be determined in this way.

Another method of particle mass measurement is electron stepping [10,11]. This method involves knocking off elec-

trons from the particle surface with an ultraviolet light source. Equation 3.4 has two unknowns, particle mass and number of charges. If the number of charges is reduced by some integral amount, the mass will remain constant and the balancing voltage will increase. By performing enough steps, the difference in balancing voltage for a one electron loss can be determined and the particle mass can be calculated. The electron stepping technique is independent of particle shape, but is limited to particles less than 20 μm in diameter [7]. Larger particles require large numbers of charges to be suspended and it becomes impossible to distinguish changes in balancing voltage for a one electron loss.

Davis and Periasamy [18] used aerodynamic drag as a means of determining particle diameter for particles of known density. They introduced an upward flow of gas into the chamber through the bottom electrode. The flow rate needed to reach terminal velocity (i.e. the flow rate needed to suspend the particle with no DC field) is measured and is a known function of particle diameter. Sageev et al. [19] also used aerodynamic drag to determine particle diameter in an electrodynamic balance. By turning off the electric field momentarily, the particle begins to fall due to gravity and quickly reaches terminal velocity. The terminal velocity is determined by measuring the time required for the particle to fall a specific distance. The terminal velocity methods are strictly valid only for particles with known drag force coefficients. More recently, Davis et al. [20] used aerodynamic drag at low flow velocities to determine particle mass or diameter.

3.2.3 Theory.

Since in this work, particle density is generally not known, aerodynamic drag has been used as a method of particle mass measurement. If the particle is spherical and the diameter can be determined, the particle mass can be calculated by measuring the drag force as a function of volumetric flow rate of gas around the suspended particle. The volumetric flow rates of gas were selected to yield velocities well under the terminal velocity.

Figure 3.2 depicts the vertical forces on an unheated, suspended particle with an upward gas flow. The corresponding force balance yields an equation slightly more complicated than equation 3.1:

$$mg = qE + F_a \tag{3.5}$$

where F_a is the aerodynamic drag force on the particle.

Since Re $\ll$ 1, the aerodynamic drag on the particle is described by Stokes' law:

$$F_a = 3\pi\mu vd \tag{3.6}$$

where μ is the gas viscosity, v is the gas velocity, and d the particle diameter.

With no gas flow around the particle:

$$mg = qCV_i/z_0 \tag{3.7}$$

where V_i is the DC voltage across the endcap electrodes required to balance the levitated particle in the absence of aerodynamic drag.

With gas flow in the upward direction:

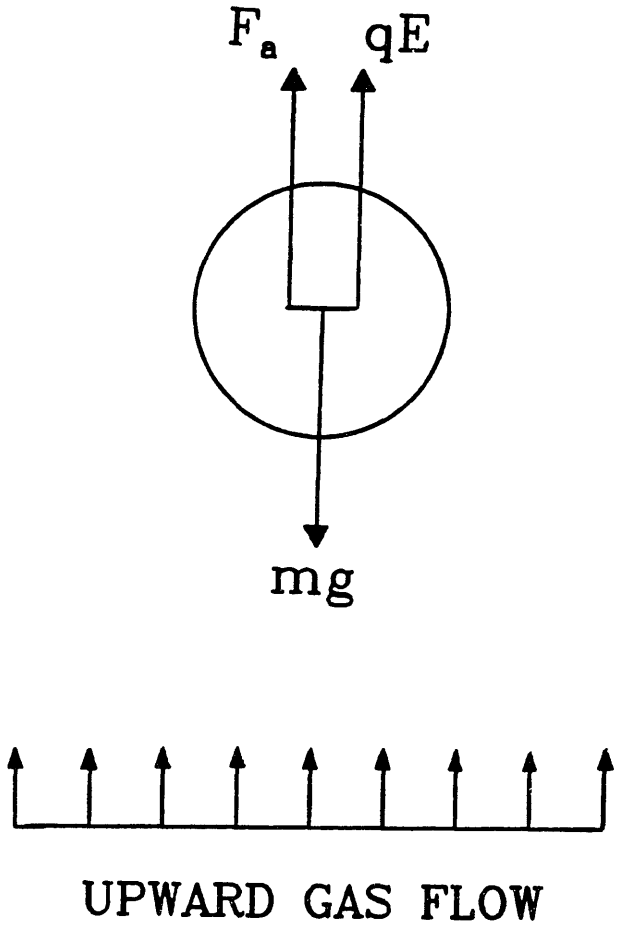

Figure 3.2 : Vertical force balance on an unheated particle suspended in an electrodynamic balance experiencing an upward gas flow.

$$mg = qCV/z_0 + 3\pi\mu vd \qquad (3.8)$$

where V is the DC voltage across the electrodes required to balance the difference between weight of the particle and the aerodynamic drag resulting from the gas flowing around the particle at velocity, v.

Over a small range of volumetric flow rates:

$$v = KQ \qquad (3.9)$$

where K is a constant determined primarily by the chamber configuration (e.g. shape of electrodes, z_0, and diameter of holes in top and bottom electrodes through which gas flows) and Q is the volumetric flow rate.

For spherical particles:

$$mg = (\pi/6)d^3\rho_p g \qquad (3.10)$$

where ρ_p is the apparent particle density.

Combining equations 3.7, 3.8, 3.9, and 3.10 and rearranging yields:

$$\Delta V_{aero} = \bar{K}V_i Q/(\rho d^2) \qquad (3.11)$$

where $\Delta V_{aero} = V_i - V$, and $\bar{K} = 18\mu K/g = 18\mu v/gQ$ is a proportionality constant that can be determined by means of a calibration procedure using particles of known density. From equation 3.11, the apparent particle density, and hence its mass and charge, can be determined from measurement of V_i and ΔV_{aero} versus Q for a particle of known diameter.

3.2.4 Calibration Runs.

Because the flow field of gas through the chamber is not known, calibration runs must be performed to back out the velocity of gas over the suspended particle as a function of volumetric flow rate. Eight calibration runs were performed on glass spheres with a known density of 2.5 g/cm^3 and diameters ranging from 50 μm to 130 μm. The particle diameter, d, and the balancing voltage in the absence of flow, V_i, are determined first, then the change in balancing voltage, ΔV, at different flow rates, Q, are measured. Typical results are shown in Figure 3.3 for spheres of 72, 74, 109, and 124 μm. The linearity of the data shown in Figure 3.3 indicates the validity of the aerodynamic drag technique in the range of gas flow rates tested. The slopes of the voltage versus flow rate data, together with measurements of V_i and particle diameter, can be substituted in equation 3.11 to determine the constant $\bar{K}$, which was found to have a value of 0.848 kg sec m^{-4}. The standard deviation for the eight calibration runs was 0.0153.

3.2.5 Gas flow field inside the electrodynamic balance.

Given the $\bar{K}$ determined from calibration in the previous section, it is possible to say something about the gas flow field in the EDB. $\bar{K}$ can be written:

$$\bar{K} = 18\mu v/gQ \qquad (3.12)$$

Substituting values for the viscosity of N_2 at 300 K and

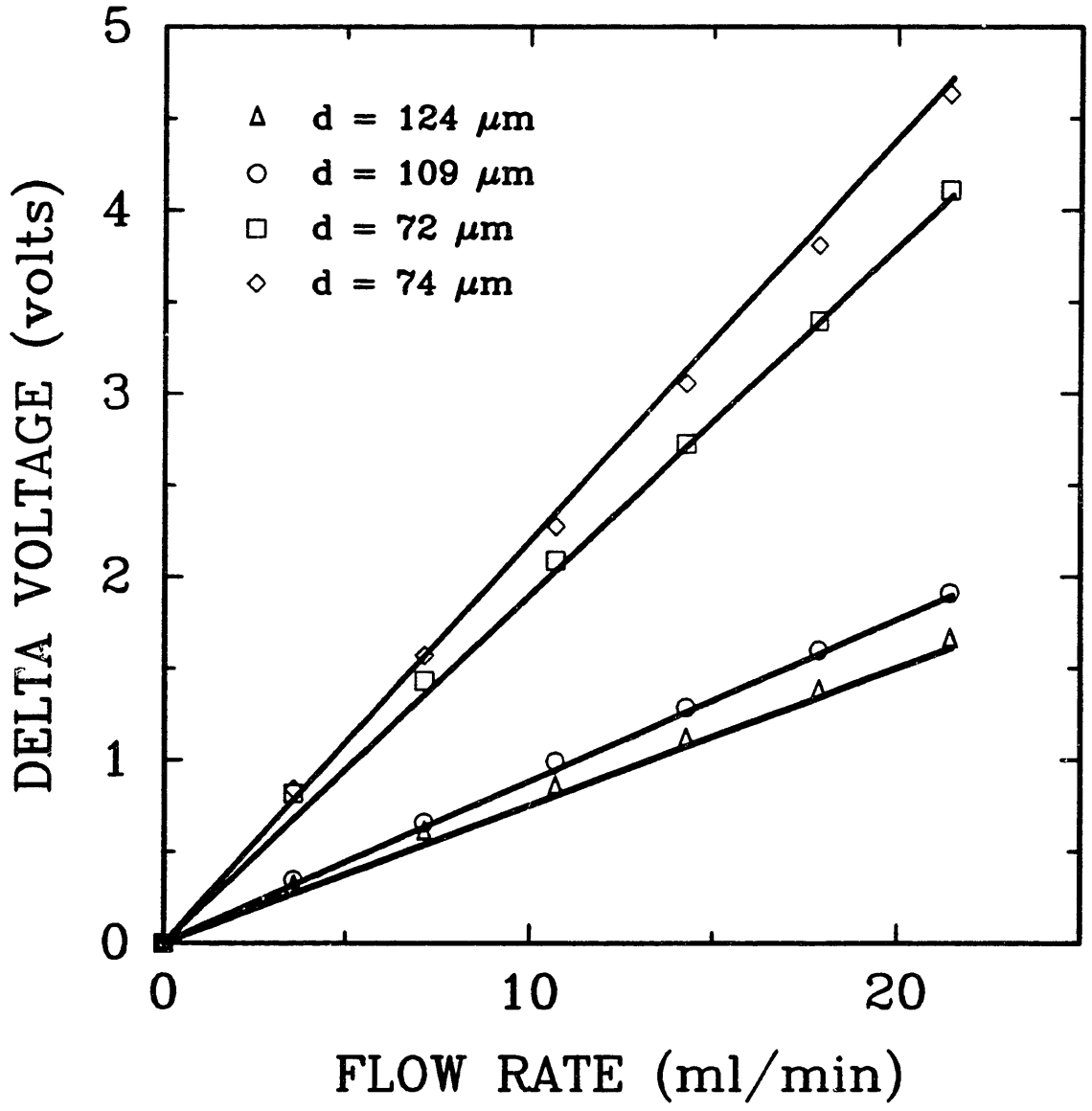

Figure 3.3 : Change in balancing voltage versus volumetric flow rate for four calibration runs performed on glass spheres with a density of 2.5 g/cm^3.

the gravitational acceleration yields:

$$\bar{K} = 3.275 \times 10^{-5} \ (v/Q) \qquad (3.13)$$

where $\bar{K}$ has the units of kg sec m^{-4}, v has units of m/sec, and Q has units of m^3/sec. Figure 3.4 shows two theoretical limiting cases of the gas flow field inside the EDB. In one case the gas flow field expands to completely fill the chamber and in the other case the flow field does not expand. By examining the predictions of $\bar{K}$ from these two limiting cases, we can get an idea of what the actual flow field looks like in the EDB during weighing by the aerodynamic technique.

For example, Figure 3.4a depicts a fully developed parabolic flow field moving through the bottom electrode. Due to the slow movement of the gas, upon entering the EDB chamber, the flow field expands completely to the walls of the ring electrode and forms a plug flow profile going through the hole in the ring electrode. Therefore, the gas velocity over the particle would be:

$$v = Q/A \qquad (3.14)$$

where: A = cross sectional area of the hole in the ring electrode.

$= 2\pi(z_0)^2$

$= 0.000101 \ m^2$

Therefore, the smallest $\bar{K}$ possible would be:

$$\bar{K}_{smallest} = 3.275 \times 10^{-5} \ (1/A)$$

$$\bar{K}_{smallest} = 0.324 \text{ kg sec } m^{-4}$$

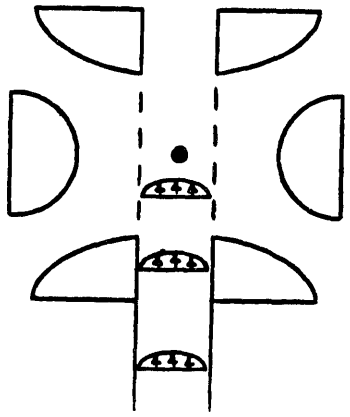

Figure 3.4b : Fast volumetric gas flow rate producing a nonexpanding parabolic gas flow field through the electrodynamic balance.

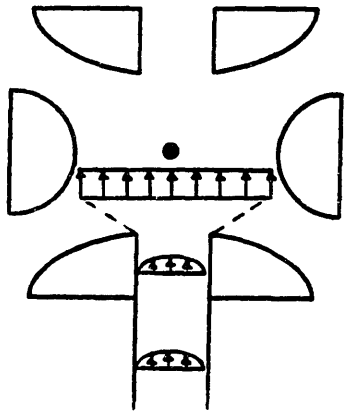

Figure 3.4a : Slow volumetric gas flow rate producing an expanded plug flow field through the electrodynamic balance.

On the other hand, Figure 3.4b depicts a fast moving gas stream that does not expand upon entering the chamber. In this limiting case, the gas would retain its parabolic profile through the chamber. In this case the gas velocity over the particle would be:

$$v = 2\langle v \rangle \tag{3.15}$$

where $\langle v \rangle$ represents the average velocity of gas through the chamber. Therefore, the gas velocity over the particle can be written:

$$v = 2Q/A \tag{3.16}$$

where: A = cross sectional area of the hole in the bottom electrode.

$= \pi(2.78 \text{ mm})^2$

$= 2.428 \times 10^{-5} \text{ m}^2$

Therefore, the largest $\bar{K}$ possible would be:

$$\bar{K}_{largest} = 3.275 \times 10^{-5} \ (2/A)$$

$$\bar{K}_{largest} = 2.697 \text{ kg sec m}^{-4}$$

Our calibrated value of 0.848 kg sec m^{-4} lies in between these two limits but much closer to the expanded plug flow case. The difference may be due to the fact that the flow is not fully developed, before engaging the particle.

Figure 3.5 is a plot of balancing DC voltage needed to suspend a "Spherocarb" particle versus volumetric flow rate of N_2 through the chamber. At lower flow rates (<30

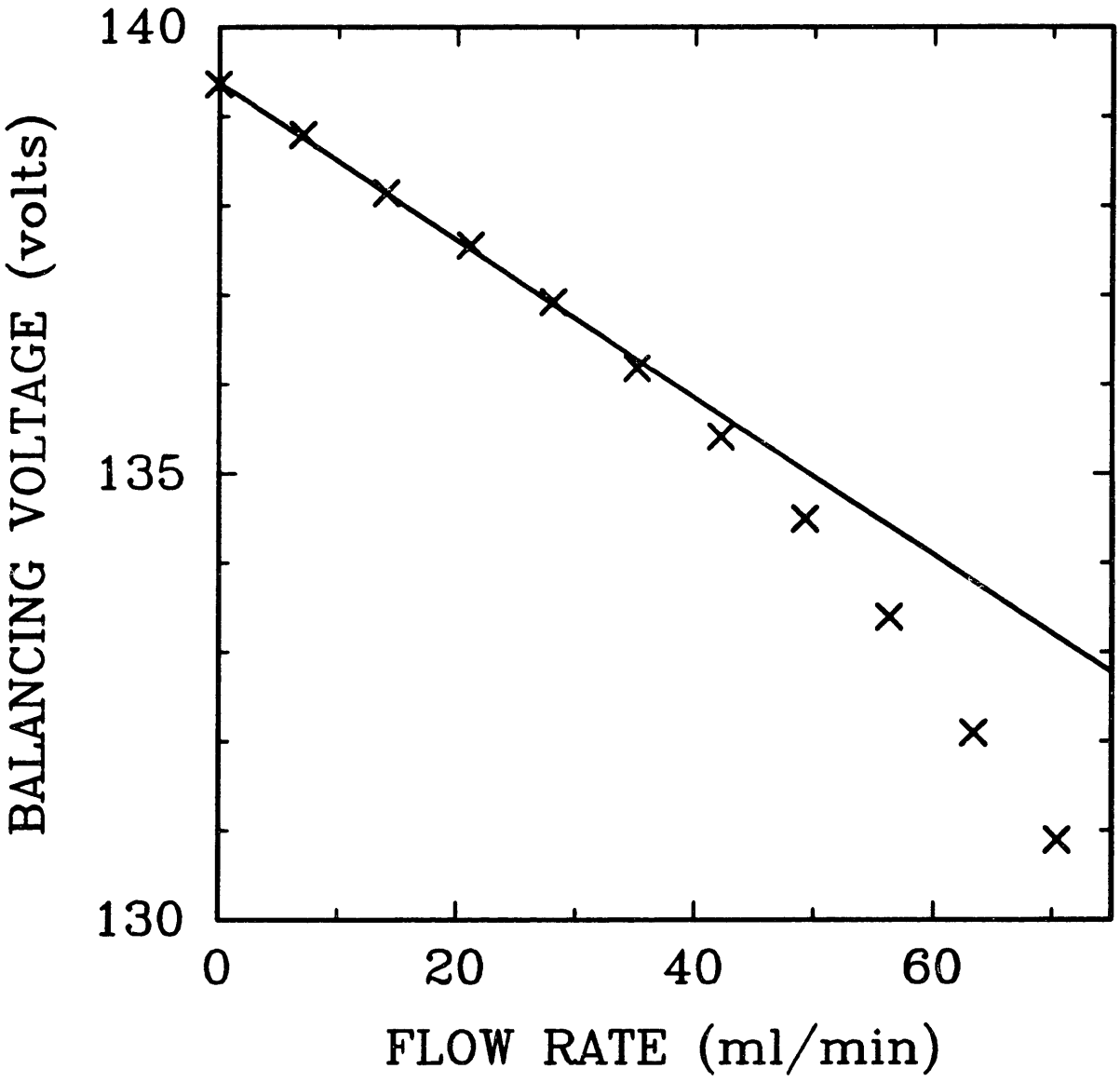

Figure 3.5 : Balancing DC voltage required for levitating a "Spherocarb" particle versus volumetric flow rate of nitrogen through the chamber.

ml/min), the plot is linear, which means that the velocity profile is not changing with volumetric flow rate. Therefore, our assumption in equation 3.9 that v is proportional to Q is valid. The true gas velocity profile probably looks something like the profile in Figure 3.4a. At higher flow rates (>30 ml/min), however, it is believed that the velocity profile is changing, probably not expanding as much before reaching the particle. Therefore, the particle (which sits on the centerline of this profile) sees a faster velocity than expected. This can be seen in Figure 3.5, as the measured balancing voltages become less than that predicted by assuming v is proportional to Q.

It can be concluded that $\bar{K}$ is constant up to a volumetric flow rate of 30 ml/min. At higher flow rates, $\bar{K}$ becomes a function of the volumetric flow rate.

From equation 3.13 and our calibrated value of $\bar{K}$ = 0.848 kg sec m^{-4}, the gas velocity in the vicinity of the suspended particle can be calculated:

$$v = 0.0432Q \tag{3.17}$$

where: v = gas velocity in the vicinity of the particle (cm/sec).
Q = volumetric flow rate of gas through the chamber (ml/min).

Figure 3.6 is a plot of gas velocity versus volumetric flow rate. Using this plot, the Reynold's number of a particle can determined.

$$Re = \langle v \rangle \rho d/\mu \tag{3.18}$$

At a volumetric flow rate of 21.4 ml/min, the Re for a

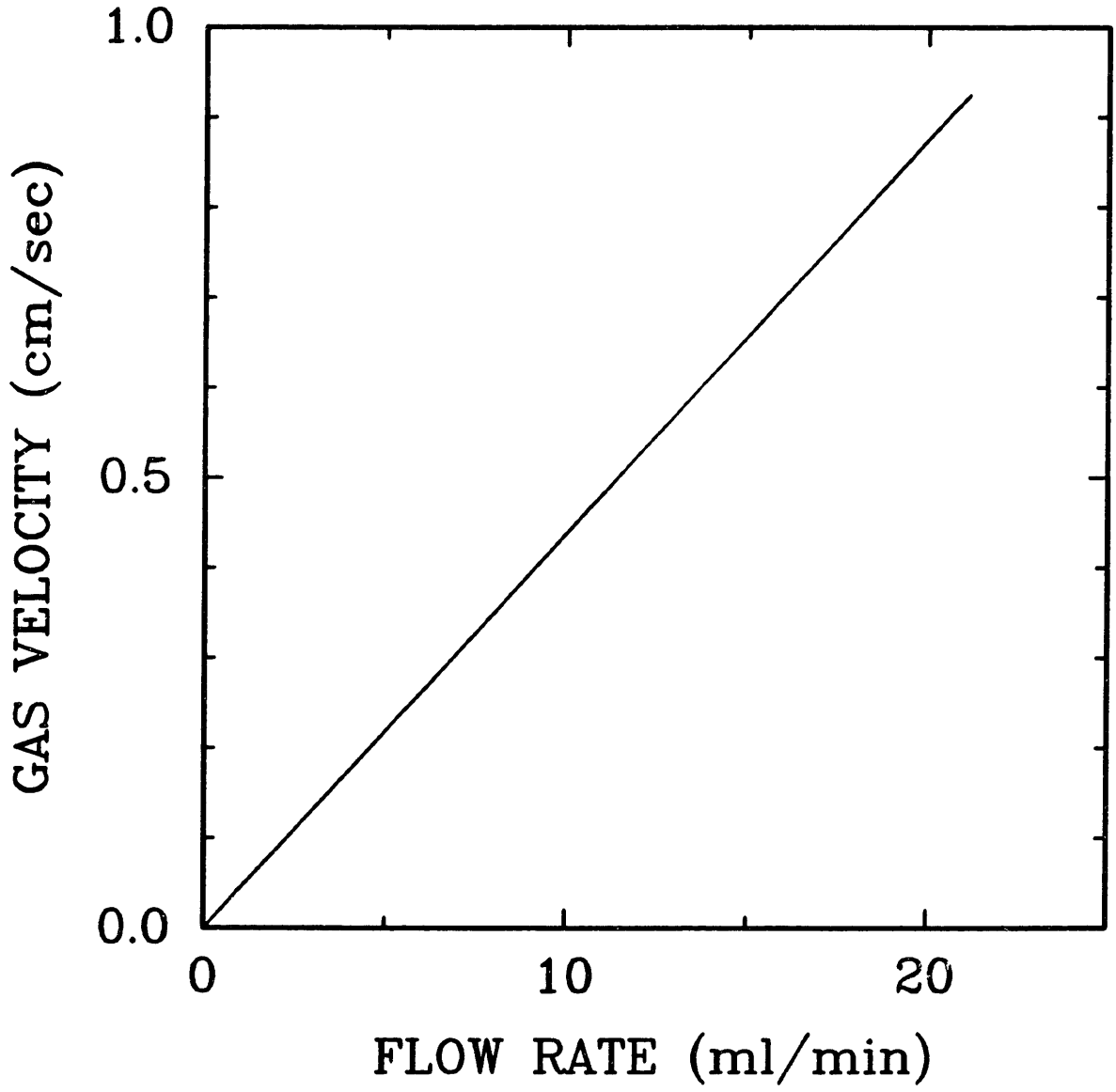

Figure 3.6 : Gas velocity around a particle levitated in the electrodynamic balance versus volumetric gas flow rate.

100 μm diameter particle is 0.06.

3.2.6 Experimental procedure.

The aerodynamic weighing procedure begins by capturing a single particle in the EDB. The EDB chamber is then flushed for 20 minutes at 42.9 ml N_2/min. This will ensure a uniform gas mixture inside the 1.0 ml EDB chamber in which the particle is suspended. Chromatographic-grade N_2 gas is supplied via cylinders and its flow rate is monitored by a Brooks mass flow meter (0-71.4 ml N_2/min). After the chamber is flushed, the flow rate of N_2 is decreased to 21.4 ml/min (or a value of 300 on the digital scale of the Brooks mass flow meter). Less than one minute is required for the flow field inside the chamber to reach an equilibrium state. The program WEIGH is then activated on the LABTECH 70. This program will record the voltages on the Keithley multimeter whenever a footpetal is pressed. The DC voltage is then manually adjusted to exactly balance the suspended particle. This DC voltage is then recorded on the computer by pressing the footpetal. This process is repeated until four separate DC balancing voltages have been recorded for this specific flow rate. The flow rate is then decreased by 3.6 ml/min (or to a value of 250 on the digital scale of the Brooks mass flow meter) and four more DC balancing voltages are recorded. The process is repeated until four DC balancing voltages have been recorded for N_2 flow rates of 21.4, 17.9, 14.3, 10.7, 7.1, 3.6, and 0.0 ml/min (or Brooks mass flow meter readings of 300, 250, 200, 150, 100, 50, and 0). After all of the DC balancing voltages have been recorded, the program STOKESLO is activated on the LABTECH 70. This program calculates the average DC balancing voltage for each of the seven N_2 flow rates and plots the

change in DC balancing voltage versus volumetric N_2 flow rate. The program then uses the slope and intercept of this plot, along with the measured diameter of the particle, to calculate the particle density and mass. This procedure for weighing takes approximately 10 minutes to perform (not including the 20 minute N_2 flush time). Printouts of the programs WEIGH and STOKESLO are found in Appendix A.

3.2.7 Examples of weighings.

An example of the aerodynamic weighing technique is presented in Figure 3.7. Two separate weighings were performed on a 245 μm diameter "Spherocarb" particle and the results are presented in the form of DC balancing voltage versus volumetric flow rate. The "Spherocarb" particle is balanced with respect to a graticule on the lens of the Ealing microscope. The small systematic difference in balancing voltage at each flow rate between the two weighings was due to a movement of the microscope between the weighings. Also, the upward curvature of the data at flow rates close to zero is probably due to diffusion of water into the chamber and absorption in the "Spherocarb" which results in a real weight gain.

The raw data are displayed in Table 3.1, along with the slopes, intercepts, and correlation coefficients of the lines in Figure 3.7, and the particle mass and density measurements. The two mass measurements from the separate weighings were 5.08 and 5.15 μg, a 1.4 % difference.

3.2.8. Error estimation in mass measurement.

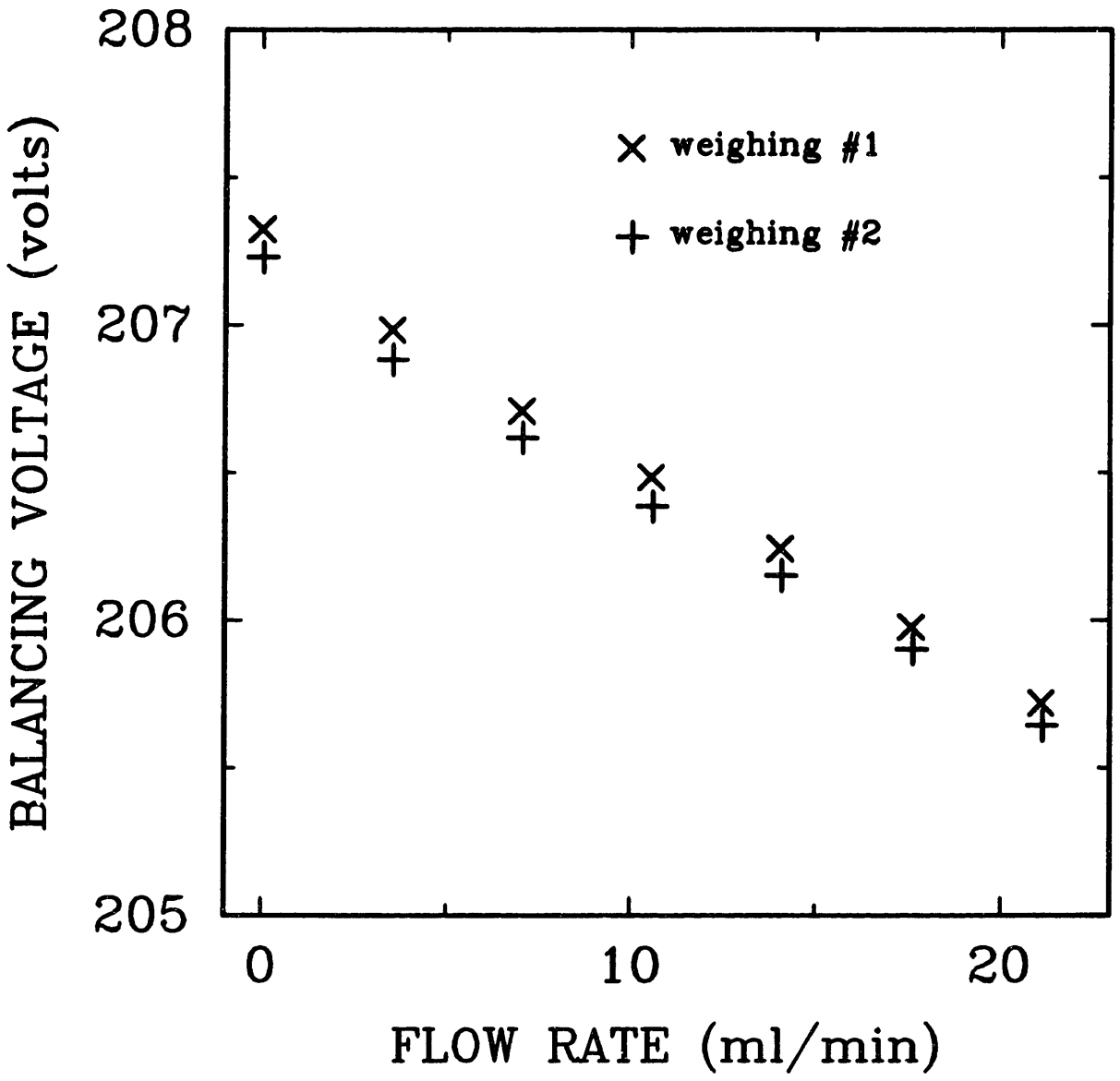

Figure 3.7 : Balancing voltage versus volumetric flow rate for two separate weighings of a 245 μm diameter "Spherocarb" particle.

Table 3.1 : Raw voltage versus flow rate data for two separate weighings of a 245 μm diameter "Spherocarb" particle.

Weighing #1		Weighing #2	
flow rate (ml/min)	Voltage (volts)	flow rate (ml/min)	Voltage (volts)
0.0	207.373	0.0	207.247
0.0	207.298	0.0	207.230
0.0	207.295	0.0	207.244
0.0	207.320	0.0	207.207
0.0	207.345		
3.5	206.956	3.5	206.880
3.5	206.984	3.5	206.874
3.5	207.008	3.5	206.907
3.5	206.993	3.5	206.878
7.0	206.734	7.0	206.645
7.0	206.700	7.0	206.619
7.0	206.714	7.0	206.621
7.0	206.691	7.0	206.596
10.6	206.484	10.6	206.366
10.6	206.494	10.6	206.415
10.6	206.478	10.6	206.371
10.6	206.488	10.6	206.399
14.1	206.214	14.1	206.119
14.1	206.261	14.1	206.157
14.1	206.255	14.1	206.168
14.1	206.249	14.1	206.175
17.6	205.972	17.6	205.909
17.6	205.989	17.6	205.893
17.6	205.987	17.6	205.918
17.6	205.970	17.6	205.901
21.1	205.723	21.1	205.651
21.1	205.737	21.1	205.624
21.1	205.714	21.1	205.634
21.1	205.712	21.1	205.673

particle density =	661 kg/m^3	670 kg/m^3
particle diameter =	245 μm	245 μm
particle mass =	5.08 μg	5.15 μg
experimental slope =	0.07394	0.07286
experimental intercept =	207.27 volts	207.17 volts
correlation coefficient =	0.9985	0.9982

The particle weight can be written in the following form:

$$mg = (\pi/6)\rho_p d^3 g \tag{3.19}$$

If equation 3.11 is rearranged, particle density may be rewritten:

$$\rho_p = \bar{K} V_i Q/(d^2 \Delta V_{aero}) \tag{3.20}$$

If we then substitute equation 3.20 into 3.19 and solve for particle mass:

$$m = (\pi/6)[\bar{K} d V_i Q/\Delta V_{aero}] \tag{3.21}$$

By taking the derivative of both sides of equation 3.21 yields:

$$\begin{aligned} \partial m = (\pi/6)[&\partial(\bar{K}Q)(d\ V_i/\Delta V_{aero}) + \partial(d)(\bar{K}Q\ V_i/\Delta V_{aero}) \\ &+ \partial(V_i)(\bar{K}Q\ d/\Delta V_{aero}) - \partial(\Delta V_{aero})(\bar{K}Q\ d\ V_i/\Delta V_{aero}^2)] \end{aligned} \tag{3.22}$$

Equation 3.22 may be rewritten in more compact form by dividing through by m, yielding:

$$\begin{aligned} |\partial m/m| = &|\partial(\bar{K}Q)/\bar{K}Q| + |\partial(d)/d| + |\partial(V_i)/V_i| \\ &+ |\partial(\Delta V_{aero})/\Delta V_{aero}| \end{aligned} \tag{3.23}$$

The following are considered reasonable error limits:

$V_i = V_i \pm 1.0$ volt.

$d = d \pm 5.0\ \mu m$.

$$K_Q = \bar{K}_Q \pm 1.8\%.$$

$$\Delta V_{aero} = \Delta V_{aero} \pm 0.10 \text{ volt.}$$

The term $\bar{K}_Q$ has been linked together and represents any systematic error due to calibration. The ± 1.8% was taken from the calibration runs. If we substitute equation 3.11 into equation 3.23, equation 3.23 can be written:

$$|\partial(m)/m| = |\partial(\bar{K}_Q)/\bar{K}_Q| + |\partial(d)/d| + |\partial(V_i)/V_i| + |\partial(\Delta V_{aero})\, d^2\, \rho/(\bar{K}_Q\, V_1)| \quad (3.24)$$

We see that error in mass measurement can be caused by errors in measuring the (1) calibration parameter, (2) particle diameter, (3) initial balancing voltage, and (4) changes in balancing voltage. The error in mass measurement is also affected by the overall magnitude of the (1) initial balancing voltage, (2) particle diameter, (3) calibration parameter, and (4) particle density.

Figure 3.8 is a plot of relative error in mass measurement versus particle diameter for a particle with a density of 500 kg/m^3. For smaller particles (<50 μm diameter), the error in measuring particle diameter dominates the total error in measuring particle mass. This error could be reduced and the range of the aerodynamic drag technique could be extended down to smaller particles if (1) a more powerful microscope were used, or (2) a different technique (e.g. diffraction or light scattering) for measuring particle diameter were employed.

For larger particles, the error in measuring the

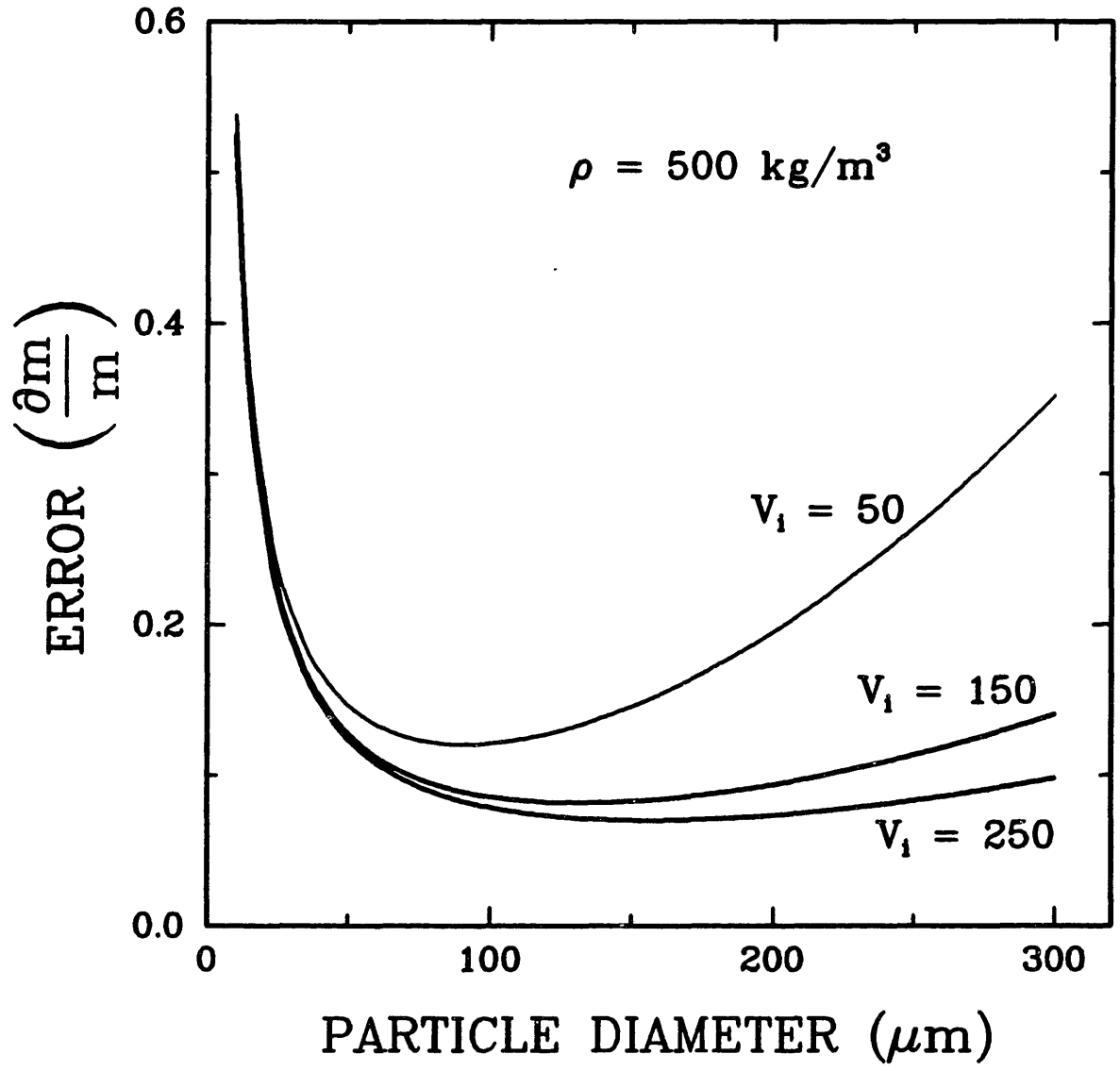

Figure 3.8 : Predicted relative error in mass measurement versus particle diameter for a particle density of 500 kg/m^3 and initial balancing voltages of 50, 150, and 250 volts.

change in balancing voltage for different flow rates dominates the total error in measuring particle mass. This is especially important when the balancing voltage is allowed to reach low values. Fortunately, the balancing voltage for a suspended particle may be increased by applying an ultraviolet light source to the particle and knocking off some charge. This ability to increase the balancing voltage of a suspended particle can drasticly reduce the error involved in measuring the mass of larger particles by the aerodynamic method. Overall, the error in mass measurement by the aerodynamic drag force technique hovers around 10% for a particle with a diameter between 50 and 250 μm and a density of 500 kg/m^3.

Figure 3.9 is a plot of relative error in mass measurement versus particle diameter for a particle with a density of 2500 kg/m^3. The increased weight of this particle exagerates the error due to measurements of balancing voltage changes.

3.2.9 Nonspherical particles.

The drag force, $F_{a,s}$, encountered by a sphere of diameter, d_s, in a fluid of viscosity, μ, and velocity, v_s, can be expressed as follows:

$$F_{a,s} = 3\pi\mu v_s d_s \tag{3.25}$$

The net gravitational force on this particle is written:

$$F_{gravity} = mg = (\pi/6)d_s^3(\rho_s-\rho_f)g \tag{3.26}$$

where ρ_s is the density of the sphere and ρ_f is the density of the fluid. At terminal velocity, $F_{a,s}$ =

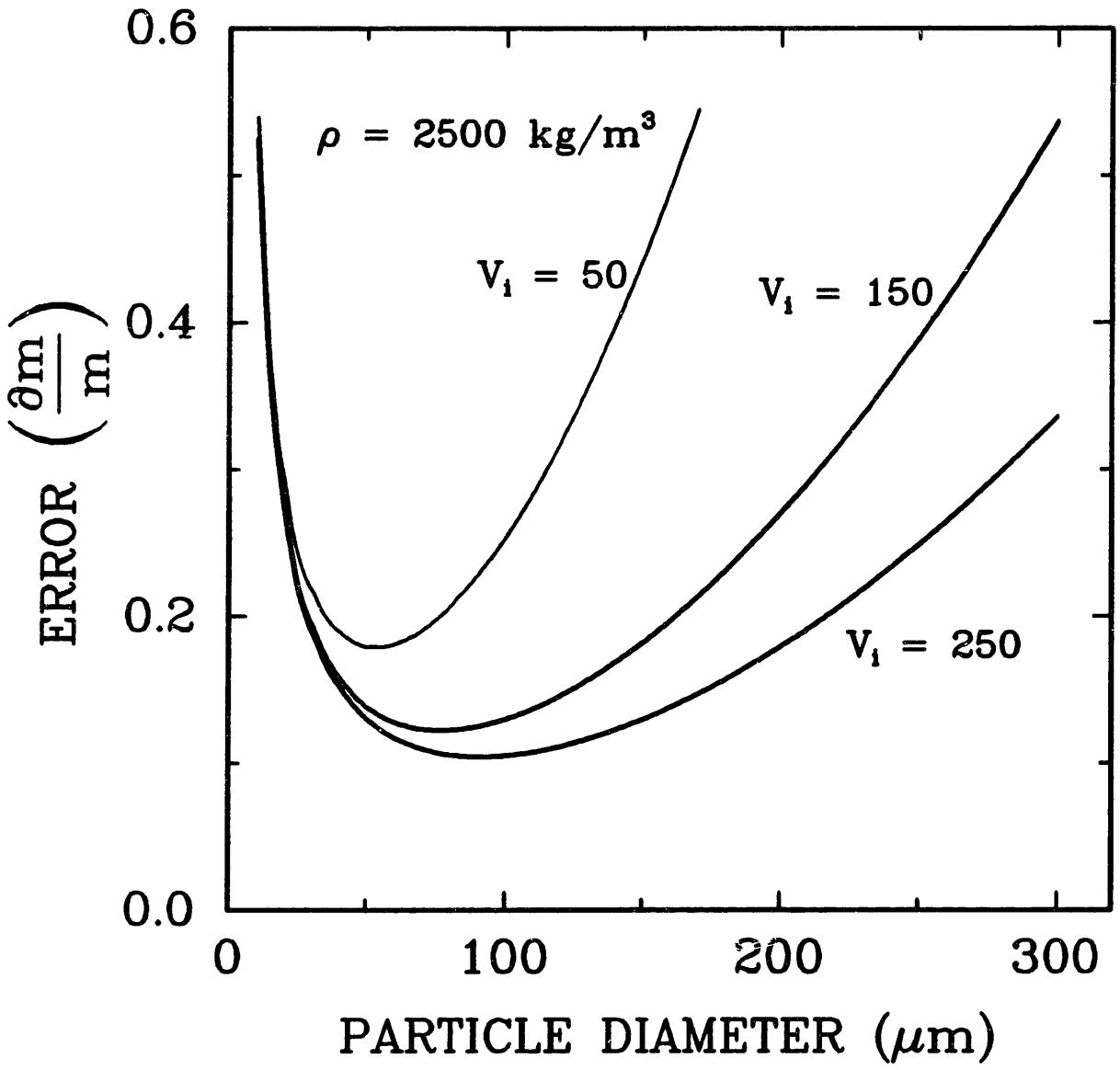

Figure 3.9 : Predicted relative error in mass measurement versus particle diameter for a particle density of 2500 kg/m^3 and initial balancing voltages of 50, 150, and 250 volts.

$F_{gravity}$ and equations 3.25 and 3.26 can be combined to obtain Stokes' law:

$$v_s = (g/18)[d_s^2(\rho_s-\rho_f)/\mu] \tag{3.27}$$

For nonspherical particles, the shape correction factor, K, is defined by the following ratio:

$$K = (v/v_s)_V \tag{3.28}$$

where v is the settling velocity of any shaped particle and the subscript V indicates that the volume of the spherical and nonspherical particles is held constant. Equation 3.28 can be substituted into equation 3.25 to yield:

$$F_{a,ns} = 3\pi\mu d_s(v/K) \tag{3.29}$$

where $F_{a,ns}$ is the drag force on a nonspherical particle, and d_s is the diameter of a sphere of equivalent volume to the nonspherical particle of interest. For nonspherical particles, K can be calculated from the following equation:

$$K = 18\mu v/[gd_s^2(\rho_{ns}-\rho_f)] \tag{3.30}$$

where ρ_{ns} is the density of the nonspherical particle. Since K is usually less than 1.0, the drag force for irregularly shaped particles is usually greater than the drag force for spheres of the same volume.

Heiss and Coull [21] concluded that three variables d_s, d_n, and ψ were necessary to determine the shape correction factor, K, for a given position of orientation. d_s has already been defined. d_n is the diameter equal to the diameter of a circle having an area equal to that of the projected area of the particle. The sphericity,

ψ, is defined as the ratio of the surface area of a sphere to that of an irregularly shaped particle of equivalent volume.

Pettyjohn and Christiansen [22] concluded from their study on drag coefficients of isometric particles that:

$$K = 0.843[\log(\psi/0.065)] \qquad (3.31)$$

This result is shown graphically in Figure 3.10. The sphericity of some common particle shapes are tabulated below:

sphere = 1.000
cube octahedron = 0.906
octahedron = 0.846
cube = 0.806
tetrahedron = 0.670

Heiss and Coull [21] performed a similar study on nonisometric particles. Figures 3.11, 3.12, and 3.13 are taken from Heiss and Coull [21]. Figure 3.11 is a plot of K versus ψ that shows the effect of the orientation in the fluid stream of various cylinders on the K value. Figure 3.12 is a plot of K versus height-diameter ratio for cylinders, rectangular parallelepipeds, and spheroids. A correlation of all of Heiss and Coull's [21] data is depicted in Figure 3.13 in the form of K versus d_s/d_n with ψ as a parameter.

3.3 Single particle surface area measurements.

3.3.1 Introduction.

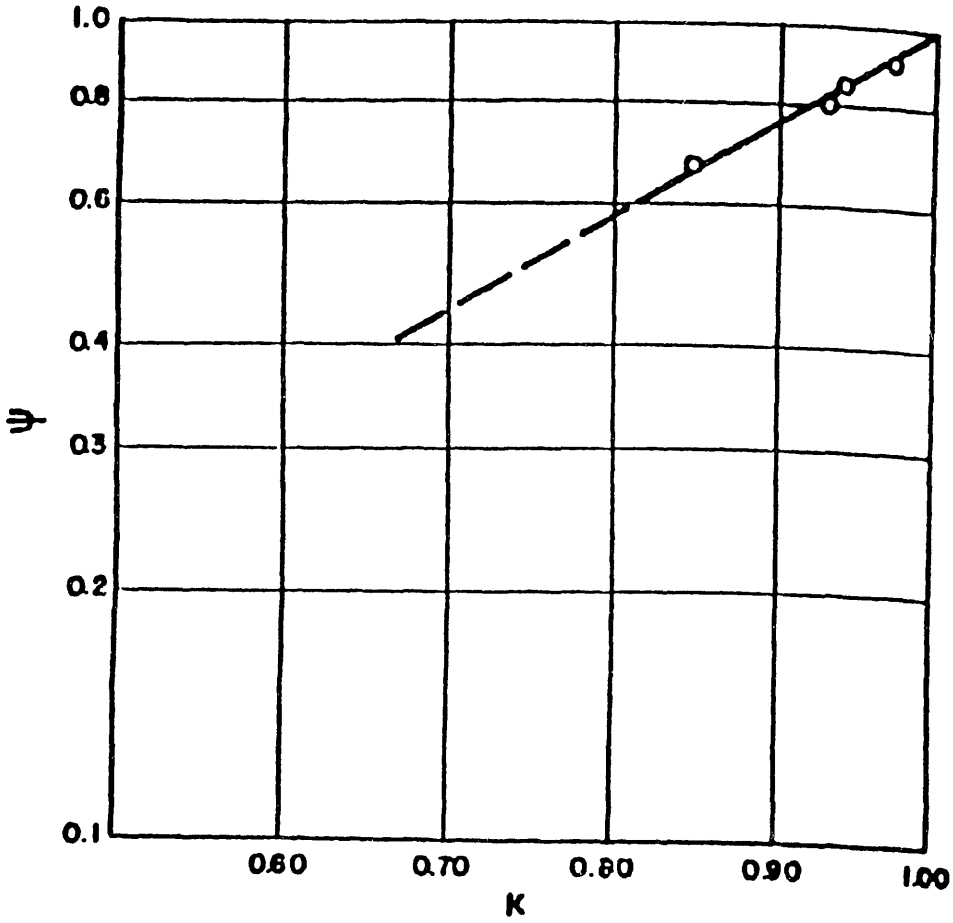

Figure 3.10 : Sphericity versus shape correction factor for isometric particles (from Pettyjohn and Christiansen [22]).

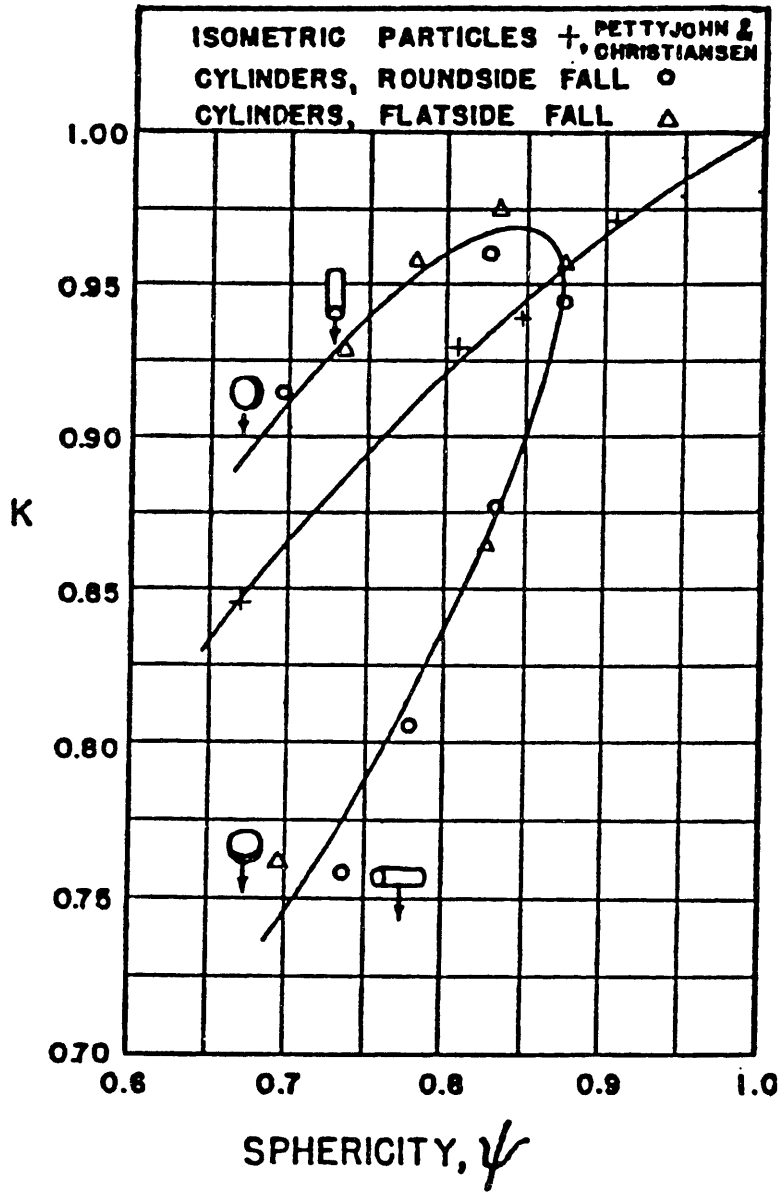

Figure 3.11 : Shape correction factor versus sphericity for isometric particles, cylinders falling roundside down, and cylinders falling flat-side down (from Heiss and Coull [21]).

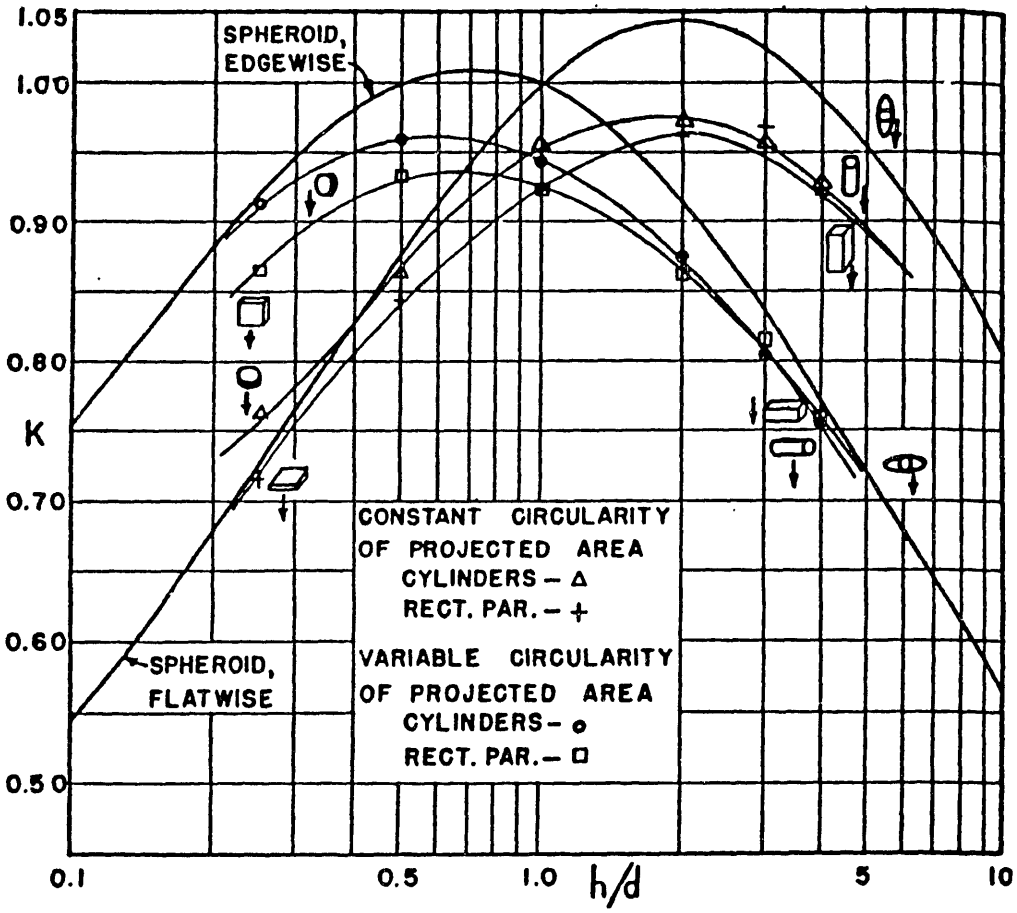

Figure 3.12 : Shape correction factor versus height–diameter ratio for cylinders, rectangular parallelepipeds, and spheroids (from Heiss and Coull [21]).

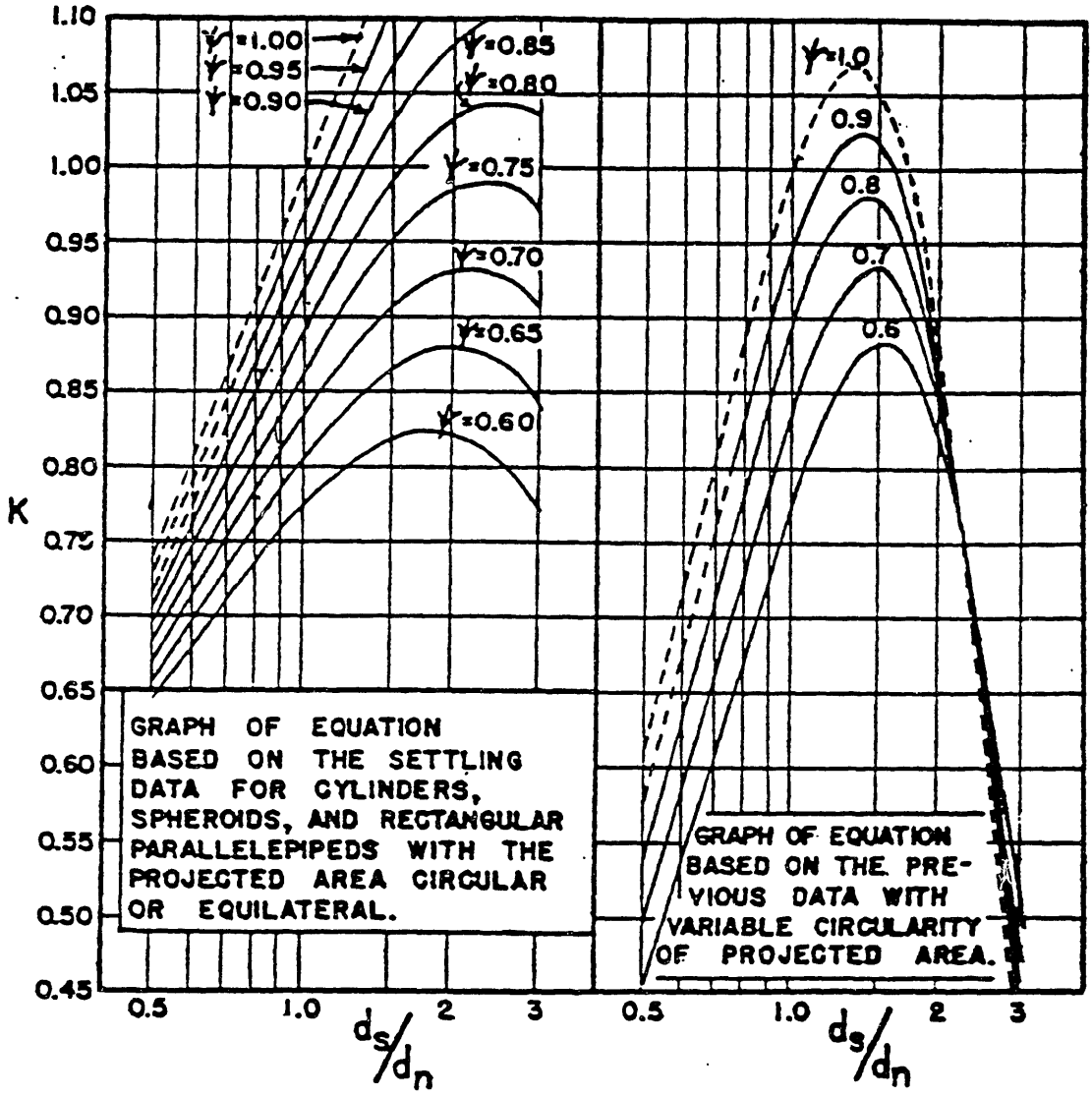

Figure 3.13 : Correlation of shape correction factor versus d_s/d_n with sphericity as a parameter (from Heiss and Coull [21]).

Since the overall rate of reaction of the suspended particle is a function of its surface area available to gaseous reactants, it is desirable to measure this surface area. Traditionally, methods for surface area measurement fall into four categories, 1) heat of wetting and calorimetric methods, 2) adsorption methods, 3) porosimetry, and 4) small-angle x-ray scattering (SAXS).

Heat of wetting methods have lost their importance in measuring surface areas of coals and coal chars after it was discovered that the adsorption of methanol involves specific interactions between the hydroxyl group of methanol and oxygen functionalities present on coal surfaces [23]. Mercury porosimetry is used primarily as a method for measuring the pore size distribution in a porous solid, however, if the correct contact angle between the mercury and the pore surface is known, porosimetry can also be used to measure surface area. On the other hand, SAXS has not been used enough on coals and coal chars to allow for easy interpretation of the scattering data [24].

Methods involving the adsorption of gases are used most commonly to measure surface areas of porous and nonporous solids. Nitrogen at 77 K, carbon dioxide at 195 K, 273 K, and 298 K, neon at 298 K, xenon at 273 K, krypton at 195 K, ethyl chloride at 273 K and 298 K, and other hydrocarbons at 298 K have all been used to measure the surface area of coal and coal char. Nitrogen and carbon dioxide are the most commonly used gases.

Two problems of using N_2 adsorption for surface area measurements of coals and coal chars have been reported. First, because of the low temperature (77 K) used with N_2 adsorption, activated diffusion can be important in

microporous networks which then leads to experimentally unattainable equilibrium coverage of the N_2 molecules on the microporous surface and, therefore, in some cases, unrealistically low surface areas [25]. Anderson et al. [26] have suggested that N_2 adsorption at 77 K provides a measure of the surface area contained in pores having diameters greater than about 5 Å. Also, Zwietering and van Krevelen [27] found that the adsorption of N_2 at 77 K in a particular coal had a half coverage time of ~1000 years.

Secondly, Marsh and Wynne-Jones [28] have also reported the opposite problem with N_2 adsorption in activated carbons. When some pores in the carbon are several N_2 diameters wide, N_2 is capable of filling these pores at extremely low relative pressures. This capillary condensation can cause the BET equation to predict an unrealistically high value of surface area.

Adsorption of CO_2 at higher temperatures (195, 273, 298 K) reduces the diffusion problems of N_2 at 77 K for two reasons. First, CO_2 is a smaller molecule than N_2 with a minimum dimension of 3.3 Å compared to 3.64 Å [25]. Secondly, diffusion at 195, 273, and 298 K is much faster than at 77 K. Thomas and Damberger [29] calculated the diffusion time of an N_2 molecule at 77 K through a pore 5 Å in diameter and 10 μm in length to be 10^5 times the diffusion time of a CO_2 molecule at 195 K through the same pore. It should be noted, however, that capillary condensation may still be a problem when using CO_2 adsorption.

When using the BET equation for calculating surface area, it is essential to measure sorption isotherms up to a relative vapor pressure of about 0.2 [30]. For CO_2 at

273 and 298 K, the saturation vapor pressure is much higher than atmospheric pressure, therefore, for measuring surface areas with the BET equation using CO_2, a high pressure adsorption system must be used. Marsh and Siemieniewska [31] overcame this difficulty by using the Dubinin-Polanyi (D-P) equation instead of the BET equation to calculate surface areas of coals using CO_2 adsorption at 273 and 293 K. Walker and Patel [32] measured surface areas of 10 different coals and chars with CO_2 adsorption at 298 K using both the D-P and BET equations in two different pressure ranges and found excellent agreement. Therefore, it can be concluded that a conventional volumetric adsorption apparatus and the D-P equation is as adequate for measuring CO_2 surface areas of coals as a high pressure adsorption apparatus and the BET equation.

In this work, single particle surface areas of coals and synthetic chars are evaluated from the adsorption isotherm of CO_2 at 298 K using the Dubinin-Polanyi equation.

3.3.2 Dubinin-Polanyi theory.

The use of the Dubinin-Polanyi equation is discussed by Lamand and Marsh [33] and is written as follows:

$$\log(n/mg) = \log(n/mg)_0 - (BT^2/\beta)\log^2(P_0/P) \qquad (3.32)$$

where (n/mg) is the number of mols of CO_2 adsorbed per sample weight at the CO_2 equilibrium pressure P, $(n/mg)_0$ is the micropore capacity in (mol/g), P_0 is the saturation vapor pressure of CO_2 at temperature T (K), β is the affinity coefficient of CO_2 relative to N_2, and B is a constant.

A plot of log(n/mg) versus $\log^2(P_0/P)$ should yield a straight line with the intercept at $\log^2(P_0/P) = 0$ equal to $\log(n/mg)_0$. If the adsorption of CO_2 is resricted to a monolayer then $(n/mg)_0$ multiplied by the cross-sectional area of a CO_2 molecule and Avagadro's number yields the microporous surface area. The cross-sectional area of the CO_2 molecule is a function of temperature and was taken from Walker and Kini [34].

3.3.3. Experimental procedure.

Rewriting the vertical force balance on a suspended particle from equation 3.3 yields:

$$mg = qCV/z_0 \tag{3.33}$$

If equation 3.33 is solved twice for the same particle, once with CO_2 adsorption and once without, and the equations are subtracted from each other, the following expression results:

$$(m-m_i)/m_i = (V - V_i)/V_i \tag{3.34}$$

where m_i and V_i are the initial mass and voltage when no CO_2 has been adsorbed and m and V are the mass and voltage when CO_2 has been adsorbed. In other words, the change in particle mass due to CO_2 adsorption divided by initial mass is equal to the change in DC voltage required for balancing divided by the initial voltage.

Experiments were initiated by capturing one particle in the center of the chamber. Degassing was then accomplished by passing ultra high purity nitrogen

through the chamber and over the particle at 42 ml/min for 30 minutes. The n/mg ratio can be measured directly from the balancing voltages (equation 3.34) and dividing by the molecular weight of CO_2.

The temperature of the chamber and the gas mixture inside the chamber was taken to be in equilibrium with the surrounding atmosphere and was measured with a thermometer to ±0.1 C. This temperature was then used along with data from Perry [35] to determine P_0, the saturation vapor pressure of CO_2.

Five different gas mixtures were utilized in these adsorption studies, pure N_2, a 20% CO_2/80% N_2 mixture, a 35% CO_2/65% N_2 mixture, a 50% CO_2/50% N_2 mixture, and pure CO_2. Some raw data for a "Spherocarb" particle is plotted in Figure 3.14 in the form of balancing voltage versus the mass flow meter reading. The mass flow meter reading was used instead of volumetric flow rate because the mass flow meter is only calibrated for nitrogen. A mass flow meter reading of 600 corresponds to a nitrogen flow rate of 42 ml/min. Three balancing voltage measurements (at mass flow meter readings of 400, 500, and 600) were taken for each gas mixture. These measurements are shown as the open boxes in Figure 3.14. Programs SA and SACALC2 are used in the surface area measurements and printouts are found in Appendix A.

Since the chamber is not leak proof, in order to ensure that the suspended particle is experiencing the same environment that is in the gas cylinders, a finite gas flow rate must be maintained. Gas flow rates corresponding to mass flow meter readings of 400, 500, and 600 have been shown to be experimentally adequate.

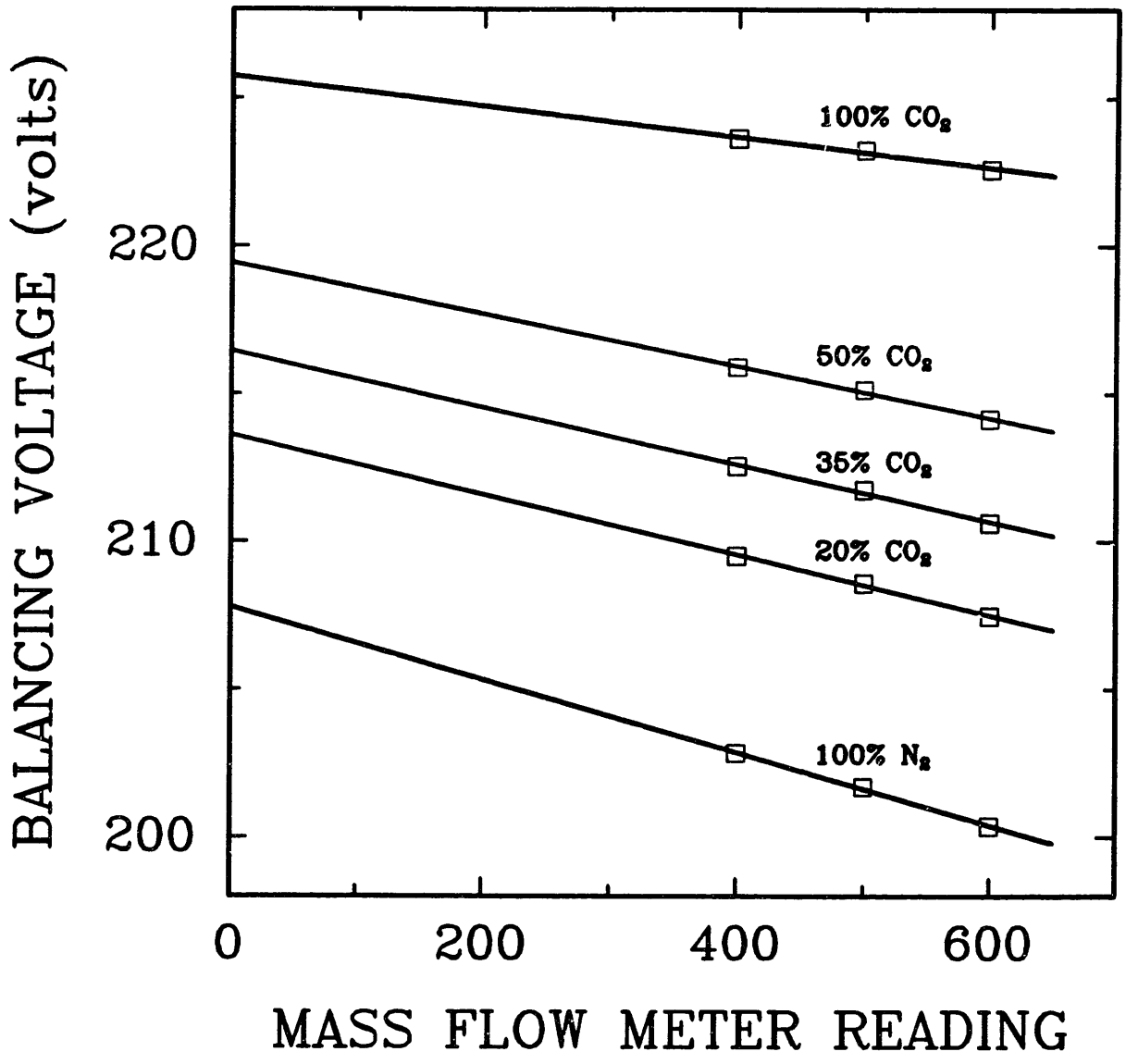

Figure 3.14 : Balancing voltage of a single "Spherocarb" particle versus mass flow meter reading for five different gas mixtures.

Unfortunately, the introduction of a gas flowing upward past the suspended particle produces an aerodynamic drag force, F_a, on the particle which affects the DC voltage required for stable balancing of the particle. This aerodynamic drag force can be described using Stokes' law:

$$F_a = 3\pi d\mu v \tag{3.35}$$

where d is the particle diameter, μ is the viscosity of the gas mixture, and v is the velocity of the gas mixture over the particle. From Figure 3.14, it can be seen that the higher the gas flow rate, the less voltage required for balancing. This is because the aerodynamic drag force is pushing the particle upward, helping suspend the particle.

The solid lines in Figure 3.14 represent a least squares linear regression that was performed on each group of three experimental points. By extrapolating the experimental data to a zero mass flow meter reading, the "true" balancing voltage without the aerodynamic drag force included can be obtained. These "true" balancing voltages can then be used directly to form a Dubinin-Polanyi plot and thus a surface area calculation. One surface area measurement performed in this fashion takes approximately 1.5 hours.

Equation 3.34 predicts that the increase in balancing voltage with increasing CO_2 partial pressure is due to particle mass increases caused by increased CO_2 adsorption.

3.3.4. Examples of surface area measurements.

In order to ensure that the changes in balancing voltage shown in Figure 3.14 are really due to CO_2 adsorption and not some hydrodynamic effect, the data from Figure 3.14 is plotted in (n/mg) versus $\log^2(P_0/P)$ form in Figure 3.15 along with similar data from a glass sphere. As expected, the glass sphere, which is known to have a very low surface area, adsorbs practically no CO_2; therefore, the adsorption of CO_2 in the "Spherocarb" particle is assumed to be real.

Figure 3.16 is a Dubinin-Polanyi plot for a 181 μm diameter "Spherocarb" particle. The data points are represented as open squares, and the line is a least squares linear regression through these points. The slope of this line is -0.1524, the intercept is -2.229, and the correlation coefficient is 0.9994. An intercept of -2.229 corresponds to a surface area of 860 m^2/g.

3.3.5. Comparison with conventional apparatus.

A comparsion of the Dubinin-Polanyi plot between data collected in a conventional volumetric adsorption apparatus and data collected on a single particle in the electrodynamic balance is made in Figure 3.17 [36]. The conventional apparatus, which utilized 0.294 g of "Spherocarb" particles and operated at 273 K, could be operated over a much broader range of CO_2 pressures. Although not readily apparent, the points from the conventional apparatus do not form a straight line, but are curved concave upward, therefore, the intercept and hence the surface area will depend on which points are chosen. The intercept of the Dubinin-Polanyi plot, which is determined from a least

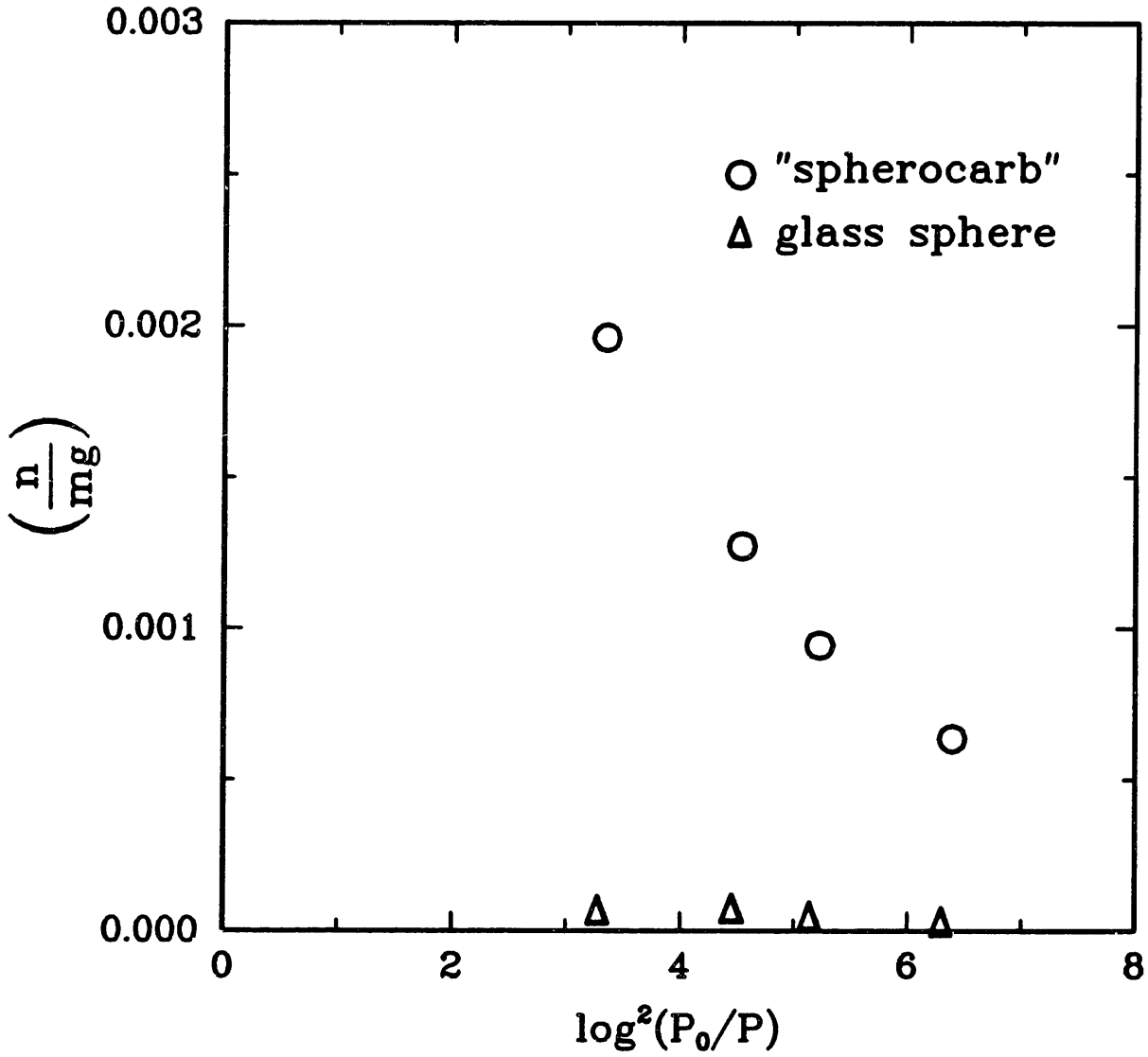

Figure 3.15 : Ratio of mols CO_2 adsorbed to particle weight versus $\log^2(P_0/P)$ for a "Spherocarb" particle and a glass sphere.

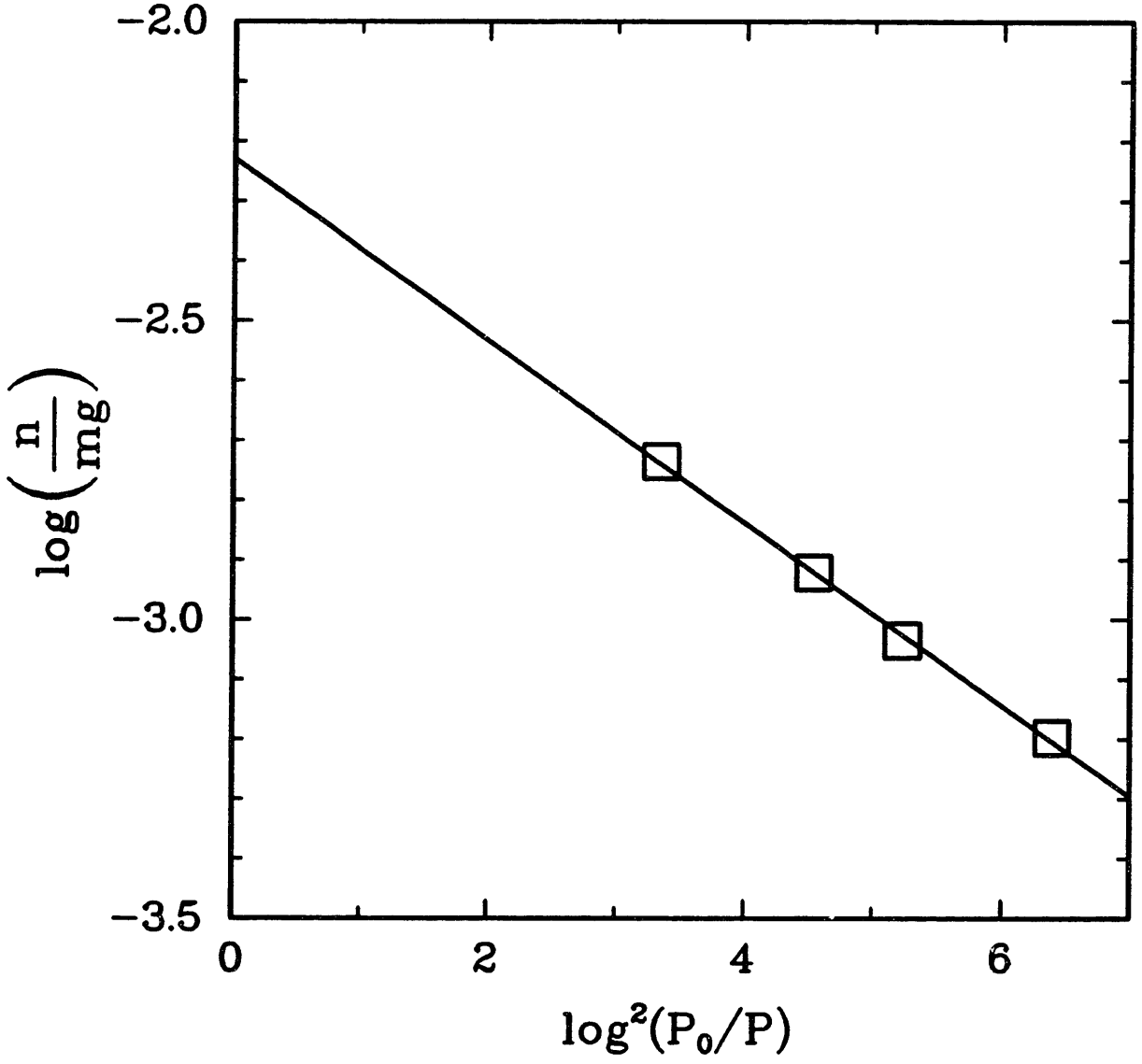

Figure 3.16 : Dubinin–Polanyi plot for a 181 μm diameter "Spherocarb" particle.

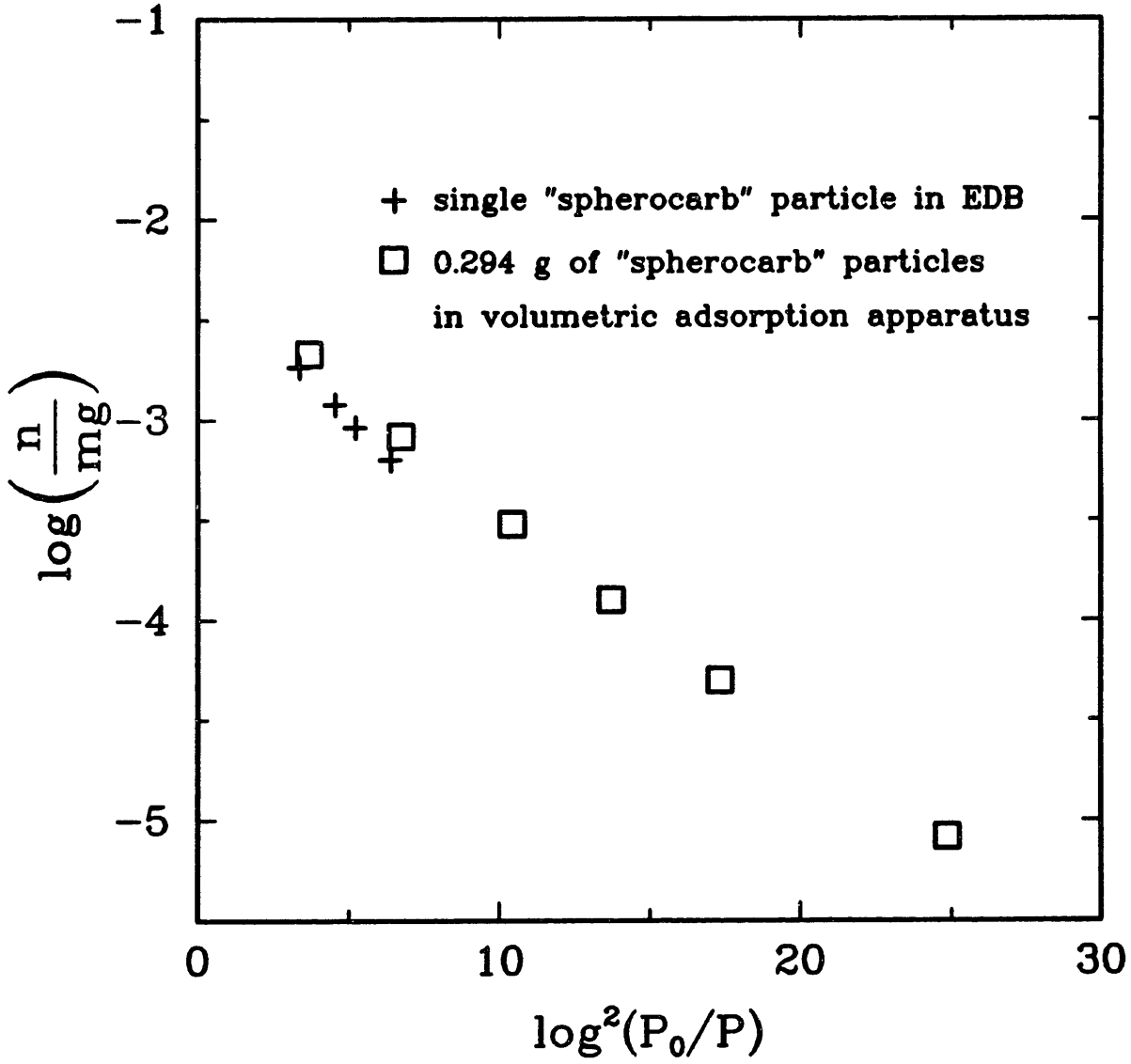

Figure 3.17 : Comparison of a Dubinin–Polanyi plot for a "Spherocarb" particle and 0.294 g of "Spherocarb" particles.

squares linear regression, is used to determine surface area. Using only high values of CO_2 pressure or low values of $\log^2(P_0/P)$, will yield higher calculated values of surface area than using only low values of CO_2 pressure or high values of $\log^2(P_0/P)$. It is not surprising, therefore, that the conventional apparatus (weighted more heavily toward the low values of CO_2 pressure) yields a surface area for "Spherocarb" particles of 636 m^2/g compared to values ranging from 821 to 1120 m^2/g for single "Spherocarb" particles measured in the electrodynamic balance. The points from the electrodynamic balance shown in Figure 3.17 yield a surface area of 860 m^2/g. A surface area of 965 m^2/g is calculated from the conventional apparatus data if only the two points with the highest values of CO_2 pressure are used. In section 6.1 the "Spherocarb" surface area is plotted versus percent conversion for eight separate "Spherocarb" particles. The initial surface area from these eight runs ranged from 821 to 1116 m^2/g, with the average initial surface area being 960 m^2/g. In a recent "Spherocarb" pore structure characterization study, Niksa [37] reports "Spherocarb" BET and Langmuir surface areas of 828 and 1100 m^2/g, respectively.

It can be argued, therefore, that the absolute value of the measured surface area depends on the values of the CO_2 pressure used in the Dubinin-Polanyi equation. Reasonable surface areas are obtained by use of any of the CO_2 pressures reported in Figure 3.17, however, if valid comparisons are to be made from one particle to the next or from the same particle at different extents of conversion or from the same particle using different apparatuses, care must be taken in choosing the same range of CO_2 pressure.

3.4 Single particle temperature measurement.

Temperature measurement is critical in kinetic studies. The EDTGA used in this thesis was equipped with a two color (2 μm and 4 μm) infrared pyrometer by Spjut [7,9]. The response times of the 2 μm and 4 μm detectors used in this system along with a corresponding error analysis of temperature measurement via this technique is discussed fully by Spjut [7,8].

3.4.1 Two color pyrometry.

According to Wien's law:

$$I_{\lambda a} = (2c_1 \epsilon_a / \lambda^5) \exp(-c_2 / \lambda_a T) \qquad (3.36)$$

where: $I_{\lambda a}$ = monochromatic emissive power at wavelength λ (ergs/cm^3 sec).
c_1 = Planck's first constant = $2\pi hc^2$ = 3.740×10^{-5} (erg cm^2/sec).
ϵ_a = emissivity at wavelength λ_a.
λ_a = wavelength (cm).
c_2 = Planck's second constant = ch/k = 1.4388 (cm K).
T = temperature (K).
h = Planck's constant = 6.6256×10^{-27} (erg sec).
k = Boltzmann's constant = 1.3805×10^{-16} (erg/K).
c = 2.9979×10^{10} (cm/sec).

The signal intensity of a photodetector that is being illuminated by a heated object is given by:

$$V_a = A_d F_{dp} G I_{\lambda a} \Delta\lambda \qquad (3.37)$$

where: V_a = signal voltage from photodetector (volts).
A_d = sensitive area of photodetector (cm^2).
F_{dp} = viewfactor between detector and particle.
G = gain of photodetector.
$\Delta\lambda$ = optical bandwidth of photodetector.

Substituting equation 3.36 into 3.37 yields:

$$V_a = (2c_1 \epsilon_\lambda A_d F_{dp} G \Delta\lambda / \lambda_a^5) \exp(-c_2/\lambda_a T) \qquad (3.38)$$

Taking the natural logs of both sides of equation 3.38 yields:

$$\ln(V_a) = \ln(K_a) - M_a/T \qquad (3.39)$$

where: $K_a = (2c_1 \epsilon_\lambda A_d F_{dp} G \Delta\lambda / \lambda_a^5)$

$M_a = c_2/\lambda_a$

When equation 3.39 is combined with an equivalent expression for detector b, the following equation is obtained:

$$\ln(V_a/V_b) = \ln(K_a/K_b) + (M_b - M_a)/T \qquad (3.40)$$

Equation 3.40 has an advantage over equation 3.39 since the factor $A_d F_{dp}$ that is dependent on particle size is ratioed out. Also, the absolute value of the emissivity at a specific wavelength need not be known, only the ratio of the emissivities. Equation 3.40 will be the working equation for particle temperature measurement in the EDTGA. The two wavelengths that are used are 2 μm and 4 μm.

The theoretical slopes are easily calculated in the

following manner:

$$M_{2\mu m} = 1.4388 \text{ cm K}/2.0\text{x}10^{-4} \text{ cm} = 7158 \text{ K}$$

$$M_{4\mu m} = 1.4388 \text{ cm K}/4.0\text{x}10^{-4} \text{ cm} = 3597 \text{ K}$$

yielding:

$$M_{4\mu m} - M_{2\mu m} = -3561 \text{ K}$$

The theoretical intercept is given by:

$$\ln(K_{2\mu m}/K_{4\mu m}) = \ln(e_{2\mu m}/e_{4\mu m}) + 5\ln(\lambda_{4\mu m}/\lambda_{2\mu m}) + \ln[(A_{d2\mu m}F_{dp2\mu m}G2\mu m\Delta\lambda_{2\mu m})/(A_{d4\mu m}F_{dp4\mu m}G4\mu m\Delta\lambda_{4\mu m})] \quad (3.41)$$

Since $F_{dp}G$ is not easily determined, the intercept will be determined by calibration.

3.5.2 Temperature calibration.

The two color pyrometer is calibrated with a type S thermocouple. The results are shown in Figure 3.18 in the form of ln(2μm signal/4μm signal) versus 1/T.
The slope of this line is -3290 and the intercept is 4.773. The correlation coefficient is 0.9988. The problem with calibrating our system with a Pt/Pt 10% Rh thermocouple is that the emissivity of Pt is known to change with wavelength and temperature. This change in emissivity with wavelength will change the intercept and will have to be taken into account. Also, the emissivity ratio will change with temperature, causing the slope to change.

From equation 3.41:

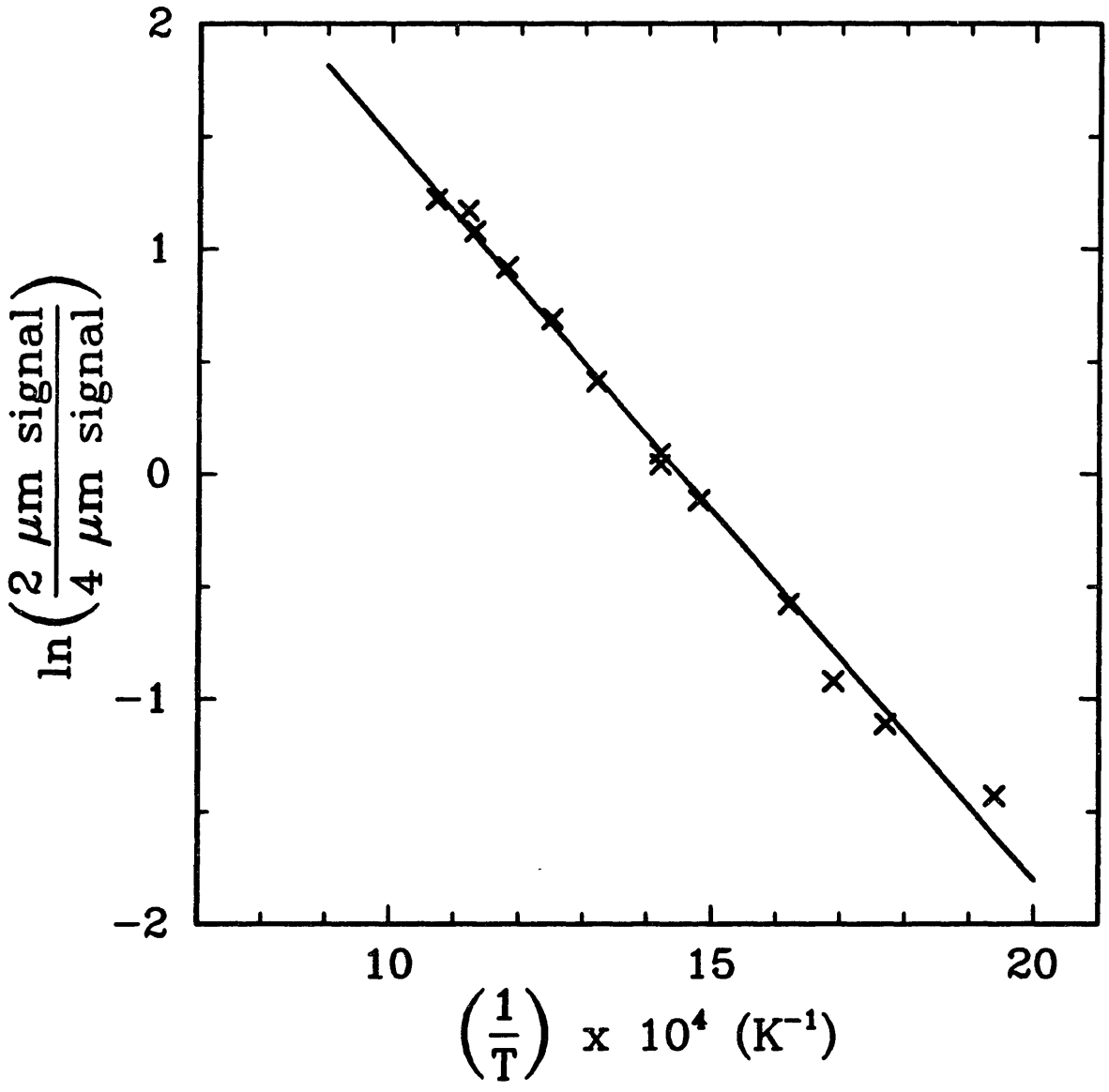

Figure 3.18 : ln[(2 μm detector signal)/(4 μm detector signal)] versus 1/T for a type S thermocouple heated by a CO_2 laser.

$$\ln(K_{2\mu m}/K_{4\mu m}) = \ln(e_{2\mu m}/e_{4\mu m}) + \ln(K) \quad (3.42)$$

or

$$\ln(K) = \ln(K_{2\mu m}/K_{4\mu m}) - \ln(e_{2\mu m}/e_{4\mu m}) \quad (3.43)$$

where: $\ln(K)$ = intercept for gray bodies.

$\ln(K_{2\mu m}/K_{4\mu m})$ = intercept from calibration curve of Figure 3.18.

$\ln(e_{2\mu m}/e_{4\mu m})$ = correction due to difference in wavelength and changes in temperature.

In order for the calibration curve of Figure 3.18 to be useful in gray body experiments (such as char oxidation) the correction of emissivities due to differences in wavelength and changes in temperature must be estimated.

Figure 3.19 is a plot of the normal spectral emissivity of platinum. The spectral emissivity of wavelengths greater than 6 μm is estimated by the Hagen-Rubens relation:

$$\epsilon_{n,\lambda} = 0.365(r/\lambda)^{0.5} \quad (3.44)$$

where: r = resistivity (ohms cm).
λ = wavelength (cm).

The resistivity of Pt is linear with temperature [38]. Three different temperatures, 600, 833, and 1111 K are depicted in Figure 3.19. Emissivity increases with increasing temperature. At 0.7 μm the emissivity of Pt becomes temperature invariant [39]. This is called the x-point. In

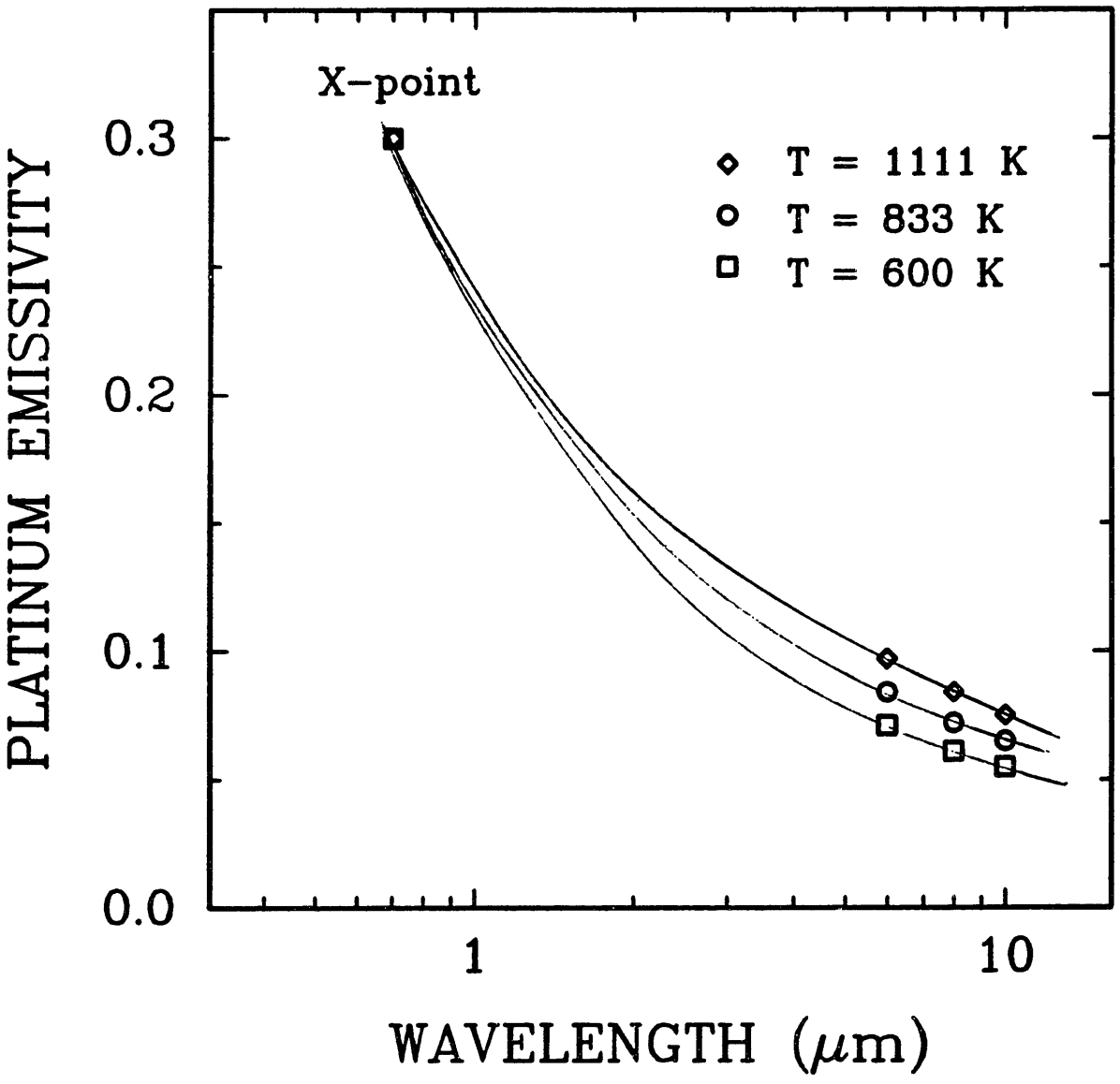

Figure 3.19 : Platinum emissivity versus wavelength at T = 600, 833, and 1111 K.

Figure 3.19, curves are drawn from the Hagen-Rubens relation to the x-point for each of the three temperatures.

Figure 3.20 is a plot of the ratio of emissivity at 2 μm to the emissivity at 4 μm taken from Figure 3.19 versus temperature. Although absolute emissivity of Pt increases with increasing temperature, the emissivity ratio decreases with increasing temperature.

If equation 3.42 is inserted into equation 3.40, the following result is obtained:

$$\ln(2\mu m \text{ signal}/4\mu m \text{ signal}) - \ln(\epsilon_{2\mu m}/\epsilon_{4\mu m}) = \ln(K) + \text{slope}/T \qquad (3.45)$$

where the left hand side of equation 3.45 is the emissivity corrected log ratio of the 2 μm detector signal to the 4 μm detector signal.

Figure 3.21 is a plot of emissivity corrected ln(2μm signal/4μm signal) and uncorrected ln(2μm signal/4μm signal) versus 1/T. The diamonds are emissivity corrected and the x's are not emissivity corrected. This plot yields a gray body intercept of 4.579 and a slpe of -3472 K. The measured slope is 2.5% lower than the theoretical slope of -3561 K.

Combining equation 3.45 with the slope and intercept of Figure 3.21 yields the following temperature equation for this two color pyrometer:

$$T(K) = 3472/[4.579 - \ln(2\mu m \text{ signal}/4\mu m \text{ signal})] \qquad (3.46)$$

or

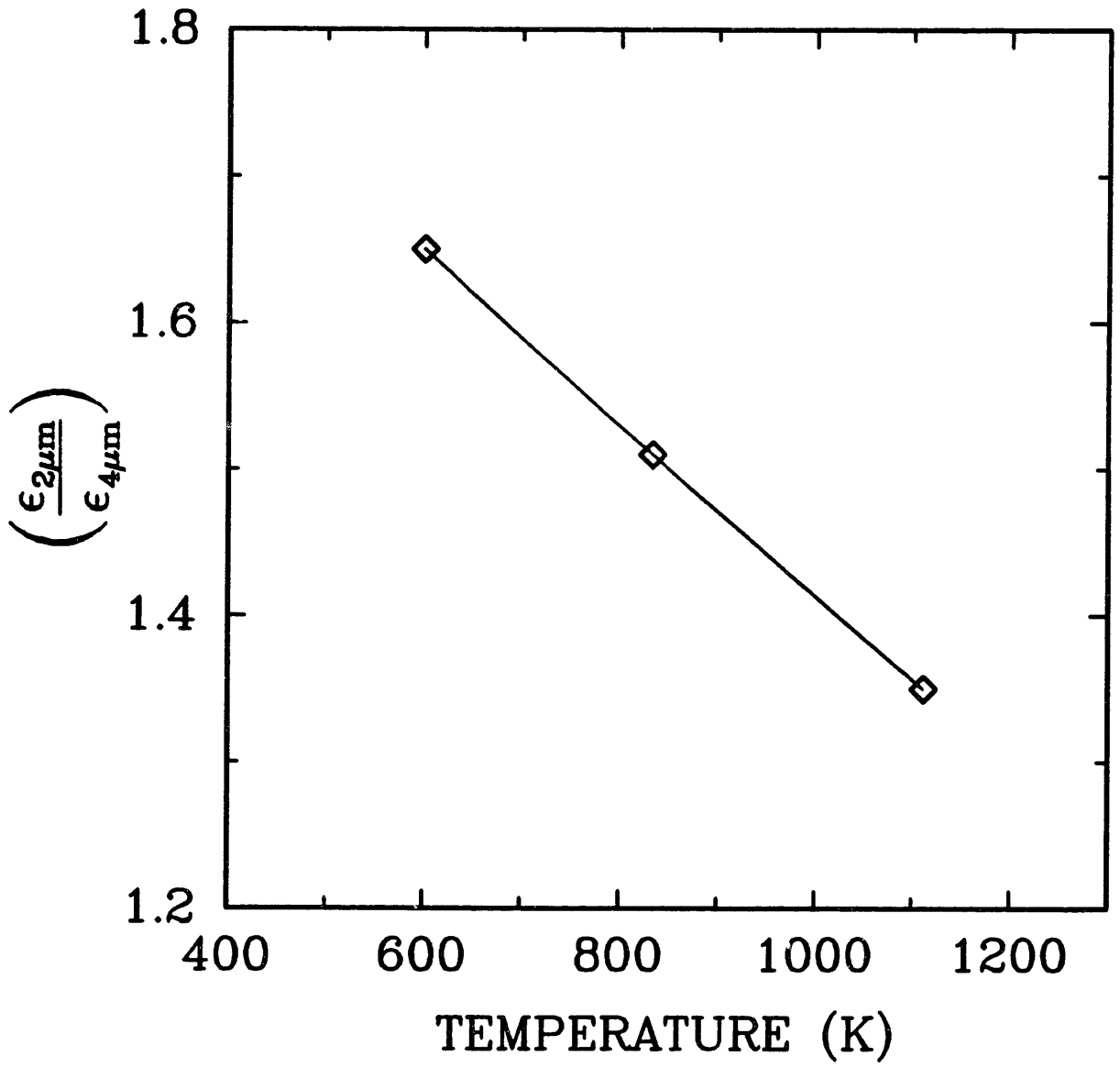

Figure 3.20 : Ratio of platinum emissivity at 2 μm to platinum emissivity at 4 μm versus temperature.

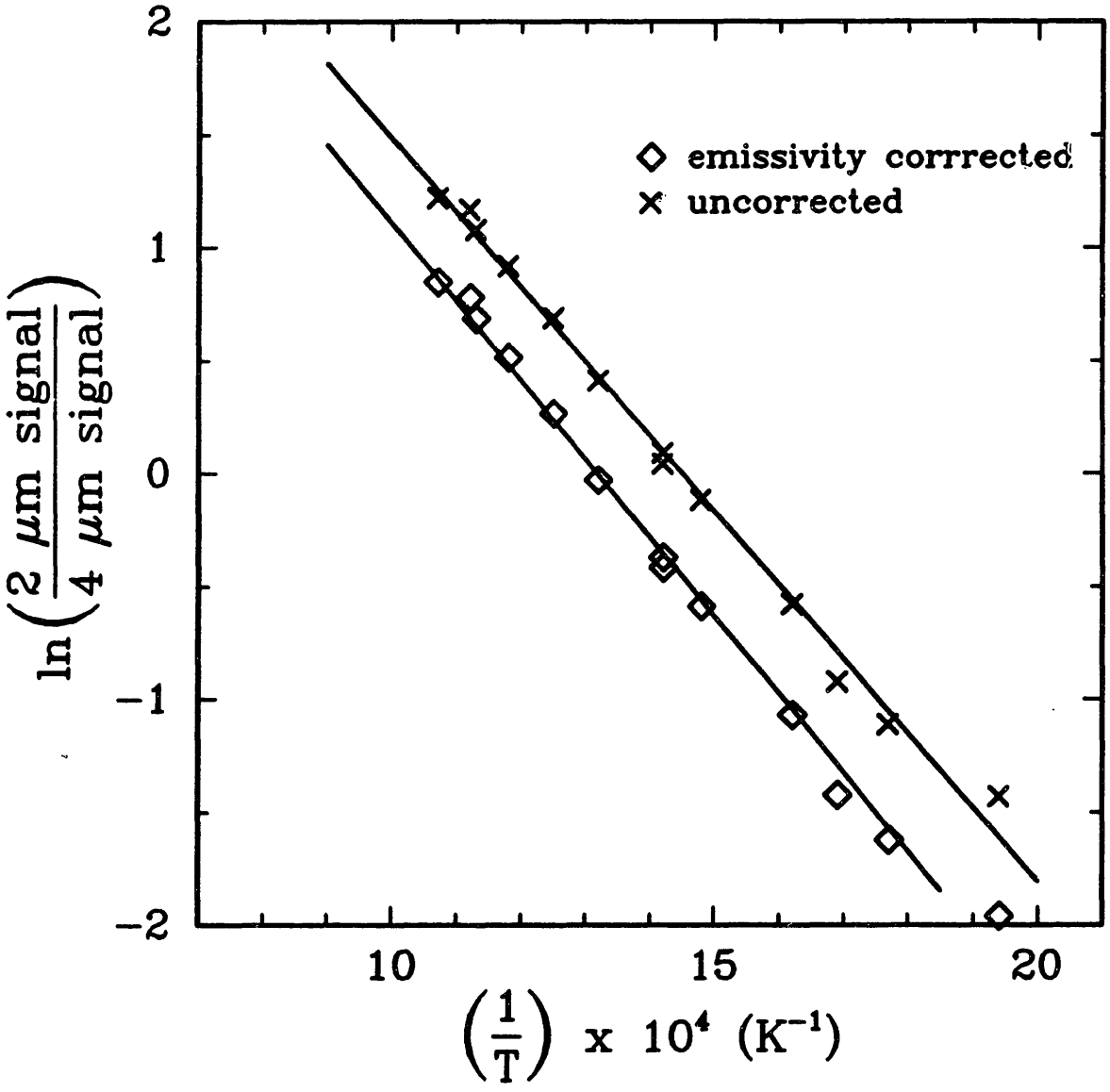

Figure 3.21 : Emissivity corrected and uncorrected ln[(2 μm detector signal)/(4 μm detector signal)] versus 1/T.

$$T(K) = 1508/[1.989 - \log(2\mu m \text{ signal}/4\mu m \text{ signal})] \quad (3.47)$$

or if the theoretical slope is used:

$$T(K) = 3561/[4.701 - \ln(2\mu m \text{ signal}/4\mu m \text{ signal})] \quad (3.48)$$

or

$$T(K) = 1547/[2.042 - \log(2\mu m \text{ signal}/4\mu m \text{ signal})] \quad (3.49)$$

3.5 Natural convective drag measurement.

When a < 250 μm diameter particle is heated in the ambient environment of the EDTGA, it has been experimentally noticed [7,12] that a natural convective drag force pushes the suspended particle upward. This natural convective drag force was as great as the particle weight in some instances [7]. In developing the EDTGA, it was first proposed that single particle kinetics could be studied continuously by following mass versus time. Since particle mass of an unheated particle is directly proportional to the DC balancing voltage, it was thought that particle mass could be followed continuously by following voltage continuously. Unfortunately, with the introduction of a natural convective drag force upon particle heating, mass was no longer proportional to DC balancing voltage. It was then decided that the natural convective drag force be measured and characterized, in order that it be cancelled out of the particle force balance and particle mass could be measured continuously by measuring DC balancing voltage.

3.5.1 Material used.

A synthetic char with a tradename "Spherocarb" manufactured by Foxboro/Analabs was used for all the drag force measurements. "Spherocarb" particles were used for three reasons. First, they are very spherical. This enables them to be weighed by the aerodynamic drag force method. "Spherocarb" sphericity also promotes more uniform particle heating which helps minimize thermophoretic forces (forces induced on the particle due to temperature gradients on the surface). Secondly, the "Spherocarb" particles are approximately black at the wavelengths of interest. This allows for relatively easy particle heating and relatively easy particle temperature measurement. Thirdly, the available size range of "Spherocarb" particles (125-250 μm) allows particle diameter measurements to be made optically using a microscope. The large size also increases the magnitude of the 2.0 and 4.0 μm signals reaching the pyrometers, allowing for more accurate temperature measurement. Finally, the large size helps to reduce the relative magnitude of the thermophoretic forces exerted on the particle.

3.5.2 Experimental procedure.

Experiments were performed varying three parameters: particle diameter, particle temperature, and surrounding gas. Particle diameter was varied between 127 and 236 μm. Particle temperature ranged from 600 to 1200 K. Two surrounding gases were used, nitrogen and carbon dioxide.

An experiment is initiated by injecting a "Spherocarb" particle into the electrodynamic balance and purging the chamber with nitrogen at 20 ml/min for 20 minutes. The diameter of the particle is measured to ±5 μm with the

Ealing microscope. The particle is then weighed two times using the aerodynamic drag force technique. If the two weights deviate by more than 5%, a third weighing is performed or the particle is discarded and a new particle captured. Once the particle has been weighed, the nitrogen atmosphere in the chamber is maintained using a steady flow of 5 ml/min of nitrogen. The carbon dioxide laser is then turned on and warmed up for approximately 20 minutes in order to reduce fluctuations in the power to approximately ±15%. After the carbon dioxide laser is warmed up, the balancing voltage is recorded to within ±1.0 volt and the laser heating of the particle initiated. The DC balancing voltage is adjusted to balance the natural convective drag force and recorded to within ±0.5 volts along with the 2 and 4 μm detector signals used for particle temperature measurement. Particle temperatures could be measured to within ±30 K.

A force balance on the heated particle reveals that:

$$\Delta V_{nat}/V_i = F_{nat}/mg \qquad (3.50)$$

where

ΔV_{nat} = change in balancing voltage between an unheated and a heated particle (volts).

V_i = balancing voltage of an unheated particle (volts).

F_{nat} = natural convective drag force (N).

mg = particle weight (N).

When heating is discontinued, the balancing voltage should equal the initial balancing voltage. This serves as a check that the particle charge to mass ratio did not change during the experiment. This process is repeated 5-15 times

with varying carbon dioxide laser powers; i.e. varying particle temperatures. The particle is also periodically reweighed to provide a check that the particle mass did not change. Carbon dioxide is then purged through the chamber and the process is repeated.

3.5.3 Error estimation of natural convective drag measurements.

Taking the derivative of each side of equation 3.50 yields:

$$\partial(F_{nat}/mg) = \partial(\Delta V_{nat})/V_i - \partial(V_i)\Delta V_{nat}/V_i^2 \qquad (3.51)$$

Dividing equation 3.51 by the natural convective drag to weight ratio results in the following equation:

$$|\partial(F_{nat}/mg)/(F_{nat}/mg)| = |\partial(\Delta V_{nat})/\Delta V_{nat}| + |\partial(V_i)/V_i| \qquad (3.52)$$

Rearranging equation 3.50 yields:

$$\Delta V_{nat} = V_i F_{nat}/mg \qquad (3.53)$$

where

$$mg = (\pi/6)d^3\rho_p g \qquad (3.54)$$

We also know that F_{nat} is a function of particle diameter, particle temperature, and surrounding gas. F_{nat} is discussed in detail in Chapter 4. For the purposes of this error analysis, however, the numerical solution discussed in Chapter 4 will be used to estimate F_{nat} as a function of dia-

meter, temperature, and surrounding gas.

Substituting equations 3.53 and 3.54 into 3.52 yields:

$$|\partial(F_{nat}/mg)/(F_{nat}/mg)| = |\partial(\Delta V_{nat})(\pi/6)d^3\rho_p g/V_i F_{nat}| + |\partial(V_i)/V_i| \quad (3.55)$$

In experimentally measuring F_{nat}/mg, the only measured quantities are ΔV_{nat} and V_i, which can be measured with the following accuracy:

$$\Delta V_{nat} = \Delta V_{nat} \pm 0.5 \text{ volts.}$$

$$V_i = V_i \pm 1.0 \text{ volt.}$$

Figures 3.22, 3.23, and 3.24 are plots of $\partial(F_{nat}/mg)/(F_{nat}/mg)$ versus particle surface temperature for 50 μm, 100 μm, 200 μm diameter spheres, respectively. The density of the spheres was taken as 500 kg/m^3 and the surrounding gas was assumed to be nitrogen. Three initial balancing voltages, 50, 150, and 250 volts were examined in each case. The error involved in measuring the natural convective drag force divided by particle weight decreased with increasing balancing voltages and with increasing temperature. Little difference in error is predicted between particle diameters of 50 μm and 100 μm, however, larger errors are predicted with 200 μm diameter particles.

The following equation is taken from the dimensional analysis performed in section 4.3:

$$F_{nat} = (\mu^2/\rho)C_{DT} \quad (3.56)$$

where:

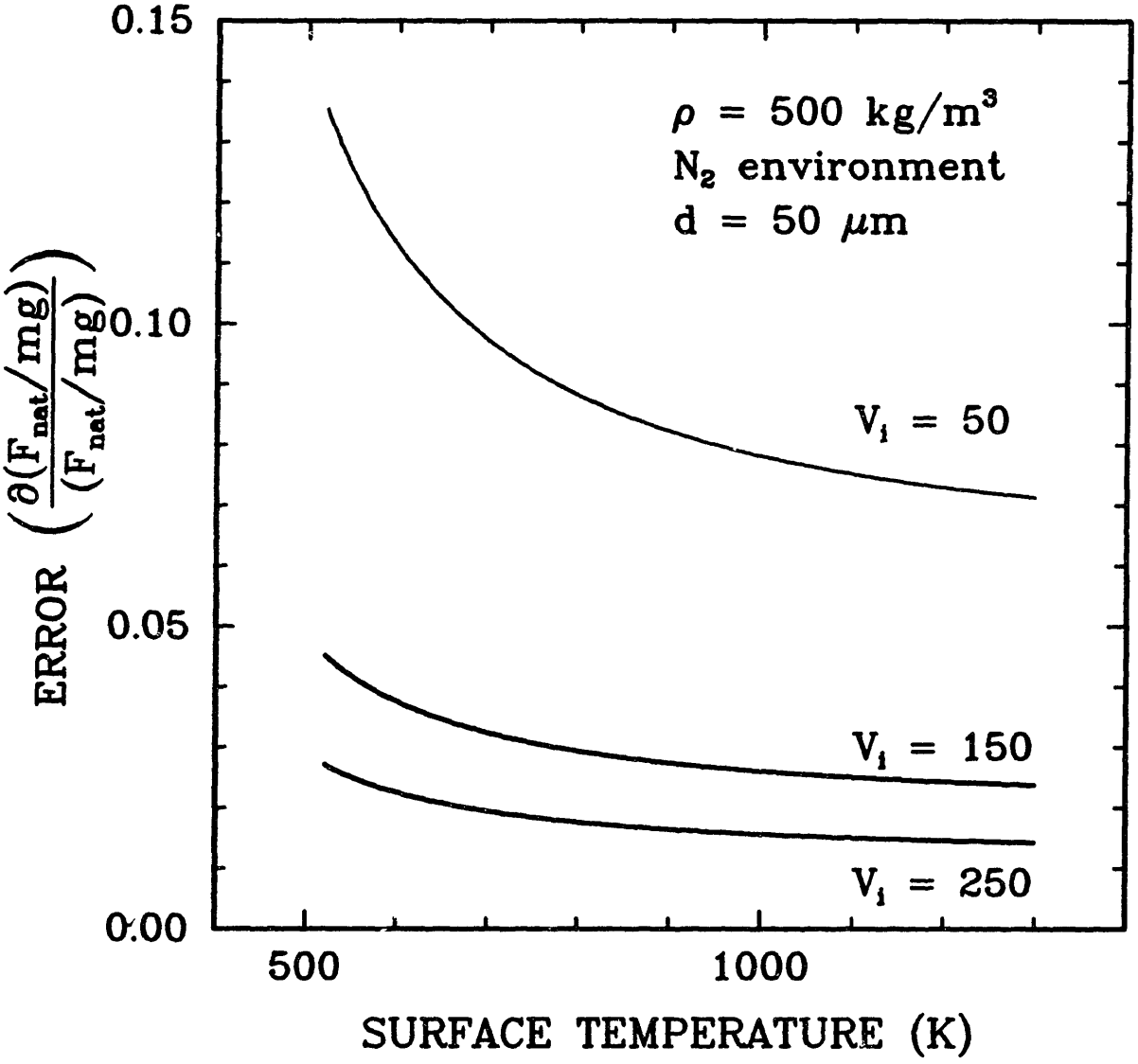

Figure 3.22 : Predicted relative error in (F_{nat}/mg) measurement versus particle surface temperature for a particle density of 500 kg/m^3, particle diameter of 50 μm, initial balancing voltages of 50, 150, and 250 volts, and a nitrogen environment.

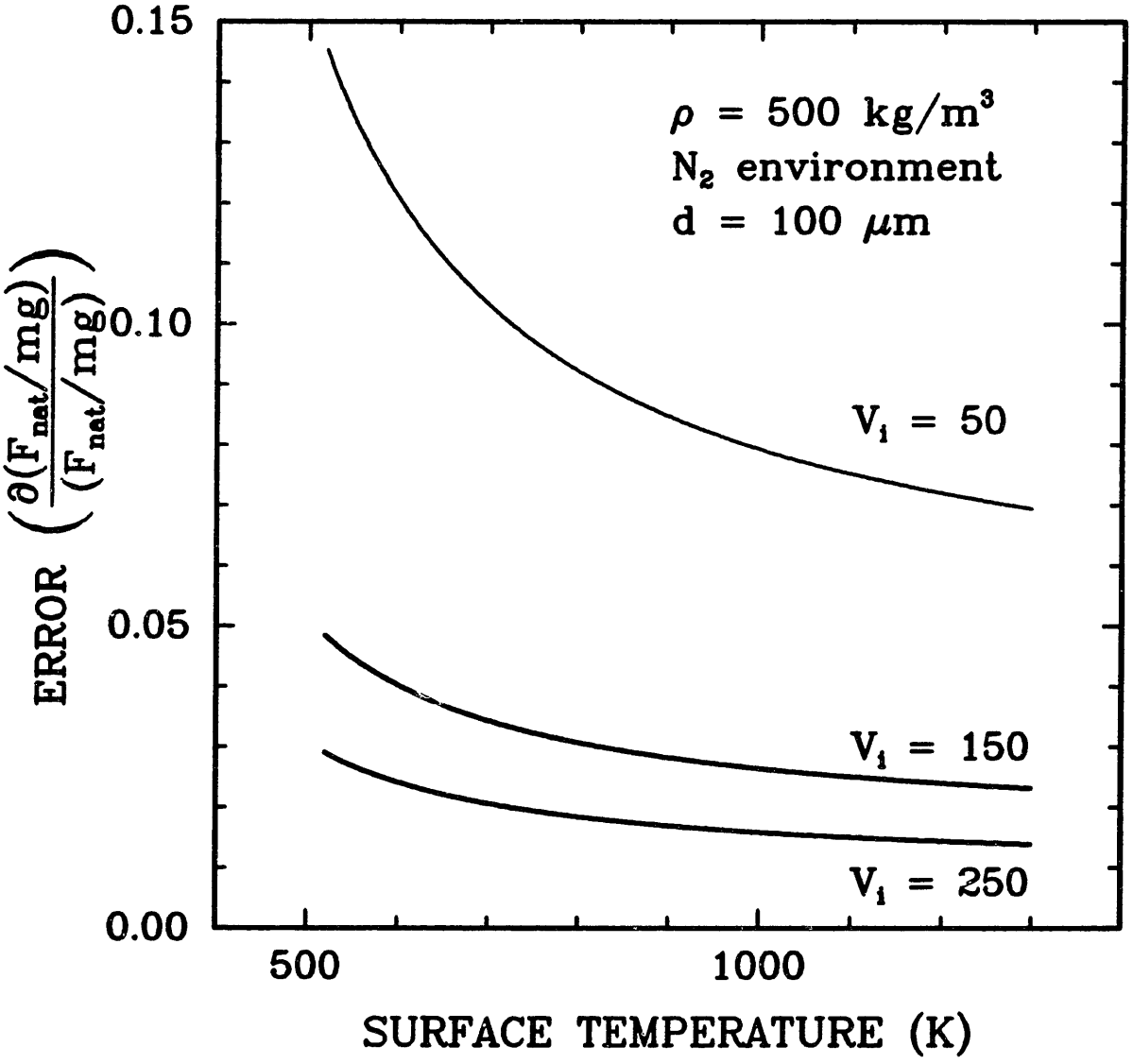

Figure 3.23 : Predicted relative error in (F_{nat}/mg) measurement versus particle surface temperature for a particle density of 500 kg/m^3, particle diameter of 100 μm, initial balancing voltages of 50, 150, and 250 volts, and a nitrogen environment.

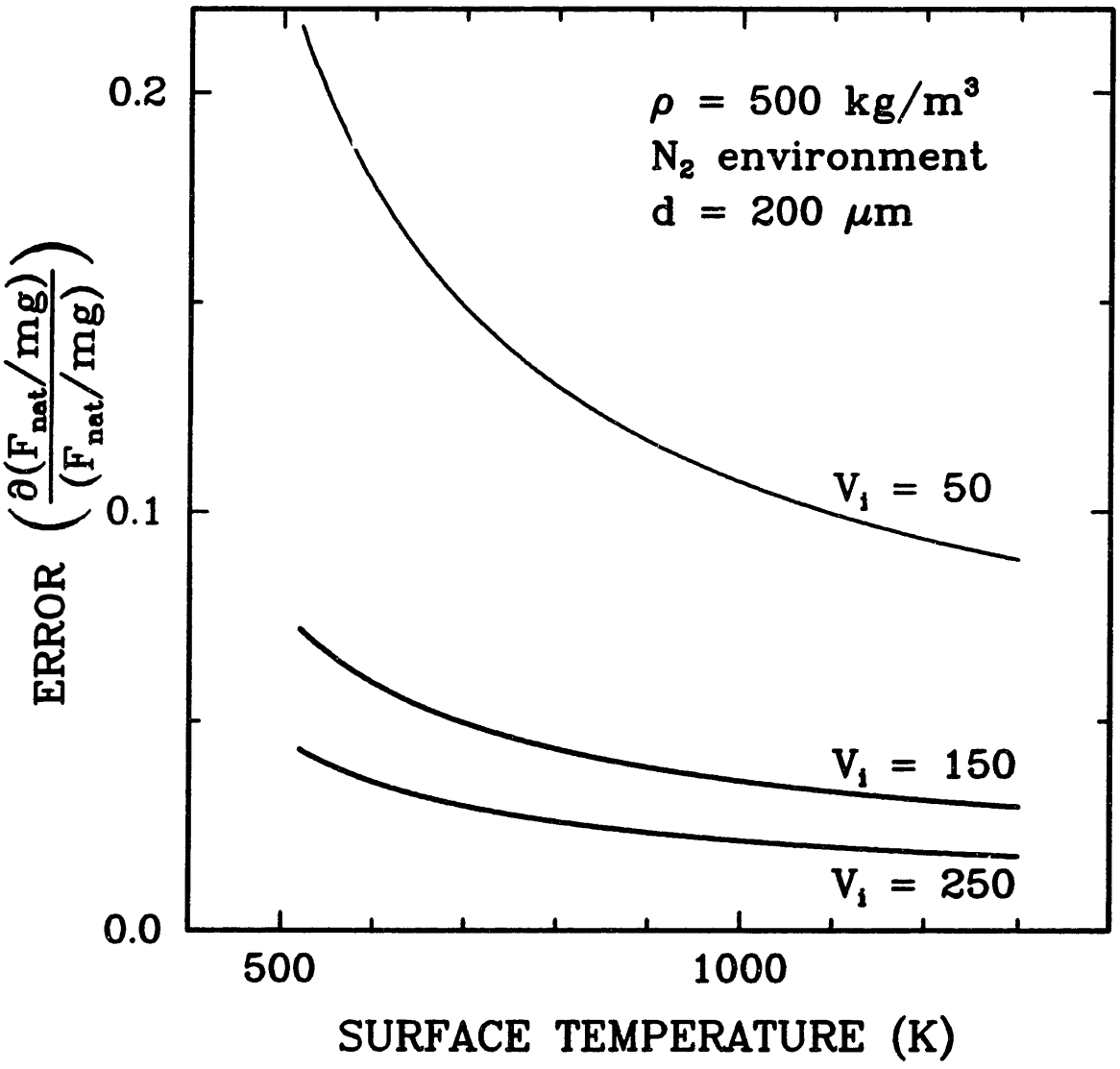

Figure 3.24 : Predicted relative error in (F_{nat}/mg) measurement versus particle surface temperature for a particle density of 500 kg/m^3, particle diameter of 200 μm, initial balancing voltages of 50, 150, and 250 volts, and a nitrogen environment.

$$C_{DT} \sim f(Gr) \tag{3.57}$$

and

$$Gr = g\beta\Delta T R^3/\nu^2 \tag{3.58}$$

We will first examine the error involved in measuring the Grashof number of a suspended particle. Taking the derivative of both sides of equation 3.58 yields:

$$\partial(Gr) = \partial(\Delta T)(g\beta R^3/\nu^2) + \partial(R)(3g\beta R^2\Delta T/\nu^2) - \partial(\nu)(2g\beta R^3/\nu^3) \tag{3.59}$$

Dividing through by the Grashof number results in:

$$\partial(Gr)/Gr = \partial(\Delta T)/\Delta T + 3\partial(R)/R + 2\partial(\nu)/\nu \tag{3.60}$$

It should be noted that the first and the third terms on the right hand side of equation 3.60 are not independent of each other. Both are a function of the particle surface temperature. For example, if the particle surface temperature measurement were 30 K greater than the actual particle surface temperture, the ΔT term in the Grashof number would cause the Grashof number measurement to be larger. The $1/\nu^2$ term, however, would cause the Grashof number measurement to be smaller. Because of these compensating terms, the Grashof number measurement error is buffered against bad temperature measurements. In terms of equation 3.60, the error due to an incorrect particle surface temperature should not be the sum of the absolute values of the first and third terms, but the difference of the absolute values. Equation 3.60 can then be rewritten as:

$$|\partial(Gr)/Gr| = | \, |\partial(\Delta T)/\Delta T| - |2\partial(\nu)/\nu| \, |$$

(3.61)

$$+ |3\partial(R)/R|$$

The particle surface temperature and particle radius can be measured with the following accuracy:

$$T_s = T_s \pm 30 \text{ K.}$$

$$R = R \pm 2.5 \ \mu m.$$

$\partial(Gr)/Gr$ is plotted against particle diameter in Figure 3.25 for three different particle surface temperatures, 500, 900, and 1300 K. Different surface temperatures have almost no effect on the uncertainty of measuring particle Grashof numbers. The error in measuring Grashof numbers is almost all associated with the uncertainty of measuring particle radius. $\partial(Gr)/Gr$ decreases from 18% for a 100 μm diameter particle to 8% for a 250 μm diameter particle.

Rearranging equation 3.56 yields:

$$C_{DT} = F_{nat}/(\mu^2/\rho) \tag{3.62}$$

Rearranging equation 3.50 results in the following:

$$F_{nat} = mg(\Delta V_{nat}/V_i) \tag{3.63}$$

If equations 3.62 and 3.63 are combined, the following equation will result:

$$C_{DT} = mg\Delta V_{nat}/((\mu^2/\rho)V_i) \tag{3.64}$$

Taking the derivative of both sides of equation 3.64, and then dividing through by equation 3.64 yields:

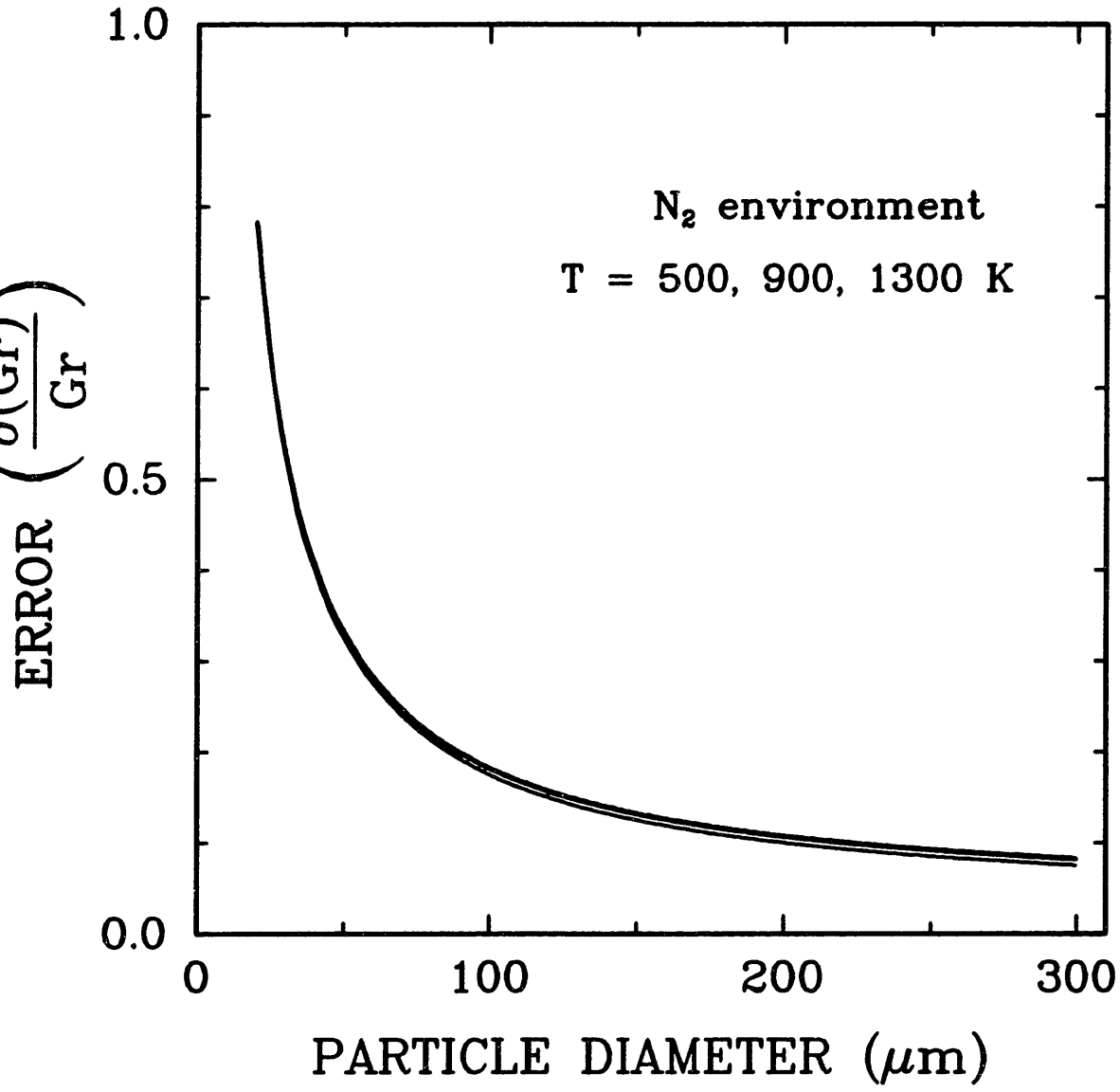

Figure 3.25 : Predicted relative error in Grashof number versus particle diameter for particle surface temperatures of 500, 900, and 1300 K in a nitrogen environment.

$$|\partial(C_{DT})/C_{DT}| = |\partial(m)/m| + |\partial(\Delta V_{nat})/\Delta V_{nat}| + |\partial(V_i/V_i| + |\partial(\mu^2/\rho)/(\mu^2/\rho)| \quad (3.65)$$

$|\partial(m)/m|$ is described in section 3.2.8. $|\partial(\Delta V_{nat}/\Delta V_{nat}|$ and $|\partial(V_i)/V_i|$ are described earlier in this section and $\partial(\mu^2/\rho)/(\mu^2/\rho)$ is a function of the error in measuring particle surface temperature.

The following are the quantities that need to be measured and the accuracy in which they can be measured:

$T_s = T_s \pm 30$ K.

$\Delta V_{nat} = \Delta V_{nat} \pm 0.5$ volts.

$d = d \pm 5$ μm.

$V_i = V_i \pm 1.0$ volt.

$\Delta V_{aero} = \Delta V_{aero} \pm 0.1$ volt.

Particle density and surrounding gas properties also are important in determining the uncertainty involved in measuring C_{DT}.

Figure 3.26 is a plot of $\partial(C_{DT})/C_{DT}$ versus particle diameter for initial balancing voltages of 50, 150, and 250 volts. This plot assumes a particle density of 650 kg/m^3 and a nitrogen atmosphere.

3.6 Kinetic measurements on single particles.

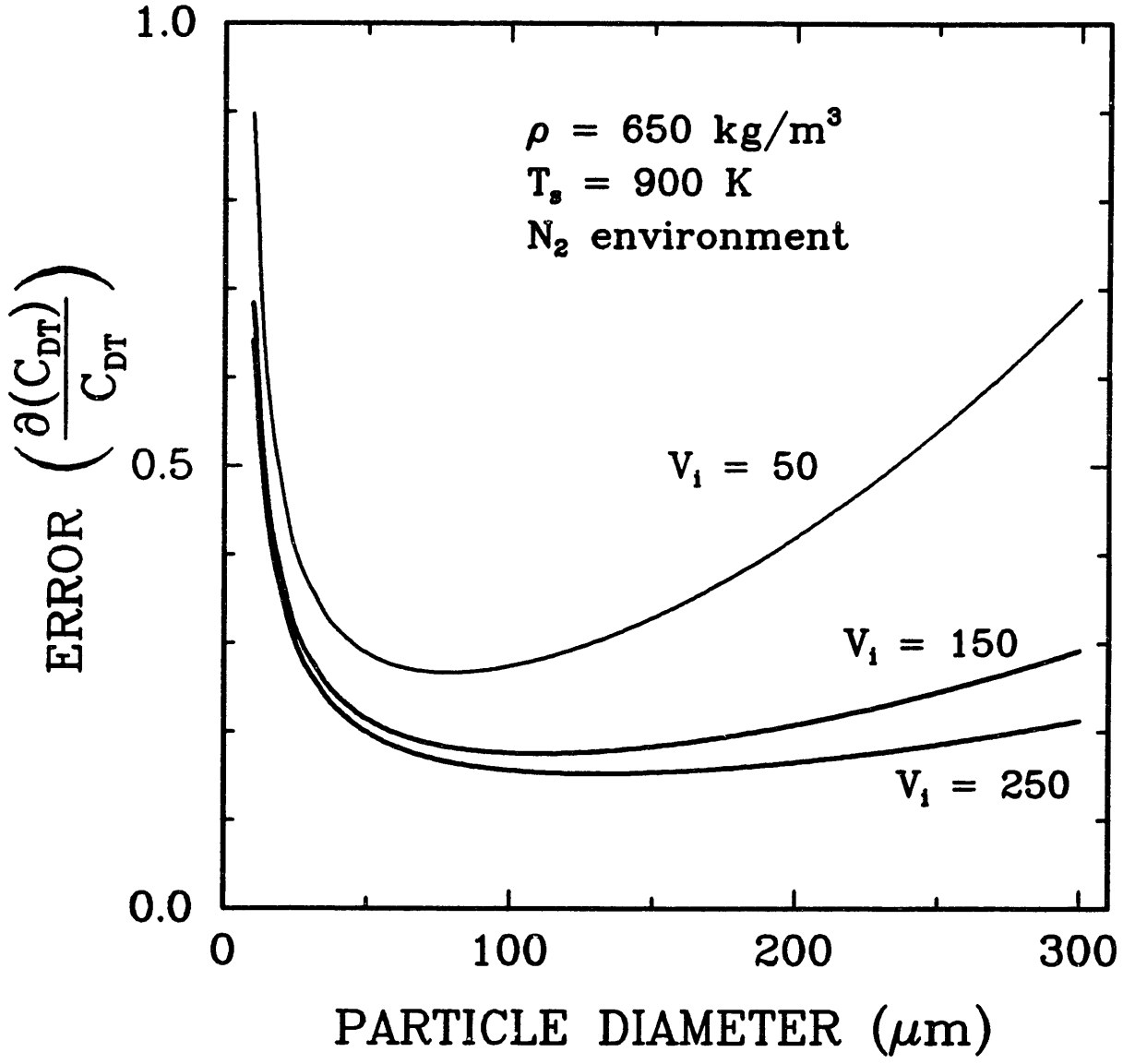

Figure 3.26 : Predicted relative error in overall dimensionless drag force coefficient versus particle diameter for a particle density of 650 kg/m^3, particle surface temperature of 900 K, initial balancing voltages of 50, 150, and 250 volts, and a nitrogen environment.

One very important measurement that can be performed in the EDB is gas-solid reaction kinetics and the simplest method for measuring kinetics is by measuring mass versus time at a specific temperature. Since particle balancing voltage is proportional to particle mass, mass versus time measurements can be performed on reacting particles by monitoring the particle balancing voltage as long as the reacting particle experiences no charge loss. Kinetic measurements are performed in the EDB by using the program FOLLOW2. A printout of FOLLOW2 is found in Appendix A. FOLLOW2 monitors the balancing voltage required to suspend a particle and the log ratio of the signals from the infrared pyrometers.

Temperature measurement by two color (2 μm and 4 μm) infrared pyrometry is discussed in detail in section 3.4. An example of the log ratio of the 2 μm signal to the 4 μm signal for a reaction of a 207 μm diameter "Spherocarb" in oxygen lasting 1050 seconds is shown in Figure 3.27. The average value of the log ratio signal is plotted versus time in Figure 3.28. The open squares represent the average values of the log ratio. Also shown in Figure 3.28 is the average signal ± one standard deviation. These points are represented as open triangles. The CO_2 laser control system seems to be doing a reasonable job keeping the log ratio signal constant through the first 500 seconds of the reaction. After 500 seconds, the log ratio signal began to creep up. The standard deviation is also increasing as the reaction proceeds. The increase in the standard deviation with time means that the particle is experiencing greater temperature fluctuations at later stages of the reaction. If the rate of reaction of the "Spherocarb" was linear in temperature, the standard deviation of the log ratio signal would have no effect on the reaction rate. Unfortunately,

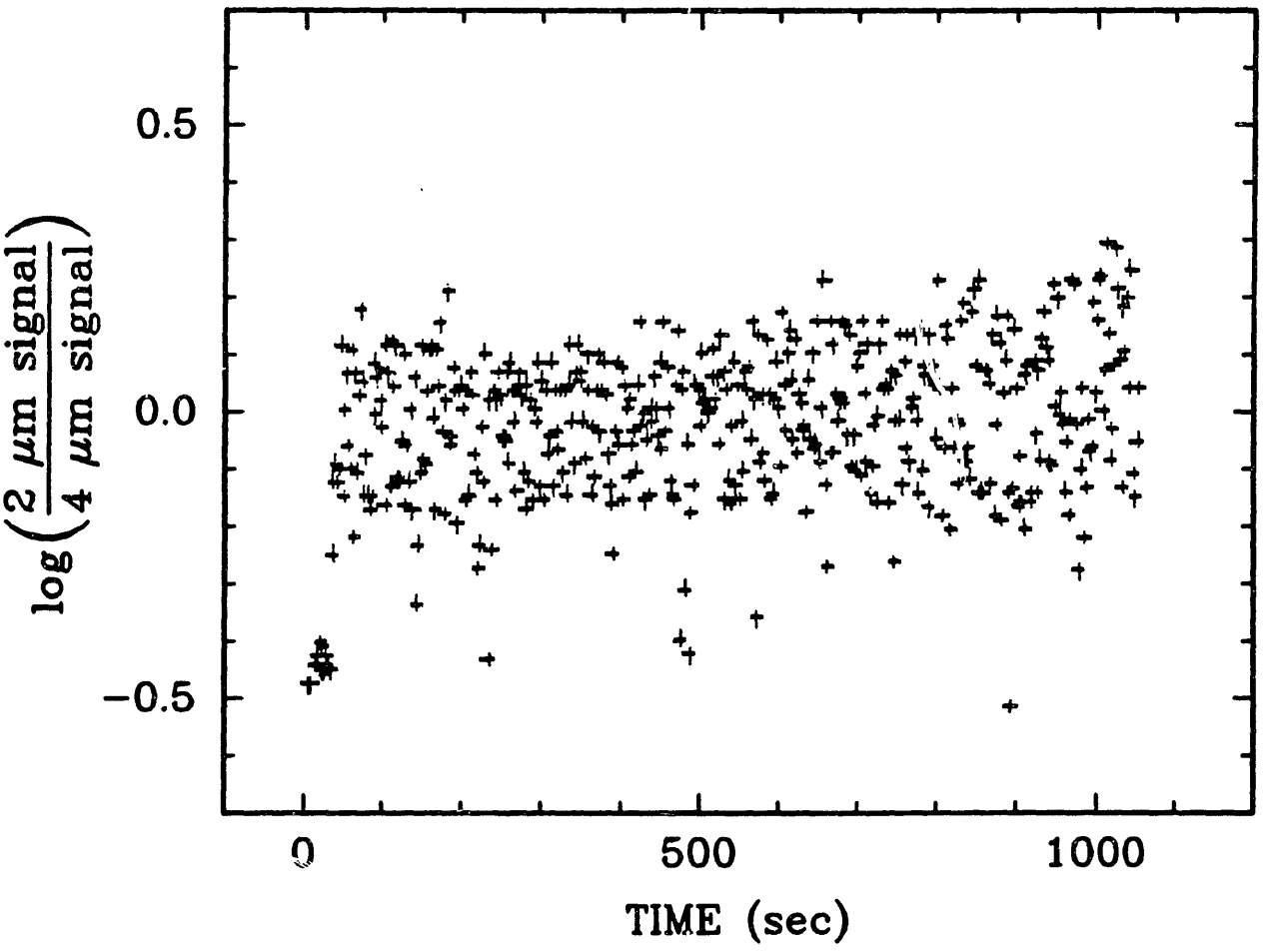

Figure 3.27 : log[(2 μm detector signal)/(4 μm detector signal)] versus time for a 207 μm diameter "Spherocarb" reacting in oxygen at 773 K.

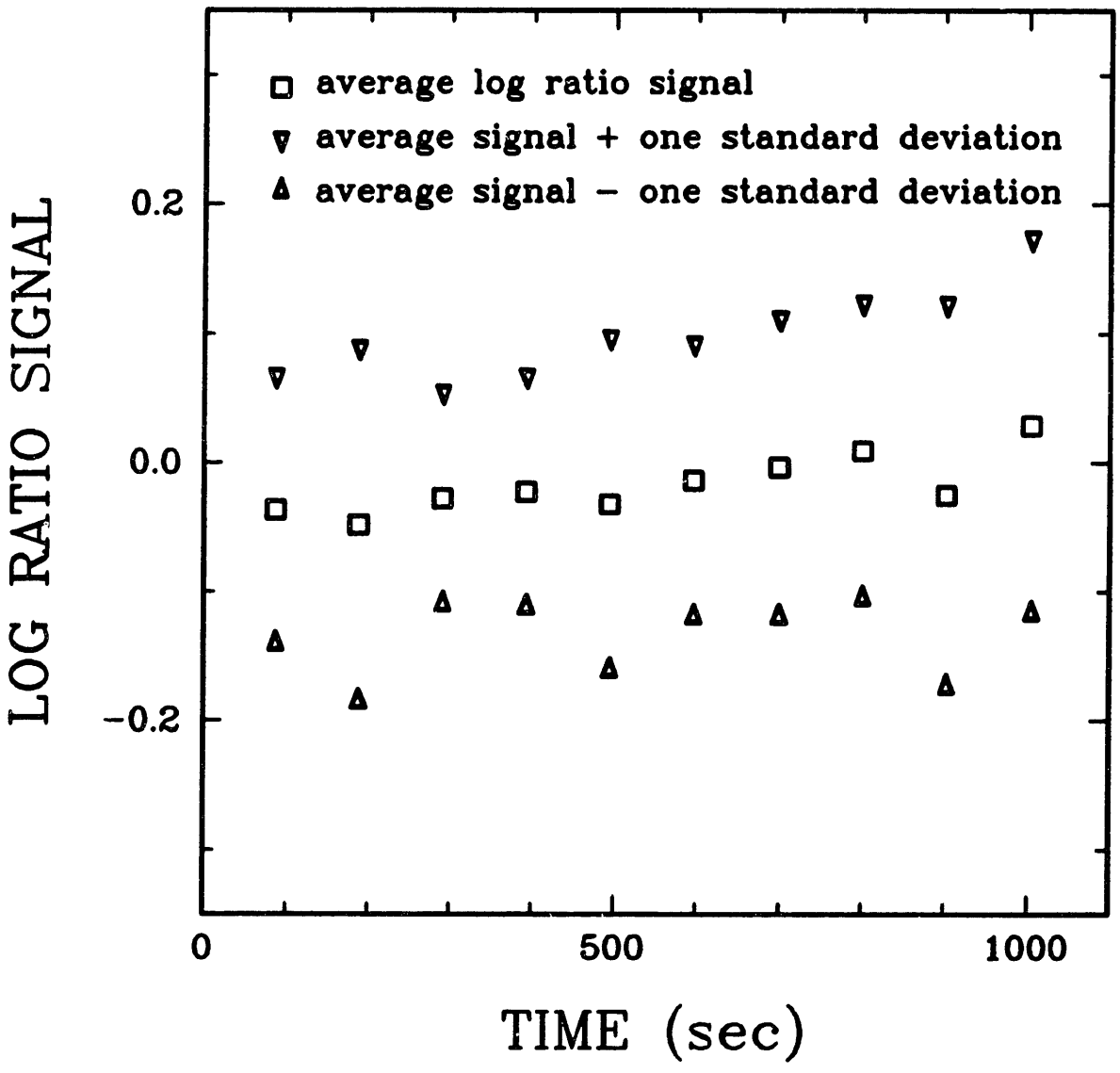

Figure 3.28 : Average log[(2 μm detector signal)/(4 μm detector signal)] ± one standard deviation versus time for a 207 μm diameter "Spherocarb" particle reacting in oxygen at 773 K.

the reaction rate of "Spherocarb" has been shown to be proportional to exp[-36,000/RT] [41,42]. An increase in temperature causes an exponential increase in reaction rate. Therefore, the average of the log ratio is not the correct value to be used in determining the average temperature of reaction.

Figure 3.29 shows the distribution of the log ratio signals shown in Figure 3.27 in the form of the fraction of total log ratio signals above a certain log ratio value versus that log ratio value. The average value of the log ratio signal is -0.0232 and the standard deviation is 0.1172.

A better method of determining the average temperature of reaction would be to insert each individual value of the log ratio signal presented in Figure 3.27 into equation 3.49 to determine the particle temperature at each stage of the reaction. These temperatures could then be inserted into the following expression to determine a dimensionless rate at each stage of reaction:

$$\text{rate} = \exp[-36{,}000/(RT)] \qquad (3.66)$$

The arithmetic average of all these reaction rates would then be used to back calculate an average temperature for the reaction. When this is done using the points up through 50% conversion, an average temperature of 773 K is calculated. If the arithmetic log ratio average is used without taking into consideration the exponential effect of temperature on rate, an average temperature of 749 K is calculated. In conclusion, when comparing two reactions occurring with the same average log ratio signal but different standard deviations, a higher average temperature will be calculated for the reaction with the higher stand-

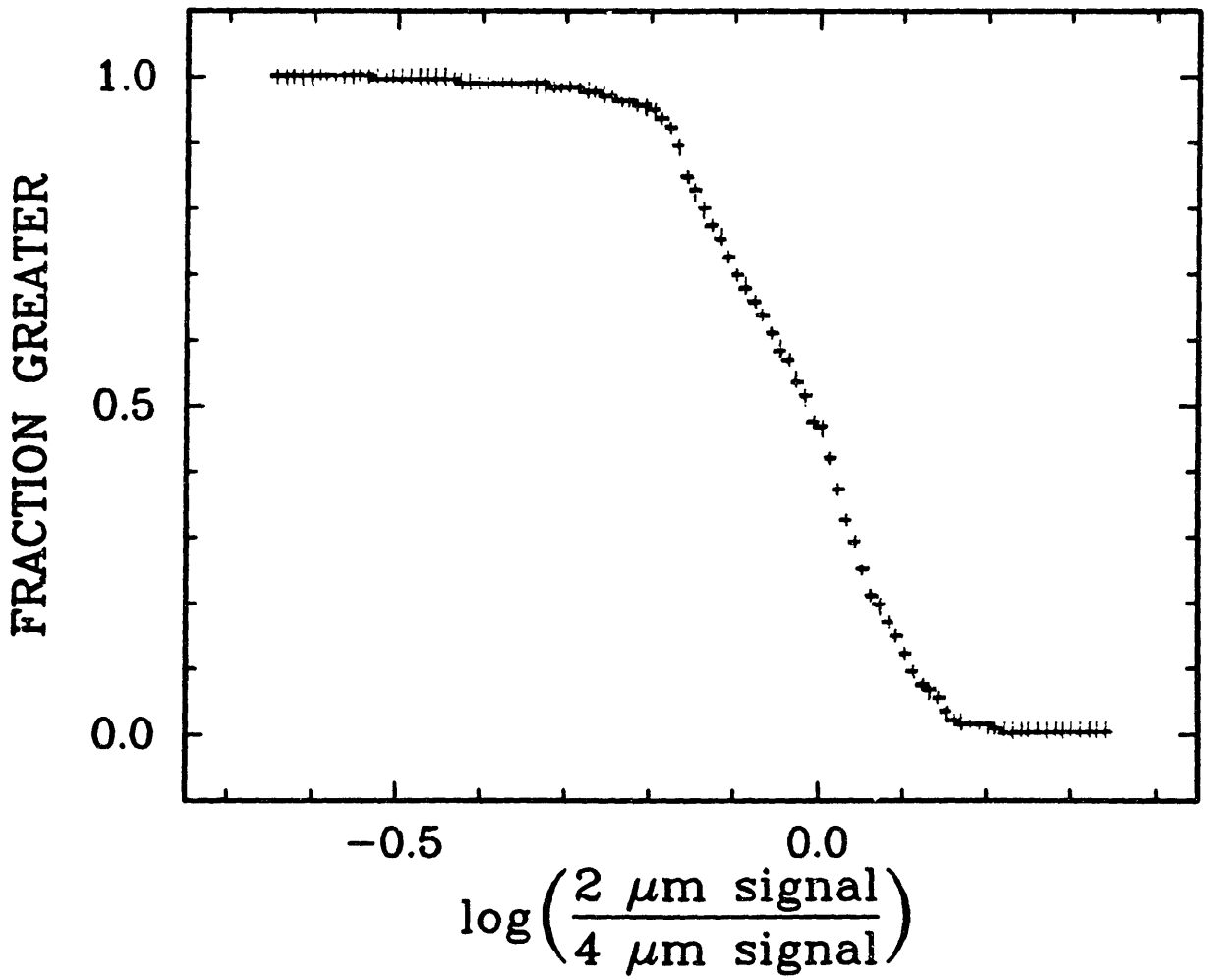

Figure 3.29 : Distribution of the log ratio signals depicted in Figure 3.27.

ard deviation in the log ratio signal when the exponential effect of temperature on rate is taken into consideration.

An even simpler method would be to calculate two log ratios:

log ratio(high) = average log ratio + standard deviation.
log ratio(low) = average log ratio - standard deviation.

From these two log ratios and equation 3.49, a high and low temperature can be calculated, from which the following high and low reaction rates may be calculated:

rate(high) = exp[-36,000/RT(high)]
rate(low) = exp[-36,000/RT(low)]

The arithmetic average of these two reaction rates would then be used to back calculate an average temperature for the reaction. When this simpler method is used an average temperature of 773 K is again calculated. It is this simpler method of determining average temperature that is utilized in this thesis.

Figure 3.30 is a plot of balancing voltage versus time for the same "Spherocarb" as Figures 3.27, 3.28, and 3.29. The log ratio data in Figure 3.27 has been broken up into ten equal divisions and the average temperature calculated for each division by the procedure proposed in the preceeding paragraph. The average temperatures are also plotted in Figure 3.30. The reaction proceeds with a relatively constant temperature up to about 600 sec, after which the average temperature begins to rise. This rise in temperature corresponds to a rise in reaction rate as measured as a function of the change in balancing voltage over the change in time. In the case of "Spherocarb", a

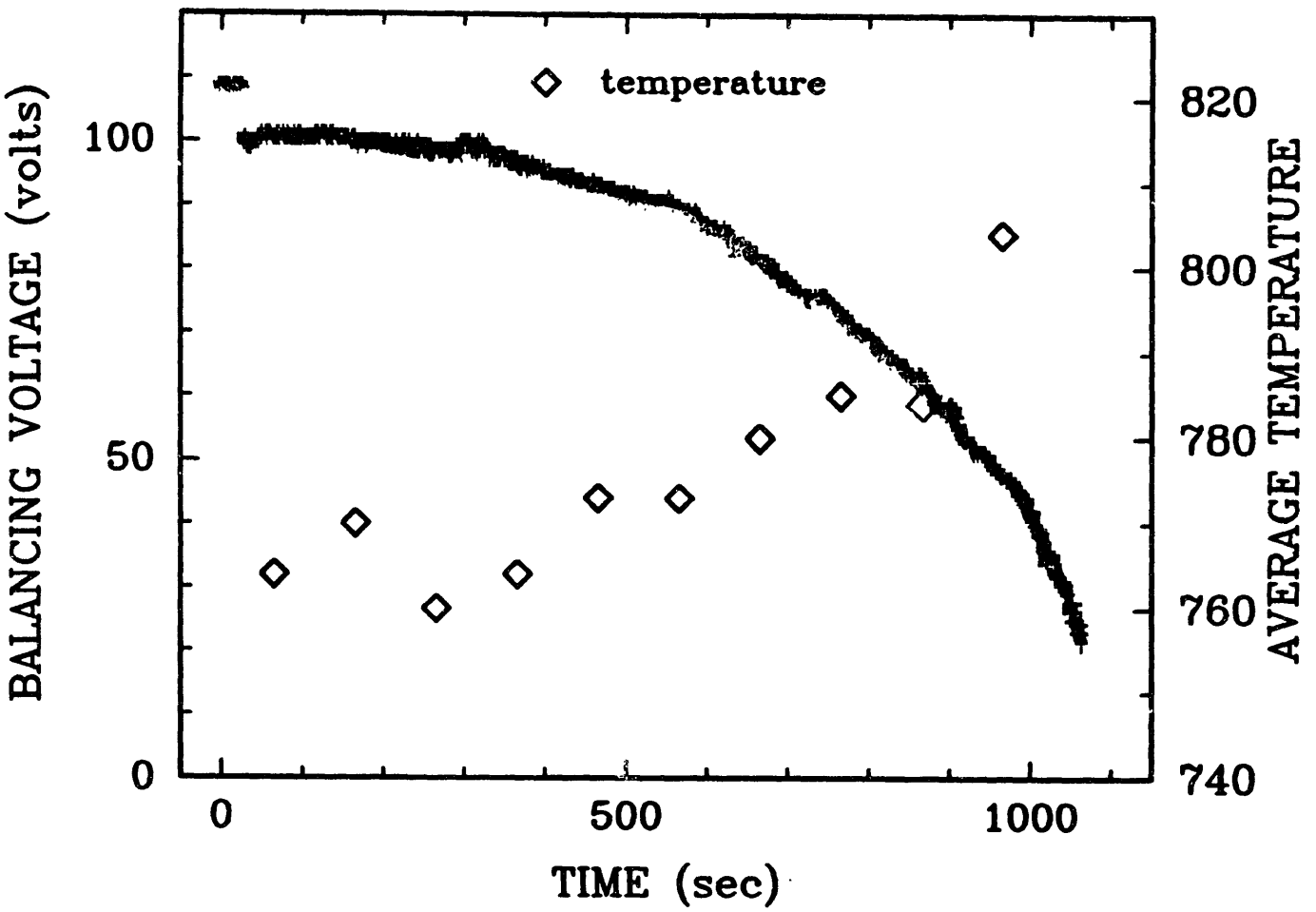

Figure 3.30 : Balancing voltage and temperature versus time for a single 207 μm diameter "Spherocarb" particle reacting in oxygen at 773 K.

20 K change in particle temperature results in a doubling of the reaction rate. It is believed that greater particle instability at later stages of the reaction is causing the greater fluctuations in temperature which in turn cause the particle to experience a larger average temperature. Since the average temperature of the particle is increasing with extent of reaction, kinetic interpretation of these data becomes more difficult in later stages of the reaction.

3.7 Conclusions for experimental measurement techniques.

1) By taking photographs of suspended particles, single particle diameter measurements can be performed to within ± 3 μm.

2) The aerodynamic drag force technique has been shown to be useful in measuring single particle mass, density, porosity, and excess charge.

3) Carbon dioxide adsorption and the Dubinin-Polanyi equation have successfully been used to measure single particle surface areas of the synthetic char "Spherocarb".

4. NATURAL CONVECTIVE DRAG.

4.1 Introduction.

4.1.1 Description of problem / motivation.

A vertical force balance on an unheated suspended particle reveals that:

$$mg = qCV/z_0 \tag{4.1}$$

where m is the particle mass, g is the gravitational acceleration, q is the number of excess charges on the suspended particle, C is a chamber constant, V is the DC voltage required for stable balancing of the particle, and z_0 is the characteristic length of the chamber. If no other forces are acting on the particle, changes in particle mass can be followed continuously by monitoring the DC voltage required for particle balancing. Upon laser heating of the suspended particle, however, the fluid near the particle surface is heated due to conduction. Since the ambient fluid is cool, the fluid near the particle surface rises, and a natural convective flow field is set up which introduces a natural convective drag force, F_{nat}, on the particle. The vertical force balance now becomes:

$$mg = qCV/z_0 + F_{nat} \tag{4.2}$$

This upward drag force on the particle complicates interpretation of the particle weight change data. Arnold and Lewittes [12] were the first to report such a force.

Later, Spjut [7] reported drag force magnitudes as great as the particle mass. In order to determine particle reaction rate, changes in particle mass must be distinguished from changes in drag force. Therefore, characterization of the natural convective drag force is necessary if the electrodynamic balance is to be used for continuous mass versus time measurements.

Due to the small size of the particles being examined in the electrodynamic balance, the corresponding Grashof number will also be small, with the range of interest being between 0.0005 and 1.0. The Reynold's number based on the maximum convective velocity is much less than one.

4.1.2 Example of natural convective drag.

An example of how the natural convective drag affects the balancing voltage of a heated "Spherocarb" particle is depicted in Figure 4.1. At time zero, the 183 μm diameter "Spherocarb" particle is balanced in the chamber and is at ambient temperature. Laser heating begins at 0.28 sec and ends at 1.94 sec and was performed in an inert N_2 environment to prevent any chemical reaction. After the particle is heated to 610 K, the natural convective drag force develops and the voltage required for balancing decreases. The initial, unheated balancing voltage is 125 volts. According to Figure 4.1, the balancing voltage changes by ~ 6.5 volts which means that the heated balancing voltage for this particle is lowered to ~ 118.5 volts. This represents a 5% decrease in balancing voltage that is caused solely by the natural convective drag force.

4.2 Previous work.

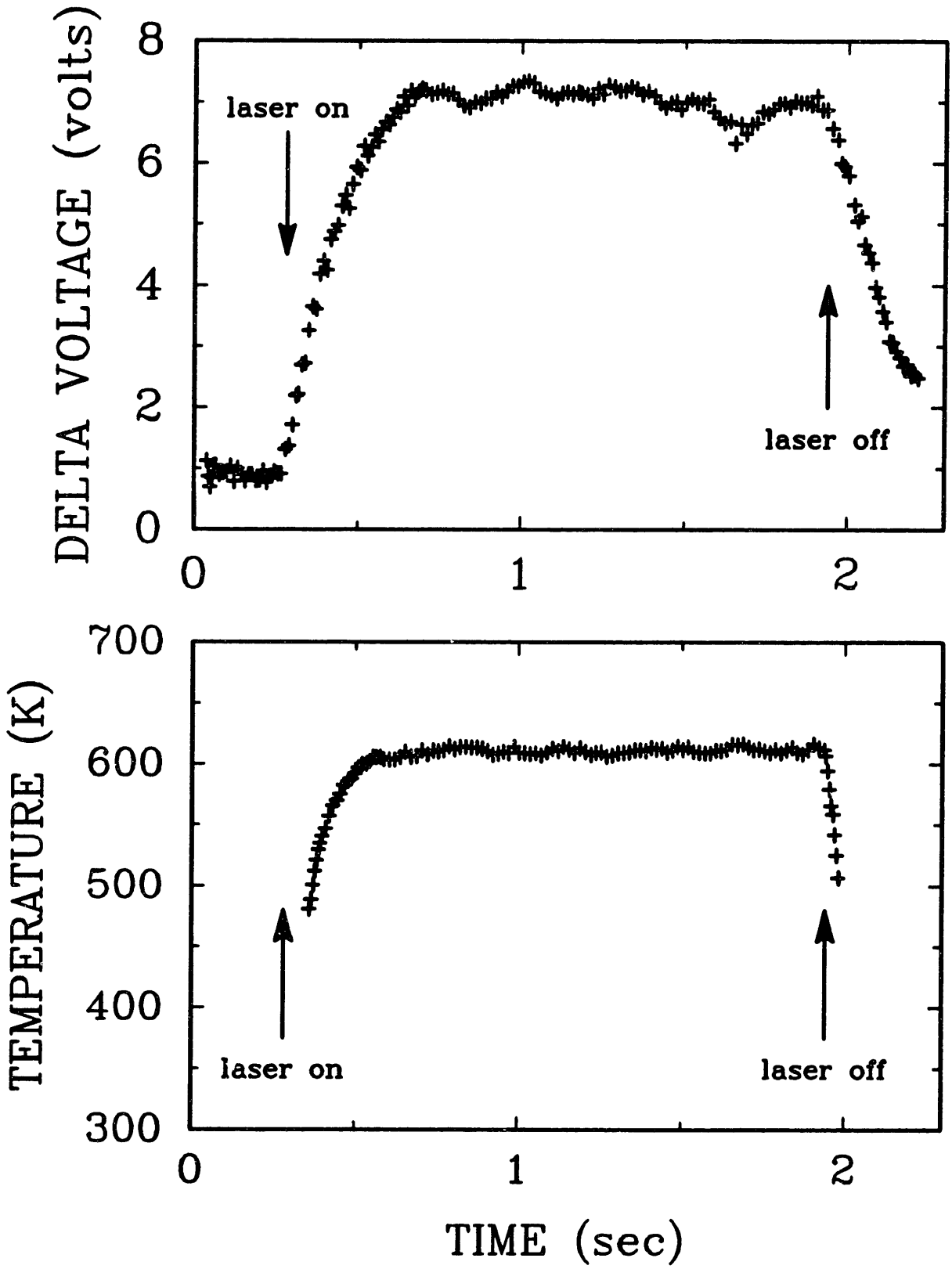

Figure 4.1 : Change in balancing voltage and temperature for a 183 μm diameter "Spherocarb" heated to 610 K in nitrogen.

Experimental studies of natural convection around a heated sphere at small Grashof number have been conducted by Meyer [42], Elenbaas [43], Ranz and Marshall [44], Mathers, Madden, and Piret [45], Tsubouchi and Sato [46], and Yuge [47]. These authors, however, were interested in heat transfer, and only measured the overall Nusselt number. No experimental measurements of the drag force induced on a sphere by a natural convective flow field are found in the literature.

The classic references to analytical treatments of natural convection around spheres at small Grashof numbers are Mahony [48], Fendell [49], Hossain and Gebhart [50], and Hieber and Gebhart [51]. Each attempted to solve the problem by a perturbation method, but a suitable outer solution could not be obtained so as to match with the inner expansion. This problem can, however, be solved by a series truncation method [52] or using finite difference methods to obtain solutions [53-56]. The Boussinesq approximation is used in all of the above-referenced studies. Only Geoola and Cornish [55,56] calculate a natural convective drag force; all previous studies concentrate on the heat transfer aspects of the problem.

4.3 Dimensional analysis.

Dimensional analysis reveals that:

$$F_{nat} = \frac{\mu^2}{\rho} C_{DT} \qquad (4.3)$$

where

F_{nat} = natural convective drag force (N).

μ = surrounding gas viscosity (kg/m sec).

ρ = surrounding gas density (kg/m^3).

C_{DT} = dimensionless drag force coefficient.

The dimensionless drag force coefficient is some unknown function of the Grashof number, Gr, and the Prandtl number, Pr, which are defined as follows:

$$Gr = g\beta(T_s - T_\infty)R^3/\nu^2$$

$$Pr = C_{p\mu/k}$$

where

g = gravitational acceleration (m/sec^2).
β = coefficient of volume expansion ($1/K$).
T_s = particle surface temperature (K).
T_∞ = ambient gas temperature (K).
R = particle radius (m).
ν = gas kinematic viscosity (m^2/sec).
C_p = gas heat capacity at constant pressure per unit mass ($m^2/sec^2\ K$).
k = gas thermal conductivity ($kg\ m/sec^3\ K$).

Note that we have used the convention of Geoola and Cornish to define Gr, where R is used as the characteristic length instead of particle diameter. All gas properties are evaluated at the gas film temperature, T_f, defined as $(T_s + T_\infty)/2$. The value of β used in the definition of Gr is $1/T_\infty$ [57]. The numerical results will be presented primarily as a function of the dimensionless drag force coefficient and the Grashof number. It should be noted that evaluating the surrounding gas properties at the ambient gas temperature or the particle surface temperature has little effect on the comparison between numerical and experimental results for the two gases utilized in this work. With both N_2 and CO_2, when the evaluation temperature of the gas properties are increased from the ambient temperature to the particle surface

temperature, the Grashof number decreases and the factor, μ^2/ρ, increases. Numerically, when the Grashof number decreases, the predicted C_{DT} also decreases. Experimentally, the increase in the factor, μ^2/ρ, will by equation 4.3, cause C_{DT} to decrease also. This behavior of the surrounding gas properties with temperature makes the choice of evaluation temperature less critical. The dependence of the gas property evaluation temperature on the magnitude of the natural convective drag force is discussed more thoroughly in section 4.6.1.5.

4.4 Theoretical Model.

A numerical technique modeled after that of Geoola and Cornish [55,56] is used to solve the conservation equations of mass, momentum, and energy in two dimensions for the gas phase near the particle. Methods were developed to obtain both a steady-state and a transient solution. The governing equations are expressed in spherical polar coordinates $(\tilde{r},\theta,\phi)$. Radial distance, temperature, velocities, and time are nondimensionalized in the following manner:

$$r = \tilde{r}/R \tag{4.4}$$

$$T = (\tilde{T} - T_\infty)/(T_S - T_\infty) \tag{4.5}$$

$$u_r = \tilde{u}_r \tilde{r}/\nu \tag{4.6}$$

$$u_\theta = \tilde{u}_\theta \tilde{r}/\nu \tag{4.7}$$

$$t = \tilde{t}\nu/\tilde{r}^2 \tag{4.8}$$

where the tilda over a variable represents the dimensional form of the variable. The assumptions used in this model are

that: 1) the particle is spherical; 2) the particle has a uniform, constant surface temperature; 3) the particle is not rotating; 4) flow is axisymmetric (all the dependent variables are independent of ϕ); 5) the only body force is gravity; 6) the Boussinesq approximation applies; and 7) other fluid properties (such as viscosity, specific heat, and thermal conductivity) are constant. The Navier-Stokes and continuity equations were combined and expressed in stream function-vorticity form. The energy, vorticity transport, and stream function equations are then transformed from polar coordinates (r,θ) to rectangular coordinates (z,θ) by means of the transformation:

$$r = e^{z} \tag{4.9}$$

The dimensionless energy conservation equation becomes:

$$e^{2z}\frac{\partial T}{\partial t} + \frac{1}{e^{z}\sin\theta}\left(\frac{\partial\psi\partial T}{\partial z\partial\theta} - \frac{\partial\psi\partial T}{\partial\theta\partial z}\right) = \frac{1}{Pr}\left(\frac{\partial^2 T}{\partial z^2} + \frac{\partial T}{\partial z} + \frac{\partial^2 T}{\partial\theta^2} + \cot\theta\frac{\partial T}{\partial\theta}\right) \tag{4.10}$$

where the velocity components are:

$$u_z = -\frac{1}{e^{2z}\sin\theta}\frac{\partial\psi}{\partial\theta} \tag{4.11}$$

$$u_\theta = \frac{1}{e^{2z}\sin\theta}\frac{\partial\psi}{\partial z} \tag{4.12}$$

The vorticity transport equation is given by:

$$e^{2z}\frac{\partial G}{\partial t} + \frac{1}{e^{z}\sin\theta}\left[\frac{\partial\psi}{\partial z}\left(\frac{\partial G}{\partial\theta} - 2G\cot\theta\right) - \frac{\partial\psi}{\partial\theta}\left(\frac{\partial G}{\partial z} - 2G\right)\right] = e^{2z}E^2(G) + e^{2z}Gr\sin^2\theta\left(\frac{\partial T}{\partial z} + \cot\theta\frac{\partial T}{\partial\theta}\right) \tag{4.13}$$

where G is the modified dimensionless vorticity, defined as follows:

$$G = \zeta e^{z} \sin \theta \tag{4.14}$$

The "E^2" operator is defined as:

$$e^{2z}E^2 = \frac{\partial^2}{\partial z^2} - \frac{\partial}{\partial z} + \frac{\partial^2}{\partial \theta^2} - \cot \theta \frac{\partial}{\partial \theta} \tag{4.15}$$

The stream function equation is written:

$$e^{2z}G = e^{2z}E^2(\psi) \tag{4.16}$$

The steady-state boundary conditions are as follows. At the sphere surface ($z = 0$):

$$\psi = 0$$
$$G = \frac{\partial^2 \psi}{\partial z^2}$$
$$T = 1$$

Along the axis of symmetry ($\theta = 0$ or $\theta = \pi$):

$$\psi = 0$$
$$G = 0$$
$$\frac{\partial T}{\partial \theta} = 0$$

At the outer boundary ($z = z_\infty$):

$$\psi = \text{smooth}$$
$$G = \text{smooth}$$
$$T = 0$$

The dependent variable is made smooth at the outer boundary by approximating its value using a first-order polynomial in z and specific values at the two adjacent nodes. The time-dependent terms were included in the energy and the vorticity transport equations for the transient

solution. The initial conditions (t=0) for the transient case are as follows:

ψ = 0 for all z and θ.
G = 0 for all z and θ.
T = 1 at z = 0,
T = 0 for all other z.

Upon solution of the steady-state stream function, vorticity, and temperature, other quantities are calculated as follows [55,56]:

Local Nusselt number at the sphere surface:

$$Nu_\theta = -2\frac{\partial T}{\partial z}\Big|_{z=0} \tag{4.17}$$

Average or overall Nusselt number:

$$Nu = \frac{1}{2}\int_0^\pi Nu_\theta \sin\theta d\theta \tag{4.18}$$

Dimensionless pressure at the front stagnation point:

$$K_0 = 4\int_0^{z_\infty}\frac{\partial\zeta}{\partial\theta}dz - 2\int_0^{z_\infty}\frac{1}{e^z}\frac{\partial}{\partial t}\left(\frac{\partial^2\psi}{\partial\theta^2}\right)dz + 2Gr\int_0^{z_\infty}Te^z dz \tag{4.19}$$

Dimensionless pressure at the sphere surface (surface pressure):

$$K_\theta = K_0 + 2Gr(1-\cos\theta) + 2\int_0^\theta\left(\frac{\partial\zeta}{\partial z} + \zeta\right)d\theta \tag{4.20}$$

Dimensionless pressure drag (form drag):

$$C_{DP} = \int_0^\pi K_\theta \sin 2\theta d\theta \tag{4.21}$$

Dimensionless viscous drag (frictional drag):

$$C_{DF} = 4\int_0^{\pi} \zeta_s \sin^2\theta d\theta \tag{4.22}$$

Dimensionless total drag:

$$C_{DT} = C_{DP} + C_{DF} \tag{4.23}$$

The integrands in equations (4.19) and (4.20) are evaluated at $\theta = 0$ and at $z = 0$, respectively.

4.5 Numerical Method.

Finite differencing was used to solve equations 4.10, 4.13, and 4.16. Central differences were used to approximate the first-order derivatives of temperature, vorticity, and the stream function, except in the convective terms of the energy and vorticity equations where an upwind differencing method was used for stability purposes. The upwind or upstream differencing method utilizes backward differencing when the velocity of the fluid is positive and forward differencing when the velocity of the fluid is negative. Therefore, the one-sided difference is always on the upwind side of the node point. In the steady-state case, the energy, vorticity, and stream function equations were solved simultaneously using an extrapolated Gauss-Seidel method [58]. The Gauss-Seidel method updates the coefficients point by point using the following relationship:

$$W_{i,j}^{(L)} = W_{i,j}^{(L-1)} + \omega_w(W_{i,j}^{(L)} - W_{i,j}^{(L-1)}) \tag{4.24}$$

where W represents either temperature, vorticity, or the

stream function, ω_w is a relaxation parameter used to accelerate the rate of convergence, and L is the iteration number. The convergence criteria used was:

$$\sum_{i=1}^{M} \sum_{j=1}^{N} |W_{i,j}^{(L)} - W_{i,j}^{(L-1)}| < \epsilon_w \qquad (4.25)$$

for all three dependent variables: T, G, and ψ. For all the steady-state computations, $\epsilon_T = 0.00001$, $\epsilon_G = 0.001$, $\epsilon_\psi = 0.0001$, $\omega_T = 1.5$, $\omega_G = 1.2$, and $\omega_\psi = 1.3$. In the transient computations, the energy and vorticity transport equations were solved using Peaceman and Rachford's ADI method [59]. The stream function equation was solved at each time step using an extrapolated Gauss-Seidel method. In both the steady and transient cases derivative boundary conditions along the axis of symmetry were approximated by third-order polynomials and the derivative boundary conditions at the particle surface were approximated by fifth-order polynomials. The boundary conditions at the outer boundary were approximated by first order polynomials.

The typical number of mesh points that was used in the calculations was M = 100 and N = 31. M is the number of nodes in the radial direction and N is the number of nodes in the theta direction. Typical values of m and n, mesh spacings in the z and θ directions, respectively, were 0.04 and 0.1047. Printouts of both the steady-state and transient algorithms are found in Appendix B.

4.6 Discussion of numerical results.

4.6.1 Steady-state solutions.

4.6.1.1 Dependence of solution on boundary conditions and grid size.

Both the steady-state and transient solutions were solved with the same boundary conditions as Geoola and Cornish [55,56] except at the outer boundary. Instead of forcing the vorticity and the stream function to zero at the outer boundary, these dependent variables were approximated by linear polynomial extrapolations in the z-direction using the values of the vorticity and the stream function at the two preceeding nodes. For example, the the case of vorticity:

$$G(z_{\infty},j) = 2G(z_{\infty}-1,j) - G(z_{\infty}-2,j) \qquad (4.26)$$

When the vorticity and the stream function are forced to zero, no mass is allowed to leave through the outer boundary. Therefore, a recirculation pattern is set up. When the vorticity and stream function at the outer boundary are not set to zero and are approximated using adjacent values, mass is permitted to cross the outer boundary, and no recirculation pattern is set up. Gas flows into the bottom of the outer sphere and out of the top. The overall drag coefficient was found to be independent of the type of outer boundary condition used as long as the outer boundary tended toward infinity. The drag coefficient was found to be very sensitive to grid size in the radial direction until some critical grid size was obtained, however. Figure 4.2 is a plot of computed steady-state drag coefficient, C_{DT}, for Grashof number = 0.05 versus location of the outer boundary for the two types of outer boundary conditions examined. The value of the critical grid size was a function of the outer boundary condition used. If the outer boundary condition approximates the vorticity and stream function using

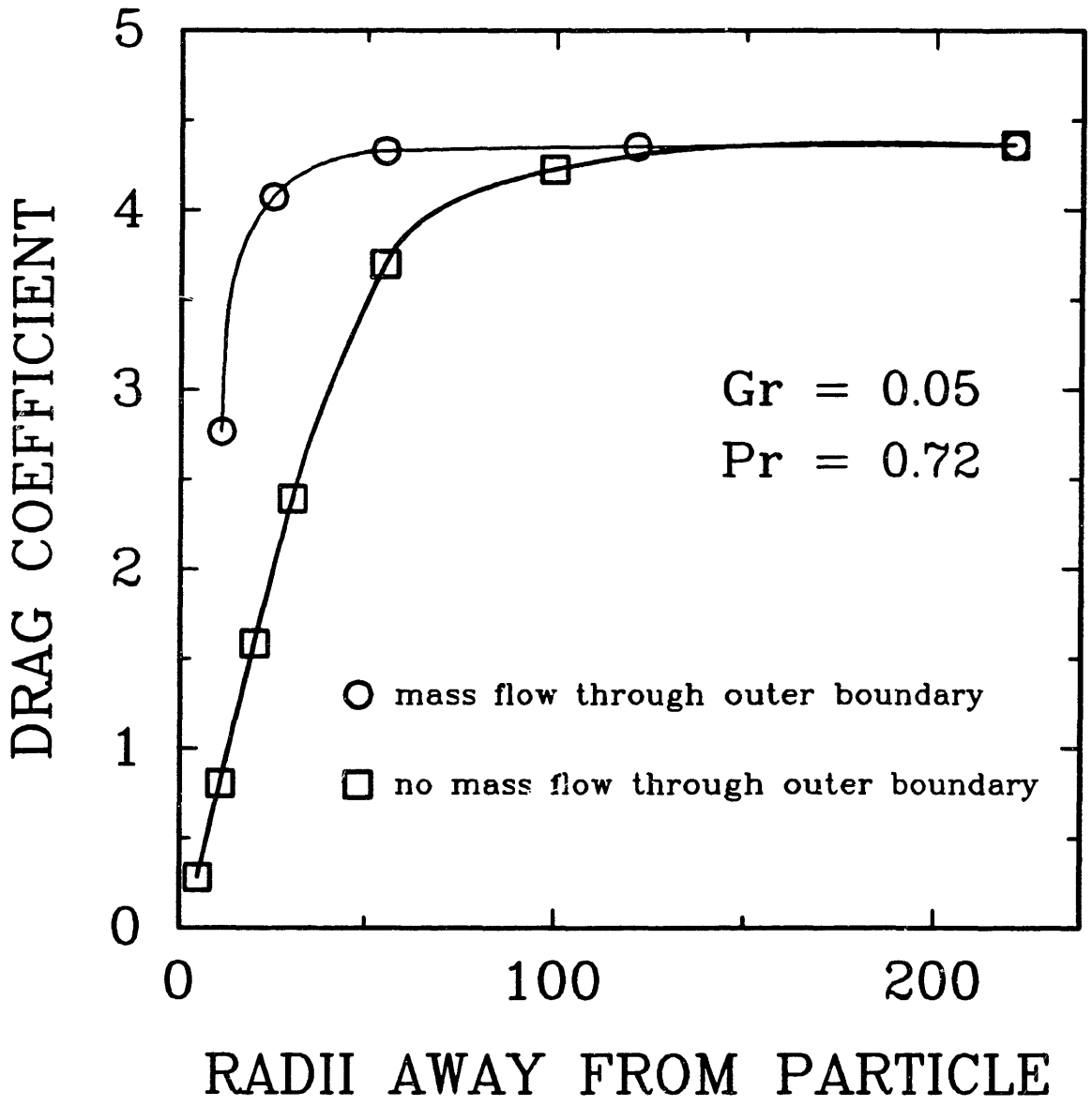

Figure 4.2 : Numerically calculated steady-state drag force coefficient for Gr = 0.05 and Pr = 0.72 versus location of outer boundary with type of outer boundary condition as a parameter.

adjacent values, the critical grid size is 50 times the radius of the particle. If Geoola and Cornish's boundary conditions are used, the critical grid size is at least 120 times the radius of the particle. The former type of outer boundary condition is preferred because it is physically more realistic and because of the savings in computer storage and computational time. Therefore, the boundary condition allowing mass flow through the outer boundary is utilized for all of the cases examined in this paper. The grid size used by Geoola and Cornish [55,56] was below the critical grid size; they had an outer boundary at 24.5 radii away from the particle surface and reported a drag coefficient of 1.17. If the outer boundary is placed farther away from the particle, past the critical grid size of 120 times the radius of the particle, a dimensionless drag force coefficient of 4.33 would have been calculated.

Figures 4.3 and 4.4 are plots of the steady-state dimensionless drag force coefficient versus number of nodes in the radial and theta directions, respectively, for the case of Gr = 0.05 and Pr = 0.72. The position of the outer boundary is kept constant at $z_\infty = 3.96$.
This sensitivity analysis of the number of mesh points reveals that a 30x30 grid adequately describes the natural convective drag force phenomenon.

4.6.1.2 Dimensionless drag force coefficient versus Prandtl number.

Figure 4.5 reveals that the steady-state drag force coefficient has a weak negative dependence on Prandtl number. A linear regression of the data in Figure 4.5 shows that:

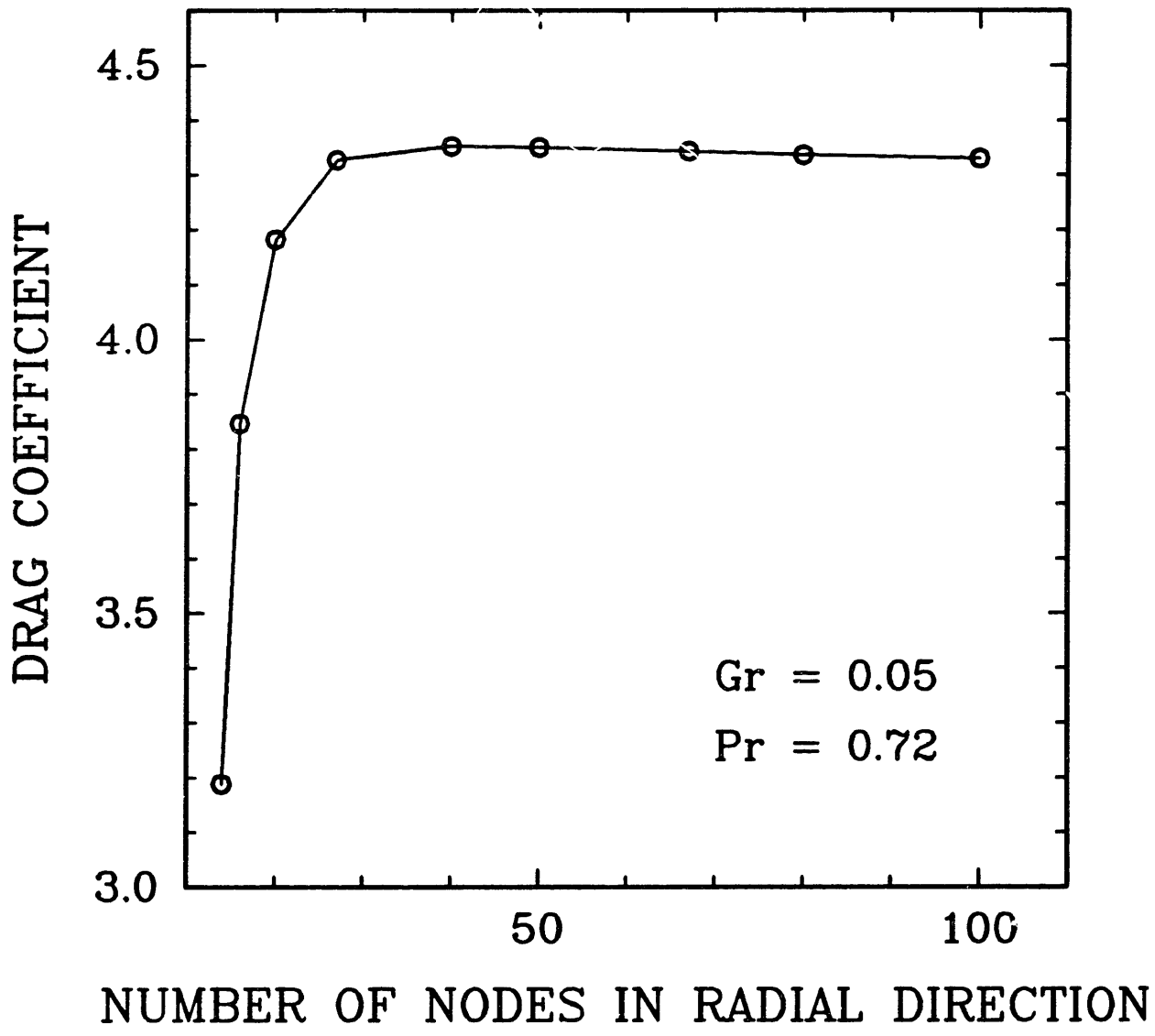

Figure 4.3 : Steady-state dimensionless drag force coefficient versus number of radial nodes for Gr = 0.05 and Pr = 0.72.

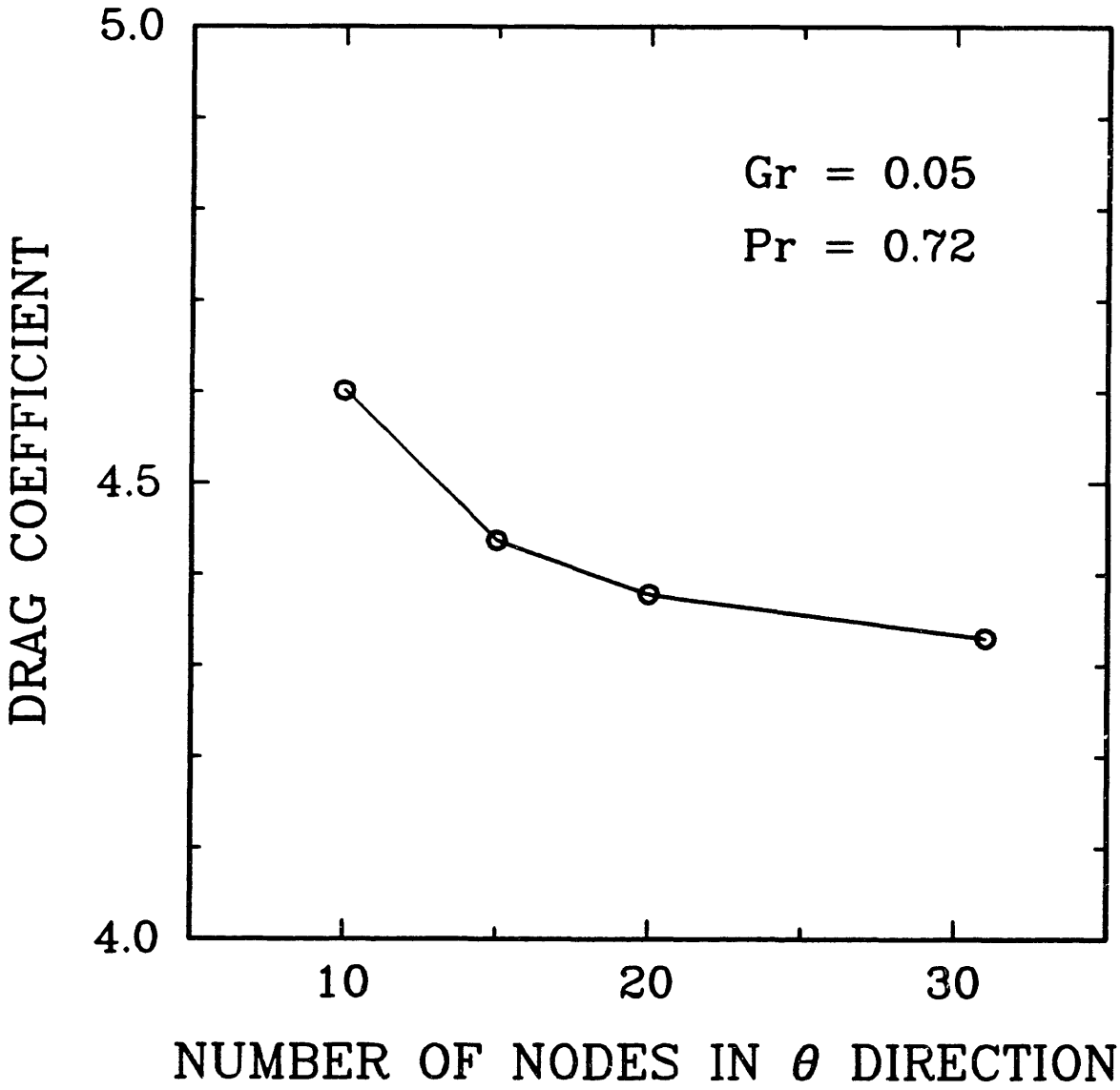

Figure 4.4 : Steady-state dimensionless drag force coefficient versus number of θ nodes for Gr = 0.05 and Pr = 0.72.

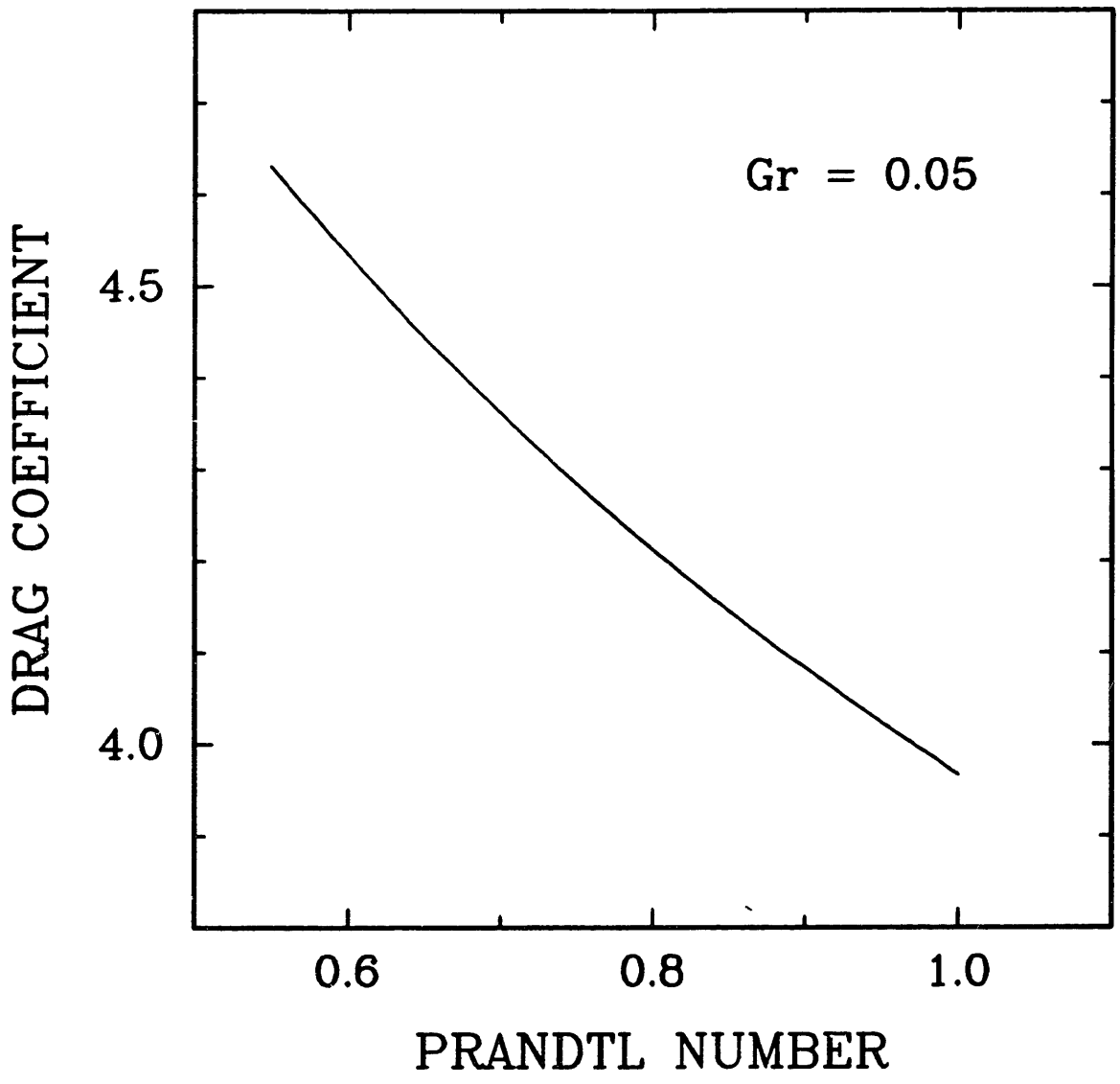

Figure 4.5 : Steady-state dimensionless drag force coefficient versus Prandtl number for Gr = 0.05.

$$C_{DT} \sim Pr^{-0.26} \qquad (4.27)$$

For the gases and temperature range examined experimentally, the Prandtl number would have a maximum of 0.78 and a minimum of 0.69. This corresponds to only a 3.5% difference in the dimensionless drag force coefficient. Therefore, for the purposes of most of this thesis, the dimensionless drag force coefficient will be assumed to only be a function of the Grashof number.

4.6.1.3 Dimensionless drag force coefficient and Nusselt number versus Grashof number.

Figure 4.6 is a plot of the steady-state dimensionless pressure, viscous, and total drag coefficients versus Grashof number. The ratio of the dimensionless viscous drag over the dimensionless pressure drag remains constant at a value of 2.0 over the range of Grashof number examined. This implies that there is no change in the basic flow patterns, such as the separation of the boundary layer.

Figure 4.7 is a plot of Nusselt number versus Grashof number for a Prandtl number of 0.72. The Nusselt number asymptotically approaches 2.03 as Grashof number goes to zero.

4.6.1.4 Dimensionless surrounding gas velocity profiles.

Figures 4.8, 4.9, and 4.10 are plots of the steady-state dimensionless tangential velocity at θ = 90 degrees versus radial distance from the particle. The angle θ is measured from a line connecting the sphere center to

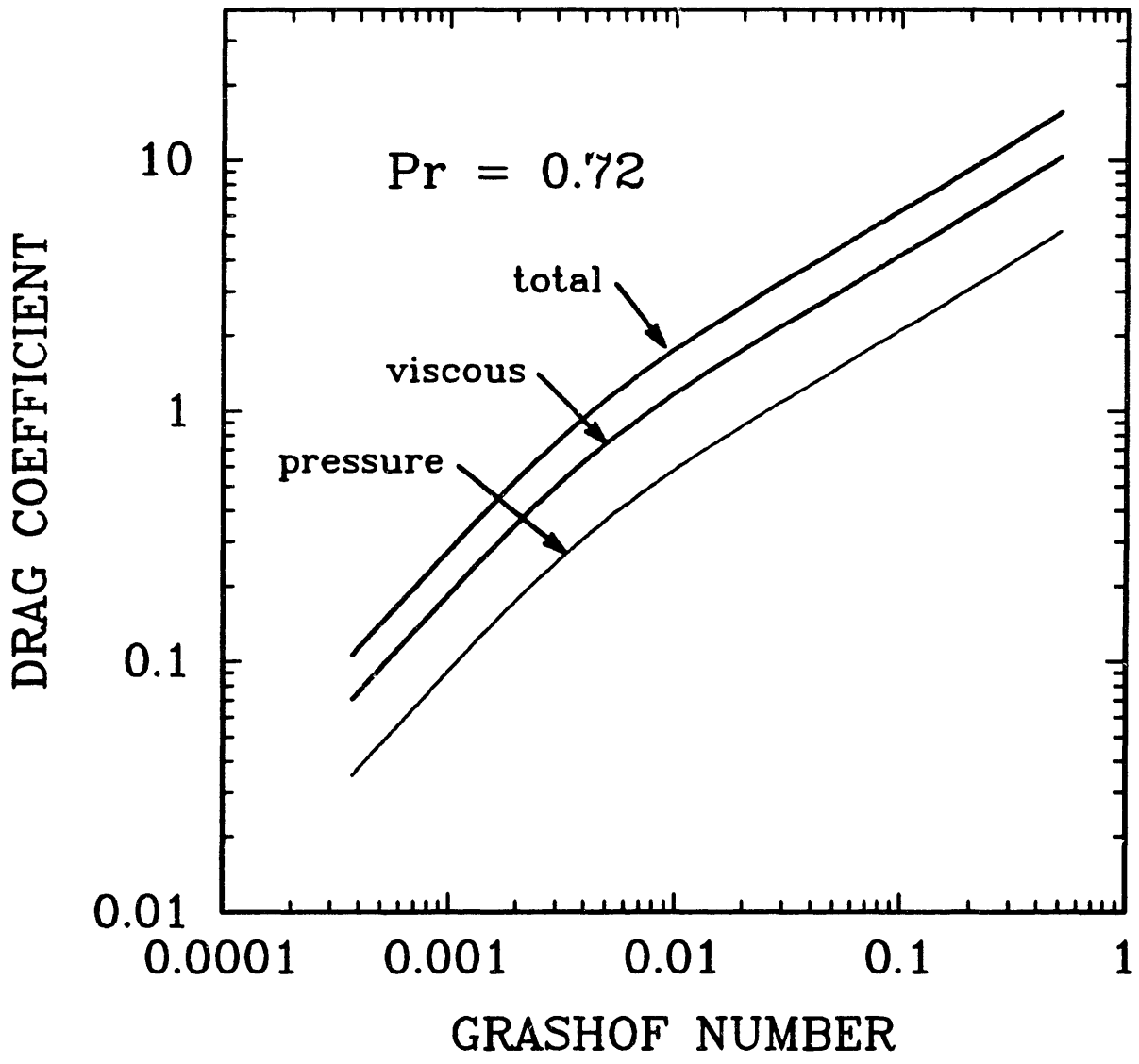

Figure 4.6 : Steady–state dimensionless pressure, viscous, and total drag force coefficients versus Grashof number for Pr = 0.72.

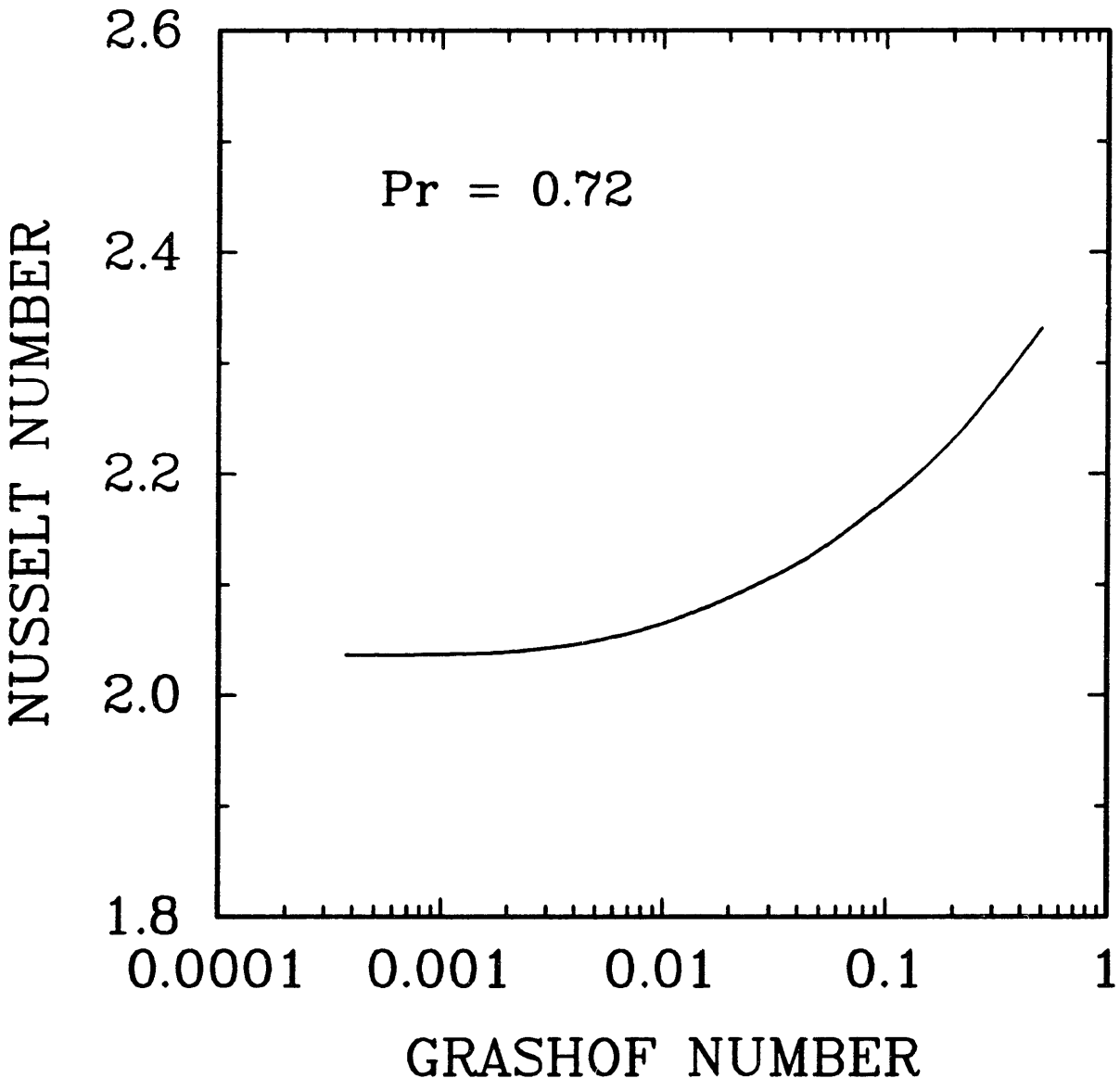

Figure 4.7 : Overall Nusselt number versus Grashof number for Pr = 0.72.

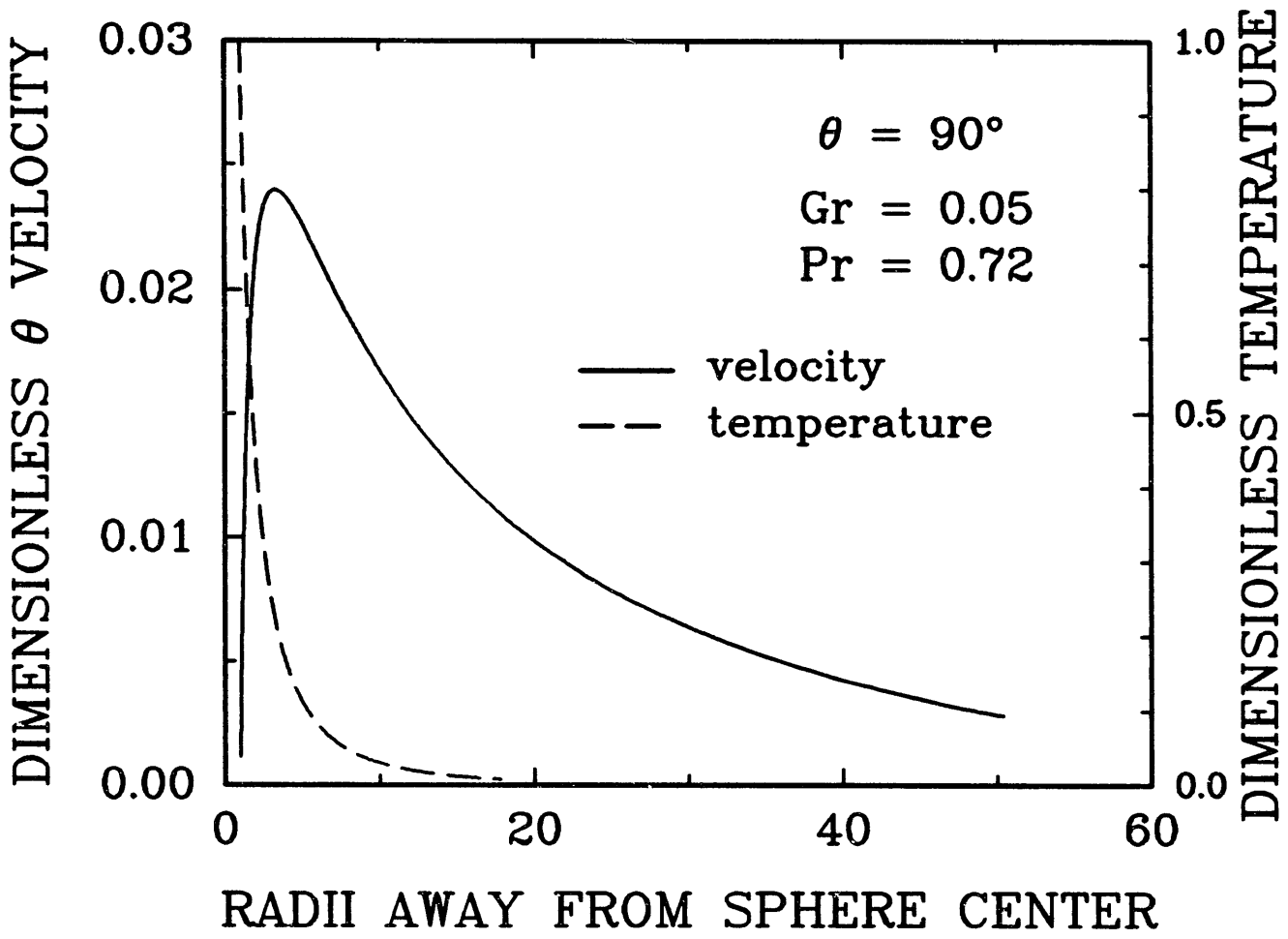

Figure 4.8 : Numerically calculated steady-state tangential velocity and dimensionless temperature for a sphere heated in an ambient environment versus radial distance from the sphere's center at $\theta = 90°$, Gr = 0.05, and Pr = 0.72.

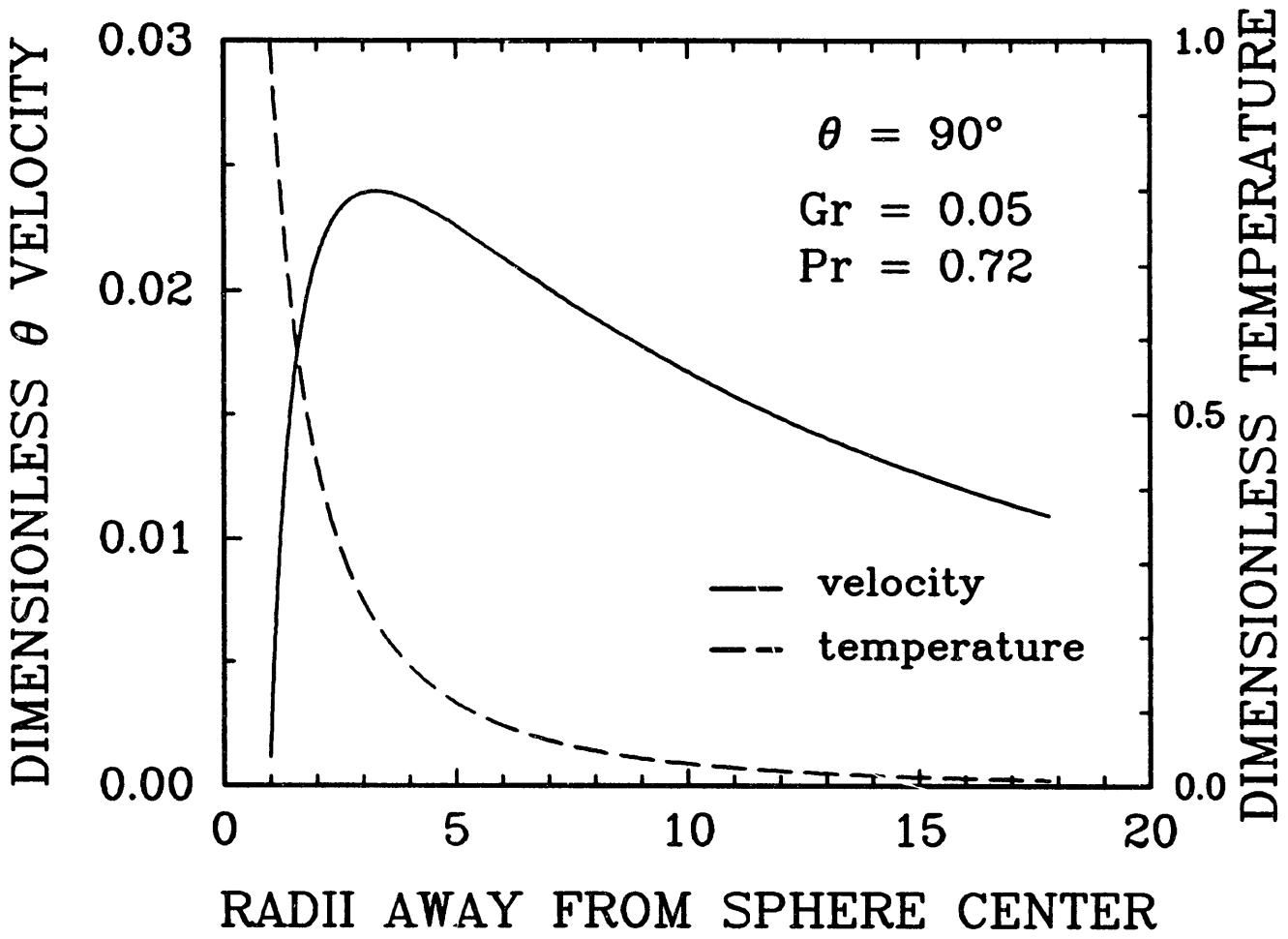

Figure 4.9 : Numerically calculated steady–state tangential velocity and dimensionless temperature for a sphere heated in an ambient environment versus radial distance from the sphere's center at θ = 90°, Gr = 0.05, and Pr = 0.72.

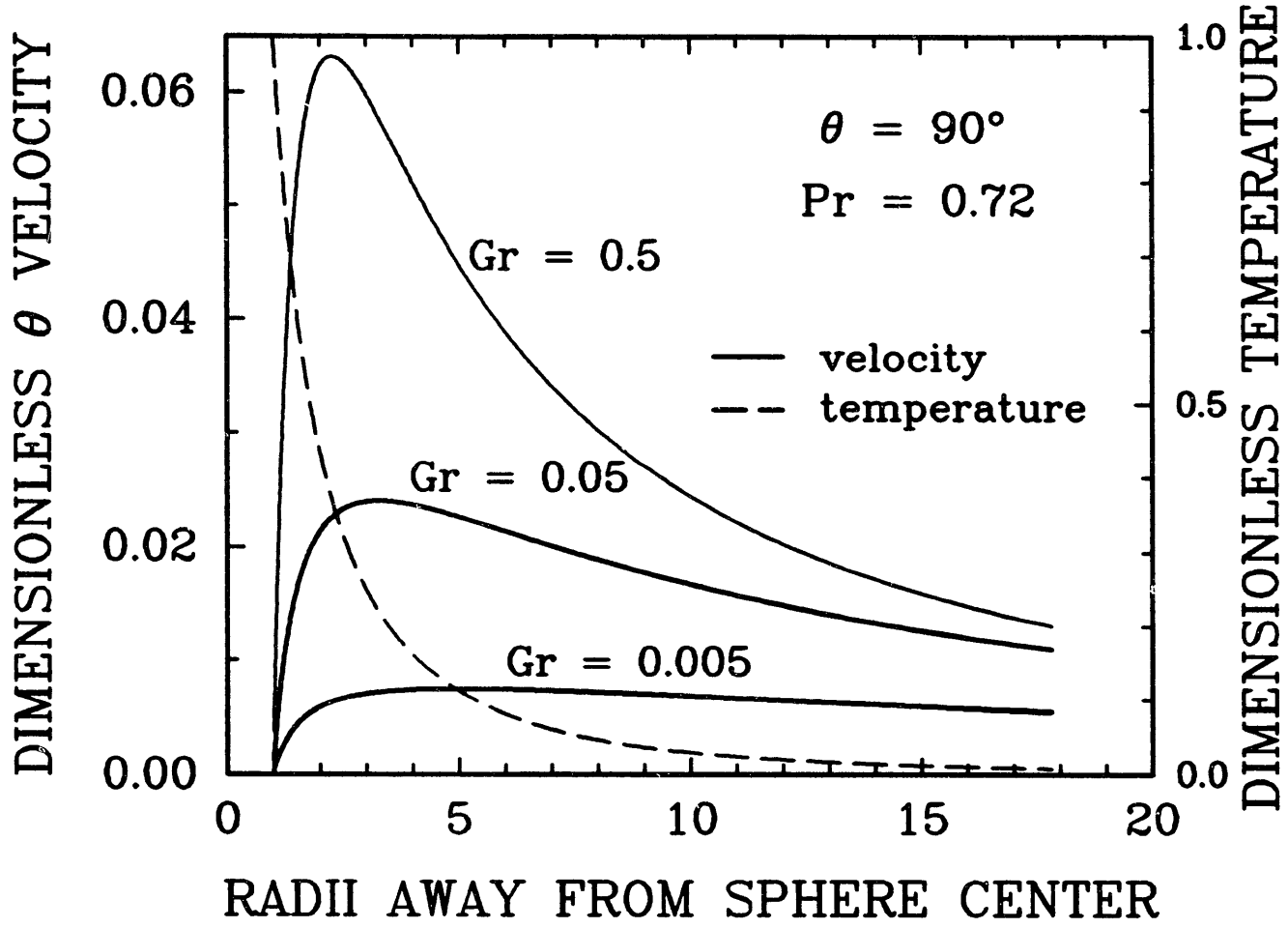

Figure 4.10 : Numerically calculated steady–state tangential velocity and dimensionless temperature for a sphere heated in an ambient environment versus radial distance from the spheres's center at θ = 90°, Pr = 0.72, and Gr = 0.005, 0.05, and 0.5.

the bottom of the sphere. Therefore, an angle of $\theta = 0$ degrees would correspond to the bottom of the sphere and an angle of $\theta = 180$ degrees would correspond to the top of the sphere. Superimposed on these plots are the dimensionless temperature profiles. Figure 4.8 shows the Gr = 0.05 case. The outer boundary used was 52 radii away from the sphere center. Note that the tangential velocity is zero at the sphere surface but not zero at the outer boundary. Also note how much farther the flow field extends past the temperature field. Figure 4.9 is the same plot as Figure 4.8 except the variables of interest are only shown out to 20 radii away from the sphere to give more spatial resolution near the sphere's surface. For this case, the maximum tangential velocity is approximately four radii away from the sphere center.

Figure 4.10 is a plot of the steady-state dimensionless tangential velocity at theta = 90 degrees versus radial distance from the particle for Grashof numbers of 0.005, 0.05, and 0.5. Again, the temperature profiles are superimposed. The temperature profiles are essentially the same for these three values of Grashof number. The maximum dimensionless velocity increases with increasing Gr. Also, the radial distance at which the maximum dimensionless velocity occurs moves closer to the particle surface with increasing Gr.

Figure 4.11 is a plot of steady-state dimensionless radial velocity at theta = 6 degrees versus radial distance from the particle. Radial velocity is defined as positive if flowing outward, away from the sphere surface. A negative value of the radial velocity at the outer boundary indicates fluid flowing into the bottom of the outer boundary.

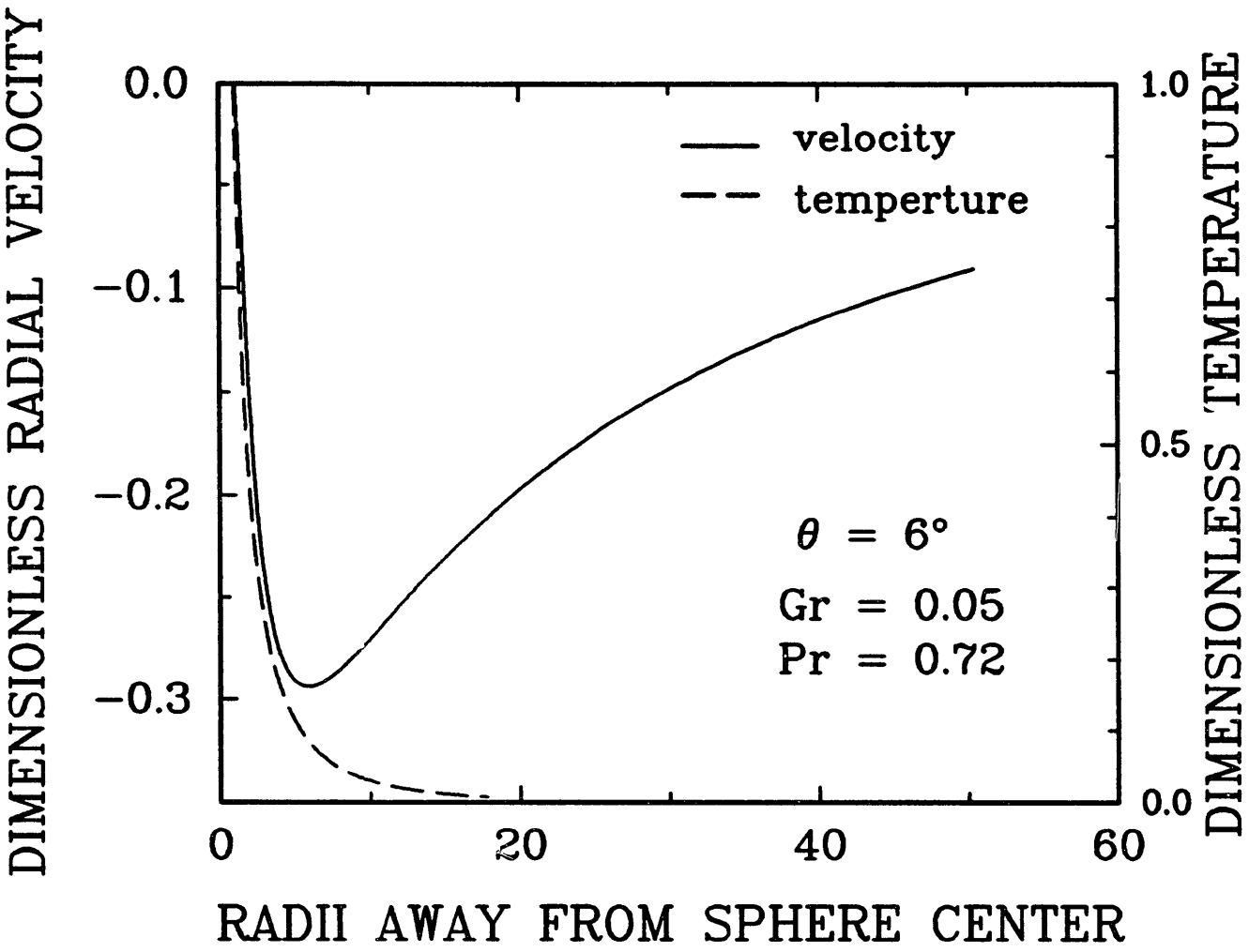

Figure 4.11 : Numerically calculated steady–state radial velocity and dimensionless temperature for a sphere heated in an ambient environment versus radial distance from the sphere's center at θ = 6°, Gr = 0.05, and Pr = 0.72.

4.6.1.5 Dependence of solution on gas property evaluation temperature.

The overall goal of numerically solving this problem is to have the ability to predict the natural convective drag force. Remebering that this force can be written:

$$F_{nat} = (\mu^2/\rho)C_{DT} \tag{4.28}$$

where: F_{nat} = natural convective drag force (N).
μ = viscosity of the surrounding gas (kg/m sec).
ρ = density of the surrounding gas (kg/m^3).
C_{DT} = overall steady-state dimensionless drag force coefficient.

From equation 4.28 two terms are important in predicting F_{nat}, (1) μ^2/ρ, and (2) C_{DT}. Both of these terms are functions of gas properties, therefore, it is important to determine the sensitivity of the solution for F_{nat} to the temperature at which these gas properties are evaluated.

The first term, μ^2/ρ, is plotted versus temperature in Figure 4.12 for both N_2 and CO_2. The data is taken from Holman [60]. Linear regressions of the logs of these data indicate that μ^2/ρ varies with temperature to the 2.31 power for N_2 and to the 2.70 power for CO_2.

The second term, C_{DT}, is a function of the Grashof number (see Figure 4.6) which is defined as:

$$Gr = g\beta(T_s - T_\infty)R^3/\nu^2 \tag{4.29}$$

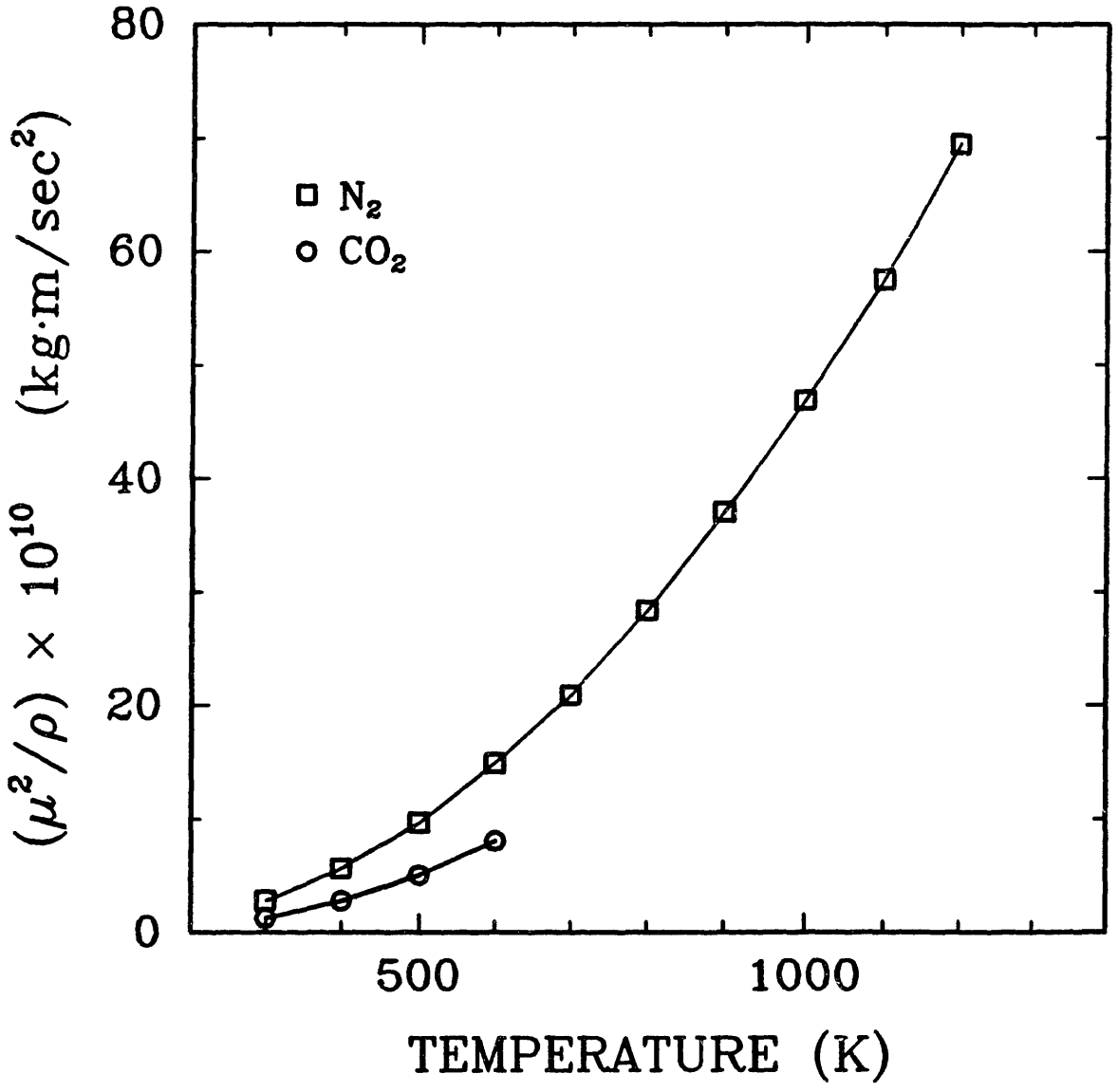

Figure 4.12 : (μ^2/ρ) versus gas temperature for nitrogen and carbon dioxide. Data taken from Holman [60].

where: g = gravitational acceleration (m/sec^2).
β = coefficient of thermal expansion ($1/K$).
T_s = particle surface temperature (K).
T_∞ = ambient temperature (K).
R = particle radius (m).
ν = kinematic viscosity of surrounding gas (m^2/sec).

Typically in natural convection problems, the temperature difference is relatively small (a couple of degrees K), therefore, the temperature at which the kinematic viscosity is evaluated really does not matter too much. In this natural convection problem, however, the temperature difference between the particle surface and the ambient gas surroundings can be as great as 1000 K. This can lead to drastically different values of Grashof number depending on the temperature at which the gas kinematic viscosity is evaluated and how β is defined. In this thesis, β will be assumed to be a constant equal to $1/T_\infty$ [57].

Figure 4.13 is a plot of the kinematic viscosity of both N_2 and CO_2 versus temperature. Again, the data is taken from Holman [60]. Linear regressions of these data indicate that ν varies with temperature to the 1.64 power for N_2 and to the 1.85 power for CO_2.

Three separate cases will be examined (each involving a different method of determining the temperature at which gas properties will be evaluated) to determine the sensitivity of the gas property evaluation temperature on the final value of the natural convective drag force. The three cases to be examined are described below:

Case I : gas properties evaluated at T_∞.
Case II : gas properties evaluated at $T_f = (T_s+T_\infty)/2$.

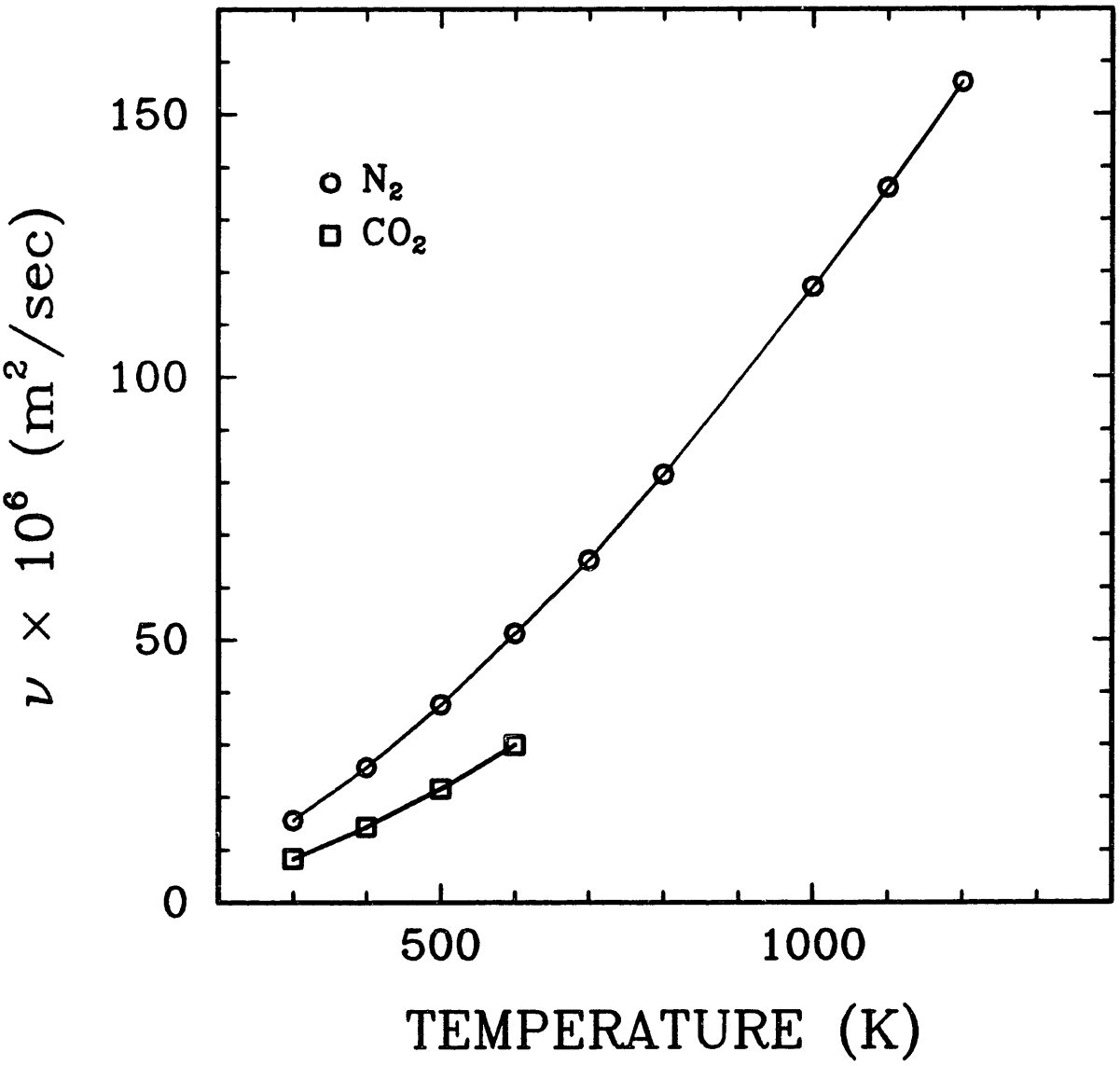

Figure 4.13 : Kinematic viscosity versus gas temperature for nitrogen and carbon dioxide. Data taken from Holman [60].

Case III : gas properties evaluated at T_s.

Grashof numbers, dimensionless drag coefficients, and natural convective drag forces will be determined for each case for two different gases, N_2 and CO_2.

Grashof numbers for the three cases versus particle surface temperatures are shown in Figures 4.14 and 4.15 for N_2 and CO_2, respectively. Grashof numbers were evaluated for spherical particles with radii of 100 μm. For case I, the Grashof number increases linearly with T_s, since ν is fixed. The Grashof numbers for CO_2 are approximately 3.5 times those for N_2. Cases II and III are shown in more detail in Figures 4.16 and 4.17 for N_2 and CO_2, respectively. In each of these cases ν is allowed to vary as a function of T_s. The linear dependence of Grashof number on T_s due to the (T_s-T_∞) term is soon swamped by the negative dependence of the Grashof number on T_s due to the $1/\nu^2$ term. This leads to the characteristic maximums in the Grashof number versus T_s curves of Figures 4.16 and 4.17.

From Figure 4.6, it can be seen that C_{DT} monotonically increases with Grashof number, therefore, it should be no surprise that the C_{DT} versus T_s plots should resemble the Grashof number versus T_s plots. This is shown in Figures 4.18 and 4.19 for N_2 and CO_2, respectively.

Figures 4.20 and 4.21 are plots of the natural convective drag force versus particle surface temperature for N_2 and CO_2, respectively, for the three cases being examined. These figures show F_{nat} to be relatively insensitive to the temperature at which the gas properties are evaluated. For N_2, the three extreme cases examined differ only by approximately 25%. For CO_2, the difference

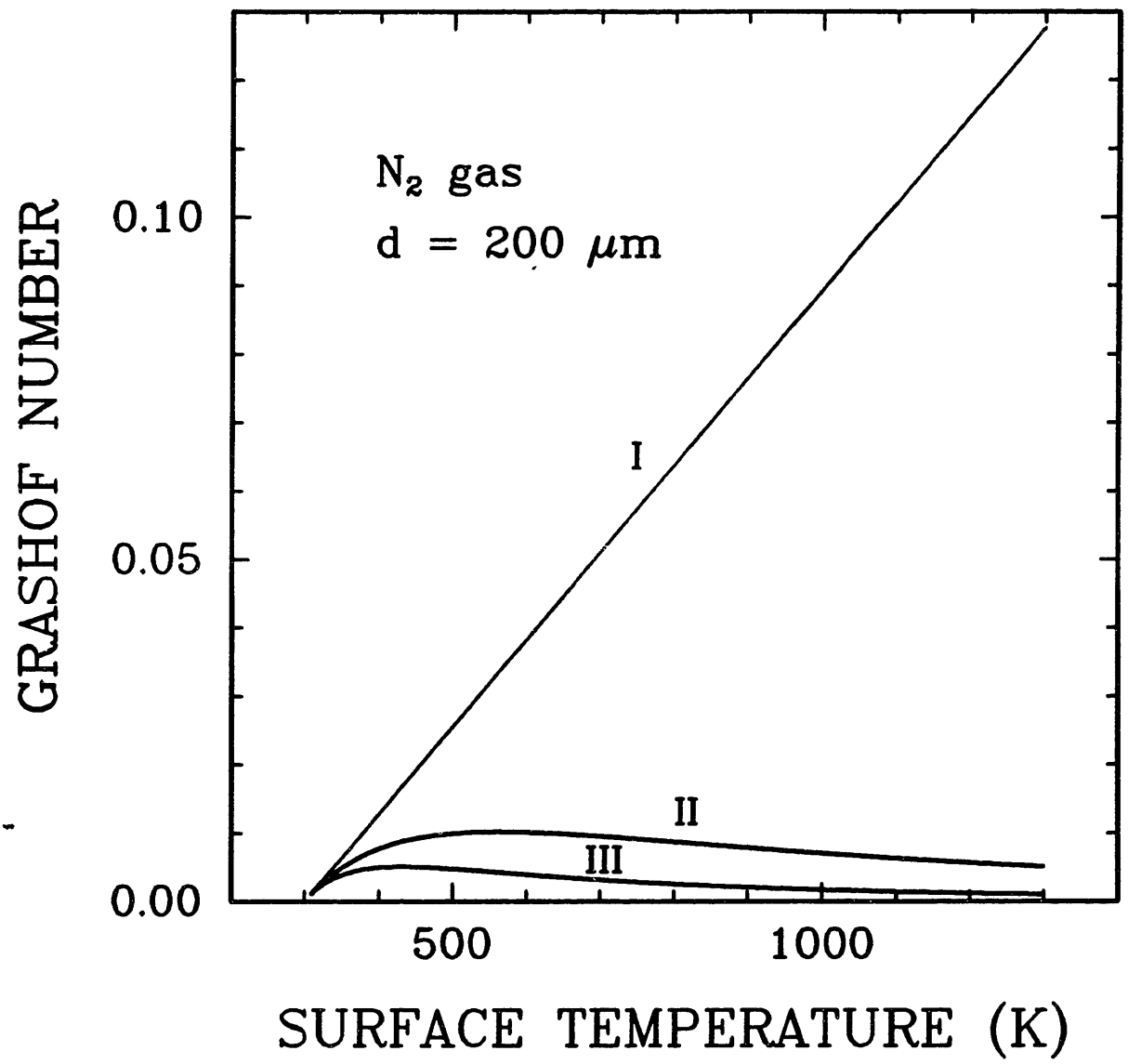

Figure 4.14 : Grashof number versus particle surface temperature for a 200 μm diameter sphere in a nitrogen environment with gas kinematic viscosity evaluated at the ambient temperature (I), the film temperature (II), and the particle surface temperature (III).

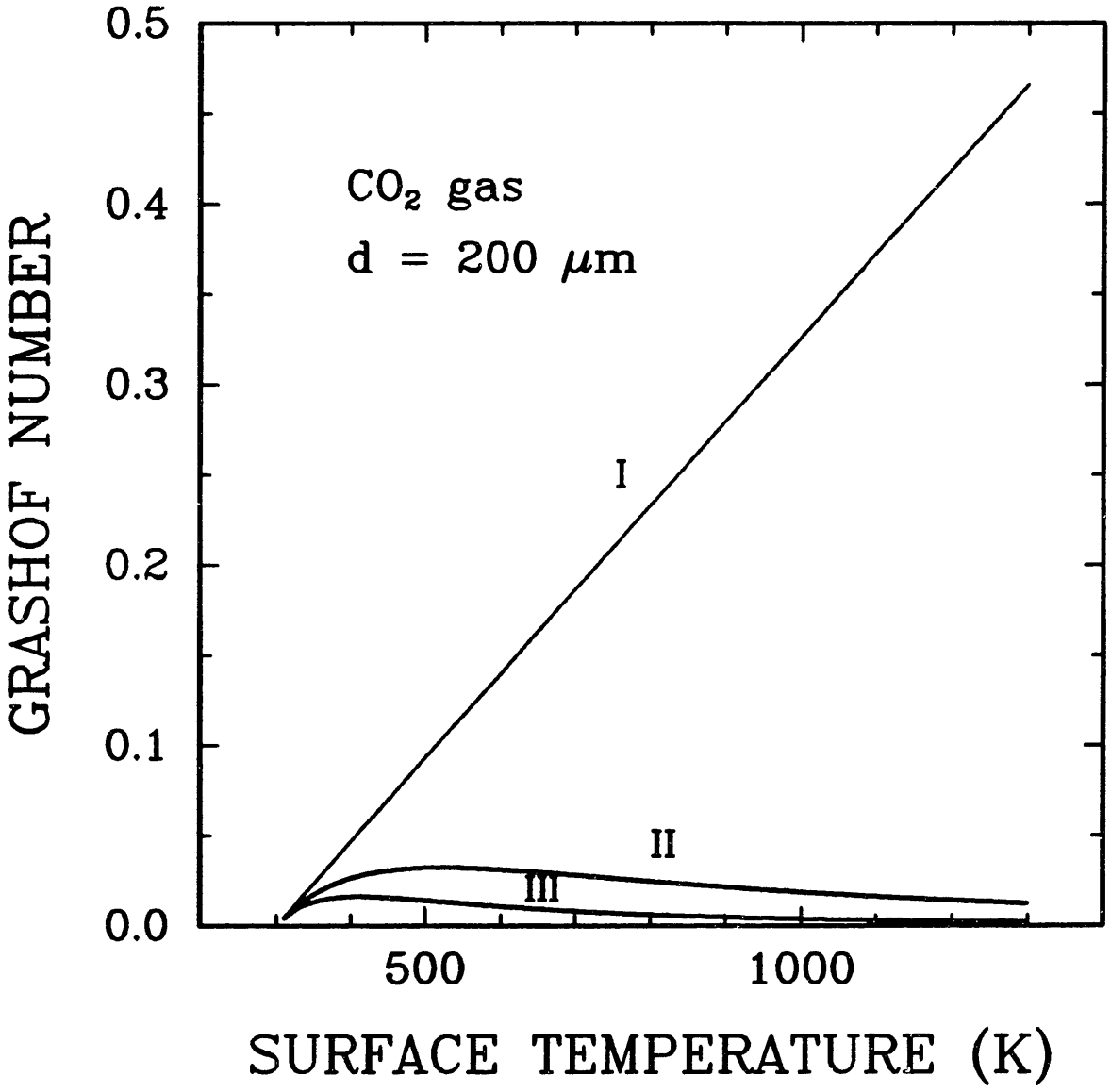

Figure 4.15 : Grashof number versus particle surface temperature for a 200 μm diameter sphere in a carbon dioxide environment with gas kinetic viscosity evaluated at the ambient temperature (I), the film temperature (II), and the particle surface temperature (III).

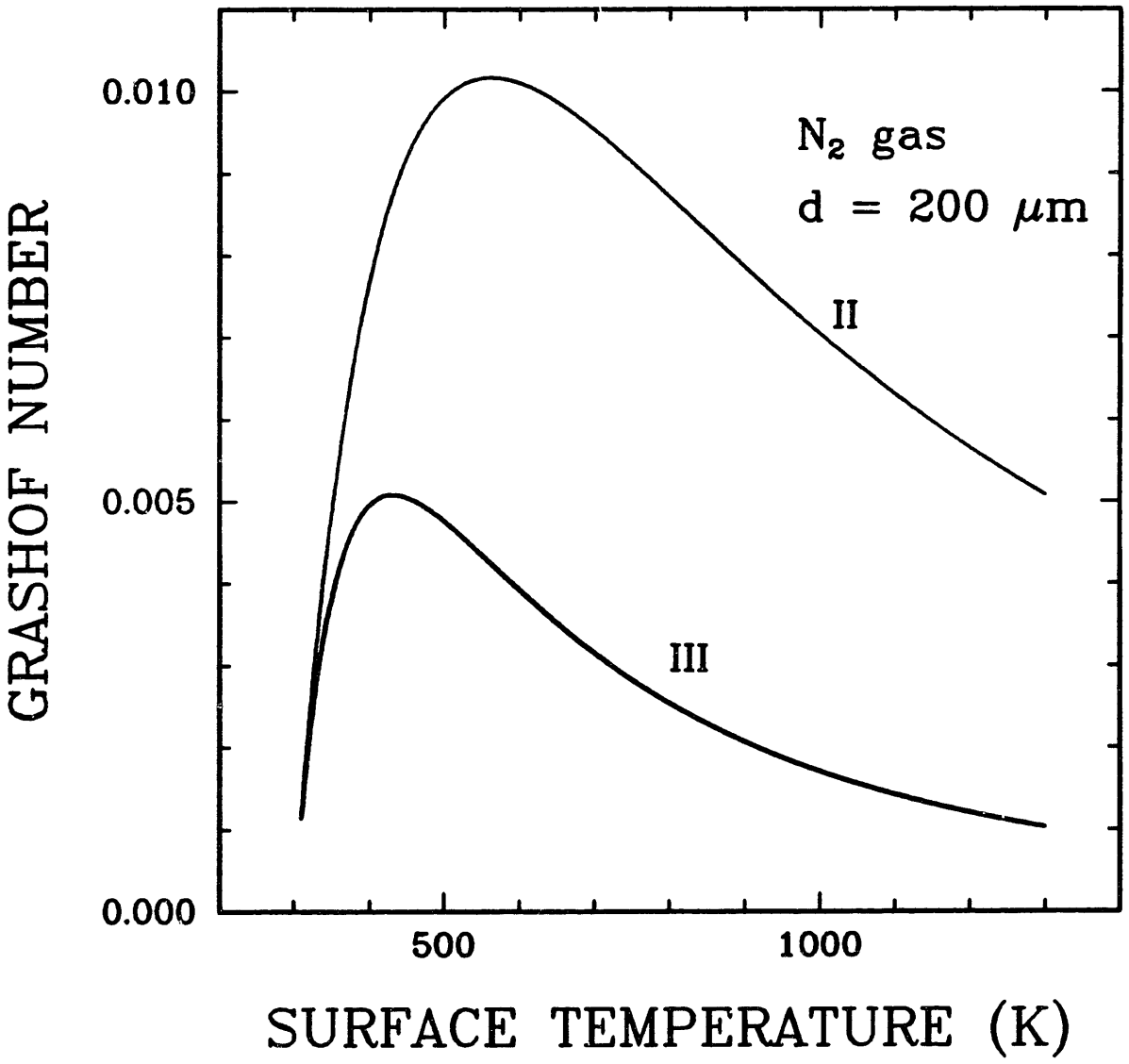

Figure 4.16 : Grashof number versus particle surface temperature for a 200 μm diameter sphere in a nitrogen environment with gas kinematic viscosity evaluated at the film temperature (II) and the particle surface temperature (III).

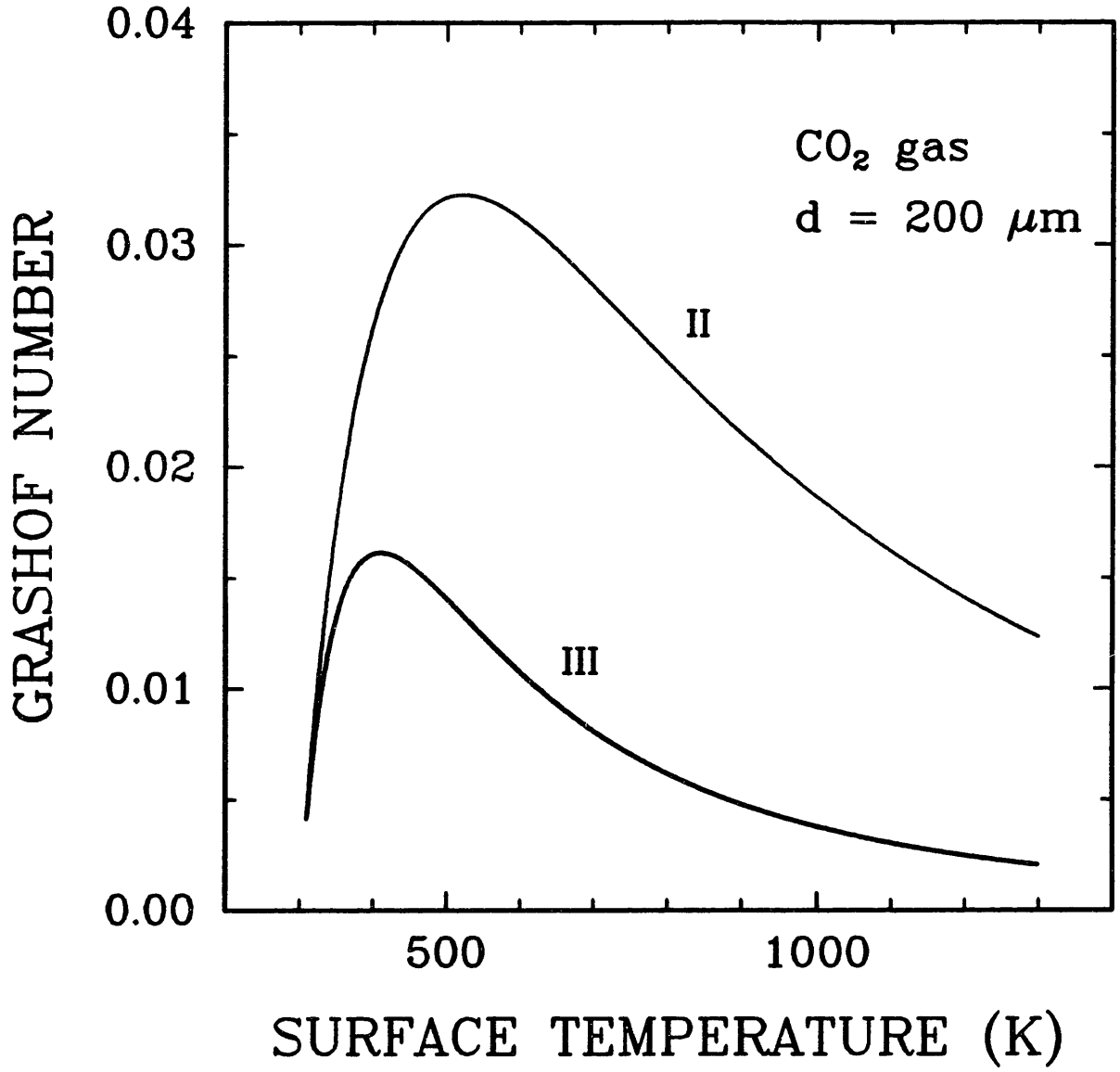

Figure 4.17 : Grashof number versus particle surface temperature for a 200 μm diameter sphere in a carbon dioxide environment with gas kinematic viscosity evaluated at the film temperature (II) and the particle surface temperature (III).

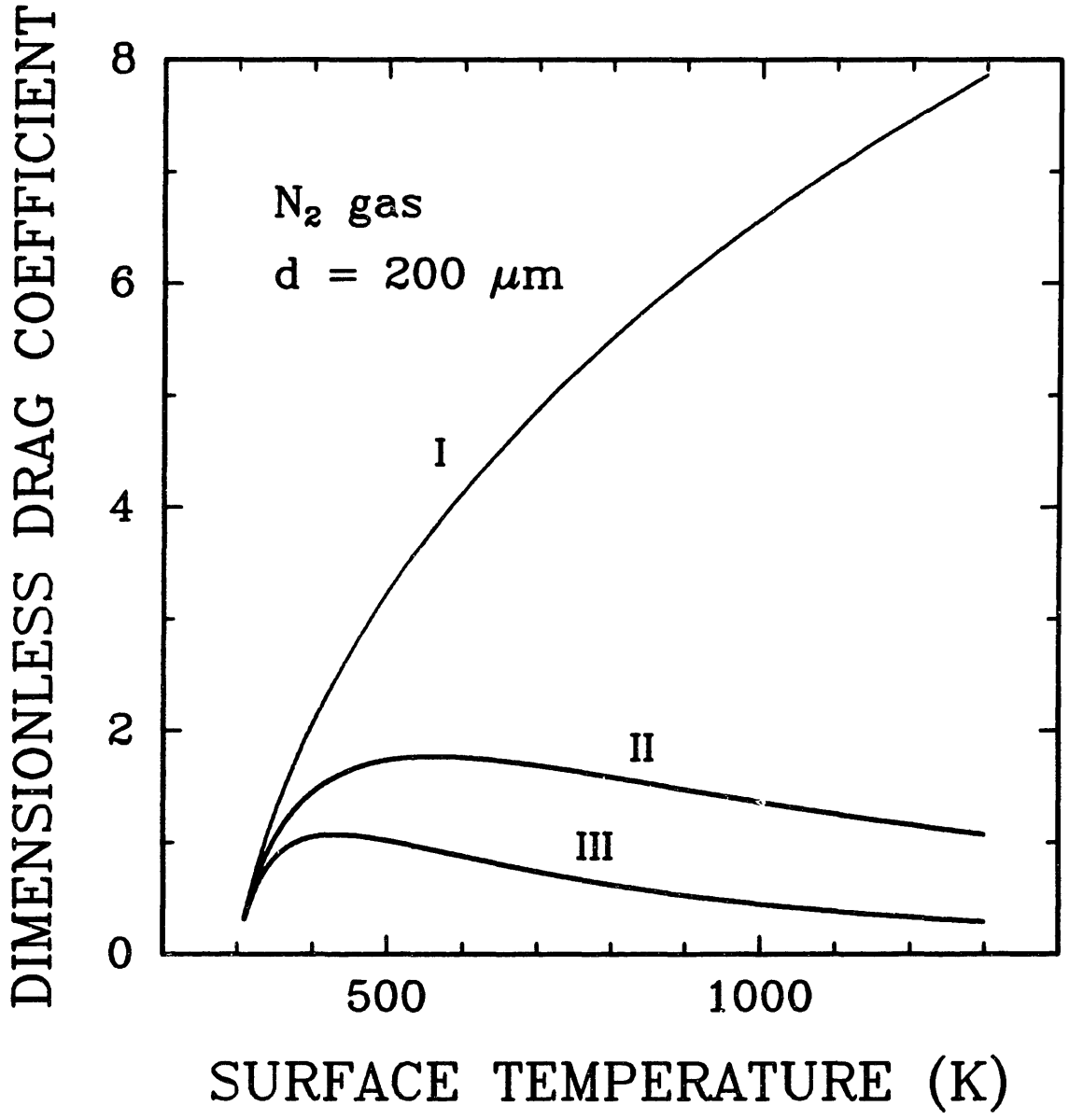

Figure 4.18 : Numerically calculated steady-state dimensionless drag force coefficient versus particle surface temperature for a 200 μm diameter sphere in a nitrogen environment with gas kinematic viscosity evaluated at the ambient temperature (I), the film temperature (II), and the particle surface temperature (III).

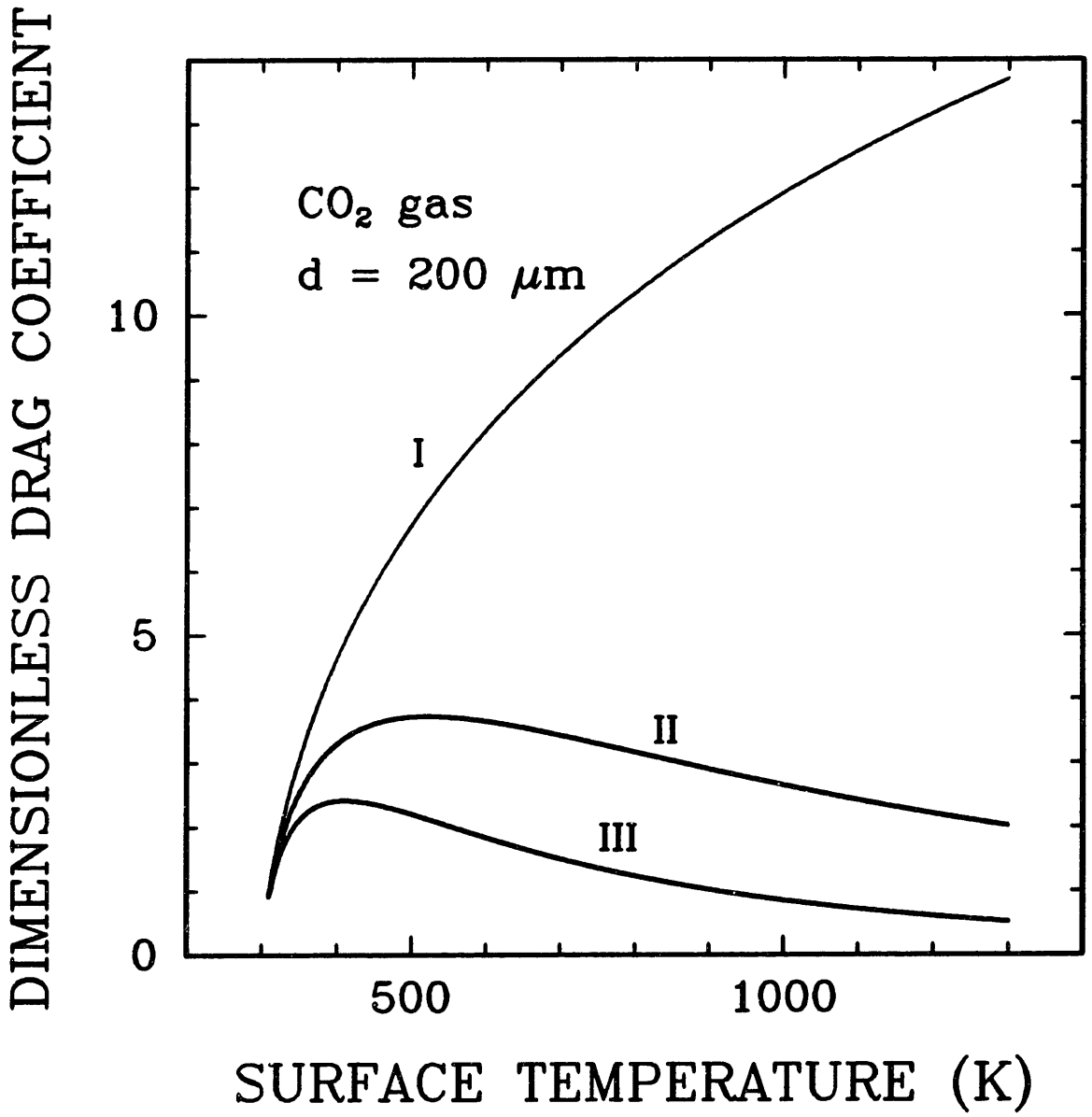

Figure 4.19 : Numerically calculated steady-state dimensionless drag force coefficient versus particle surface temperature for a 200 μm diameter sphere in a carbon dioxide environment with gas kinematic viscosity evaluated at the ambient temperature (I), the film temperature (II), and the particle surface temperature (III).

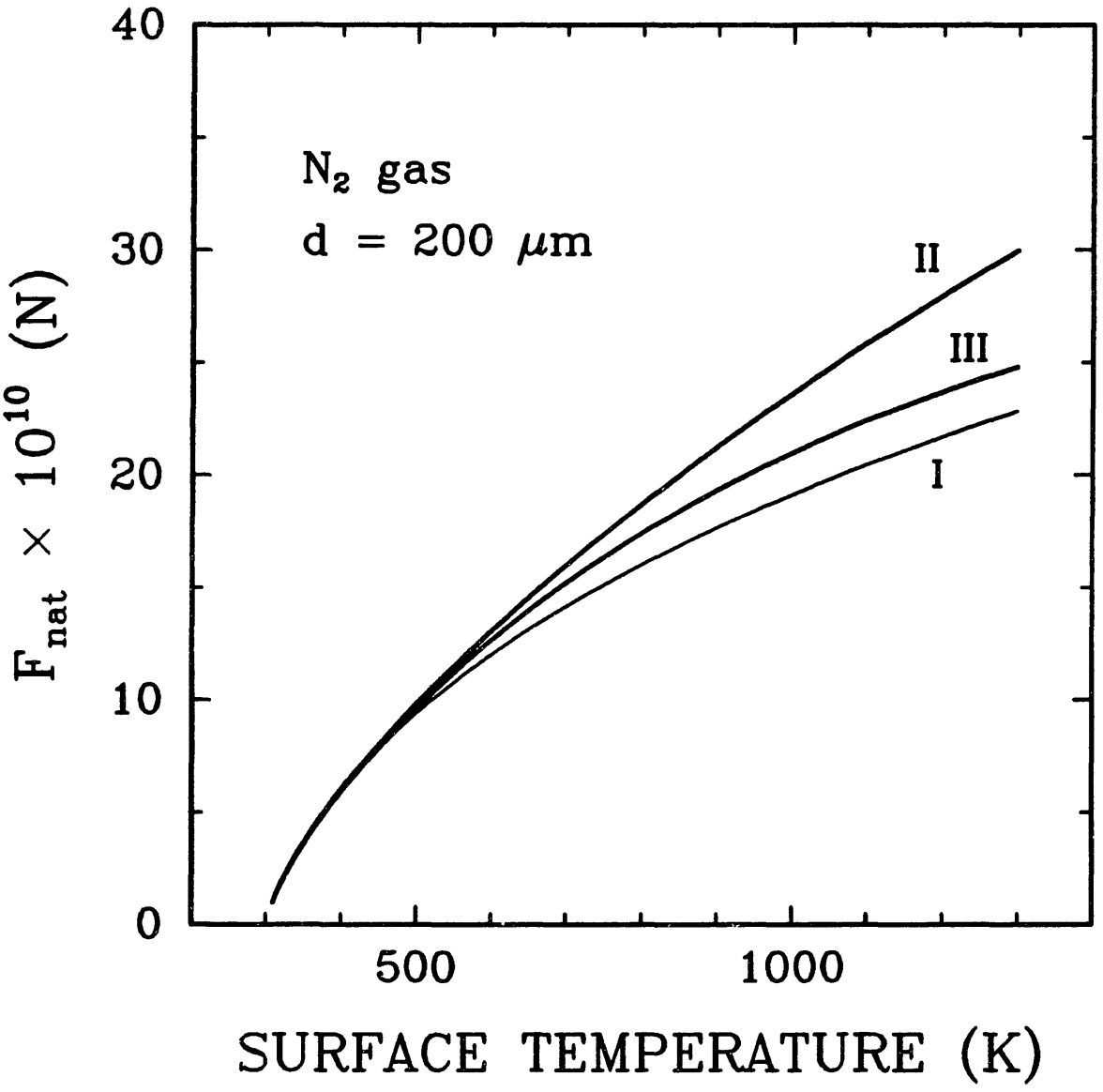

Figure 4.20 : Numerically calculated steady-state natural convective drag force versus particle surface temperature for a 200 μm diameter sphere in a nitrogen environment with gas kinematic viscosity evaluated at the ambient temperature (I), the film temperature (II), and the particle surface temperature (III).

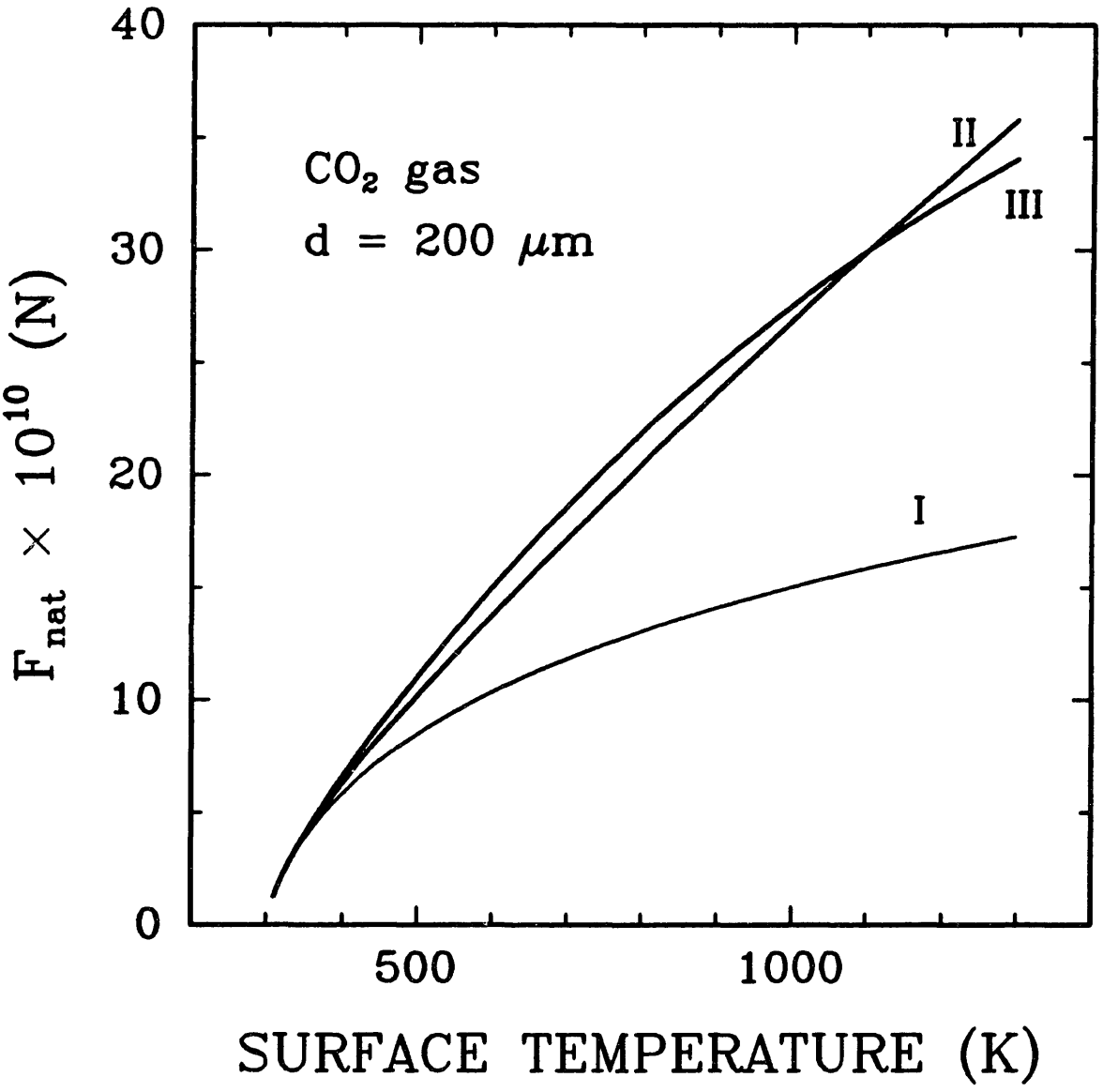

Figure 4.21 : Numerically calculated steady-state natural convective drag force versus particle surface temperature for a 200 μm diameter sphere in a carbon dioxide environment with gas kinematic viscosity evaluated at the ambient temperature (I), the film temperature (II), and the particle surface temperature (III).

is approximately 50%. These figures also show that F_{nat} is remarkably similar for both surrounding gases studied, N_2 and CO_2. The fact that μ^2/ρ for N_2 is greater than μ^2/ρ for CO_2 is counteracted by the fact that C_{DT} for N_2 is less than C_{DT} for CO_2. Even though F_{nat} has been shown (in these cases) to be relatively insensitive to the temperature at which the gas properties are evaluated, it is recommended that all gas properties be evaluated at the film temperature (case II).

4.6.2 Transient solutions.

Figure 4.22 is a plot of the total drag force coefficient and Nusselt number versus dimensionless time for Gr = 0.05 and Pr = 0.72. The transient drag coefficient is within 10% of steady-state at a dimensionless time of 280. The Nusselt number is within 10% of steady-state at a dimensionless time of 15. The Nusselt number reaches steady-state in less than 1/10 of the time it takes the drag force coefficient to reach steady-state. This indicates that the temperature profile is set up one order of magnitude faster than the flow field.

Figure 4.23 is a plot of dimensionless drag force coefficient versus dimensionless time for Gr = 0.005, 0.05, 0.5. As Grashof number increases, the dimensionless time required to reach steady-state decreases. This inverse relationship between dimensionless time and Grashof number is shown more clearly in Figure 4.24, which is a log-log plot of the dimensionless time required to reach 90% of the steady-state total drag force coefficient versus Grashof number.

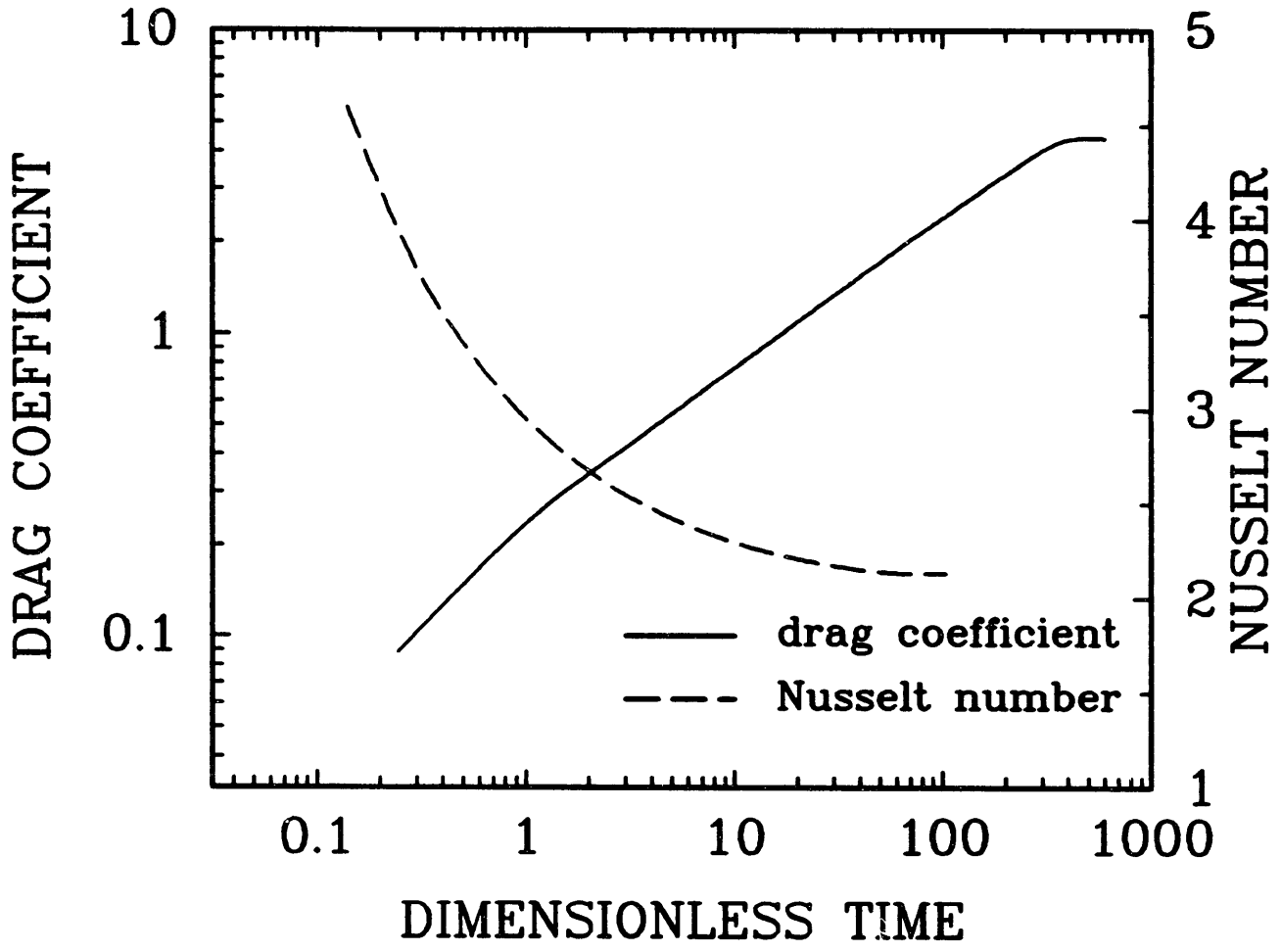

Figure 4.22 : Numerically calculated steady-state dimensionless drag force coefficient and Nuseelt number versus dimensionless time for Gr = 0.05 and Pr = 0.72.

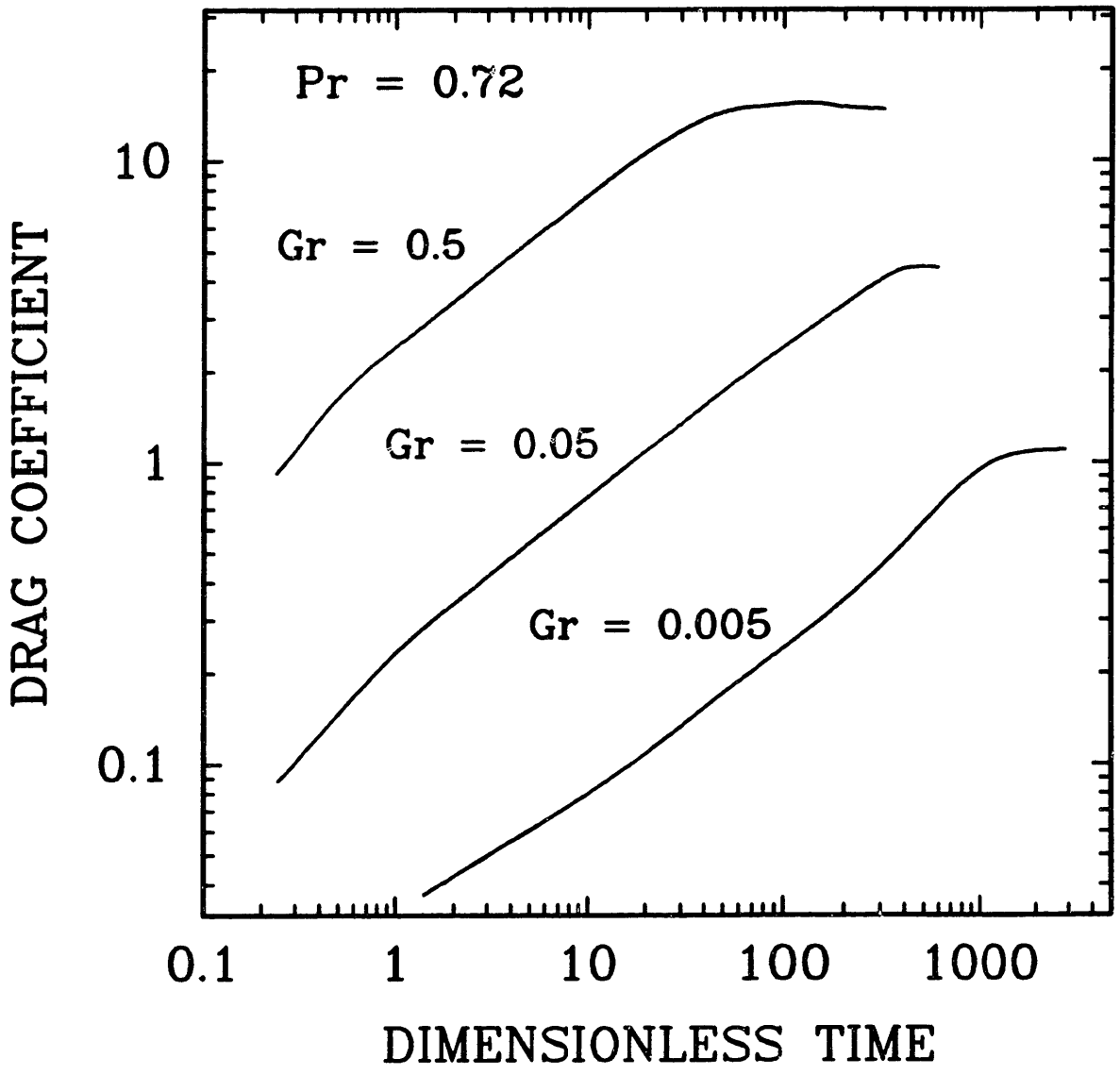

Figure 4.23 : Numerically calculated steady-state dimensionless drag force coefficient versus dimensionless time for Pr = 0.72 and Gr = 0.005, 0.05, and 0.5.

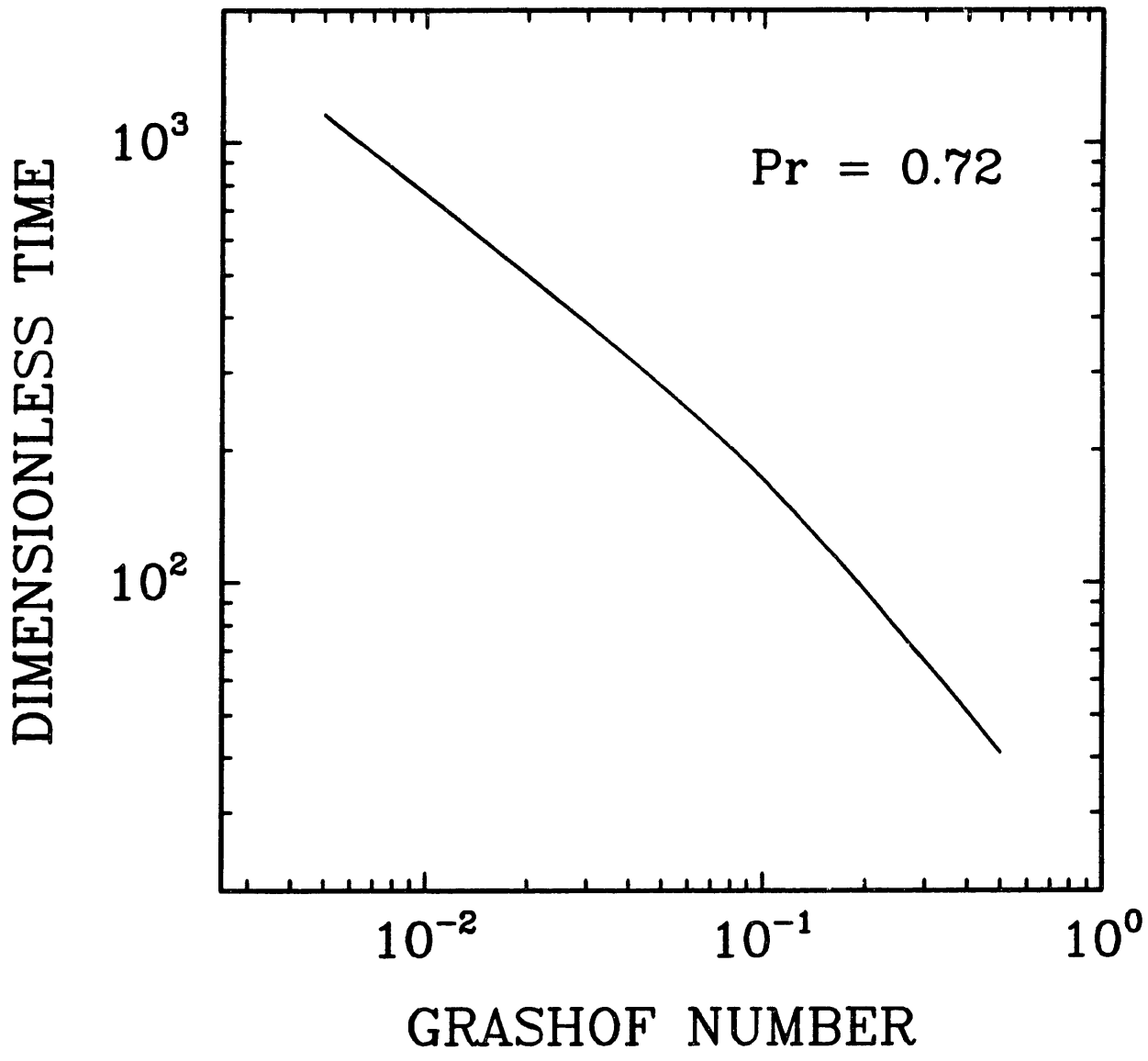

Figure 4.24 : Dimensionless time versus Grashof number for Pr = 0.72.

4.7 Experimental results.

4.7.1 Steady-state results.

The experimental program examined the effect of three parameters, particle temperature, particle size, and surrounding gas on the natural convective drag force. Particle temperature was varied in the range of 600 to 1200 K. Five different diameter spheres were examined, 127, 153, 168, 192, and 236 μm. In each case, the material used was the synthetic char "Spherocarb". Also, two different surrounding gases were used, N_2 and CO_2.

Figures 4.25, 4.26, 4.27, 4.28, and 4.29 are plots of the natural convective drag force, F_{nat}, divided by particle weight versus particle temperature for each of the five separate "Spherocarbs". For example, Figure 4.25 represents F_{nat}/mg versus particle temperature for the same 127 μm diameter "Spherocarb" particle in both N_2 and CO_2. A total of 90 natural convective drag experiments were performed. The experiments performed in nitrogen are shown as open triangles and the experiments performed in carbon dioxide are open circles. For each "Spherocarb", F_{nat}/mg increases with increasing temperature. Also, there is little difference between the natural convective drag force in N_2 and the natural convective drag force in CO_2. Overall, the natural convective drag force ranged from 7% to 16% of the particle weight over the range of conditions examined. Also, F_{nat}/mg decreases with increasing diameter.

Figures 4.30 and 4.31 are plots of the natural convective drag force versus particle temprature for the five "Spherocarb" particles in N_2 and CO_2, respectively.

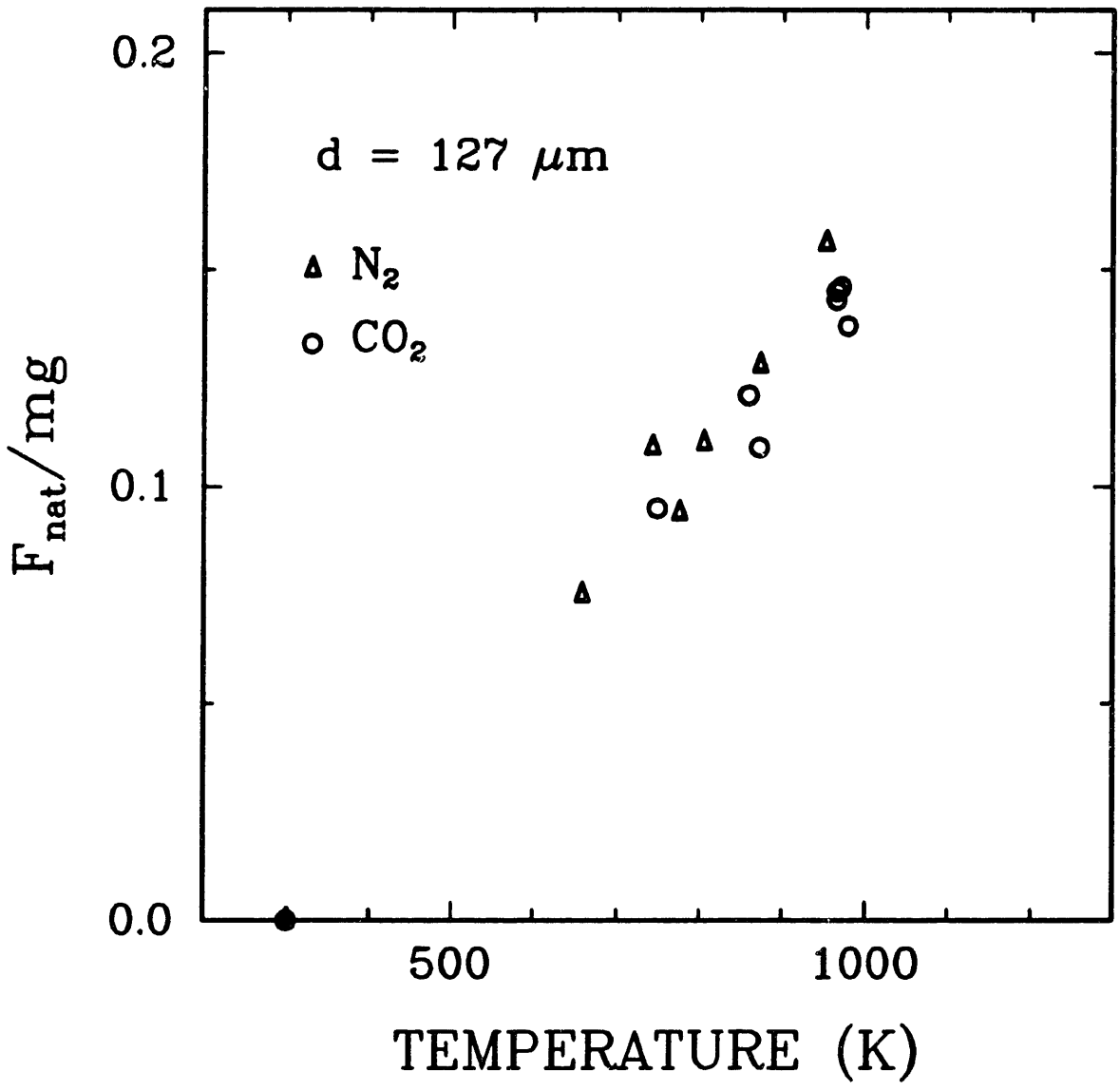

Figure 4.25 : Experimental measurements of the ratio of natural convective drag force to particle weight versus particle temperature for a 127 μm diameter "Spherocarb" particle in nitrogen and carbon dioxide.

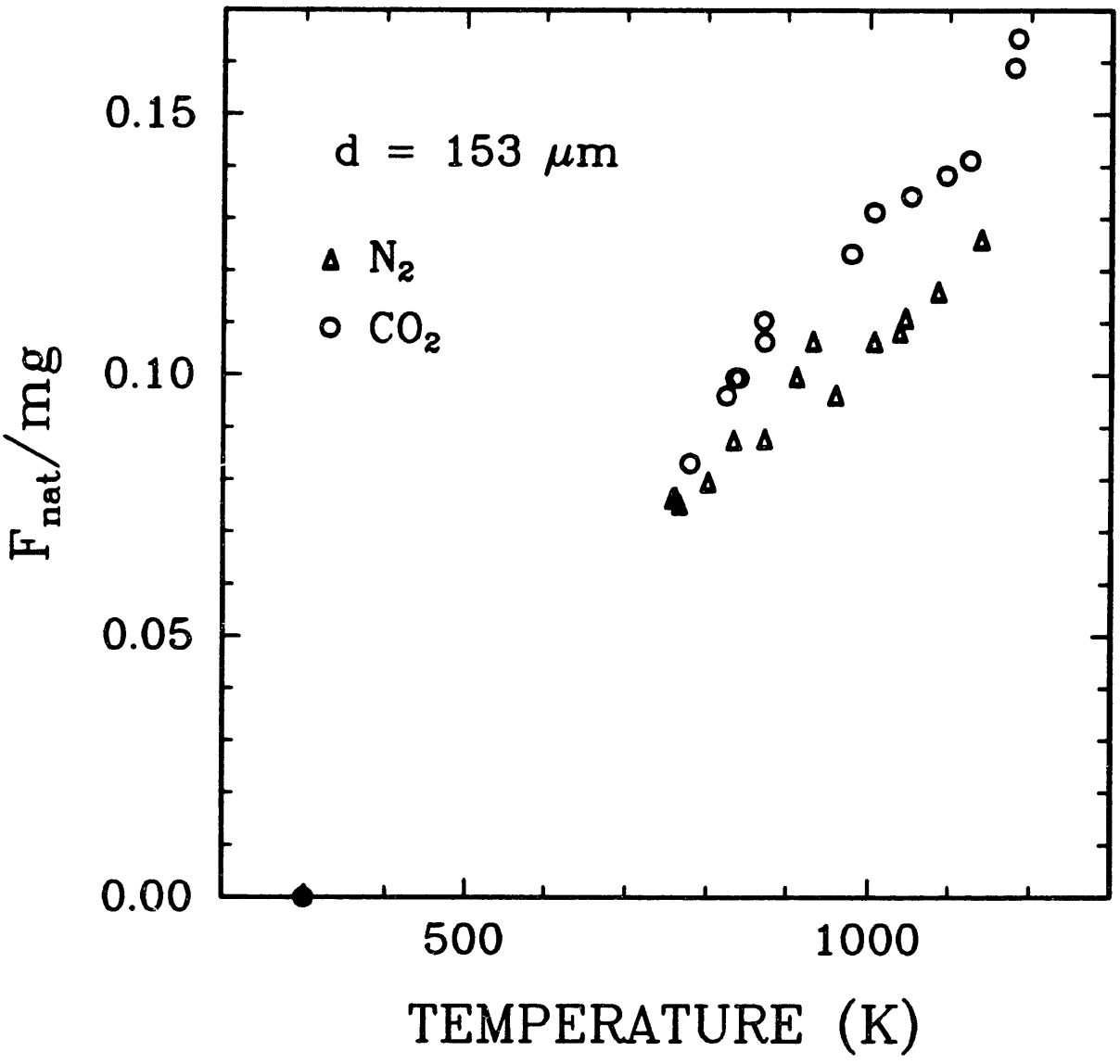

Figure 4.26 : Experimental measurements of the ratio of natural convective drag force to particle weight versus particle temperature for a 153 μm diameter "Spherocarb" particle in nitrogen and carbon dioxide.

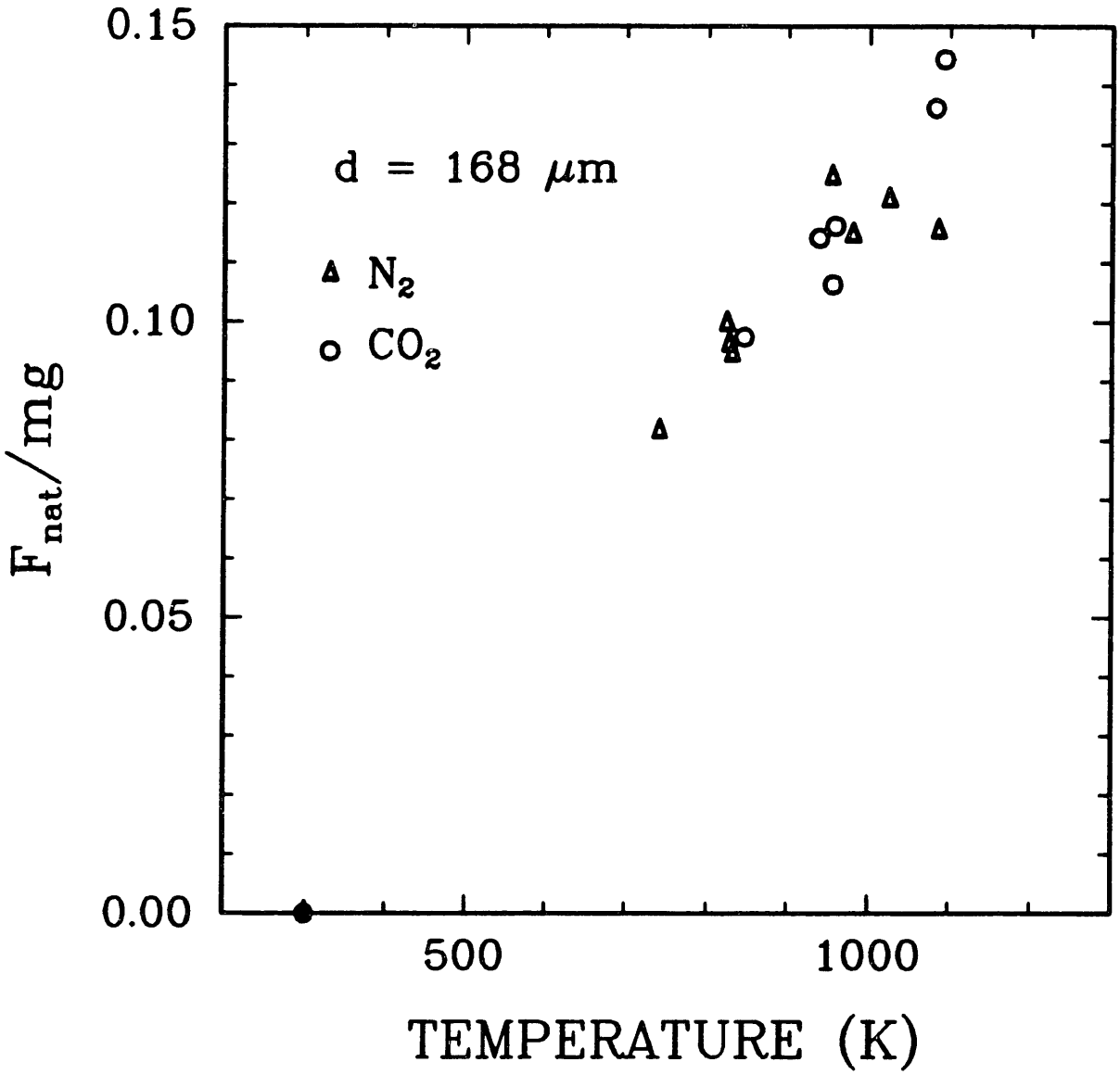

Figure 4.27 : Experimental measurements of the ratio of natural convective drag force to particle weight versus particle temperature for a 168 μm diameter "Spherocarb" particle in nitrogen and carbon dioxide.

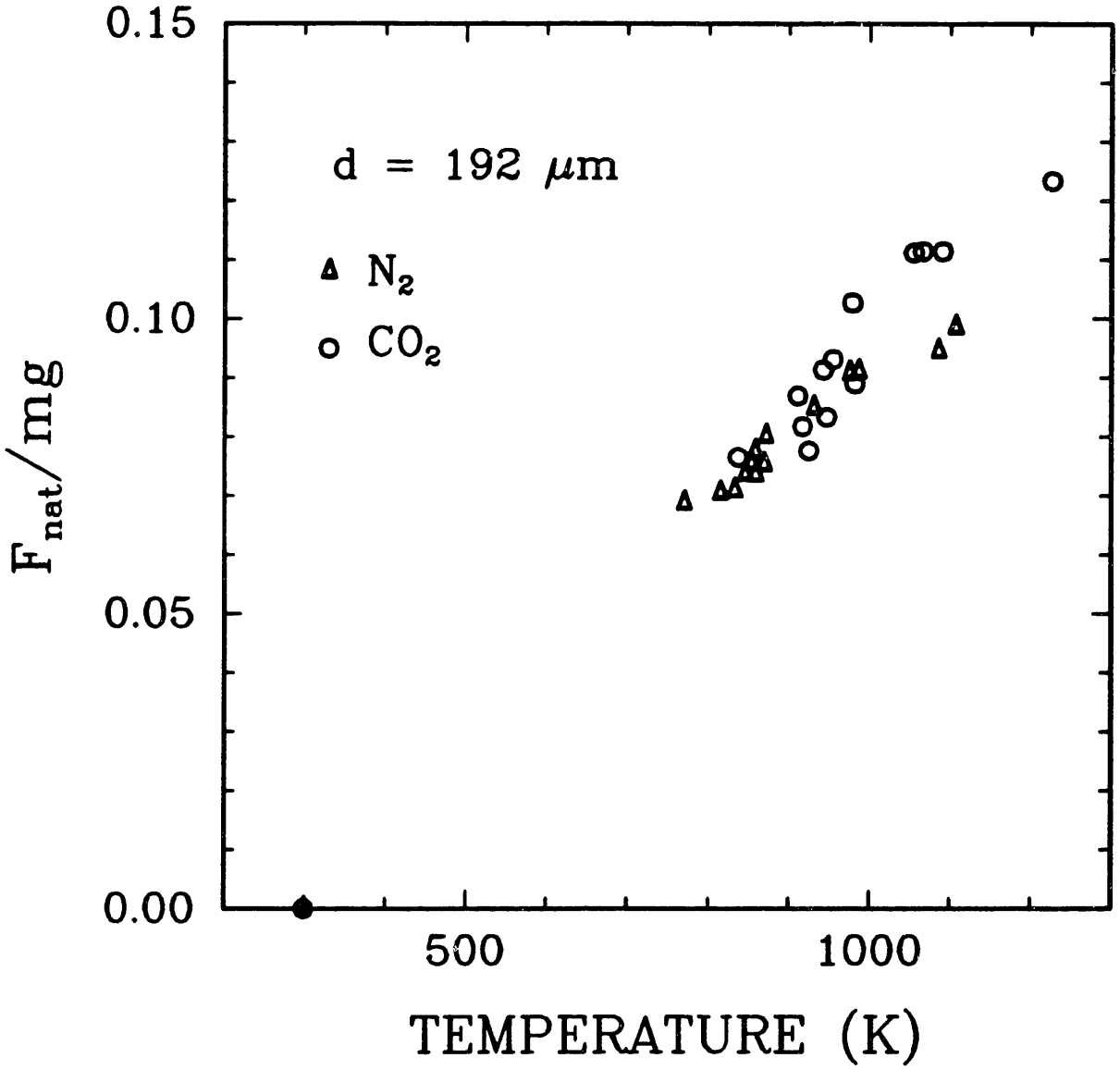

Figure 4.28 : Experimental measurements of the ratio of natural convective drag force to particle weight versus particle temperature for a 192 μm diameter "Spherocarb" particle in nitrogen and carbon dioxide.

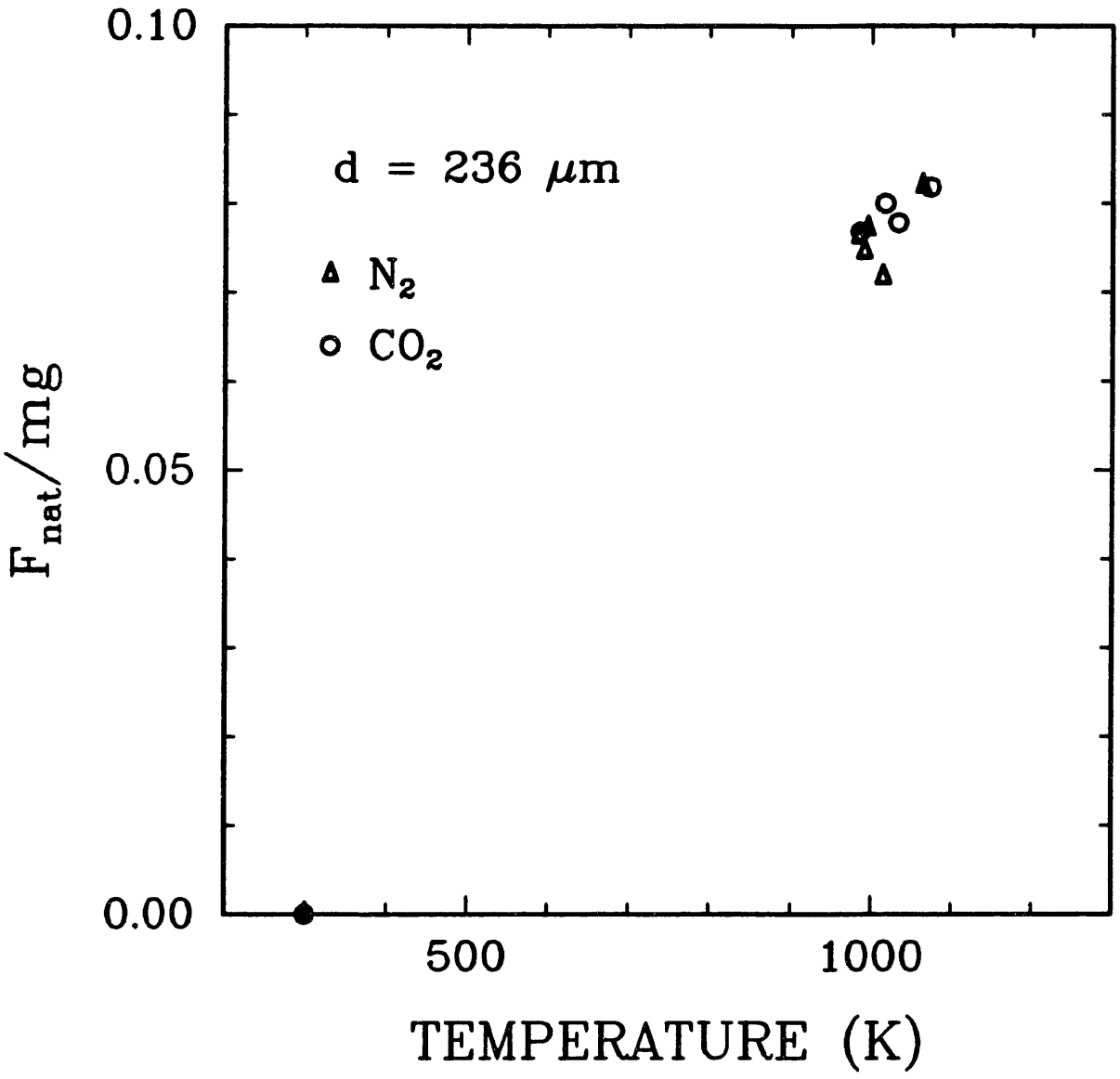

Figure 4.29 : Experimental measurements of the ratio of natural convective drag force to particle weight versus particle temperature for a 236 μm diameter "Spherocarb" particle in nitrogen and carbon dioxide.

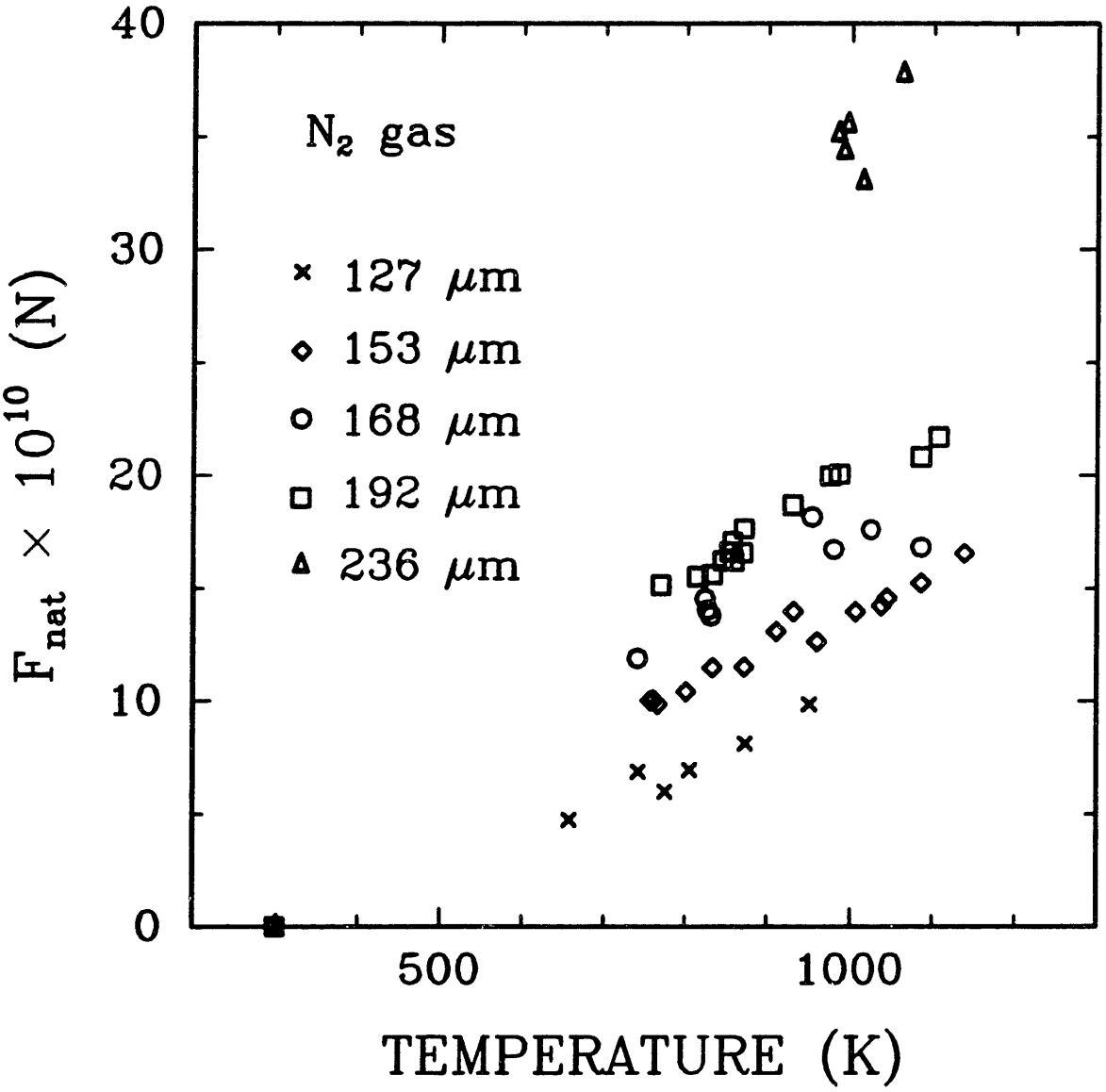

Figure 4.30 : Experimental measurements of natural convective drag force versus particle temperature for five different diameter "Spherocarb" particles in nitrogen.

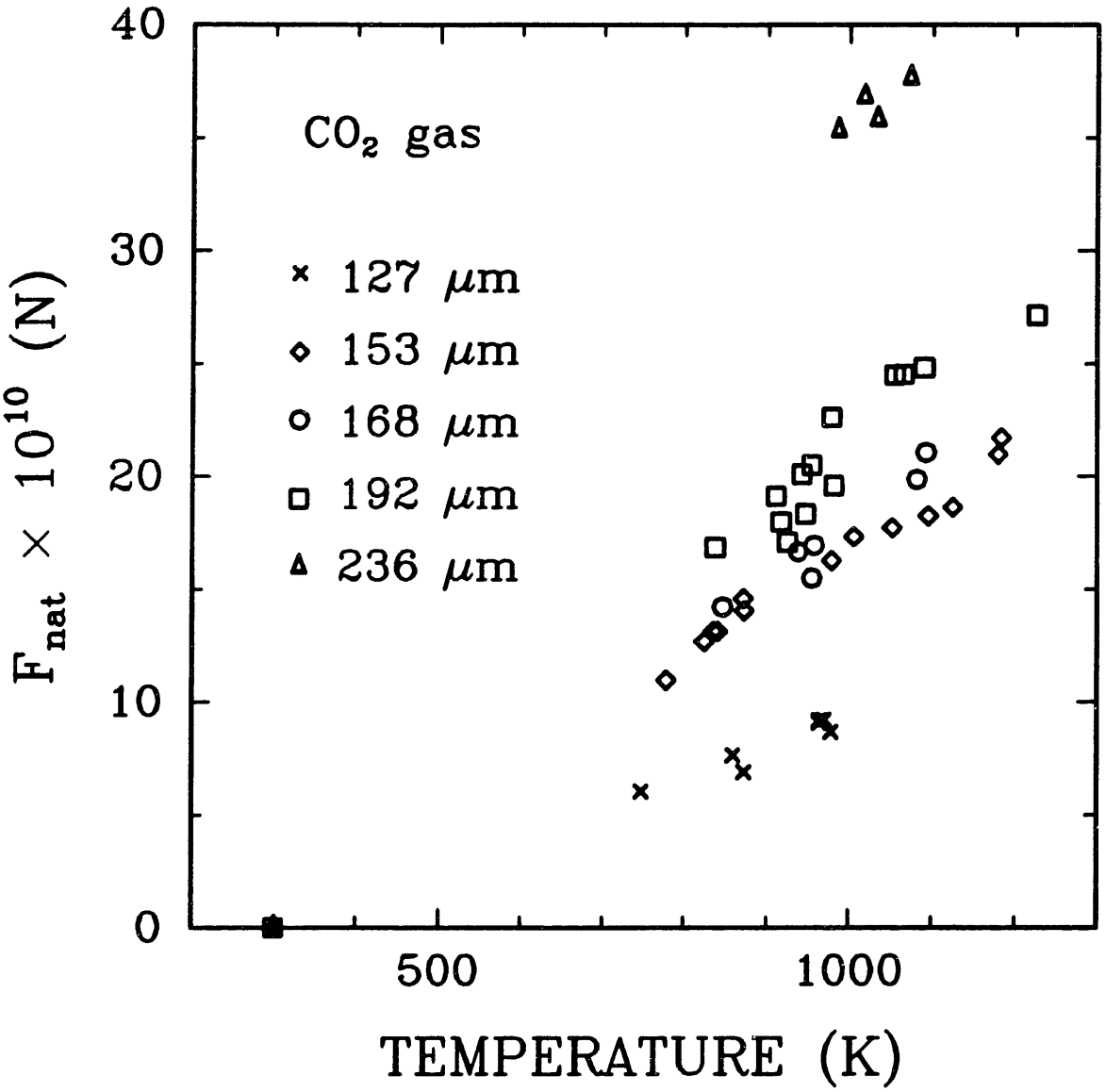

Figure 4.31 : Experimental measurements of natural convective drag force versus particle temperature for five different diameter "Spherocarb" particles in carbon dioxide.

The overall magnitude of the natural convective drag force increases with increasing diameter.

All of the data of Figures 4.25-4.29 can be collapsed onto the overall steady-state dimensionless drag coefficient versus Grashof number plot of Figure 4.32. From equation 4.3, C_{DT} is defined as $F_{nat}/(\mu^2/\rho)$, where μ^2/ρ is evaluated at the film temperature, $T_f = (T_S+T_\infty)/2$. The kinematic viscosity in the Grashof number is also evaluated at the film temperature.

4.7.2 Transient results.

Figure 4.33 is a plot of the change in balancing voltage due to the natural convective drag force versus time. The original, unheated balancing voltage for this 183 μm diameter "Spherocarb" particle was 125 volts and the particle temperature was 610 K. The natural convective drag takes about 300 msec to get set up.

4.8 Comparison of experimental and numerical results.

4.8.1 Steady-state results.

Figures 4.34, 4.35, 4.36, 4.37, and 4.38 are plots of the natural convective drag force divided by particle weight versus particle temperature for each of the five "Spherocarb" particles examined. The triangles represent experiments performed in nitrogen, the circles represent experiments performed in carbon dioxide, and the solid lines represent the numerical solutions. The surrounding gas properties are evaluated at the film temperature which is defined as the

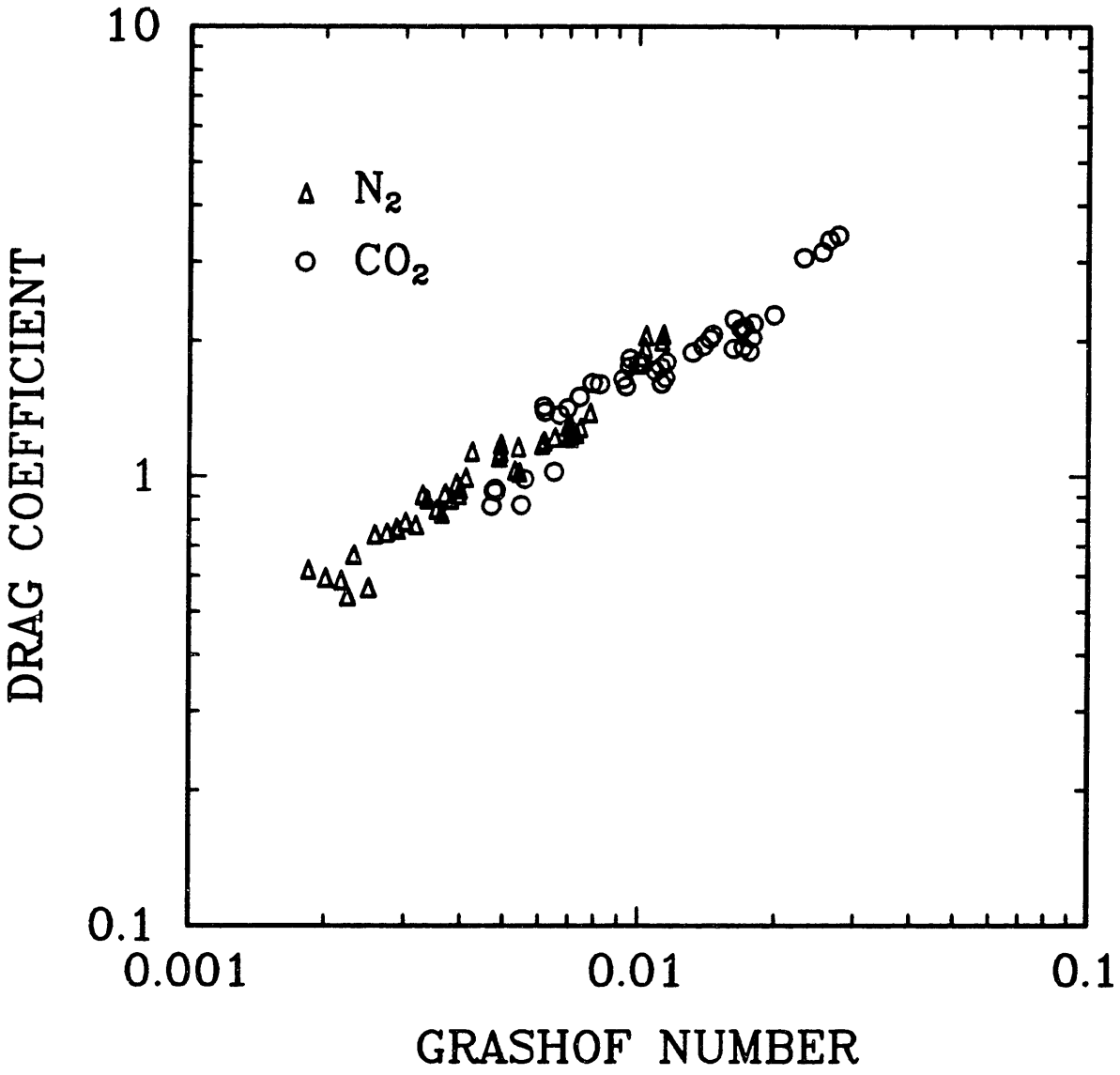

Figure 4.32 : Experimental measurements of steady-state dimensionless drag force coefficient versus Grashof number for five different diameter "Spherocarb" particles being heated in nitrogen and carbon dioxide.

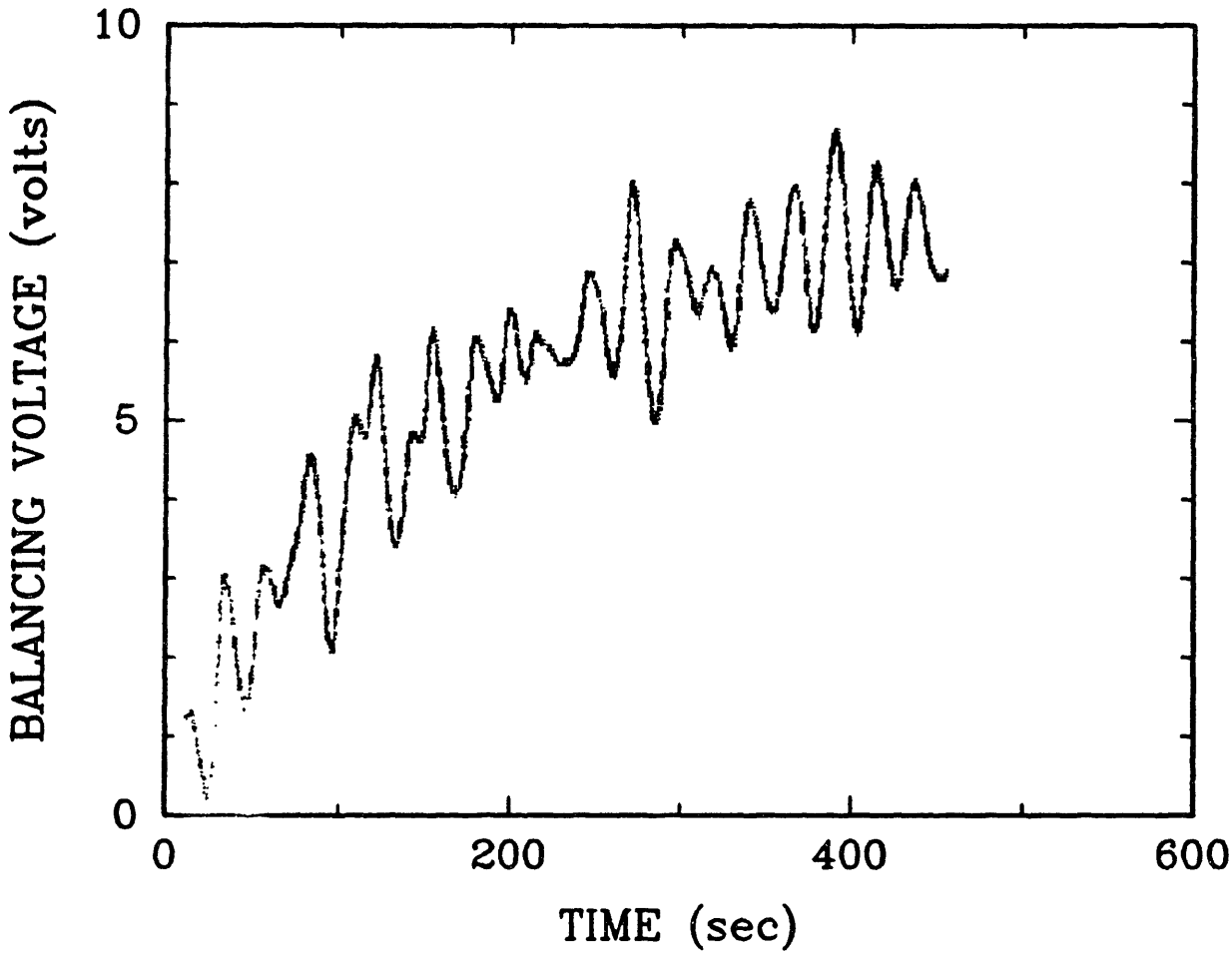

Figure 4.33 : Experimental measurement of the change in balancing voltage due to the natural convective drag force versus time for a 183 μm diameter "Spherocarb" particle being heated to 610 K in nitrogen.

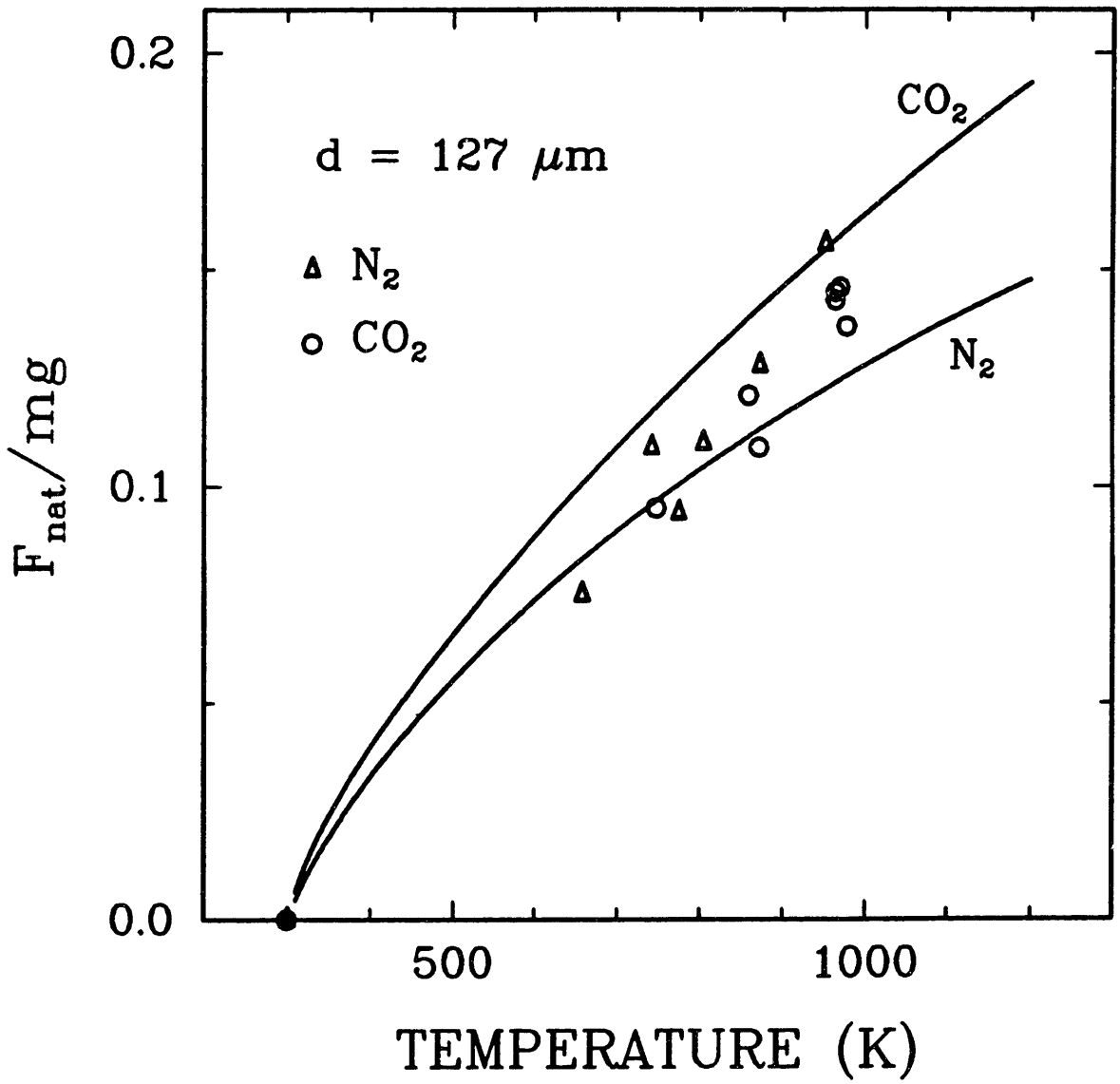

Figure 4.34 : Experimental measurements and numerical calculations of the ratio of natural convective drag force to particle weight versus temperature for a 127 μm diameter "Spherocarb" particle in nitrogen and carbon dioxide.

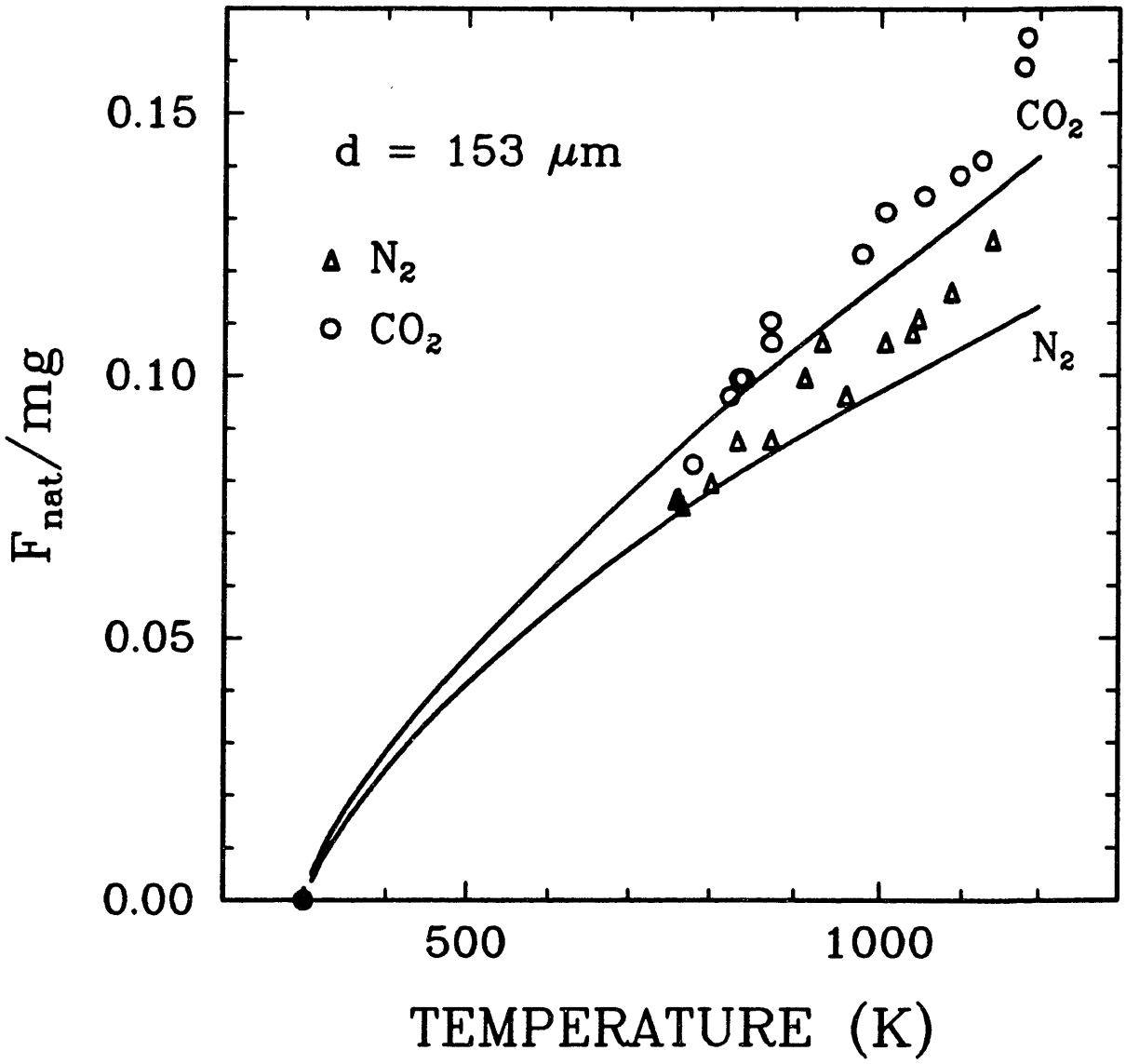

Figure 4.35 : Experimental measurements and numerical calculations of the ratio of natural convective drag force to particle weight versus temperature for a 153 μm diameter "Spherocarb" particle in nitrogen and carbon dioxide.

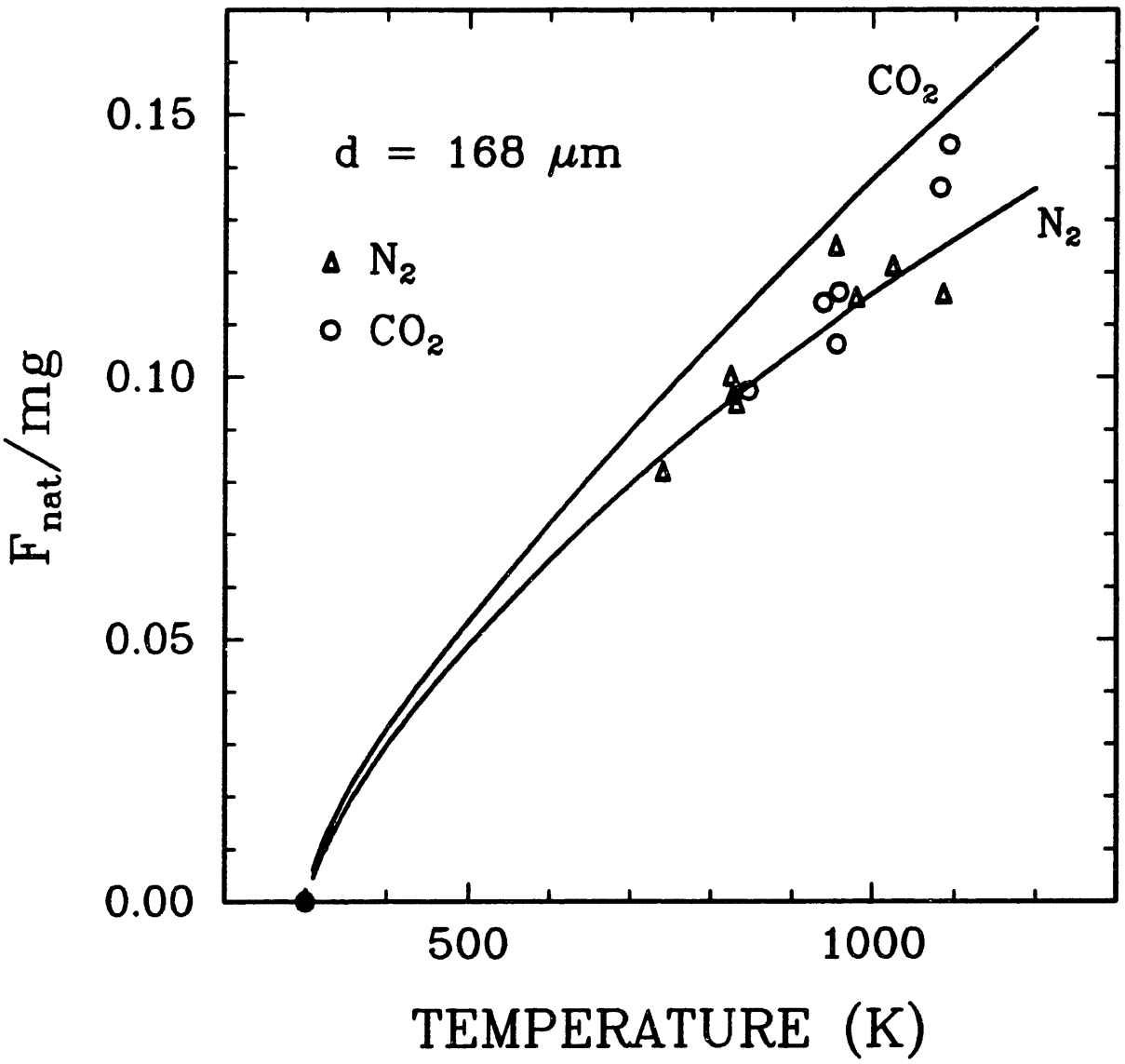

Figure 4.36 : Experimental measurements and numerical calculations of the ratio of natural convective drag force to particle weight versus temperature for a 168 μm diameter "Spherocarb" particle in nitrogen and carbon dioxide.

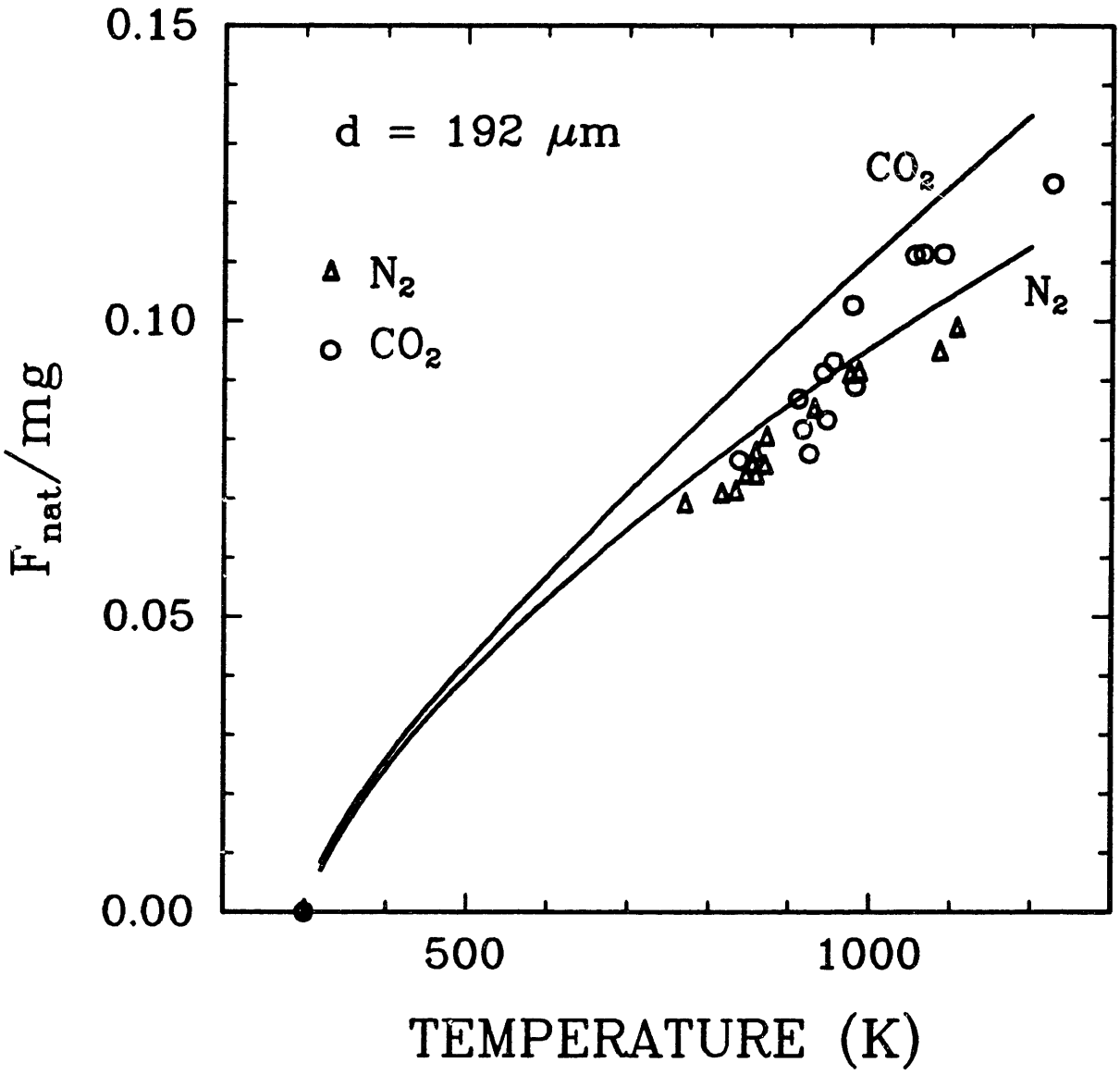

Figure 4.37 : Experimental measurements and numerical calculations of the ratio of natural convective drag force to particle weight versus temperature for a 192 μm diameter "Spherocarb" particle in nitrogen and carbon dioxide.

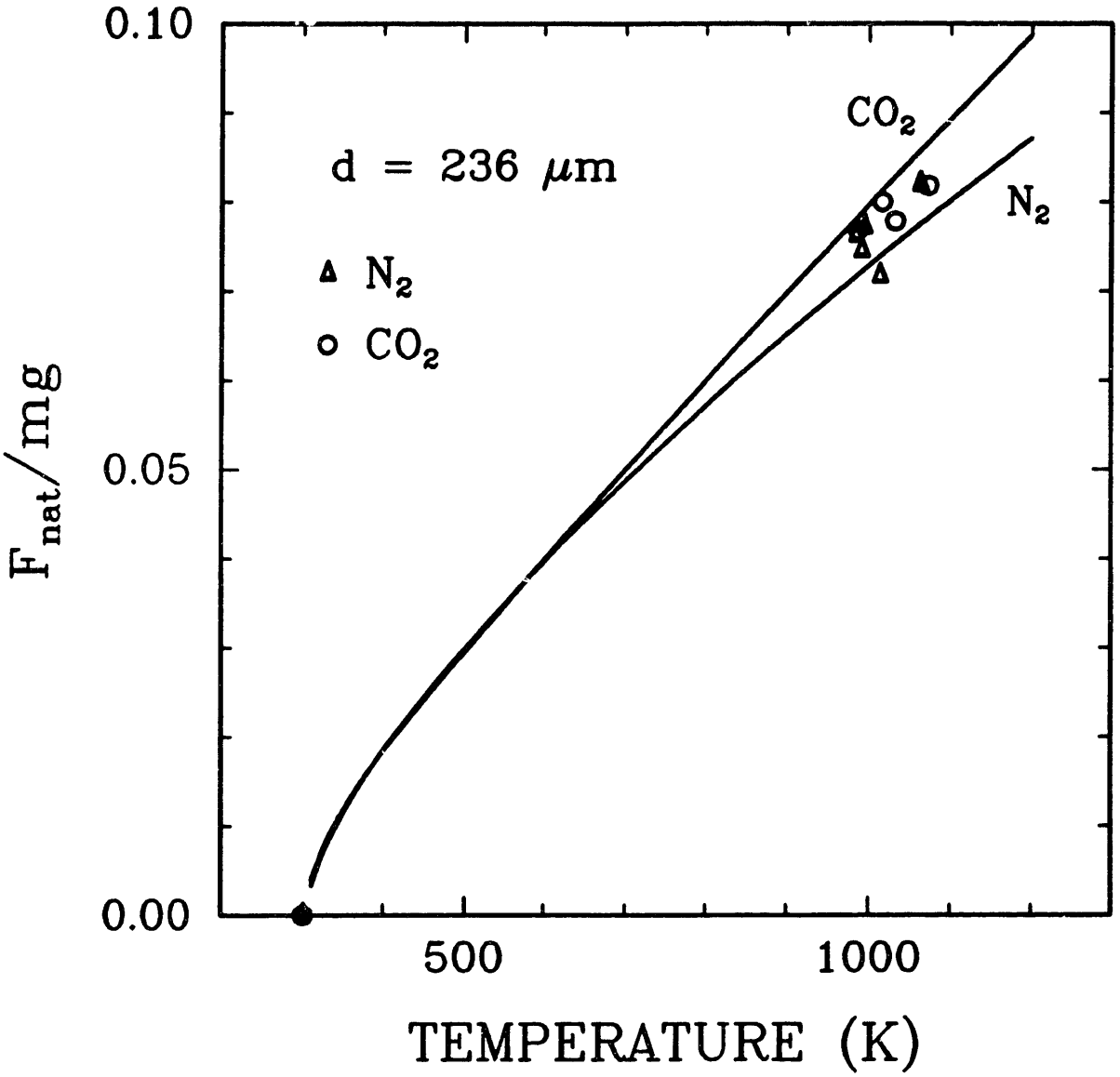

Figure 4.38 : Experimental measurements and numerical calculations of the ratio of natural convective drag force to particle weight versus temperature for a 236 μm diameter "Spherocarb" particle in nitrogen and carbon dioxide.

arithmetic mean between the particle surface temperature and the ambient gas temperature. The numerical solution agrees well with the experimental results, even though the Boussinesq criterion has been violated due to the large temperature differences in the problem [61].

Figure 4.39 is a plot of steady-state dimensionless drag force coefficient versus Grashof number. Again, the triangles represent experiments performed in nitrogen, the circles represent experiments performed in carbon dioxide, and the solid line represents the numerical solution.

4.8.2 Transient results.

Figure 4.40 is a plot of the change in balancing voltage versus real time for a 183 μm diameter "Spherocarb" particle heated to 610 K in nitrogen. The initial, unheated voltage was 125 volts. The small points represent experimental results and the smooth solid line represents the transient numerical solution. The experimental points were smoothed with a moving average filter. Again we see good agreement between experiment and theory. According to the heat transfer model developed by Spjut [7], the particle should reach 90% of its equilibrium temperature in 70-80 msec.

4.9 Numerical predictions.

4.9.1 Steady-state predictions.

Figure 4.41 is a plot of the numerical solution of the steady-state natural convective drag force for a heated

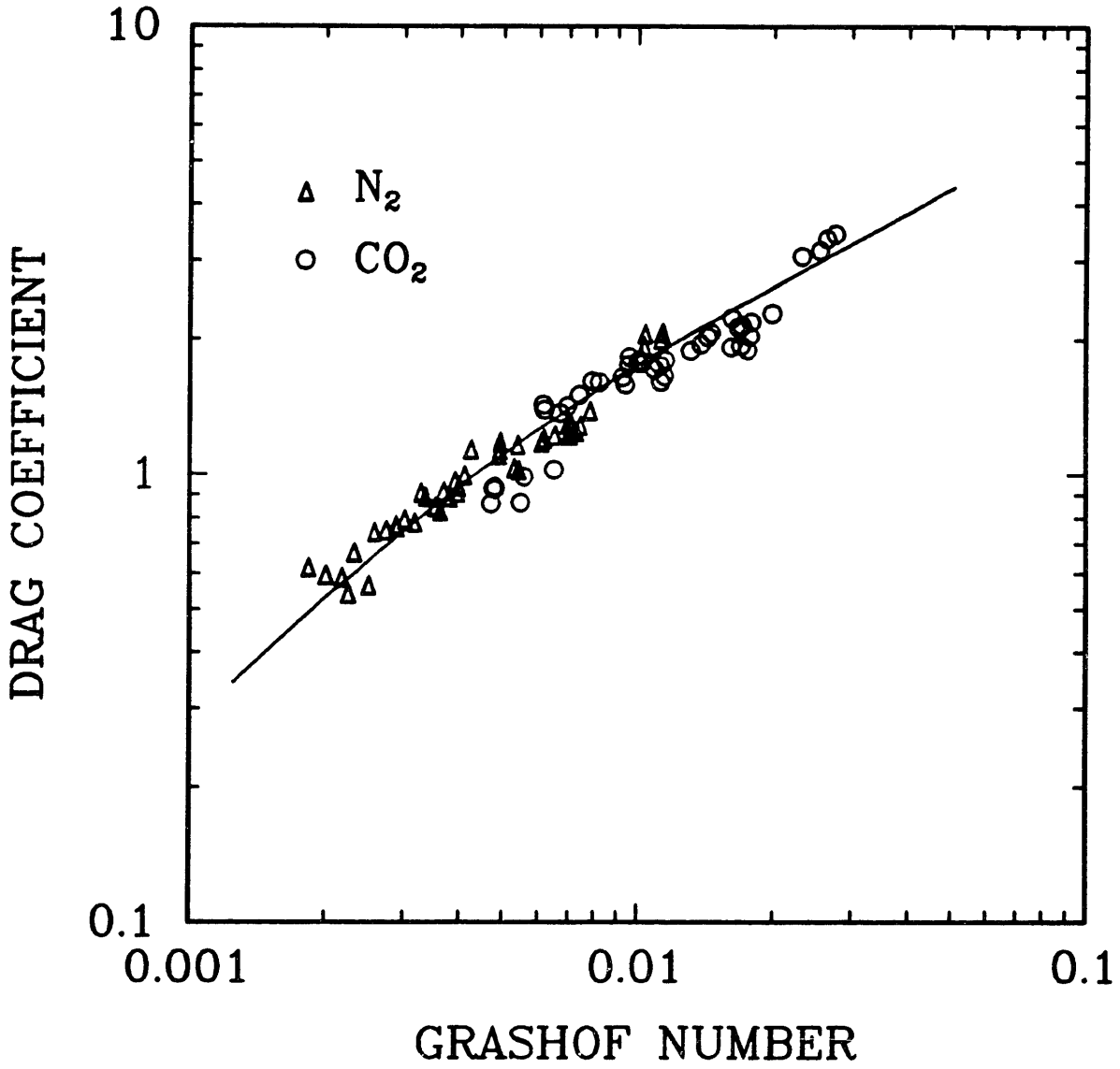

Figure 4.39 : Experimental measurements and numerical calculations of the steady-state dimensionless drag coefficient versus Grashof number for five different diameter "Spherocarb" particles heated in nitrogen and carbon dioxide.

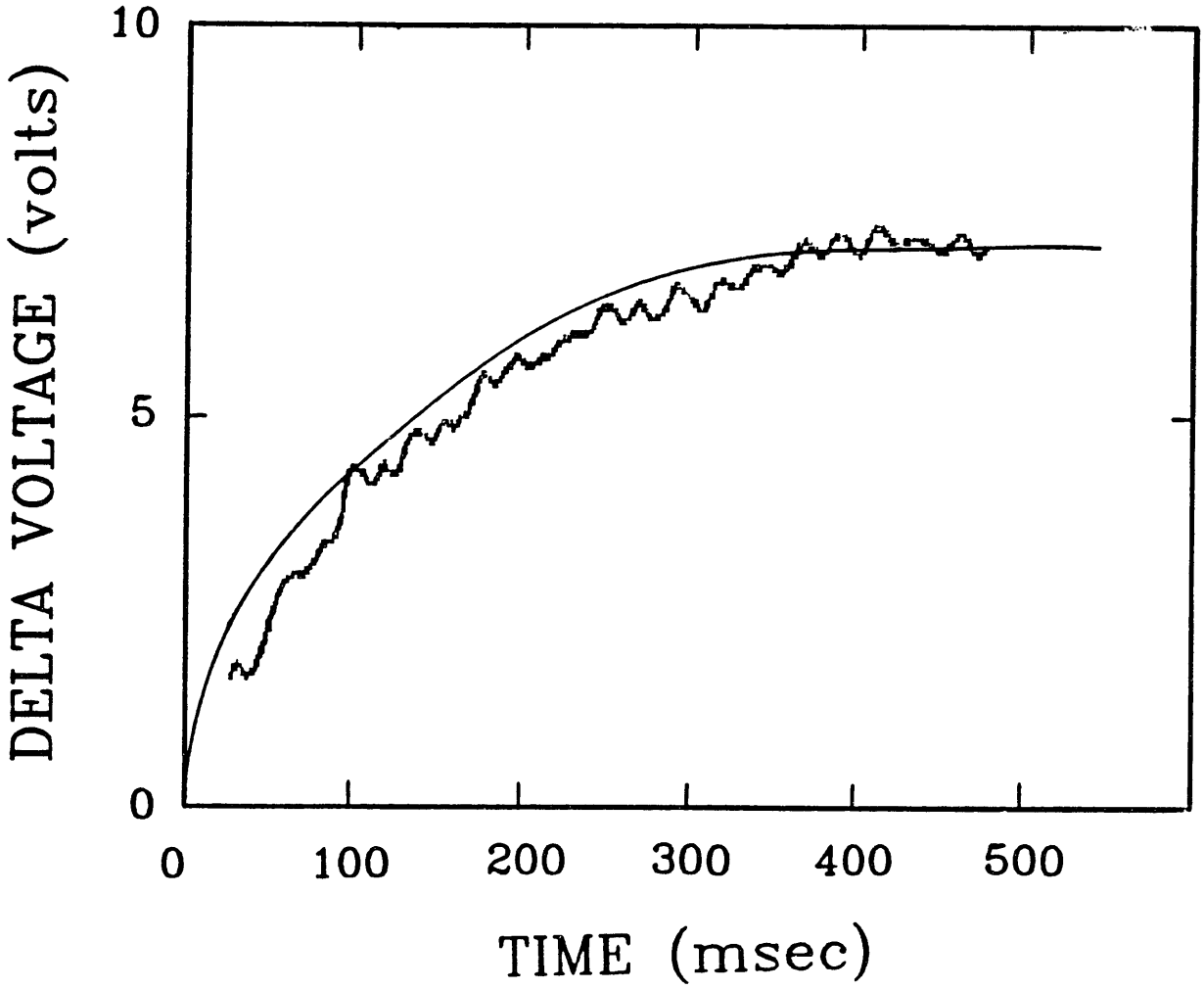

Figure 4.40 : Experimental measurements and numerical calculations of the change in balancing voltage versus time for a 183 μm diameter "Spherocarb" particle heated to 610 K in nitrogen.

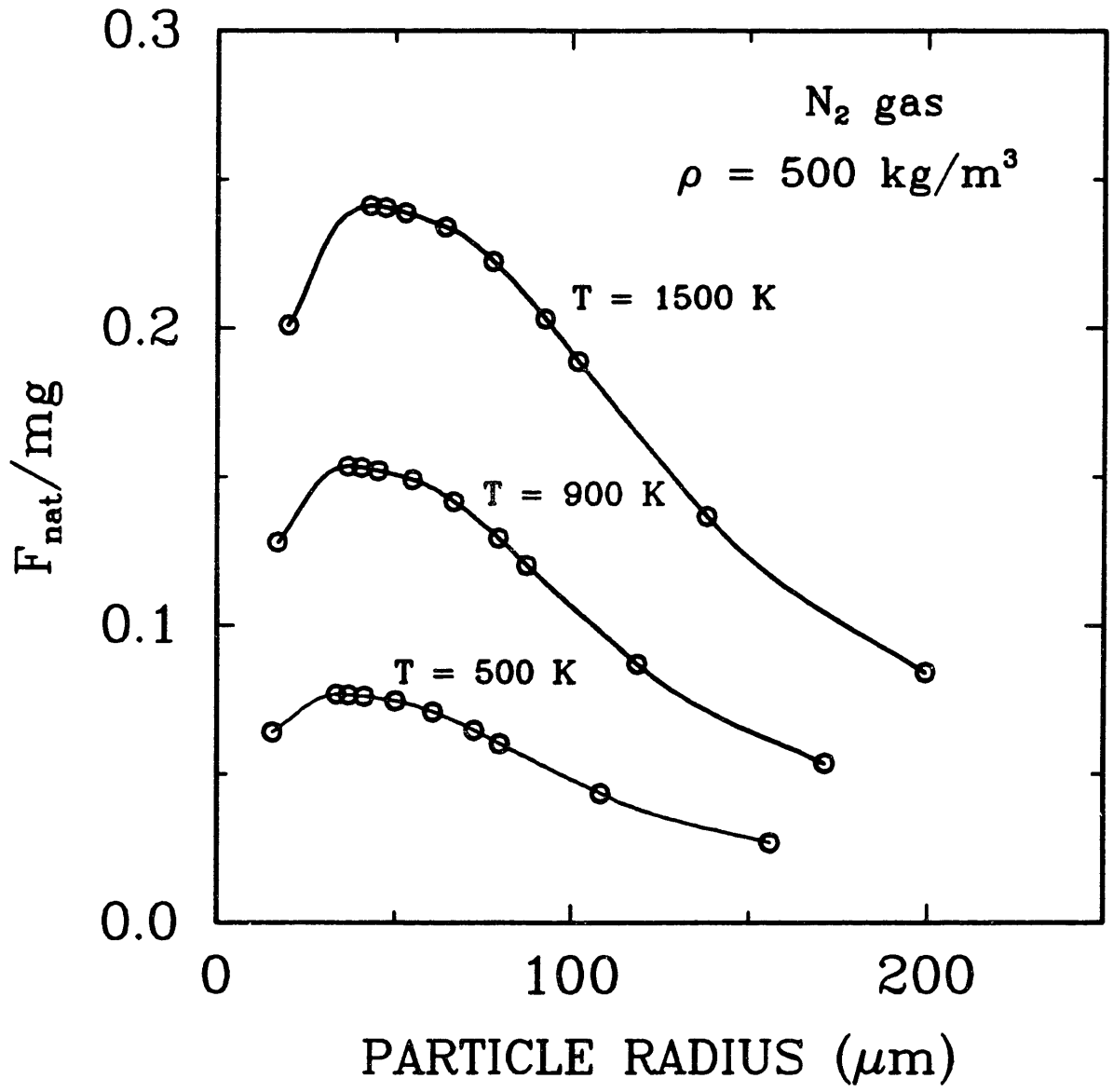

Figure 4.41 : Numerically predicted ratio of the steady-state natural convective drag force to particle weight versus particle radius for a particle density of 500 kg/m^3 and three different particle temperatures, 500 K, 900 K, and 1500 K.

sphere in ambient nitrogen divided by the particle weight versus particle radius for a particle density of 500 kg/m^3 and three different particle surface temperatures, 1500 K, 900 K, and 500 K. The circles represent predictions of the drag force/weight using the numerical solution and the solid lines are "best fit" lines through these points. The numerical solution predicts a peak in drag force divided by weight for a particle radius of approximately 40 μm. The numerical solution predicts that the natural convective drag force around aerosol particles less than 10 μm in diameter with a density greater than 500 kg/m^3 will be less than 5% of the particle weight if particle temperatures are kept under 1500 K. Furthermore, since the drag force divided by weight is inversely proportional to particle density, heavy particles with densities greater than 2500 kg/m^3 will also not experience drag forces greater than 5% of their weights if particle temperatures are kept under 1500 K.

4.9.2 Transient predictions.

Figure 4.42 is a prediction based on the transient numerical results of the real time required to reach 90% of the steady-state drag coefficient in nitrogen versus particle temperature for three different particle radii of 40, 80, and 120 μm. The time required to set up the natural convective flow field decreases with increasing particle temperature and decreases with decreasing particle radius.

For slow reactions, when the time required to set up the natural convective flow field is much less than the time required for chemcial reaction, the steady-state solution can be used to describe the natural convective drag throughout the reaction. This allows the use of the electrodynamic

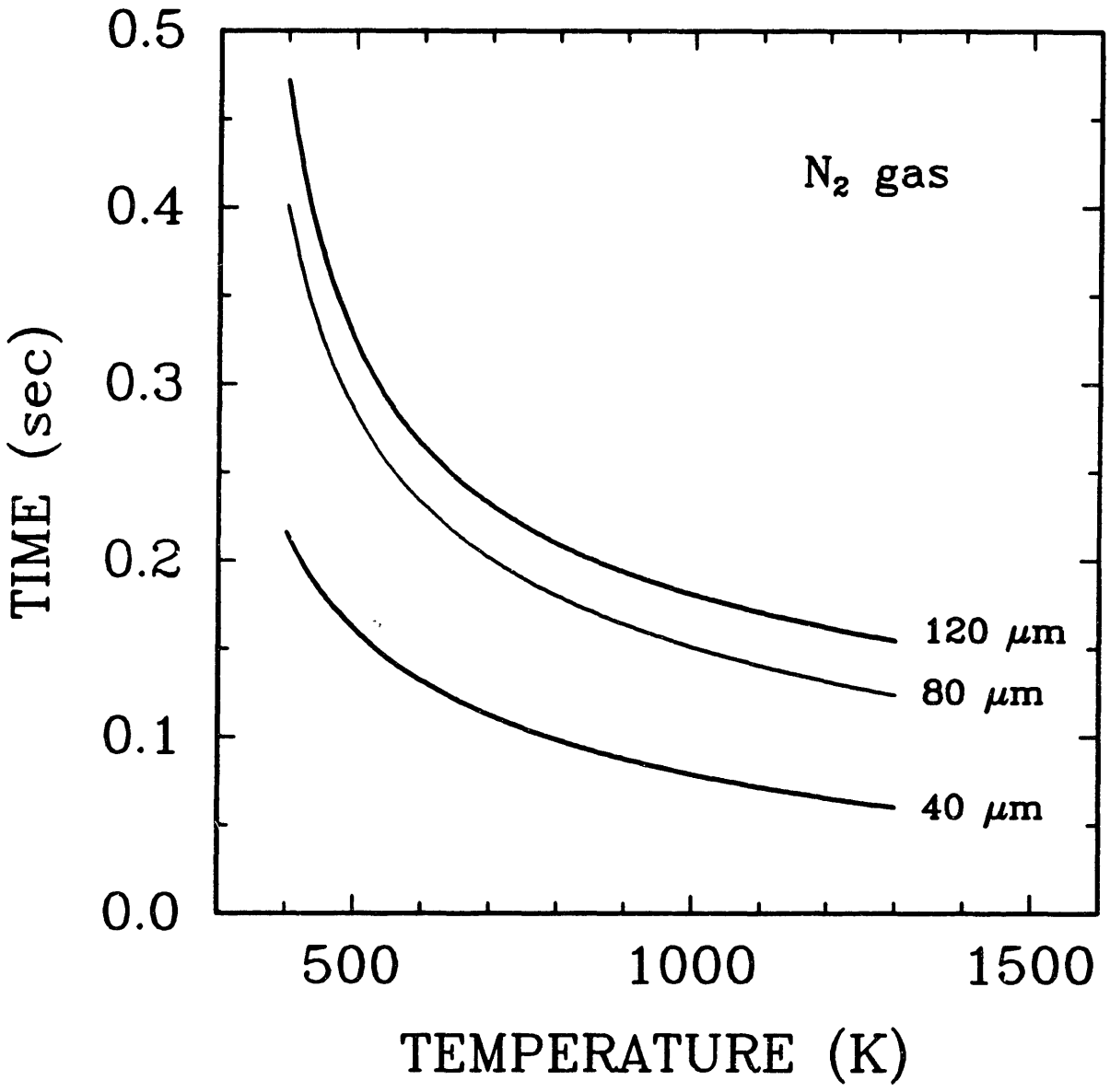

Figure 4.42 : Numerical predictions of real time required to reach 90% of the steady-state drag force coefficient versus particle temperature for particle radii of 40, 80, and 120 μm.

balance to follow mass in a continuous fashion. For fast reactions, when the time required to set up the natural convective flow field is slightly less than the time required for chemical reaction, the transient solution can be used to predict the natural convective drag throughout the reaction. For very fast reactions, when the time required to set up the natural convective flow field is longer than the time required for chemical reaction, neither the steady-state or transient solutions can be used to predict the natural convective drag. However, if the position control system can respond fast enough to keep the reacting particle in the center of the chamber, continuous mass versus time data can be collected by following balancing voltage versus time and neglecting the natural convective drag which will not have had enough time to set up. If the position control system cannot respond fast enough, discrete mass versus time points will then be required.

4.9.3 Polynomial approximations.

Since the steady-state program takes approximately 5-15 minutes on a VAX 8600, it is desirable to approximate the numerical solution, shown graphically in Figure 4.6, by a correlation. A discrete least squares method [61] was used to obtain the following second-order polynomial which describes the steady-state dimensionless total drag force coefficient:

$$\log(C_{DT}) = 1.25 + 0.31[\log(Gr)] - 0.097[\log(Gr)]^2 \quad (4.30)$$

The correlations's prediction of C_{DT} versus Grashof number is shown as the solid line in Figure 4.43. The crosses are the actual numerical solution. This correlation is good to within 5% over the range $0.0004 < Gr$

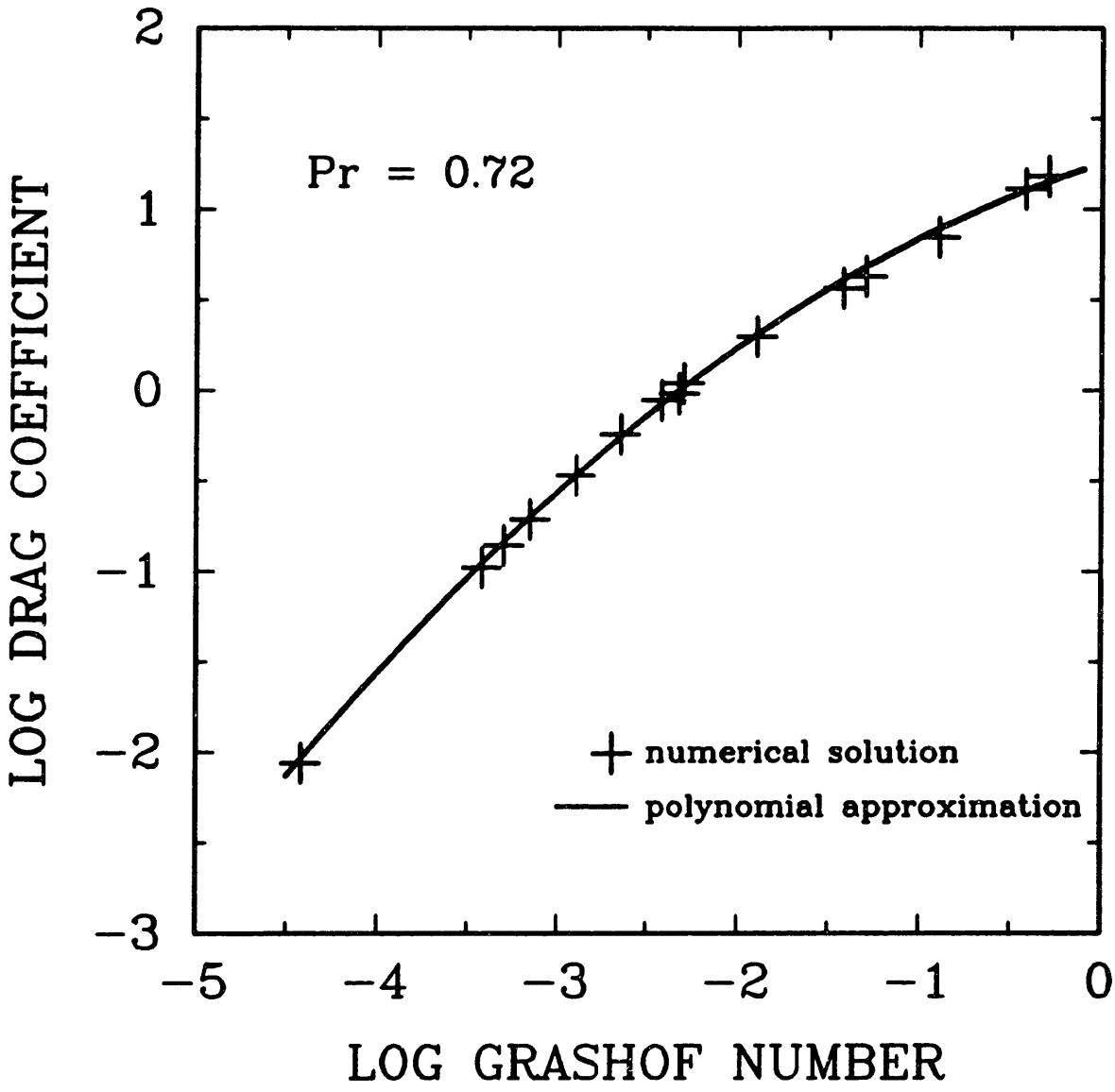

Figure 4.43 : Comparison of the polynomial approximation and the numerical calculation of the steady-state dimensionless drag force coefficient versus Grashof number.

< 0.5 for Pr = 0.72. The steady-state correlation is used to calculate F_{nat}/mg versus particle radius and this calculation is compared to the numerical solution in Figure 4.44. The open circles connected by the solid line represent the numerical solution and the open triangles connected by the dotted line represent the F_{nat}/mg values calculated by the correlation.

The transient program takes approximately 5-24 hours on a VAX 8600. The same discrete least squares method was used to obtain the following second-order polynomial that approximates the dimensionless time required to reach 90% of the steady-state drag force coefficient:

$$\log(t_{90\%}) = 1.32 - \log(Gr) - 0.11[\log(Gr)]^2 \qquad (4.31)$$

The correlation's prediction of dimensionless time versus Grashof number is shown as the solid line in Figure 4.45. The crosses are the actual numerical solution.

4.10 Examples of natural convective drag solution's use.

By examining a typical "Spherocarb" reaction in air, the effect of the natural convective drag force can be better appreciated. Figure 4.46 is a plot of balancing voltage versus time for a 207 μm diameter "Spherocarb". At a time of about 30 seconds, the particle was heated to 774 K. Immediately the natural convective drag force can be seen as the balancing voltage drops from 110 volts to 100 volts. If equation 4.30 is used to predict the natural convective drag force and a "Spherocarb" density of 650 kg/m^3 is assumed, the natural convective drag may be cancelled out and the "true" balancing voltage may be calculated. The "true" balancing voltage versus time is plotted in Figure

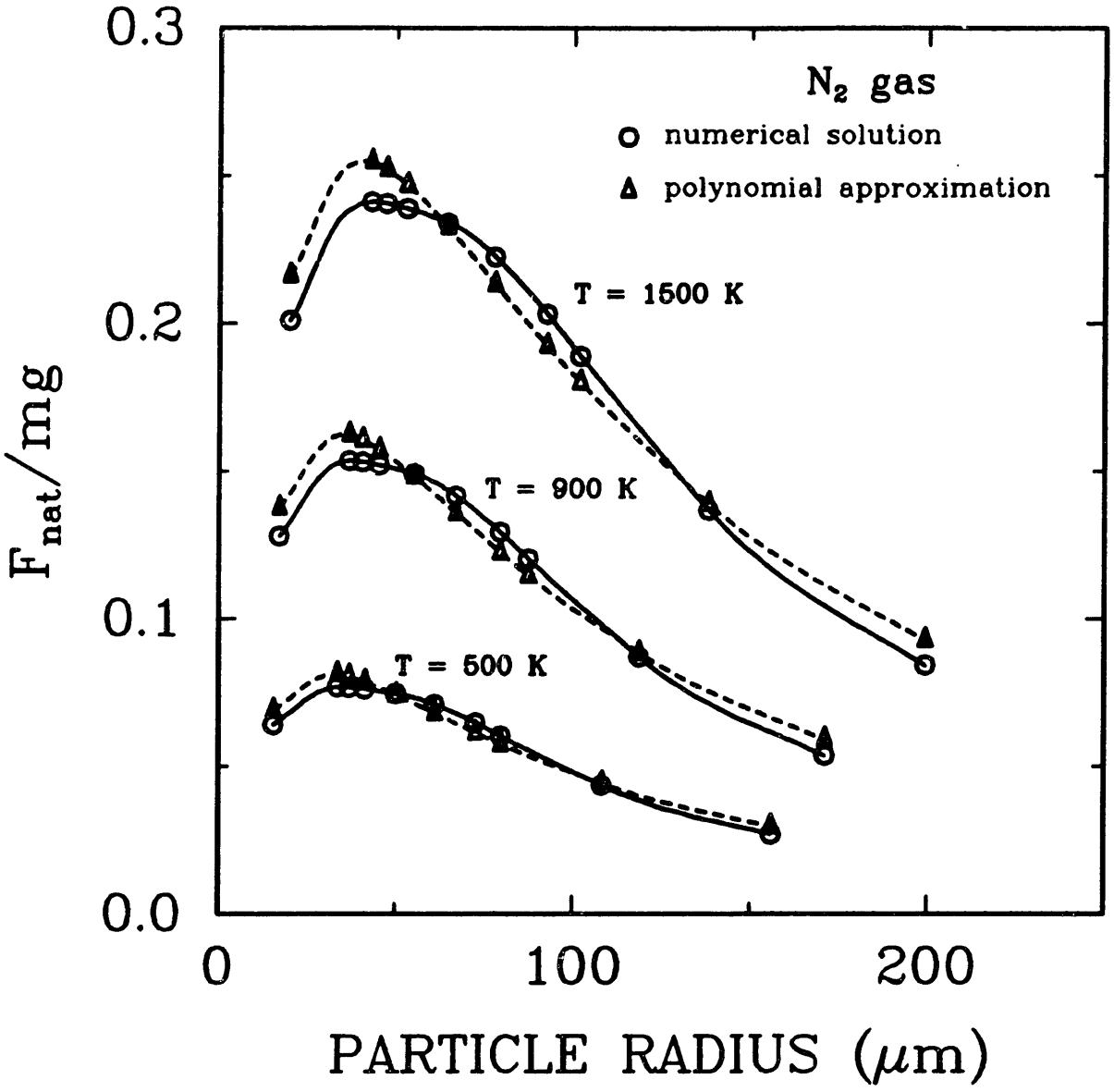

Figure 4.44 : Comparison of the polynomial approximation and the numerical calculation of the ratio of state natural convective drag force to particle weight versus particle radius for particle temperatures of 500, 900, and 1300 K.

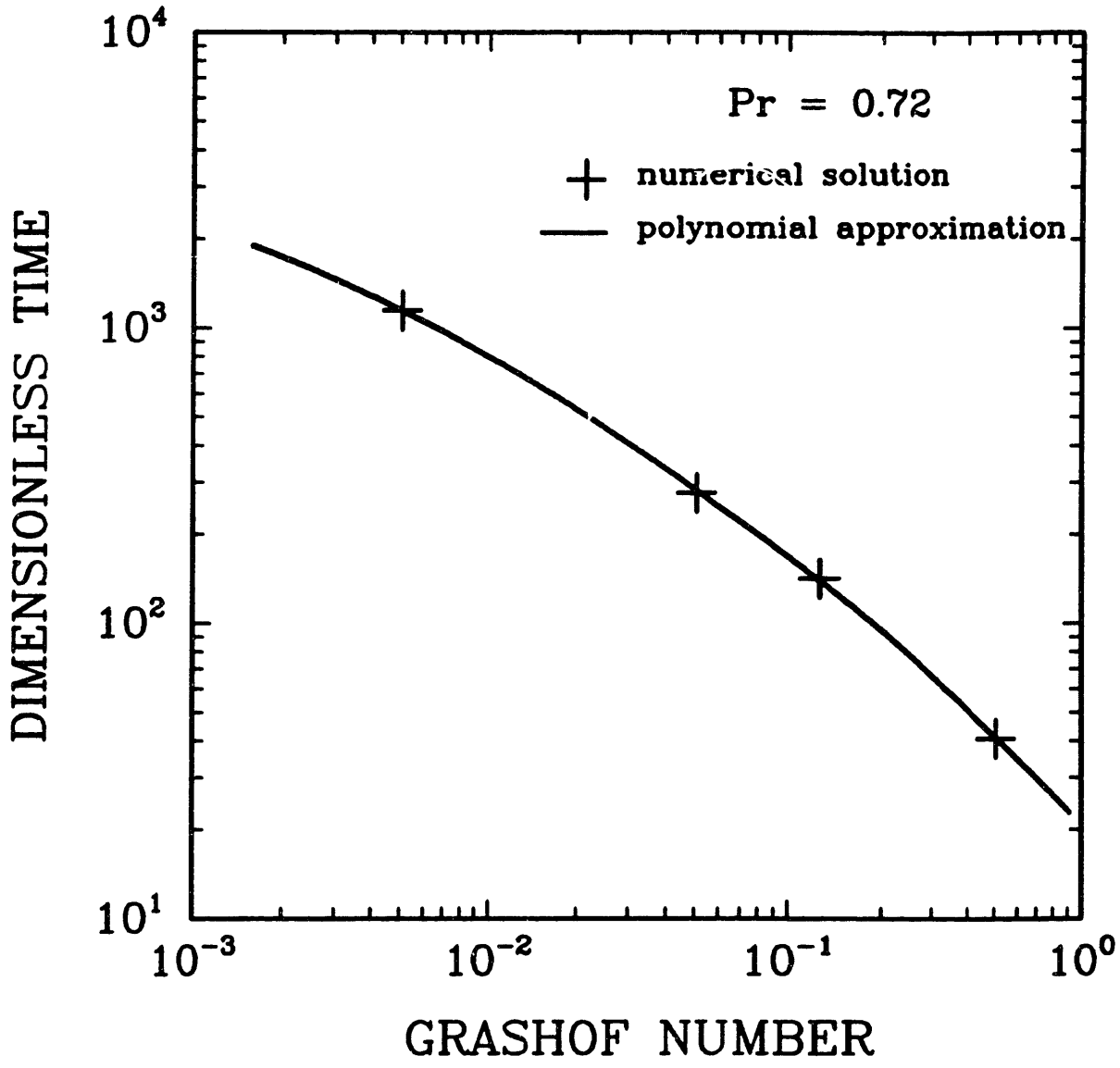

Figure 4.45 : Comparison of the polynomial approximation and the numerical calculation of dimensionless time versus Grashof number.

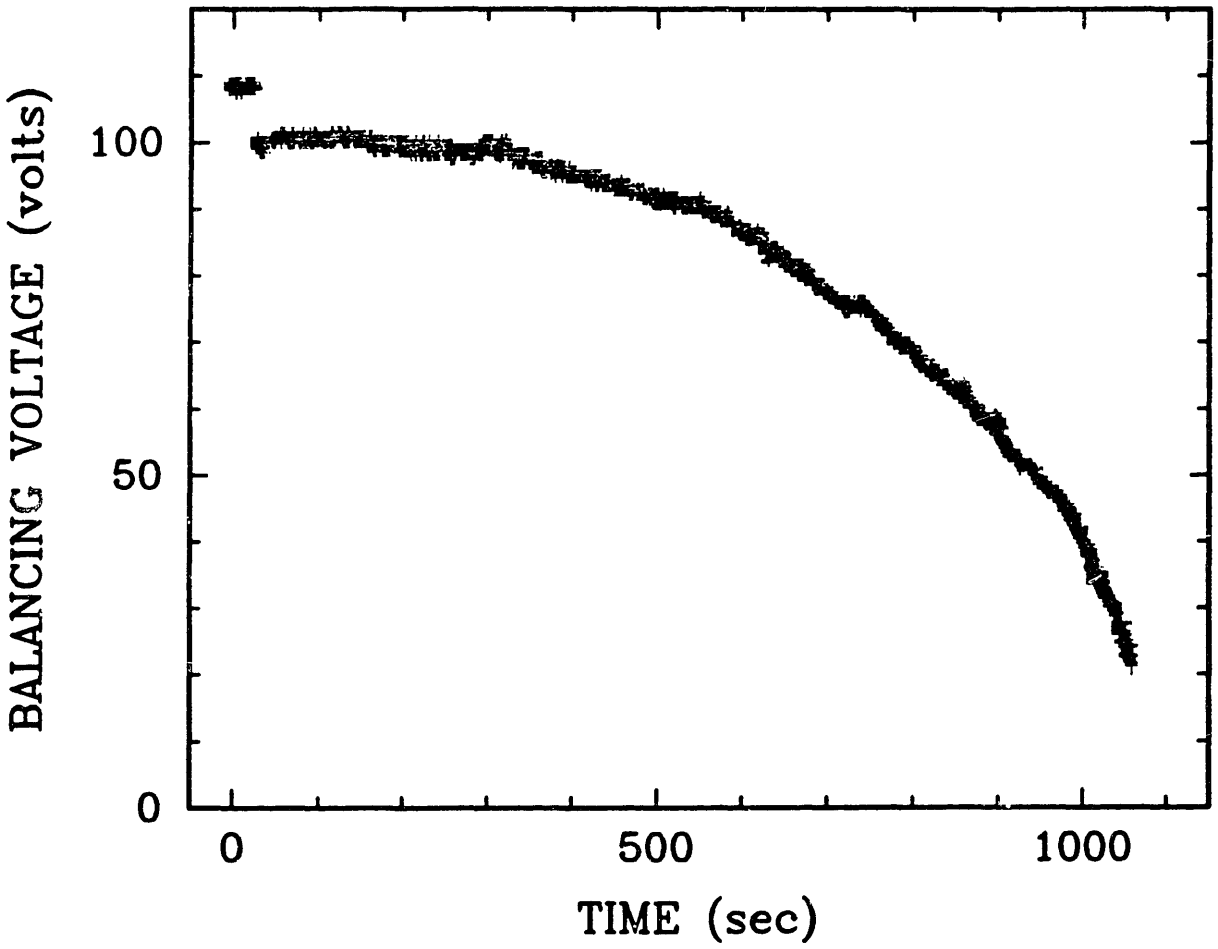

Figure 4.46 : Experimentally measured balancing voltage versus time for a single 207 μm diameter "Spherocarb" particle reacting in oxygen at 773 K.

4.47. It should be noted that the diameter and density history of the particle must be known or predicted at each stage of the reaction in order for the "true" balancing voltage to be calculated.

4.11 Conclusions for natural convection.

1) The computational method of Geoola and Cornish [55,56] for describing the heat transfer and fluid mechanics surrounding a heated solid sphere was modified to correctly calculate the drag force due to natural convection.

2) The experimental steady-state and transient results of the natural convective drag force agree well with the Boussinesq numerical solutions, indicating that the Boussinesq approximation is valid over the experimental parameter range examined.

3) The numerical calculations were used to develop the following empirical correlation to approximate the steady-state natural convective drag force:

$$\log(C_{DT}) = 1.25 + 0.31[\log(Gr)] - 0.097[\log(Gr)]^2$$

where C_{DT} is the overall steady-state dimensionless drag force coefficient and Gr is the Grashof number. This correlation is good to within 5% over the range $0.0004 < Gr < 0.5$ for Prandtl number = 0.72.

4) The numerical calculations were also used to develop the following empirical correlation to approximate, $t_{90\%}$, the dimensionless time required to reach 90% of the steady-state drag coefficient:

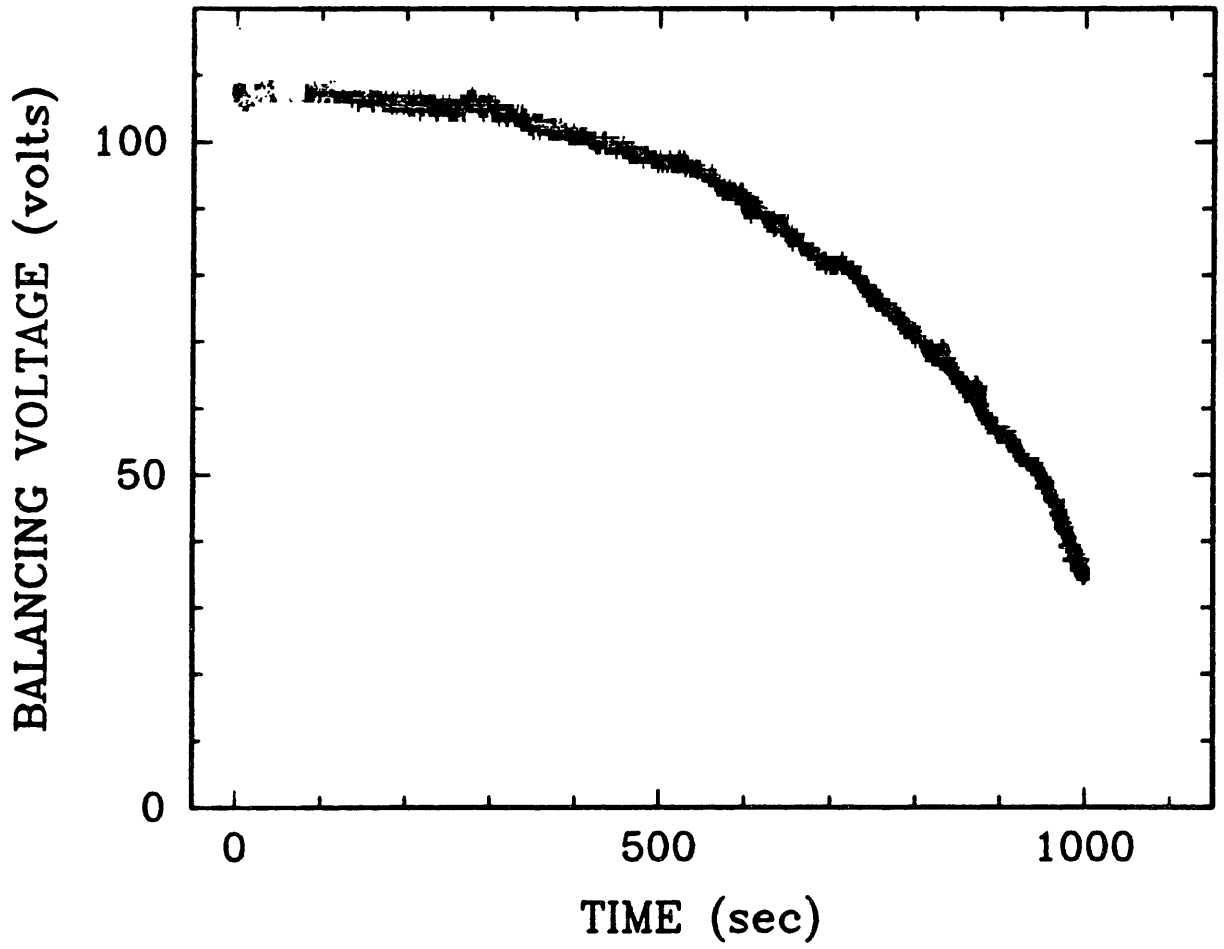

Figure 4.47 : "True" balancing voltage (after correcting for the natural convective drag force) versus time for a single 207 μm diameter "Spherocarb" particle reacting in oxygen at 773 K.

$$\log(t_{90\%}) = 1.32 - \log(Gr) - 0.11[\log(Gr)]^2$$

5) The steady-state and transient empirical correlations presented here may be used to cancel out the natural convective drag force from the reacting particle force balance, thereby, allowing continuous mass versus time measurements to be calculated from balancing voltage versus time measurements.

6) The numerical solution predicts that the steady-state natural convective drag force relative to the particle weight should increase with particle radius up to a maximum value at a particle radius of approximately 40 μm and then start to decrease. The natural covective drag force increases monotonically with increasing temperature. The natural convective drag force around aerosol particles, heated to under 1500 K, with radii less the 5 μm and density greater than 500 kg/m^3 should be less than 5% of the particle weight.

7) The steady-state natural convective drag force relative to particle weight is inversely proportional to particle density. Therefore, if a particle is to be heated to a temperature under 1500 K and has a density greater than 2500 kg/m^3, its natural convective drag force should be less than 5% of the particle weight.

8) The time required to set up the natural convective flow field decreases with increasing particle temperature and decreases with decreasing particle radius. The time was in the range of 100-300 msec for the experiments performed.

5. CHARGE LOSS FROM HEATED PARTICLES LEVITATED IN THE EDB.

5.1 Motivation.

The electrodynamic balance (EDB) is a device capable of suspending a single, charged, less than 250 μm particle in a dynamic electric field. It is being developed as a tool for studying single particle, high temperature, gas-solid reactions. The following vertical force balance reveals the importance of the charge on the particle:

$$mg = qE \tag{5.1}$$

where m is the particle mass, g is the gravitational acceleration, q is the excess charge on the particle, and E is the electric field strength in the vertical direction. E is used to counteract the gravitational force on the particle and balance it in the center of the chamber. If q = 0, then particle suspension in this manner is impossible, therefore, charging the particle and keeping it charged is extremely important. The term "catastrophic" charge loss will be used to describe an event where enough charge is lost from a particle to prevent it from being stably balanced.

Experimentally, it has been found that initial charging of particles (most probably by tribo or frictional electrification) is not a problem. Particles with both positive and negative excess charge have been successfully captured in the EDB. A typical number of excess charges on a captured particle in our EDB is in the range of 10^6 to 10^8.

Although initial charging of particles is not difficult, keeping the particle charged during heating has been shown

experimentally to be a problem. All particles suspended in our EDB, regardless of material, polarity of charge, size, or shape, have been shown to experience charge loss at some temperature. To date, C, SiO_2, BaO, CaO, KI, KCl, NaCl, $Ca(OH)_2$, $CaSO_4$, Al coated SiO_2, Fe coated SiO_2, Ag coated Cu, and Au coated Ni particles have all experienced charge loss. The size range examined was between 20 and 250 μm.

Since charge loss and subsequent loss of the ability to suspend the particle in the chamber using an electric field has been shown to occur as the particle is heated, it is desirable to (1) understand the mechanism by which this charge loss occurs, (2) be able to predict when this charge loss will occur, and (3) determine the conditions for which charge loss is minimized. Knowledge of when charge loss is likely to occur will dictate how the EDB can be used in studying high temperature gas-solid reactions. For example, if it is determined that catastrophic charge loss occurs in every material at 1000 K, direct mass, density, diameter, and surface area measurements versus time cannot be made on reactions above 1000 K. For very fast reactions ($\tau_{reaction}$ < 100 msec) at temperatures >1000 K, however, temperature versus time data may still be obtained as the particle falls from the chamber center. The temperature history along with a heat balance may then be used to determine particle reaction rates.

To date, it has been found that single particle mass, density, diameter, surface area, and temperature can all be measured in the EDB as a function of extent of reaction, as long as catastrophic charge loss does not occur. It can be argued, therefore, that charge loss from a heated particle represents the single most important limitation in using the EDB as a tool to study single particle high temperature gas-solid reactions.

5.2 Potential charge loss mechanisms.

Charge may be lost from a particle levitated in the EDB by six different mechanisms, (1) photoemission, (2) field emission, (3) secondary emission, (4) thermionic emission of electrons or ions, (5) fragmentation, and (6) surrounding gas ionization. Two of these mechanisms, photoemission and secondary emission, can be discarded a priori. Since the energy of a photon emitted from the CO_2 laser at 10.6 μm is 0.12 eV (at least one order of magnitude lower than the work function of the solids tested) photoemission of electrons due to incident 10.6 μm radiation is assumed negligible. Secondary emission of electrons is caused by the bombardment of the solid by charged particles. Since charged particles are usually not hitting the suspended particle, secondary emission can also be assumed negligible. Field emission of electrons occurs from a solid which is subject to high surface fields. Cold field emission may be excluded as well because charge loss has not been detected under nonheating conditions. The remaining mechanisms for further consideration are:

(1) emission of electrons or ions originated from either a thermionic process alone or a thermionic process magnified by an existing electric field. The symmetry of charge loss with charge sign indicates that the charge carriers should be positive or negative ions rather than electrons.

(2) A fragmentation process which may be defined as a cluster of molecules leaving in a condensed phase. Although it seems a reasonable mechanism, observable fragmentation usually does not accompany charge loss and it would seem

reasonable to assume that quite a large section of the particle would have to fragment off in order for the particle to lose enough charge to no longer be stable in the chamber.

(3) Surrounding gas ionization cannot be ruled out, but due to the large ionization potentials of typical surrounding gases (~11-16 eV) compared to the work functions of typical solids (1-6 eV), it is assumed that a thermionic emission of ions from the solid would occur at a lower temperature than the ionization of the surrounding gas. Also, if gas ionization were the sole mechanism of charge loss, charge loss would not be a function of material but a function solely of gas type. Experimentally, this has been found not to be the case. One can still, however, use the temperature at which gas ionization becomes appreciable as an upper limit on the temperature to which a particle can successfully be heated without charge loss. The gas molecules most likely to undergo ionization would be the heated molecules adjacent to the heated particle. The gas and the solid would be undergoing essentially the same electric field at this point in space, therefore, it is assumed that the work function of the solid and the ionization potential of the gas would be lowered by equivalent amounts.

From this short discussion alone, we can infer that the most viable mechanism of charge loss from heated levitated particles is thermionic emission of ions.

5.3 Literature background.

To understand thermionic emission, the work function and threshold energy of the solid must first be defined. The valence electrons of any solid are prevented from escaping by a potential barrier at the surface of the solid. The work

function is a measure of the strength of this potential barrier. The energy levels of the electrons in metals are shown in Figure 5.1a. The bottom of the conduction band is used as the reference energy level (E = 0). The vacuum level, W, represents the energy of an electron at rest outside at a large distance from the metal. The Fermi energy level, E_f, represents the highest filled energy level of a metal at T = 0 K. The work function, ϕ, is defined as the energy required to bring an electron from the Fermi level to the vacuum level, $W - E_f$. In the words of Gallo [63], "the work function is defined as the minimum energy required to extract the weakest electrons from its maximum natural surface excursion distance to infinity."

The energy levels for semiconductors and insulators are depicted in Figure 5.1b. The Fermi level usually lies above the highest occupied energy level, $-E_d$. E_d, sometimes referred to as the energy gap between the valence band and the conduction band, is larger for insulators than for semiconductors. The threshold energy, E_{th}, is defined as the energy required to bring an electron from the highest occupied level to the vacuum level. The threshold energy of a semiconductor or insulator is usually larger than the work function.

Thermionic emission of ions or electrons from a solid surface is usually written in the form of the Richardson-Dushman equation.

$$I = A\, T^2 \exp[-\phi/kT] \qquad (5.2)$$

where I = total emitted current per unit area.

A = $4\pi emk^2/h^3$ = 120 amps/cm^2K^2

= the Richardson constant.

e = elementary charge = 1.6 X 10^{-19} coul.

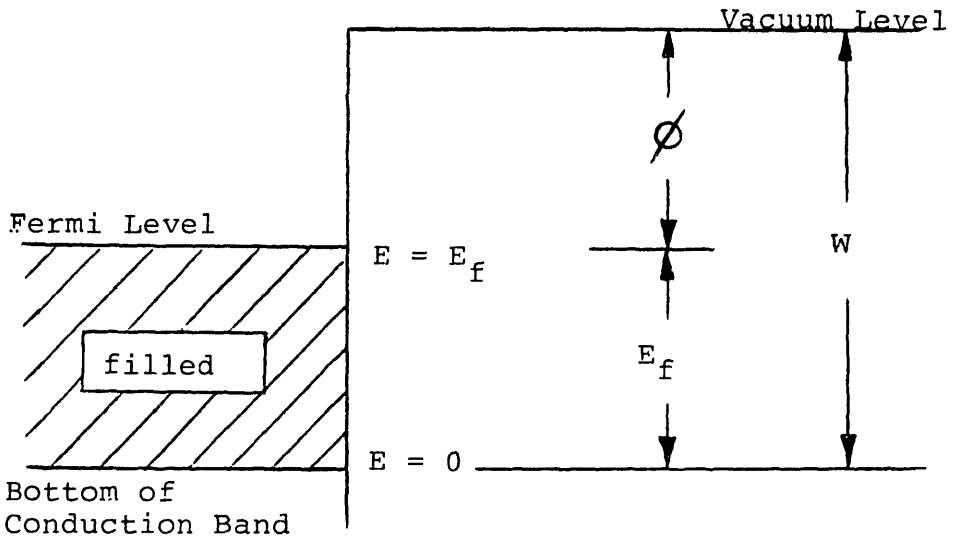

Figure 5.1a : Energy levels of electrons in metals.

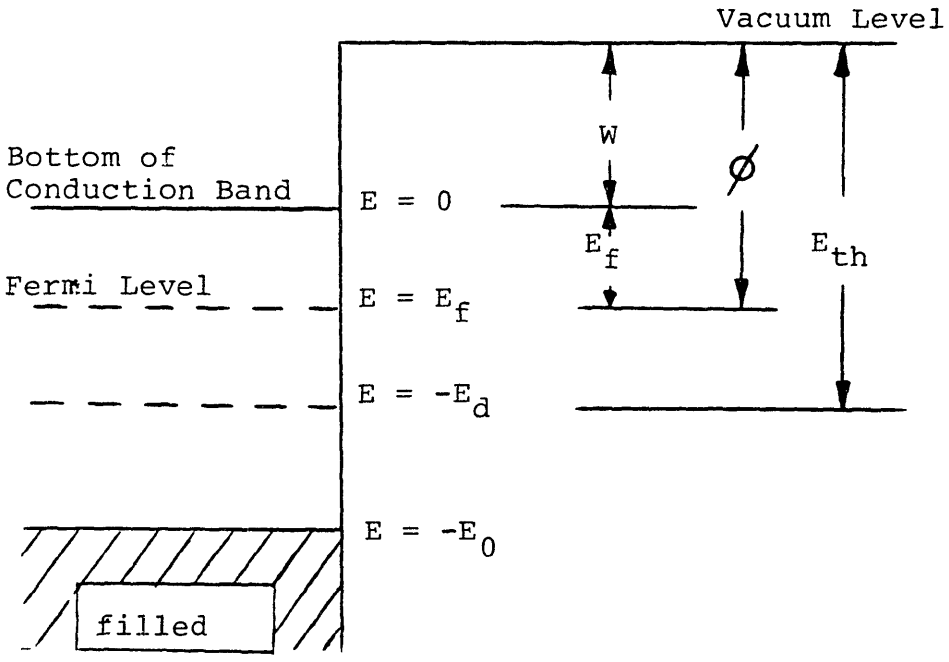

Figure 5.1b : Energy levels of electrons in semiconductors and insulators.

m = mass of an electron = 9.107 X 10-31 kg.

k = Boltzmann's constant = 8.63 X 10^{-5} eV/molecule K.

h = Planck's constant = 4.14 X 10^{-15} eV sec.

T = temperature (K).

ϕ = work function (eV).

Charge loss from a heated 100 μm diameter particle (as predicted by the Richardson-Dushman equation) versus particle temperature is plotted in Figure 5.2 with particle work function as a parameter. A representative list of work functions for different materials is presented in Table 5.1 [64-67].

An electric field can lower the apparent work function of the material by $[eE/(4\pi\epsilon_0)]^{0.5}$. This is called the Schottky effect [68,69] and the total current can now be written:

$$I = A\,T^2 \exp[-\phi/kT]\exp\{[eE/(4\pi\epsilon_0)]^{0.5}/(kT)\} \qquad (5.3)$$

where E = electric field strength at the surface of the material (volts/m).

ϵ_0 = permittivity of free space
= 8.85 X 10^{-12} farad/m.

Therefore, the electric field of a levitated particle (created by the excess charge on the surface) acts to lower the work function of the particle and aids in charge loss. The extent to which the electric field affects the work function is shown in Figure 5.3

The Richardson-Dushman equation modified for the Schottky effect (equation 5.3) has been derived for the emission of electrons from a perfectly clean, smooth metal surface in a vacuum. The system under study will almost

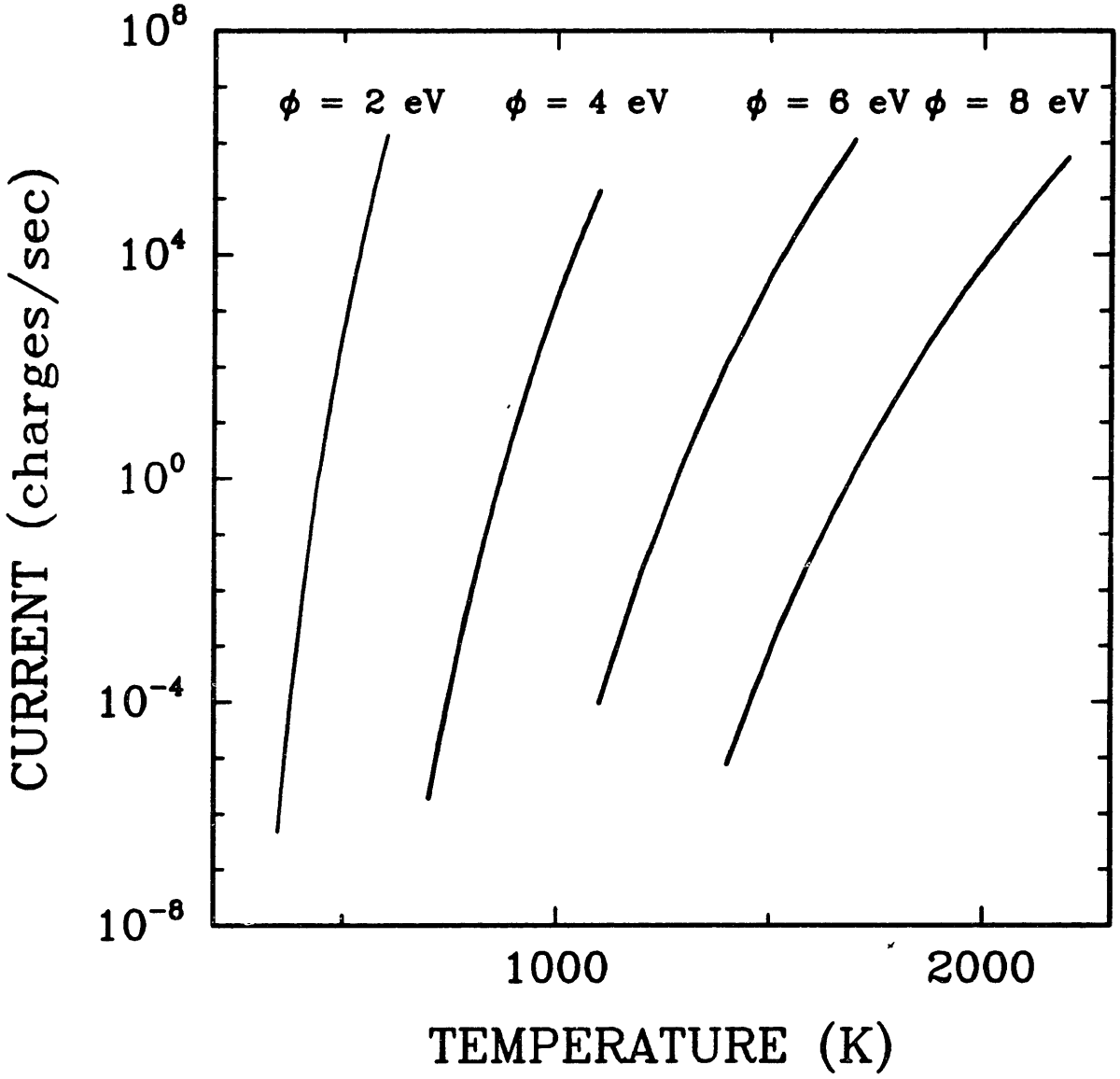

Figure 5.2 : Richardson–Dushman equation prediction of charge loss from a 100 μm diameter sphere versus temperature for work functions of 2, 4, 6, and 8 eV.

Table 5.1 : Work functions of various materials [64-67].

material	ϕ (eV)
Ag	4.3-4.7
Al	4.0-4.4
Ba	2.1-2.7
C	4.4-5.0
Ca	2.8
Cs	1.8-2.1
Cu	4.5-4.9
Fe	4.5-4.8
Ge	4.8
K	2.3
Mo	4.2-5.3
Na	2.3-2.8
Ni	4.1-5.4
Pt	5.4-5.7
Si	4.6-5.2
Ta	4.0-4.8
W	4.2-5.3
BaO	1.7
CaO	1.9
CuO	5.3
SrO	1.4
SiO_2	5.0
NaCl	8.5
KF	10.4
KCl	8.7
KI	7.2
ZnS	8.7

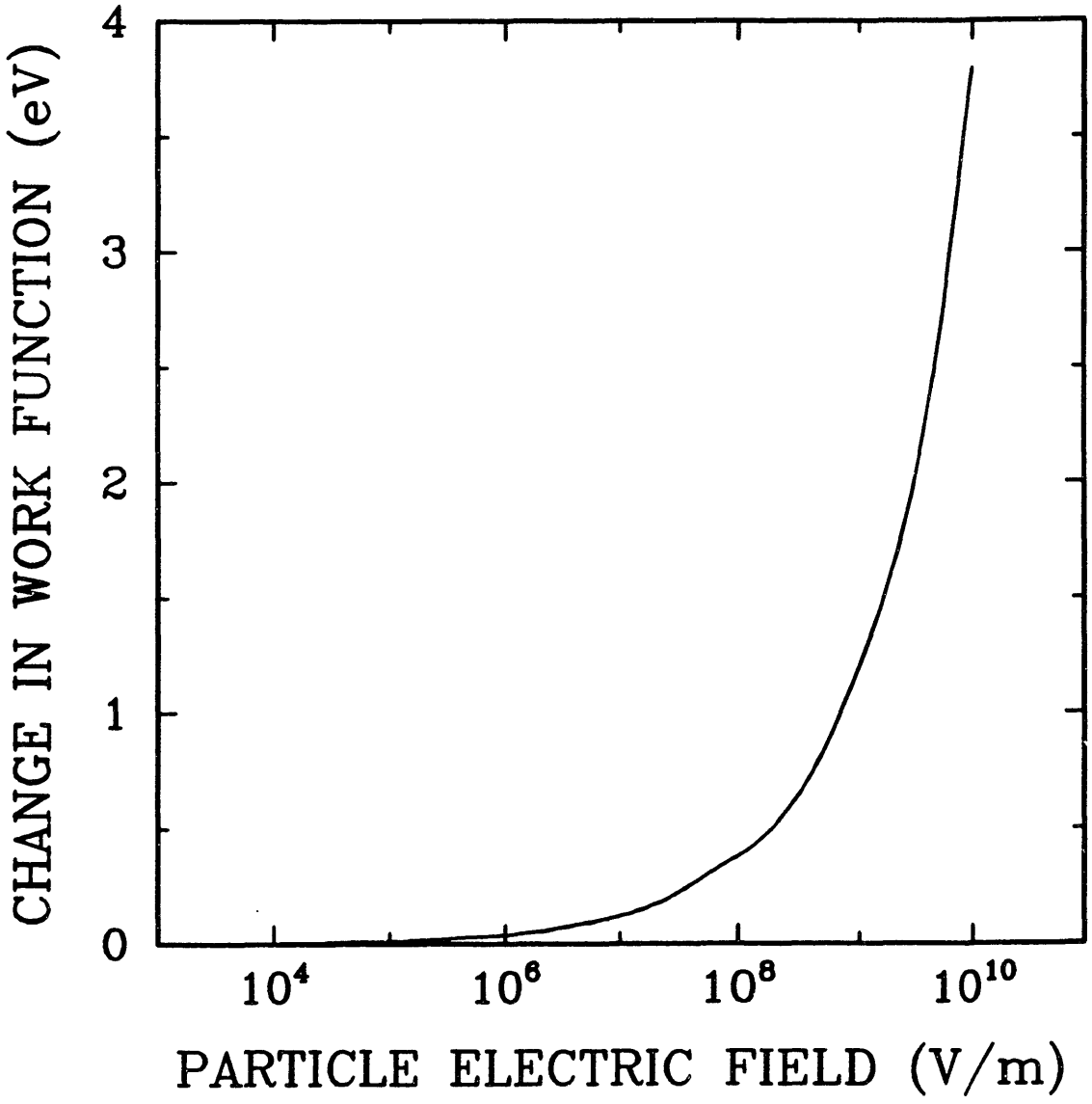

Figure 5.3 : Change in solid work function due to Schottky effect versus electric field strength at the solid surface.

always deviate from the ideal case. For example, the metal surface, unless meticulously purified, will contain adsorbed species and will not be clean. Also, most surfaces will contain either microscopic irregularities, due to defects in lattice structure, or macroscopic irregularities. Finally, the metal surface may not be in a vacuum. All of these nonidealities present in a real system can be modeled by changing the two variables of equation 5.3, A and ϕ.

Jenkins [65] proposes two factors which may change the Richardson coefficient, A, from its theoretical value of 120. One is the possible reflections of electrons at the surface barrier. A second possible explanation is that ϕ has a temperature dependence that can be described by:

$$\phi = \phi_0 + \alpha T \tag{5.4}$$

where ϕ_0 = the work function at some reference temperature, and α = the thermal expansion coefficient. Therefore, if both of these factors are present:

$$A = 120(1-r)\exp(-\alpha/k) \tag{5.5}$$

where r = the fraction of electrons reflected back at the surface.

The nonidealities previously stated, surface contamination, surface irregularities, and nonvacuum conditions, all can be described by changes in the work function, ϕ. Jenkins [65] states that adsorbed layers of atoms either neutral or ionized "can greatly modify the potential barrier, since it generally results in a double layer of charges. A monatomic layer of 10^{14} atoms/cm^2 can lower the work function by two or three eV." Jenkins [65] also describes the emission of ions by thermal exci-

tation or by the influence of a high electric field. Their work functions are greater, however, than those of electrons by several electron volts. In the case of evaporation of contaminated species, the number of ions to atoms can be derived from the Langmuir-Saha equation:

$$\nu_i/\nu_a = \gamma \exp[-(I-\phi)/kT] \qquad (5.6)$$

where ν_i/ν_a = ratio of number ions to number of atoms evaporated per second.

γ = statistical weight ratio.

I = ionization energy of the atom evaporated.

ϕ = work function of the surface.

Jenkins [65] also states that many metals which have alkali metal impurities emit positive ions at temperature below 1000 C. As an example, Na^+, K^+, and Ca^+ are emitted from platinum. The salts of the alkali metals have been found to emit the positive alkali ions at temperatures as low as 400 C.

Loeb [70] discusses the role of the surface irregularities in the lowering of the work function. In studying vacuum sparks from a wire he noticed a disagreement in the experimental electric field necessary for sparking (10^6 V/m) and the theoretical value ($>10^8$ V/m) predicted from the wire temperature and work function. After working with the same wire for a long period of time (many sparks), the surface became polished and the experimental electric field necessary for sparking increased 100 times. The smoothing of the surface irregularities was concluded to be responsible for the increase in electric field required for sparking. In a separate experiment [70] with a tungsten wire (ϕ = 4.5 eV), a detectable current was obtained at 10^5 V/cm instead of the 2 X 10^7 to 3 X 10^7 V/cm predicted from

theory. Again the discrepancy was explained by the existence of surface irregularities. Schottky modeled the electric field surrounding an irregularity by:

$$X = \beta X_m \tag{5.7}$$

where X = microscopic or point electric field around irregularity (V/m).

β = correction factor.

X_m = macroscopically imposed electric field (V/m).

Values of β as high as 200 have been reported [70]. Lawton and Weinberg [67] have described the same effect. It can be concluded that surface irregularities seem to act in a way as to magnify the electric field found on charged particles, and this in turn can be thought of as decreasing the particle work function.

Finally the effect of the surrounding gas is described by Jenkins [65] as a "poisoning" effect. Electronegative gases such as O_2, CO_2, and H_2O can adsorb on the surface and result in a depression or "poisoning" of emission. This can also be thought of as an increase in work function. The role of adsorption of electropositive materials can be thought to work in the reverse manner; thereby, lowering the work function [67].

Direct experimental work on electrical discharge from isolated charged particles has not been found in the literature.

5.4 Proposal of modified Richardson-Dushman equation.

Taking into consideration that the particle work

function and particle temperature are of primary importance in describing charge loss, and that electric field strength, adsorbed species, and surface irregularities are of secondary importance and act to lower the particle work function, a modified Richardson-Dushman equation is proposed and can be written:

$$I = AT^2 \exp[(-\phi_0 + \xi + \Phi)/(kT)] \qquad (5.8)$$

Where:

$\xi = [e\beta E/(4\pi\epsilon_0)]^{0.5}$
= the lowerering of the work function due to the electric field and the enhancement of the electric field by surface irregularities (eV).

Φ = the lowering of the work function due to surface contamination (eV).

$A = 120(1-r)\exp[-\alpha/k]$ = the Richardson constant (amps/cm^2 K^2).

r = fraction of ions or electrons reflected back at the surface (dimensionless).

T = particle temperature (K).

ϕ_0 = work function at some reference temperature (eV).

k = Boltzmann's constant = 8.63 x 10^{-5} eV/molecule K.

α = thermal expansion coefficient of solid (eV/K).

e = elementary charge = 1.6 x 10^{-19} coul.

β = correction factor due to surface irregularities (dimensionless).

E = electric field at the particle surface (V/m).

Work functions of different materials are listed in Table 5.1.

5.5 The electric field strength experienced by a levitated

particle.

The total electric field at the particle surface, E_{total}, is a combination of the electric fields produced by 1) the DC endcap electrodes, E_{DC}, 2) the AC ring electrode, E_{AC}, and 3) the excess surface charge, E_s. E_{DC} can be written:

$$E_{DC} = CV/z_0 \tag{5.9}$$

where: C = the EDB chamber constant = 0.4.
V = the DC voltage between the endcap electrodes (volts).
z_0 = the characteristic length of the EDB = 0.004 m.

E_{AC} can be written:

$$E_{AC} = (V_{AC}L/z_0^2)\cos(\Omega t) \tag{5.10}$$

where: V_{AC} = the amplitude of the AC voltage applied to the ring electrode (volts).
L = distance of the particle surface from the chamber center (m).
Ω = oscillating frequency of the AC field (Hz).
t = time (sec).

We are concerned with the maximum electric field the particle is experiencing, therefore, cos(Ωt) will be taken as equal to 1.0 and equation 5.10 can be rewritten:

$$E_{AC} = V_{AC}L/z_0^2 \tag{5.11}$$

The minimum L would be the radius of the particle. L will usually be larger, however, due to movement of the particle

during heating.

E_s can be written:

$$E_s = (1/4\pi\epsilon_0 B)(q/R^2) \tag{5.12}$$

where: $B = 1 + 2[(\epsilon_r-1)/(\epsilon_r+1)]$.
ϵ_r = relative permittivity of particle.
q = total excess charge on particle (coul).
R = particle radius (m).

A typical value of ϵ_r is 2 [71], therefore, a typical value of B is 1.67.

If equation 3.3 is rearranged, the excess charge may be written:

$$q = mgz_0/(CV) \tag{5.13}$$

where: m = particle mass (kg).

We also know that:

$$m = (4/3)\pi R^3 \rho_p \tag{5.14}$$

where: ρ_p = particle density (kg/m^3).

Combining equations 5.12, 5.13, and 5.14:

$$E_s = gz_0\rho_p R/(3\epsilon_0 BCV) \tag{5.15}$$

The total electric field experienced at the particle surface can be written:

$$E_{total} = E_{DC} + E_{AC} + E_s \tag{5.16}$$

Figure 5.4 is a plot of E_{DC}, E_{AC}, E_s, and E_{total} versus the DC voltage between the endcap electrodes. Figure 5.4 was generated by using equations 5.9, 5.11, 5.15, and 5.16 along with the following variables:

$C = 0.4.$

$z_0 = 0.004$ m.

$V_{AC} = 1800$ volts.

$L = 3R.$

$\rho_p = 1000$ kg/m^3.

$R = 100$ μm.

$B = 1.67.$

In this particular case, the electric field produced by the excess surface charge dominates the total electric field at the particle surface. Also, the total electric field at the particle surface decreases with increasing DC voltage. This is due to the fact that as the DC voltage increases, the overall charge required to suspend the particle decreases.

Figure 5.5 is a plot of E_{DC}, E_{AC}, E_s, and E_{total} versus particle radius. In this plot, particle radius is allowed to vary and the DC balancing voltage is held constant at 250 volts. All of the other variables are the same as those used in Figure 5.4. Except for very small particles ($R<10$ μm), the electric field produced by the excess surface charge again dominates the total electric field at the particle surface. The total electric field increases with increasing particle size. This is due mainly to the fact that as particle size increases, more charge is required on the particle to suspend it. The total electric field is increased almost an order of magnitude when particle radius is increased from 10 μm to 100 μm.

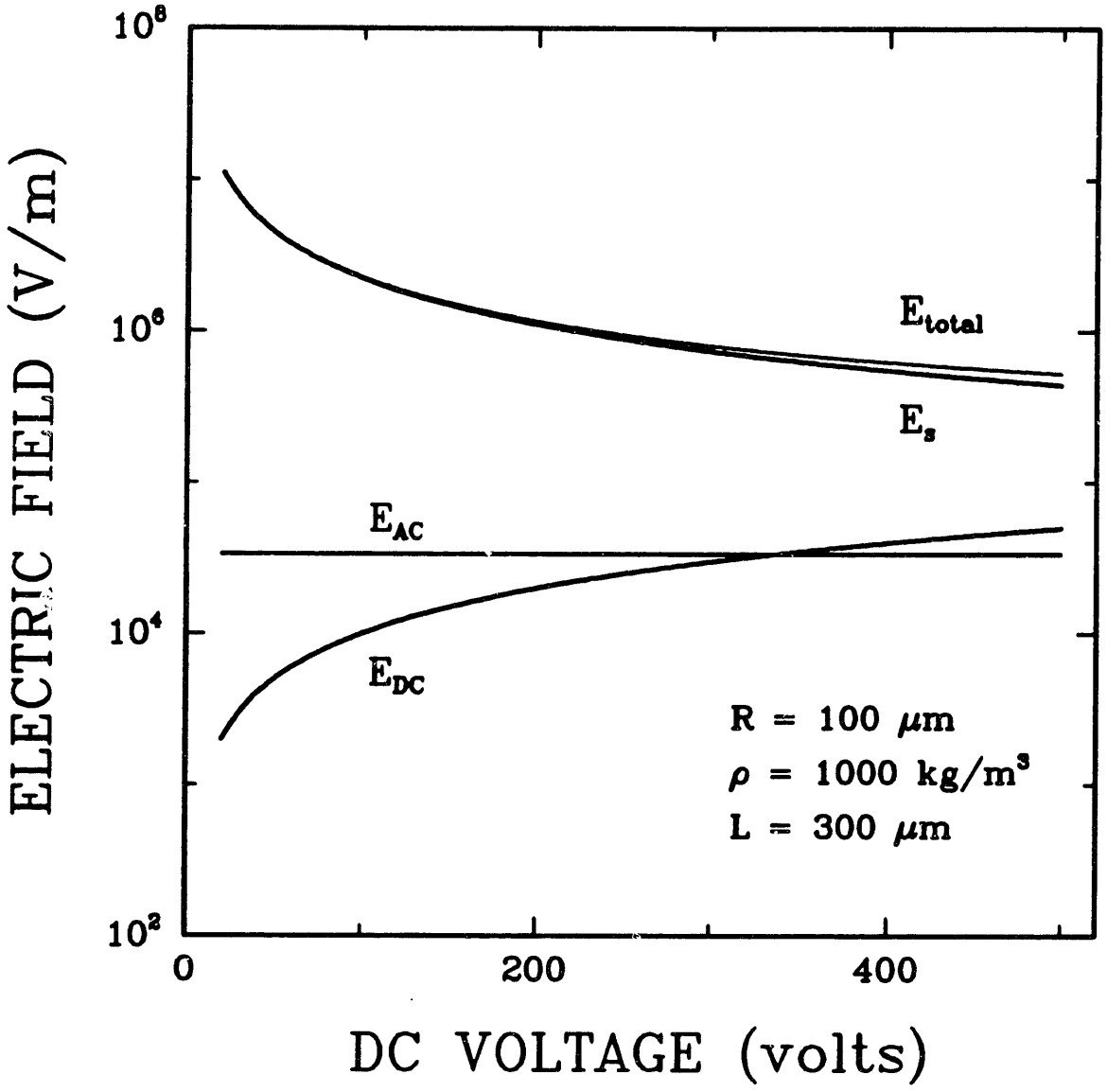

Figure 5.4 : E_{DC}, E_{AC}, E_s, E_{total} versus DC voltage for a particle levitated in the EDB. Particle radius = 100 μm, particle density = 1000 kg/m^3, and particle location = 300 μm from the chamber center.

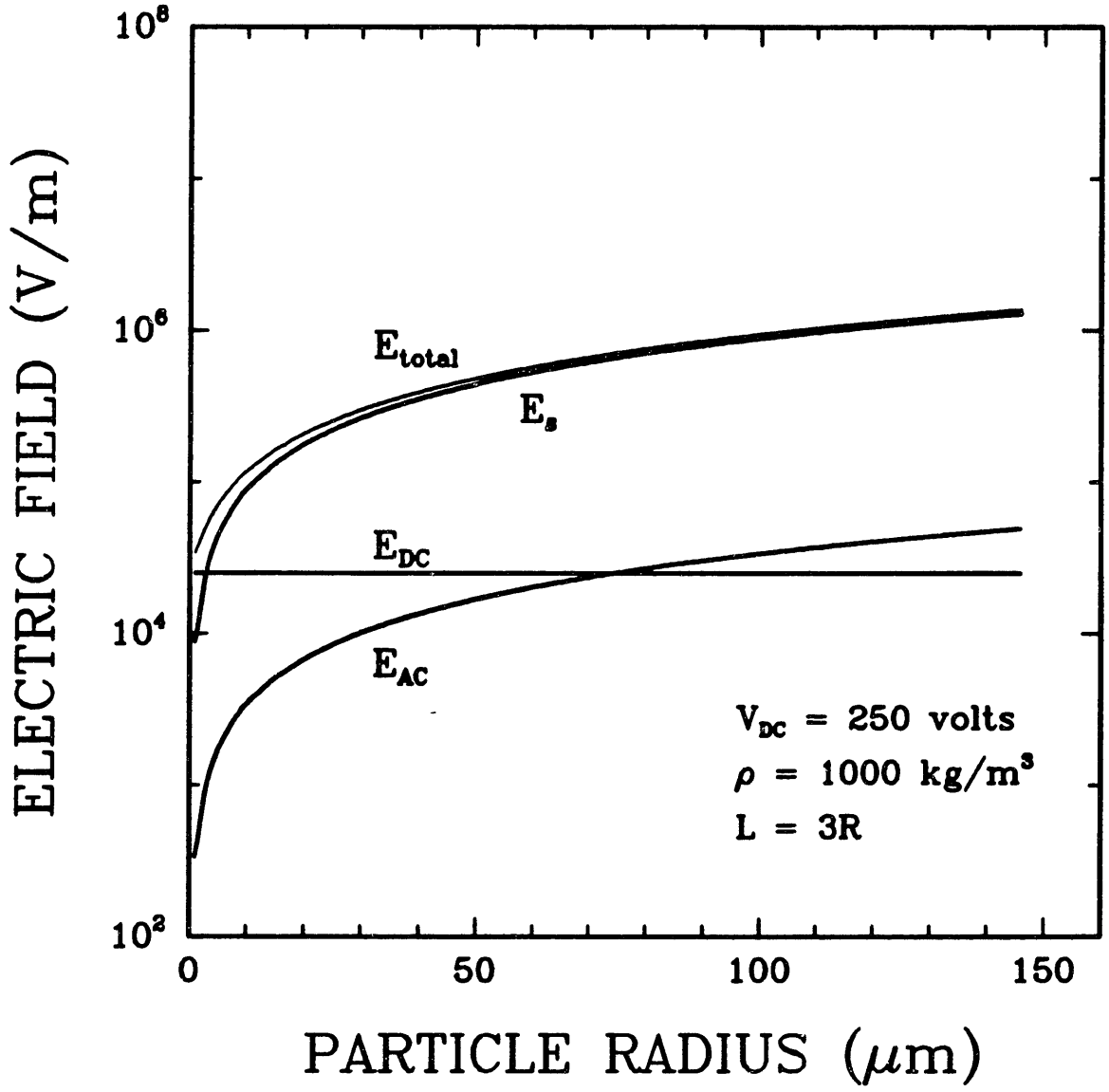

Figure 5.5 : E_{DC}, E_{AC}, E_s, E_{total} versus particle radius for a particle levitated in the EDB. Particle density = 1000 kg/m^3, DC voltage = 250 V, and particle location = three radii from the chamber center.

From Figures 5.4 and 5.5 it can be concluded that in general 1) the electric field produced by the excess surface charge dominates the total electric field at the particle surface, and that 2) the total electric field at the particle surface can be minimized by minimizing the total amount of excess charge on the levitated particle. The values of the electric fields presented in Figures 5.4 and 5.5 would (according to Figure 5.3) have little effect on the apparent work function ot the levitated particle. However, if the electric fields were enhanced 200 times due to surface irregularities as proposed by Loeb [70] and Lawton and Weinberg [67], the electric fields presented in Figures 5.4 and 5.5 could lower the apparent work function of a levitated particle by a few electron volts.

Figures 5.6 and 5.7 are plots of the total electric field at the particle surface versus particle radius for DC balancing voltages of 50, 250, and 450 volts. Particle density is 500 kg/m^3 for Figure 5.6 and 2500 kg/m^3 for Figure 5.7. All of the other variables are the same as those used in Figure 5.4. From these two plots, it can be seen again that the total electric field at the particle surface increases with increasing particle radius and increases with decreasing DC balancing voltage. It can also be concluded that the total electric field at the particle surface increases with increasing particle density.

Figure 5.8 is a plot of the electric field experienced by a levitated particle in the EDB versus the particle radius for two cases, an upper and a lower bound. The electric field surrounding the particle is independent of the type of material levitated (e.g. conductor, insulator, etc.). The total electric field was calculated using equations 5.9, 5.11, 5.15, and 5.16 along with the following variables for

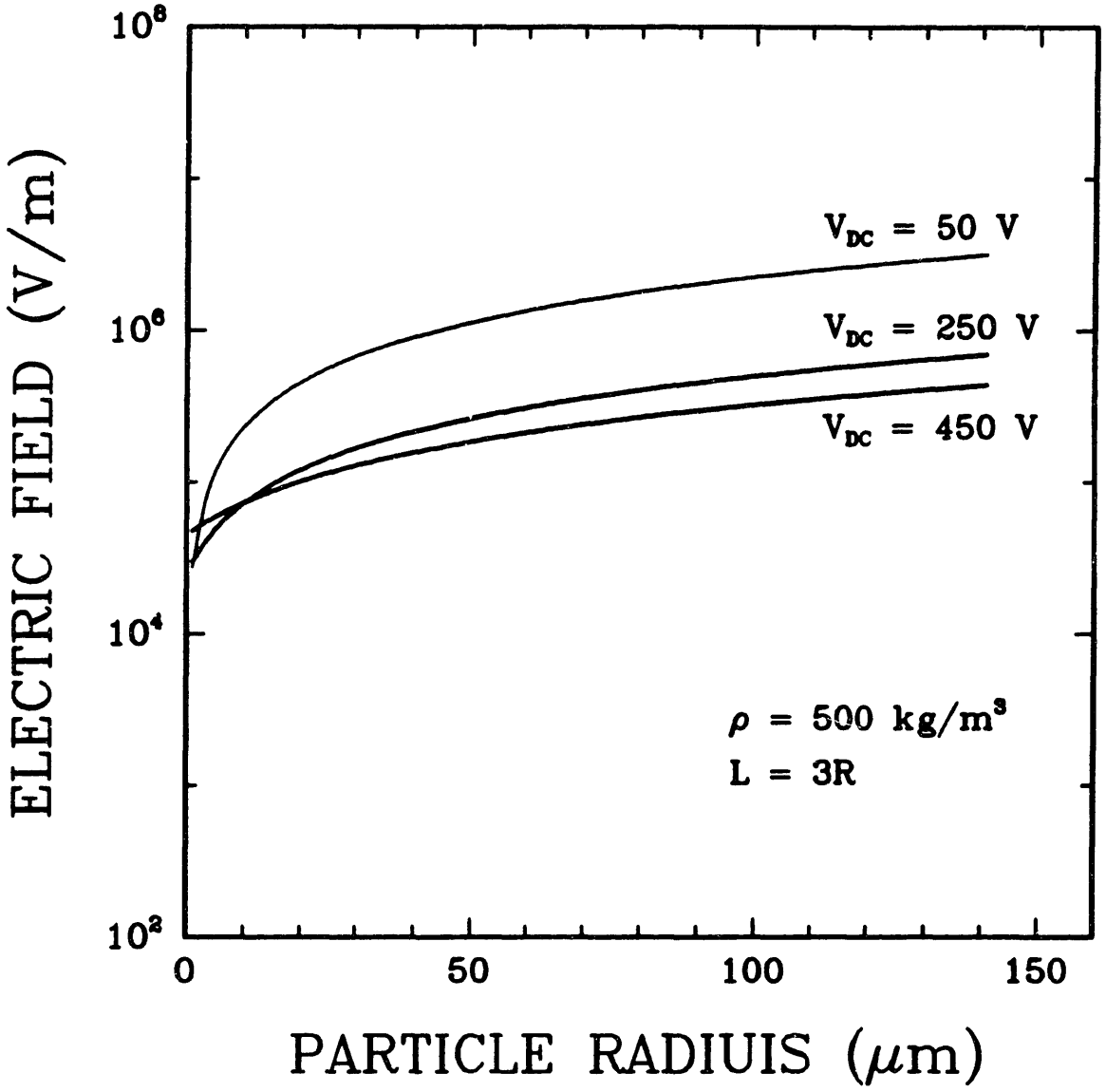

Figure 5.6 : E_{total} versus particle radius for a particle levitated in the EDB. Particle density = 500 kg/m^3, particle location = three radii from the chamber center, and DC voltage = 50, 250, and 450 V.

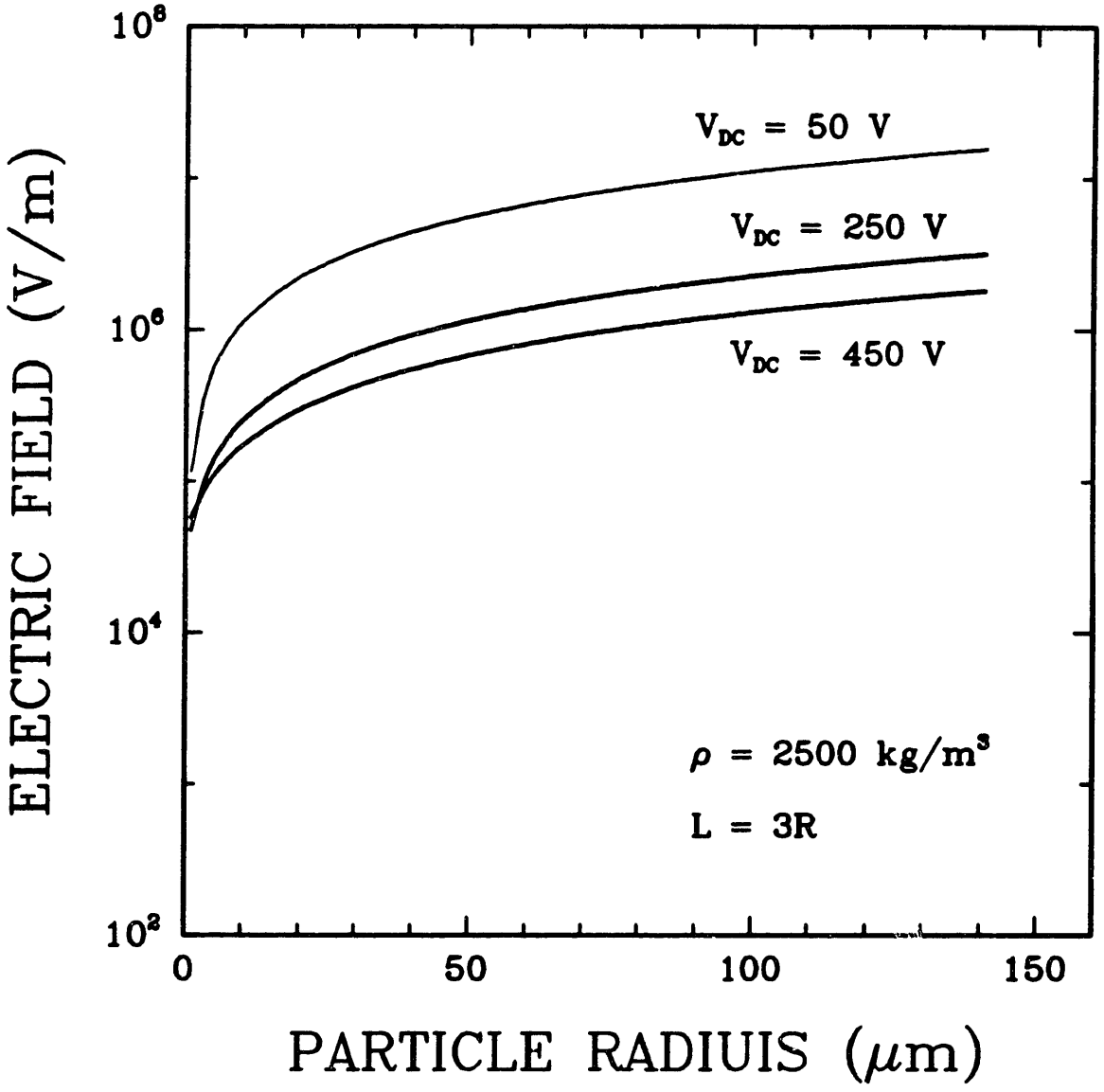

Figure 5.7 : E_{total} versus particle radius for a particle levitated in the EDB. Particle density = 2500 kg/m^3, particle location = three radii from chamber center, and DC voltages = 50, 250, and 450 V.

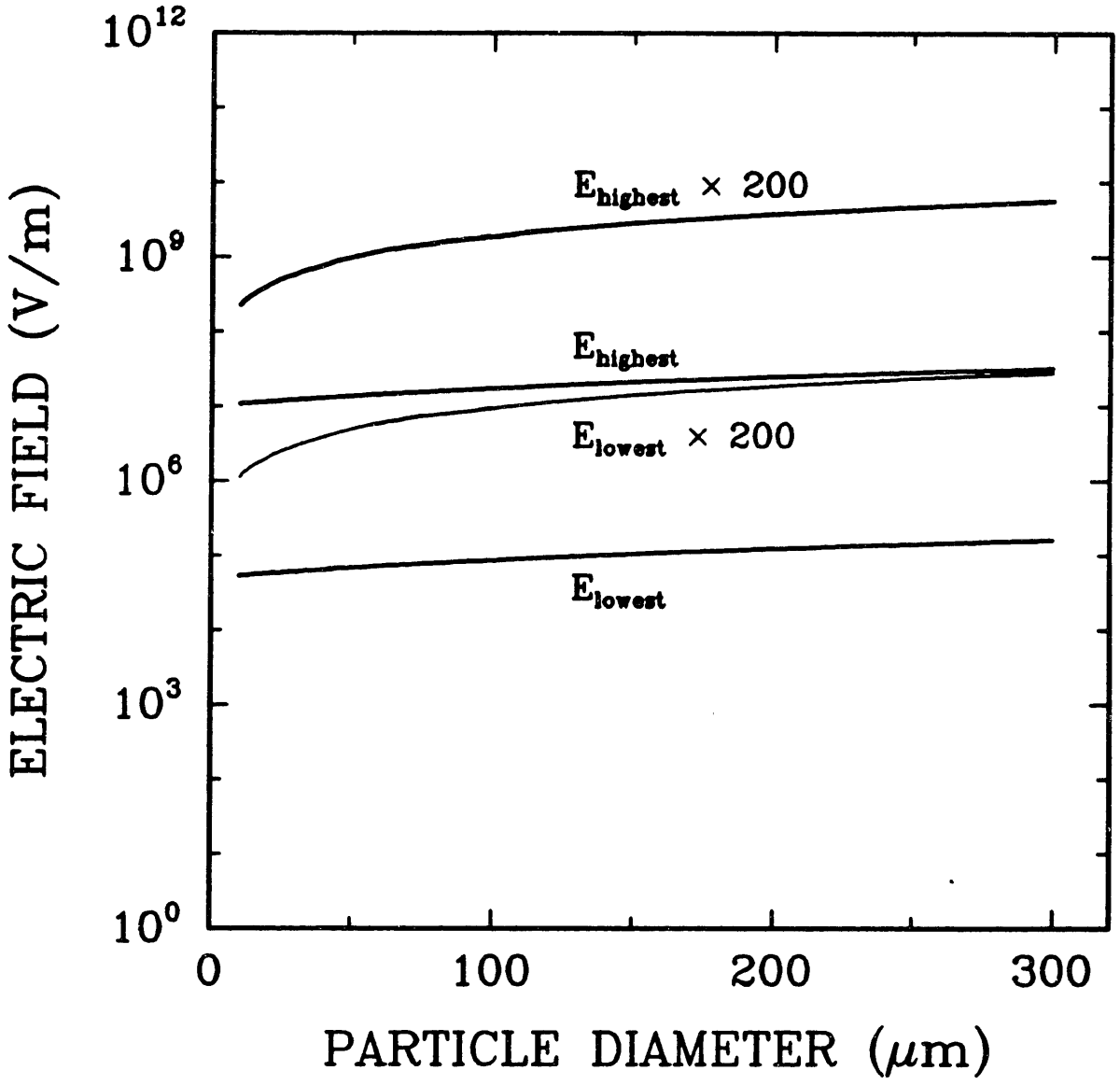

Figure 5.8 : Upper and lower bounds of total electric field strength experienced by a levitated particle in the EDB (with and without correction for surface irregularities) versus particle diameter.

the lower bound:

$C = 0.4.$

$z_0 = 0.004$ m.

$V_{AC} = 500$ volts.

$L = R.$

$\rho_p = 250$ kg/m^3.

$V_{DC} = 500$ volts.

$B = 2.5.$

The lower bound represents probably the smallest electric field that a particle would experience if levitated in our EDB.

The following are the variables used for the upper bound:

$C = 0.4.$

$z_0 = 0.004$ m.

$V_{AC} = 3000$ volts.

$L = 1000$ μm.

$\rho_p = 5000$ kg/m^3.

$V_{DC} = 100$ volts.

$B = 1.0.$

The upper bound represents probably the largest electric field that a particle would experience if levitated in our EDB.

The lower bound predicts an electric field strength of approximately 10^5 V/m, and the upper bound predicts an electric field strength of approximately 5×10^7 V/m. Also depicted in Figure 5.8 are the upper and lower limits multiplied by 200 to take into account possible surface irregularities. The range of electric field strengths is

now 5×10^7 to 10^9 V/m. According to Figure 5.3, an electric field strength of this magnitude could considerably lower the work function of a levitated particle.

An example of the potential lowering of the work function due to the electric field experienced by a levitated particle is shown in Figure 5.9. The change in work function is plotted versus particle diameter for two different materials, Si and "Spherocarb". Equations 5.9, 5.11, 5.15, and 5.16 are used along with the Schottky equation:

$$\Delta\phi = [e\beta E_{total}/(4\pi\epsilon_0)]^{0.5} \qquad (5.17)$$

and the following values for the variables:

$C = 0.4.$
$z_0 = 0.004$ m.
$V_{AC} = 1800$ V.
$L = 300$ μm.
$V_{DC} = 200$ V.
$B = 1.0$
$\beta = 200.$

The density of Si was taken to be 2.33 g/cm^3 and the density of "Spherocarb" was taken to be 0.65 g/cm^3. It can be seen from this plot that the electric fields experienced by levitated particles can be sufficient to lower the particle work function by as much as 1.4 eV for Si and 0.7 eV for "Spherocarb". The electric field experienced by a levitated particle, and hence the change in particle work function can be minimized by decreasing the number of excess charges on the particle by: 1) decreasing particle size, 2) decreasing particle density, and 3) increasing the DC voltage required for balancing.

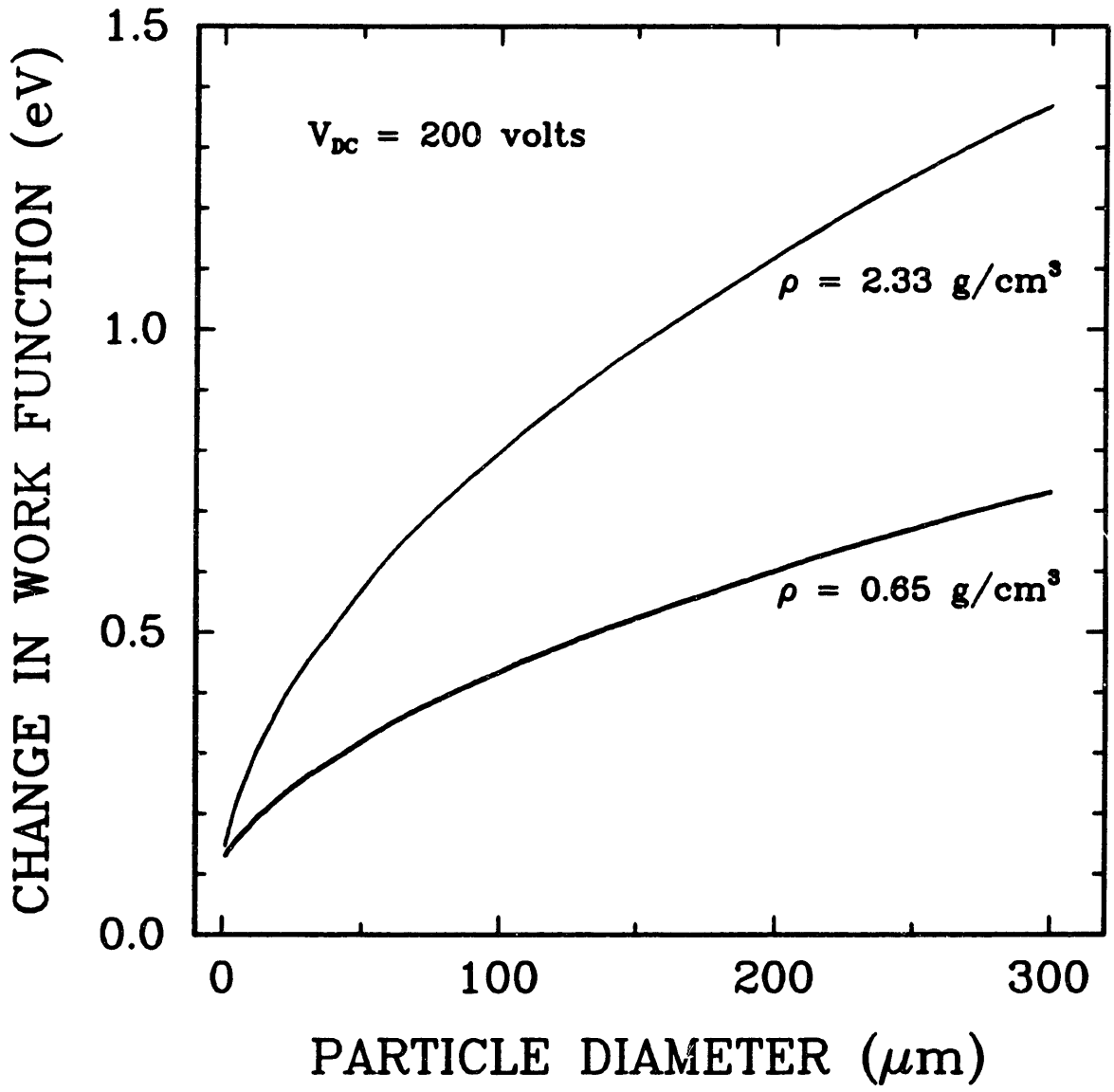

Figure 5.9 : Change in work function due to the electric field versus particle diameter for typical Si and "Spherocarb" particles levitated in the EDB.

5.6 Experimental results.

From the modified Richardson-Dushman equation proposed in section 5.4, charge loss is predicted to be a strong function of particle temperature and work function and a lesser function of electric field strength, surface contamination, and surface irregularities. Two sets of experimental measurements were performed. The first set of experiments examines the effect of particle temperature and particle work function on charge loss from heated particles levitated in the EDTGA. The second set of experiments looks at the effect of temperature, surface contamination, and electric field strength on charge loss from a heated metal thermocouple.

5.6.1 Charge loss from heated particles.

In this section, charge loss experiments performed on particles levitated in the EDB are discussed. The amount of energy being sent to the suspended particle by the CO_2 laser can be changed by adjusting one of three variables: 1) overall laser power (4-20 W), 2) laser beam diameter, and 3) laser pulse length. Particle size, shape, and absorptivity are important in determining how much of the energy sent to the suspended particle is actually absorbed.

Since excess charge on a levitated particle is inversely proportional to the DC voltage required for stable balancing, charge loss can be measured by an increase in the DC voltage required for balancing. Figures 5.10 and 5.11 are examples of typical charge loss experiments. Figure 5.10 is a plot of the balancing

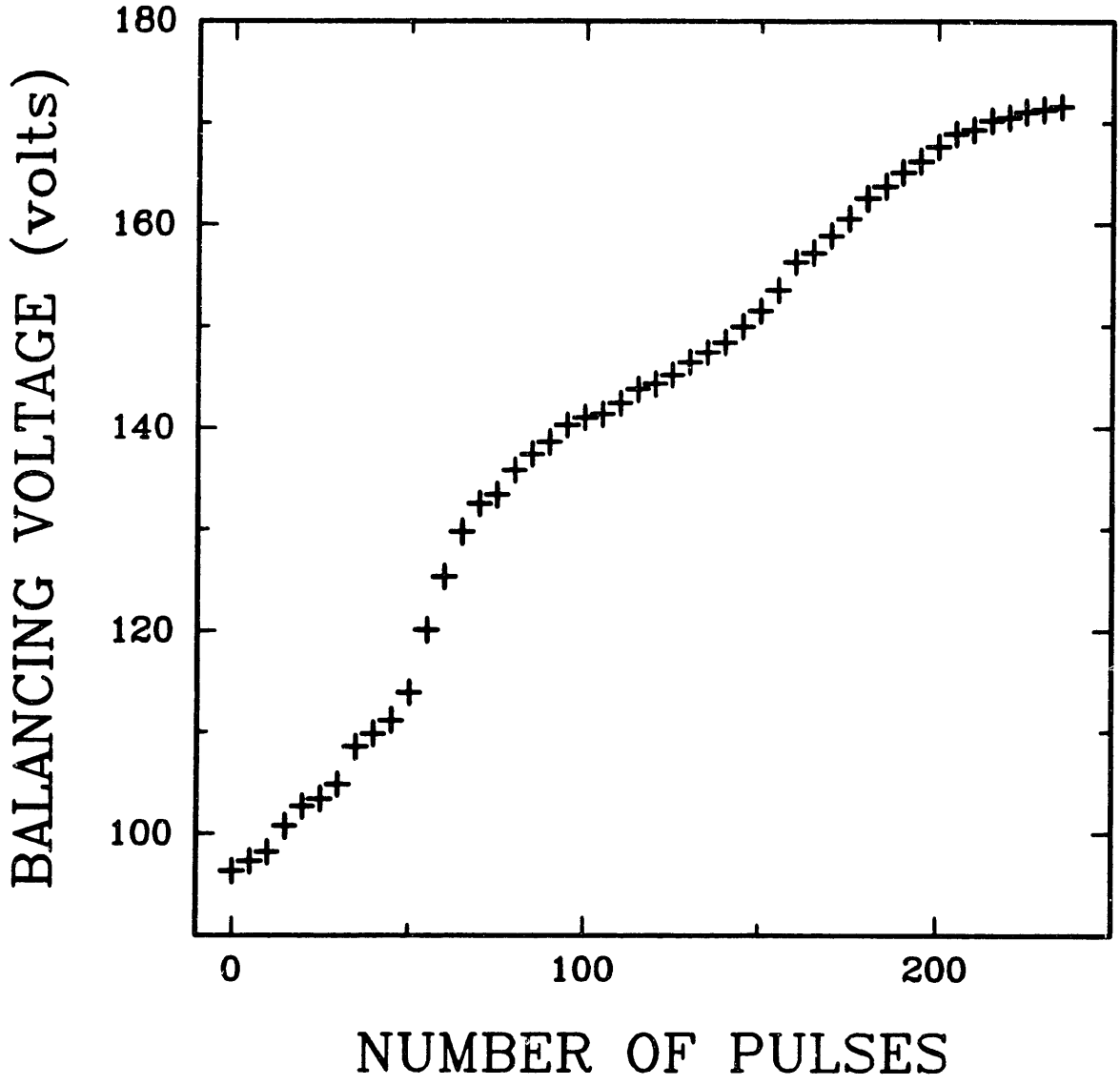

Figure 5.10 : Balancing DC voltage versus number of 2.8 msec CO_2 laser pulses for a negatively charged 162 μm diameter "Spherocarb" particle.

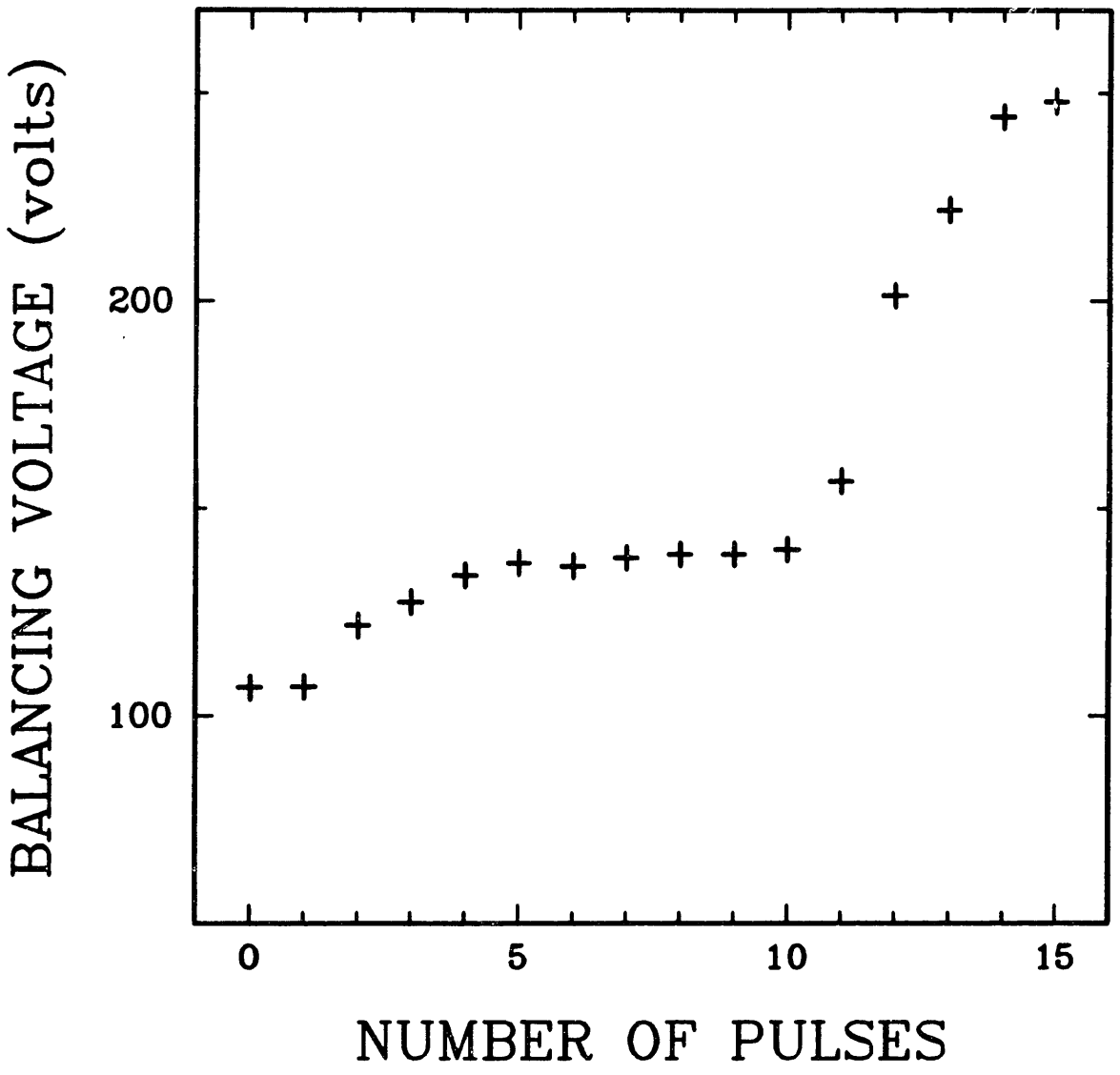

Figure 5.11 : Balancing DC voltage versus number of 2.8 msec CO_2 laser pulses for a CaO_3 particle.

voltage of a 162 μm diameter "Spherocarb" particle versus number of CO_2 laser pulses. This particular "Spherocarb" particle was negatively charged and levitated in a nitrogen environment. The overall laser power was 18 W, the laser beam diameter was 330 μm, and the laser pulse length was 2.8 msec. The increase in balancing voltage shown in Figure 5.10 indicates charge loss from the particle. Since overall charge is decreasing, a larger electric field is required for particle balancing. The increase in balancing voltage per CO_2 laser pulse is not constant. This is most likely due to fluctuations in the power of the CO_2 laser pulse.

Figure 5.11 is a similar plot of balancing voltage versus number of 2.8 msec laser pulses for a $CaCO_3$ particle. The increases in balancing voltage are even more random in this case. This is probably due to the plate-like shape of the $CaCO_3$ particle. Depending on how the plate-like particle was oriented in the CO_2 laser beam, different amounts of energy could be absorbed.

All materials heated in the EDB to date have experienced charge loss at and above certain CO_2 laser intensities. According to Spjut's [7] single particle heat balance:

$$T_{eq} - T_{\infty} = IQ_{abs}d/(8k) \qquad (5.18)$$

where: T_{eq} = equilibrium particle temperature (K).
T_{∞} = ambient temperature (K).
I = CO_2 laser intensity (W/m^2).
Q_{abs} = absorption efficiency (dimensionless).
d = particle diameter (m).
k = gas thermal conductivity (W/m K).

Therefore, equilibrium temperature should be directly proportional to the CO_2 laser intensity.

Figure 5.12 is a plot of the change in balancing voltage due to a 2.8 msec CO_2 laser pulse versus the CO_2 laser intensity for seven different "Spherocarb" particles. Four of the experiments were performed on negatively charged "Spherocarb" particles and three of the experiments were performed on positively charged "Spherocarb" particles. No difference in charge loss was detected between negatively and positively charged particles. Below a CO_2 laser intensity of 25 MW/m^2, no charge loss is detected. Above 80 MW/m^2, catastrophic charge loss always occurs and the particle is lost from the chamber. In this experiment the beam diameter was approximately 350 μm. The step change shape of this plot indicates an intensity threshold, beyond which charge loss is inevitable. Due to the very short laser pulse length, temperature measurement was not possible, however, the fact that a CO_2 laser intensity threshold exists indicates the existance of a temperature threshold.

Figure 5.13 is a plot of CO_2 laser intensity versus the critical CO_2 pulse length for "Spherocarb" particles. The critical pulse length is defined as the shortest CO_2 laser pulse required for charge loss to occur. Particles undergoing CO_2 laser pulse lengths smaller than the critical will not experience any charge loss. The smaller the CO_2 laser intensity, the longer the pulse required before charge loss can occur. Since the pulse lengths being discussed are much shorter than those required for an equilibrium temperature to be reached, the length of the pulse is related to the final temperature the particle experiences. If that temperature is below a certain level, no charge loss occurs. Again we see evidence that a

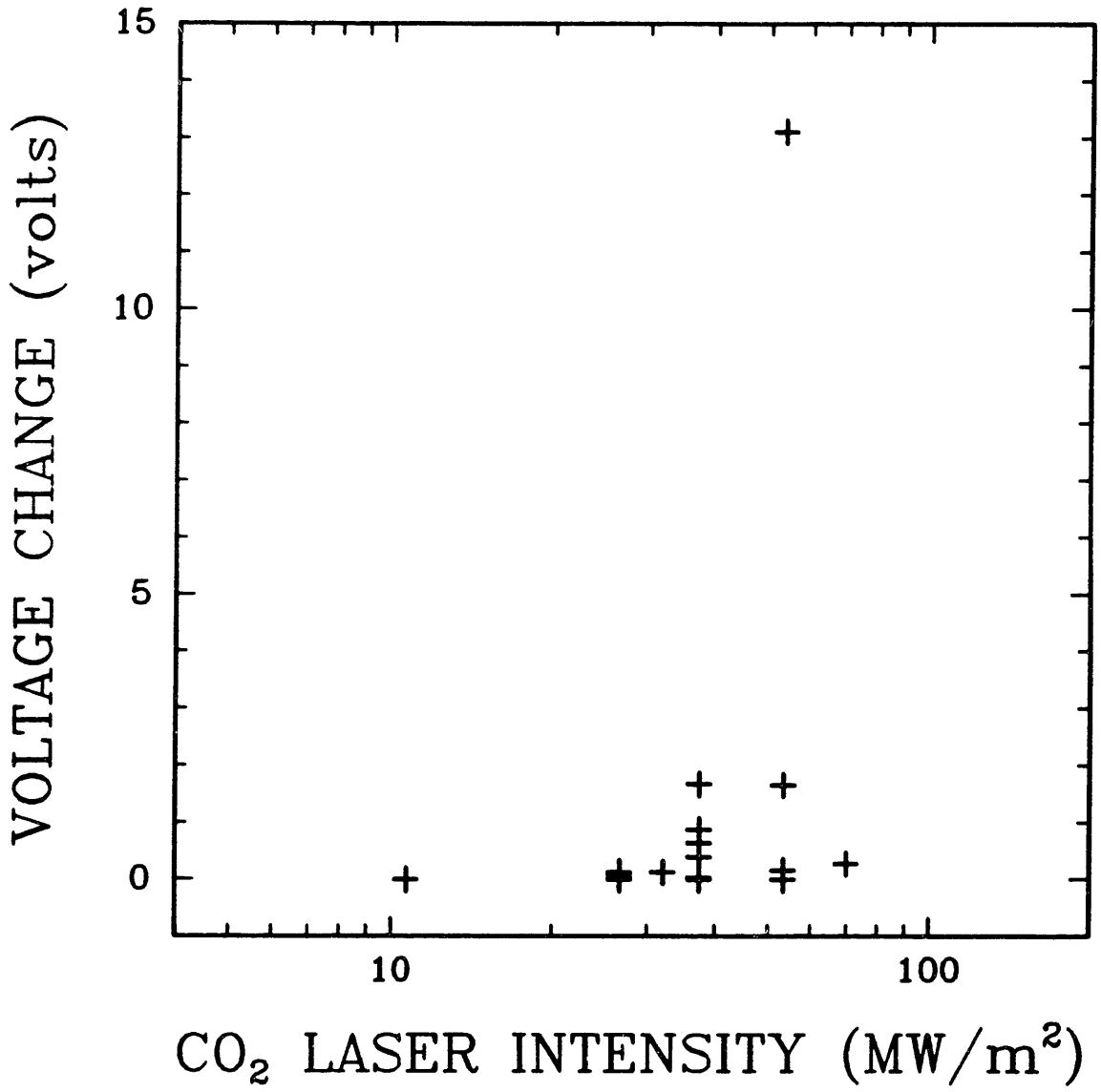

Figure 5.12 : Change in balancing DC voltage due to charge loss versus CO_2 laser intensity for seven different "Spherocarb" particles levitated in the EDB.

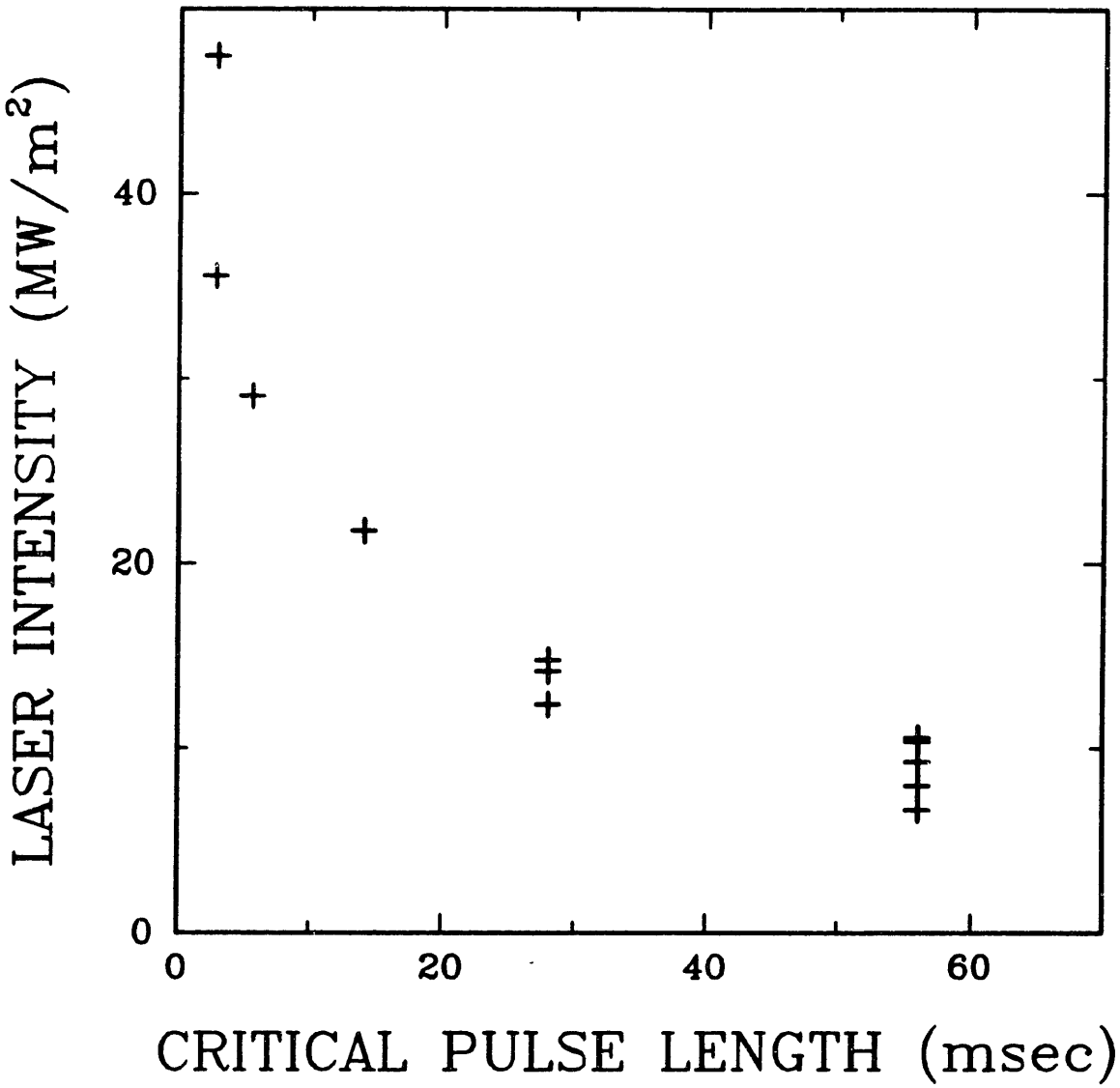

Figure 5.13 : CO_2 laser intensity versus critical pulse length for "Spherocarb" particles levitated in the EDB.

threshold temperature exists for "Spherocarb" particles.

Next we turn our attention to the effect of particle work function on charge loss. Figure 5.14 is a plot of absorbed laser intensity required for charge loss versus particle work function for seven different materials, BaO, CaO, C, SiO_2, KI, KCl, and NaCl. Absorbed CO_2 laser intensity is defined as the product of laser intensity times the particle absorptivity. Absorptivities were taken from Loewenstein et al. [72] and Blackman [73]. It appears that the larger the work function of the particle, the more laser power is required before charge loss occurs. Caution must be exercised when trying to draw conclusions from this plot, however, due to uncertainties in material absorptivities of 10.6 μm radiation and laser intensities.

"Spherocarb" oxidation has been extensively studied in the EDTGA and some of the results are presented in Chapter 6. Of the over 200 uncatalyzed "Spherocarb" oxidations performed, charge loss usually did not occur until a critical temperature of 1200-1300 K was reached. This temperature agrees well with the temperature that would be predicted by the Richardson-Dushman equation for a material, such as carbon, with a work function of approximately 4.7 eV. It is interesting to note that when K was added to the "Spherocarb" particles as a catalyst, charge loss became noticable at a much lower temperature of approxiamately 750 K. Potassium is known to wet the particle surface, therefore, charge loss should be dependent on potassium's work functin instead of carbon. Charge loss from "Spherocarb" particles at lower temperatures due to addition of K is very much consistant with the fact that potassium's work function of 2.3 eV is much lower than carbon's work function of 4.7 eV. Again, 750 K agrees well with the critical temperature for onset of charge loss predicted by the

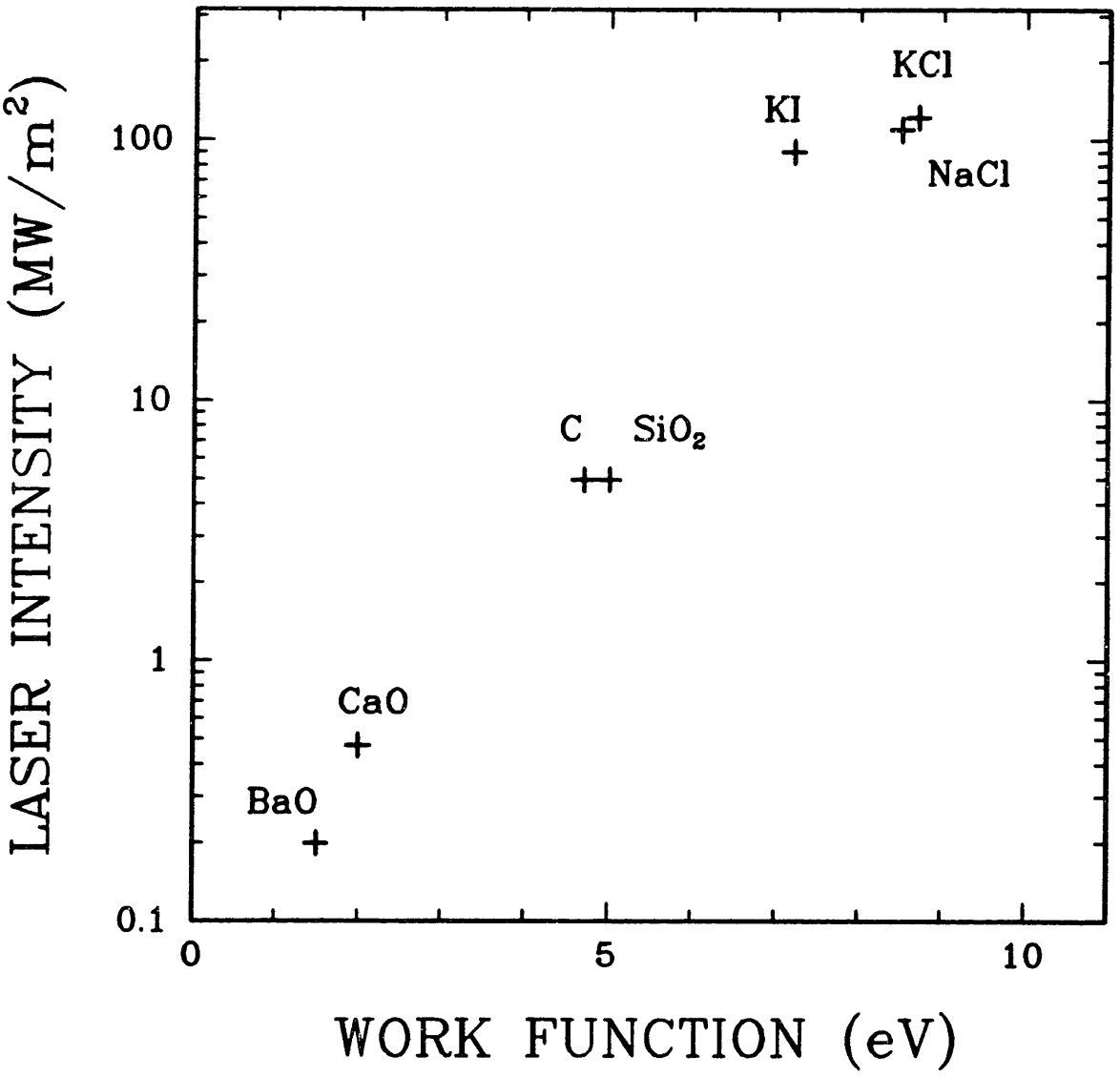

Figure 5.14 : Absorbed CO_2 laser power required for charge loss versus particle work function for seven different materials, BaO, CaO, C, SiO_2, KI, KCl, and NaCl.

Richardson-Dushman equation for K with a work function of 2.3 eV. Another example of the importance of work function on charge loss is the inability (due to charge loss) of $CaCO_3$ to be heated to temperatures above 1173 K in order to form CaO. CaO has a work function of 1.9 eV. The Richardson-Dushman equation would predict charge loss at around 500 K for CaO.

One general observation is that charge loss has been observed to occur very quickly (<100 msec) and sporadically. Also, fragmentation has been observed with $CaCO_3$ and BaO but with no other materials. This implies that fragmentation can be important, but is not the sole mechanism for charge loss.

Evidence has also been presented in this section against thermionic emission of electrons as the only mechanism for charge loss. Even though charge loss does appear to be a function of the particle's temperature and work function or threshhold energy, there is no noticable difference in charge loss from positively charged particles as compared to negatively charged particles. If thermionic emission of electrons was the mechanism for loss of negative charge, it would seem reasonable that the mechanism for loss of positive charge would yield different results. For example, when photoemission is the mechanism for charge loss, as is the case when an ultraviolet light source is incident on the levitated particle, negatively charged particles lose charge much more readily than do positively charged particles. This is shown in Figure 5.15 in a plot of relative voltage of both a negatively and a positively charged "Spherocarb" versus the time exposed to an ultraviolet light source. Relative voltage is defined as the ratio of the particle balancing voltage to the initial particle balancing voltage.

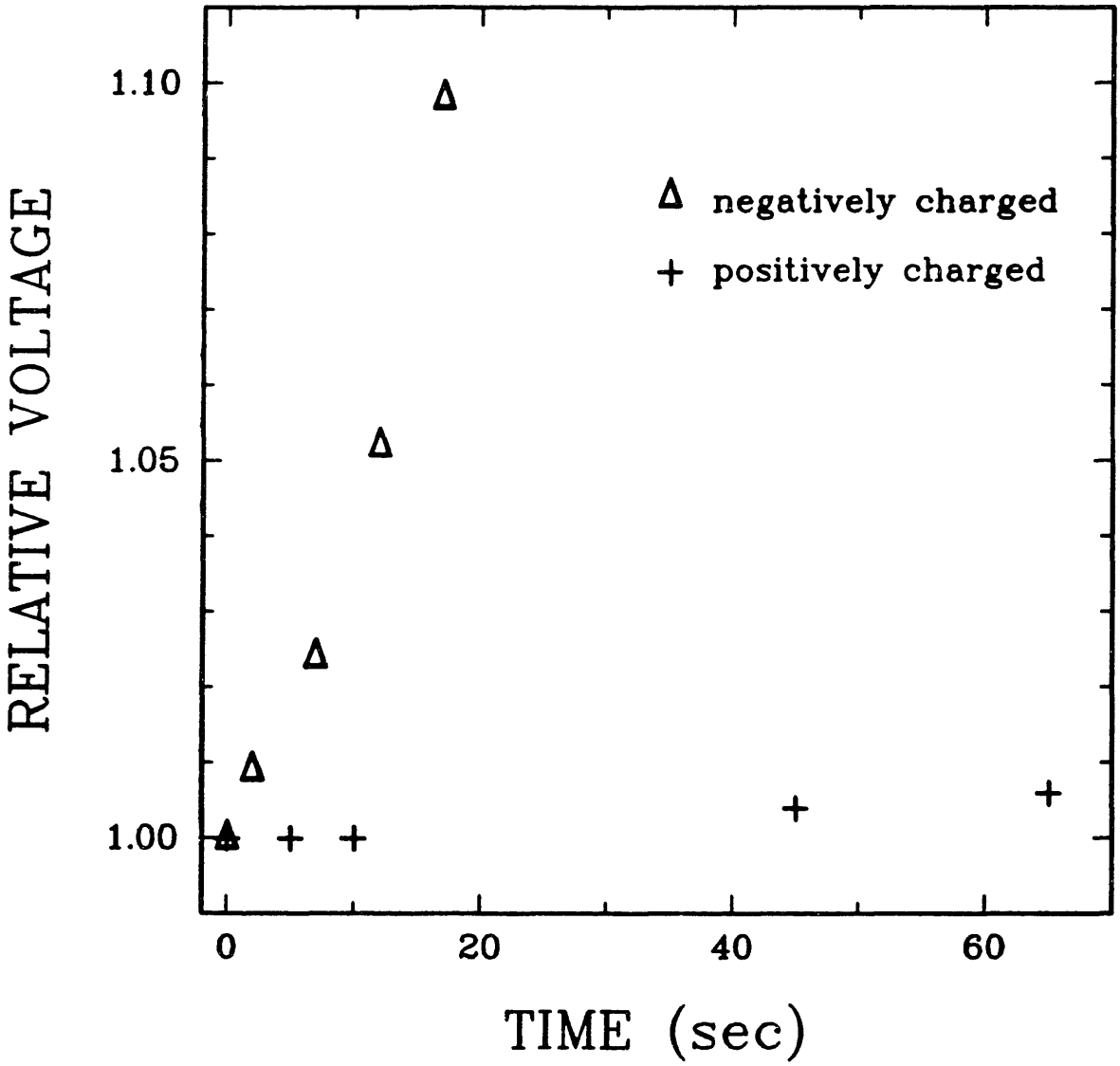

Figure 5.15 : Ratio of voltage to initial voltage versus time exposed to an ultraviolet light source for positively and negatively charged "Spherocarbs".

Preliminary experimental results on levitated particles, therefore, indicate that the mechanism for charge loss is not thermionic emission of electrons, but perhaps the thermionic emission or desorption of ions, which still, however, appears to be related to work function (Figure 5.14).

5.6.2 Charge loss from heated metal wires.

The advantage of studying charge loss from particles levitated in the EDB is that general trends may easily be established. For example, charge loss increases with increasing CO_2 laser intensity, and charge loss decreases with increasing particle work function. The disadvantage of studying charge loss from particles suspended in the EDB is that systematically studying the effects of independent parameters is difficult.

The literature survey on thermionic emission theory presented in section 5.3 indicates that emission depends on the particle's work function and temperature. However, the work function is a function of, not only the material, but of the adsorbed species on the particle and the electric field to which the particle is exposed. The adsorbed species are a function of the material's past history and current gas surroundings. Also, the electric field is not only a strong function of the macroscopically applied electric field, but also the surface irregularites which potentially could create microscopic electric fields 200 times greater than the macroscopic field. Because surface contamination and surface irregularities are difficult to measure, it is difficult to determine the quantitative effect of these two variables on charge loss from a single charged particle. Since each experiment in the EDB that involves charge loss, and subsequent loss of the particle,

each experiment would involve different particles. Particle-to-particle variations in both surface contamination and surface irregularities make a systematic, quantitative study of charge loss from charged particles heated in the EDB very difficult. Particle heating would also present difficulties in getting systematic results. It would be difficult to heat the suspended particle to the same temperature each time due to CO_2 laser fluctuations, particle variations, and particle movements. Therefore, it has been proposed to further study charge loss in a simplified system which resembles the EDB as closely as possible.

5.6.2.1 Apparatus.

The simplified experimental system is designed to measure the charge transfer or current from an isolated metal surface inside the EDB to the surrounding electrode walls. The EDB used in these experiments had the same configuration and dimensions as the one described in Chapter 2. The isolated metal surface was either a single metal wire or a thermocouple which was inserted into the center of the EDB through a hole in the top electrode and insulated from the electrodes by a ceramic tube.

Two types of heating systems were utilized, CO_2 laser heating and resistance heating. The first set of experiments were performed by heating a single wire or thermocouple probe with two 3 W CO_2 lasers. The second set of experiments was carried out with a 4 mm length of 0.010" Pt wire which was heated by passing an AC current through it. The Pt was welded on each end to separate 4" lengths of 0.020" Ag wire which were inserted into the ceramic insulating tube. Since the Pt wire had a smaller diameter, it had a greater resistance. This enabled the Pt wire section to be heated to a

geater extent than the Ag wire section.

The electrical system varied depending on the type of heating utilized. With CO_2 laser heating, the electrical system consists of two main circuits, one for thermocouple voltage measurement, and the other for current detection (see Figure 5.16). The system is designed so that the single wire or thermocouple probe is connected to the electrodes only through a common ground. Therefore, current flowing in the system must pass from the probe to the electrodes through the atmosphere. It is this movement of charged species through the atmosphere that is measured in an attempt to shed light on how charges are lost from a charged, isolated particle suspended in the EDB. A DC voltage of up to positive or negative 1000 V is simultaneously supplied to each electrode, forming an electric field around the wire or thermocouple bead which is analagous to the electric field present at the surface of an isolated charged particle. Each thermocouple leg or single wire is connected through switches to both main circuits. A voltmeter is used to monitor thermocouple voltage in one circuit, and an oscilloscope or separate voltmeter monitors current once it has passed through a total outer resistance of 91 kΩ.

With resistance heating, alternating current from a wall outlet is passed through a variac to a 10 A step down transformer with a secondary voltage of 6.3 V (See Figure 5.17). One voltmeter monitors the AC voltage to the Ag wires while another voltmeter monitors current.

5.6.2.2 Experimental procedure.

Although the experiments performed with this apparatus involved a wide range of materials, the procedure

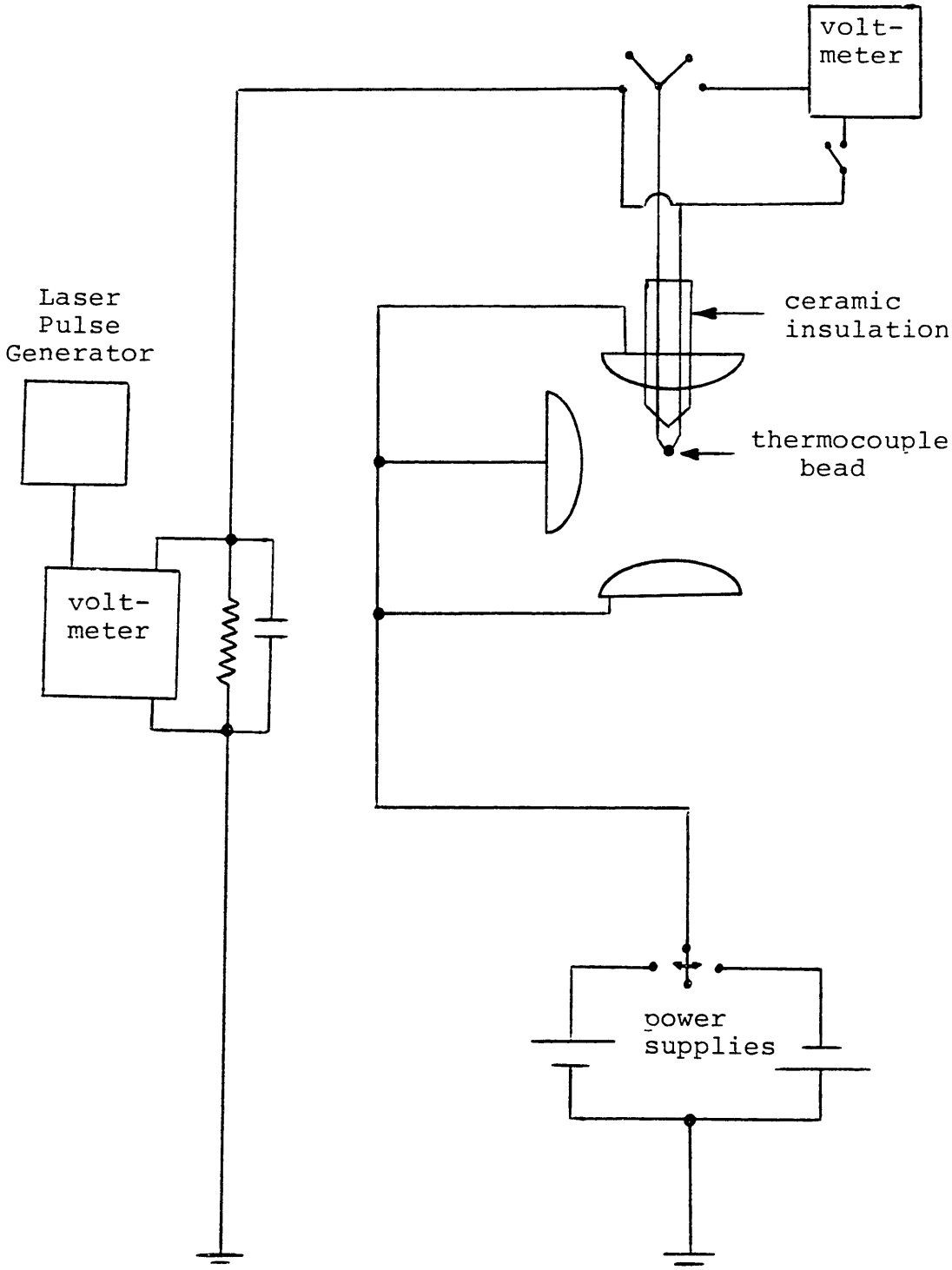

Figure 5.16 : Schematic of charge loss detection system with CO_2 laser heating.

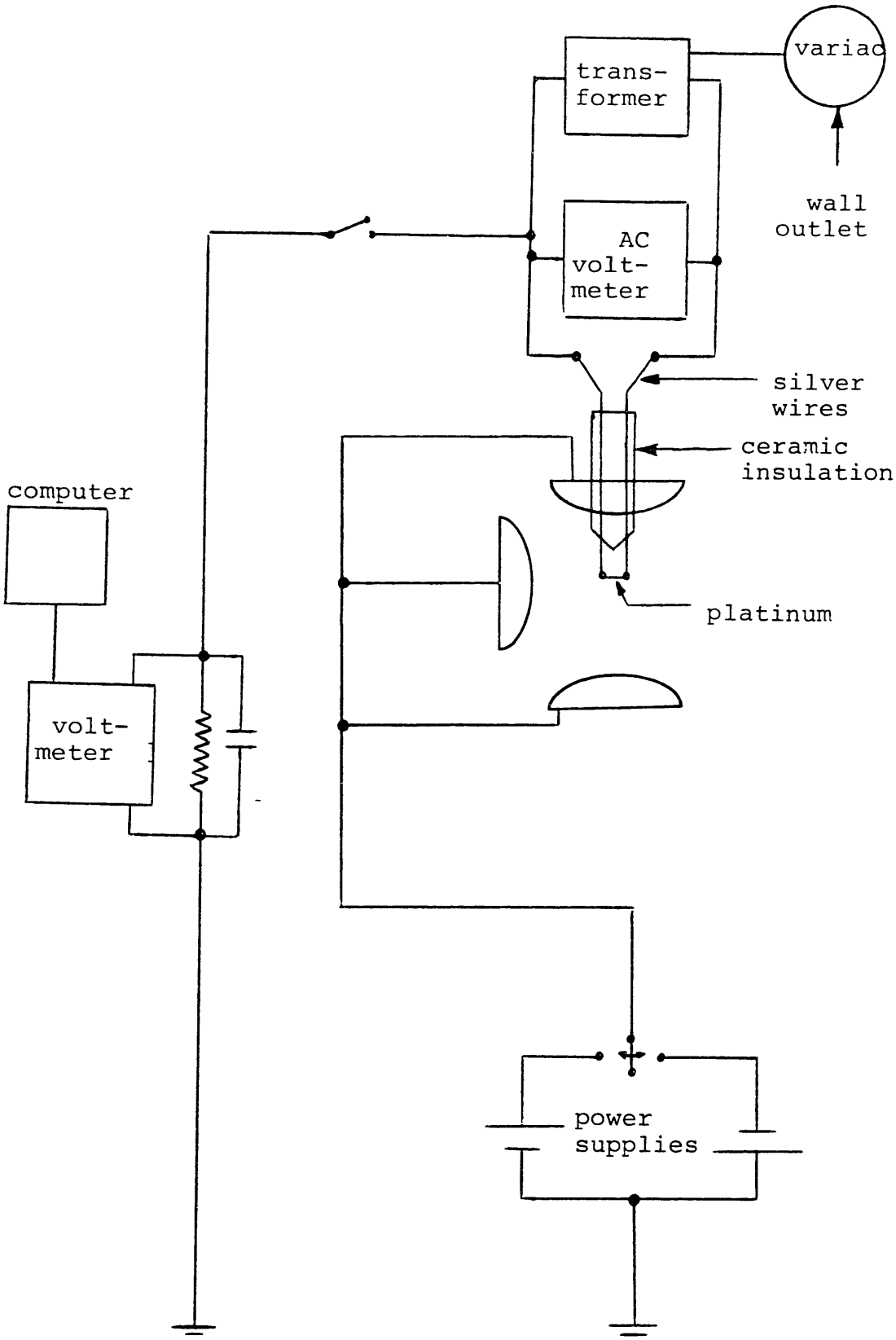

Figure 5.17 : Schematic of charge loss detection system with resistance heating.

remained essentially the same. Four-inch lengths of ceramic tubing of 0.060" diameter were filed to a point on one end. A single wire or thermocouple was then housed within these lengths for insulation and rigidity and were positioned in a manner such that the wire tip or thermocouple bead was pulled flush with the ceramic tip, and their legs were cemented into place at the other end. This ceramic tube was then inserted and affixed into a dolirene mechanism which was threaded into the top electrode. This allowed the metal probe tip to be held stationary in the center of the EDB and to be moved vertically without rotation.

Once the desired metal probe was inserted, it could be positioned into the center by using the microscope and HeNe laser. Next, the atmosphere of the probe could be adjusted and fixed by flowing cylinder gas into the chamber through the bottom electrode. Probe heating was then initiated, either by the CO_2 lasers or by allowing an AC current to flow through the wire. Time was then allowed for stabilization of temperature before beginning current measurements.

Besides altering the DC voltage supplied to the surrounding electrodes, several different metals were utilized as probes. Also, different probe coatings and gas surroundings were used. Many combinations of probes, coatings, and surrounding gases were attempted which resulted in many different current patterns which could then be compared. Probes were either single wires (0.008" Pt, 0.005" W, or 0.010" W) or thermocouples (0.008" Type R or 0.003"-0.010" Type K). Within the sealed EDB, various gases would be pumped in at a rate of 2.5-3.5 l/min. Ar, O_2, N_2, dry air, and wet air were used in the experiments. By dipping the thermocouple bead into ethanol solutions, various compounds such as SiO_2, ZrO_2, carbon black, $Ca(Ac)_2$,

and KCl were used as surface coatings. Soot was also used for this purpose by simply placing the bead into a flame. The soot coating could be preserved by heating in an Ar flow rate of 3.5 l/min. Finally, various hydroxyl and salt solutions including EtOH, KOH, HCl, and KCl were also applied to the probe tip.

5.6.2.3 Experimental results and discusion.

Figures 5.18-5.22 highlight results taken from a thermocouple or metal wire probe held in place by a ceramic tube with heat being provided by a CO_2 laser.

Figure 5.18 is a plot of positive ion current (in mV) versus the negative voltage being applied to the electrodes. In order to get the ion current in amps, divide by the resistance of the system, which in this case is 91 kΩ. Temperature is unknown for this experiment because a single Pt wire was used as the probe. The parameter being adjusted is the surrounding gas environment. Four different surrounding gases were used, Ar, N_2, wet air, and dry air. Two observations are readily apparent. First, increasing DC voltage to the surrounding electrodes, increases the positive ion current. This can be thought of as a decreasing of the surface work function, allowing ions to be released from the surface more easily. Secondly, an argon environment allows the flow of a substanially higher current, with N_2, wet air, and finally dry air allowing lower currents. This phenomenon probably correlated with argon's lower breakdown potential. This can also be used as evidence against the theory that ionization of the surrounding gas is the most important mechanism of charge loss, since the ionization energies of Ar and N_2 are approximately the same at around 15.6 eV.

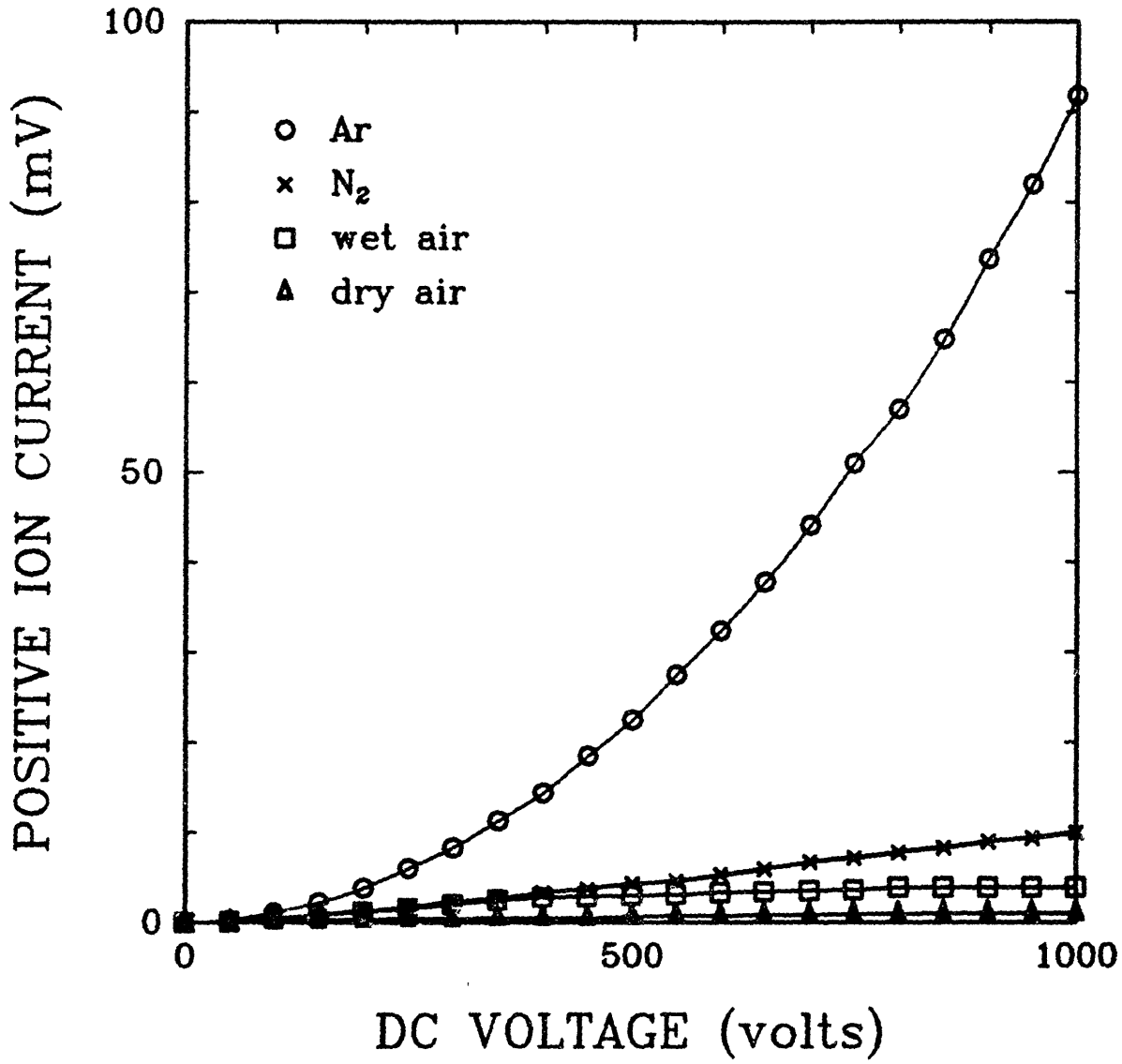

Figure 5.18 : Positive ion charge loss from a CO_2 laser heated, Pt wire versus negative DC voltage applied to surrounding electrodes. Surrounding gas is the parameter.

Figure 5.19 is a plot of ion current (in mV) versus the DC voltage being applied to the electrodes. The parameter being adjusted is the type R thermocouple temperature. Again we see the current is very much a function of the DC voltage being applied to the electrodes. This was always the case for the experiments performed with the CO_2 laser. We also see from Figure 5.19 that thermocouple temperature is also an important parameter. As temperature was increased, current was also increased. In this particular case negative ion current was also measured. It should be pointed out, however, that negative ion current was not always detected in these experiments. It is believed that negative ions were released only after heating to a higher temperature than was needed for positive ions to be released.

Figure 5.20 is a plot of positive ion current versus negative DC voltage being applied to the electrodes, with thermocouple temperature as a parameter. Here we see a very systematic dependence of positive ion current versus type K thermocouple temperature.

Figure 5.21 is a plot of positive ion current versus type R thermocouple temperature for various negative DC voltages applied to the electrodes. An attempt was made to extrapolate the data to zero current, thereby determining at what temperature charge loss (or current) becomes noticable. Table 5.2 highlights these results. It can be seen that charge loss (or current) becomes measurable at 1000 K if 25 volts DC are applied to the electrodes. On the other hand, if 400 volts DC are applied, current becomes measurable at 400 K.

Finally, Figure 5.22 is a plot of positive ion current

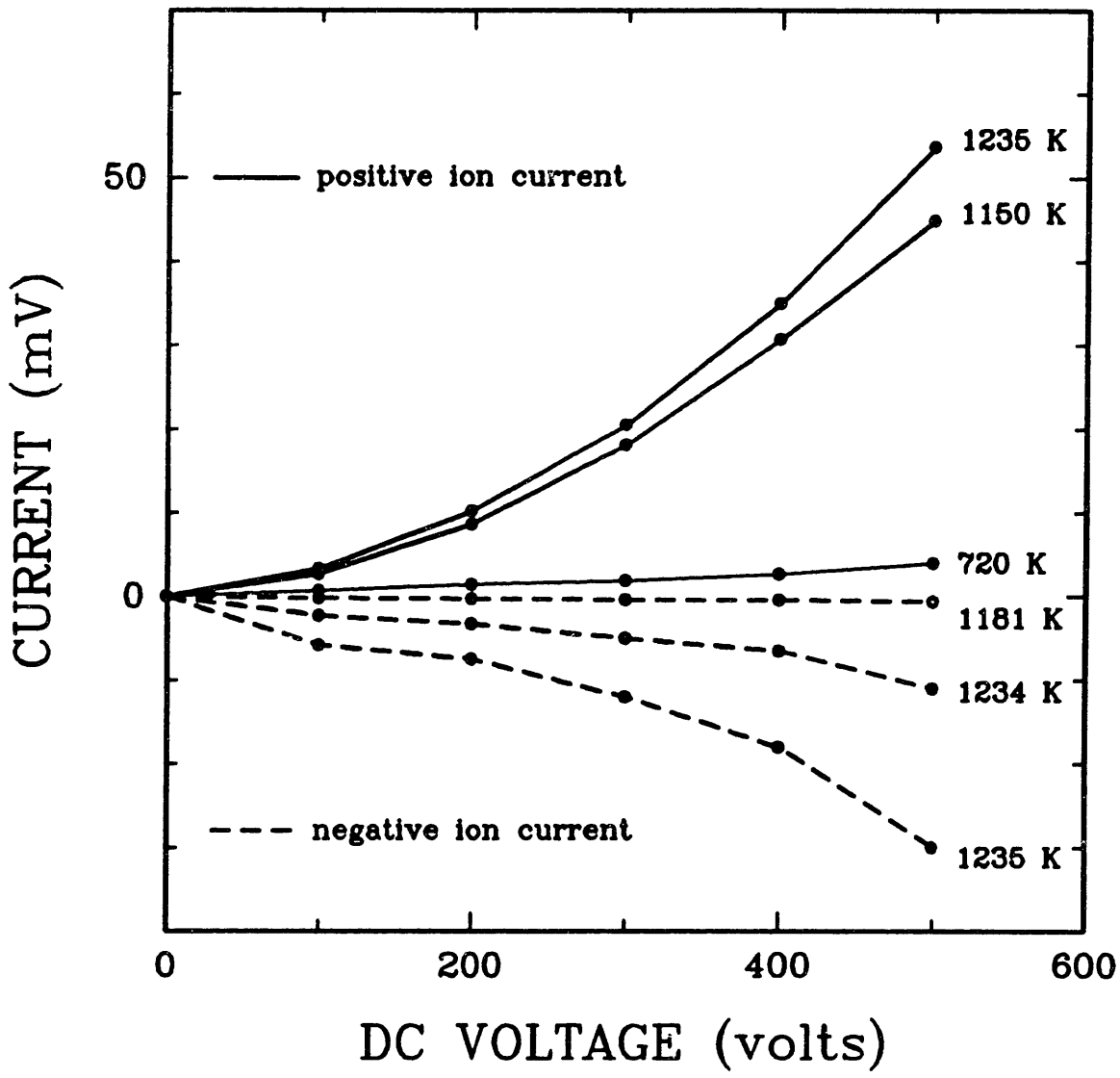

Figure 5.19 : Charge loss from a CO_2 laser heated, type R thermocouple versus DC voltage applied to surrounding electrodes. Thermocouple temperature is the parameter.

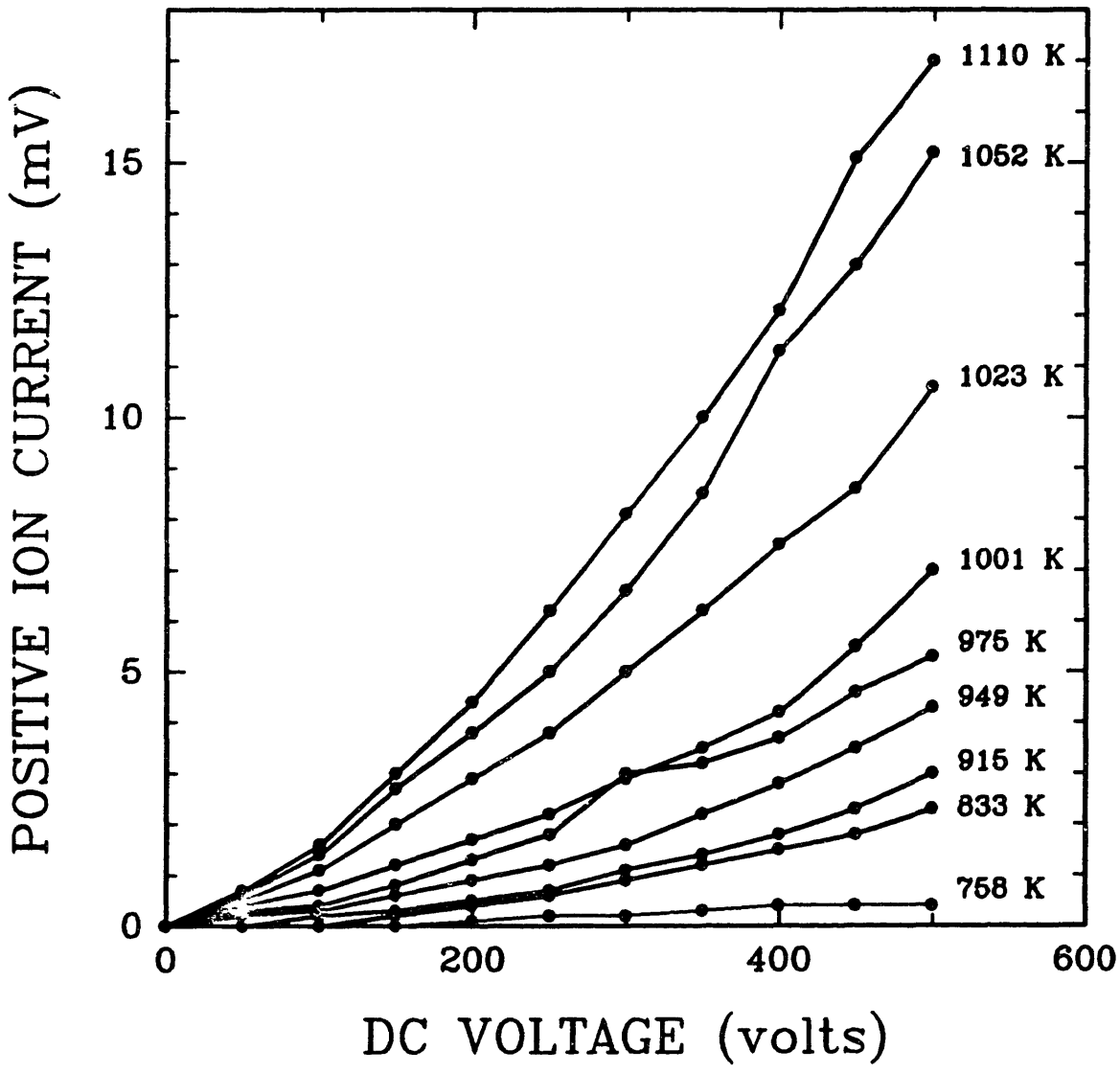

Figure 5.20 : Positive ion charge loss from a CO_2 laser heated, type K thermocouple versus DC voltage applied to surrounding electrodes. Thermocouple temperature is the parameter.

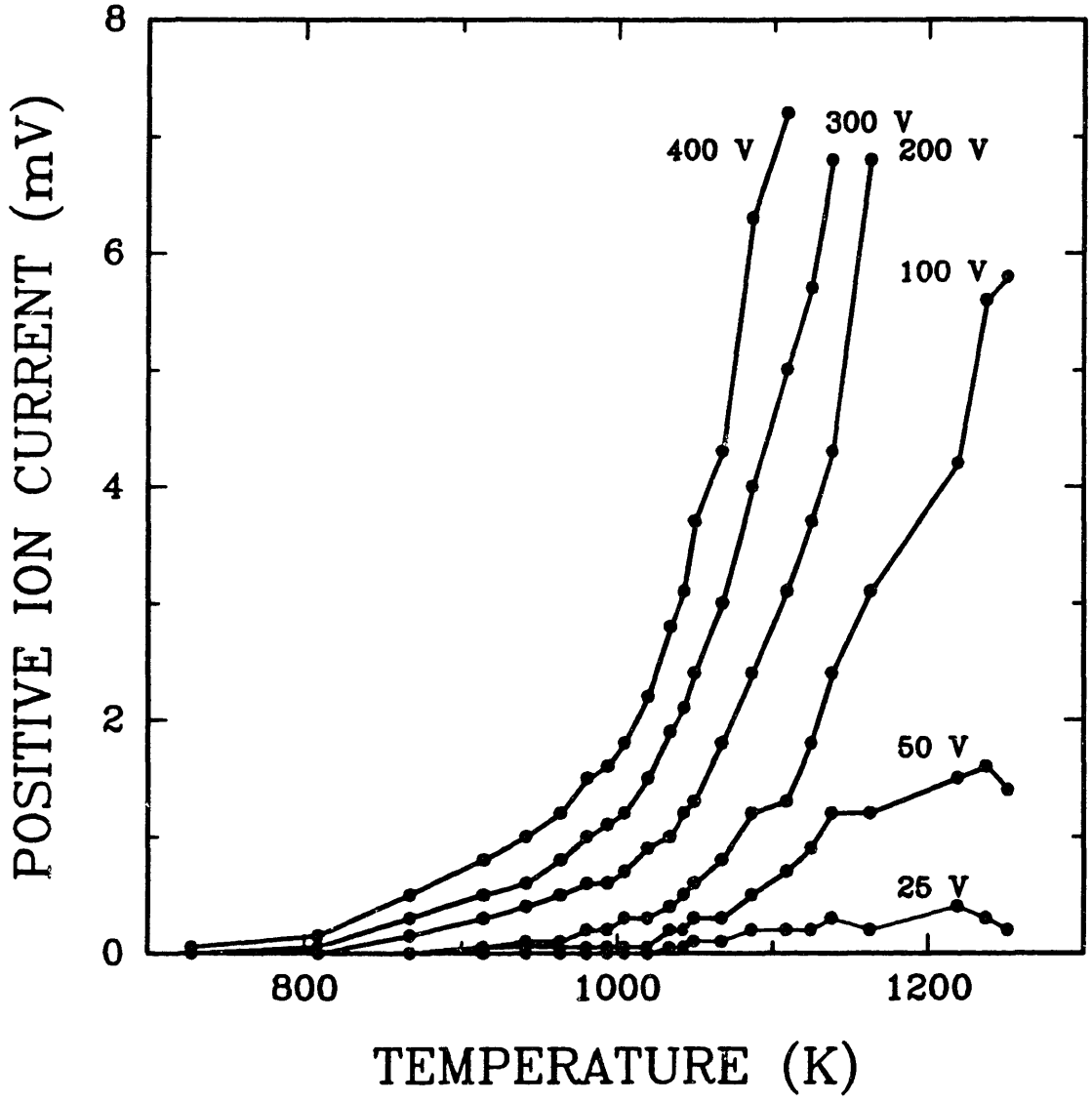

Figure 5.21 : Positive ion charge loss from a CO_2 laser heated, type R thermocouple versus thermocouple temperature. Negative DC voltage applied to surrounding electrodes is the parameter.

Table 5.2 : Temperature at 0.0 mV intercept versus applied DC voltage.

Voltage	Temperature (K)
25	1000
50	900
100	875
150	850
200	800
250	700
300	600
350	500
400	400

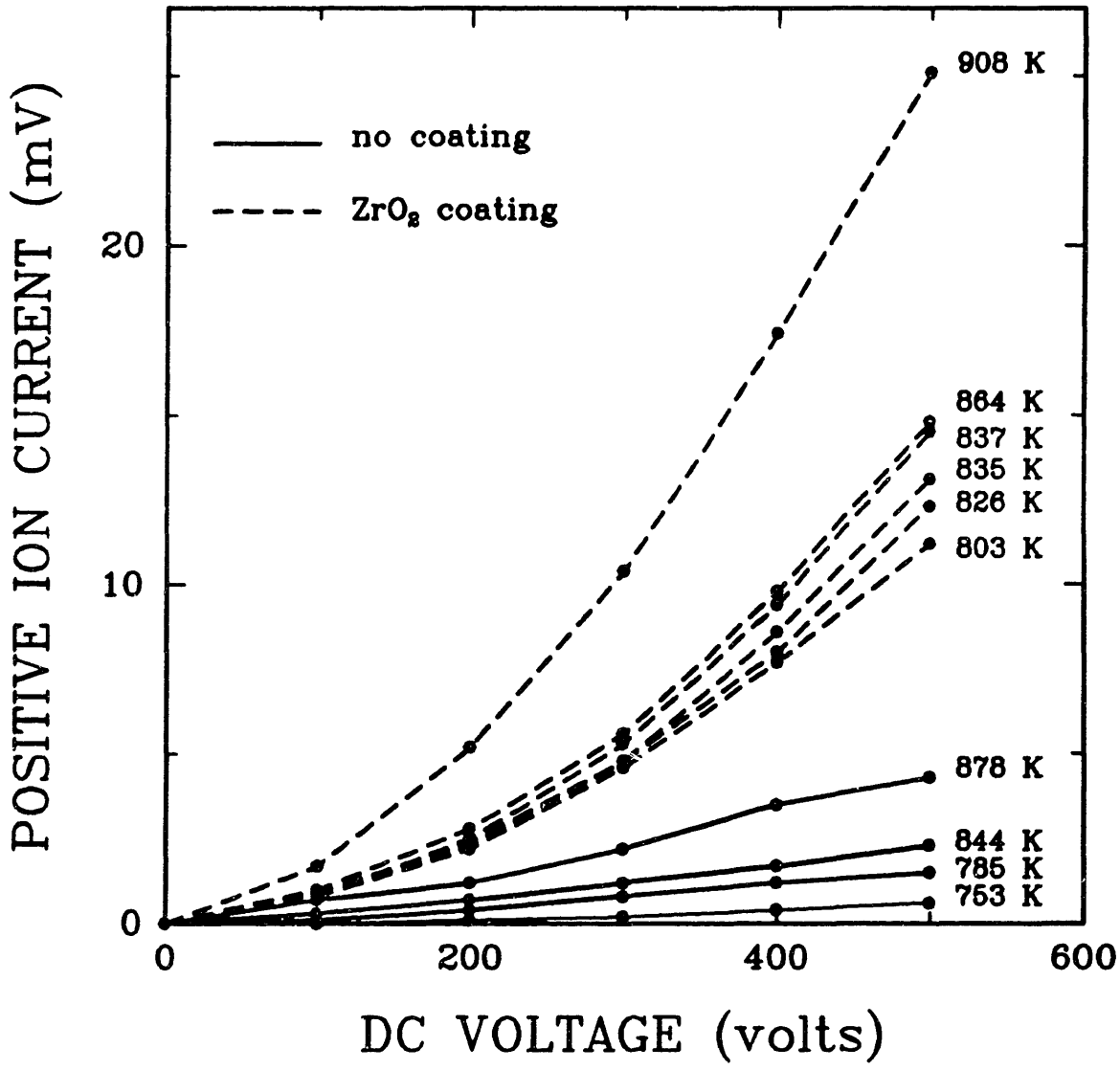

Figure 5.22 : Positive ion charge loss from a CO_2 laser heated, type R thermocouple versus DC voltage applied to surrounding electrodes for an uncoated and a ZrO_2 coated thermocouple. Thermocouple temperature is the parameter.

versus negative DC voltage applied to the electrodes, with type R thermocouple temperature as a parameter. This plot highlights the results of work performed with doped thermocouples. In this case, a ZrO_2 coating was attached to the thermocouple. The solid lines in Figure 5.22 represent results with no coating on the thermocouple and the dotted lines represent results with a ZrO_2 coating. The ZrO_2 coating increases the positive ion current by approximately one order of magnitude. Other experiments were performed with various coatings: SiO_2, carbon black, soot, $Ca(Ac)_2$, KCl, H_2O, and EtOH. All the results were very similar in that the doping of the thermocouple caused a drastic increase in current flow. Negative ion current also became very enhanced with some of the coatings.

When we heated the thermocouple or bare wire with the CO_2 laser, we believe we saw positive ion current to the electrodes due to heating of the ceramic. Due to the low emissivity of Pt, it was impossible to make the Pt wire glow without hitting the ceramic with the laser and heating it up first. On the plus side of this conclusion is that we are able to get nice stable positive ion currents versus time curves when we use the CO_2 laser for heating. However, we think that the reason for the nice stable positive ion currents is that the ceramic provides an infinite supply of positive ions.

It is believed that we have been unable to see electron flow through the surrounding gas. All thermionic emission experiments in the literature are performed in a vacuum. Since we have been unable to observe thermionic emission of electrons with our apparatus, we are really studying desorption or thermionic emission of ions from the metal or ceramic surface.

Using the CO_2 laser heated system, we discovered that different: surrounding gases, DC voltages, temperatures, and thermocouple materials all create different positive ion currents. We also discovered that doping of the thermocouples increased positive ion currents by one order of magnitude. Doping sometimes also allowed for negative ion current.

When the Pt wire is heated by resistance, the ceramic is no longer heated to such high temperatures that it glows. In this case it is believed that we are really looking at desorption of positive ions from the Pt wire itself. Figure 5.23 is a plot of positive ion current versus time for a resistance heated Pt wire. A total of nine cycles were performed on the same Pt wire. A cycle consisted of 65 sec of heating followed by a period where the wire is allowed to cool back to room temperature. We see that positive ion current from the Pt wire is very much a function of how long the positive ions have been flowing, both during a specific cycle and from cycle to cycle. For example, the positive ion current during cycle 9 is much less than the positive ion current during cycle 3. We believe that the positive ions are impurities in the Pt wire and are being used up, so that at infinite time no more positive ions would remain in the wire and positive ion current would stop completely.

For all of the experiments performed, a higher positive ion current was measured from the heated probe to the electrodes than would be predicted from the Richardson-Dushman equation for electron emission. In these cases, positive ions are emitted at much lower temperatures than electrons or negative ions. Therefore, it apears that positive ions have a lower surface work function. For the

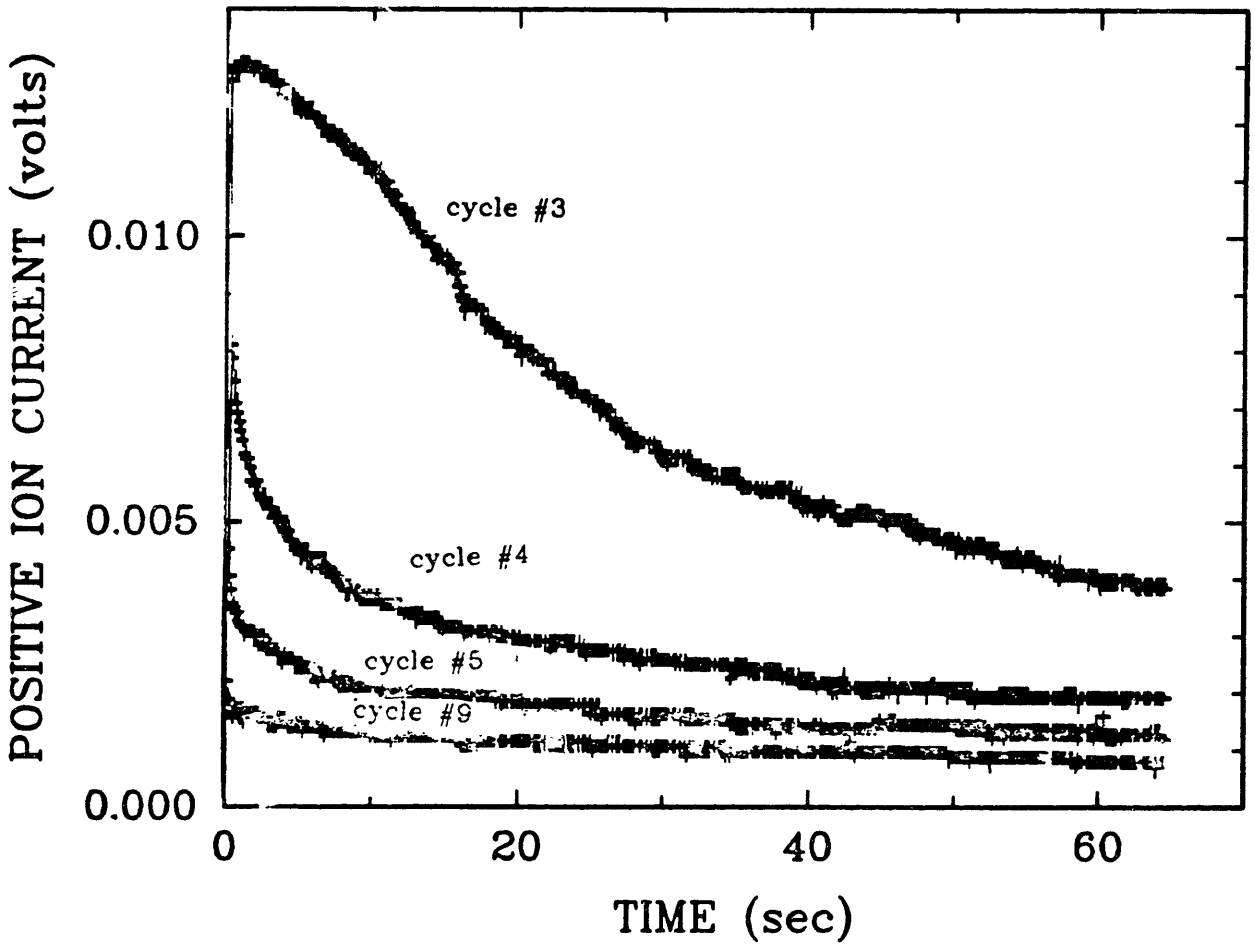

Figure 5.23 : Positive ion charge loss from a resistance heated Pt wire versus time with cycle number as the parameter.

experiments performed on the resistance heated Pt wire, the work function can be calculated to be 4.25 eV for positive ions instead of the theoretical value of 5.4 eV for electrons.

5.7 Summary of charge loss from heated particles.

1) Catastrophic charge loss due to particle heating has experimentally been found to represent the most serious limitation in studying single particle, high temperature, gas-solid reactions in the EDB.

2) Six different charge loss mechanisms have been proposed:
   a) photoemission,
   b) field emision,
   c) secondary emission,
   d) thermionic emission of electrons or ions,
   e) fragmentation, and
   f) surrounding gas ionization.

3) Photoemission, secondary emission, and "cold" field emission have been shown not to be viable mechanisms.

4) A fragmentation process which may be defined as a cluster of molecules leaving in a condensed phase. Although it seems a reasonable mechanism, observable fragmentation usually does not accompany charge loss and it would seem reasonable to assume that quite a large section of the particle would have to fragment off in order for the particle to lose enough charge to no longer be stable in the chamber.

5) Surrounding gas ionization cannot be ruled out, but due to the large ionization potentials of typical

surrounding gases (~11-16 eV) compared to the work functions of typical solids (1-6 eV), it is assumed that a thermionic emission of ions from the solid would occur at a lower temperature than the ionization of the surrounding gas. One can, however, use the temperature at which gas ionization becomes appreciable as an upper limit on the temperature to which a particle can successfully be heated without charge loss.

6) Experimentally, charge loss appears to be a function of particle work function, particle temperature, electric field strength, and adsorbed species concentration. There is also no noticable difference in charge loss from positively charged particles as compared to negatively charged particles.

7) After examining evidence from experiments performed in this lab as well as evidence presented in the literature, thermionic emission of ions remains the most viable mechanism for charge loss. The Richardson-Dushman equation describes thermionic emission from a clean surface and predicts the maximum temperature at which a material can be heated without experiencing charge loss. The Richardson-Dushman equation successfully predicts charge loss from "Spherocarb" particles (work function of carbon = 4.7 eV) at 1200-1300 K and charge loss from K catalyzed "Spherocarb" particles (work function of K = 2.3 eV) at 750 K. This equation also successfully predicts the inability of $CaCO_3$ to be heated to temperatures above 1173 K in order to form CaO.

8) Taking into consideration that the particle work function and particle temperature are of primary importance in describing charge loss, and that electric field strength, adsorbed species, and

surface irregularities are of secondary importance and act to lower the particle work function, a modified Richardson-Dushman equation has been proposed.

5.8 Charge loss recommendations.

When performing experiments where charge loss is known to be a problem, charge loss can be minimized by: 1) minimizing the electric field at the particle surface, 2) minimizing the adsorbed species, 3) minimizing surface irregularities, and 4) using positively charged particles. Since the electric field at the particle surface is dominated by the amount of excess charge on the surface, the electric field at the particle surface can be minimized by using smaller particles and as large a DC balancing voltage as possible. Although never attempted, it is recommended that a technique for minimizing adsorbed species be developed. Vacuum degassing may be a viable solution. There is no known method of decreasing surface irregularities. Finally, positively charged particles should be used since the work function for the thermionic emission of ions is usually a couple of electron volts greater than the work function for the thermionic emission of electrons. This is true in theory, however, it has not yet been experimentally observed in the EDB.

6. SINGLE PARTICLE "SPHEROCARB" OXIDATION.

It has been shown in the preceeding chapters that diameter, mass, density, surface area, and reactivity measurements can be performed on single particles levitated in the electrodynamic balance (EDB). In this chapter we utilize these measurement techniques on char to examine the changes in these variables during oxidation. The uncatalyzed synthetic char "Spherocarb" was chosen as a base case and is examined in section 6.1. Since "Spherocarb" has been widely studied, results from the electrodynamic thermogravimetric analyzer (EDTGA) can be compared with those of conventional gas-solid reaction apparatuses to test the overall usefulness, credibility, and uniqueness of the EDTGA in studying gas-solid reactions. "Spherocarb" particles doped with Fe, K, and Ca are examined in section 6.2 to determine the effect of catalyst on diameter, surface area, and reactivity versus extent of reaction.

6.1 Uncatalyzed "Spherocarb".

6.1.1 Charge loss versus conversion.

By rearranging equation 3.3, the excess charge on a suspended particle can be written in the following manner:

$$q = mgz_0/(CV) \qquad (6.1)$$

where the particle mass, m, is measured via the aerodynamic drag technique discussed in section 3.2.

Figure 6.1 is a plot of overall excess charge versus percent conversion for six separate "Spherocarb" oxidation runs. Three of the oxidations were performed in oxygen, two in carbon dioxide, and one in a dilute stream of oxygen in nitrogen. Although temperature measurements for these runs were not made, reaction times indicate that temperatures probably ranged from 750 to 830 K for the oxidations performed in oxygen and 1200 to 1250 K for the oxidations performed in carbon dioxide. Each excess charge measurement was performed discretely, i.e. an excess charge measurement was performed, the "Spherocarb" was reacted until a specific conversion was reached, the reaction was stopped, another excess charge measurement was performed, etc. The excess charge on the six particles ranges from 2 to 9 million elementary charges and appears to be relatively constant for each run throughout the reaction.

Error bars are included on the points of Figure 6.1 in Figure 6.2. Error estimation for charge measurement were performed in the same manner as error estimation for mass measurement found in section 3.1.7. From Figure 6.2 it can be concluded that the excess charge on the "Spherocarb" particles for these six particular runs remains constant within experimental error during conversion. Therefore, "Spherocarb" mass can be followed continuously inder these conditions by following balancing voltage versus time.

Figure 6.3 is a plot of relative charge versus percent conversion for nine "Spherocarb" oxidation runs, the six runs discussed in Figures 6.1 and 6.2 along with two other runs performed in oxygen and one other run performed in air. The reason the other three runs were not plotted in Figures 6.1 and 6.2 is

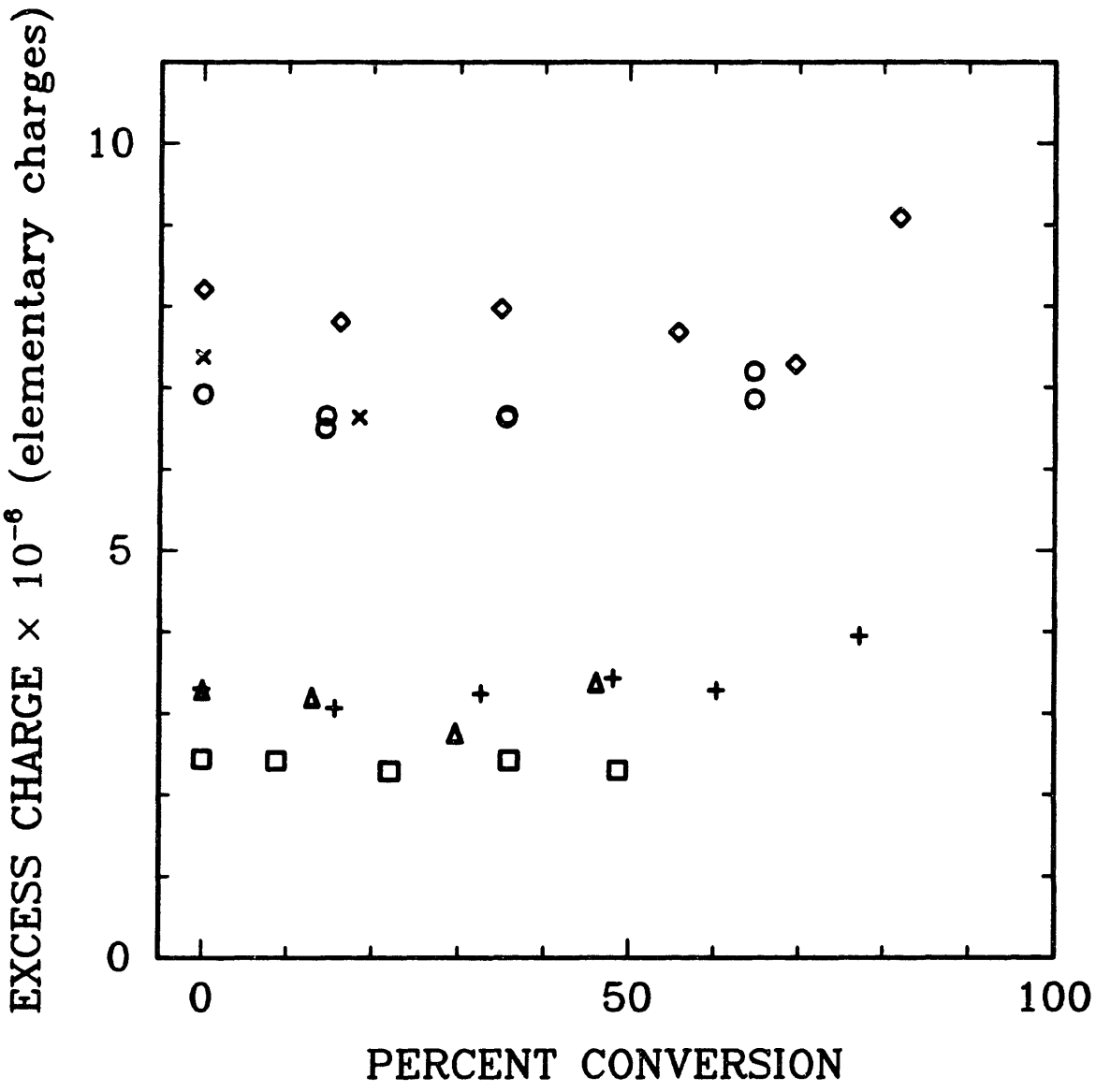

Figure 6.1 : Excess charge versus percent conversion for six separate, single particle, uncatalyzed "Spherocarb" oxidations performed in the EDTGA.

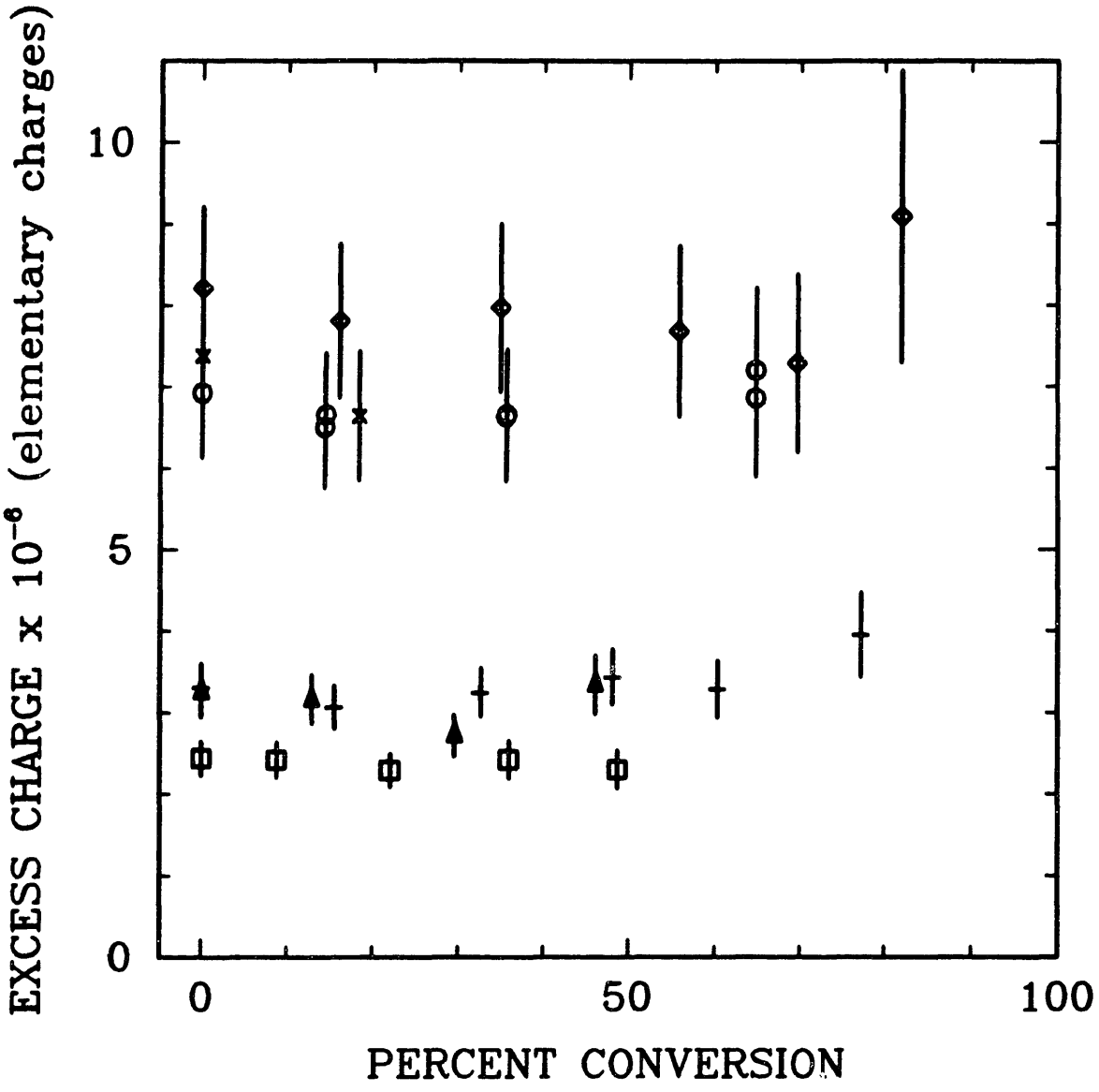

Figure 6.2 : Excess charge + error bars versus percent conversion for six separate, single particle, uncatalyzed "Spherocarb" oxidations performed in the EDTGA.

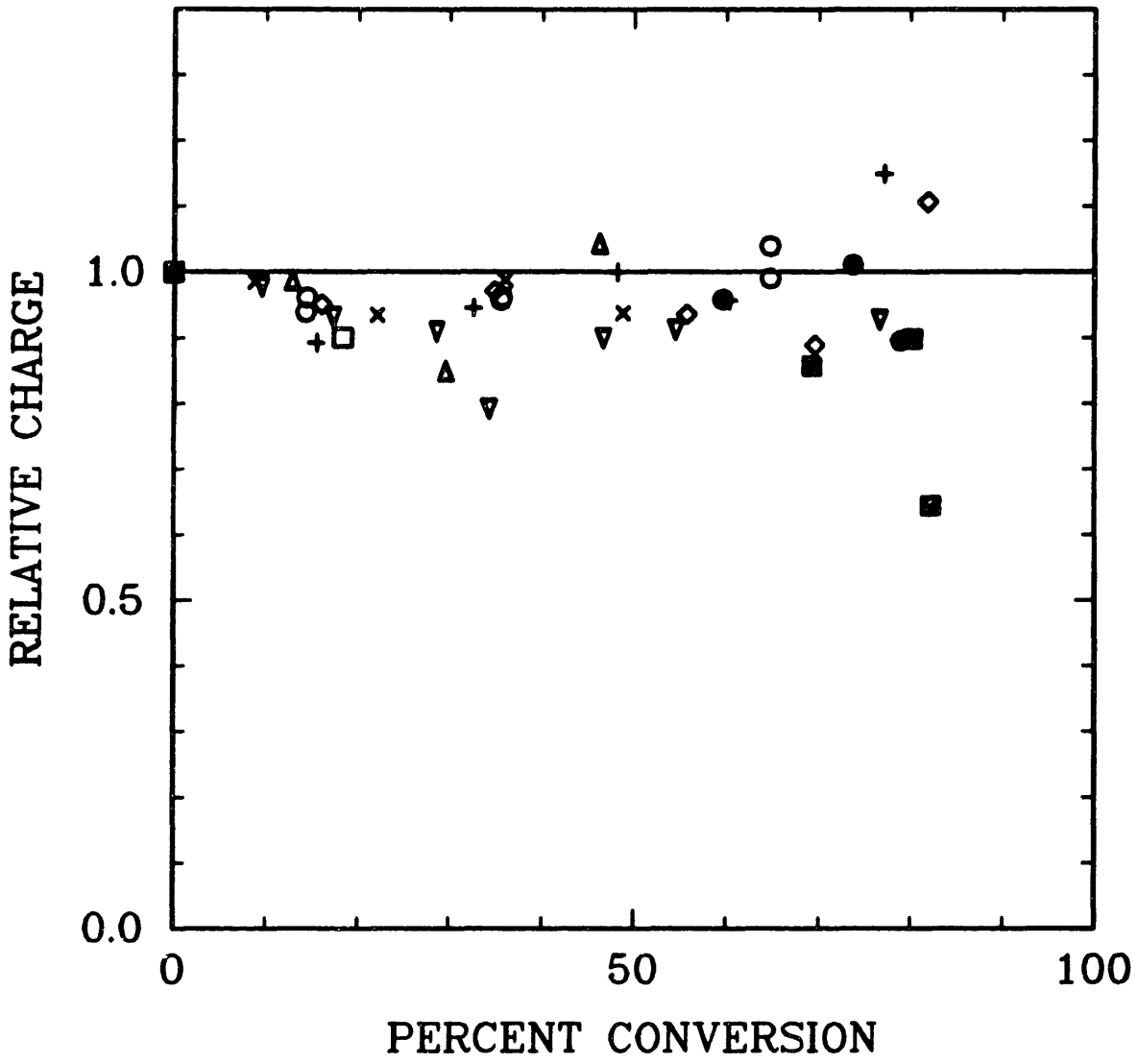

Figure 6.3 : Ratio of excess charge to initial excess charge versus percent conversion for nine separate, single particle, uncatalyzed "Spherocarb" oxidations performed in the EDTGA.

that charge was purposely removed from the particles during these runs to keep the balancing voltage large and the error in mass measurement low. Charge was removed from the particles by irradiation by an ultraviolet light source. Relative charge is defined as the charge on the particle divided by the initial charge on the particle. With the exception of only a couple points, we can again conclude that charge loss from "Spherocarbs" undergoing oxidations at these conditions is not a problem.

6.1.2 Density and porosity versus conversion.

Figure 6.4 is a plot of density versus percent conversion for nine separate, uncatalyzed "Spherocarb" oxidations. Intitial densities ranged from 670 to 920 kg/m^3. Percent conversion is defined as follows:

$$\% \text{ conversion} = (1.0 - m/m_i)100\% \qquad (6.2)$$

Five of the oxidations were performed in oxygen, one in air, two in carbon dioxide, and one in a dilute stream of oxygen in nitrogen. These are the same nine oxidations discussed in section 6.1.1. It is believed that the "Spherocarbs" are oxidizing in the kinetically controlled regime under these conditions [41]. Density measurements were performed discretely using the aerodynamic drag force technique discussed in section 3.2. From Figure 6.4 it can be seen that "Spherocarb" density decreases with conversion at these reaction conditions. Conventional theory would predict particle density to decrease linearly with conversion under regime I conditions, however, the data suggest a minimum density of approximately 400 kg/m^3 that "Spherocarb" cannot go below, even at high conversions of

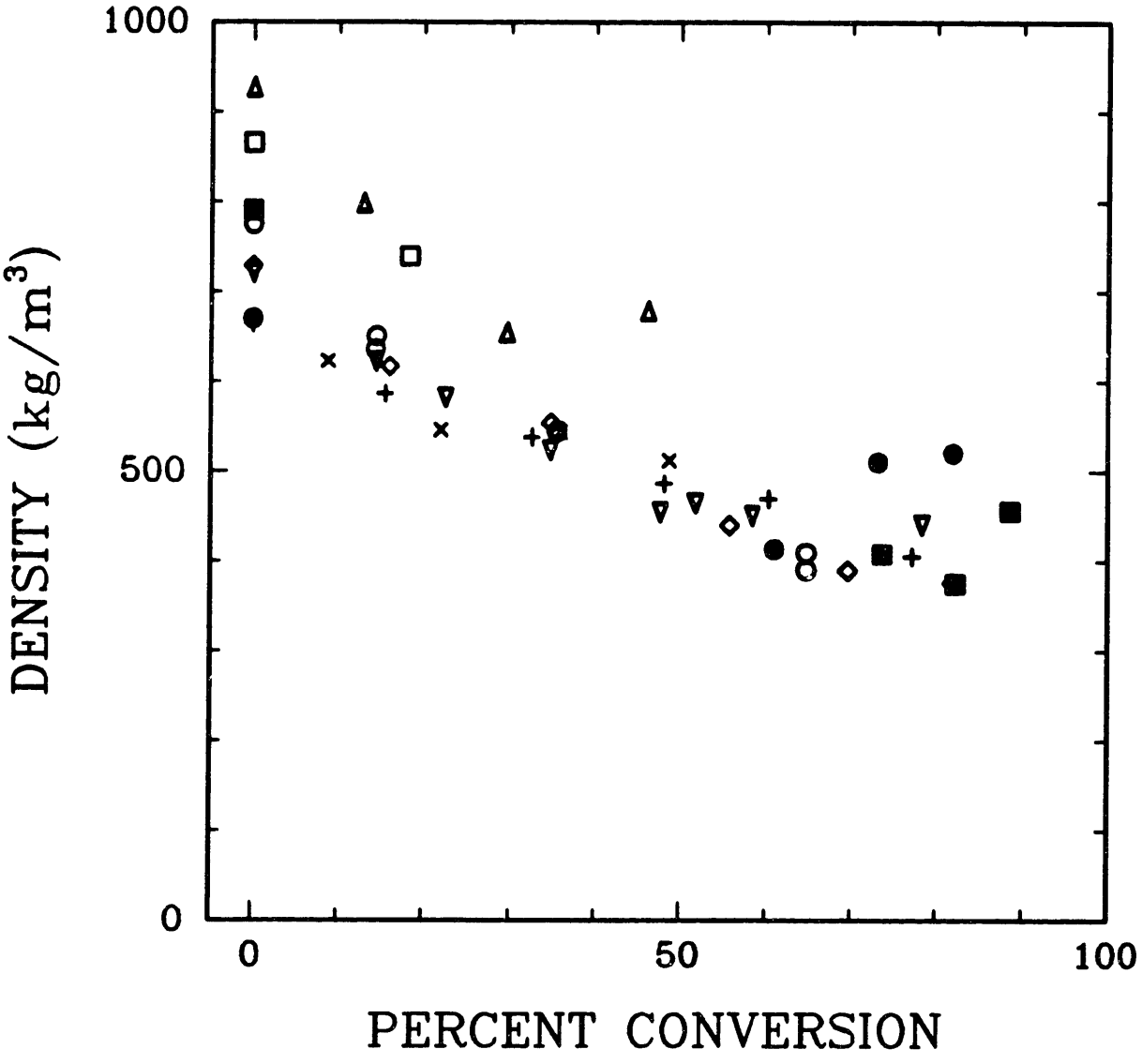

Figure 6.4 : Apparent density versus percent conversion for nine separate, single particle, uncatalyzed "Spherocarb" oxidations performed in the EDTGA.

60-90%. These data are consistent with the shrinkage-densification model proposed by Hurt et al. [74] for chars undergoing regime I or kinetically controlled oxidation. All of the reaction is occurring in the micropores, however, instead of just reacting out the inside of the particle and decreasing the particle density linearly with conversion, molecular rearrangement occurs inside the micropores during reaction causing concurrent densification of the remaining particle.

Figure 6.5 is a plot of relative density versus percent conversion for the same nine "Spherocarb" oxidations. Relative density is defined as density divided by initial density. The two solid lines represent the two extreme cases of gas-solid reactions, regimes I and III. Regime I indicates kinetic control, where the reacting gas concentration is uniform throughout the particle and equal to the surrounding bulk gas concetration. Under regime I or kinetically controlled conditions the relative density would linearly decrease to zero at 100% conversion. Regime II indicates pore diffusion control. Under these conditions the reacting gas concentration decreases toward the particle center and reaction would take place preferentially near the particle surface. Particle density and diameter could both decrease. Regime III indicates external mass transfer control or severe pore diffusion limitations. Here reaction would occur only on the particle surface. Particle density would remain constant and the particle would shrink.

Figure 6.6 is a plot of "Spherocarb" overall porosity versus percent conversion for the same nine runs as in Figures 6.4 and 6.5. Overall porosity is defined as:

$$\text{porosity} = (1.0 - \rho_p/2100) \qquad (6.3)$$

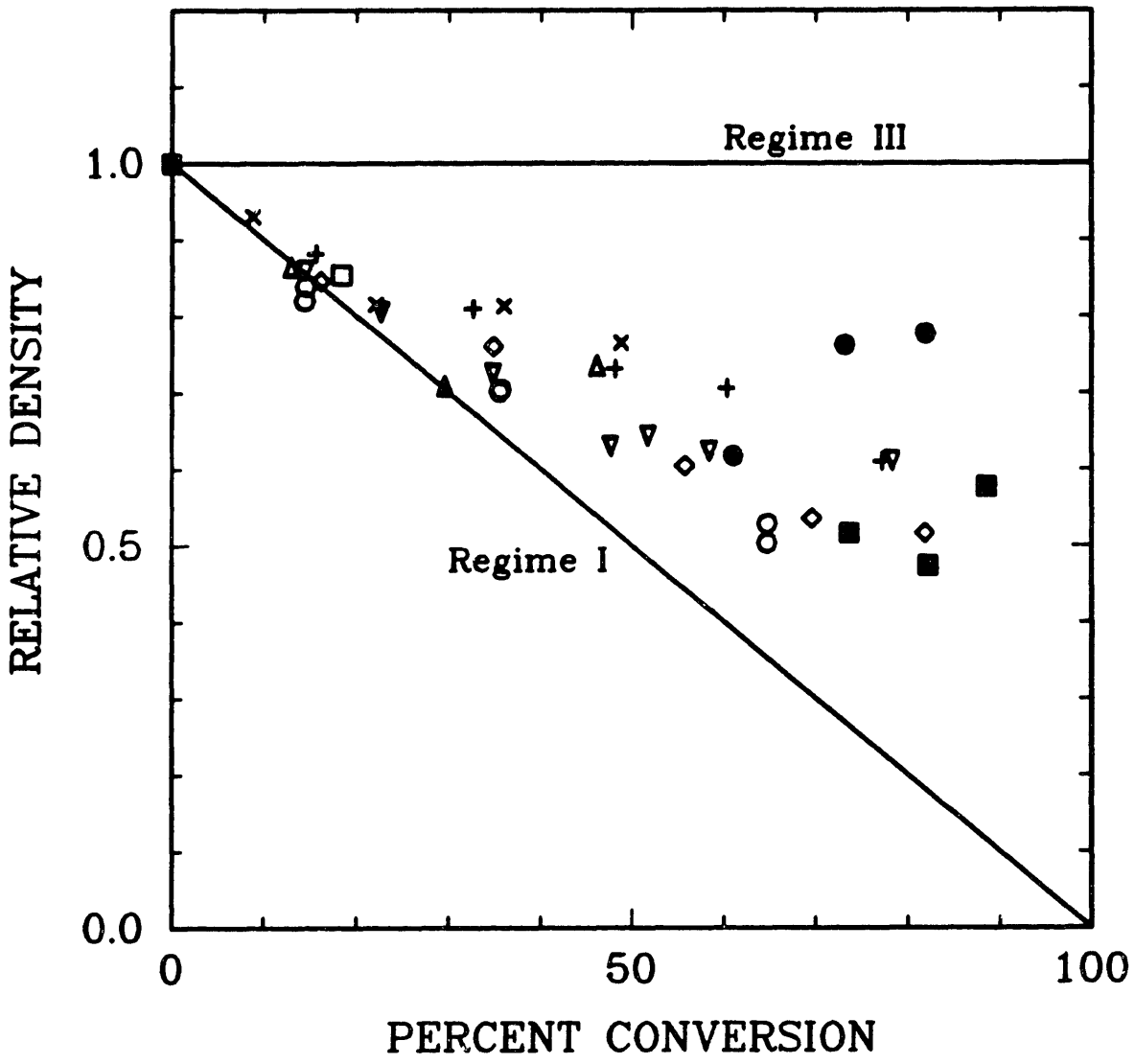

Figure 6.5 : Ratio of density to initial density versus percent conversion for nine separate, single particle, uncatalyzed "Spherocarb" oxidations performed in the EDTGA.

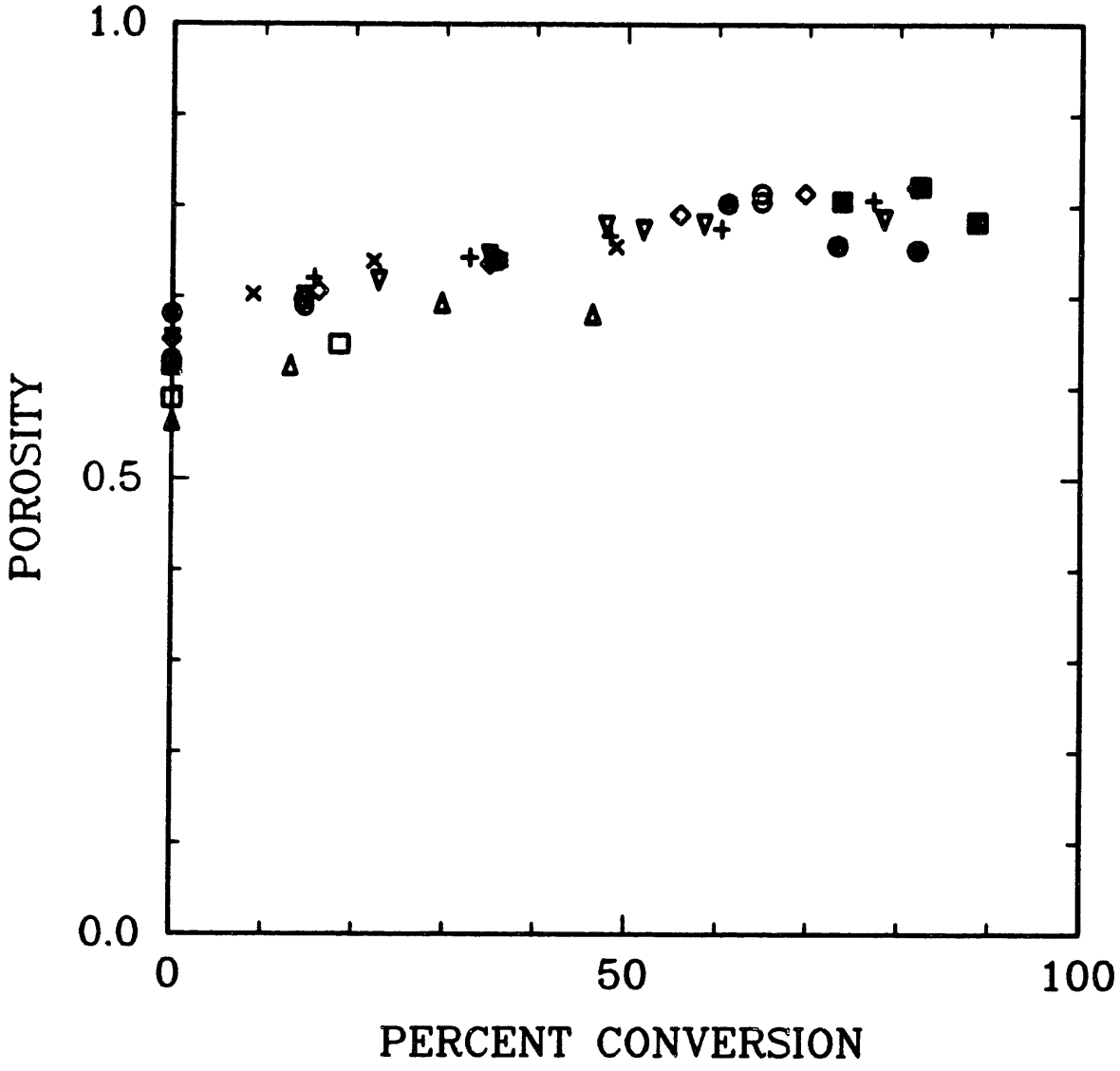

Figure 6.6 : Porosity versus percent conversion for nine separate, single particle, uncatalyzed "Spherocarb" oxidations performed in the EDTGA.

where a skeletal density of 2100 kg/m^3 was assumed. The initial overall porosity ranges from 0.56 to 0.68. As the reaction proceeds, the overall porosity increases steadily until it plateaus at a value of 0.82 at about 60% conversion. Since the overall porosity is just another way of plotting density versus conversion, the same conclusion about a maximum obtainable porosity can be made.

6.1.3 Shrinkage versus conversion.

Diameter measurements of particles suspended in the EDB can be obtained from one or both of the microscopes attached to the system. Figure 6.7 is a series of eight photographs taken of one uncatalyzed "Spherocarb" particle at various stages of conversion, 0, 14, 23, 35, 48, 52, 58, and 78% conversion. The photographs were taken from a 35 mm camera mounted on a (x100) Wild microscope that observed the particle through a hole in the top endcap electrode. This particular "Spherocarb" particle was reacting in air at 770 K. The particle's spherical shape was retained up to a conversion of 50%, afterwhich the particle became first oval shaped and finally almost triangular. In section 6.1.6, the variation from particle to particle of "Spherocarb" density is discussed. It is concluded that the variation in density is caused by cavities (on the order of tens of microns in size) unevenly distributed from particle to particle. It is believed that these rather large cavities are responsible for the nonsphericity of the "Spherocarb" particles at high conversions. It appears, therefore, that the particle shape at high conversions is dependent on its original internal macroporosity.

An average "Spherocarb" diameter at each conversion

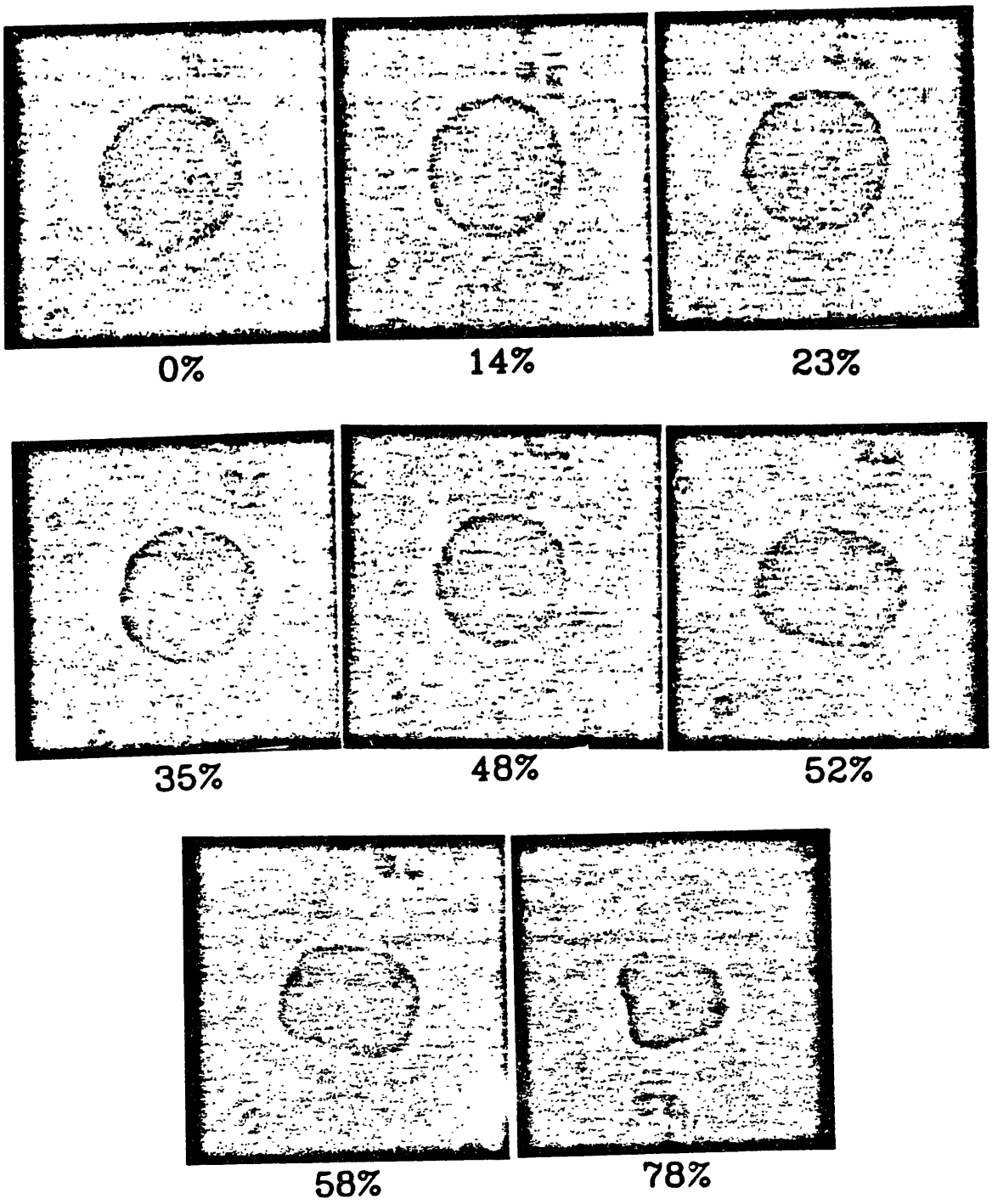

Figure 6.7 : Photographs at different conversions of a single, uncatalyzed "Spherocarb" particle reacting in air in the EDTGA at 770 K.

can be measured from 1) the photographs of Figure 6.7 and 2) optical measurements from the x70 Ealing microscope. This average "Spherocarb" diameter is plotted versus conversion in Figure 6.8. The unreacted "Spherocarb" has a diameter of 181 μm. This diameter decreases to a value of 128 μm at a conversion of 78%.

Another example of "Spherocarb" shrinkage versus conversion is given in Figure 6.9. This particular "Spherocarb" was reacted in air at 830 K and is depicted at conversions of 0, 20, 38, 63, 79, and 94 %. The initial diameter was 205 μm. This particle retains its spherical shape up through 63% conversion.

Diameter versus conversion measurements were obtained for 13 separate, single particle, uncatalyzed "Spherocarb" reactions, with the results depicted in Figure 6.10 in the form of the ratio of diameter to intial diameter versus percent conversion. The results are amazingly consistent. The curved solid line in Figure 6.10 represents regime III conditions and the solid line at d/d_i equal to 1.0 represents regime I conditions. Nine of the runs were performed in oxygen, three in carbon dioxide, and one in air. Reaction times for 50% conversion ranged from 2 minutes in oxygen to 30 minutes in carbon dioxide, with a corresponding temperature range of 750-830 K for reactions in oxygen and 1200-1250 K for reactions in carbon dioxide. At 50% conversion, the "Spherocarb" diameter is typically 90% of its original value, and at 90% conversion, the diameter is reduced to 50% of its original value. Since it is believed that all of the runs took place under regime I conditions, the Hurt shrinkage-densification model must be incorporated to interpret the data. The data indicate that the extent of "Spherocarb" shrinkage is not a function of

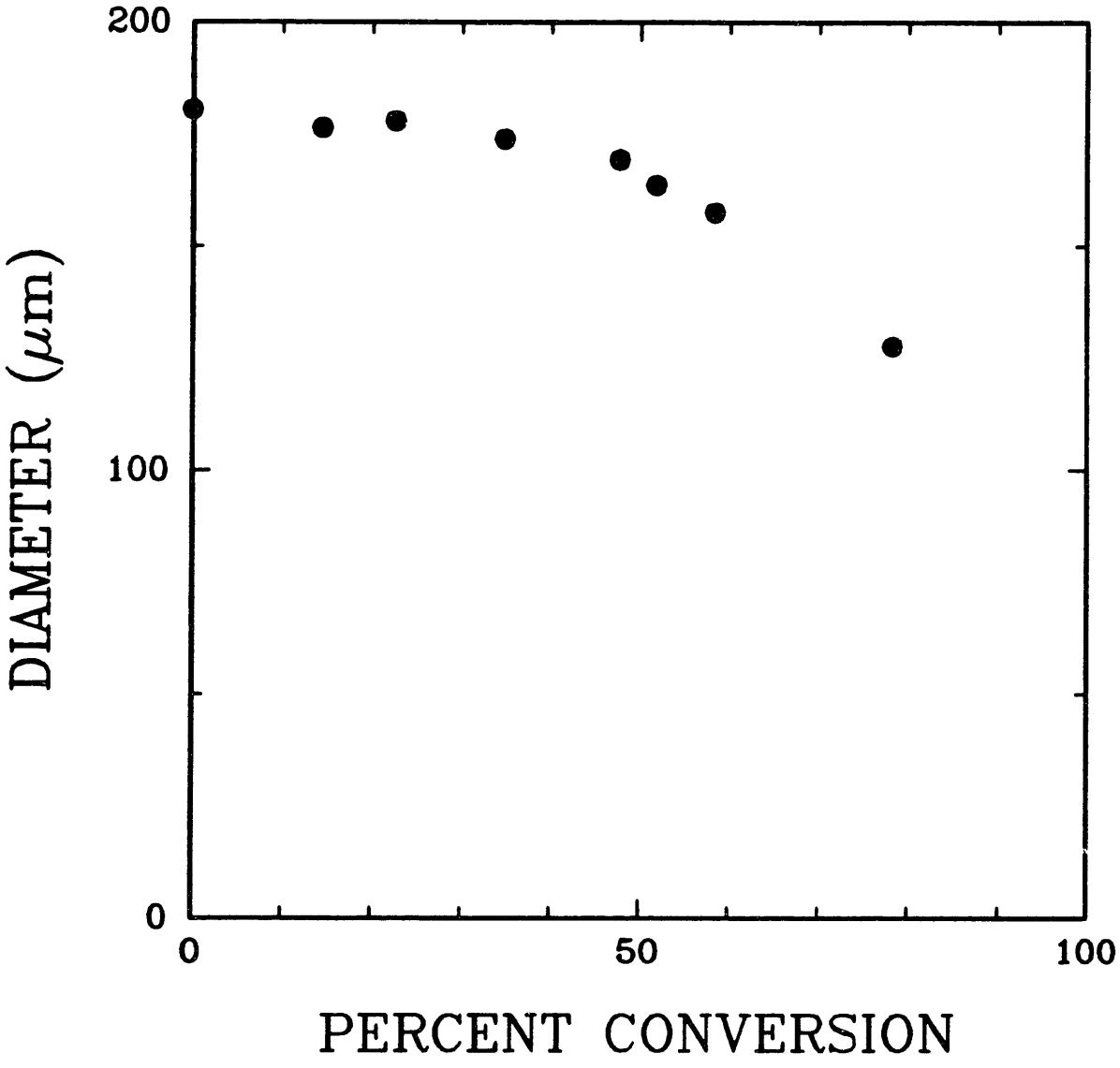

Figure 6.8 : Diameter versus percent conversion for a single, uncatalyzed "Spherocarb" particle reacting in air in the EDTGA at 770 K.

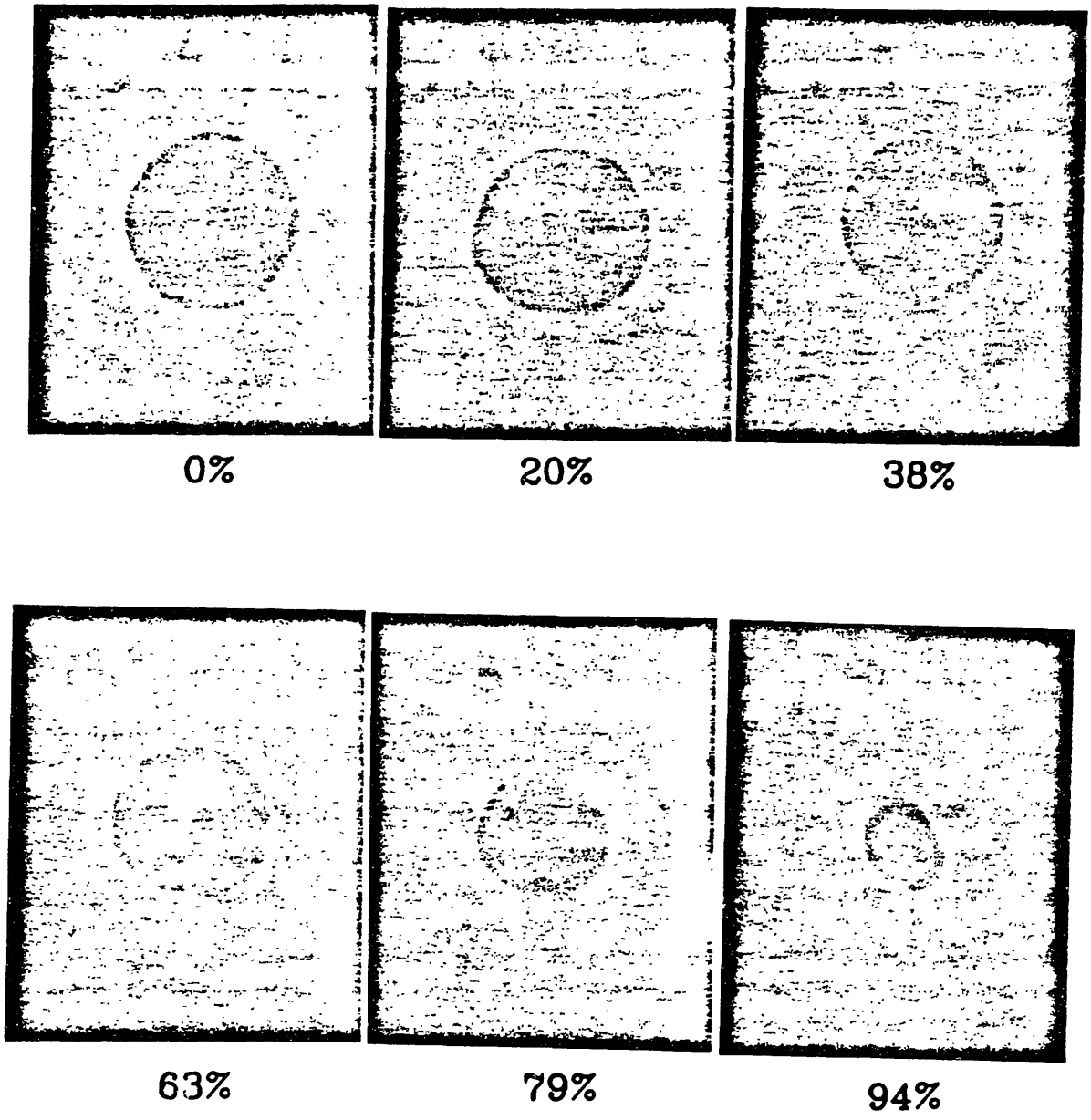

Figure 6.9 : Photographs at different conversions of a single, uncatalyzed "Spherocarb" particle reacting in air in the EDTGA at 830 K.

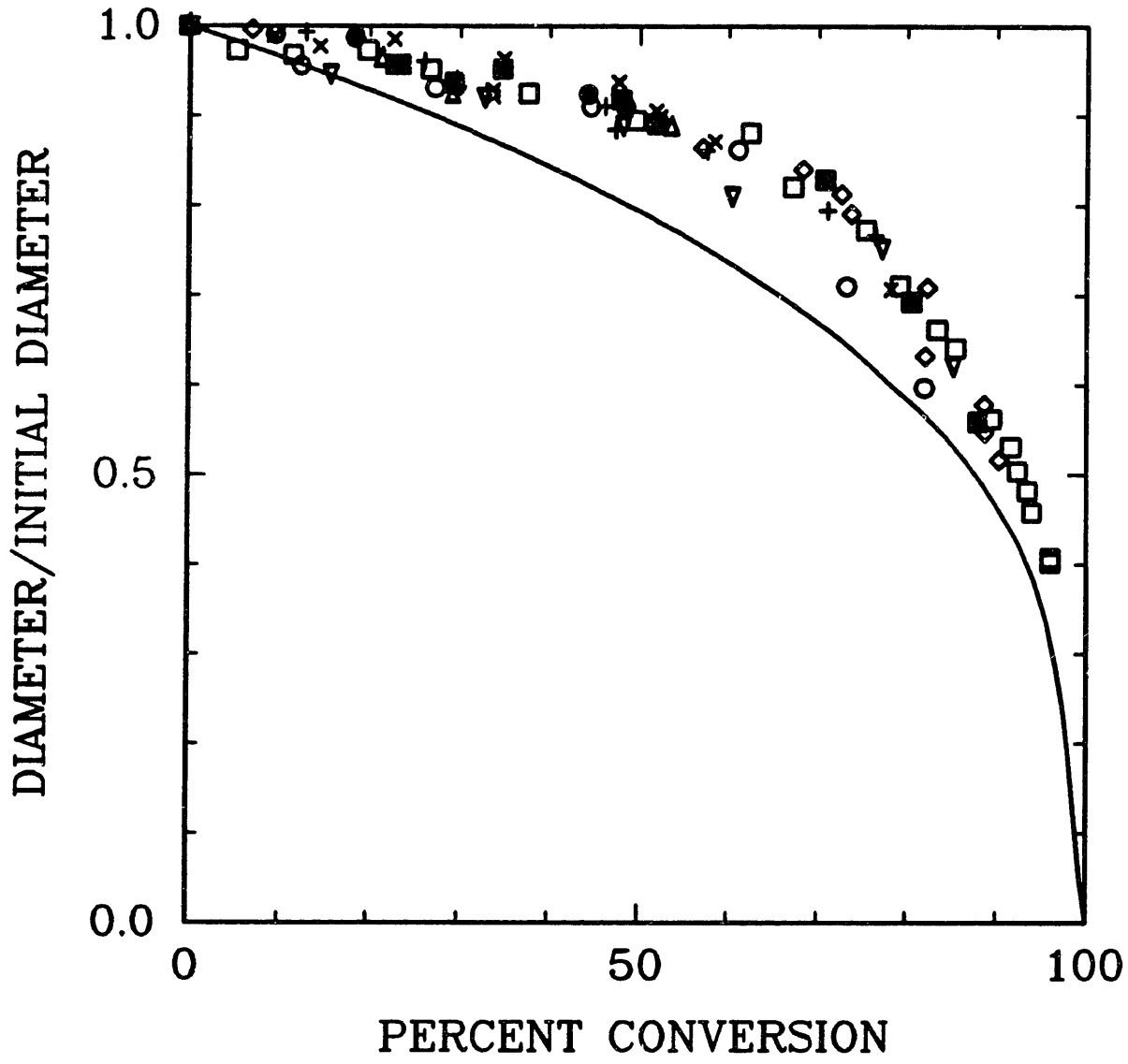

Figure 6.10 : Ratio of diameter to initial diameter versus percent conversion for 13 separate, single particle, uncatalyzed "Spherocarb" oxidations performed in the EDTGA.

temperature or reacting gas, but only a function of conversion.

In Figure 6.11, the same data plotted in Figure 6.10 is plotted as $(d/d_i)^3$ versus percent conversion. The solid line represents regime III conditions.

Figure 6.12 is a plot of $\log(d/d_i)$ versus $\log(m/m_i)$ for the same 13 separate runs of Figures 6.10 and 6.11. Again, the solid line represents regime III conditions which has a slope of 0.33. Up to a value of 60% conversion or a $\log(m/m_i)$ of -0.4, the slope of the data is approximately 0.15. The data above 60% conversion or greater than $\log(m/m_i) = -0.4$, has a slope of approximately 0.333. From these data, it appears that the extent of shrinkage is smaller at conversions below 60%. This is the stage of conversion associated with sharp density decreases which are characteristic of regime I oxidation. At conversions greater than 60%, the density decreases level off and shrinkage accelerates. This phenomenon is consistent with Hurt's [74] hypothesis that shrinkage is due to solid state rearrangements facilitated by the removal of cross links during oxidation. Once the cross links have been sufficiently removed, shrinkage accelerates.

As discussed by Hurt [47], the observation of particle shrinkage versus conversion under regime I conditions has important implications. First, particle shrinkage by itself can no longer imply external mass transfer control or extreme pore diffusion limitations. Secondly, shrinkage will affect particle fragmentation. It was previously believed that particles undergoing regime I oxidation would react to some critical porosity and then fragment. Experiments performed in this lab indicate particle conversions up to 96% are

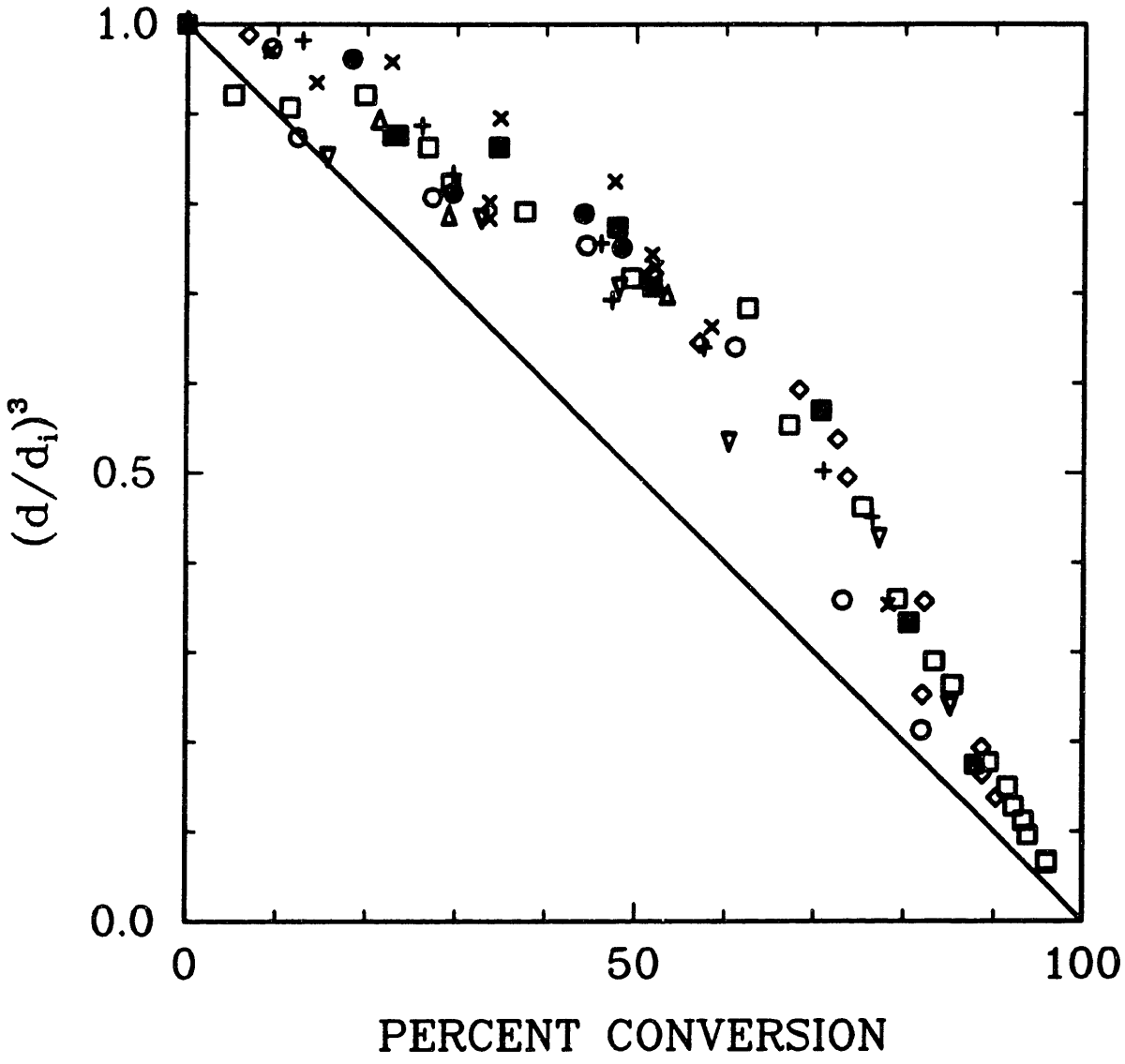

Figure 6.11 : Ratio of diameter to initial diameter cubed versus percent conversion for 13 separate, single particle, uncatalyzed "Spherocarb" oxidations performed in the EDTGA.

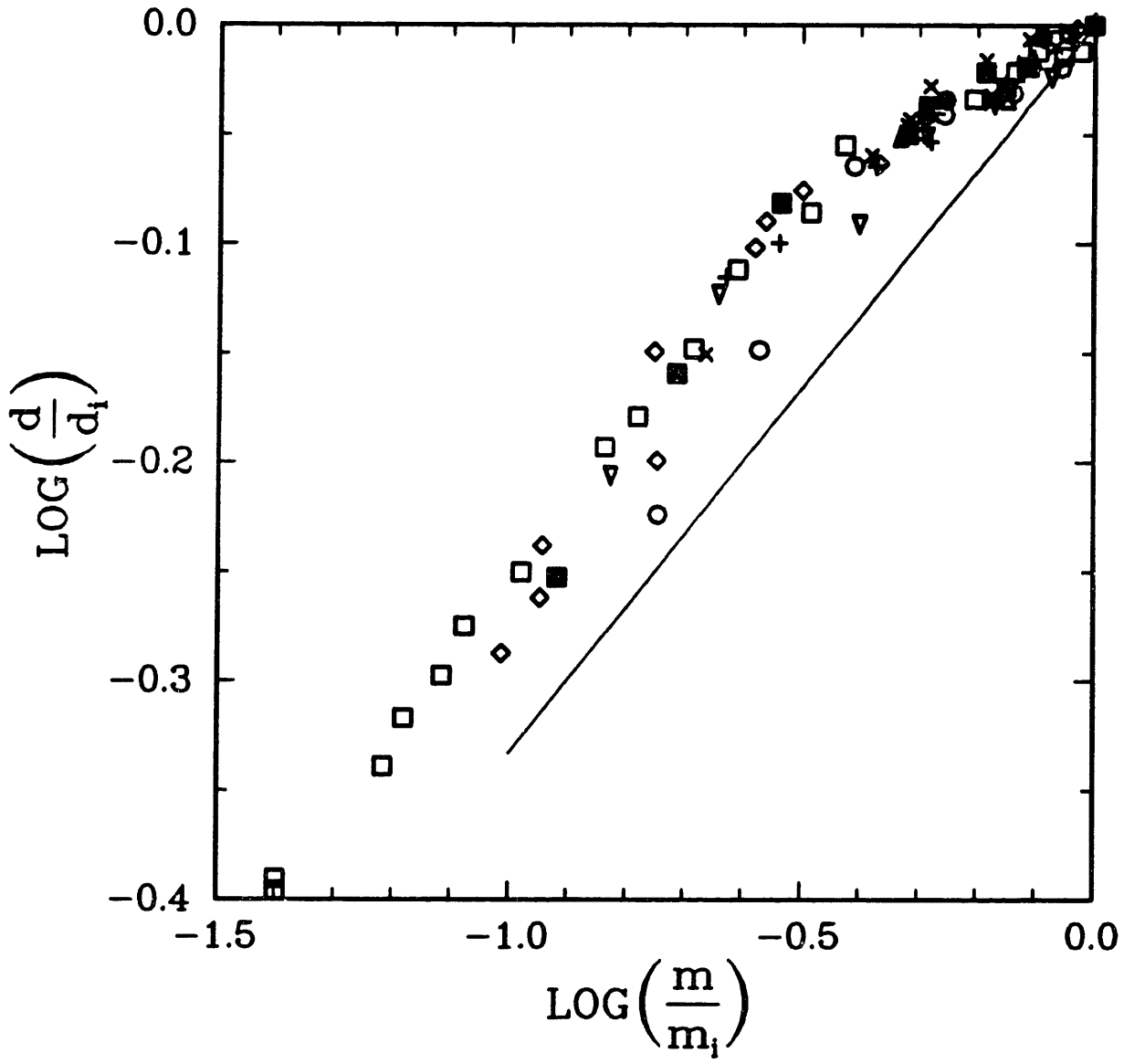

Figure 6.12 : Log of the ratio of diameter to initial diameter versus log of the ratio of mass to initial mass for 13 separate, single particle, uncatalyzed "Spherocarb" oxidations performed in the EDTGA.

possible without fragmentation.

It is believed that molecular rearrangements occur during oxidation of "Spherocarb" causing densification or graphitization of the original amorphous material. Using X-ray diffraction, Smith and Tyler [75] noticed a sharp increase in the diffuse graphite (002) band at a half scattering angle of about 25 degrees during combustion of a semi-anthracite coal at high temperatures (greater than 2000 K). It was unsuccessfully attempted to confirm graphitization of "Spherocarb" at low temperatures (700-900 K) using powder X-ray diffraction. Figure 6.13 is a plot of intensity of X-ray diffraction versus half scattering angle for graphite, unreacted "Spherocarb", 80% reacted "Spherocarb", and a glass microscope slide. The characteristic peak at 25 degrees is readily apparent from the graphite sample. As expected, the microscope slide is completely amorphous. Both the unreacted and 80% reacted "Spherocarb" are also amorphous. More importantly, however, is the fact that there is no noticable difference between the two samples, indicating that if graphitization is occurring during oxidation at low temperatures, it is not being detected. The partially reacted "Spherocarb" was reacted to approximately 80% conversion in a furnace at 750 K in an air environment. Figure 6.14 is a close up view of the diffractograms for both the unreacted and 80% converted "Spherocarb".

6.1.4 Surface area versus conversion.

Single particle surface areas are obtained using CO_2 adsorption and the Dubinin-Polanyi equation. The technique for surface area measurement is discussed in detail in section 3.3. The Dubinin-Polanyi plot for a

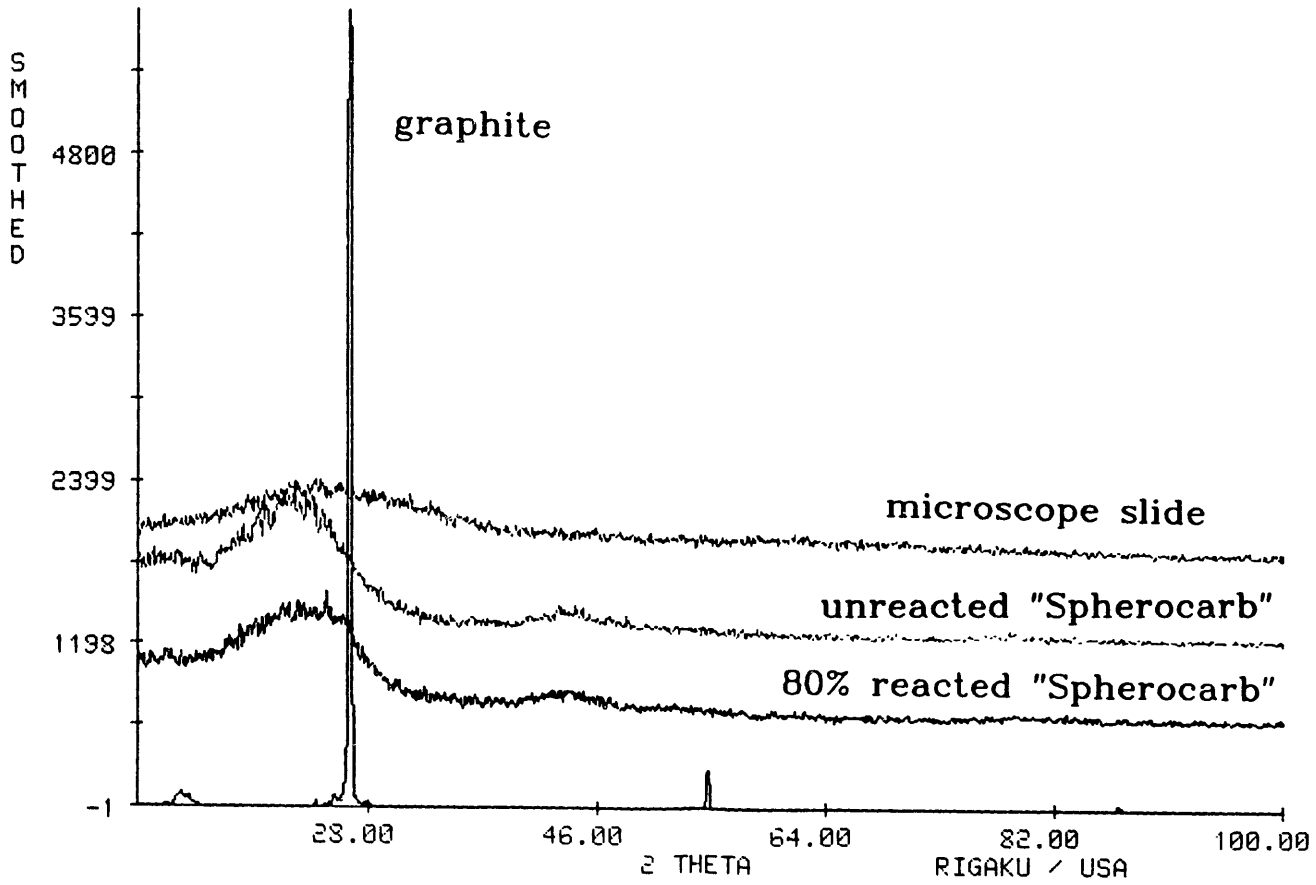

Figure 6.13 : Diffractogram of graphite, unreacted "Spherocarb", 80% reacted "Spherocarb", and a glass microscope slide.

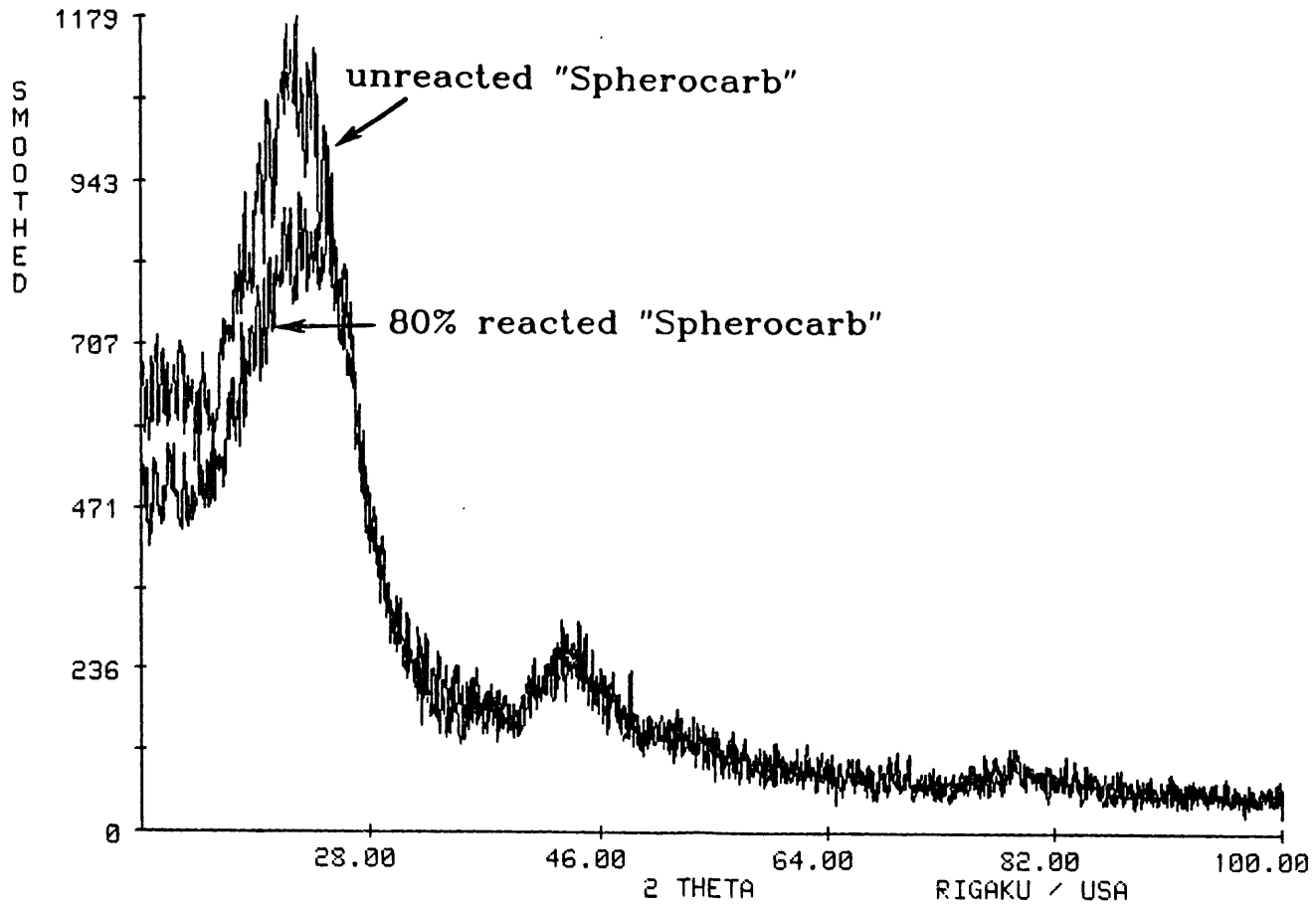

Figure 6.14 : Diffractogram of unreacted "Spherocarb" and 80% reacted "Spherocarb".

single 181 μm diameter "Spherocarb" at three different conversions is shown in Figure 6.15. The slopes of these three sets of data are relatively constant, but the intercept is decreasing, indicating a reduction in surface area. This particular "Spherocarb" particle was reacting in air at approxiamately 770 K. Figure 6.16 is a plot of specific surface area versus percent conversion for this particular "Spherocarb" oxidation. The specific surface area, measured in m^2 per gram of "Spherocarb" remaining increases from its initial value of 860 m^2/g to 990 m^2/g at approximately 15% conversion and then decreases with conversion.

Figure 6.17 is a plot of specific surface area versus percent conversion for eight separate, single particle, "Spherocarb" oxidations. Five of the runs were performed in oxygen, two in carbon dioxide, and one in air. The reaction time required for 50% conversion ranged from 2 to 16 min for the oxygen runs, from 20 to 30 min for the carbon dioxide runs, and 110 min for the air run. The temperatures corresponding to these reaction times are 750 to 830 K for oxygen, 1200 to 1250 K for carbon dioxide, and 770 K for air. The initial specific surface area varied from 821 to 1116 m^2/g, with the average initial surface area being 960 m^2/g. These surface areas can be compared to a value of 965 m^2/g obtained from a 0.294 g sample of "Spherocarb" particles from Hurt [36] in a conventional volumetric adsorption apparatus. The surface area appears to increase slightly up to a conversion of 10-15% and then monotonically decrease to an average value of 660 m^2/g at about 81% conversion. A value of 647 m^2/g was obtained at 65% conversion from Hurt [36] using a conventional volumetric adsorption apparatus.

The data indicate that "Spherocarb" surface area

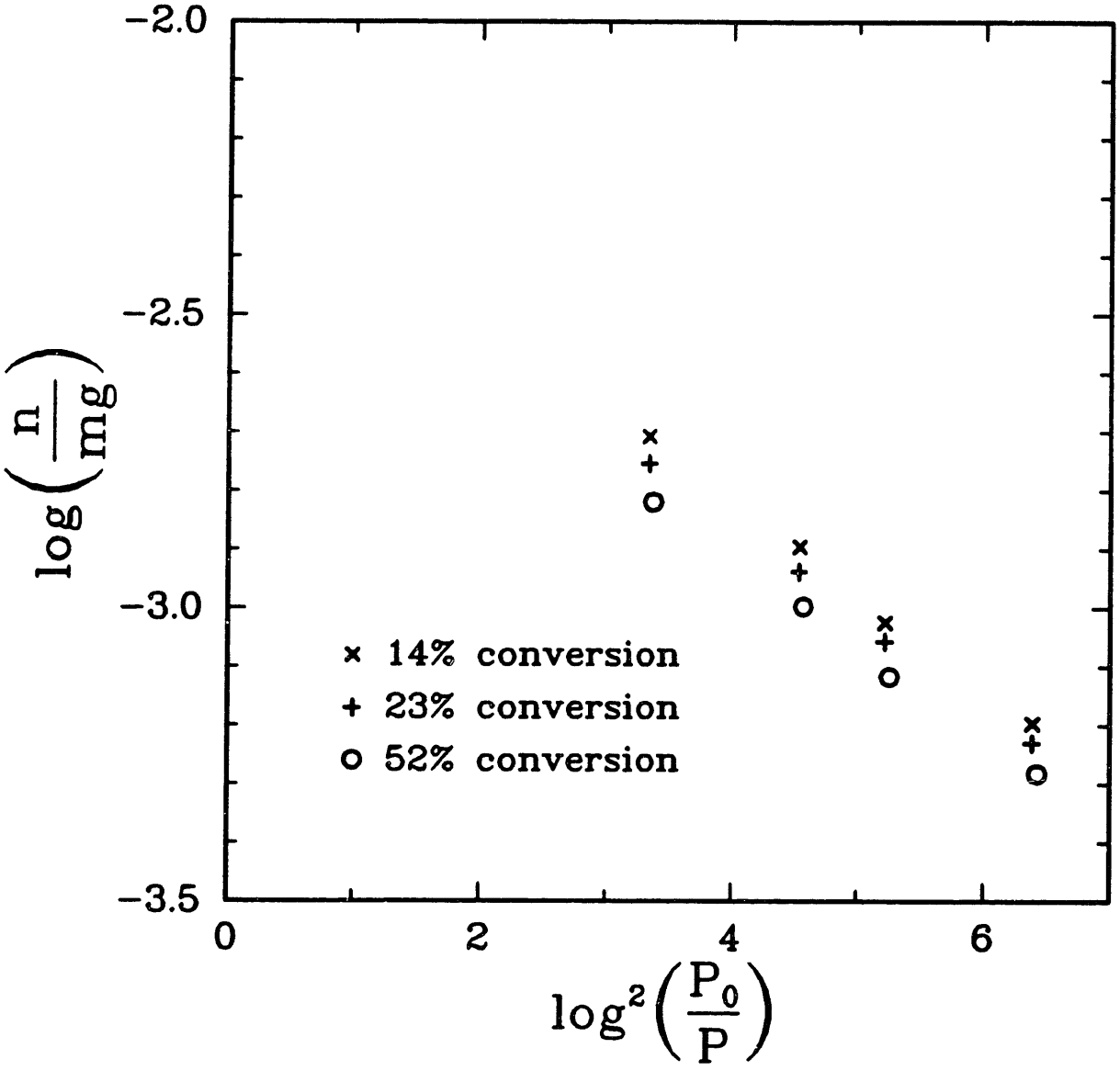

Figure 6.15 : Dubinin–Polanyi plot for a single, uncatalyzed "Spherocarb" particle at three different conversions.

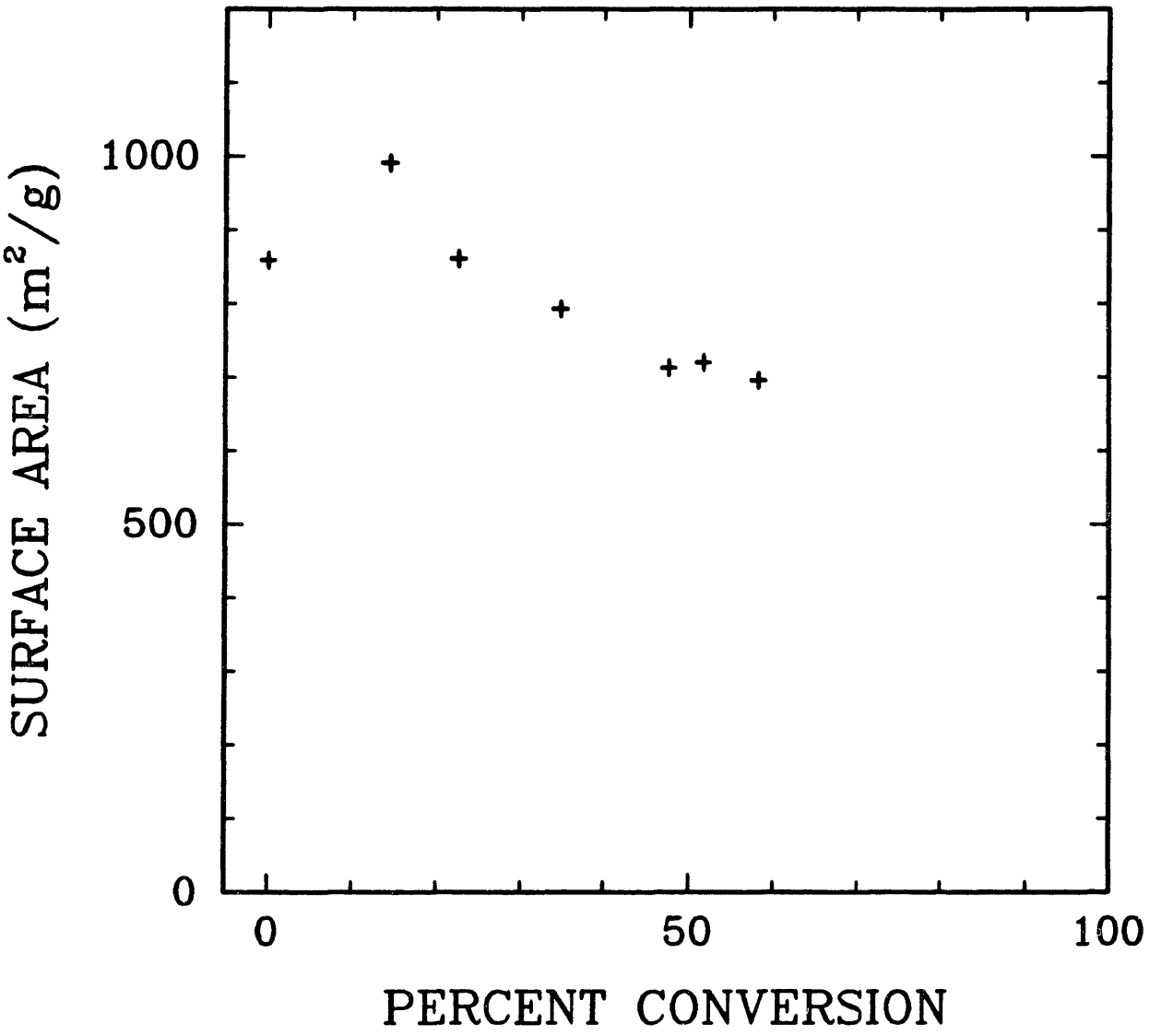

Figure 6.16 : Surface area versus percent conversion for a single, uncatalyzed "Spherocarb" particle reacting in air in the EDTGA at 770 K.

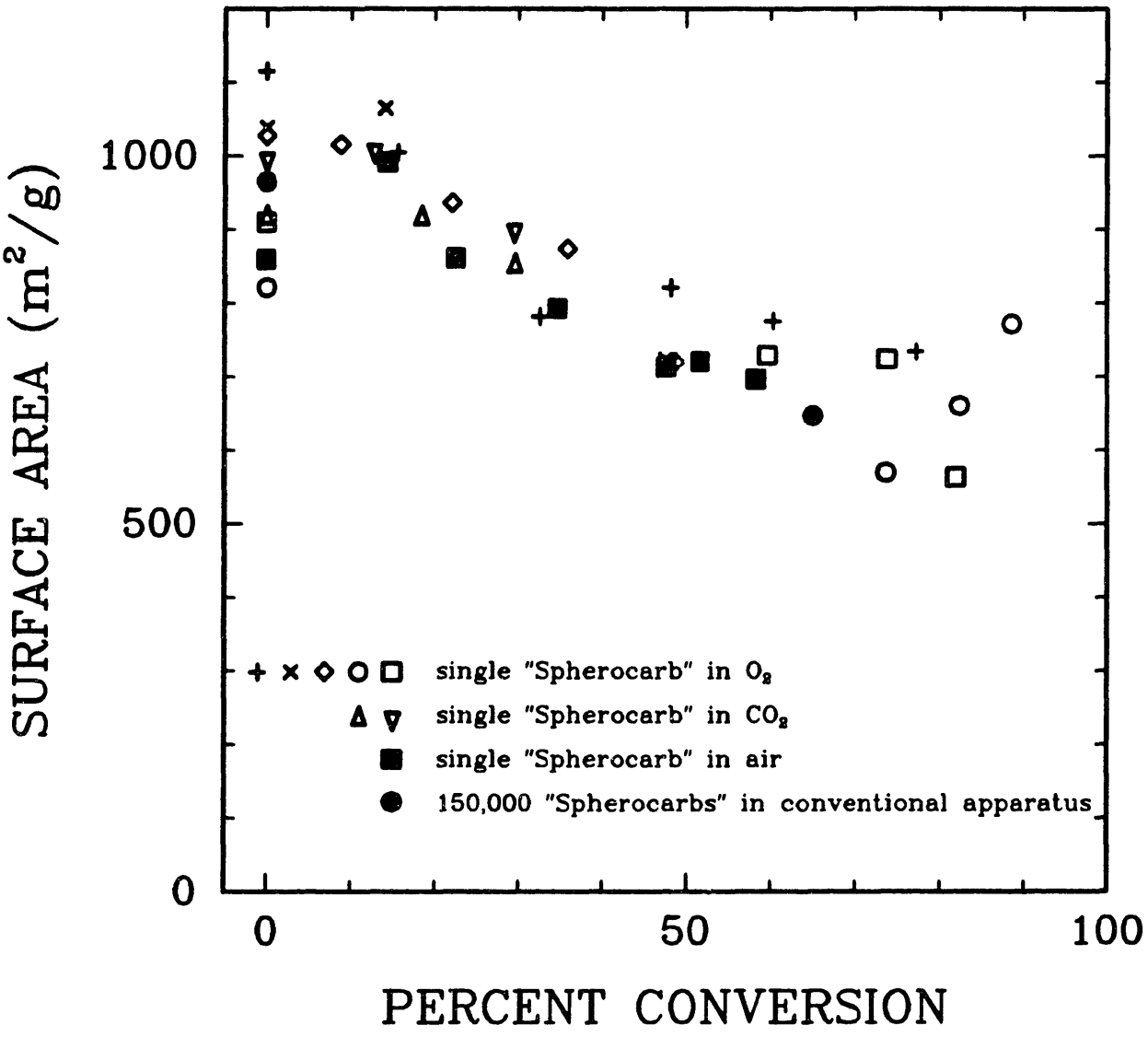

Figure 6.17 : Specific surface area versus percent conversion for eight separate, single particle, uncatalyzed "Spherocarb" oxidations performed in the EDTGA.

evolution is not a function of temperature or reacting gas, but only a function of conversion. It is also interesting to note that Gavalas' random pore model predicts an increase in specific surface area versus conversion. Hurt et al. [47] recently resolved the discrepancy between the experimental results and the Gavalas model prediction by incorporating shrinkage into Gavalas' model. By accounting for particle shrinkage, the decrease in surface area could now be explained. The decreasing surface area emphasizes another important implicatin of shrinkage in char oxidation. Shrinkage can play a major role in the surface area evolution of a reacting char particle.

6.1.5 Reactivities.

A total of 19 separate, uncatalyzed "Spherocarb" particles were reacted in air. Particle temperatures ranged from 740 to 1170 K and the corresponding times required for 50% conversion ranged from 2.2 to 17,000 sec. Four of the 19 runs will be discussed individually in this section. The entire 19 runs will be summarized on an Arrhenius plot later in this section.

Figures 6.18, 6.19, and 6.20 correspond to a 204 μm diameter "Spherocarb" particle reacting in air at a temperature of 764 K. Figure 6.18 shows the rms value of the 2 μm signal, the rms value of the 4 μm signal, and the log ratio of the 2 μm signal to the 4 μm signal. Data was collected at a rate of 1 point every 4.7 sec. The average value of the log ratio signal is 0.134 with a standard deviation of 0.087. Figure 6.19 is a plot of the balancing voltage versus time for the same reaction. After heating begins, the initial balancing voltage of 117 volts is reduced immediately to 108 volts due to the

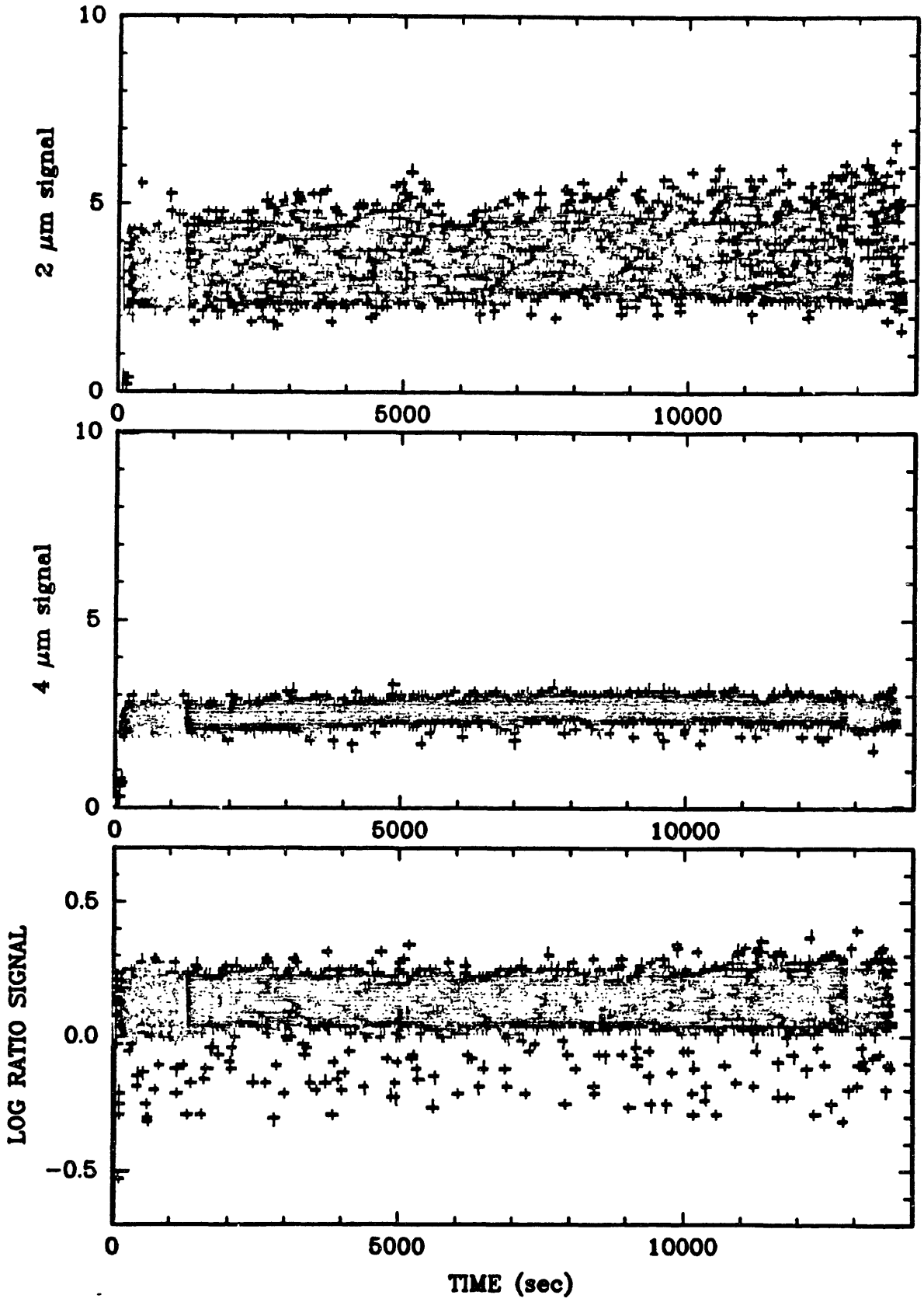

Figure 6.18 : 2 μm, 4 μm, and log ratio signals versus time for a 204 μm diameter, uncatalyzed "Spherocarb" reacting in air at 764 K.

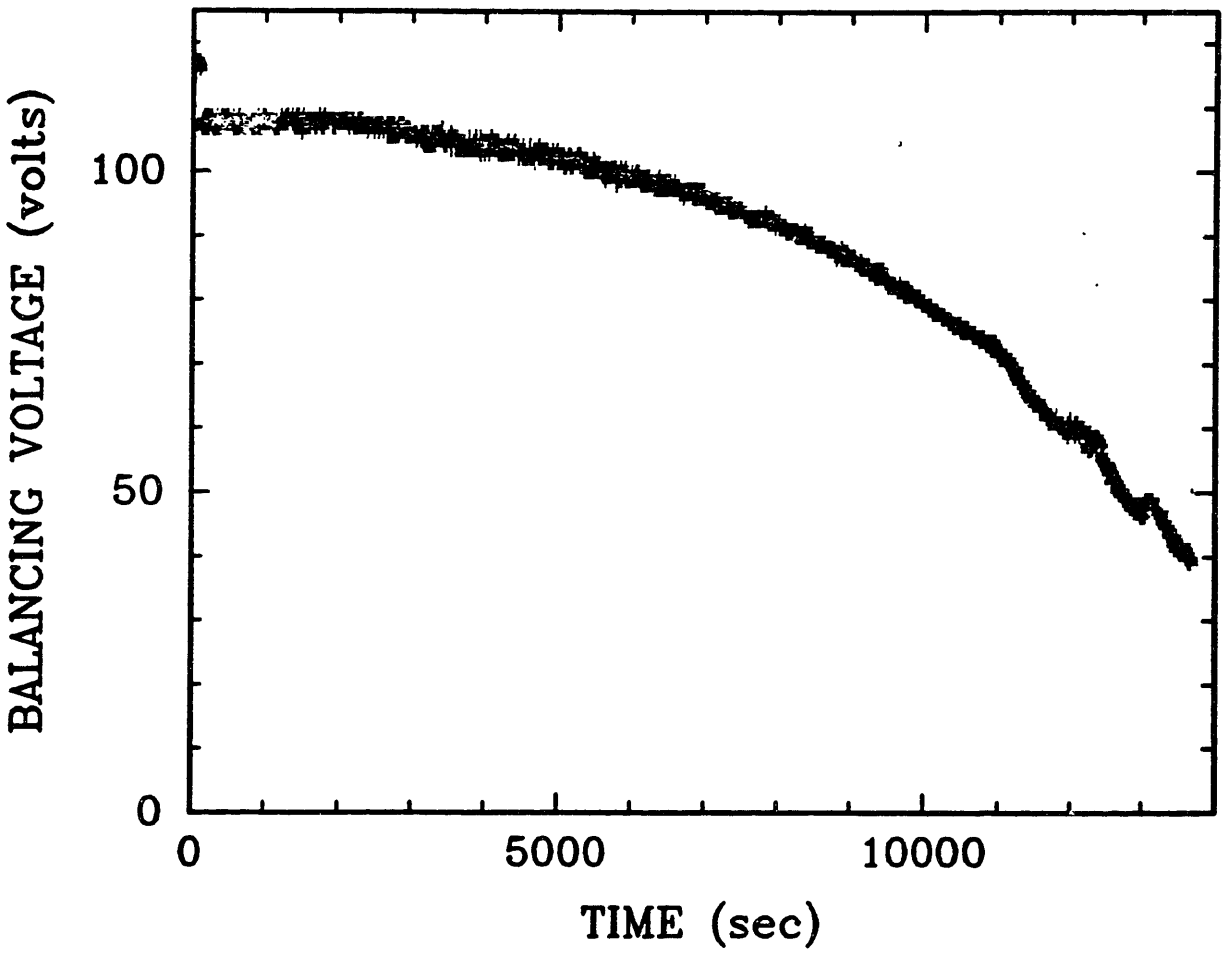

Figure 6.19 : Experimentally measured balancing voltage versus time for a 204 μm diameter, uncatalyzed "Spherocarb" particle reacting in air in the EDTGA at 764 K.

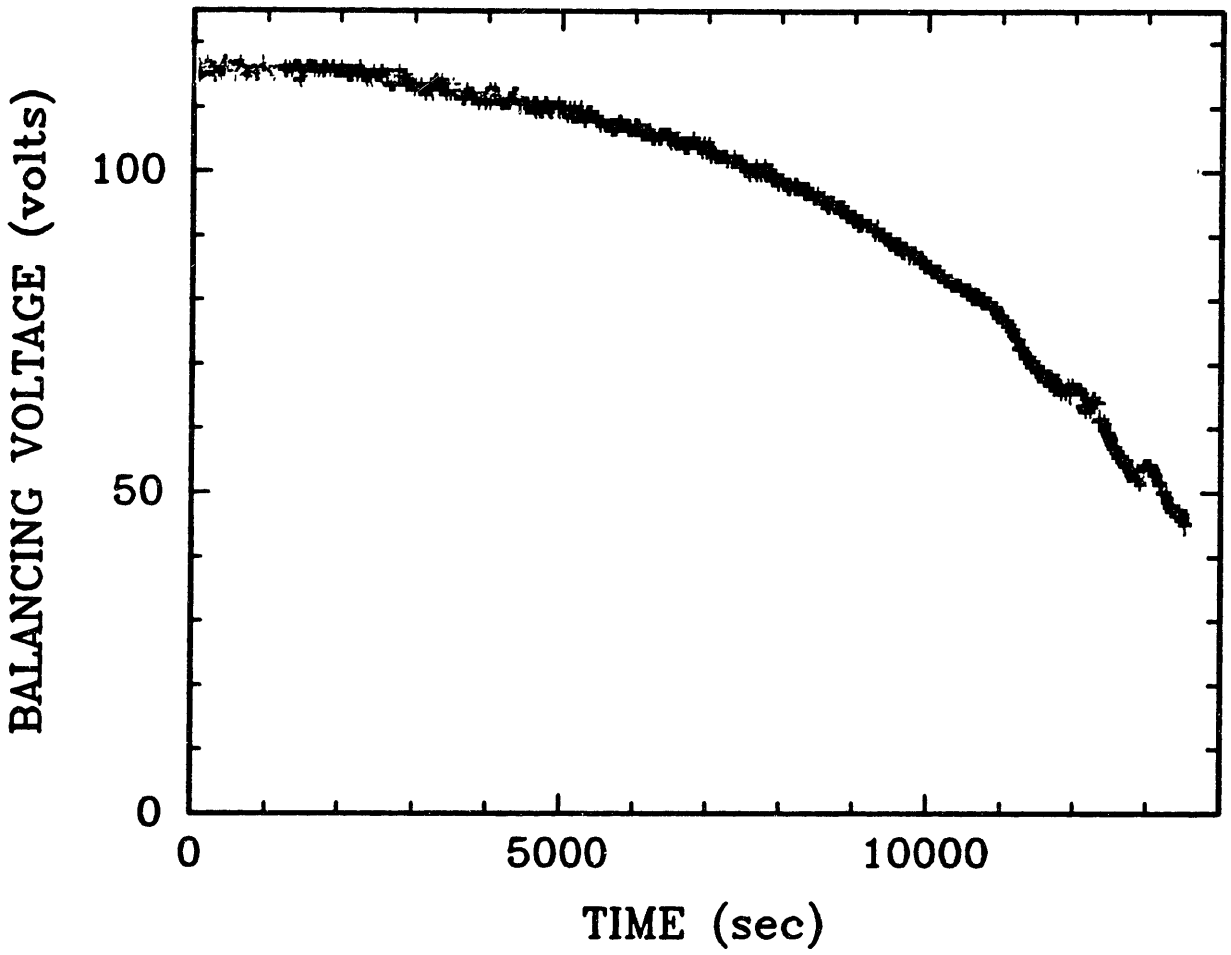

Figure 6.20 : "True" balancing voltage (after correcting for the natural convective drag force) versus time for a 204 μm diameter, uncatalyzed "Spherocarb" particle reacting in air in the EDTGA at 764 K.

natural convective drag force. In Figure 6.20, the natural convective drag force is cancelled out and the "true" balancing voltage is plotted versus time. Also, zero time is shifted to the moment heating commences. The natural convective drag force is predicted by the correlation of the numerical solution presented in equation 4.30. From Figure 6.20, the time required for 50% conversion can be calculated to be 12,600 sec or approximately 3.5 hours.

Figures 6.21, 6.22, and 6.23 are plots of the 2 μm, 4 μm, log ratio, balancing voltage, and corrected balancing voltage signals versus time for a 207 μm diameter "Spherocarb" particle reacting in air at a temperature of 804 K. For these plots data was collected at a rate of 1 point every 0.47 sec. The average value of the log ratio signal is 0.064 with a standard deviation of 0.107. The time required for 50% conversion is 2420 sec for this reaction.

Figures 6.24, 6.25, and 6.26 are plots of the 2 μm, 4 μm, log ratio, balancing voltage, and corrected balancing voltage signals versus time for a 201 μm diameter "Spherocarb" particle reacting in air at a temperature of 948 K. For these plots data was collected at a rate of 1 point every 0.47 sec. The average value of the log ratio signal is 0.394 with a standard deviation of 0.054. The time required for 50% conversion is 106 sec for this reaction.

Figures 6.27, 6.28, and 6.29 are plots of the 2 μm, 4 μm, log ratio, balancing voltage, and corrected balancing voltage signals versus time for a 162 μm diameter "Spherocarb" particle reacting in air at a temperature of 1033 K. For these plots data was collected

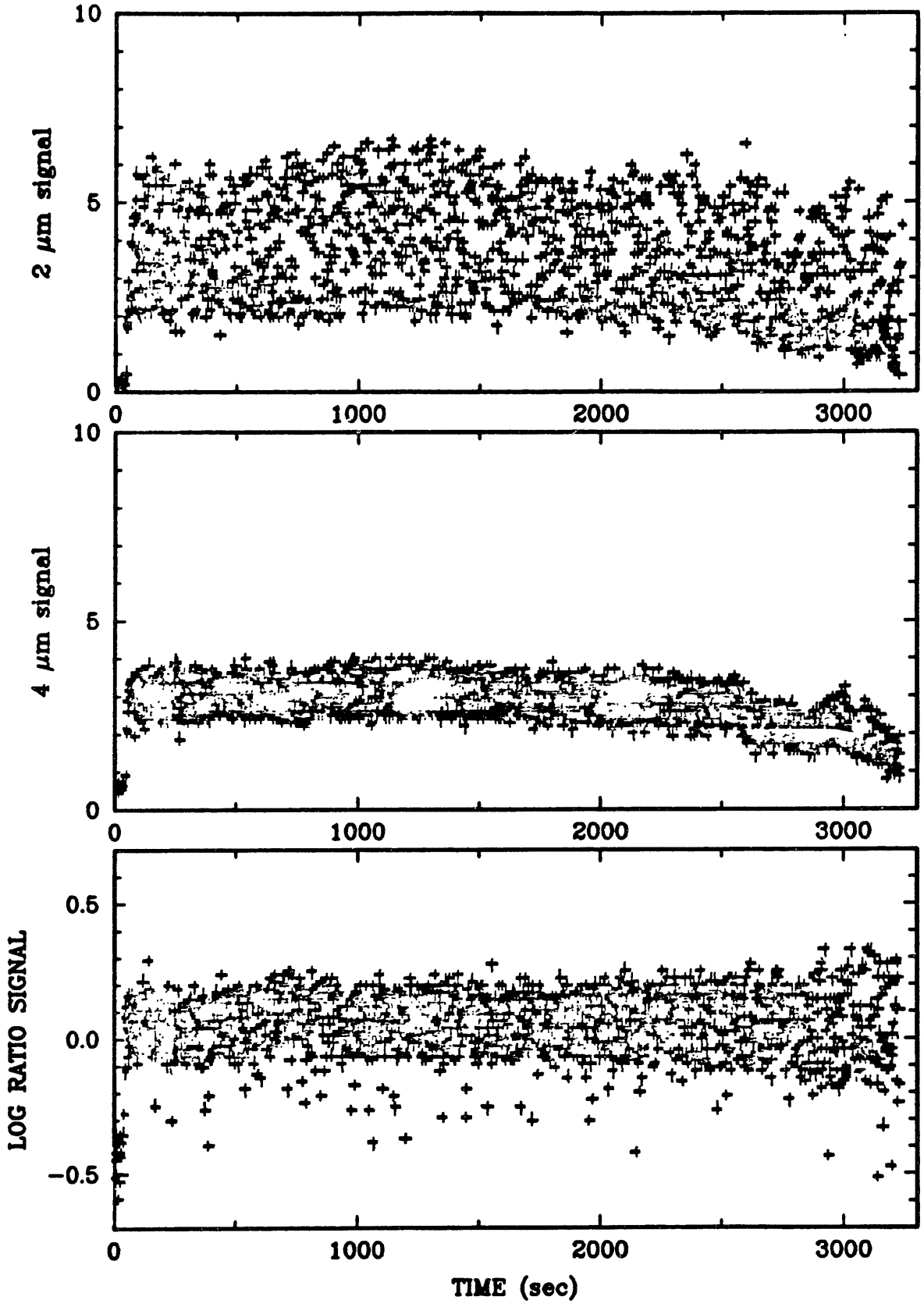

Figure 6.21 : 2 μm, 4 μm, and log ratio signals versus time for a 207 μm diameter, uncatalyzed "Spherocarb" reacting in air at 804 K.

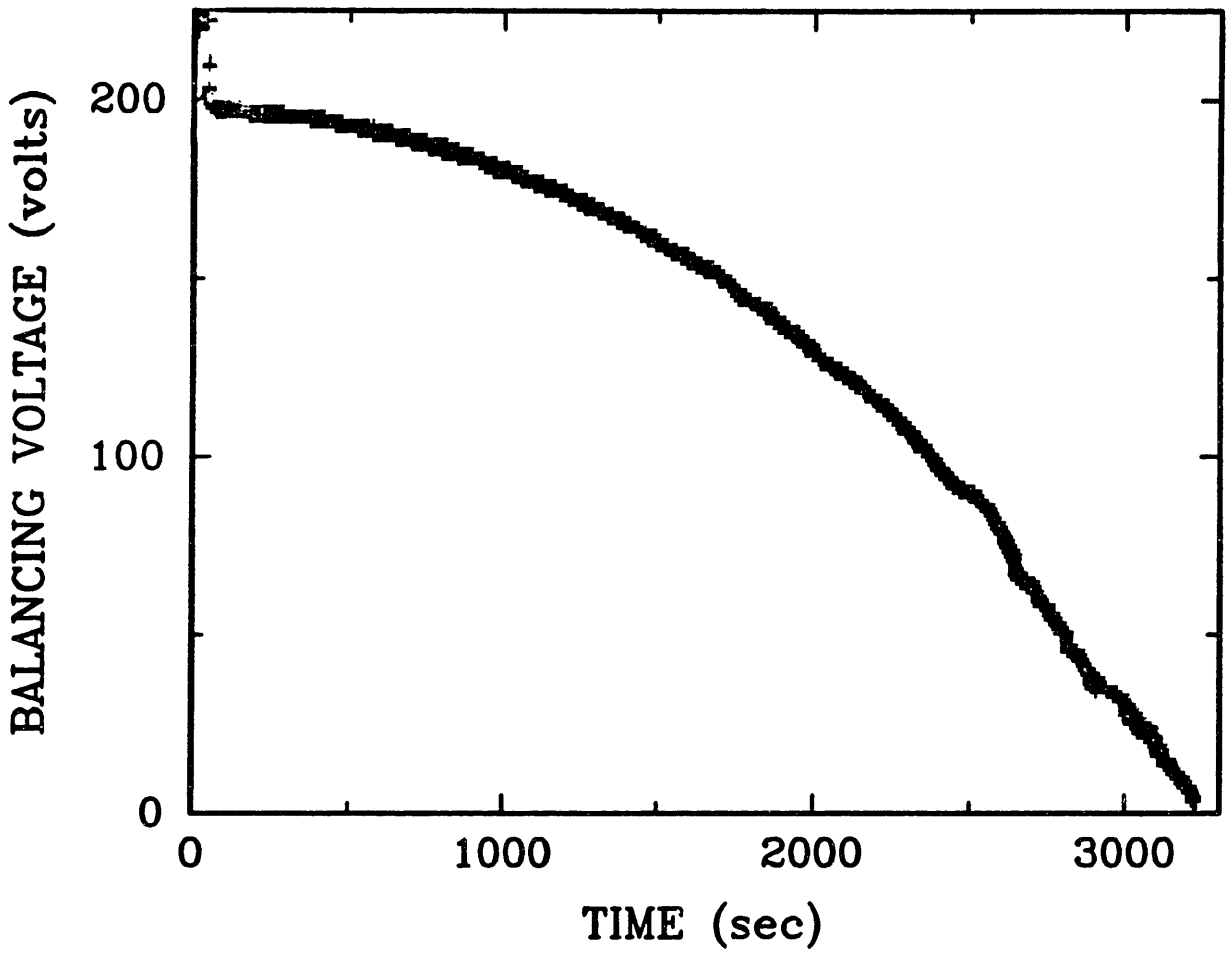

Figure 6.22 : Experimentally measured balancing voltage versus time for a 207 μm diameter, uncatalyzed "Spherocarb" particle reacting in air in the EDTGA at 804 K.

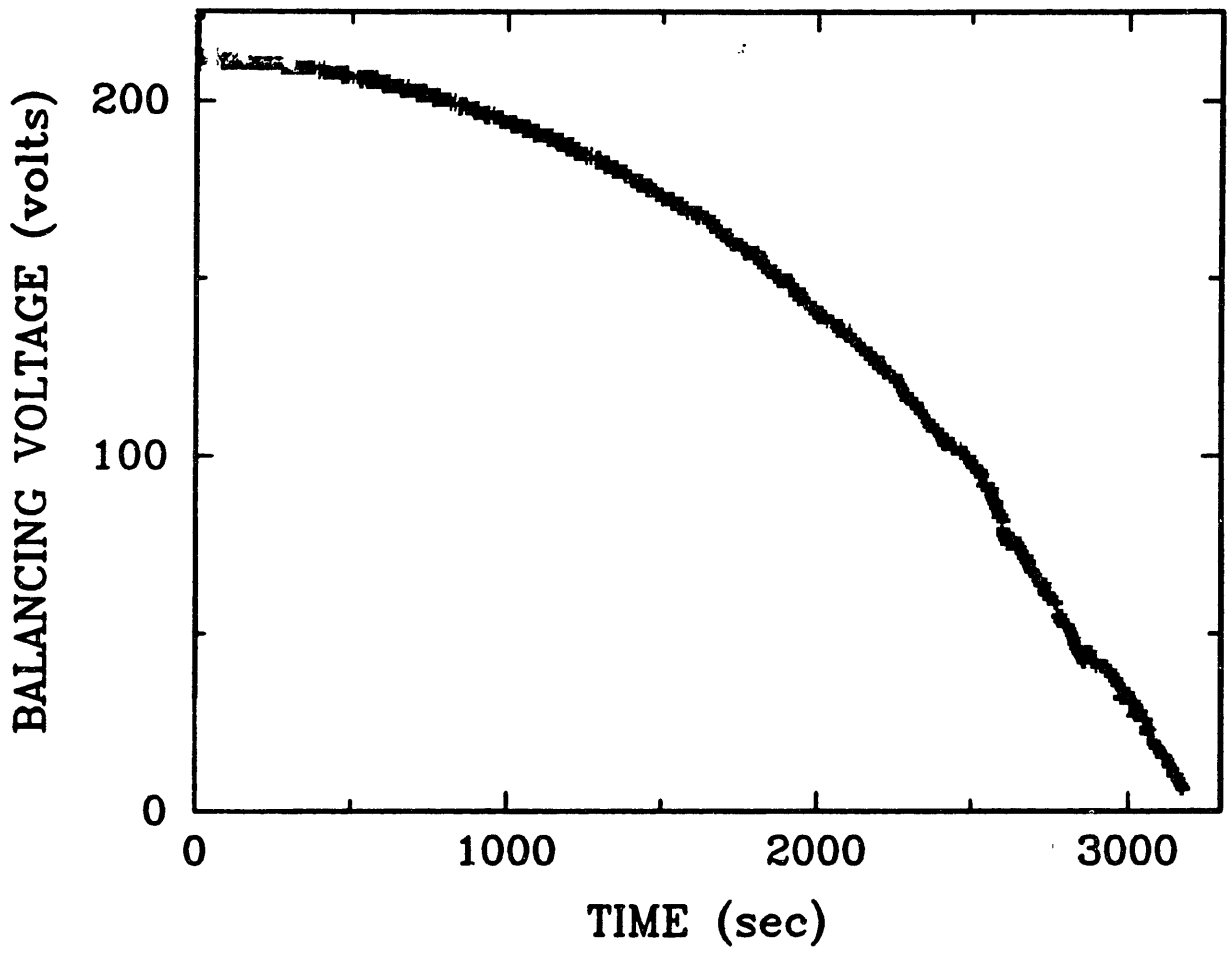

Figure 6.23 : "True" balancing voltage (after correcting for the natural convective drag force) versus time for a 207 μm diameter, uncatalyzed "Spherocarb" particle reacting in air in the EDTGA at 804 K.

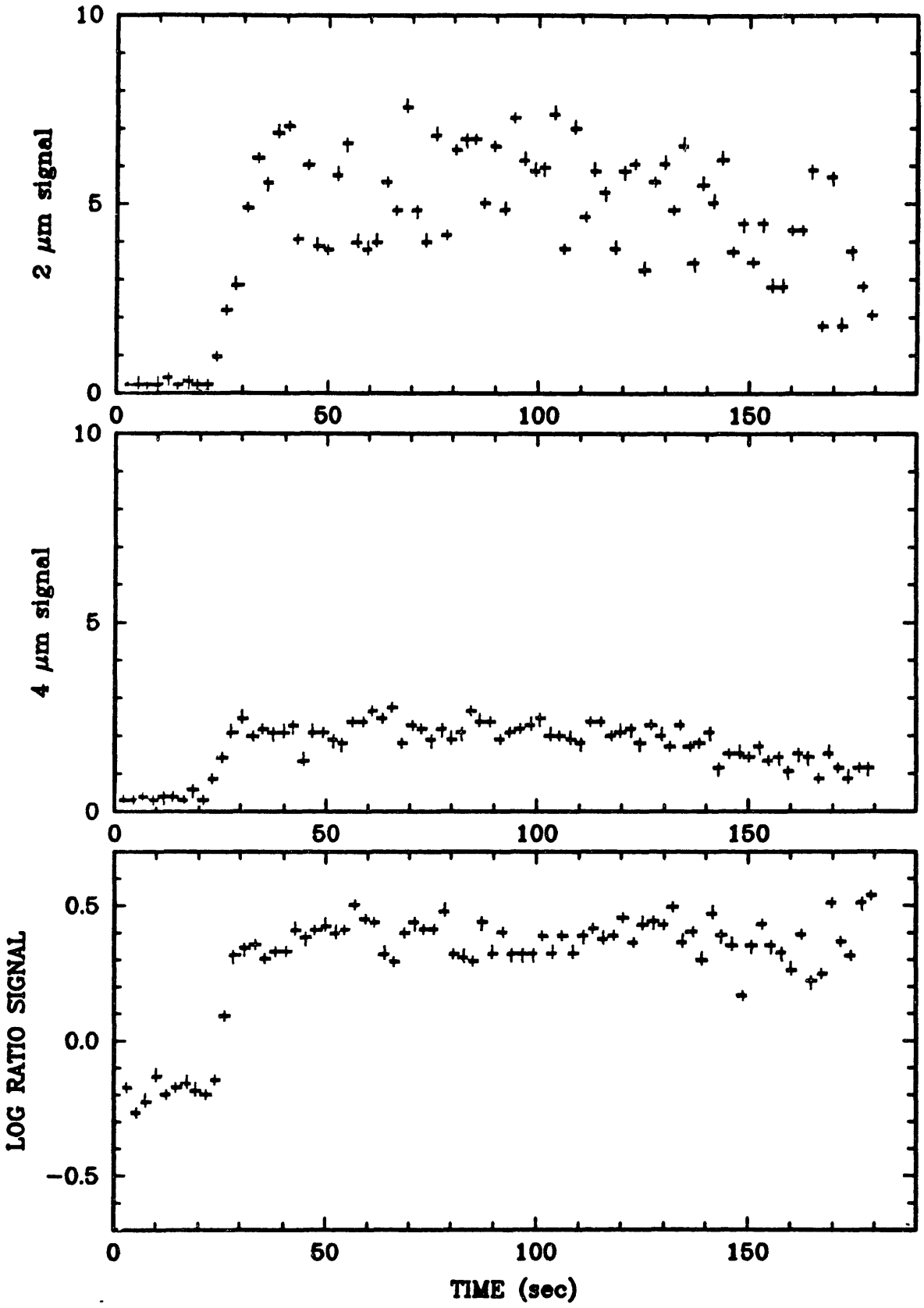

Figure 6.24 : 2 μm, 4 μm, and log ratio signals versus time for a 201 μm diameter, uncatalyzed "Spherocarb" reacting in air at 948 K.

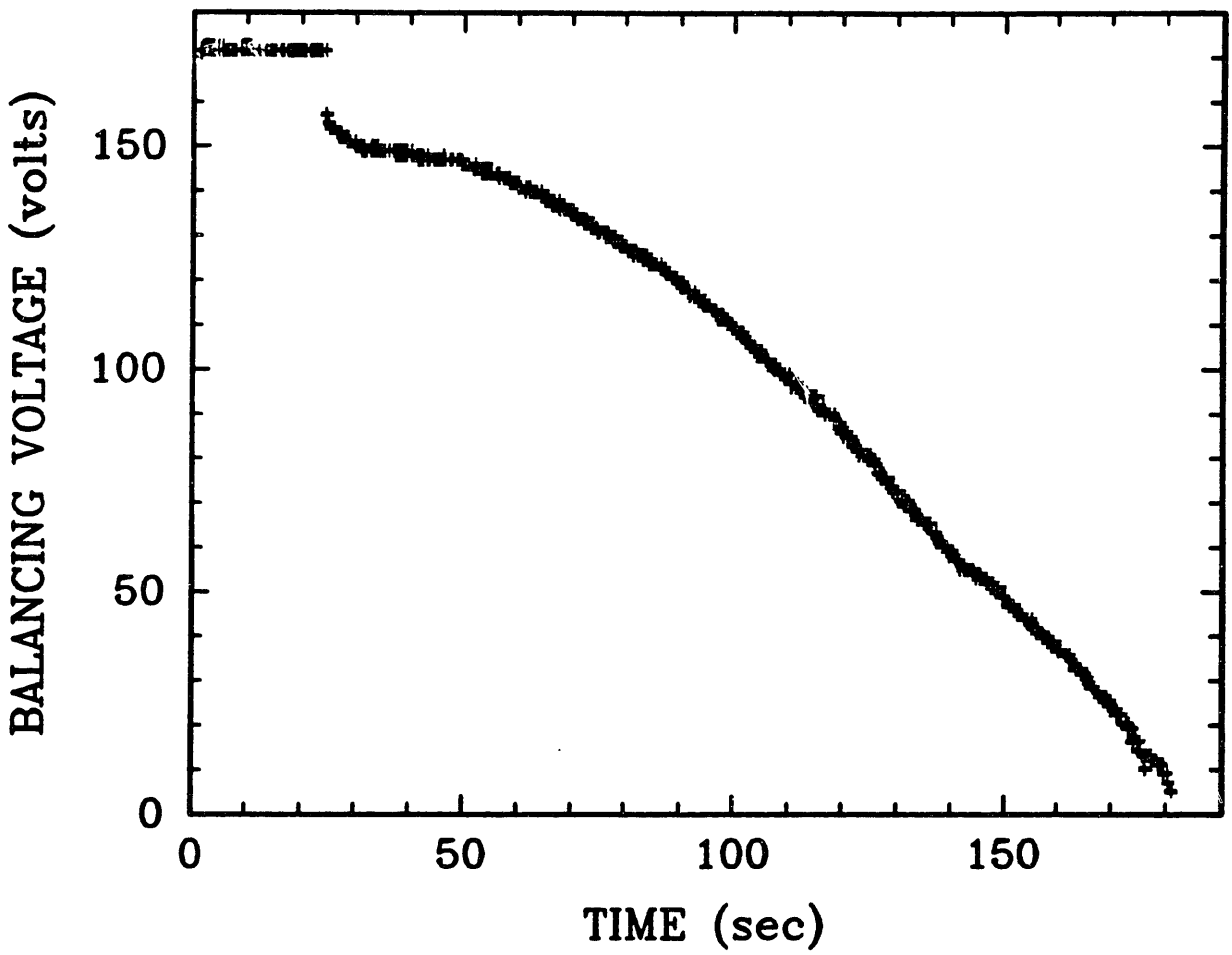

Figure 6.25 : Experimentally measured balancing voltage versus time for a 201 μm diameter, uncatalyzed "Spherocarb" particle reacting in air in the EDTGA at 948 K.

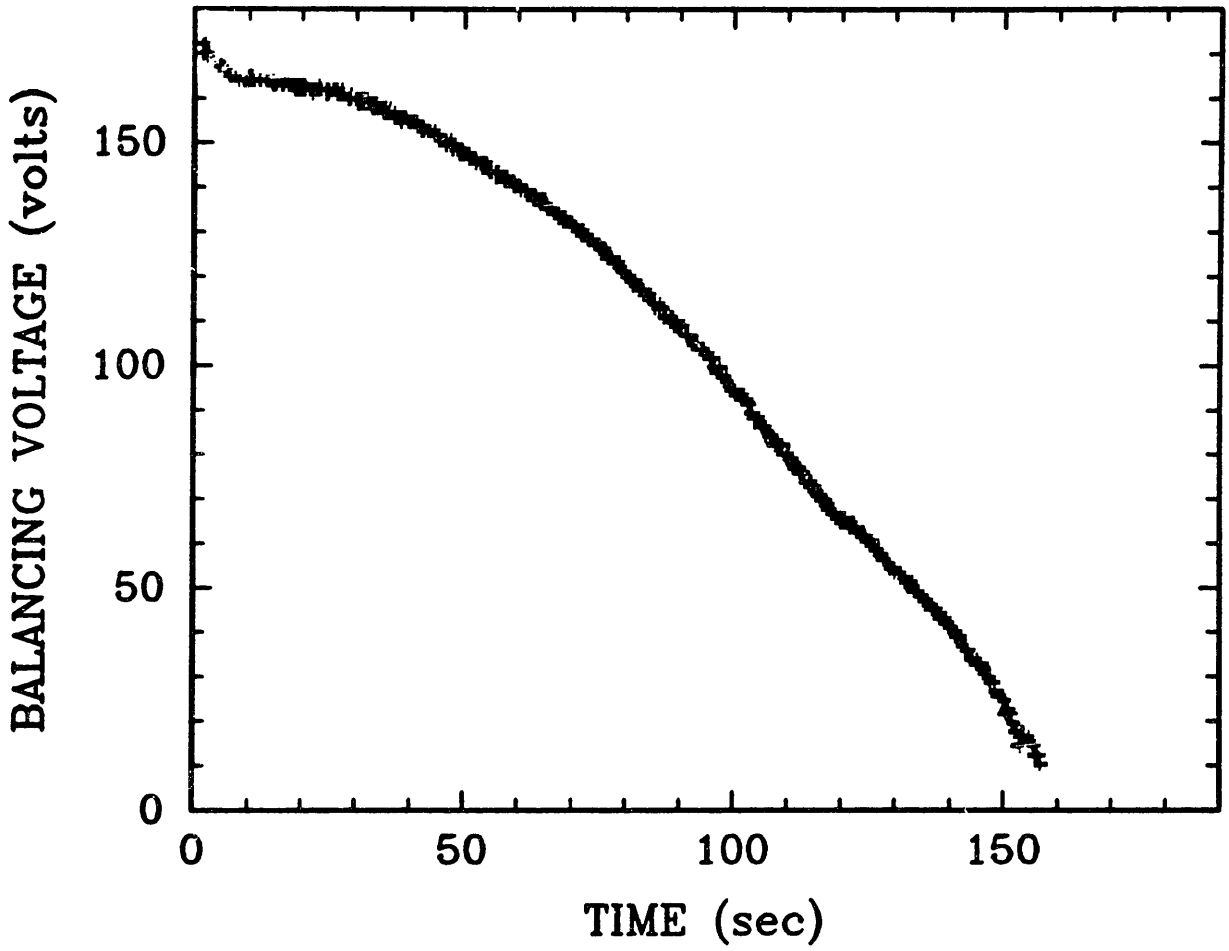

Figure 6.26 : "True" balancing voltage (after correcting for the natural convective drag force) versus time for a 201 μm diameter, uncatalyzed "Spherocarb" particle reacting in air in the EDTGA at 948 K.

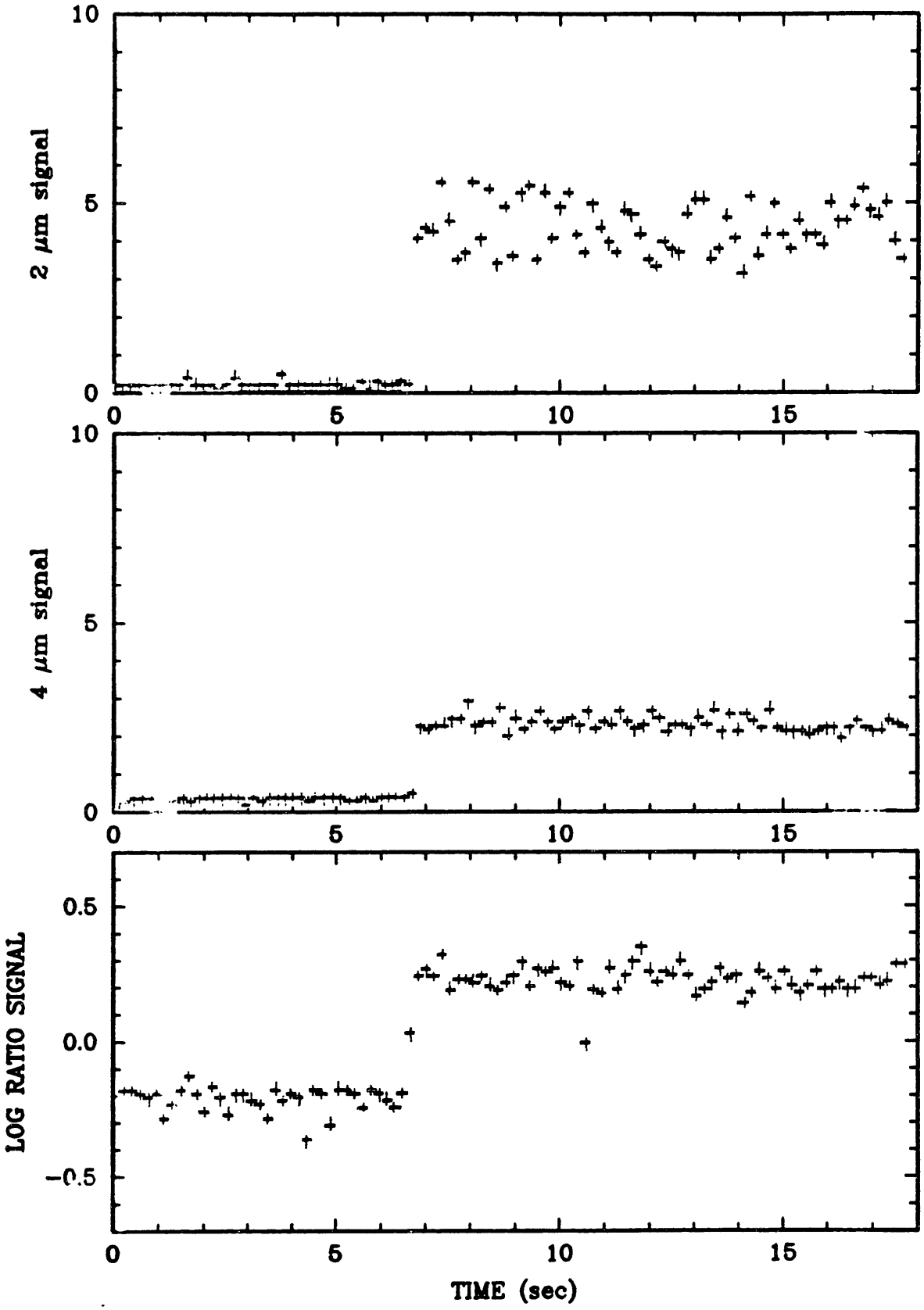

Figure 6.27 : 2 μm, 4 μm, and log ratio signals versus time for a 162 μm diameter, uncatalyzed "Spherocarb" reacting in air at 1033 K.

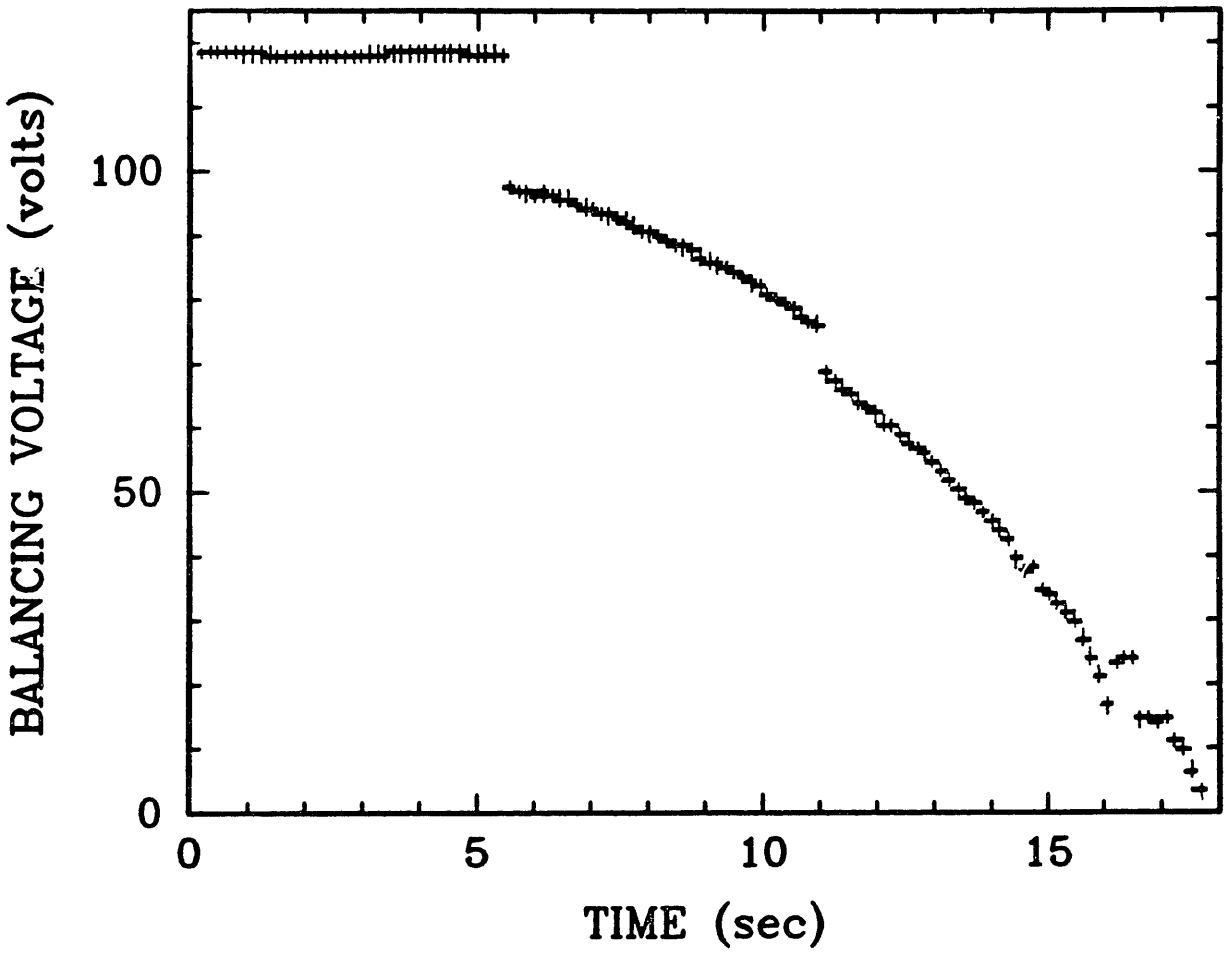

Figure 6.28 : Experimentally measured balancing voltage versus time for a 162 μm diameter, uncatalyzed "Spherocarb" particle reacting in air in the EDTGA at 1033 K.

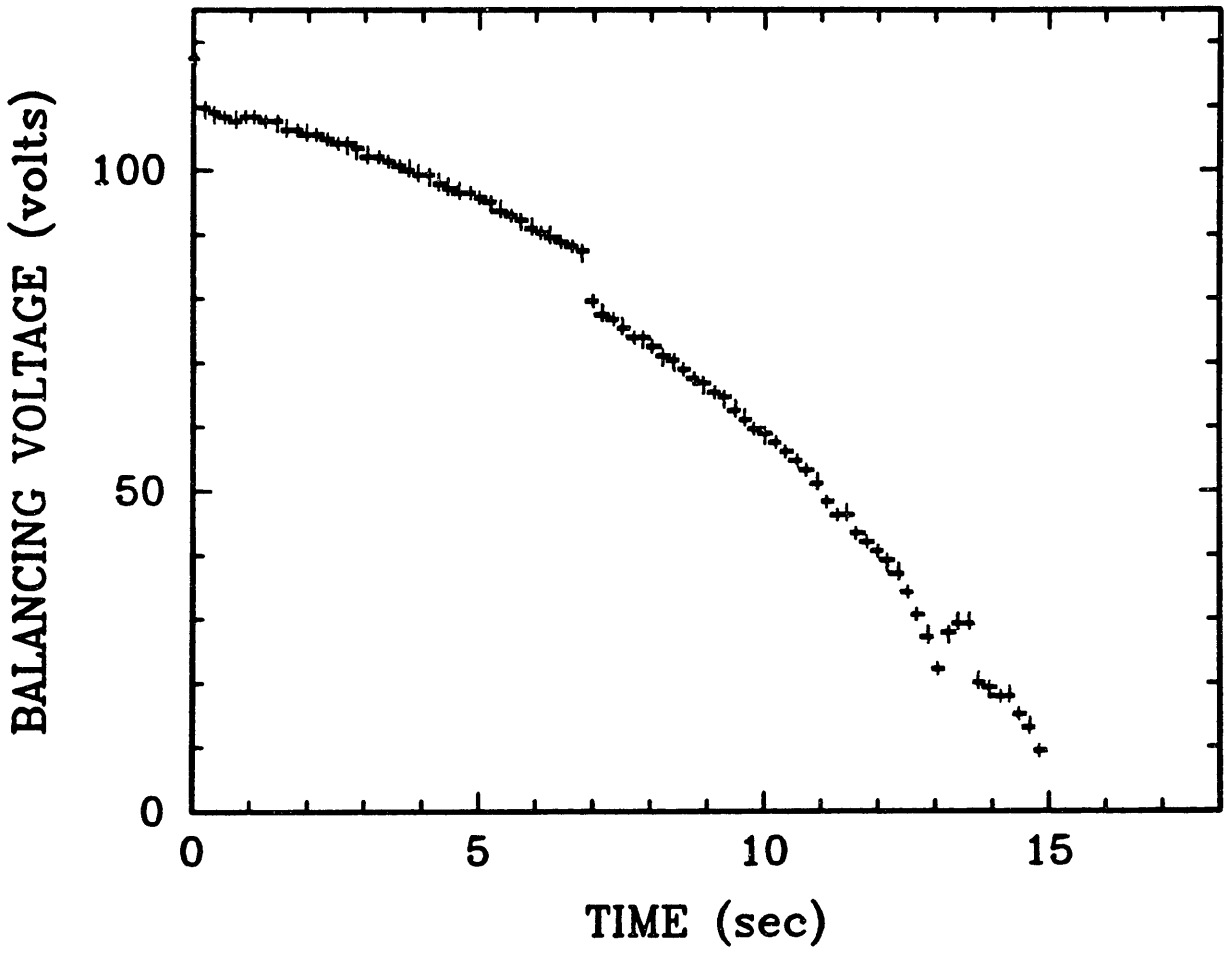

Figure 6.29 : "True" balancing voltage (after correcting for the natural convective drag force) versus time for a 162 μm diameter, uncatalyzed "Spherocarb" particle reacting in air in the EDTGA at 1033 K.

at a rate of 1 point every 0.47 sec. The average value of the log ratio signal is 0.241 with a standard deviation of 0.049. The time required for 50% conversion is 11.4 sec for this reaction.

Figure 6.30 is a plot of the natural log of $1/\tau_{0.5}$ versus 1/T for all of the 19 "Spherocarb" particles that were reacted in air. $\tau_{0.5}$ is defined as the time in seconds required for 50% of the particle to have reacted. In this figure, the solid black circles represent data collected by Floess [40] and Hurt [41] in a conventional TGA. Their data cover the range of $\tau_{0.5}$ = 372 to 167,900 sec, approximately 2.5 orders of magnitude in reaction rate. The x's represent data collected in the EDTGA. These data cover the range of $\tau_{0.5}$ = 2.2 to 17,000 sec, almost 4 orders of magnitude in reaction rate. More significant, however, is the fact that the EDTGA results are reproducible at rates over 2 orders of magnitude faster than obtainable in a conventional TGA. Both TGA and EDTGA results yield an activation energy of 36 kcal/mol for the "Spherocarb"-air reaction. These results indicate for the first time that the EDTGA is a viable tool in studying the kinetics of high temperature gas-solid reactions.

Figure 6.31 is the same plot as Figure 6.30 with the addition of seven "Spherocarb" runs performed in oxygen.

6.1.6 Density distribution.

The single particle density measurements presented in this section were obtained by measuring particle mass by the aerodynamic drag force technique discussed in detail in

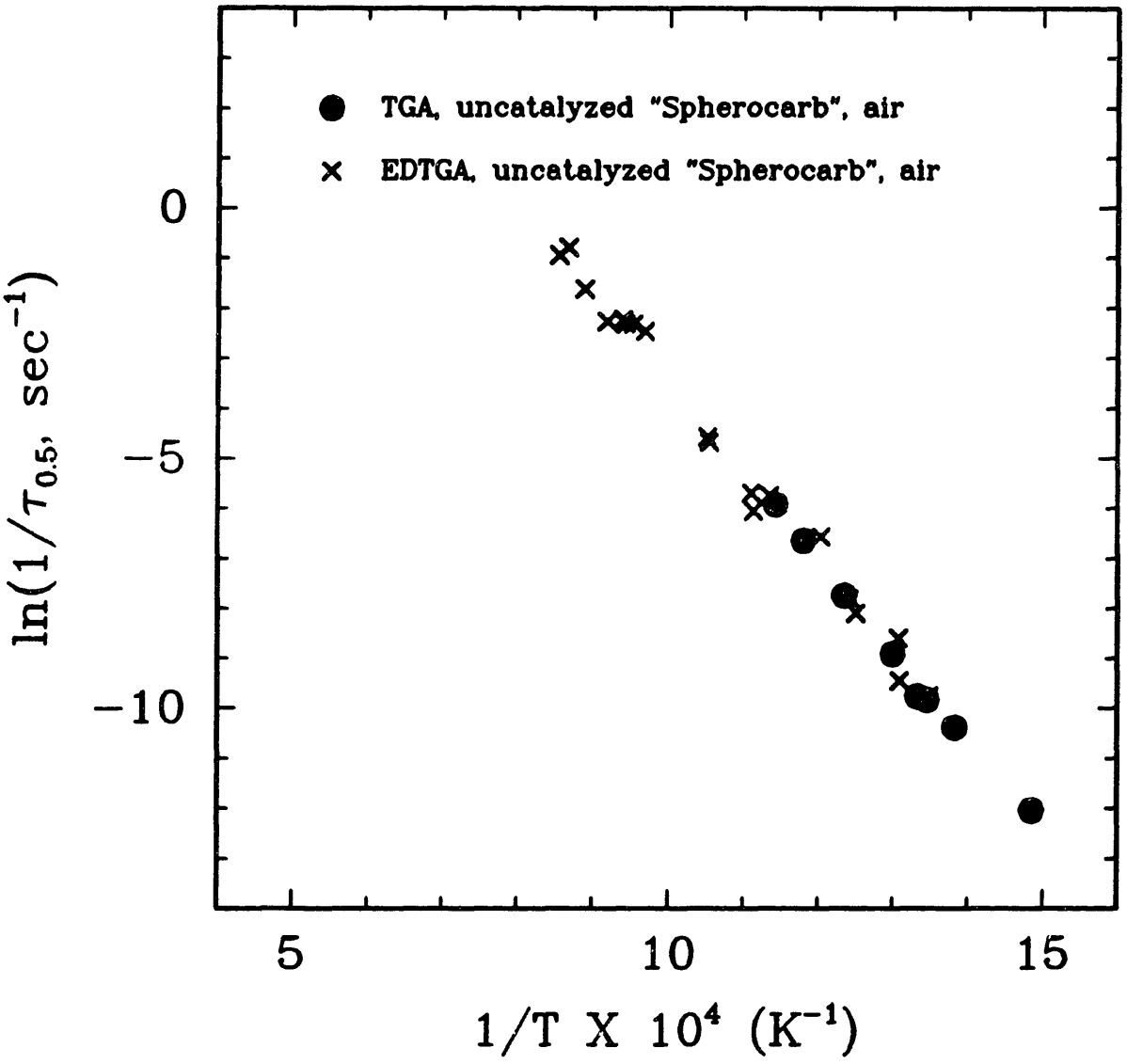

Figure 6.30 : $\ln(1/\tau_{0.5})$ versus 1/T for 19 separate, single particle, uncatalyzed "Spherocarb"–air reactions performed in the EDTGA and eight "Spherocarb"–air reactions performed in a conventional TGA.

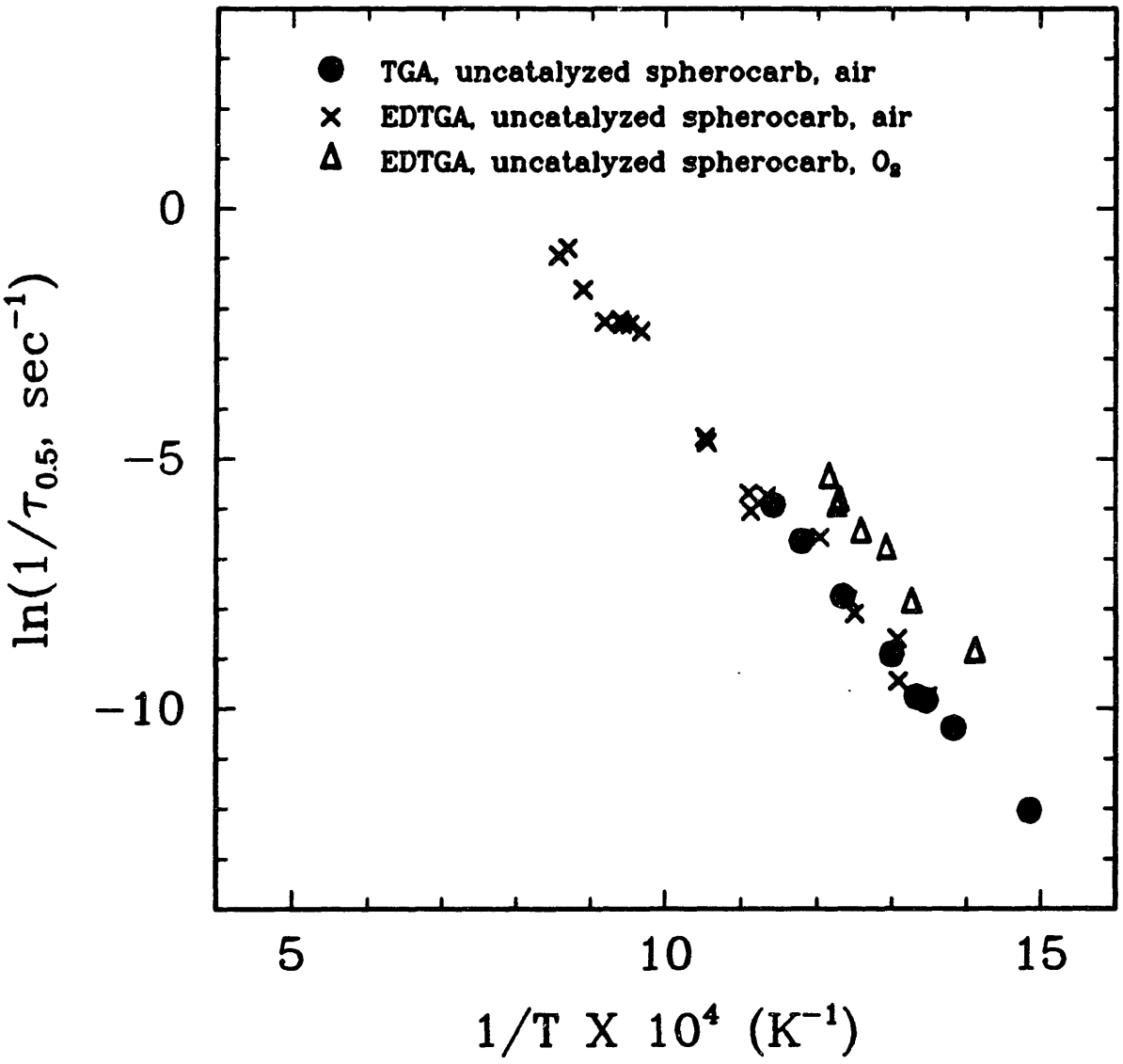

Figure 6.31 : $\ln(1/\tau_{0.5})$ versus 1/T for 19 single particle uncatalyzed "Spherocarb"–air reactions performed in the EDTGA, 7 single particle uncatalyzed "Spherocarb"–O_2 reactions performed in the EDTGA, and 8 "Spherocarb"–air reactions performed in a conventional TGA.

section 3.2 and dividing by the volume of a sphere, $(\pi/6)d^3$, where the sphere diameter, d, was measured by an optical microscope. A sample of 35 particles in the size range 60-100 U.S. Mesh has been tested by D'Amore et al. [76]. The discrete distributions of the "Spherocarb" particle's density on a number basis, where $f_n d\rho$ is the number fraction of particles with a density of ρ to $\rho+d\rho$, and on a mass basis, where $f_m d\rho$ is the mass fraction of particles with a density ρ to $\rho+d\rho$ are reported in Figure 6.32. The results indicate that the "Spherocarb" particle density varies from a minimum of 0.42 to a maximum of 0.80 g/cm^3. The mean particle densities on numerical and on mass bases are 0.62 and 0.64 g/cm^3, respectively. No correlation seems to hold between particle density and diameter for the sample tested. More recently, "Spherocarb" particles with densities as high as 940 kg/m^3 have been weighed.

The reason for the variability in particle density may be appreciated from an optical examination of the "Spherocarb" particles. The particles (Figure 6.33A) appear spherical in shape and homogeneous on a 100 μm scale. However, on closer examination (Figure 6.33B), macropores or cavities on a 10 μm scale randomly distributed on the particle surface are observed. A photograph of polished cross sections of these particles [76] in Figure 6.34 show the three typical patterns that have been observed in analyzing a sample of about a hundred particles:

i) very small ($\sim$1 μm) cavities finely dispersed in the whole particle;

ii) a few relatively big cavities, of the order of tens of microns;

iii) a cenosphere-like particle (i.e. only one cavity present in the middle).

The variation in macroporosity of the particles is the

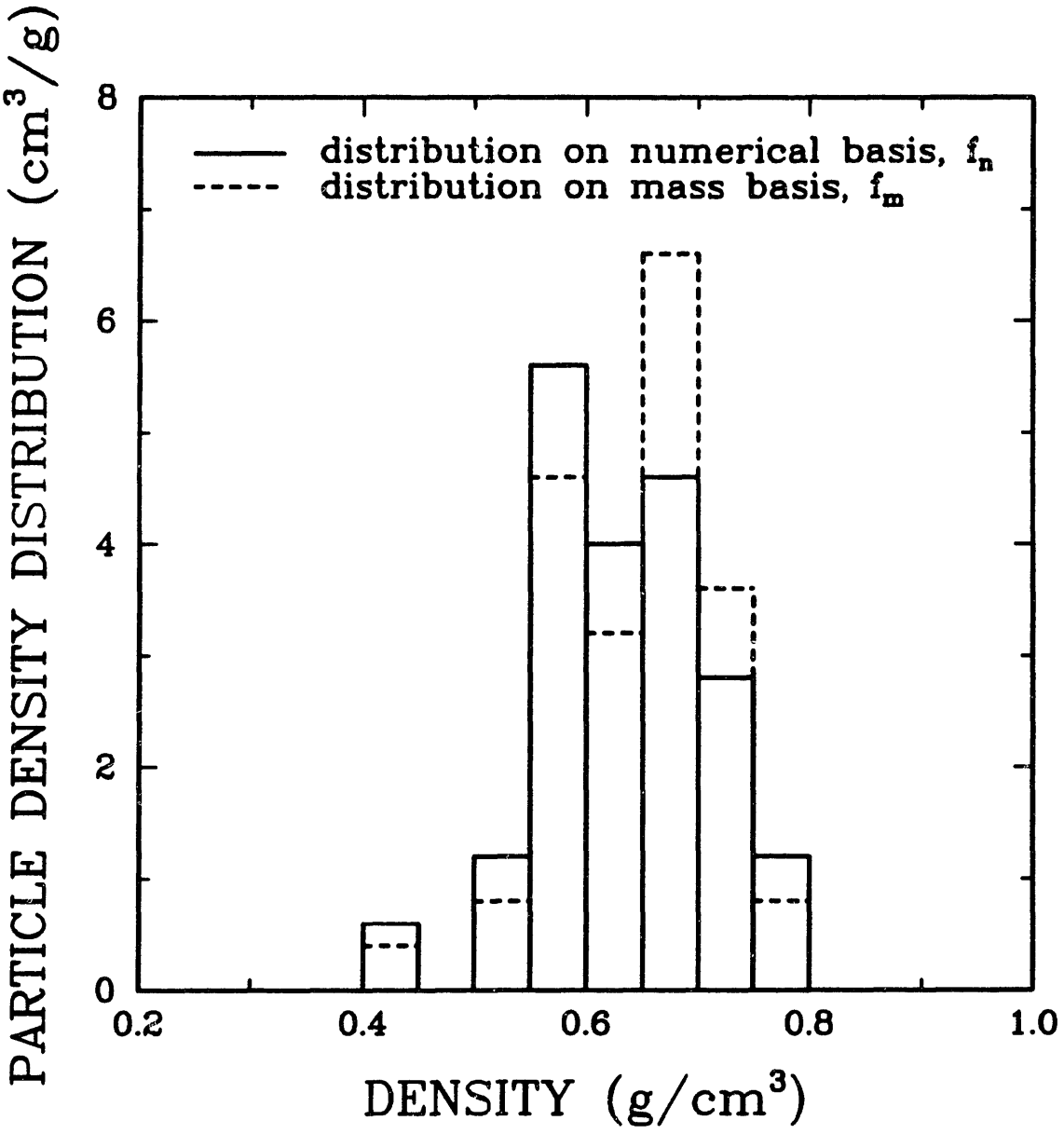

Figure 6.32 : Density distribution of 35 aerodynamically weighed "Spherocarb" particles.

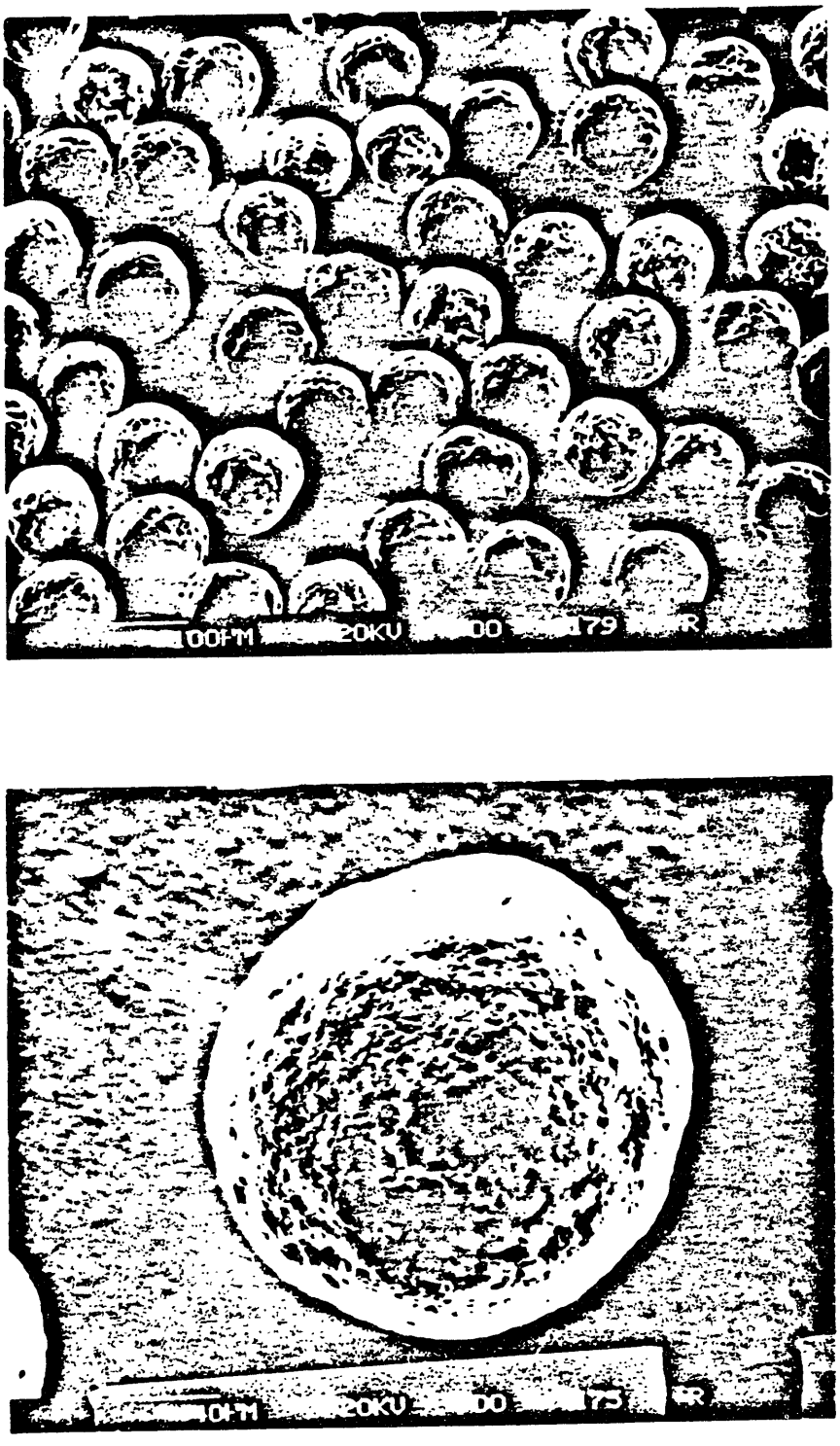

Figure 6.33 : SEM photographs of "Spherocarb" particles.

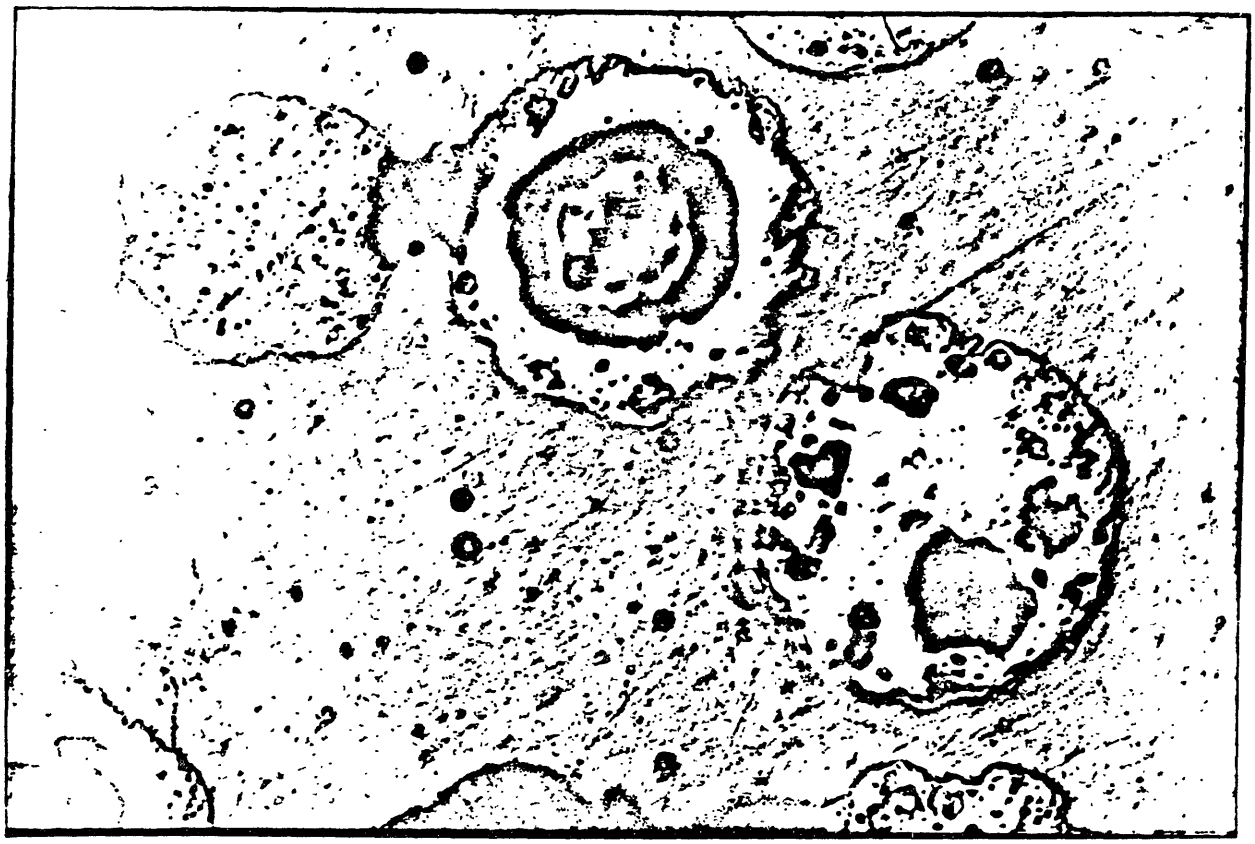

Figure 6.34 : Polished cross-sections of "Spherocarb" particles.

probable cause of the density distribution reported in Figure 6.32. An examination of the cross-section of about a hundred particles provided two cenospheres (class iii), 32 particles with big cavities (class ii), and 59 particles with smaller holes or no macropores visible at the magnification used (class i). These results are in qualitative agreement with a macropore volume distribution that can be inferred from the density distribution. The large voids are a possible consequence of bubble formation during the release of volatiles during the formation of the synthetic char by the pyrolysis of a polymer. Similar voids are observed in chars produced by the pyrolysis of bituminous coals. The lack of correlation between particle size and density for "Spherocarb" particles indicates that the void distribution is about the same for each size, suggesting that the particles were size segregated after pyrolysis.

6.1.7 Effect of density on reactivity.

In section 6.1.6 it was shown that individual "Spherocarb" particles, although appearing uniform from the outside, have large differences in apparent densities. In this section the effect of apparent density of "Spherocarb" particles on reactivity will be examined using the EDTGA, which because of its ability to measure the density of single particles, is uniquely capable of systematically studying the effect of particle density on reactivity. Nine "Spherocarb" reactions were performed in air at temperatures ranging from 876 to 901 K. Apparent densities of the "Spherocarbs" ranged from 612 to 937 kg/m^3. Reactivities were measured by the amount of time required for 50% conversion, $\tau_{0.5}$. In an attempt to keep all variables equal except for the "Spherocarb" density, all of

the $\tau_{0.5}$'s were normalized to a constant temperature of 880 K by utilizing the following linear regression of the Arrhenius plot of Figure 6.30:

$$\ln(1/\tau_{0.5}) = -18{,}107/T + 14.6718 \qquad (6.4)$$

By Subtracting equation 6.4 by itself, the following equation results:

$$\ln(1/\tau_{0.5})_{T=880} = \ln(1/\tau_{0.5})_T + 18{,}107(1/T - 1/880) \qquad (6.5)$$

which can be used to normalize the $\tau_{0.5}$'s to the constant temperature of 880 K. The results of this normalization along with the raw data from the nine runs is shown in Table 6.1. Figure 6.35 is a plot of normalized $\tau_{0.5}$ versus "Spherocarb" density. The time required for 50% conversion is not correlated with "Spherocarb" density.

6.1.8 Particle-to-particle variations in reactivity.

Again using the data in Table 6.1, we now focus our attention on measuring the particle-to-particle variations in reactivity. The average value of $\tau_{0.5}$ for the nine runs of Table 6.1 is 252 sec with a standard deviation of 54 sec or 21%. The measured average temperatures and unnormalized $\tau_{0.5}$'s are used in the Arrhenius plot of Figure 6.36. Individual "Spherocarbs" possess amazingly uniform reactivities.

Table 6.1 : Densities, average temperatures, and times for 50% conversion for nine separate, single particle, uncatalyzed "Spherocarb" reactions performed in air.

Run #	ρ (kg/m^3)	T_{ave} (K)	$\tau_{0.5}$ (sec)	$T_{ave,n}$ (K)	$\tau_{0.5,n}$ (sec)
1	909	877	182	880	170
2	776	878	230	880	219
3	890	879	263	880	257
4	819	876	278	880	253
5	757	885	157	880	176
6	612	889	275	880	339
7	937	879	312	880	305
8	694	901	154	880	249
9	810	886	261	880	300

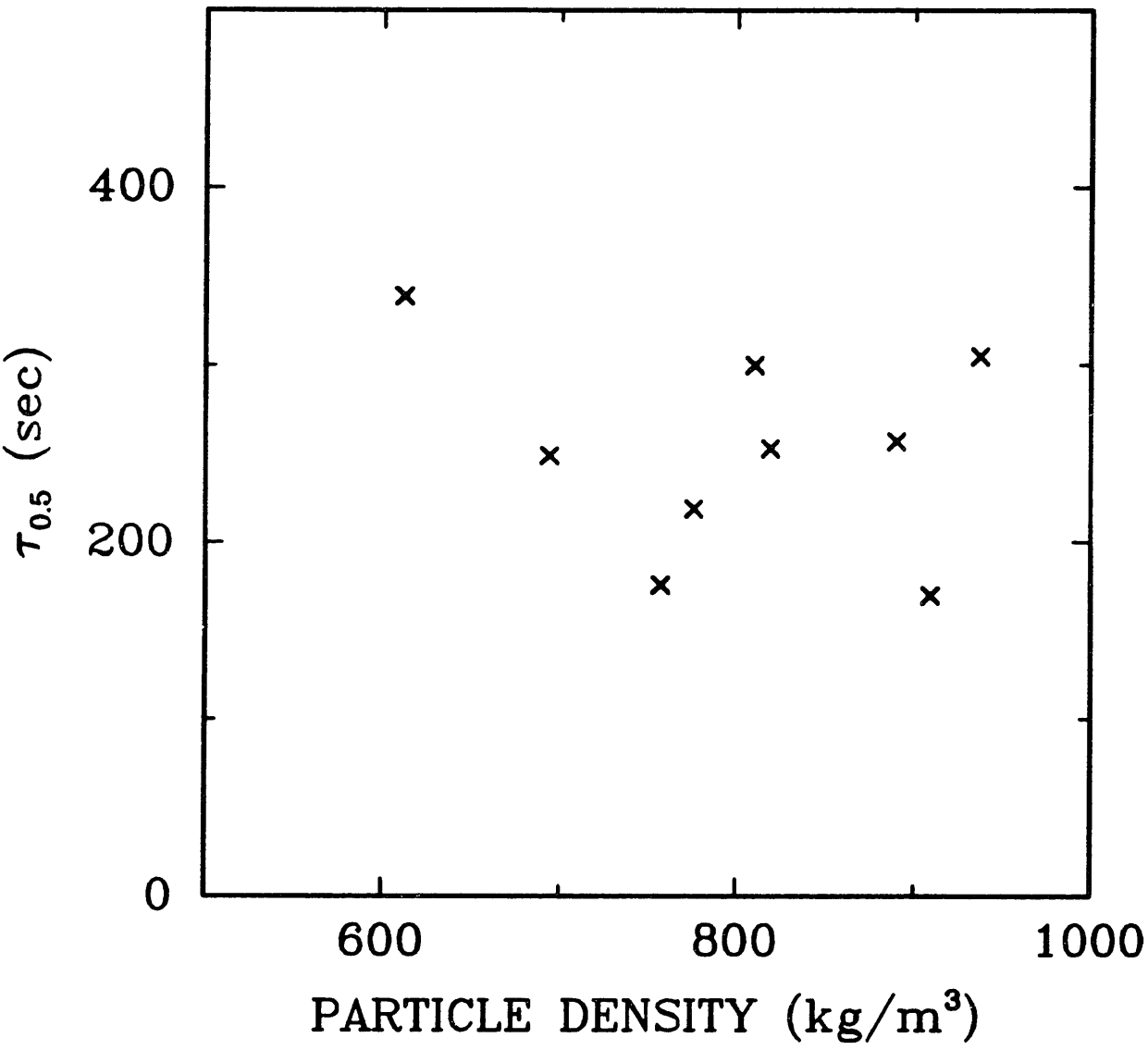

Figure 6.35 : Reaction time required for 50% conversion versus particle density for nine separate, single particle, uncatalyzed "Spherocarb"–air reactions performed in the EDTGA at 880 K.

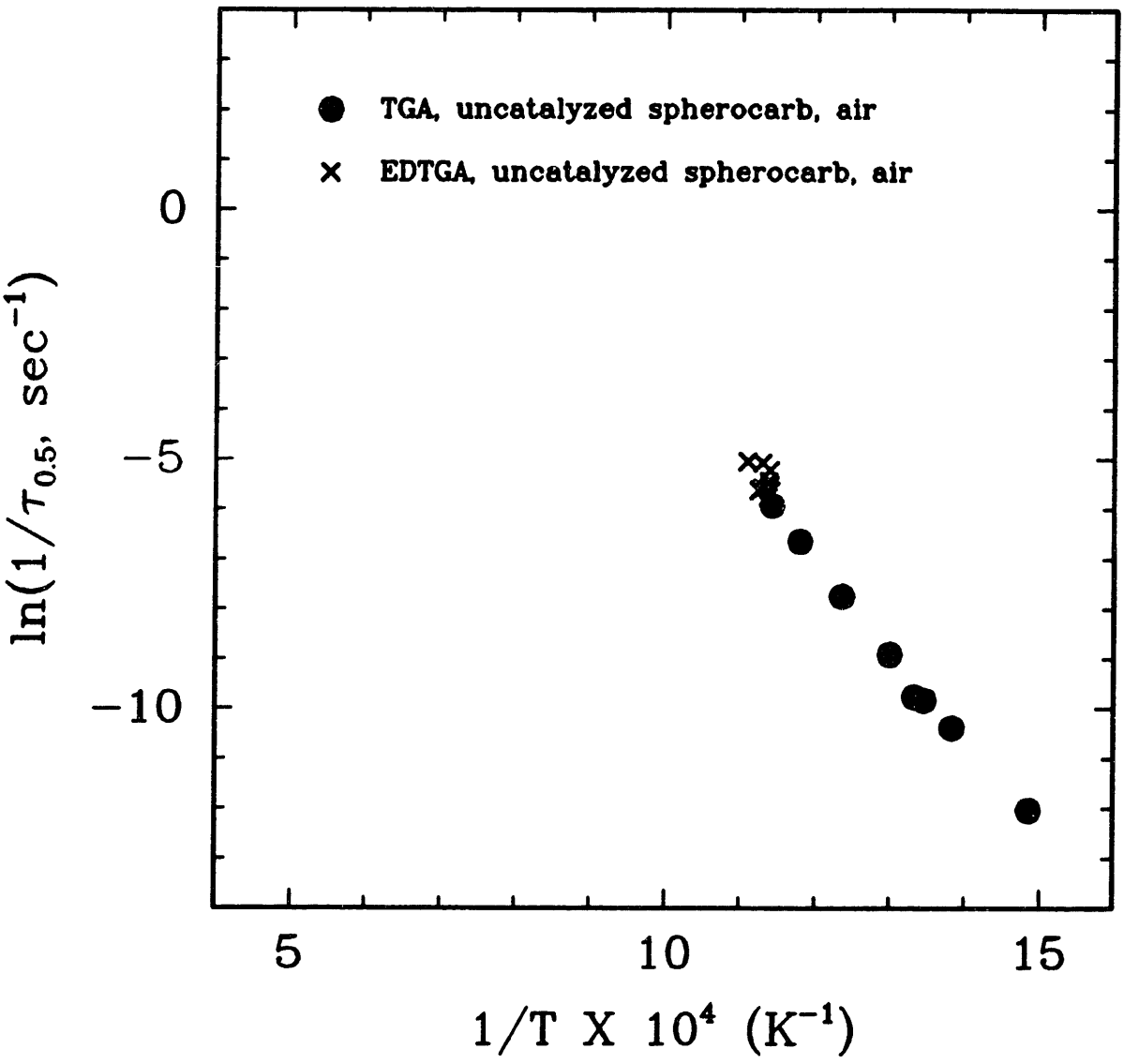

Figure 6.36 : Arrhenius plot for nine separate, single particle, uncatalyzed "Spherocarb"–air reactions performed in the EDTGA at approximately the same temperature and eight "Spherocarb"–air reactions performed in a conventional TGA.

6.2 Catalyzed "Spherocarb".

In this section the role of catalysts on "Spherocarb" oxidation is discussed. Three different catalysts (Fe, K, and Ca) were examined to determine their effect on "Spherocarb" oxidation. Potassium has been shown by Mims and Pabst [77] and Mims et al. [78] to be very mobile and to completely wet the reacting surface. Iron has been shown by McKee [79] and Baker et al. [80] to be an immobile, pitting catalyst. Calcium is ion exchanged on the "Spherocarb" surface and is assumed to be immobile. In this section, we will examine the effect of Fe, K, and Ca on shrinkage, surface area evolution, and reactivity. The effect of catalyst addition on particle-to-particle variations in reactivity will also be examined. Iron is added to the "Spherocarbs" by mixing in a solution of $FeCl_3$. Potassium is added in a similar manner, by mixing the "Spherocarb" particles in a solution of K_2CO_3. Calcium was ion exchanged in a solution of calcium acetate in a manner described by Floess [40].

6.2.1 Fe catalyzed "Spherocarb".

Figure 6.37 is two sets of three photographs taken from two Fe catalyzed "Spherocarb" particles at various stages of conversion, 0, 36, and 64% conversion for the first Fe catalyzed "Spherocarb" pictured along the top of Figure 6.37, and 0, 29, and 76% conversion for the second Fe catalyzed "Spherocarb" pictured along the bottom of Figure 6.37. The first Fe catalyzed "Spherocarb" particle was reacted in air, with a time of approximately 16 minutes required for 50% conversion. Although no temperature measurements were performed, a reaction temperature of 710 K can be estimated from the

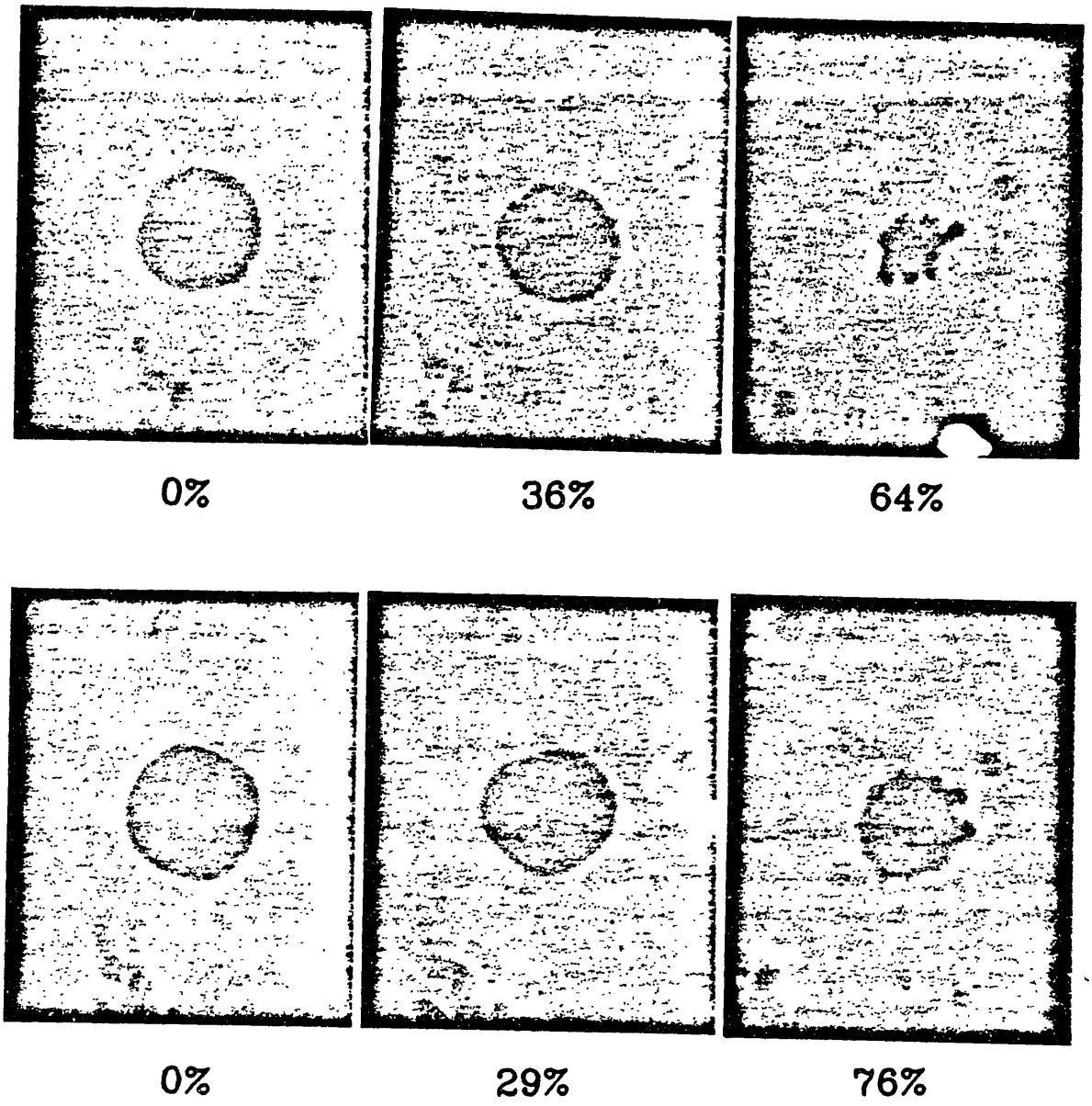

Figure 6.37 : Photographs at different conversions of two separate, Fe catalyzed "Spherocarb" particles reacting in air in the EDTGA at 710 K and 830 K, respectively.

Arrhenius plot (Figure 6.48) discussed later in this section. The initial "Spherocarb" diameter was 136 μm at 0% conversion. The particle shrank slightly to 130 μm at 36% conversion, and then at a conversion greater than 54%, the "Spherocarb" ignited momentarily and fragmented off its outer shell leaving the irregularly shaped particle depicted in the photograph at 64% conversion. No attempt was made at trying to determine the particle diameter at this conversion. It should be noted that conversion measurements were based on balancing voltages alone and that if charge loss occurred during particle ignition, the conversion in the final photograph could have been greater than 64%. The 64% represents the lower limit on conversion in this case. It is reasonable to assume that no charge loss had occurred prior to ignition.

The second Fe catalyzed "Spherocarb" particle was also reacted in air and the time required for 50% conversion was approximately 70 sec. Again, no temperature measurements were performed, but a reaction temperature of 830 K was estimated from the Arrhenius plot (Figure 6.48). The initial "Spherocarb" diameter was 148 μm at 0% conversion. The particle shrank slightly to 145 μm at 29% conversion, and then at a conversion greater than 29%, the "Spherocarb" again ignited momentarily and fragmented off its outer shell leaving the irregularly shaped particle depicted in the photograph at 76% conversion. Again, the 76% conversion represents the lower limit on conversion in this case.

Diameter versus conversion measurements were obtained for eight separate, Fe catalyzed "Spherocarb" reactions, with the results depicted in Figure 6.38 in the form of the ratio of diameter to intial diameter versus percent conversion. The curved solid line in

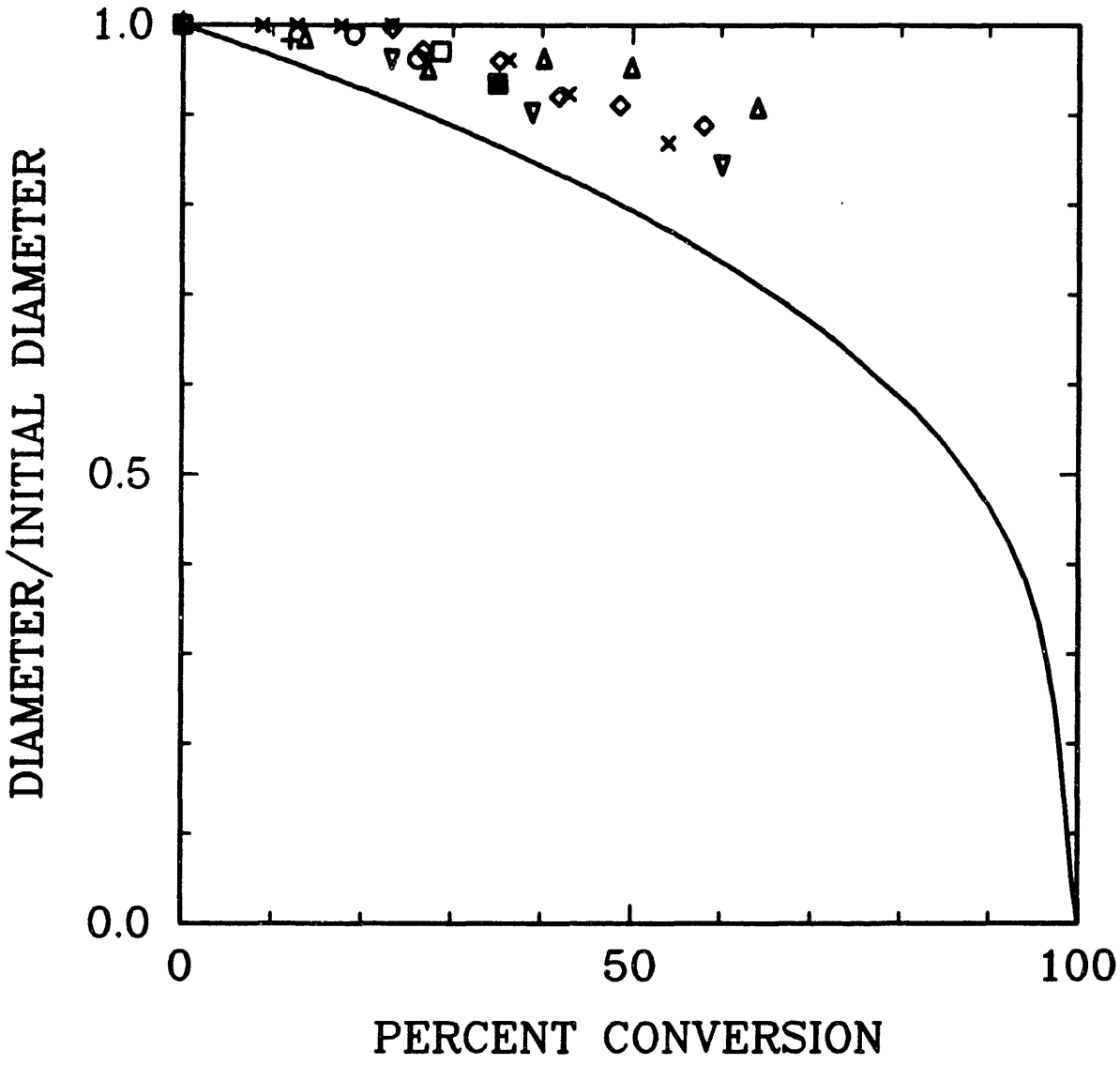

Figure 6.38 : Ratio of diameter to initial diameter versus percent conversion for eight separate, single particle, Fe catalyzed "Spherocarb" oxidations performed in the EDTGA.

Figure 6.38 represents regime III conditions and the solid line at d/d_i equal to 1.0 represents regime I conditions. All eight of the runs were performed in air. Reaction times for 50% conversion ranged from 70 sec to 28 minutes, with a corresponding temperature range of 700-830 K. At 50% conversion, the Fe catalyzed "Spherocarb" diameter is typically 94% of its original value. None of the runs got past 63% conversion before fragmentation occurred.

In Figure 6.39, the same data plotted in Figure 6.38 is plotted as $(d/d_i)^3$ versus percent conversion. The solid line represents regime III conditions.

Figure 6.40 is a plot of $\log(d/d_i)$ versus $\log(m/m_i)$ for the same eight separate runs of Figures 6.38 and 6.39. Again, the solid line represents regime III conditions which has a slope of 0.333. A linear regression of all the data of Figure 6.40 yields a slope of approximately 0.14, just slightly below the slope of 0.15 for the uncatalyzed "Spherocarb" data with conversion less than 60%. It appears that the presence of Fe catalyst in "Spherocarb" does not change the shrinkage phenomena from the uncatalyzed case.

Single particle surface areas are obtained using CO_2 adsorption and the Dubinin-Polanyi equation. The technique for surface area measurement is discussed in detail in section 3.3. The Dubinin-Polanyi plot for the same 125 μm diameter "Spherocarb" at three different conversions is shown in Figure 6.41. The slopes of these three sets of data are relatively constant, at -0.174, -0.171, -0.166, respectively, but the intercept is decreasing, indicating a reduction in surface area. This particular Fe catalyzed "Spherocarb" particle was

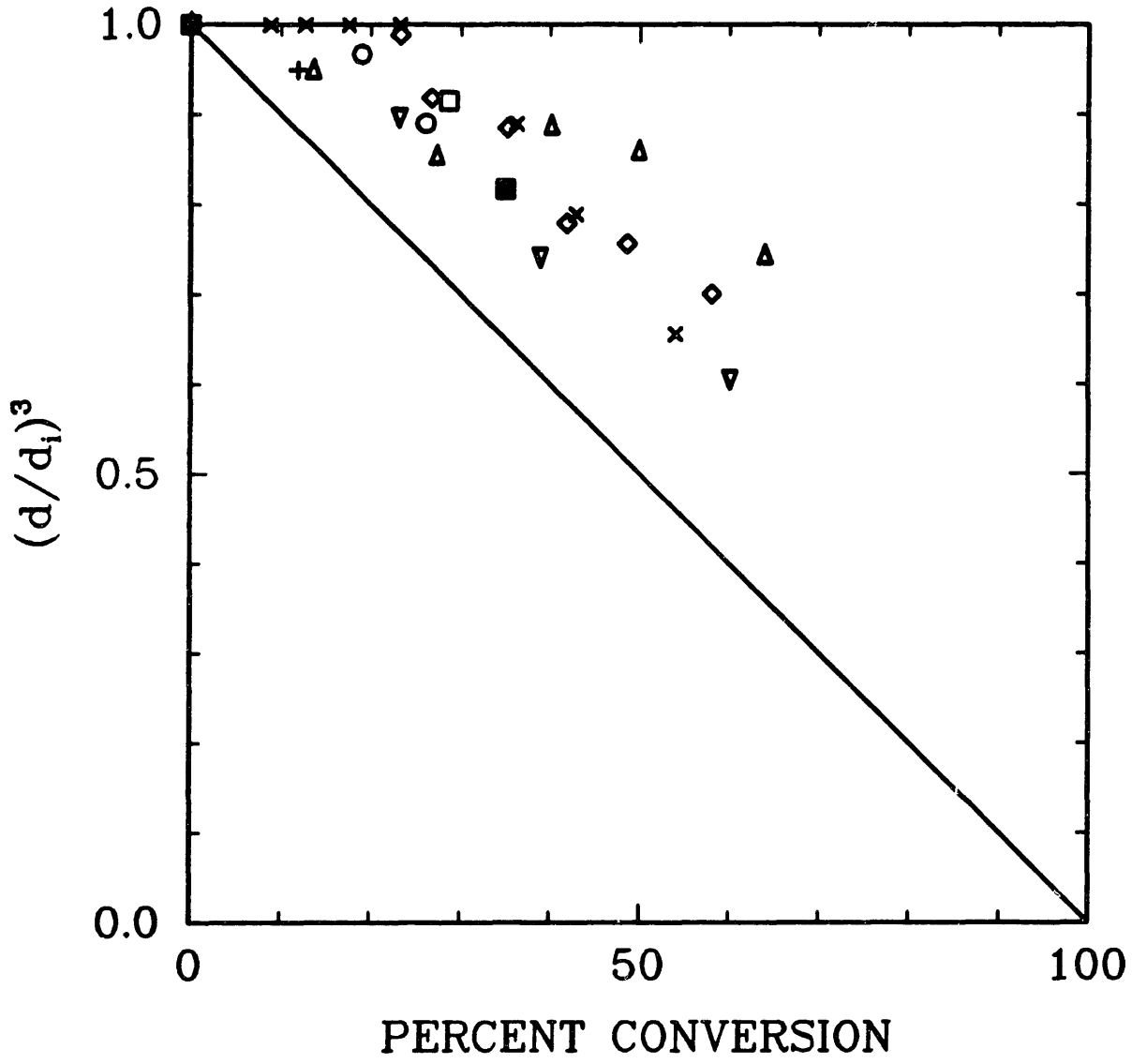

Figure 6.39 : Ratio of diameter to initial diameter cubed versus percent conversion for eight separate, single particle, Fe catalyzed "Spherocarb" oxidations performed in the EDTGA.

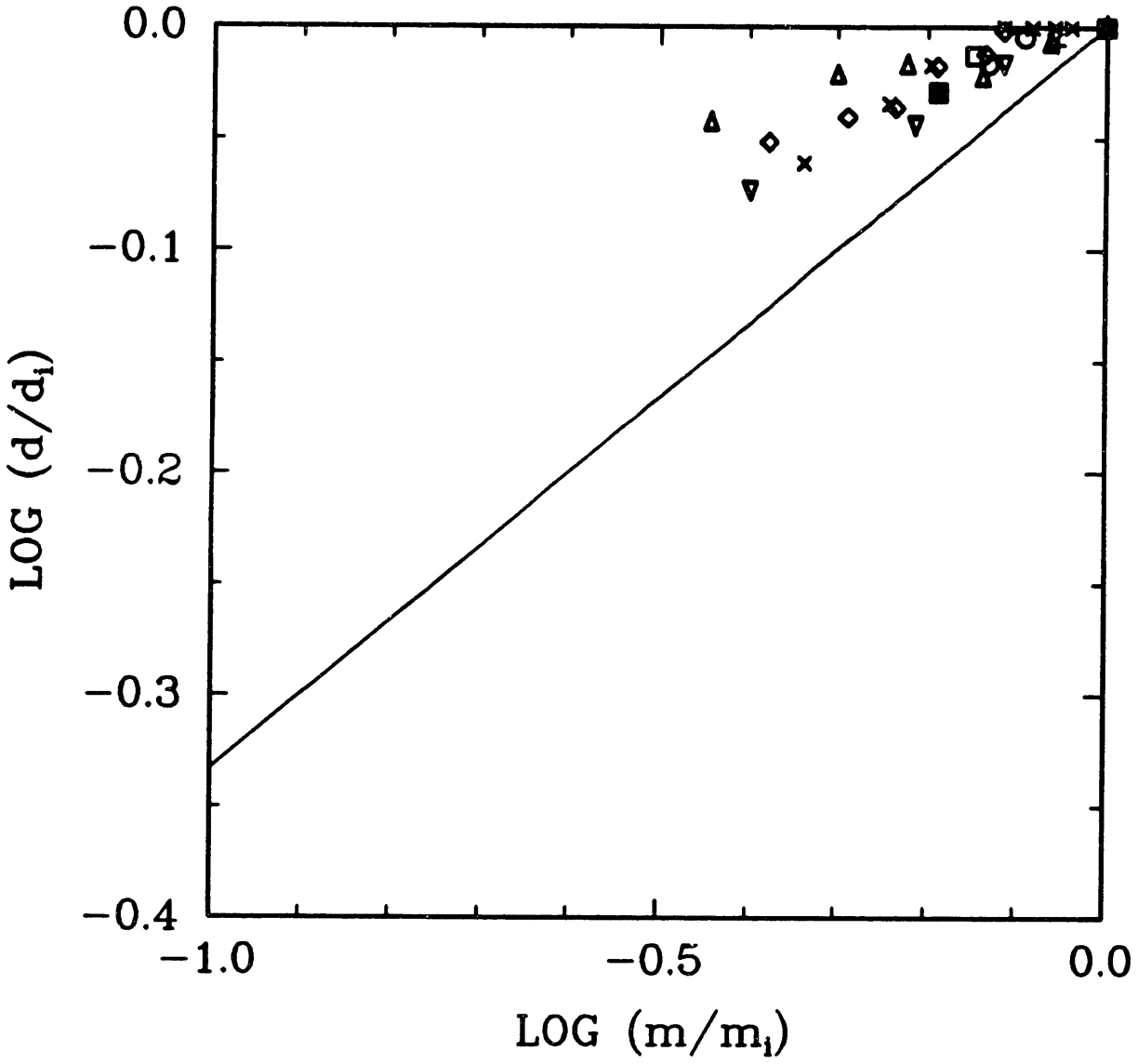

Figure 6.40 : Log of the ratio of diameter to initial diameter versus log of the ratio of mass to initial mass for eight separate, single particle, Fe catalyzed "Spherocarb" oxidations performed in the EDTGA.

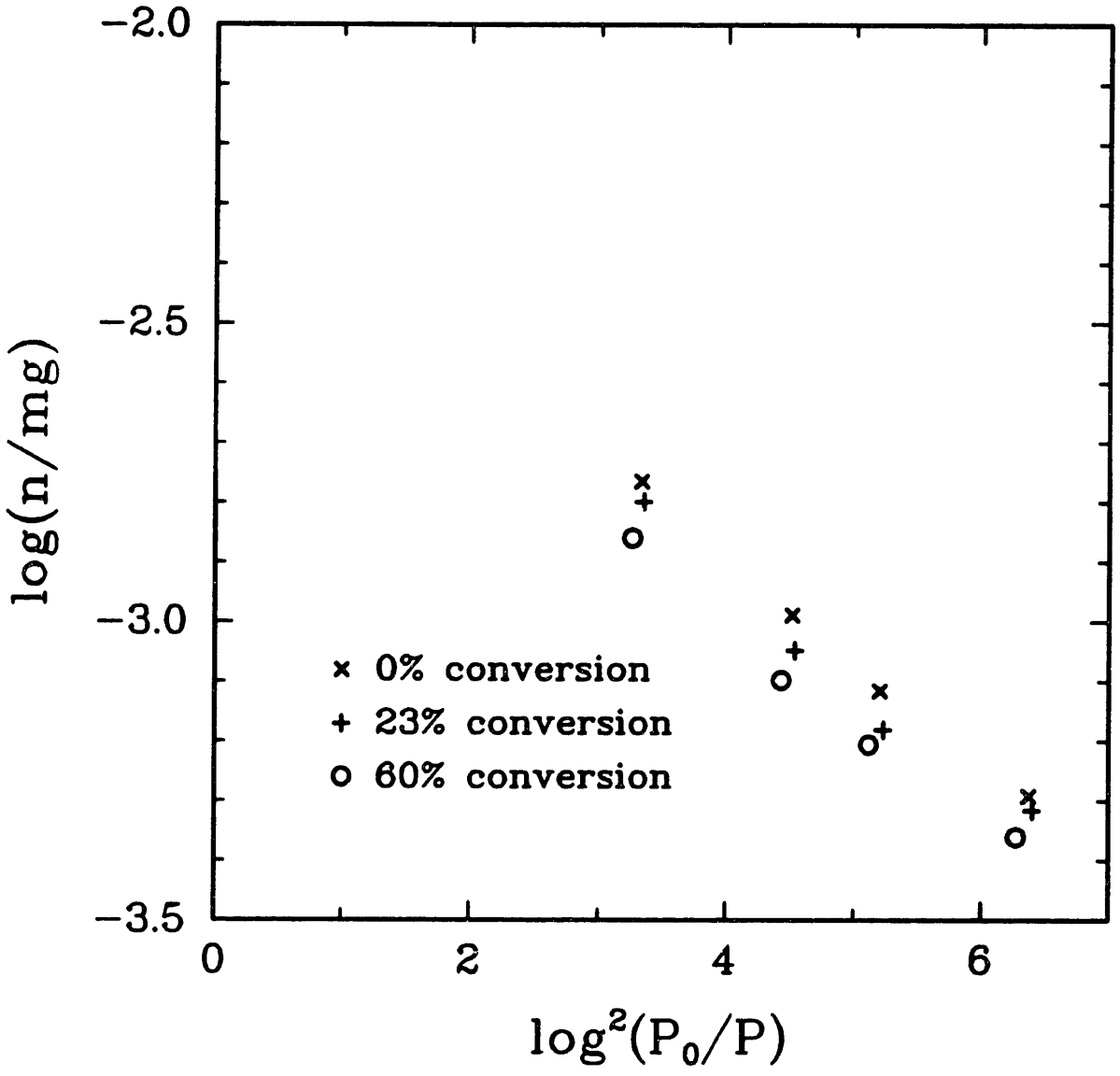

Figure 6.41 : Dubinin–Polanyi plot for a single, Fe catalyzed "Spherocarb" particle at three different conversions.

reacting in air at approxiamately 710 K.

Figure 6.42 is a plot of specific surface area versus percent conversion for five separate Fe catalyzed "Spherocarb" oxidations. All five of the runs were performed in air. The initial specific surface area varied from 930 to 1030 m^2/g, with the average initial surface area being 981 $m2/g$. These surface areas can be compared to a value of 965 m^2/g obtained from a 0.294 g sample of uncatalyzed "Spherocarb" particles from Hurt [36] in a conventional volumetric adsorption apparatus and to a value of 960 m^2/g for the eight uncatalyzed "Spherocarb" particles examined in the EDTGA in section 6.1. Aside from one stray point, the surface area appears to decrease in the same manner as the uncatalyzed "Spherocarb".

A total of 10 separate Fe catalyzed "Spherocarb" particles were reacted in air. The time required for 50% conversion ranged from 23 to 418 sec. Figures 6.43, 6.44, and 6.45 are plots of the 2 μm, 4 μm, log ratio, balancing voltage, and corrected balancing voltage signals versus time for a 125 μm diameter Fe catalyzed "Spherocarb" particle reacting in air at a temperature of 863 K. The time required for 50% conversion is 53 sec for this reaction.

The data from the 10 separate Fe catalyzed "Spherocarb" oxidations is presented in Table 6.2. $\tau_{0.5}$ and the average particle temperature are recorded for each run. A plot of $\tau_{0.5}$ versus average particle temperature is plotted in Figure 6.46. The "Spherocarb" particle that reacts at 810 K reacts about an order of magnitude slower than the other nine particles. A possible explanation for this

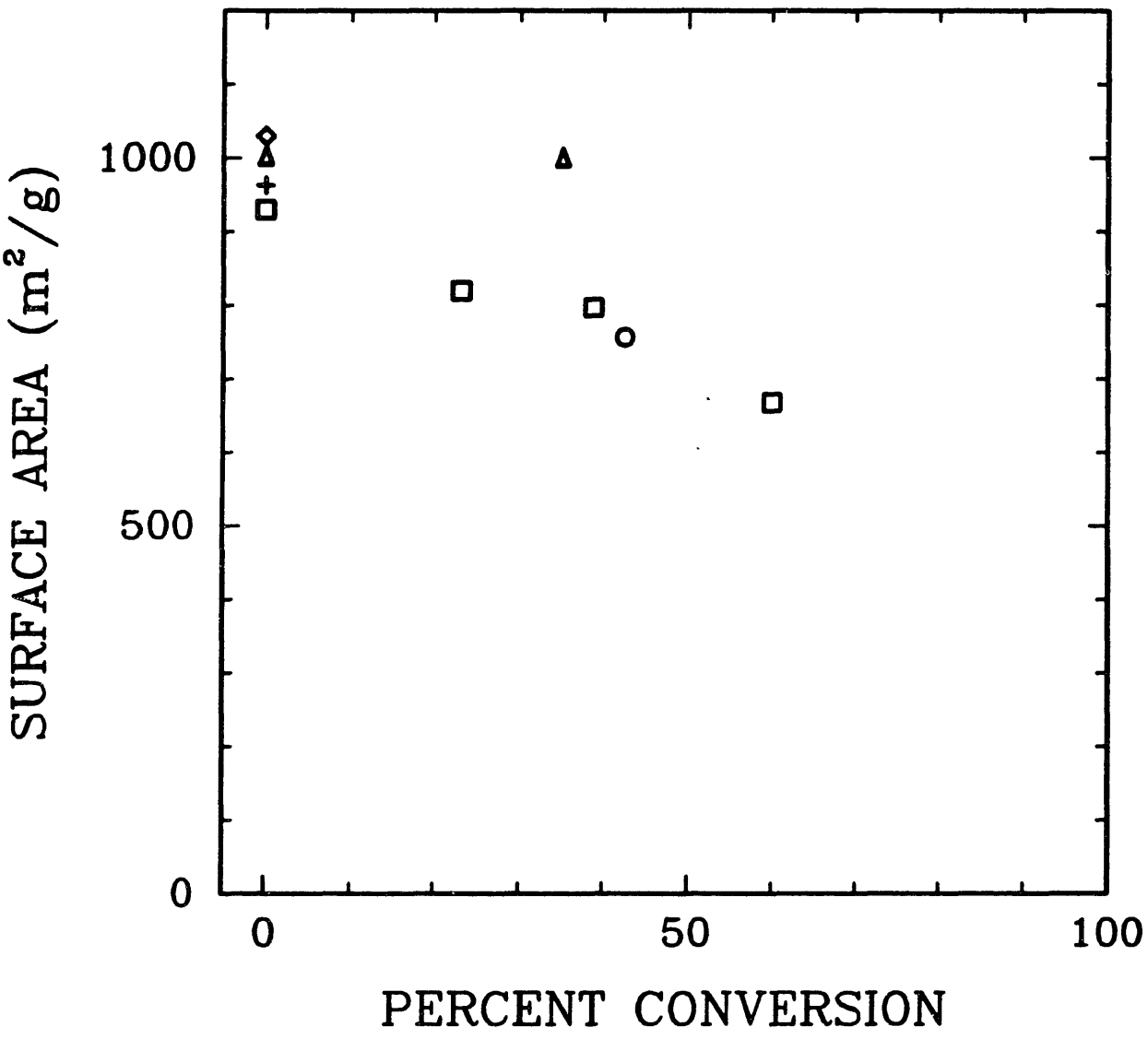

Figure 6.42 : Specific surface area versus percent conversion for five separate, single particle, Fe catalyzed "Spherocarb" oxidations performed in the EDTGA.

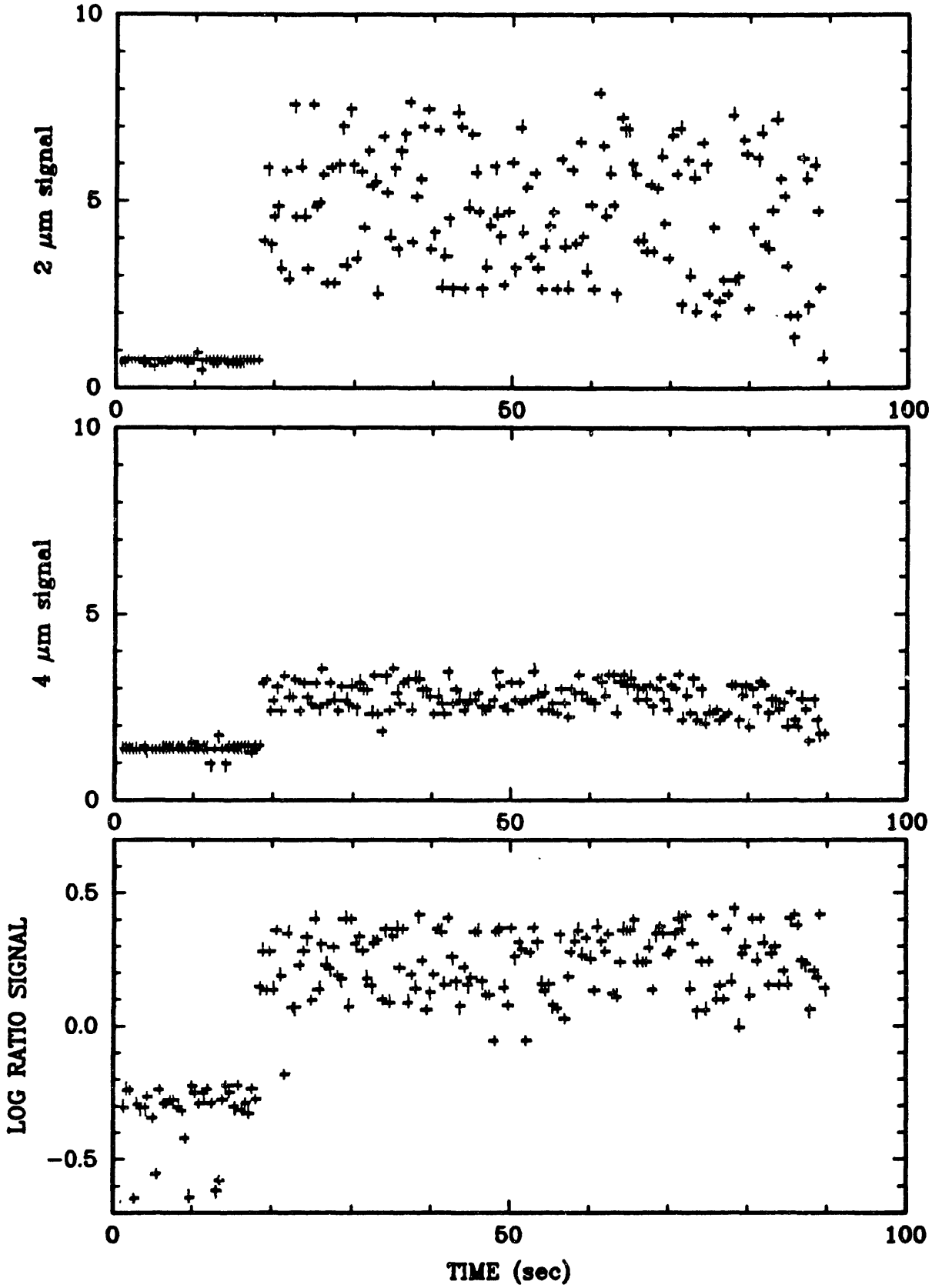

Figure 6.43 : 2 μm, 4 μm, and log ratio signals versus time for a 125 μm diameter, Fe catalyzed "Spherocarb" reacting in air at 863 K.

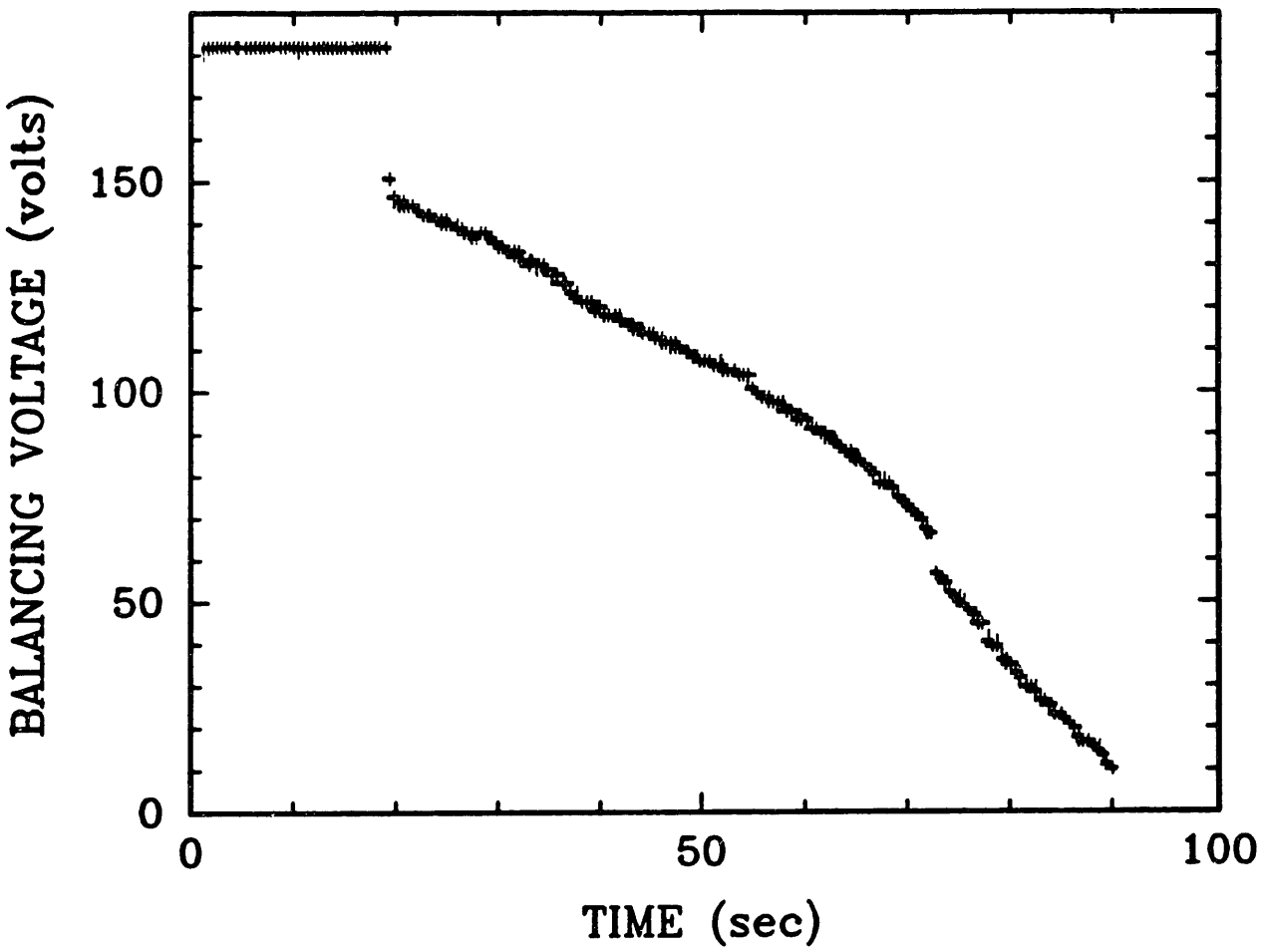

Figure 6.44 : Experimentally measured balancing voltage versus time for a 125 μm diameter, Fe catalyzed "Spherocarb" particle reacting in air in the EDTGA at 863 K.

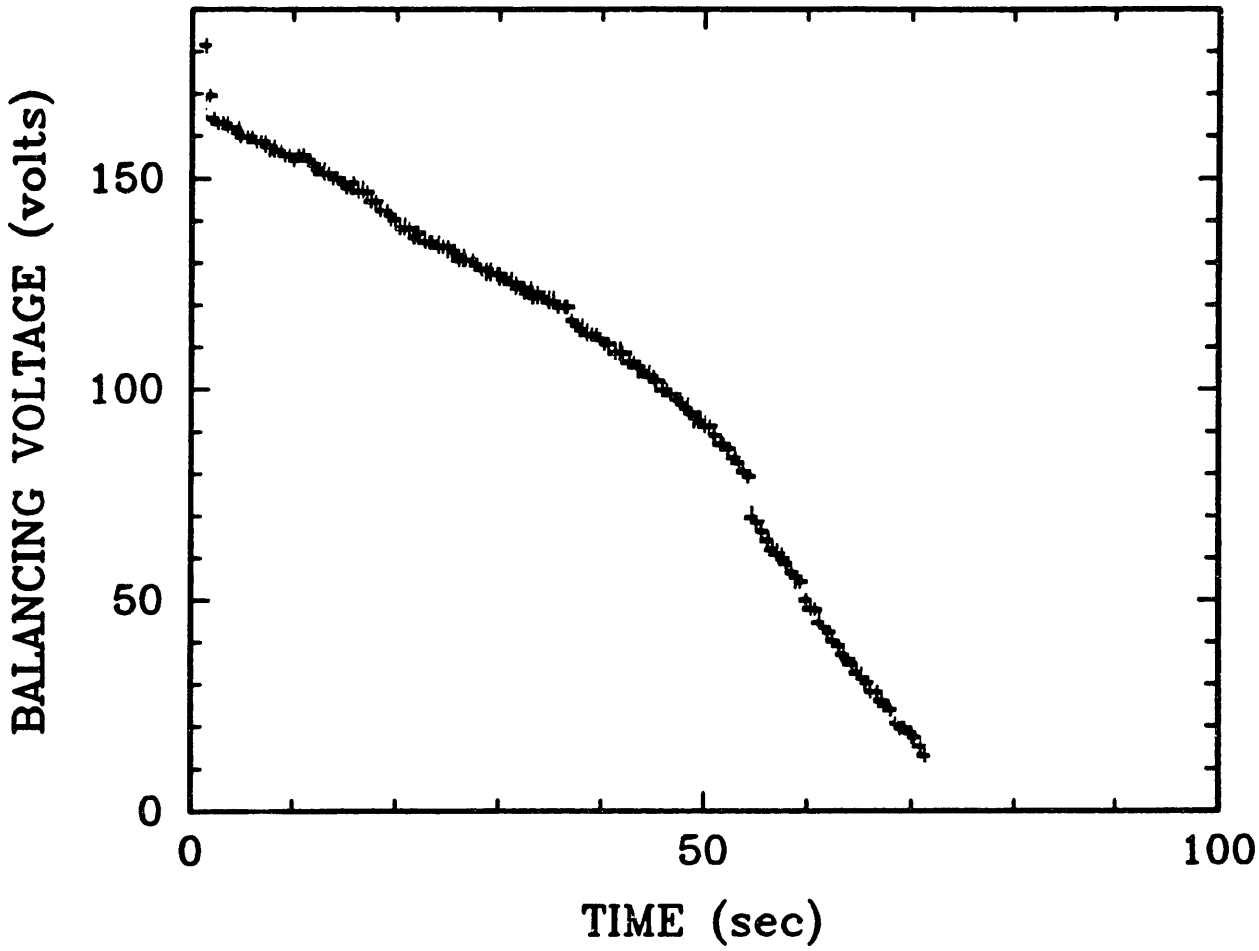

Figure 6.45 : "True" balancing voltage (after correcting for the natural convective drag force) versus time for a 125 μm diameter, Fe catalyzed "Spherocarb" particle reacting in air in the EDTGA at 863 K.

Table 6.2 : Average temperatures and times required for 50% conversion for 10 separate, single particle, Fe catalyzed "Spherocarb" reactions performed in air.

Run #	T_{ave} (K)	$\tau_{0.5}$ (sec)	$T_{ave,n}$ (K)	$\tau_{0.5,n}$ (sec)
1	846	69	845	71
2	841	24	845	22
3	810	418	845	166
4	863	53	845	83
5	842	38	845	35
6	820	56	845	29
7	842	47	845	44
8	826	26	845	16
9	848	23	845	25
10	821	24	845	13

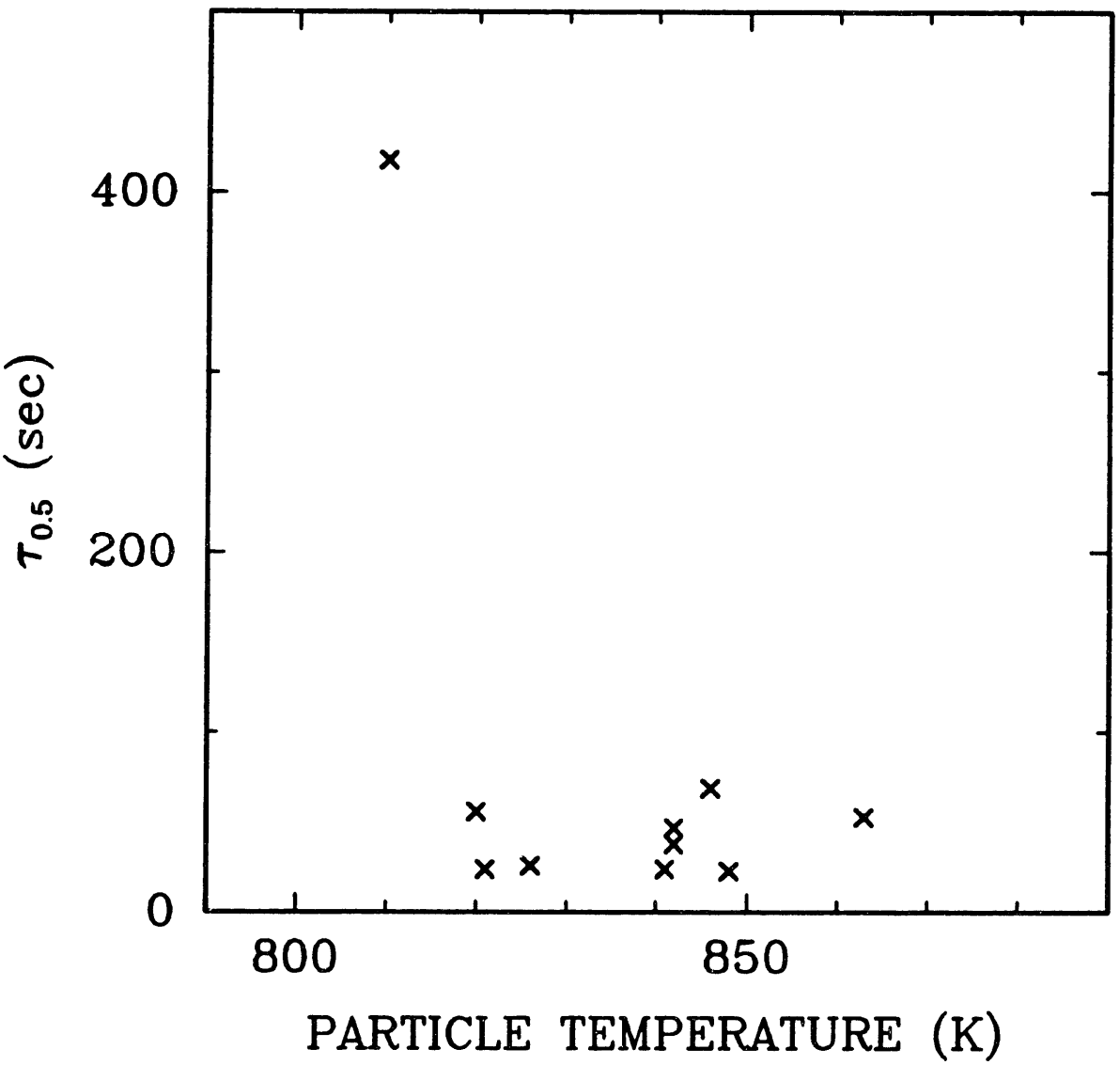

Figure 6.46 : Reaction time required for 50% conversion versus particle temperature for ten separate, single particle, Fe catalyzed "Spherocarb"–air reactions performed in the EDTGA.

decrease in reactivity is that this particular "Spherocarb" particle did not have as much Fe catalyst as the other particles. Figure 6.47 is the same plot as Figure 6.46 without the 810 K point. A fair amount of scatter in reactivity still exists from particle to particle.

In an attempt to quantitatively measure the particle-to-particle variations in reactivity the $\tau_{0.5}$'s have been normalized to a common temperature of 845 K and their values are recorded in Table 6.2. The average value of $\tau_{0.5}$ for the ten Fe catalyzed "Spherocarb" oxidations is 50.4 sec with a standard deviation of 44 sec or 88%. If the 810 K point is not used, an average normalized $\tau_{0.5}$ is 38 sec with a standard deviation of 23 sec or 61%. The measured average temperatures and unnormalized $\tau_{0.5}$'s are plotted in Arrhenius form in Figure 6.48. Due to the large particle-to-particle variations in reactivity, a large sample of particles would be needed to determine an activation energy for the Fe catalyzed "Spherocarbs". The average Fe catalyzed "Spherocarb" reacts 23 times faster than the uncatalyzed "Spherocarbs" discussed in section 6.1.

6.2.2 K catalyzed "Spherocarb".

Diameter versus conversion measurements were obtained for nine separate, K catalyzed "Spherocarb" reactions, with the results depicted in Figure 6.49 in the form of the ratio of diameter to intial diameter versus percent conversion. The curved solid line in Figure 6.49 represents regime III conditions and the solid line at d/d_i equal to 1.0 represents regime I conditions.

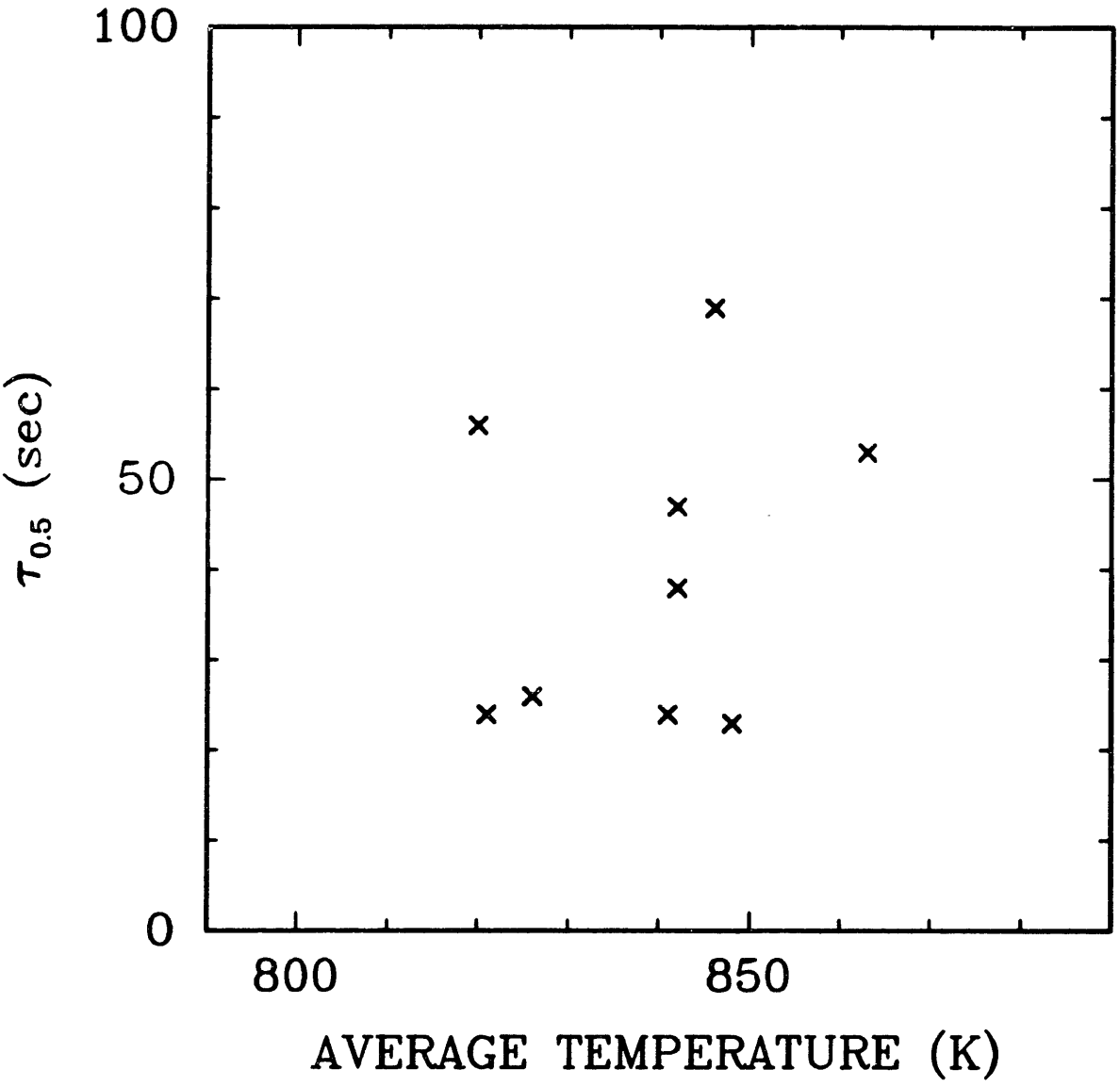

Figure 6.47 : Reaction time required for 50% conversion versus particle temperature for nine separate, single particle, Fe catalyzed "Spherocarb"–air reactions performed in the EDTGA.

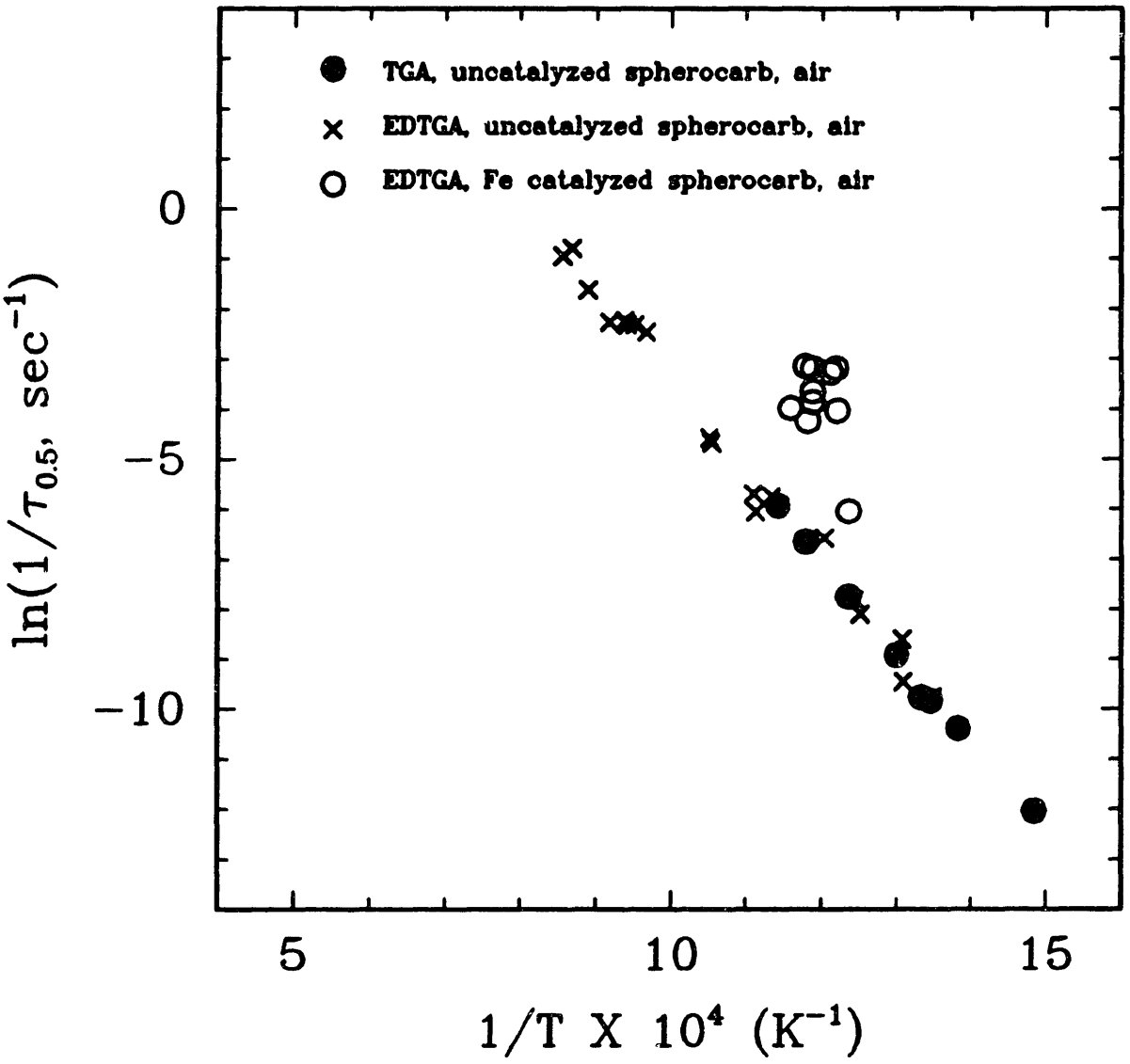

Figure 6.48 : Arrhenius plot for 10 separate, single particle, Fe catalyzed "Spherocarb"–air reactions performed in the EDTGA, 19 single particle, uncatalyzed "Spherocarb"–air reactions performed in the EDTGA, and eight "Spherocarb"–air reactions performed in a conventional TGA.

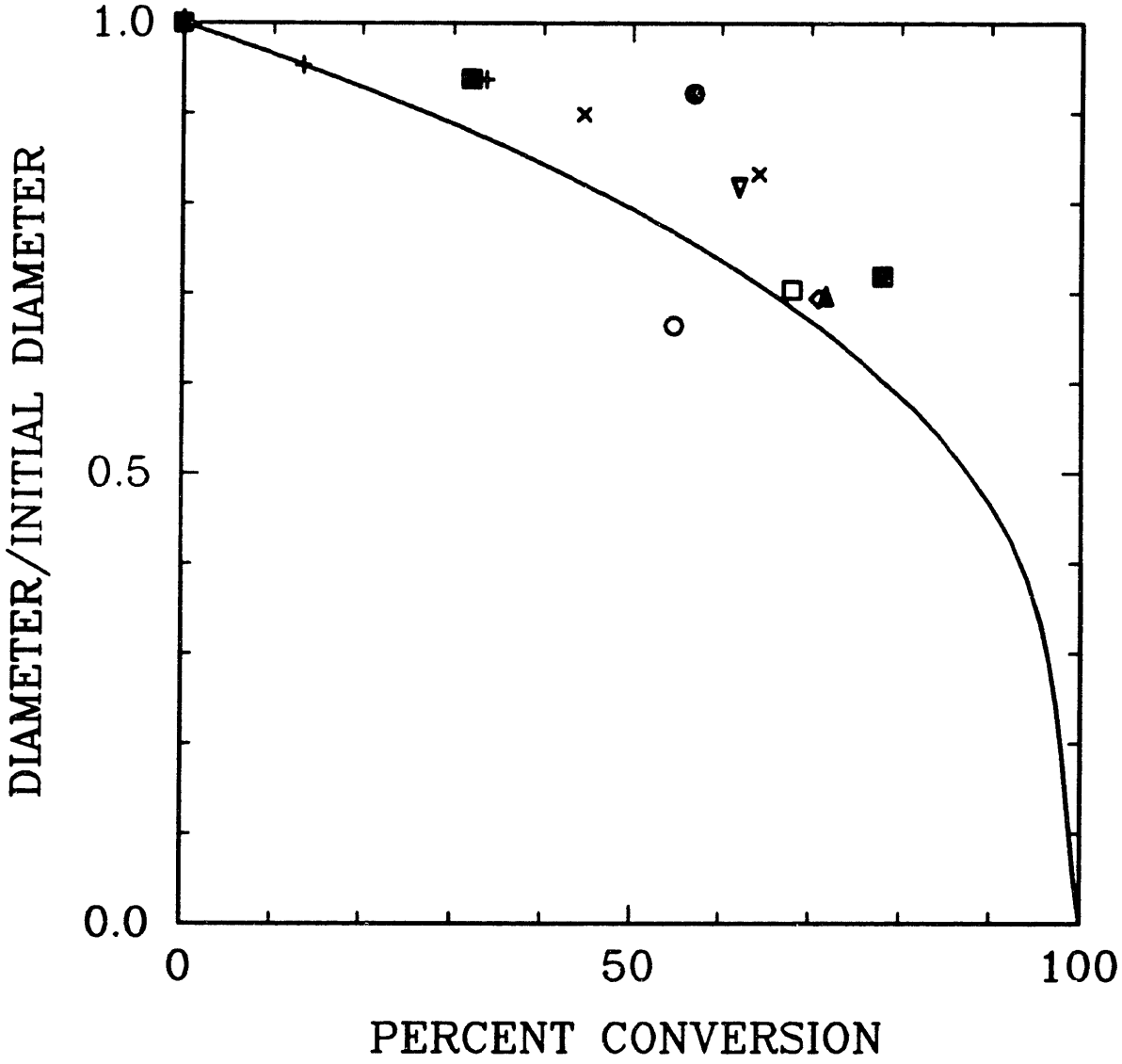

Figure 6.49 : Ratio of diameter to initial diameter versus percent conversion for nine separate, single particle, K catalyzed "Spherocarb" oxidations performed in the EDTGA.

All nine of the runs were performed in air. Reaction times for 50% conversion ranged from 89 sec to 12 minutes, with a corresponding temperature range of 670-740 K. The increased scatter in these data is due to measuring the particle diameter only by the graticule in the x70 microscope. No photographs were taken.

In Figure 6.50, the same data plotted in Figure 6.49 is plotted as $(d/d_i)^3$ versus percent conversion. The solid line represents regime III conditions.

Figure 6.51 is a plot of $\log(d/d_i)$ versus $\log(m/m_i)$ for the same eight separate runs of Figures 6.49 and 6.50. Again, the solid line represents regime III conditions which has a slope of 0.333. The presence of K catalyst in "Spherocarb" appears to enhance shrinkage slightly over the uncatalyzed case.

Figure 6.52 is a plot of specific surface area versus percent conversion for four separate K catalyzed "Spherocarb" oxidations. All four of the runs were performed in air. The surface area decreases with conversion to a greater extent than the uncatalyzed "Spherocarb".

A total of seven separate K catalyzed "Spherocarb" particles were reacted in air. The time required for 50% conversion ranged from 89 to 306 sec. The data from the seven separate K catalyzed "Spherocarb" oxidations is presented in Table 6.3. $\tau_{0.5}$ and the average particle temperature are recorded for each run. A plot of $\tau_{0.5}$ versus average particle temperature is plotted in Figure 6.53.

In an attempt to quantitatively measure the

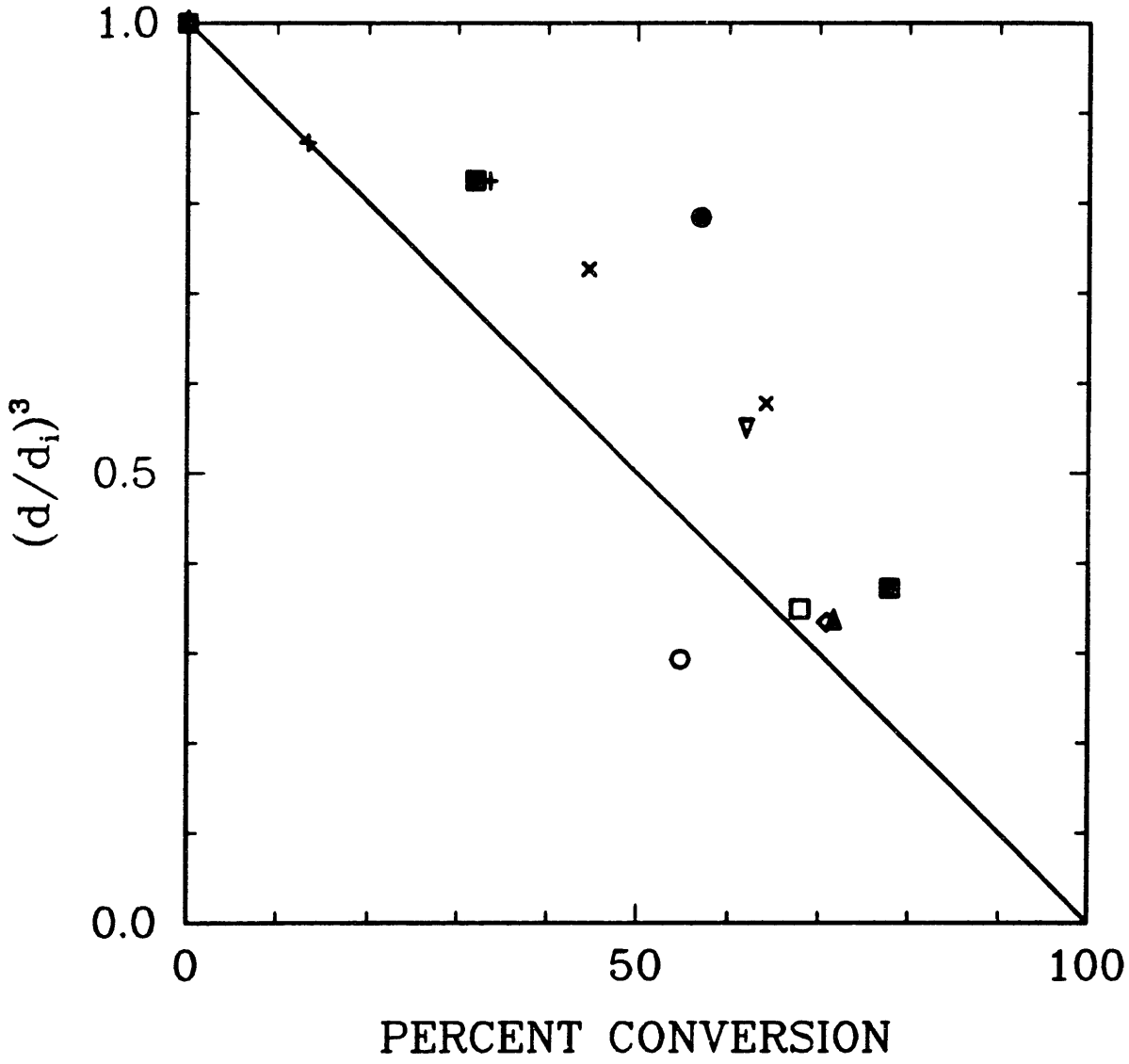

Figure 6.50 : Ratio of diameter to initial diameter cubed versus percent conversion for nine separate, single particle, K catalyzed "Spherocarb" oxidations performed in the EDTGA.

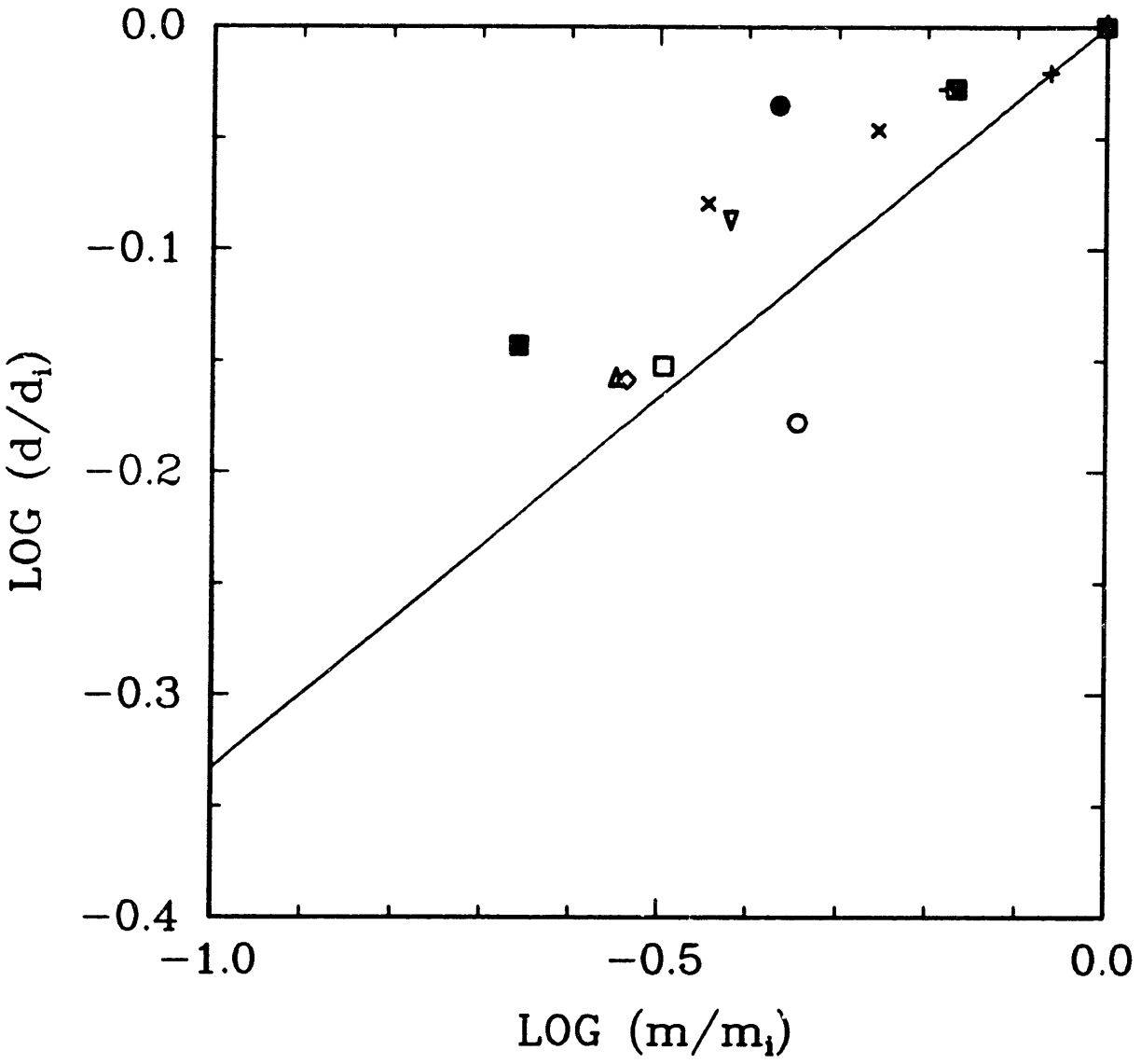

Figure 6.51 : Log of the ratio of diameter to initial diameter versus log of the ratio of mass to initial mass for nine separate, single particle, K catalyzed "Spherocarb" oxidations performed in the EDTGA.

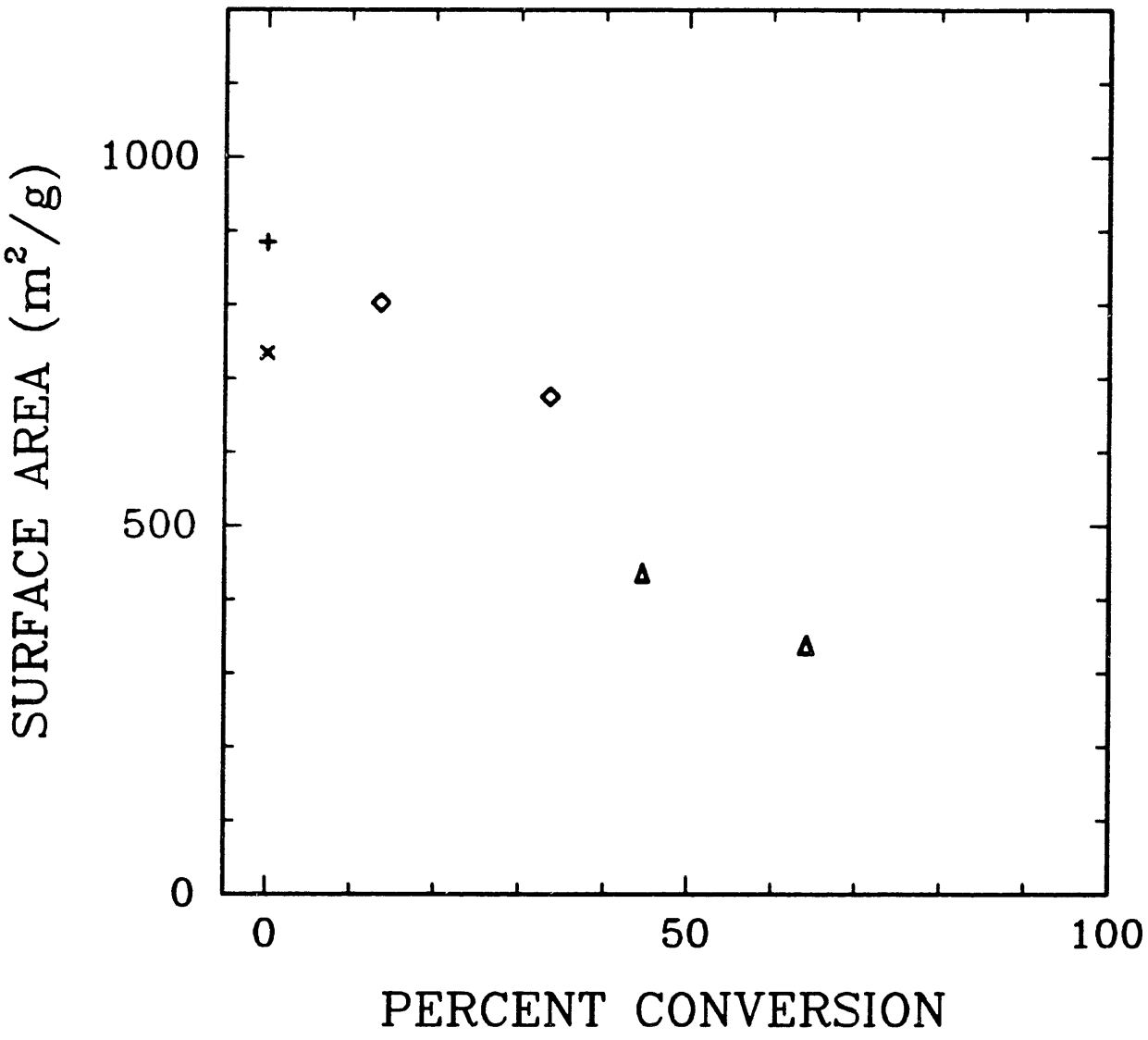

Figure 6.52 : Specific surface area versus percent conversion for four separate, single particle, K catalyzed "Spherocarb" oxidations performed in the EDTGA.

Table 6.3 : Average temperatures and times required for 50% conversion for seven separate, single particle, K catalyzed "Spherocarb" reactions performed in air.

Run #	T_{ave} (K)	$\tau_{0.5}$ (sec)	$T_{ave,n}$ (K)	$\tau_{0.5,n}$ (sec)
1	737	89	730	113
2	733	148	730	164
3	728	130	730	121
4	730	111	730	111
5	743	157	730	242
6	702	306	730	114
7	723	148	730	116

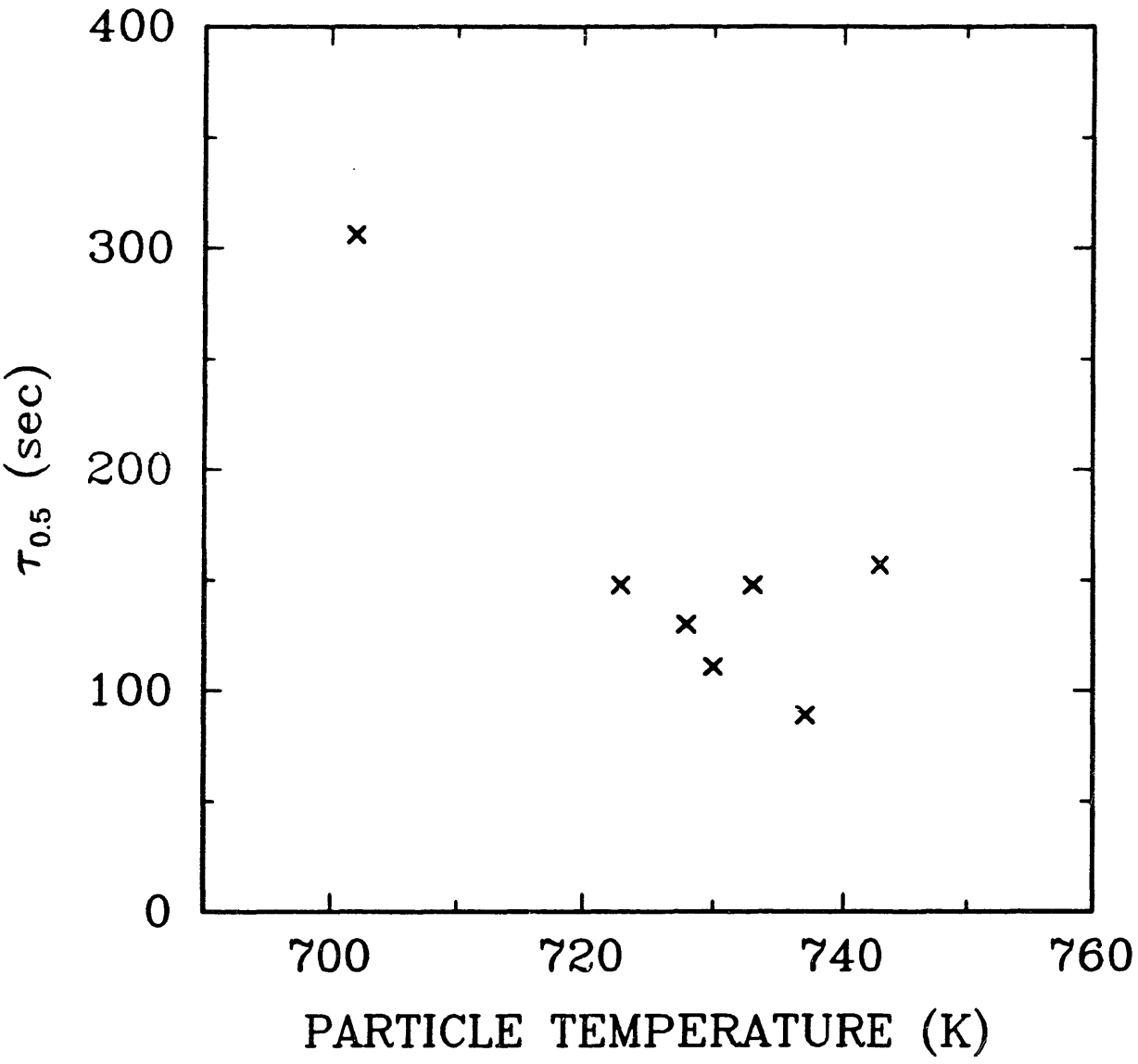

Figure 6.53 : Reaction time required for 50% conversion versus particle temperature for seven separate, single particle, K catalyzed "Spherocarb"–air reactions performed in the EDTGA.

particle-to-particle variations in reactivity the $\tau_{0.5}$'s have been normalized to a common temperature of 730 K and their values are recorded in Table 6.3. The average value of $\tau_{0.5}$ for the seven K catalyzed "Spherocarb" oxidations is 140 sec with a standard deviation of 45 sec or 32%. The measured average temperatures and unnormalized $\tau_{0.5}$'s are plotted in Arrhenius form in Figure 6.54. Particle-to-particle variations in reactivity for K catalyzed "Spherocarbs" are much smaller than those of Fe catalyzed "Spherocarbs" and are nearly as uniform as uncatalyzed "Spherocarbs". The average K catalyzed "Spherocarb" reacts 180 times faster than the uncatalyzed "Spherocarbs" discussed in section 6.1.

6.2.3 Ca catalyzed "Spherocarb".

Figure 6.55 is a plot of diameter/initial diameter versus conversion for three separate, single particle, Ca catalyzed "Spherocarb" oxidations. No other measurements were performed on Ca catalyzed "Spherocarb".

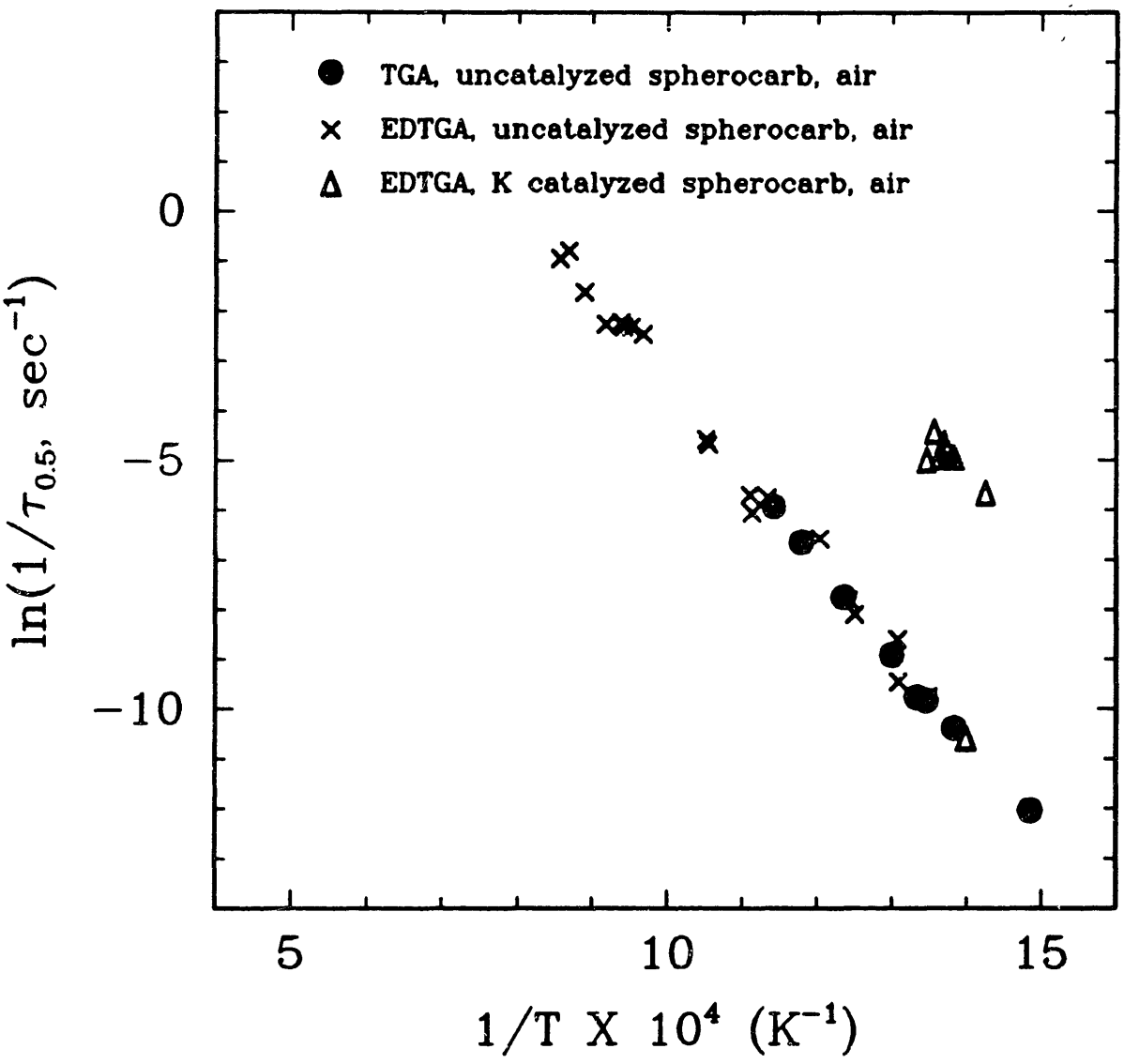

Figure 6.54 : Arrhenius plot for 7 separate, single particle, K catalyzed "Spherocarb"–air reactions performed in the EDTGA, 19 single particle, uncatalyzed "Spherocarb"–air reactions performed in the EDTGA, and eight "Spherocarb"–air reactions performed in a conventional TGA.

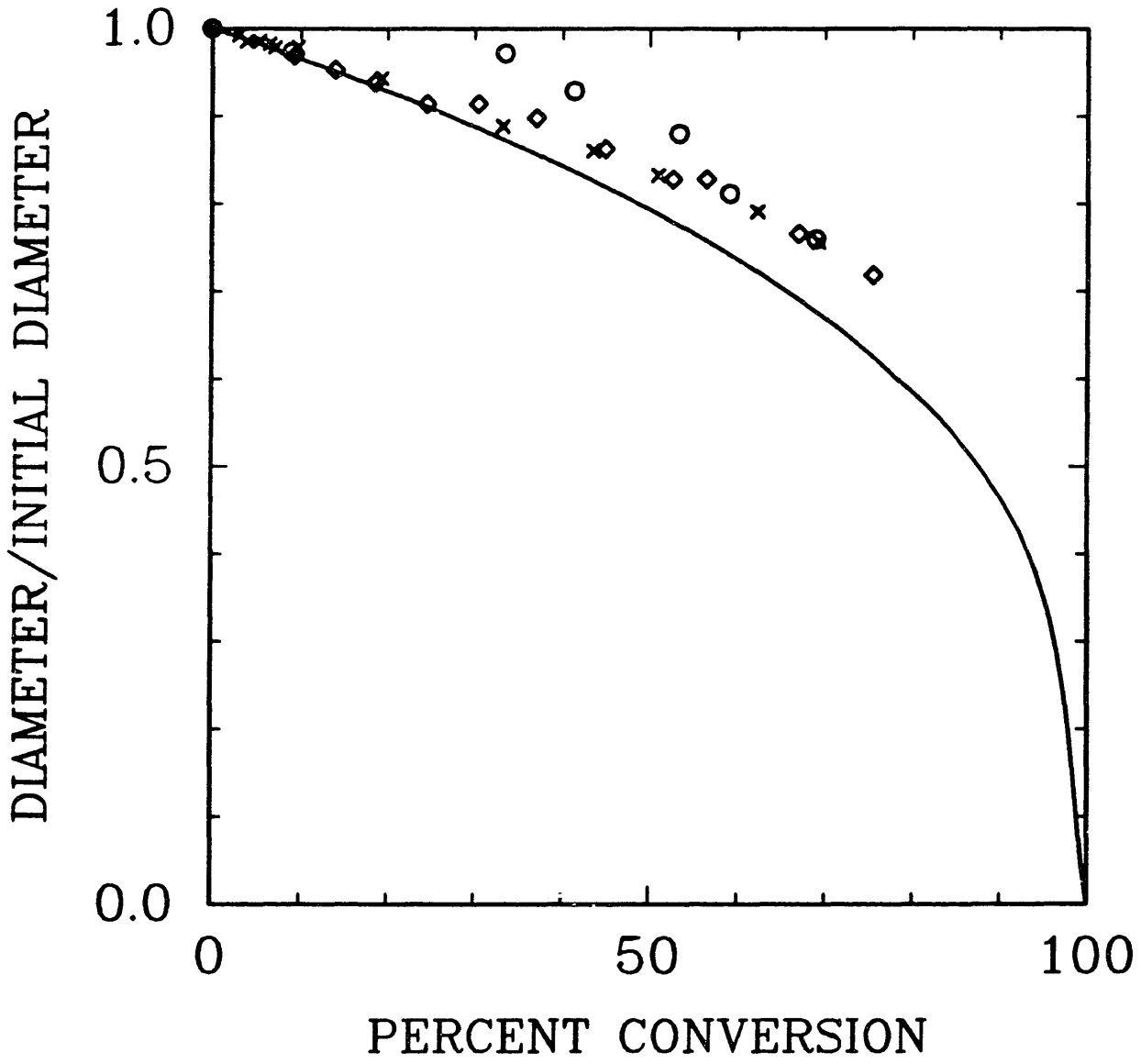

Figure 6.55 : Ratio of diameter to initial diameter versus percent conversion for three separate, single particle, Ca catalyzed "Spherocarb" oxidations performed in the EDTGA.

7. CONCLUSIONS.

7.1 Experimental techniques for single particle characterization.

1) By taking photographs of suspended particles, single particle diameter measurements can be performed to within ± 3 μm.

2) The aerodynamic drag force technique has been shown to be useful in measuring single particle mass, density, porosity, and excess charge.

3) Carbon dioxide adsorption and the Dubinin-Polanyi equation have successfully been used to measure single particle surface areas of the synthetic char "Spherocarb".

7.2 Natural convection.

1) The computational method of Geoola and Cornish [55,56] for describing the heat transfer and fluid mechanics surrounding a heated solid sphere was modified to correctly calculate the drag force due to natural convection.

2) The experimental steady-state and transient results of the natural convective drag force agree well with the Boussinesq numerical solutions, indicating that the Boussinesq approximation is valid over the experimental parameter range examined.

3) The numerical calculations were used to develop the following empirical correlation to approximate the steady-state natural convective drag force:

$$\log(C_{DT}) = 1.25 + 0.31[\log(Gr)] - 0.097[\log(Gr)]^2$$

where C_{DT} is the overall steady-state dimensionless drag force coefficient and Gr is the Grashof number. This correlation is good to within 5% over the range $0.0004 < Gr < 0.5$ for Prandtl number = 0.72.

4) The numerical calculations were also used to develop the following empirical correlation to approximate, $t_{90\%}$, the dimensionless time required to reach 90% of the steady-state drag coefficient:

$$\log(t_{90\%}) = 1.32 - \log(Gr) - 0.11[\log(Gr)]^2$$

5) The steady-state and transient empirical correlations presented here may be used to cancel out the natural convective drag force from the reacting particle force balance, thereby, allowing continuous mass versus time measurements to be calculated from balancing voltage versus time measurements.

6) The numerical solution predicts that the steady-state natural convective drag force relative to the particle weight should increase with particle radius up to a maximum value at a particle radius of approximately 40 μm and then start to decrease. The natural covective drag force increases monotonically with increasing temperature. The natural convective drag force around aerosol particles, heated to under 1500 K, with radii less the 5 μm and density greater

than 500 kg/m^3 should be less than 5% of the particle weight.

7) The steady-state natural convective drag force relative to particle weight is inversely proportional to particle density. Therefore, if a particle is to be heated to a temperature under 1500 K and has a density greater than 2500 kg/m^3, its natural convective drag force should be less than 5% of the particle weight.

8) The time required to set up the natural convective flow field decreases with increasing particle temperature and decreases with decreasing particle radius. The time was in the range of 100-300 msec for the experiments performed.

7.3 Charge loss.

1) "Catastrophic" charge loss due to particle heating has experimentally been found to represent the most serious limitation in studying single particle gas-solid reactions in the EDB. Every material to date that has been levitated in our EDB has experienced charge loss at some temperature.

2) Six different charge loss mechanisms have been proposed:
   a) photoemission,
   b) field emission,
   c) secondary emission,
   d) thermionic emission of electrons or ions,
   e) fragmentation, and
   f) surrounding gas ionization.

3) Experimentally, charge loss appears to be a function of particle work function, particle temperature, electric field strength, and adsorbed species concentration. There is also no noticable difference in charge loss from positively charged particles as compared to negatively charged particles.

4) From a literature survey, it was determined that:
   a) Particle surface irregularities coupled with the electric field at the particle surface could drasticly increase the charge loss from the particle at a specific temperature, potentially decreasing the particle surface work function by a couple of electron volts.
   b) Surface impurities can also lead to a drastic increase in charge loss.

5) The electric field at the particle surface can be decreased by minimizing the number of charges on the levitated particle.

6) After examining evidence from experiments performed in this lab as well as evidence presented in the literature, thermionic emission of ions remains the most viable mechanism for charge loss. The Richardson-Dushman equation describes thermionic emission from a clean surface and predicts the maximum temperature at which a material can be heated without experiencing charge loss. The Richardson-Dushman equation successfully predicts charge loss for uncatalyzed "Spherocarb" at 1200-1300 K and charge loss for K catalyzed "Spherocarb" at around 750 K. It also successfully predicts the inability to heat $CaCO_3$ above 1173 K without

charge loss.

7) Taking into consideration that the particle work function and particle temperature are of primary importance in describing charge loss, and that electric field strength, adsorbed species, and surface irregularities are of secondary importance and act to lower the particle work function, a modified Richardson-Dushman equation is proposed and can be written:

$$I = AT^2 \exp[(-\phi_0 + \xi + \Phi)/(kT)]$$

where:

$\xi = [e\beta(E_s + E_{AC} + E_{DC})/(4\pi\epsilon_0)]^{0.5}$
= the lowering of the work function due to the electic field at the particle surface (eV).

Φ = the lowering of the work function due to surface contamination (eV).

A = the Richardson constant = 120 amps/cm^2 K^2.

T = particle temperature (K).

ϕ_0 = work function at some reference temperature (eV).

k = Boltzmann's constant = 8.63 x 10^{-5} eV/molecule K.

e = elementary charge = 1.6 x 10^{-19} coul.

β = correction factor due to surface irregularities (dimensionless).

E_s = electric field at particle surface due to excess surface charges (V/m).

E_{AC} = electric field at particle surface due to AC electric field (V/m).

E_{DC} = electric field at particle surface due to DC electric field (V/m).

ϵ_0 = permittivity of free space
= 8.85 x 10^{-12} farad/m.

Work functions of various materials are tabulated in Table 5.1.

7.4 "Spherocarb" oxidation.

7.4.1 Uncatalyzed "Spherocarb".

1) Charge loss from "Spherocarb" particles does not occur at temperatures below 1200-1300 K. Therefore, continuous mass versus time measurements are obtainable via continuous voltage versus time measurements in a temperature range of interest for gasification and combustion.

2) "Spherocarb" density decreases versus conversion in a manner consistent with Hurt's shrinkage-densification model. It appears that "Spherocarb" porosity cannot exceed 82%. Density evolution is not a function of reacting gas or particle temperature.

3) "Spherocarb" particles have been observed to undergo shrinkage while reacting under regime I or kinetically controlled conditions. At 50% conversion, "Spherocarb" diameter is approximately 90% of its original value, and at 90% conversion, "Spherocarb" diameter is approximately 50% of its original value. The extent of "Spherocarb" shrinkage is not a function of temperature or reacting gas, but only a function of conversion.

4) "Spherocarb" specific surface area, as measured by

CO_2 adsorption, has an initial average value of 960 m^2/g. The surface area appears to increase slightly up to a conversion of 10-15% and then decreases monotonically to an average value of 660 m^2/g at approximately 80% conversion. "Spherocarb" surface area evolution is not a function of temperature or reacting gas, but only a function of conversion.

5) Nineteen separate "Spherocarb" particles were reacted in the EDTGA in air at temperatures ranging from 740 to 1170 K. Corresponding reaction times required for 50% conversion covered almost four orders of magnitude, ranging from 2.2 to 17,000 sec. The reaction rates obtained from the EDTGA agree favorably with those obtained from a conventional TGA, with both apparatuses yielding an activation energy of 36 kcal/mol for the "Spherocarb"-air reaction. No pore diffusion limitations are detectable over the entire four orders of reaction rates examined, indicating that the "Spherocarbs" are reacting in the kinetic regime.

6) Density measurements on individual "Spherocarb" particles revealed a large variability in "Spherocarb" apparent density from particle to particle. A systematic study of "Spherocarb" density versus reactivity showed no correlation.

7) A series of nine single particle "Spherocarb" oxidations at 880 K revealed a standard deviation in reaction rate of only 21% indicating that individual "Spherocarb" particles possess a uniform reactivity.

7.4.2 Catalyzed "Sperocarb".

1) Up to a conversion of approximately 50-60%, Fe catalyst had little or no effect on "Spherocarb" shrinkage or surface area evolution.

2) During many of the Fe catalyzed "Spherocarb" oxidations a sudden increase in reaction rate occurred at a conversion of approximately 50-60%, igniting the particle momentarily and fragmenting off the outer shell.

3) A series of 10 single particle Fe catalyzed "Spherocarb" oxidations in air at 845 K revealed a standard deviation in reaction rates of 88% indicating particle-to-particle variations in reactivity that are much greater than the uncatalyzed "Spherocarb" particles.

4) The average Fe catalyzed "Spherocarb" particle reacted 23 times faster than the average uncatalyzed "Spherocarb" particle at the same temperature.

5) Although scatter in the diameter versus conversion data was larger for the K catalyzed "Spherocarb" reactions, it appeared that the K catalyst enhanced "Spherocarb" shrinkage.

6) The surface area of K catalyzed "Spherocarb" particles decreased more than the uncatalyzed "Spherocarb" particles.

7) A series of seven single particle K catalyzed "Spherocarb" oxidations in air at 730 K revealed a standard deviation in reaction rates of 32% indicat-

ing particle-to-particle variations in reactivity that are much smaller than the Fe catalyzed "Spherocarbs" but greater than the uncatalyzed "Spherocarbs".

8) The average K catalyzed "Spherocarb" particle reacted 180 times faster than the average uncatalyzed "Spherocarb" at equal temperatures.

9) Ca catalyst showed "Spherocarb" shrinkage versus conversion similar to that observed for the uncatalyzed case.

7.5 Usefulness of EDB.

7.5.1 Advantages.

1) If charge loss does not occur, the EDB can be used as a TGA and reacting particle mass may be followed continuously in time.

2) The range of reactivities that potentially can be studied is greater than conventional devices due to the minimal heat and mass transfer limitations associated with a single particle device.

3) Because of the fast heat/quench times (<100 msec) associated with laser heating, discrete measurements of single particle:
    1. mass
    2. density
    3. charge
    4. porosity

5. diameter
6. surface area

versus conversion are possible.

4) Reacting single particles allows for a systematic study of specific variables (such as particle density particle size, particle surface area, coal composition, etc.) on particle reactivity.

7.5.2 Limitations.

1) Charge loss remains the single largest problem plaguing the EDTGA. If a particle does not hold its charge, interpretation of balancing voltage versus time is meaningless. Also, "catastrophic" charge loss results in loss of the particle, which prevents further characterization.

2) The temperature control system fails to keep the particle at a constant temperature when the particle is undergoing large movements in the chamber.

3) Mass, density, charge, and porosity measurements are not as accurate for irregular particles whose drag coefficients are unknown.

8. RECOMMENDATIONS.

Since charge loss remains a serious limitation of the EDTGA, an attempt should be made to try to understand the charge loss phenomena better. It is recommended that a systematic study be performed to examine the effect of particle size on charge loss. With the construction of a new EDTGA (capable of high vacuums and pressures), the effect of gas pressure on charge loss can be studied. The vacuum system will also allow for desorption of many adsorbed species on the levitated particle. Since adsorbed species can lower the particle work function by a couple of electron volts, the affect of desorption on charge loss should be investigated.

It is also recommended to attempt to circumvent the problem of charge loss by levitating a particle aerodynamically or acoustically instead of electrodynamically. In order to levitate a particle aerodynamically, gas would be required to flow around the particle at terminal velocity. A system would have to be constructed to allow for a more uniform velocity profile. In this type of system, the speed of response of the gas flow system would limit the reactions that could be effectively studied.

It is recommended that particle heating be attempted from the top. Heating from two sides would not be required, therefore, the CO_2 laser beam would not have to be split and alignment would cease to be a problem. Since a single CO_2 beam would be used, a very large, uniform beam would be possible, which should help particle stability. The only problem would be how to deal with the photophoretic force, which would now act in the vertical direction. This would complicate the voltage versus time measurements.

It is also recommended to automate the EDTGA as much as possible. This would minimize differences in measurements from one experimenter to the next. This standardization would open the door for the EDTGA to be used by many different researchers in much the same way as a conventional TGA is used today. An imaging system could be used to size the levitated particle automatically. It could also detect small movements in the particle caused by an aerodynamic drag force, thereby, increasing the accuracy and relieving the boredom of the weighing and surface area measurements.

REFERENCES:

[1] Milliken, R.A., "The Isolation of an Ion, A Precision Measurement of its charge," *Phys. Rev.*, **32**, 349 (1911).

[2] Davis, E.J., "Transport Phenomena with Sigle Aerosol Particles," *Aerosol Sci. Tech.*, **2**, 121-144 (1983).

[3] Blau, H.H. Jr., McCleese, D.J., and Watson, D., *J. Atmos. Sci.*, **9**, 2522-2528 (1970).

[4] Davis, E.J., and Ray, A.K., "Single Aerosol Particle Size and Mass Measurements Using an Electrodynamic Balance," *J. Colloid Int. Sci.*, **75**, no. 2, 566-576 (1980).

[5] Rubel, G.O., "Measurement of the Condensational Growth of Single Hygroscopic Acid Aerosol Droplets," *J. Aerosol Sci.*, Vol. 12, no. 6, 551-558 (1981).

[6] Ray, A.K., "A Study of Rate Processes Associated with Single and Multiple Aerocolloidal Particles," Ph.D. Thesis, Clarkson College of Technology (1980).

[7] Spjut, R.E., "Heat Transfer to and Position Control of Electrodynamically Suspended Micron-sized Particles," Ph.D. Thesis, Massachusetts Institute of Technology, Cambridge, MA (1985).

[8] Spjut, R.E., Bar-Ziv, E., Sarofim, A.F., and Longwell, J.P., "Electrodynamic Thermogravimetric Analyzer," *Rev.*

Sci. Instrum., **57**(8), 1604-1610 (1986).

[9] Spjut, R.E., Sarofim, A.F., and Longwell, J.P., "Laser Heating and Particle Temperature Measurement in an Electrodynamic Balance," *Langmuir*, **1**, 355-360 (1985).

[10] Arnold, S., "Determination of Particle Mass and Charge by One Electron Differentials", *J. Aerosol Sci.*, **10**, 49-53 (1979).

[11] Philip, M.A., Gelbard, F., and Arnold, S., "An Absolute Method for Aerosol Particle Mass and Charge Measurement," *J. Colloid Int. Sci.*, **91**, no. 2, 507-515 (1983).

[12] Arnold, S., and Lewittes, M., "Size Dependence of the Photophoretic Force," *J. Appl. Phys.*, **53**(7), 5314-5319 (1982).

[13] Wuerker, R.F., Shelton, H., and Langmuir, R.V., "Electrodynamic Containment of Charged Particles," *J. Appl. Phys.*, **30**, no. 3, 342-349 (1959).

[14] Frickel, R.H., Shaffer, R.E., and Stamatoff, J.B., Technical Report ARCSL-TR77041, U.S. Command, Aberdeen, MD (1978).

[15] Philip, M.A., "An absolute method for aerosol particle mass measurement," M.S. Thesis, Massachusetts Institute of Technology, Cambridge, MA 02139 (1981).

[16] Spjut, R.E., personal communication, Massachusetts Institute of Technology (1987).

[17] Meek, J.M., and Craggs, J.D., *Electrical Breackdown*

of Gases, Clarendon Press, Oxford (1953).

[18] Davis, E.J., and Periasamy, R., "Light-Scattering and Aerodynamic Size Measurements for Homogeneous and Inhomogeneous Microspheres," *Langmuir*, **1**, 373-379 (1985).

[19] Sageev, G., Seinfeld, J.H., and Flagan, R.C., "Particle Sizing in the Electrodynamic Balance," *Rev. Sci. Instrum.*, **57**, no. 5, 933-936 (1986).

[20] Davis, E.J., Zhang, S.H., Fulton, J.H., and Periasamy, R., "Measurement of the Aerodynamic Drag Force on Single Aerosol Particles", *Aerosol Sci. Tech.*, **6**, 273-287 (1987).

[21] Heiss, J.F., and Coull, J., "The effect of orientation and shape on the settling velocity of non-isometric particles in a viscous medium," *Chem. Eng. Prog.*, **48**, 3, 133-140 (1952).

[22] Pettyjohn, E.S., and Christiansen, E.B., "Effect of particle shape on free settling rates of isometric particles," *Chem. Eng. Prog.*, **44**, 2, 157-172 (1948).

[23] Marsh, H., "The determination of Surface Areas of Coals-Some Physichemical Considerations," *Fuel*, **44**, 253-268 (1965).

[24] Kalliat, M., Kwak, C.Y., and Schmidt, P.W., presented at the Symposium "New Approaches in Coal Chemistry," Regional ACS meeting, Pittsburgh, PA (1980).

[25] Meyers, R.A., editor, Coal Structure, p. 60-75, Academic Press, New York (1982).

[26] Anderson, R.B., Hall, W.K., Leckye, J.A., and Stein, K.C., "Sorption Studies on American Coals," *J.Phys. Chem.*, **60**, 1548-1558 (1956).

[27] Zwietering, P., and van Krevelen, D.W., "Chemical Structure and Properties of Coal IV- Pore Structure," *Fuel*, **33**, 331-337 (1954).

[28] Marsh, H., and Wynne-Jones, W.F.K., "The Surface Properties of Carbon-I The Effect of Activated Diffusion in the Determination of Surface Area," *Carbon*, **1**, (1964).

[29] Thomas, T., Jr., and Damberger, H.H., *Circ.- Ill. State Geol. Surv.*, 493 (1976).

[30] Brunauer, S., Emmett, P.H., and Teller, E., "Adsorption of Gases in Multimolecular Layers," *J. Am. Chem. Soc.*, **60**, 309-319 (1938).

[31] Marsh, H., and Siemieniewska, T., "The Surface Areas of Coals as Evaluated from the Adsorption Isotherms of Carbon Dioxide Using the Dubinin-Polanyi Equation," *Fuel, London*, **44**, 355-367 (1965).

[32] Walker, P.L., Jr., and Patel, R.L., "Surface Areas of Coals from Carbon Dioxide Adsorption at 298 K," *Fuel*, **49**, 91-94 (1970).

[33] Lamond, T.G., and Marsh, H., "The Surface Properties of Carbon-II The Effect of Capillary Condensation at Low Relative Pressures Upon the Determination of Surface Area," *Carbon*, **1**, 281-292 (1964).

[34] Walker, P.L., Jr., and Kini, K.A., "Measurement of the

Ultrafine Surface Area of Coals," *Fuel*, **44**, 453-459 (1965).

[35] Perry, R.H., and Chilton, C.H., editors, Chemical Engineers' Handbook, fifth edition, McGraw-Hill Book Company, New York (1973).

[36] Hurt, R.H., personal communiacation, conventional volumetric adsorption apparatus data, Massachusetts Institute of Technology, Dept. of Chemical Engineering (1987).

[37] Niksa, S., "Spherocarb" pore size distribution.

[38] Goldsmith, A., Waterman, T.E., and Hirschhorn, H.J., "Thermophysical Properties of Solid Materials," WADC Technical Report, 58-476, vol. 1 (Aug. 1960).

[39] Hottel, H.C., and Sarofim, A.F., *Radiative Transfer*, McGraw-Hill Book Company, New York (1967).

[40] Floess, J.K., "The Effect of Calcium on the Gasification Reactions of Carbon," Ph.D. Thesis, Massachusetts Institute of Technology, Cambridge, MA (1985).

[41] Hurt, R.H., "Chemical and Physical Phenomena Determining Carbon Gasification Reactivity," Ph.D. Thesis, Massachusetts Institute of Technology, Cambridge, MA (1987).

[42] Meyer, P., "Heat Transfer to Small Particles by Natural Convection," *Inst. Chem. Engrs.*, **15**, 127-131 (1937).

[43] Elenbaas, W., "The Dissipation of Heat by Free Convection

of Spheres and Horizontal Cylinders," *Physica*, **9**, no. 3, 285-296 (1942).

[44] Ranz, W.E., and Marshall, W.R. Jr., "Evaporation from Drops," *Chem. Engng. Prog.* **48**, no. 4, 173-180 (1952).

[45] Mathers, W.G., Madden, A.J. Jr., and Piret, E.L., "Simultaneous Heat and Mass Transfer in Free Convection," *Ind. Engng. Chem.*, **49**, no. 6, 961-968 (1957).

[46] Tsubouchi, T., and Sato, S., "Heat Transfer from Fine Wires and Particles by Natural Convection," res. of the Inst. of high speed mech., Tohoku Univ. **12**, pp. 127-132 (1960).

[47] Yuge, T., "Experiments on Heat Transfer from Spheres Including Combined Natural and Forced Convection," *Trans. ASME*, **C82**, 214-220 (1960).

[48] Mahony, J.J., "Heat Transfer at Small Grashof Numbers," *Proc. R. Soc., London*, **A238**, 412-423 (1956).

[49] Fendell, F.E., "Laminar Natural Convection about an Isothermally Heated Sphere at Small Grashof Number," *J. Fluid Mech.*, **34**, part 1, 163-176 (1968).

[50] Hossain, M.A., and Gebhart, B., "Natural Convection about a Sphere at Low Grashof Number," Fourth International Heat Transfer Conference, Paris-Versailles, **5**, NCl.6, A.I.Ch.E., New York (1970).

[51] Hieber, C.A., and Gebhart, B., "Mixed Convection from a Sphere at Small Reynolds and Grashof Numbers," *J. Fluid Mech.*, **38**, part 1, 137-159 (1969).

[52] Singh, S.N., and Hasan, M.M., "Free Convection about a Sphere at Small Grashof Number," *Int. J. Heat Mass Transfer*, **26**, no. 5, 781-783 (1983).

[53] Farouk, B., "Natural Convection Heat Transfer from an Isothermal Sphere," *Therm. Sci.*, **16**, vol. 1, 347-364 (1982).

[54] Fujii, T., Honda, T., and Fujii, M., "A Numerical Analysis of Laminar Free Convection around an Isothermal Sphere: Finite-Difference Solution of the Full Navier-Stokes and Energy Equations Between Concentric Spheres," *Num. Heat Transfer*, **7**, 103-111 (1984).

[55] Geoola, F., and Cornish, A.R.H., "Numerical Solution of Steady-State Free Convective Heat Transfer from a Solid Sphere," *Int. J. Heat Mass Transfer*, **24**, no. 8, 1369-1379 (1981).

[56] Geoola, F., and Cornish, A.R.H., "Numerical Simulation of Free Convective Heat Transfer from a Sphere," *Int. J. Heat Mass Transfer*, **25**, no. 11, 1677-1687 (1982).

[57] Sparrow, E.M., and Gregg, J.L. Jr., "The Variable Fluid-Property Problem in Free Convection," *Trans. ASME*, **a46**, 879-8867 (1958).

[58] Smith, G.D., *Numerical Solution of Partial Differential Equations*, Chapters 2 and 5, Oxford University Press, London (1965).

[59] Peaceman, D.W., and Rachford, H.H. Jr., "The Numerical Solution of Parabolic and Elliptic Differential Equations," *J. Soc. Ind. Appl. Math.*, **3**, 28-41 (1955).

[60] Holman, J.P., *Heat Transfer*, fourth edition, McGraw-Hill Book Company, New York (1976).

[61] Boussinesq, J., *Theorie analytique de la chaleur*, Paris: Gathier-Villars, vol. 2 (1903).

[62] Burden, R.L., Faires, J.P., and Reynolds, A.C., *Numerical Analysis*, Prindle, Weber, and Schmidt, Boston, Massachusetts, 136-145 (1978).

[63] Gallo, C.F., and Lama, W.L., "Some Charge Exchange Phenomena Explained by a Classical Model of the Work Function," *J. of Electrostatics*, **2**, 145-150 (1976).

[64] Weast, R.C., editor, CRC Handbook of Chemistry and Physics, 61st edition, CRC Press, Inc., Baco Raton, Florida (1980).

[65] Jenkins, R.O., and Trodden, W.G., *Electron an Ion Emission from Solids*, Dover Publications Inc., New York (1965).

[66] Cardona, M., and Ley, L., editors, *Photoemission in Solids I, General Principles*, Springer-Verlag Berlin Heidelberg New York (1978).

[67] Lawton, J., and Weinberg, F.T., *Electrical Aspects of Combustion*, Clarendon Press, Oxford (1969).

[68] Schottky, V.W., *Physik. Zeitschr.*, **XV**, 872-878 (1914).

[69] de Bruyne, N.A., "The Action of Strong Electric Fields on the Current from a Thermionic Cathode," *Proc. Roy. Soc. (London)*, **120A**, 423-437 (1928).

[70] Loeb, L.B., *Fundamental Processes of Electrical Discharge in Gases*, John Wiley and Sons, Inc., New York, 310-335 (1939).

[71] Hughes, J.F., *Electrostatic Powder Coating*, John Wiley and Sons, Inc., New York.

[72] Loewenstein, E.U., Smith, D.R., and Morgan, R.L., "Optical Constants of Far Infrared Materials 2: Crystalline Solids", *Applied Optics*, vol. 12, no. 2, 404 (1973).

[73] Blackman, M., "On the adsorption of polar crystals in the infrared," *Trans. Roy. Soc. (London)*, **A236**, 103 (1936).

[74] Hurt, R.H., Dudek, D.R., Longwell, J.P., and Sarofim, A.F., "The Phenomenon of Gasification-Induced Carbon Densification and its Influence on Pore Structure Evolution," accepted for publication in *Carbon*, (1988).

[75] Smith, I.W., and Tyler, R.J., "Internal burning of pulverized semi-anthracite: the relation between particle structure and reactivity," *Fuel*, **51**, 312-321 (1972).

[76] D'Amore, M., Dudek, D.R., Sarofim, A.F., and Longwell, J.P., "Apparent Particle Desity of a Fine Particle," submitted to *Powder Technology* (1988).

[77] Mims, C.A., and Pabst, J.K., "Role of Surface Salt Complexes in Alkali-Catalyzed Carbon Gasification," *Fuel*, **62**, 176-179 (1983).

[78] Mims, C.A., Chludzinski, J.J. Jr., Pabst, J.K., and Baker, R.T.K., "Potassium-Catalyzed Gasification of Graphite in Oxygen and Steam," *J Catalysis*, **88**, 97-106 (1984).

[79] McKee, D.W., "Metal Oxides as Catalysts for the Oxidation of Graphite", *Carbon*, **8**, 623-635 (1970).

[80] Baker, R.T.K., Chludzinski, J.J. Jr., and Sherwood, R.D., "A Comparison of the Catalytic Influence of Nickel, Iron, and Nickel-Iron on the Gasification of Graphite in Various Gaseous Environments," *Carbon*, **23**, no. 3, 245-254 (1985).

APPENDIX A : Working Programs.

```
A      PROGRAM WEIGH_PARTICLE
C*************************************************************************
C
C  This program records a voltage from the KEITHLEY 192 voltmeter every
C     time that the footpedal is pressed. The voltmeter is set for
C     6-1/2 digits with no filtering, DC volts and autoranging  The
C     results are displayed to the screen and stored in
C     '/USER/DATA/OUTPUT/VOLTAGE'. The program is halted by depressing
C     any key on the keyboard. The VM instructions are stored
C     as INSTRUCTIONS  They are then converted
C     to integer form as OUT_DATA  The data are sent to the VM and the
C     device is triggered. The voltages are read from the
C     VM as IN_DATA and converted to characters in RESULTS
C     The GPIB routines are documented in the GPIB directory.
C     ADDR, TADDR, and LADDR are the VM's address, talker address and
C     listener address respectively.
C
C
C*************************************************************************
      INTEGER*1,OUT_DATA(20),IN_DATA(18),ADDR(3),TADDR(3),LADDR(3)
      INTEGER*1 LETTER
      INTEGER*2 EOSO,EOSI,STATUS,STAT,IREAD
      CHARACTER INSTRUCTIONS*20,RESULTS*16,ANSWER*5
      logical yes
      integer*2 level,exep

      data level/'46h/
C  The keyboard buffer is on interrupt level 46H

      DATA ADDR,TADDR,LADDR/'6H,2**5FFH,'48H,2**0FFH,'28H,2**0FFH/
      DATA INSTRUCTIONS/'T0F0R0K0G0S?M1Z0W0X'/

      PARAMETER (IREAD = 200)

      OPEN (1,FILE='/USER/DATA/OUTPUT/VOLTAGE')

      CALL GPIBINIT
      EOSO = 88
      EOSI = 10


      DO 300 I = 1,20
       OUT_DATA(I) = ICHAR(INSTRUCTIONS(I:I))
       IF (INSTRUCTIONS(I:I) .EQ. 'X') J = I
300   CONTINUE
      STATUS = 0

      CALL GPIBWRITE(LADDR,OUT_DATA,J,EOSO)

310   STATUS = 0
```

```
      WRITE (6,*) 'READ DATA?'
      READ (5,100) ANSWER
100   FORMAT (A)

      IF (ANSWER(1:1) .NE. 'Y') GO TO 320

C Disable the keyboard buffer
      call rqdisable(%val(level),exep)

      ML = 18
      IPREV = 0
      RESULTS((ML-1):ML) = '  '

340   CALL OUTPUT(#0BH,4)

C Check to see if a key has been pressed to stop the program.
      call key_press_check(yes)
      if (yes) GO TO 320

C Check to see if the footpedal has been depressed. If so
C       read voltmeter.
      CALL INW(#0CH,IANS)
      IF (IANS.GT.2048) IANS=IANS.OR.#08000H
      IF ((IANS.GE.IREAD).AND.(IPREV.LT.IREAD)) THEN
        CALL GPIBREAD(TADDR,IN_DATA,ML,EOSI,STAT)
        DO 330 L = 1,ML-2
           RESULTS(L:L) = CHAR(IN_DATA(L))
330     CONTINUE
        WRITE (6,*) RESULTS
        WRITE (1,*) RESULTS
        IPREV = IANS
        GO TO 340
      ELSE
        IPREV = IANS
        GO TO 340
      END IF

320   CONTINUE
      CALL INPUT(#2EH,LETTER)

C Reenable the keyboard buffer.
      call rqenable(%val(level),exep)

C Reset the voltmeter
      INSTRUCTIONS = 'T4F0R0K0G0E7X'
      DO 337 I = 1,20
        OUT_DATA(I) = ICHAR(INSTRUCTIONS(I:I))
        IF (INSTRUCTIONS(I:I) .EQ. 'X') J = I
337   CONTINUE

      CALL GPIBWRITE(LADDR,OUT_DATA,J,EOSO)
```

```
CALL GPIBEND
END
```

```
      PROGRAM WEIGHT_ANALYSIS

C*************************************************************************
C  This program calculates the weight of a particle using Stoke's law,
C       surrounding gas velocities, and the voltages stored in /USER/
C       DATA/OUTPUT/VOLTAGE.  The data are averaged until a 'Y' is
C       lencountered at the end of a line. Thus repeated measurements
C       of the same balancing voltage are permitted
C
C*************************************************************************

      IMPLICIT REAL*10 (A-H)
      IMPLICIT REAL*10 (O-Z)
      REAL*10 MASS,M,M2
      INTEGER*4 NC,NCT
      INTEGER*2 K(99)
      LOGICAL FINAL
      CHARACTER NEXT*2,ANSWER*3
      DIMENSION V(100),Q(7)
      DATA M,M2,SUM,IV,N/3*0.0,1.0/
      DATA FINAL/.FALSE./

      OPEN (1,FILE='/USER/DATA/OUTPUT/VOLTAGE')
      OPEN (2,FILE='/USER/DATA/OUTPUT/WEIGHT')
      OPEN (3,FILE='/USER/DATA/EP/stokes')

      WRITE (3,100)
100   FORMAT('CRTP 1'/'SYMB 4'/'XLEN 6'/'XLAB FLOW RATE (ml/min)'/
     &  'YLAB BALANCING VOLTAGE'/'TITL BALANCING VOLTAGE VS. FLOW RATE'/
     & 'SYHT .25')

300   READ(1,110,ERR=777,END=333) VOLTAGE,NEXT
110   FORMAT(4X,F12.0,A1)
C
C
C  CALCULATE MASS OF PARTICLE USING STOKE'S DRAG LAW
C
C
       IF ( (NEXT .EQ. 'Y')  OR. (NEXT .EQ. 'y') ) THEN
C
          V(IV) = SUM/N
          SUM = VOLTAGE
          N = 1
          IV = IV + 1
       ELSE
          SUM = SUM + VOLTAGE
          N = N + 1
       END IF

       GO TO 300
```

```
 333   V(IV) = SUM/N
 C
 C
 C
 C  CONVERT DISPLAY ON DIGITAL ROTAMETER TO ACTUAL FLOW RATE IN ml/min.
 C
 C
      Q(1) = 0.0704286*300
      Q(2) = 0.0704286*250
      Q(3) = 0.0704286*200
      Q(4) = 0.0704286*150
      Q(5) = 0.0704286*100
      Q(6) = 0.0704286*50
      Q(7) = 0.0
 C
 C
      DO 301 I = 1,7
      J = 8 - I
      WRITE(3,101) Q(J), V(J)
 301 CONTINUE
 101 FORMAT(1X,F10.4,',',F10.5)
 C
 C
 C  CALCULATE SLOPE OF VOLTAGE VS. FLOW RATE CURVE
 C
 C
      SUMV = 0.0
      SUMQ = 0.0
      SUMVQ = 0.0
      SUMV2 = 0.0
      SUMQ2 = 0.0
      DO 302 I = 1,7
      SUMV = SUMV + V(I)
      SUMQ = SUMQ + Q(I)
      SUMVQ = SUMVQ + Q(I)*V(I)
      SUMV2 = SUMV2 + V(I)**2
      SUMQ2 = SUMQ2 + Q(I)**2
 302 CONTINUE
 C
 C
      SLOPE = (SUMVQ-(SUMV*SUMQ/7.0))/(SUMQ2-((SUMQ**2)/7.0))
      XINT = (SUMV-(SLOPE*SUMQ))/7.0
      SIGMAQ = ((SUMQ2-((SUMQ**2)/7.0))/6.0)**0.5
      SIGMAV = ((SUMV2-((SUMV**2)/7.0))/6.0)**0.5
      CC = SLOPE*SIGMAQ/SIGMAV
      DELTAV = XINT - V(7)
 C
 C
 C  ENTER PARTICLE DIAMETER
 C
 C
```

```
      WRITE(6,102)
  102 FORMAT(1X,'DIAMETER IN MICRONS ?')
      READ(5,*) D
      WRITE(6,99)
   99 FORMAT(1X,'FACTOR ?')
      READ(5,*) FACTOR
      FACTOR = FACTOR*0.000000001
C
C
C  CALCULATE PARTICLE DENSITY AND PARTICLE MASS
C
C
      DEN = FACTOR*XINT/(((D*0.000001)**2)*SLOPE)
C
      WEIGHT = 3.14159265*DEN*((D*0.000001)**3)/6.0
C
C
C  PRINT OUT PARTICLE DENSITY, DIAMETER, MASS, SLOPE, INTERCEPT, AND
C  CORRELATION COEFFICIENT
C
C
      WRITE(6,103) DEN
      WRITE(2,103) DEN
  103 FORMAT(1X,'PARTICLE DENSITY = ',F10.1,' kg/m3')
      WRITE(6,104) D
      WRITE(2,104) D
  104 FORMAT(1X,'PARTICLE DIAMETER = ',F10.2,' microns')
      WRITE(6,105) WEIGHT
      WRITE(2,105) WEIGHT
  105 FORMAT(1X,'PARTICLE MASS = ',F20.15,' kg')
      WRITE(6,106) SLOPE
      WRITE(2,106) SLOPE
  106 FORMAT(1X,'EXPERIMENTAL SLOPE = ',F10.6)
      WRITE(6,107) XINT
      WRITE(2,107) XINT
  107 FORMAT(1X,'EXPERIMENTAL INTERCEPT = ',F10.3,' volts')
      WRITE(6,108) CC
      WRITE(2,108) CC
  108 FORMAT(1X,'CORRELATION COEFFICIENT = ',F10.6)
      WRITE(6,109) DELTAV
      WRITE(2,109) DELTAV
  109 FORMAT(1X,'INTERCEPT - VOLTAGE WITH ZERO FLOW = ',F10.5)
C
C
  777 WRITE(6,*) 'ERROR IN VOLTAGE FILE READ'
  400 CONTINUE
C
C
      STOP
      END
```

```
      PROGRAM WEIGH_PARTICLE
C*************************************************************************
C
C  This program records a voltage from the KEITHLEY 192 voltmeter every
C       time that the footpedal is pressed. The voltmeter is set for
C       6-1/2 digits with no filtering, DC volts and autoranging. The
C       results are displayed to the screen and stored in
C       '/USER/DATA/OUTPUT/VOLTAGE'. The program is halted by depressing
C       any key on the keyboard. The VM instructions are stored
C       as INSTRUCTIONS. They are then converted
C       to integer form as OUT_DATA. The data are sent to the VM and the
C       device is triggered. The voltages are read from the
C       VM as IN_DATA and converted to characters in RESULTS.
C       The GPIB routines are documented in the GPIB directory.
C       ADDR, TADDR, and LADDR are the VM's address, talker address and
C       listener address respectively
C
C
C*************************************************************************
      INTEGER*1,OUT_DATA(20),IN_DATA(16),ADDR(3),TADDR(3),LADDR(3)
      INTEGER*1 LETTER
      INTEGER*2 EOSO,EOSI,STATUS,STAT,IREAD
      CHARACTER INSTRUCTIONS*20,RESULTS*16,ANSWER*5
      logical yes
      integer*2 level,exep

      data level/'46h/
C  The keyboard buffer is on interrupt level 46H

      DATA ADDR,TADDR,LADDR/'8H,2*'0FFH,'48H,2*'0FFH,'28H,2*'0FFH/
      DATA INSTRUCTIONS/'T0F0R0K000S7M1Z0W0X'/

      PARAMETER (IREAD = 200)

      OPEN (1,FILE='/USER/DATA/OUTPUT/SURFACE')

      CALL GPIBINIT
      EOSO = 66
      EOSI = 10


      DO 300 I = 1,20
        OUT_DATA(I) = ICHAR(INSTRUCTIONS(I:I))
        IF (INSTRUCTIONS(I:I) .EQ. 'X') J = I
300   CONTINUE
      STATUS = 0

      CALL GPIBWRITE(LADDR,OUT_DATA,J,EOSO)

310   STATUS = 0
```

```
      WRITE (6,*) 'READ DATA?'
      READ (5,100) ANSWER
100   FORMAT (A)

      IF (ANSWER(1:1) .NE. 'Y') GO TO 320

C Disable the keyboard buffer.
      call rqdisable(%val(level),exep)

      ML = 16
      IPREV = 0
      RESULTS((ML-1):ML) = '  '

340   CALL OUTPUT(#0BH,4)

C Check to see if a key has been pressed to stop the program
      call key_press_check(yes)
      if (yes) GO TO 320

C Check to see if the footpedal has been depressed  If so
C       read voltmeter
      CALL INW(#0CH,IANS)
      IF (IANS.GT.2048) IANS=IANS OR #08000H
      IF ((IANS.GE.IREAD) AND.(IPREV.LT.IREAD)) THEN
        CALL GPIBREAD(IADDR,IN_DATA,ML,EOSI,STAT)
        DO 330 L = 1,ML-2
           RESULTS(L:L) = CHAR(IN_DATA(L))
330     CONTINUE
        WRITE (6,*) RESULTS
        WRITE (1,*) RESULTS
        IPREV = IANS
        GO TO 340
      ELSE
        IPREV = IANS
        GO TO 340
      END IF

320   CONTINUE
      CALL INPUT(#2EH,LETTER)

C Reenable the keyboard buffer.
      call rqenable(%val(level),exep)

C Reset the voltmeter.
      INSTRUCTIONS = 'T4F0R0K0Q0S7X'
      DO 337 I = 1,20
        OUT_DATA(I) = ICHAR(INSTRUCTIONS(I:I))
        IF (INSTRUCTIONS(I:I) .EQ. 'X') J = I
337   CONTINUE

      CALL GPIBWRITE(IADDR,OUT_DATA,J,EOSO)
```

```
CALL GPIBEND
END
```

```
      PROGRAM SURFACE_AREA_ANALYSIS

C*************************************************************************
C  This program calculates the SURFACE AREA of a single particle using
C      carbon dioxide adsorption as measured by the
C      voltages stored in /USER/DATA/OUTPUT/SURFACE
C
C      The final surface area is displayed on the screen
C      and in the file /USER/DATA/OUTPUT/SA.  A plot of log(mols of
C      carbon dioxide adsorbed divided by the particle weight) versus
C      [log(P0/P)]**2 is stored in/USER/DATA/EP/SA.
C*************************************************************************

      DIMENSION V(14), p(5), slope(5), v0(5), xnlog(5), plog(5)

      OPEN (1,FILE='/USER/DATA/OUTPUT/SURFACE')
      OPEN (2,FILE='/USER/DATA/OUTPUT/SA')
      OPEN (3,FILE='/USER/DATA/EP/SA')

      WRITE (3,100)
100   FORMAT('CRTP 1'/'SYMB 4'/'XLEN 6'/'XLAB [LOG(P0/P)]**2'/
     & 'YLAB LOG(n/W)'/'TITL DUBININ-POLANYI PLOT'/
     & 'SYHT .25'/'XMIN 0.0'/'XMAX 8.0'/'YMIN -3.5'/'YMAX -2.0')

110   FORMAT(4X,F12.0)
C
C
      P(2) = 0.2
      P(3) = 0.35
      P(4) = 0.5
      P(5) = 1.0
C
C     READ BALANCING VOLTAGES FROM DATA FILE
C
      DO 10 I = 1,14
      READ(1,110) V(I)
   10 CONTINUE
C
C     READ CHAMBER TEMPERATURE
C
      WRITE(6,130)
130 FORMAT(1X,'CHAMBER TEMP (degrees C) ?')
      READ(5,*) T
C
C     DETERMINE ZERO FLOW BALANCING VOLTAGES FOR FIVE GAS MIXTURES
C
      DO 20 I = 1,7
      J = 2*I - 1
      V(I) = (V(J) + V(J+1))/2.0
   20 CONTINUE
C
```

```
      SUMX = 1500.0
      SUMX2 = 770000
C
      SUMY = 0.0
      SUMXY = 0.0
      DO 40 J = 1,3
      K = J
      L = 700 - J*100
      SUMY = SUMY + V(K)
      SUMXY = SUMXY + V(K)*L
   40 CONTINUE
      SLOPE(1) = (SUMXY-SUMX*SUMY/3.)/(SUMX2-SUMX**2/3.)
      V0(1) = (SUMY - SLOPE(1)*SUMX)/3.
C
C
      V0(2) = -0 88*SLOPE(1)*600.0 + V(4)
      V0(3) = -0.89*SLOPE(1)*600.0 + V(5)
      V0(4) = -0.77*SLOPE(1)*600.0 + V(6)
      V0(5) = -0.62*SLOPE(1)*600.0 + V(7)
C
C     CALCULATE THE SATURATION VAPOR PRESSURE, P0
C
      TEMP = T + 273 15
      POLOG = -874.34/TEMP + 4 7366
      P0 = 10**POLOG
C
      DO 50 I = 2,5
      RATIO = P0/P(I)
      X = ALOG10(RATIO)
      PLOG(I) = X**2
   50 CONTINUE
C
      DO 60 I = 2,5
      RATIO = (V0(I)/V0(1) - 1.0)/44.01
      XNLOG(I) = ALOG10(RATIO)
   60 CONTINUE
C
C
C
      DO 65 I = 2,5
      WRITE(3,120) PLOG(I), XNLOG(I)
   65 CONTINUE
120 FORMAT(1X,F15.5,' , ',F15.5)
C
C
      SUMX = 0.0
      SUMY = 0.0
      SUMXY = 0.0
      SUMX2 = 0.0
      SUMY2 = 0.0
C
```

```
      DO 70 I = 2,5
      SUMX = SUMX + PLOG(I)
      SUMY = SUMY + XNLOG(I)
      SUMXY = SUMXY + PLOG(I)*XNLOG(I)
      SUMX2 = SUMX2 + PLOG(I)**2
      SUMY2 = SUMY2 + XNLOG(I)**2
   70 CONTINUE
C
      SLOPESA = (SUMXY-SUMX*SUMY/4.)/(SUMX2-SUMX**2/4.)
      XINT = (SUMY - SLOPESA*SUMX)/4.0
      SIGX = ((SUMX2-SUMX**2/4.0)/3.0)**0.5
      SIGY = ((SUMY2-SUMY**2/4 0)/3.0)**0.5
      R = SLOPESA*SIGX/SIGY
C
      AREA = (10.0**XINT)*1.457566E05
C
      WRITE(6,103) AREA
      WRITE(2,103) AREA
  103 FORMAT(1X,'SURFACE AREA = ',F10 1,' m2/g')
      WRITE(2,104) xint
  104 FORMAT(1X,'intercept = ',F10 5)
      WRITE(2,105) slopesa
  105 FORMAT(1X,'slope = ',F20.15)
      WRITE(2,125) r
  125 format(1x,'correlation coefficient = ',f10.6)
      WRITE(6,106) temp
      WRITE(2,106) temp
  106 FORMAT(1X,'chamber temperature = ',F10.2,' K')
      WRITE(2,107) p0
  107 FORMAT(1X,'saturation vapor pressure = ',F10 3,' atm.')
      WRITE(2,108)
  108 FORMAT(1X,'           ')
      WRITE(2,109)
  109 FORMAT(1X,'log(n/W) versus [log(P0/P)]**2')
      DO 80 I = 2,5
      WRITE(2,111) XNLOG(I), PLOG(I)
   80 CONTINUE
  111 FORMAT(1X,2F15.5)
      WRITE(2,108)
      WRITE(2,112)
  112 FORMAT(1X,'BALANCING VOLTAGES AT ZERO FLOW')
      WRITE(2,108)
      WRITE(2,113)
  113 FORMAT(1X,'    VOLTAGE          SLOPE   ')
      WRITE(2,114) VG(1), SLOPE(1)
  114 FORMAT(1X,2F15.5,' PURE NITROGEN')
      WRITE(2,115) VG(2)
  115 FORMAT(1X,F15.5,'              20% CO2')
      WRITE(2,116) VG(3)
  116 FORMAT(1X,F15.5,'              35% CO2')
      WRITE(2,117) VG(4)
```

```
117 FORMAT(1X,F15.5,'              50% CO2')
    WRITE(2,118) V0(5)
118 FORMAT(1X,F15.5,'             100% CO2')
C
C
C
C
    STOP
    END
```

```
      PROGRAM VOLT_TESTER
C
C
C ***************************************************************************
C
C     This program collects the 2 micon, 4 micon, log ratio, and bal-
C     voltage signals versus time at a rate controlled by /USER/DATA/
C     INPUT/VMD.
C
C***************************************************************************
C
C
      INTEGER*1,OUT_DATA(20),IN_DATA(18,7200),ADDR(3),TADDR(3),LADDR(3)
      INTEGER*2 EOSO,EOSI,STAT,IREAD, IANS
      CHARACTER INSTRUCTIONS*20,RESULTS*16,ANSWER*5,SPEED
      DATA ADDR,TADDR,LADDR/'8H,2**0FFH,'48H,2**0FFH,'28H,2**0FFH/
      OPEN (1,FILE='/USER/DATA/OUTPUT/TWO')
      OPEN (2,FILE='/USER/DATA/OUTPUT/FOUR')
      OPEN (3,FILE='/USER/DATA/OUTPUT/LOG')
      OPEN (7,FILE='/USER/DATA/OUTPUT/VM')
      OPEN (8,FILE='/USER/DATA/INPUT/VMD')
      CALL OUTPUT('0Z7H,'070H)
      CALL GPIBINIT
      EOSO = 88
      EOSI = 10
      ML = 18
      WRITE (6,*) 'HOW MANY POINTS ((7200)?'
      READ (5,*) NPOINTS



      READ (8,110) INSTRUCTIONS
      DO 300 I = 1,20
        OUT_DATA(I) = ICHAR(INSTRUCTIONS(I:I))
        IF (INSTRUCTIONS(I:I) .EQ. '5') SPEED = INSTRUCTIONS(I+1:I+1)
        IF (INSTRUCTIONS(I:I)  EQ. 'X') J = I
300   CONTINUE
      WRITE(6,*) 'XXX'
      STAT = 0
      IF (SPEED .EQ. '0') THEN
        TIME = 0 072
      ELSE IF ((SPEED .GE. '1') .AND. (SPEED .LE. '4')) THEN
        TIME = 0.13
      ELSE
        TIME = 0.47262
      END IF
      WRITE(6,*) 'YYY'
      CALL GPIBWRITE(LADDR,OUT_DATA,J,EOSO)
      WRITE (6,*) 'PROCEED?'
      READ (5,183) ANSWER
183 FORMAT(A)
```

```
      IF (ANSWER EQ.'N'.OR.ANSWER.EQ.'n') go to 777
C     CALL GPIBTRIG(LADDR)
      MCOUNT = 0
        DO 411 L = 1,NPOINTS

        CALL GPIBREAD(TADDR,IN_DATA(1,L),ML,EOSI,STAT)
C
        WRITE (6,*) '*'
C
      MCOUNT = MCOUNT + 1
      IF(MCOUNT.EQ.5) GO TO 18
      GO TO 411
C
   18 MCOUNT = 0
      CALL OUTPUT(#0BH,0)
      CALL INW(#0CH,IANS)
      TEMP = FLOAT(IANS)
      IF (IANS.GT.2048) IANS=IANS.OR.#08000H
      CALL INW(#0CH,IANS)
      IF (FLOAT(IANS).GT.10240.0) GO TO 11
      IF (FLOAT(IANS).LT.0.0) GO TO 11
      WRITE(1,200) L*TIME, FLOAT(IANS)/204.8
      GO TO 12
C
   11 CALL OUTPUT(#0BH,0)
      CALL INW(#0CH,IANS)
      IF (IANS.GT.2048) IANS=IANS.OR.#0800H
      TEMP = FLOAT(IANS)/204.8
      WRITE(1,200) L*TIME, FLOAT(IANS)/204.8
   12 CONTINUE
C
C
      CALL OUTPUT(#0BH,1)
      CALL INW(#0CH,IANS)
      TEMP = FLOAT(IANS)
      IF (IANS.GT.2048) IANS=IANS.OR.#08000H
      CALL INW(#0CH,IANS)
      IF (FLOAT(IANS).GT.10240.0) GO TO 13
      IF (FLOAT(IANS).LT.0.0) GO TO 13
      WRITE(2,200) L*TIME, FLOAT(IANS)/204.8
      GO TO 14
C
   13 CALL OUTPUT(#0BH,1)
      CALL INW(#0CH,IANS)
      IF (IANS.GT.2048) IANS=IANS.OR.#0800H
      TEMP = FLOAT(IANS)/204.8
      WRITE(2,200) L*TIME, FLOAT(IANS)/204.8
   14 CONTINUE
C
C
      CALL OUTPUT(#0BH,2)
```

```
      CALL INW(#0CH,IAN5)
      TEMP = FLOAT(IAN5)
      IF (IAN5.GT.2048) IAN5=IAN5.OR.#C000H
      CALL INW(#0CH,IAN5)
      IF (FLOAT(IAN5).GT.10240.0) GO TO 15
      IF (FLOAT(IAN5).LT.0.0) GO TO 15
      WRITE(3,200) L*TIME, FLOAT(IAN5)/204.8
      GO TO 16
C
   15 CALL OUTPUT(#0BH,2)
      CALL INW(#0CH,IAN5)
      IF (IAN5.GT.2048) IAN5=IAN5.OR.#0800H
      TEMP = FLOAT(IAN5)/204.8
      WRITE(3,200) L*TIME, FLOAT(IAN5)/204.8
   16 CONTINUE
C
C
411   CONTINUE
      WRITE (6,*) 'THE RAIN IN SPAIN FALLS MAINLY ON THE PLAIN.'
      DO 450 IT = 1,NPOINTS
        DO 430 L = 1,16
           RESULTS(L:L) = CHAR(IN_DATA(L,IT))
430     CONTINUE
        WRITE (7,100) IT*TIME,RESULTS
450   CONTINUE
777   CONTINUE
100   FORMAT(F12.3,',',A)
200   FORMAT(F12.3,',',F12.5)
110   FORMAT(A)
      CALL GPIBEND
      CALL OUTPUT(#027H,#076H)
      CALL OUTPUT(#025H,#0D4H)
      CALL OUTPUT(#025H,#050H)
      END
```

APPENDIX B : Natural Convective Drag Algorithms.

```
c
c
c
c     This program solves the energy, vorticity, and stream function
c     equations for natural convection around a heated sphere using
c     a finite difference method.  The Boussenesq approximation is utilized.
c
c
c     important variables:
c     xm_int = interval length in i, radial, or z direction.
c     xn_int = interval length in j or theta direction.
c     M = total number of i, radial, or z intervals.
c     N = total number of j or theta intervals.
c     omega_g = relaxation factor for vorticity.
c     omega_t = relaxation factor for temperature.
c     omega_psi = relaxation factor for the stream function.
c     eps_g = convergence criteria for vorticity.
c     eps_t = convergence criteria for temperature.
c     eps_psi = convergence criteria for the stream function.
c     Pr = Prandtl number of surrounding gas.
c     Gr = Grashof number.
c     t = dimensionless temperature.
c     psi = stream function.
c     g = vorticity.
c     err_t = maximum difference between temperature and updated temperature.
c     err_psi = maximum difference between stream function and updated stream
c               function.
c     err_g = maximum difference between vorticity and updated vorticity.
c     ncount = iteration counter.
c     a1-a16, a20, a111, a112 = factors
c     del_i = change in the stream function in the radial direction.
c     del_j = change in the stream function in the theta direction.
c     omega_th = weighting factor for upwind difference representation of a
c                first-order derivative with respect to theta.
c     omega_z = weighting factor for upwind difference representation of a
c               first-order derivative with respect to z.
c     pre_1 = factor
c     pre_t = factor for temperature equation.
c     pre_g = factor for vorticity equation.
c     res_t = residual for temperature.
c     res_psi = residual for the stream function.
c     res_g = residual for vorticity.
c     L, x1, x2 = factors.
c     xnu = local Nusselt number.
c     xnuss = overall Nusselt number.
c     xk0 = dimensionless pressure at front stagnation point.
c     xk = dimensionless pressure at sphere surface.
c     dgdth = derivative of vorticity wrt theta at theta = 0.0.
c     dgdz = derivative of vorticity wrt z at z = 0.0.
c     cdp = dimensionless pressure drag.
c     cdf = dimensionless viscous drag.
c     cdt = dimensionless total drag.
c
c
c
      program natdrag
c
c
      implicit double precision (A-H)
      implicit double precision (O-Z)
```

```
c
      common /all/ M, N, t(10000), psi(10000), g(10000), xm_int, xn_int
      common /up1/ pr, gr, omega_t, omega_psi, omega_g
      common /up2/ err_t, err_psi, err_g
      common /calc/ xnu(63), xnuss, xk0, xk(63), cdp, cdf, cdt
c
c
      open(unit=20,name='out.dat1',type='new')
c      open(unit=21,name='start1.dat',type='old')
      open(unit=22,name='invar1.dat',type='old')
      open(unit=23,name='invar2.dat',type='old')
c
c
      read(22,*) xm_int
      read(22,*) xn_int
      read(22,*) M
      read(22,*) N
      read(22,*) omega_g
      read(22,*) omega_t
      read(22,*) omega_psi
      read(23,*) eps_g
      read(23,*) eps_t
      read(23,*) eps_psi
      read(23,*) pr
      read(23,*) gr
c
      call iv_set
c
      call bc_set
c
c     Set iteration counter.
c
      ncount = 0
c
c     Begin main program loop.
c
1     continue
      ncount = ncount + 1
c
c     If desirable, the iteration number can be printed after each iteration.
c
      write(6,200) ncount
200   format(1x,'iteration number = ',i5)
c
c
c     Check to see if the number of iteratons is excessive.  If it is,
c     get out of loop, print error messege, and print results.
c
      if(ncount.gt.10000) go to 991
c
      call bc_set
c
      call update
c
c
c     If desirable, residuals can be printed after each iteration.
c
      write(6,606) err_t
      write(6,607) err_psi
      write(6,608) err_g
```

```
606   format(1x,'total temperature residual = ',d20.10)
607   format(1x,'total stream function residual = ',d20.10)
608   format(1x,'total vorticity residual = ',d20.10)
c
c     Check to see if residuals are within error tolerances.  If they are,
c     get out of loop and print the results.  If they aren't, go through
c     another iteration.
c
      if(err_t.lt.eps_t) go to 15
      go to 1
15    if(err_g.lt.eps_g) go to 16
      go to 1
16    if(err_psi.lt.eps_psi) go to 17
      go to 1
17    continue
c
c
c     Print results into output file.
c
      write(20,105) ncount
105   format(1x,i6,'  iterations')
c
c     Print input variables read from invar1.dat and invar2.dat.
c
      write(20,106) eps_t
106   format(1x,'conv. criterion for temp = ',d20.10)
      write(20,107) eps_g
107   format(1x,'conv. criterion for vorticity = ',d20.10)
      write(20,108) eps_psi
108   format(1x,'conv. criterion for stream fun = ',d20.10)
c
      write(20,109) pr
109   format(1x,'Prandtl number = ',d10.5)
      write(20,110) gr
110   format(1x,'Grashof number = ',d10.5)
c
      write(20,111) M
111   format(1x,'total number of radial intervals = ',i4)
      write(20,112) N
112   format(1x,'total number of theta intervals = ',i4)
      write(20,113) xm_int
113   format(1x,'radial mesh size = ',d20.10)
      write(20,114) xn_int
114   format(1x,'theta mesh size = ',d20.10)
c
c
      write(20,135)
c      write(20,455)
c455   format(1x,'    r    theta velocity (cm/sec)    radial velocity')
c
c
c      If desirable, velocities can be calculated from stream functions.
c
c
c      theta = 1.*xn_int
c      do 44 i = 1,M-1
c      k = 1.*M + i
c      k1 = k + 1
c      k2 = k - 1
c      k3 = k + M
```

```
c       k4 = k - M
c       z = (i-1)*xm_int
c       r = dexp(z)
c       pre_v = 1./(dexp(2.*z)*dsin(theta))
c       dpsidth = (psi(k3)-psi(k))/xn_int
c       dpsidz = (psi(k1)-psi(k))/xm_int
c       vrdim = - pre_v*dpsidth
c       vthdim = pre_v*dpsidz
c       vr = 15.63*vrdim
c       vth = 15.63*vthdim
c       write(20,456) r, vth, vr, t(k)
c456    format(1x,1x,d20.10,1x,d20.10,1x,d20.10,1x,d20.10)
c44     continue
c
c
      write(20,135)
c
c     Print temperature, stream function, and vorticity as a function
c     of theta and r.
c
      do 2 j = 1,N
      write(20,120)
120   format(1x,'      r       temp     stream fun     vorticity')
      theta = (j-1)*xn_int
      write(20,125) theta
125   format(1x,'theta =  ',d20.10)
      do 3 i = 1,M
      z = xm_int*(i-1)
      r = dexp(z)
      k2 = (j-1)*M + i
      if(j.eq.1.or.j.eq.N) go to 18
      g(k2) = g(k2)/(dexp(z)*dsin(theta))
      go to 680
18    g(k2) = g(k2)
c680   continue
680   write(20,130) r, t(k2), psi(k2), g(k2)
130   format(1x,' ',d10.5,' ',d20.10,' ',d15.5,' ',d20.10)
3     continue
2     continue
c
c
      call calc
c
c     Print Nusselt numbers, pressures, and dimensionless drag coeffients.
c
      write(20,135)
135   format(1x,'  ')
      write(20,140) xnuss
140   format(1x,'The overall Nusselt number =  ',d10.5)
      write(20,145) xk0
145   format(1x,'dimen. pressure at stag. point = ',d20.10)
      write(20,150) cdp
150   format(1x,'dimensionless pressure drag = ',d20.10)
      write(20,155) cdf
155   format(1x,'dimensionless viscous drag = ',d20.10)
      write(20,160) cdt
160   format(1x,'dimensionless total drag = ',d20.10)
c
      write(20,135)
c
```

```
c     Print local Nusselt number and dimensionless pressure at sphere
c     surface as a function of theta.
c
      write(20,165)
165   format(1x,'       theta        Nusselt        pressure')
c
      do 4 i = 1,N
      theta = (i-1)*xn_int
      write(20,170) theta, xnu(i), xk(i)
170   format(1x,3d20.10)
4     continue
c
      go to 990
c
c     ERROR MESSEGES
c
991   write(6,175)
      write(20,175)
175   format(1x,'over 10,000 iterations; did not converge!!!! ')
      go to 17
c
c
990   stop
      end
c
c
      subroutine iv_set
c
      implicit double precision (A-H)
      implicit double precision (O-Z)
c
      common /all/ M, N, t(10000), psi(10000), g(10000), xm_int, xn_int
c
c     This subroutine sets the initial values of temperture, vorticity, and
c     stream function.
c
c      Set initial values to zero.
c
      k = M*N
      do 10 i = 1,k
      t(k) = 0.0
      psi(k) = 0.0
      g(k) = 0.0
10    continue
c
c
c     Read initial values from input file.
c
c      do 34 j = 1,N
c      do 35 i = 1,M
c      k = (j-1)*M + i
c      z = (i-1)*xm_int
c      theta = (j-1)*xn_int
c      read(21,305) xjunk, t(k), psi(k), g(k)
c305   format(1x,1x,d10.5,1x,d20.10,1x,d15.5,1x,d20.10)
c      g(k) = g(k)*dexp(z)*dsin(theta)
c35    continue
c34    continue
c
      return
```

```
      end
c
c
c
      subroutine bc_set
c
      implicit double precision (A-H)
      implicit double precision (O-Z)
c
      common /all/ M, N, t(10000), psi(10000), g(10000), xm_int, xn_int
c
c     This subroutine sets the boundary conditions for the problem.
c
c     Along the bottom of the grid, i.e. theta = 0.0, is an axis of symmetry.
c
      b1 = 18./11.
      b2 = - 9./11.
      b3 = 2./11.
      b4 = - 5./12.
      b5 = 61./24.
      b6 = - 13./2.
      b7 = 107./12.
      b8 = - 77./12.
      b9 = 2./(xm_int**2)
c
      do 11 i = 1,M
      k = i
      k1 = i + M
      k2 = k1 + M
      k3 = k2 + M
c      t(k) = t(k1)
      t(k) = b1*t(k1) + b2*t(k2) + b3*t(k3)
      psi(k) = 0.0
      g(k) = 0.0
11    continue
c
c     Along the top of the grid, i.e. theta = pi, is also an axis of symmetry.
c
      do 21 i = 1,M
      k = M*(N-1) + i
      k1 = k - M
      k2 = k1 - M
      k3 = k2 - M
c      t(k) = t(k1)
      t(k) = b1*t(k1) + b2*t(k2) + b3*t(k3)
      psi(k) = 0.0
      g(k) = 0.0
21    continue
c
c     Along the left hand side of the grid, i.e. the particle surface.
c
      z1 = xm_int
      do 31 i = 1,N
      k = M*(i-1) + 1
      k1 = k + 1
      k2 = k1 + 1
      k3 = k2 + 1
      k4 = k3 + 1
      k5 = k4 + 1
      t(k) = 1.0
```

```
      psi(k) = 0.0
      c1 = b4*psi(k5) + b5*psi(k4) + b6*psi(k3)
      c2 = b7*psi(k2) + b8*psi(k1)
      c = c1 + c2
c      c = (3.*psi(k1) - 3.*psi(k2)/4. + psi(k3)/9.)/(z1**2)
c      c = 2.*psi(k1) - psi(k2)/4.
c      c = psi(k2)/2. - psi(k1)
c      c=25.*psi(k4)/24.-14.*psi(k3)/3.+33.*psi(k2)/4.-20.*psi(k1)/3.
      g(k) = b9*c
c      g(k) = 2.0*psi(k1)/(xm_int**2)
c      g(k) = (-5.*psi(k1)+4.*psi(k2)-psi(k3))/(xm_int**2)
31    continue
c
c     Along the right hand side of the grid, i.e. the outer boundary.
c
      zin = xm_int*(M-1)
      do 41 i = 1,N
      k = M*i
      k1 = k - 1
      k2 = k1 - 1
      k3 = k2 - 1
      k4 = k3 - 1
      k5 = k4 - 1
      t(k) = 0.0
      psi(k) = 2.*psi(k1) - psi(k2)
c      psi(k) = 0.0
c      c1 = -5.*psi(k5)/12. + 61.*psi(k4)/24. - 13.*psi(k3)/2.
c      c2 = 107.*psi(k2)/12. - 77.*psi(k1)/12.
c      c = c1 + c2
c      c = psi(k2)/2. - psi(k1)
c      g(k) = 2.*c/(xm_int**2)
c      g(k) = 0.0
      g(k) = 2.*g(k1) - g(k2)
41    continue
c
      return
      end
c
c
      subroutine update
c
      implicit double precision (A-H)
      implicit double precision (O-Z)
c
      common /all/ M, N, t(10000), psi(10000), g(10000), xm_int, xn_int
      common /up1/ pr, gr, omega_t, omega_psi, omega_g
      common /up2/ err_t, err_psi, err_g
c
c     This program updates the values for temperature, vorticity, and stream
c     function using an extrapolated Gauss-Siedel method.
c
      err_t = 0.0
      err_g = 0.0
      err_psi = 0.0
c
      a1 = 1.0/(xm_int**2) - 1.0/(2.0*xm_int)
      a2 = 1.0/(xm_int**2) + 1.0/(2.0*xm_int)
      a3 = 2.0/(xm_int**2) + 2.0/(xn_int**2)
c
      do 12 j = 1,N-2
```

```
      do 22 i = 1,M-2
      k = j*M + i + 1
c
      k1 = k + 1
      k2 = k - 1
      k3 = k + M
      k4 = k - M
c
      theta = j*xn_int
      z = xm_int*i
      a4 = 1./(xn_int**2) - 1./(dtan(theta)*2.*xn_int)
      a5 = 1./(xn_int**2) + 1./(dtan(theta)*2.*xn_int)
c
c     Check sign of del psi's
c
      del_i = psi(k1) - psi(k2)
      del_j = psi(k3) - psi(k4)
      if(del_i.gt.0.0) go to 90
      omega_th = 1.0
      go to 91
90    omega_th = 0.0
91    continue
c
      if(del_j.lt.0.0) go to 92
      omega_z = 1.0
      go to 93
92    omega_z = 0.0
93    continue
c
      pre_1 = 1./(2.*xm_int*xn_int*dexp(z)*dsin(theta))
c
c     The energy equation is used to update the temperture at each node.
c
c
      a16 = del_i*(1. - 2.*omega_th) - del_j*(1. - 2.*omega_z)
      pre_t = pre_1*a16 + (a3/pr)
c
      a15 = (1.0/pr)*(a2*t(k1) + a1*t(k2)+a5*t(k3)+a4*t(k4) )
      a13 = -(del_i*pre_1)*(omega_th*t(k3)-(1.-omega_th)*t(k4))
      a14 = (del_j*pre_1)*(omega_z*t(k1)-(1.-omega_z)*t(k2))
      temp_t = ( a13 + a14 + a15 ) / pre_t
c
      res_t = dabs( t(k) - temp_t )
      err_t = err_t + res_t
c
c      if(res_t.gt.err_t) err_t = res_t
c
      t(k) = t(k) + omega_t*( temp_t-t(k) )
c
c     The stream function equation is used to update the stream function at
c     each node.
c
      a20 = a1*psi(k1) + a2*psi(k2) + a4*psi(k3) + a5*psi(k4)
      temp_psi = (1./a3)*( a20 - g(k)*dexp(2.*z) )
c
c      a21 = a3 + (1.-2.*omega_z)/xm_int
c      a22 = (1.-2.*omega_th)/(xn_int*dtan(theta))
c      a23 = a21 + a22
c      a24 = 1.0/(xm_int**2) - omega_z/xm_int
c      a25 = 1.0/(xm_int**2) + (1.0-omega_z)/xm_int
```

```
c       a26 = 1.0/(xn_int**2) - omega_th/(xn_int*dtan(theta))
c       a27 = 1.0/(xn_int**2) + (1.0-omega_th)/(xn_int*dtan(theta))
c       a28 = a24*psi(k+1) + a25*psi(k-1) + a26*psi(k+M) + a27*psi(k-M)
c       temp_psi = (1.0/a23)*(a28 - (dexp(2.0*z))*g(k))
c
        res_psi = dabs( psi(k) - temp_psi )
        err_psi = err_psi + res_psi
c       if(res_psi.gt.err_psi) err_psi = res_psi
        psi(k) = psi(k) + omega_psi*(temp_psi-psi(k))
c
c       The vorticity equation is used to update the vorticity at each node.
c
        a111 = del_i*pre_1
        a112 = 1. - 2.*omega_th - 2.*xn_int/dtan(theta)
        a11 = a111*a112
        a12 = (del_j*pre_1)*(1. - 2.*omega_z - 2.*xm_int)
        pre_g = a11 - a12 + a3
c
        a6 = omega_th*g(k3) - (1. - omega_th)*g(k4)
        a7 = omega_z*g(k1) - (1. - omega_z)*g(k2)
        a8 = a1*g(k1) + a2*g(k2) + a4*g(k3) + a5*g(k4)
        a9 = dexp(2.*z)*((dsin(theta))**2)*gr/(2.*xm_int*xn_int)
        a10 = xn_int*(t(k1)-t(k2))+(xm_int/dtan(theta))*(t(k3)-t(k4))
        top = -(del_i*pre_1)*a6 + (del_j*pre_1)*a7 + a8 + a9*a10
        temp_g = top/pre_g
c
        res_g = dabs( g(k) - temp_g )
        err_g = err_g + res_g
c       if(res_g.gt.err_g) err_g = res_g
        g(k) = g(k) + omega_g*(temp_g-g(k))
c
22      continue
12      continue
c
c
        return
        end
c
c
        subroutine calc
c
c
c       This subroutine calculates the Nusselt number, pressure, and drag
c       force.
c
        implicit double precision (A-H)
        implicit double precision (O-Z)
c
        common /all/ M, N, t(10000), psi(10000), g(10000), xm_int, xn_int
        common /up1/ pr, gr, omega_t, omega_psi, omega_g
        common /up2/ err_t, err_psi, err_g
        common /calc/ xnu(63), xnuss, xk0, xk(63), cdp, cdf, cdt
c
c       Calculation of the Nusselt number as a function of theta and the
c       calculation of the overall Nusselt number.  The trapezoid rule is
c       when integrals are performed.
c
        xnuss = 0.0
        do 50 I = 1,N
        J = M*(I-1) + 1
```

```
      K = J + 1
      k2 = K + 1
c      xnu(I) = -2.0*( t(K) - t(J) ) / xm_int
      xnu(I) = (-4.0*t(K) + t(k2) + 3.0)/xm_int
      theta = (I-1)*xn_int
      if(I.eq.1.or.I.eq.N) go to 19
      L = 2
      go to 20
19    L = 1
20    continue
      xnuss = xnuss + (xn_int/4.0)*(L*xnu(I)*dsin(theta))
50    continue
c
c
c     Calculation of the dimensionless pressure at the front stagnation
c     point.
c
      xk0 = 0.0
      do 51 i = 1,M
      k1 = i + M
      k2 = k1 + M
      k3 = k2 + M
      z = (i-1)*xm_int
      sub = g(k3) - 3.*g(k2) + 3.*g(k1)
c      dgdth = (g(k2)-sub)/(2.*xn_int)
c      dgdth = ( g(k1) - g(i) ) / xn_int
c      dgdth = (-3.*g(i)/2. + 2.*g(k1) - g(k2)/2.)/xn_int
      dgdth = (-11.*sub/6.+3.*g(k1)-3.*g(k2)/2.+g(k3)/3.)/xn_int
      if(i.eq.1.or.i.eq.M) go to 71
      L = 2
      go to 72
71    L = 1
72    continue
      x1 = (2.0*xm_int)*(L*dgdth)
      x2 = (gr*xm_int)*(L*t(i)*dexp(z))
      xk0 = xk0 + x1 + x2
51    continue
c
c     Calculation of the dimensionless pressure at the sphere surface, the
c     dimensionless pressure drag, and the dimensionless viscous drag.
c
      cdp = 0.0
      cdf = 0.0
      xkth1 = 0.0
      do 52 j = 1,N
      theta = (j-1)*xn_int
      k1 = (j-1)*M + 1
      k2 = k1 + 1
      k3 = k2 + 1
      k4 = k3 + 1
      if(j.eq.1.or.j.eq.N) go to 73
      L = 2
      go to 74
73    L = 1
74    continue
      sub = g(k4) - 3.*g(k3) + 3.*g(k2)
c      dgdz = (g(k3) - g(k2))/xm_int
c      dgdz = ( g(k3)-sub ) / (2.*xm_int)
c      dgdz = ( g(k2) - sub ) / xm_int
c      dgdz = (-3.*sub/2. + 2.*g(k2) - g(k3)/2.)/xm_int
```

```
      dgdz = (-11.*g(k1)/6.+3.*g(k2)-3.*g(k3)/2.+g(k4)/3.)/xm_int
      xkth1 = xkth1 + xn_int*L*( dgdz + g(k1) )
      xk(j) = xk0 + 2.0*gr*(1.0 - dcos(theta)) + xkth1
      cdp = cdp + (xn_int/2.0)*xk(j)*L*sin(2.0*theta)
      cdf = cdf + (2.0*xn_int)*L*g(k1)*(dsin(theta)**2)
52    continue
      cdt = cdp + cdf
c
      return
      end
```

```
c
c
c
c     This program solves the transient energy, vorticity, and stream function
c     equations for natural convection around a heated sphere using
c     a finite difference method.  The Boussenesq approximation is utilized.
c
c
      program trans
c
c
      implicit double precision (A-H)
      implicit double precision (O-Z)
c
      dimension tim(2000),gim(2000),pim(2000),tiim(2000),xim(2000)
      dimension xnim(2000),cpim(2000),cfim(2000),ctim(2000)
c
      common /all1/ M, N, t(100,31), psi(100,31), g(100,31)
      common /all2/ xm_int, xn_int, del_t, tmax
      common /up1/ pr, gr, omega_psi, err_psi
      common /calc/ xnu(63), xnuss, xk0, xk(63), cdp, cdf, cdt
      common /up2/ temp(100,31), tempg(100,31), tempsi(100,31)
c
c
      open(unit=21,name='start37.dat',type='old')
      open(unit=22,name='invartr1.dat',type='old')
      open(unit=23,name='invartr2.dat',type='old')
c
c
      read(22,*) xm_int, xn_int, M, N, omega_psi
      read(23,*) eps_psi, pr, gr, del_t, tmax
c
      call iv_set
c
      call bc_set
c
c     Set iteration counter.
c
      ncount = 0
      tcount = 0.0
      L = 0
      LD1 = 0
      LD2 = 0
      tstart = 10.0*del_t
c
      go to 17
c
c     Begin stream function iteration loop.
c
1     continue
      ncount = ncount + 1
c
c     If desirable, the iteration number can be printed after each iteration.
c
c      write(6,200) ncount
c200   format(1x,'iteration number = ',i5)
c
c
c     Check to see if the number of iteratons is excessive.  If it is,
c     get out of loop, print error messege, and print results.
```

```
c
      if(ncount.gt.10000) go to 991
c
      call bc_set
c
      call update
c
c      write(6,444) err_psi
c444   format(1x,'stream function error = ',d20.10)
c
c     Check to see if the stream function residual is within error
c     tolerance.  If it is, get out of loop and print the results.
c     If it isn't, go through another iteration.
c
      if(err_psi.lt.eps_psi) go to 171
      go to 1
c
171   continue
c
c      xit = abs(g(1,11) - tempg(1,11))
c      if(tcount.lt.tstart) go to 9
c      if(xit.gt.0.0005) go to 9
c      del_t = 1.1*del_t
c      if(del_t.gt.1) del_t = 0.5
c
c9     continue
      do 173 i = 1,M
      do 172 j = 1,N
      t(i,j) = temp(i,j)
      g(i,j) = tempg(i,j)
172   continue
173   continue
c
17    continue
c
c
      L = L + 1
      tcount = tcount + del_t
      time = tcount - del_t
      write(6,777) time
777   format(1x,'time = ',d20.10)
      if(L.eq.15) go to 44
      if(tcount.gt.tmax) go to 18
c
25    continue
c
      do 35 j = 1,N
      do 36 i = 1,M
      tempsi(i,j) = psi(i,j)
36    continue
35    continue
c
c
      call tempvor
c
      if(L.eq.14) go to 701
      go to 702
701   open(unit=24,name='outtr1.dat',type='old')
      LD1 = LD1 + 1
      tim(ld1) = time
```

```
      gim(ld1) = g(1,11)
      pim(ld1) = psi(2,11)
      do 703 Lit = 1,LD1
      write(24,778) tim(Lit), gim(Lit), pim(Lit)
703   continue
778   format(1x,3d20.10)
      close(unit=24)
702   continue
c
      ncount = 0
      go to 1
c
18    continue
c
      L = 0
c
c     Print results into output file.
c
      write(20,105) ncount
105   format(1x,i6,'  iterations')
c
      write(20,106) time
106   format(1x,'dimensionless time = ',d20.5)
c
c     Print input variables read from invar1.dat and invar2.dat.
c
      write(20,108) eps_psi
108   format(1x,'conv. criterion for stream fun = ',d20.10)
c
      write(20,109) pr
109   format(1x,'Prandtl number = ',d10.5)
      write(20,110) gr
110   format(1x,'Grashof number = ',d10.5)
c
      write(20,111) M
111   format(1x,'total number of radial intervals = ',i4)
      write(20,112) N
112   format(1x,'total number of theta intervals = ',i4)
      write(20,113) xm_int
113   format(1x,'radial mesh size = ',d20.10)
      write(20,114) xn_int
114   format(1x,'theta mesh size = ',d20.10)
c
c
c      theta = 1.*xn_int
c      do 44 i = 1,M-1
c      k = 1.*M + i
c      k1 = k + 1
c      k2 = k - 1
c      k3 = k + M
c      k4 = k - M
c      z = (i-1)*xm_int
c      r = dexp(z)
c      pre_v = 1./(dexp(2.*z)*dsin(theta))
c      dpsidth = (psi(k3)-psi(k))/xn_int
c      dpsidz = (psi(k1)-psi(k))/xm_int
c      vrdim = - pre_v*dpsidth
c      vthdim = pre_v*dpsidz
c      vr = 15.63*vrdim
c      vth = 15.63*vthdim
```

```
c      write(20,456) r, vth, vr, t(k,2)
c456   format(1x,1x,d20.10,1x,d20.10,1x,d20.10,1x,d20.10)
44     continue
c
       L = 0
c
       open(unit=20,name='outtr2.dat',type='old')
       open(unit=25,name='outtr6.dat',type='old')
       LD2 = LD2 + 1
c      write(20,135)
c
c      Print temperature, stream function, and vorticity as a function
c      of theta and r.
c
       do 2 j = 1,N
c      write(20,120)
c120   format(1x,'      r        temp      stream fun      vorticity')
       theta = (j-1)*xn_int
c      write(20,125) theta
c125   format(1x,'theta =  ',d20.10)
       do 3 i = 1,M
       z = xm_int*(i-1)
       r = dexp(z)
       k2 = (j-1)*M + i
       if(j.eq.1.or.j.eq.N) go to 19
       g(i,j) = g(i,j)/(dexp(z)*dsin(theta))
       go to 680
19     g(i,j) = g(i,j)
c680   continue
680    write(25,130) r, t(i,j), psi(i,j), g(i,j)
130    format(1x,' ',d10.5,' ',d20.10,' ',d15.5,' ',d20.10)
3      continue
2      continue
c
c
       call calc
c
c      Print Nusselt numbers, pressures, and dimensionless drag coeffients.
c
c      write(20,135)
135    format(1x,'  ')
c
       tiim(LD2) = time
       xnim(LD2) = xnuss
       xim(LD2) = xk0
       cpim(LD2) = cdp
       cfim(LD2) = cdf
       ctim(LD2) = cdt
c        write(20,210)
c210     format(1x,1x,'time',3x,'Nu',4x,'K0',4x,'Cdp',4x,'Cdf',4x,'Cdt')
        time = tcount - del_t
        do 211 L6 = 1,LD2
        write(20,220)tiim(L6),xnim(L6),xim(L6),cpim(L6),cfim(L6),ctim(L6)
211     continue
220     format(1x,6d15.4)
c
c        write(6,300)
c300     format(1x,'xx')
c
c       write(20,140) xnuss
```

```
c140   format(1x,'The overall Nusselt number =  ',d10.5)
c      write(20,145) xk0
c145   format(1x,'dimen. pressure at stag. point = ',d20.10)
c      write(20,150) cdp
c150   format(1x,'dimensionless pressure drag = ',d20.10)
c      write(20,155) cdf
c155   format(1x,'dimensionless viscous drag = ',d20.10)
c      write(20,160) cdt
c160   format(1x,'dimensionless total drag = ',d20.10)
c
c      write(20,135)
c
c     Print local Nusselt number and dimensionless pressure at sphere
c     surface as a function of theta.
c
c      write(20,165)
c165   format(1x,'       theta        Nusselt        pressure')
c
c      do 4 i = 1,N
c      theta = (i-1)*xn_int
c      write(20,170) theta, xnu(i), xk(i)
c170   format(1x,3d20.10)
c4     continue
c
       if(tcount.gt.tmax) go to 990
c
       do 83 j = 1,N
       theta = (j-1)*xn_int
       do 84 i = 1,M
       z = (i-1)*xm_int
       if(j.eq.1.or.j.eq.N) go to 85
       g(i,j) = g(i,j)*dexp(z)*dsin(theta)
       go to 86
85     g(i,j) = g(i,j)
86     continue
84     continue
83     continue
c
       close(unit=20)
       close(unit=25)
       go to 25
c
c      ERROR MESSEGES
c
991    write(6,175)
       write(20,175)
175    format(1x,'over 10,000 iterations; did not converge!!!! ')
       go to 17
c
c
990    stop
       end
c
c
       subroutine iv_set
c
       implicit double precision (A-H)
       implicit double precision (O-Z)
c
       common /all1/ M, N, t(100,31), psi(100,31), g(100,31)
```

```
      common /all2/ xm_int, xn_int, del_t, tmax
c
c     This subroutine sets the initial values of temperture, vorticity, and
c     stream function.
c
c      Set initial values to zero.
c
c      do 9 j = 1,N
c      do 10 i = 1,M
c      z = (i-1)*xm_int
c      zin = (M-1)*xm_int
c      fact1 = exp(zin) - 1.0
c      t(i,j) = exp(zin)*exp(-z)/fact1 - 1./fact1
c      if(i.eq.1) go to 11
c      t(i,j) = 0.0
c      go to 12
c11    t(i,j) = 1.0
c12    continue
c      psi(i,j) = 0.0
c      g(i,j) = 0.0
c10    continue
c9     continue
c
c
c     Read initial values from input file.
c
      do 34 j = 1,N
      do 35 i = 1,M
      z = (i-1)*xm_int
      theta = (j-1)*xn_int
      read(21,305) xjunk, t(i,j), psi(i,j), g(i,j)
305   format(1x,1x,d10.5,1x,d20.10,1x,d15.5,1x,d20.10)
      if(j.eq.1.or.j.eq.N) go to 71
      g(i,j) = g(i,j)*dexp(z)*dsin(theta)
71    continue
35    continue
34    continue
c
      return
      end
c
c
c
      subroutine bc_set
c
      implicit double precision (A-H)
      implicit double precision (O-Z)
c
      common /all1/ M, N, t(100,31), psi(100,31), g(100,31)
      common /all2/ xm_int, xn_int, del_t, tmax
c
c     This subroutine sets the boundary conditions for the problem.
c
c     Along the bottom of the grid, i.e. theta = 0.0, is an axis of symmetry.
c
      b1 = 18./11.
      b2 = - 9./11.
      b3 = 2./11.
      b4 = - 5./12.
      b5 = 61./24.
```

```
      b6 = - 13./2.
      b7 = 107./12.
      b8 = - 77./12.
      b9 = 2./(xm_int**2)
c
      do 11 i = 1,M
c      t(i,1) = t(i,2)
c      t(i,1) = b1*t(i,2) + b2*t(i,3) + b3*t(i,4)
      psi(i,1) = 0.0
c      g(i,1) = 0.0
11    continue
c
c     Along the top of the grid, i.e. theta = pi, is also an axis of symmetry.
c
      do 21 i = 1,M
c      t(i,N) = t(i,N-1)
c      t(i,N) = b1*t(i,N-1) + b2*t(i,N-2) + b3*t(i,N-3)
      psi(i,N) = 0.0
c      g(i,N) = 0.0
21    continue
c
c     Along the left hand side of the grid, i.e. the particle surface.
c
      z1 = xm_int
      do 31 j = 1,N
c      t(1,j) = 1.0
      psi(1,j) = 0.0
c      c1 = b4*psi(6,j) + b5*psi(5,j) + b6*psi(4,j)
c      c2 = b7*psi(3,j) + b8*psi(2,j)
c      c = c1 + c2
c      c = (3.*psi(k1) - 3.*psi(k2)/4. + psi(k3)/9.)/(z1**2)
c      c = 2.*psi(k1) - psi(k2)/4.
c      c = psi(k2)/2. - psi(k1)
c      c=25.*psi(k4)/24.-14.*psi(k3)/3.+33.*psi(k2)/4.-20.*psi(k1)/3.
c      g(1,j) = b9*c
c      g(1,j) = 2.0*psi(2,j)/(xm_int**2)
c      g(k,2) = g(k,1)
c      g(k,1) = (-5.*psi(k1)+4.*psi(k2)-psi(k3))/(xm_int**2)
c      g(k,2) = g(k,1)
31    continue
c
c     Along the right hand side of the grid, i.e. the outer boundary.
c
      zin = xm_int*(M-1)
      do 41 j = 1,N
c      t(M,j) = 0.0
      psi(M,j) = 2.*psi(M-1,j) - psi(M-2,j)
c      psi(M,j) = 0.0
c      c1 = -5.*psi(k5)/12. + 61.*psi(k4)/24. - 13.*psi(k3)/2.
c      c2 = 107.*psi(k2)/12. - 77.*psi(k1)/12.
c      c = c1 + c2
c      c = psi(k2)/2. - psi(k1)
c      g(k,1) = 2.*c/(xm_int**2)
c      g(k,2) = 2.*c/(xm_int**2)
c      g(M,j) = 0.0
c      g(M,j) = 2.*g(M-1,j) - g(M-2,j)
41    continue
c
      return
      end
```

```
c
c
      subroutine update
c
      implicit double precision (A-H)
      implicit double precision (O-Z)
c
      common /all1/ M, N, t(100,31), psi(100,31), g(100,31)
      common /all2/ xm_int, xn_int, del_t, tmax
      common /up1/ pr, gr, omega_psi, err_psi
c
c     This program updates the values for the stream
c     function using an extrapolated Gauss-Siedel method.
c
      err_psi = 0.0
c
      a1 = 1.0/(xm_int**2) - 1.0/(2.0*xm_int)
      a2 = 1.0/(xm_int**2) + 1.0/(2.0*xm_int)
      a3 = 2.0/(xm_int**2) + 2.0/(xn_int**2)
c
      do 12 j = 2,N-1
      do 22 i = 2,M-1
c
      theta = (j-1)*xn_int
      z = (i-1)*xm_int
      a4 = 1./(xn_int**2) - 1./(dtan(theta)*2.*xn_int)
      a5 = 1./(xn_int**2) + 1./(dtan(theta)*2.*xn_int)
c
c     The stream function equation is used to update the stream function at
c     each node.
c
      a20 = a1*psi(i+1,j)+a2*psi(i-1,j)+a4*psi(i,j+1)+a5*psi(i,j-1)
      temp_psi = (1./a3)*( a20 - g(i,j)*dexp(2.*z) )
c
c
      res_psi = dabs( psi(i,j) - temp_psi )
      if(res_psi.gt.err_psi) err_psi = res_psi
c      err_psi = err_psi + res_psi
      psi(i,j) = psi(i,j) + omega_psi*(temp_psi-psi(i,j))
c
22    continue
12    continue
c
c
      return
      end
c
c
      subroutine tempvor
c
      implicit double precision (A-H)
      implicit double precision (O-Z)
c
      dimension b(100,4), c(100,31), temp1(100,31), tempg1(100,31)
      common /all1/ M, N, t(100,31), psi(100,31), g(100,31)
      common /all2/ xm_int, xn_int, del_t, tmax
      common /up1/ pr, gr, omega_psi, err_psi
      common /up2/ temp(100,31), tempg(100,31), tempsi(100,31)
c
      a5 = 1./(xn_int**2)
```

```
      a6 = 1./(2.*xm_int*xn_int)
      a7 = 1./(pr*(xn_int**2))
      a8 = 1./(2.*pr*xn_int)
      a9 = 1./(pr*(xm_int**2))
      a10 = 1./(2.*pr*xm_int)
      a11 = 1./(2.*xn_int)
      a12 = 1./(xm_int**2)
      a13 = 1./(2.*xm_int)
c
      b1 = -5./12.
      b2 = 61./24.
      b3 = -13./2.
      b4 = 107./12.
      b5 = -77./12.
      b6 = 2./(xm_int**2)
      b7 = 18./11.
      b8 = -9./11.
      b9 = 2./11.
c
      go to 52
c
53    continue
c
c
      do 12 j = 2,N-1
c
      do 553 k1 = 1,M
      b(k1,1) = 0.0
      b(k1,2) = 0.0
      b(k1,3) = 0.0
      b(k1,4) = 0.0
      c(k1,1) = 0.0
      c(k1,2) = 0.0
      c(k1,3) = 0.0
      c(k1,4) = 0.0
553   continue
c
      b(1,1) = 0.0
      b(1,2) = 1.0d+30
      b(1,3) = -a9 - a10
      b(1,4) = 1.0d+30
c
      c(1,1) = 0.0
      c(1,2) = 1.0d+30
      c(1,3) = 0.0
      f3 = b1*psi(6,j) + b2*psi(5,j) + b3*psi(4,j)
      f4 = b4*psi(3,j) + b5*psi(2,j)
      c(1,4) = c(1,2)*b6*(f3+f4)
c
      do 22 i = 2,M-1
c
c
      theta = (j-1)*xn_int
      z = (i-1)*xm_int
c
      pre_1 = a6/(exp(z)*sin(theta))
c
c     check sign of del psi's
c
      del_i = psi(i+1,j) - psi(i-1,j)
```

```
      del_j = psi(i,j+1) - psi(i,j-1)
      if(del_i.gt.0.0) go to 90
      omega_th = 1.0
      go to 91
90    omega_th = 0.0
91    continue
c
      if(del_j.lt.0.0) go to 92
      omega_z = 1.0
      go to 93
92    omega_z = 0.0
93    continue
c
c     Set up coefficient matrix.
c
      b(i,1) = del_j*pre_1*(1.-omega_z) - a9 + a10
      t1 = 2.*exp(2.*z)/del_t
      t2 = -del_j*pre_1*(1.-2*omega_z) + 2.*a9
      b(i,2) = t1 + t2
      b(i,3) = -del_j*pre_1*omega_z - a9 - a10
c
      d1 = del_i*pre_1*(1.-omega_th) + a7 - a8/tan(theta)
      t3 = 2.*exp(2.*z)/del_t
      t4 = -del_i*pre_1*(1.-2.*omega_th) - 2.*a7
      d2 = t3 + t4
      d3 = -del_i*pre_1*omega_th + a7 + a8/tan(theta)
      b(i,4) = d1*temp1(i,j-1)+d2*temp1(i,j)+d3*temp1(i,j+1)
c
      c(i,1) = del_j*pre_1*(1.-omega_z) - a12 - a13
      sub1 = del_j*pre_1*(1. - 2.*omega_z - 2.*xm_int)
      c(i,2) = 2.*exp(2.*z)/del_t - sub1 + 2.*a12
      c(i,3) = -del_j*pre_1*omega_z - a12 + a13
c
      e1 = del_i*pre_1*(1.-omega_th) + a5 + a11/tan(theta)
      sub2 = 1. - 2.*omega_th - 2.*xn_int/tan(theta)
      e2 = 2.*exp(2.*z)/del_t - del_i*pre_1*sub2 - 2.*a5
      e3 = - del_i*pre_1*omega_th + a5 - a11/tan(theta)
      sub31 = xn_int*(t(i+1,j)-t(i-1,j))
      sub32 = sm_int*(t(i,j+1)-t(i,j-1))/tan(theta)
      sub3 = sub31 + sub32
      e4 = exp(2.*z)*((sin(theta))**2)*gr*a6*sub3
      c(i,4)=e1*tempg1(i,j-1)+e2*tempg1(i,j)+e3*tempg1(i,j+1)+e4

22    continue
c
      b(M,2) = 1.0d+30
      b(M,3) = 0.0
c
      c(M,1) = 0.0
      c(M,2) = 1.0d+30
      c(M,3) = 0.0
      c(M,4) = c(M,2)*(2.*g(M-1,j)-g(M-2,j))
c
c     Solve tridiagonal matrix and store values in the fourth column
c     of the temperature and vorticity matrix.
c
      do 13 i = 2,M
      b(i,2) = b(i,2) - b(i,1)/b(i-1,2)*b(i-1,3)
      b(i,4) = b(i,4) - b(i,1)/b(i-1,2)*b(i-1,4)
      c(i,2) = c(i,2) - c(i,1)/c(i-1,2)*c(i-1,3)
```

```
      c(i,4) = c(i,4) - c(i,1)/c(i-1,2)*c(i-1,4)
13    continue
c
c
      MM1 = M - 1
      b(M,4) = b(M,4)/b(M,2)
      c(M,4) = c(M,4)/c(M,2)
      do 14 i = 1,MM1
      L = M - i
      b(L,4) = (b(L,4) - b(L,3)*b(L+1,4))/b(L,2)
      c(L,4) = (c(L,4) - c(L,3)*c(L+1,4))/c(L,2)
14    continue
c
      do 25 k = 1,M
      temp(k,j) = b(k,4)
      tempg(k,j) = c(k,4)
25    continue
c
12    continue
c
c
      do 261 i = 1,M
      temp(i,N) = b7*temp1(i,N-1)+b8*temp1(i,N-2)+b9*temp1(i,N-3)
      temp(i,1) = b7*temp1(i,2) + b8*temp1(i,3) + b9*temp1(i,4)
      tempg(i,N) = 0.0
      tempg(i,1) = 0.0
261   continue
c
      go to 99
c
52    continue
c
      do 321 jx = 1,N
      temp1(1,jx) = 1.0
      f1 = b1*psi(6,jx) + b2*psi(5,jx) + b3*psi(4,jx)
      f2 = b4*psi(3,jx) + b5*psi(2,jx)
      tempg1(1,jx) = b6*(f1+f2)
321   continue
c
      do 32 i = 2,M-1
c
      do 554 k2 = 1,N
      b(k2,1) = 0.0
      b(k2,2) = 0.0
      b(k2,3) = 0.0
      b(k2,4) = 0.0
      c(k2,1) = 0.0
      c(k2,2) = 0.0
      c(k2,3) = 0.0
      c(k2,4) = 0.0
554   continue
c
      b(1,1) = 0.0
      b(1,2) = 1.0d+30
      b(1,3) = 0.0
      b(1,4) = b(1,2)*(b7*t(i,2)+b8*t(i,3)+b9*t(i,4))
c
      c(1,1) = 0.0
      c(1,2) = 1.0d+30
      c(1,3) = 1.0
```

```
      c(1,4) = 0.0
c
      do 42 j = 2,N-1
c
      theta = (j-1)*xn_int
      z = (i-1)*xm_int
c
      pre_1 = a6/(exp(z)*sin(theta))
c
c     Check sign of del psi's.
c
      del_i = psi(i+1,j) - psi(i-1,j)
      del_j = psi(i,j+1) - psi(i,j-1)
      if(del_i.gt.0.0) go to 94
      omega_th = 1.0
      go to 95
94    omega_th = 0.0
95    continue
c
      if(del_j.lt.0.0) go to 96
      omega_z = 1.0
      go to 97
96    omega_z = 0.0
97    continue
c
c     Set up coefficient matrix.
c
      b(j,1) = -del_i*pre_1*(1.-omega_th) - a7 + a8/tan(theta)
      t5 = 2.*exp(2.*z)/del_t
      t6 = del_i*pre_1*(1.-2.*omega_th) + 2.*a7
      b(j,2) = t5 + t6
      b(j,3) = del_i*pre_1*omega_th - a7 - a8/tan(theta)
c
      d1 = -del_j*pre_1*(1.-omega_z) + a9 - a10
      t7 = 2.*exp(2.*z)/del_t
      t8 = del_j*pre_1*(1.-2.*omega_z) - 2.*a9
      d2 = t7 + t8
      d3 = del_j*pre_1*omega_z + a9 + a10
      b(j,4) = d1*t(i-1,j) + d2*t(i,j) + d3*t(i+1,j)
c
      c(j,1) = -del_i*pre_1*(1.-omega_th) - a5 - a11/tan(theta)
      sub4 = del_i*pre_1*(1.-2.*omega_th-2.*xn_int/tan(theta))
      c(j,2) = 2.*exp(2.*z)/del_t + sub4 + 2.*a5
      c(j,3) = del_i*pre_1*omega_th - a5 + a11/tan(theta)
c
      e1 = -del_j*pre_1*(1.-omega_z) + a12 + a13
      sub5 = del_j*pre_1*(1. - 2.*omega_z - 2.*xm_int)
      e2 = sub5 - 2.*a12 + 2.*exp(2.*z)/del_t
      e3 = del_j*pre_1*omega_z + a12 - a13
      sub61 = xn_int*(t(i+1,j)-t(i-1,j))
      sub62 = xm_int*(t(i,j+1)-t(i,j-1))/tan(theta)
      sub6 = sub61 + sub62
      e4 = exp(2.*z)*((sin(theta))**2)*gr*a6*sub6
      c(j,4) = e1*g(i-1,j) + e2*g(i,j) + e3*g(i+1,j) + e4
c
42    continue
c
      b(N,1) = 0.0
      b(N,2) = 1.0d+30
      b(N,3) = 0.0
```

```
      b(N,4) = b(N,2)*(b7*t(i,N-1)+b8*t(i,N-2)+b9*t(i,N-3))
c
      c(N,1) = 1.0
      c(N,2) = 1.0d+30
      c(N,3) = 0.0
      c(N,4) = 0.0
c
c     Solve tridiagonal matrix and store values in the fifth column of
c     the temperature and vorticity matrix.
c
      do 15 I = 2,N
      b(I,2) = b(I,2) - b(I,1)/b(I-1,2)*b(I-1,3)
      b(I,4) = b(I,4) - b(I,1)/b(I-1,2)*b(I-1,4)
      c(I,2) = c(I,2) - c(I,1)/c(I-1,2)*c(I-1,3)
      c(I,4) = c(I,4) - c(I,1)/c(I-1,2)*c(I-1,4)
15    continue
c
      NM1 = N - 1
      b(N,4) = b(N,4)/b(N,2)
      c(N,4) = c(N,4)/c(N,2)
      do 16 ix = 1,NM1
      L = N - ix
      b(L,4) = (b(L,4) - b(L,3)*b(L+1,4))/b(L,2)
      c(L,4) = (c(L,4) - c(L,3)*c(L+1,4))/c(L,2)
16    continue
c
      do 26 k = 1,N
      temp1(i,k) = b(k,4)
      tempg1(i,k) = c(k,4)
26    continue
c
32    continue
c
c
      do 262 j = 1,N
      temp1(M,j) = 0.0
      tempg1(M,j) = 2.*g(M-1,j) - g(M-2,j)
262   continue
c
      go to 53
c
99    continue
c
      return
      end
c
c
c
      subroutine calc
c
c
c     This subroutine calculates the Nusselt number, pressure, and drag
c     force.
c
      implicit double precision (A-H)
      implicit double precision (O-Z)

      common /all1/ M, N, t(100,31), psi(100,31), g(100,31)
      common /all2/ xm_int, xn_int, del_t, tmax
      common /up1/ pr, gr, omega_psi, err_psi
```

```
      common /calc/ xnu(63), xnuss, xk0, xk(63), cdp, cdf, cdt
      common /up2/ temp(100,31), tempg(100,31), tempsi(100,31)
c
c     Calculation of the Nusselt number as a function of theta and the
c     calculation of the overall Nusselt number.  The trapezoid rule is
c     when integrals are performed.
c
      xnuss = 0.0
      do 50 j = 1,N
c      xnu(j) = -2.0*( t(2,j) - t(1,j) ) / xm_int
      xnu(j) = (-4.0*t(2,j) + t(3,j) + 3.0)/ xm_int
      theta = (j-1)*xn_int
      if(j.eq.1.or.j.eq.N) go to 19
      L = 2
      go to 20
19    L = 1
20    continue
      xnuss = xnuss + (xn_int/4.0)*(L*xnu(j)*dsin(theta))
50    continue
c
c
c     Calculation of the dimensionless pressure at the front stagnation
c     point.
c
      xk0 = 0.0
      do 51 i = 1,M
      z = (i-1)*xm_int
      sub = g(i,4) - 3.*g(i,3) + 3.*g(i,2)
c      dgdth = (g(k2,2)-sub)/(2.*xn_int)
c      dgdth = ( g(k1,2) - g(i,2) ) / xn_int
c      dgdth = (-3.*g(i,2)/2. + 2.*g(k1,2) - g(k2,2)/2.)/xn_int
      dgdth=(-11.*sub/6.+3.*g(i,2)-3.*g(i,3)/2.+g(i,4)/3.)/xn_int
c
      dpsidth1 = (psi(i,3)-2.*psi(i,2)+psi(i,1))/(xn_int**2)
      dpsidth2 = (tempsi(i,3)-2.*tempsi(i,2)+tempsi(i,1))/(xn_int**2)
      dpsidth = (dpsidth1-dpsidth2)/del_t
c
      if(i.eq.1.or.i.eq.M) go to 71
      L = 2
      go to 72
71    L = 1
72    continue
      x1 = (2.0*xm_int)*(L*dgdth)
      x2 = (gr*xm_int)*(L*t(i,1)*dexp(z))
      x3  = -xm_int*L*dpsidth*exp(-z)
      xk0 = xk0 + x1 + x2 + x3
51    continue
c
c     Calculation of the dimensionless pressure at the sphere surface, the
c     dimensionless pressure drag, and the dimensionless viscous drag.
c
      cdp = 0.0
      cdf = 0.0
      xkth1 = 0.0
      do 52 j = 1,N
      theta = (j-1)*xn_int
      if(j.eq.1.or.j.eq.N) go to 73
      L = 2
      go to 74
73    L = 1
```

```
74    continue
      sub = g(4,j) - 3.*g(3,j) + 3.*g(2,j)
c      dgdz = (g(k3,2) - g(k2,2))/xm_int
c      dgdz = ( g(k3,2)-sub ) / (2.*xm_int)
c      dgdz = ( g(k2,2) - sub ) / xm_int
c      dgdz = (-3.*sub/2. + 2.*g(k2,2) - g(k3,2)/2.)/xm_int
      dgdz=(-11.*g(1,j)/6.+3.*g(2,j)-3.*g(3,j)/2.+g(4,j)/3.)/xm_int
      xkth1 = xkth1 + xn_int*L*( dgdz + g(1,j) )
      xk(j) = xk0 + 2.0*gr*(1.0 - dcos(theta)) + xkth1
      cdp = cdp + (xn_int/2.0)*xk(j)*L*sin(2.0*theta)
      cdf = cdf + (2.0*xn_int)*L*g(1,j)*(dsin(theta)**2)
52    continue
      cdt = cdp + cdf
c
      return
      end
```